DISTINGUISHING THE CONTRACTIONAL AND TENSIONAL SIGNATURES OF DEFORMATION AND METAMORPHISM ON EVIA ISLAND, NW AEGEAN SEA

TAYLOR DUCHARME

A thesis submitted in partial fulfillment of the requirements for the doctoral degree in Earth Sciences

Department of Earth and Environmental Sciences

Faculty of Science

University of Ottawa

Abstract

Most of the circum-Mediterranean orogenic belts of southern Europe have accommodated dominantly extensional tectonic deformation since the early Miocene. The Aegean Sea, situated in the eastern Mediterranean Sea between Greece and Turkey, is an example of a back-arc basin formed by consequence of that extension. Trench retreat due to slab rollback starting in the Eocene subjected the Aegean region to tensional forces, resulting in the exhumation of high pressure, low temperature (HP-LT) metamorphic rocks characteristic of subduction zone metamorphism. The exhumed crustal fragments, composing the Cycladic islands, represent remnants of oceanic and continental crust situated offboard of the African margin. Those rocks were subducted beneath the southern margin of the European craton during convergence sustained between the two continents since the late Mesozoic. This thesis contributes a new island-scale study of Aegean exhumation by examining the record of unroofing on southern Evia island. Structural and petrological analyses and diverse radiometric dating techniques reveal a hitherto unrecognized major deformation corridor, whose strain geometry and geochronological record demonstrates its relevance to the extensional architecture governing exhumation of HP-LT rock units in the Aegean Sea. This structure, herein named the Evia Shear Zone, operated in tandem with the more regionally extensive North Cycladic Detachment System to exhume lowermost parts of the structural pile on southern Evia.

The constituent chapters presented herein illustrate challenges involved in discriminating among structural and petrological features developed during convergent stages of mountain building, as opposed to those related to extensional post-orogenic collapse. The combined work highlights analytical techniques that can overcome those ambiguities. Among them, the use of exploratory geochronology to inform subsequent targeted higher-resolution dating was effective at highlighting inconsistences in prior assumptions present in both the literature and first-order empirical inferences made over the course of this thesis. Overall, the data presented here demonstrate: (1) the potential morphological diversity among structures responsible for facilitating exhumation in deeply exhumed orogens; (2) the tenuous nature of some common petrological inferences as applied to subduction zone geodynamics; (3) the power of multiple geochronometers applied to tectonic problems in concert. The ultimate conclusions of this work should inform best practices for future refinement of orogenic models for the evolution and unroofing histories of HP-LT metamorphic complexes.

Acknowledgments

Most PhD theses owe their greatest thanks to the thesis advisor, but the abundance of opportunity and support afforded by David Schneider during this degree should not be so understated. In a short four years he managed to hammer in not only rigorous scientific training, but also explicitly reinforced invaluable soft skills that will make navigating the world of academia that little bit easier. Dave embraces the calling of training the next generation of geoscientists to a degree that very few do – no part of this thesis would be the same without his guidance, his scientific creativity, or his musings.

I thank Bernhard Grasemann for his truly significant contributions to this thesis, both by way of his direct input and careful scrutiny of the structural data, and by his growing of my own understanding of structural geology. Accompanying Bernhard in the field is an ever-humbling experience, and each successive outing with him gives new perspective on geologic structures that will follow me throughout my career. This thesis is incalculably better for his generous sharing of time and expertise.

Many collaborators were kind enough to contribute their knowledge throughout this endeavour. Alfredo Camacho aided greatly in facilitating the $^{40}Ar/^{39}Ar$ analyses that permeate this thesis, and his understanding of its particulars was indispensable. Iwona Klonowska and Michał Bukała generously contributed their time to thermodynamic modelling, and my chats with them filled many gaps in my understanding of metamorphic petrology. Kyle Larson freely shared his time processing, or guiding me in the processing and interpretation of, the $^{87}Rb/^{87}Sr$ and fabric analyzer data, while facilitating those analyses with a speed that is probably only matched by his e-mail response times. Konstantinos Soukis readily offered his formidable knowledge of Greek geology, and his contributions in this regard enriched my comprehension of the regional context. This thesis is greatly improved for each of their influences, both on the articles themselves and on my own understanding of the discipline.

Many thanks go to Glenn Poirier for sharing his expertise on both the SEM and microprobe, and to Alain Mauviel who may well have the fastest thin section-making hands in the west.

No thesis can flourish in a vacuum, and so I am grateful to the many fellow graduate students with whom I have had the pleasure of sharing a beer over the past four years. Special thanks are due to the DAS lab, who managed to ensure that no room (at least not the ones I was in) went unescaped. ‘Escaping’ MRN0011 after all these years is going to be bittersweet.

I am grateful to my examining committee for their time spent in evaluating my thesis: Brian O’Driscoll (University of Ottawa), Alexandre Zagorevski (Geological Survey of Canada), Eric DeKemp (Geological Survey of Canada), and Djordje Grujic (Dalhousie University).

I owe my continued sanity to lifelong friends Daniel, Kyle, Eric, and Jacob, who filled the past four years with memorable trips, concerts, and many good chats.

Lastly, I give my appreciation and love to my dad, sister, and mom, who never questioned my decision to chase this dream, whatever the circumstances became.

Table of Contents

Abstract.....ii

Acknowledgments.....iii

Table of Contents.....iv

Chapter 1: Introduction.....1

1.1 Exhumation mechanisms.....7

1.2 Overview of Cycladic geology.....13

1.3 Geology of Evia island.....16

1.4 Thesis motivation and structure.....19

1.5 References.....24

Chapter 2: Stretched thin: Oligocene extrusion and ductile thinning of the Basal Unit along the Evia Shear Zone, NW Cyclades, Greece.....39

2.1 Abstract……40

2.2 Introduction……..40

2.3 Tectonic setting……42

2.3.1 Geological framework of Evia……..46

2.4 Structure of southern Evia……49

2.4.1 Hanging wall – Cycladic Blueschist Unit……..50

2.4.2 Footwall – Basal Unit……51

2.5 Thermodynamic modeling……58

2.5.1 Albite-pumpellyite schist (sample EV19-03)……59

2.5.2 Glaucophane schist (sample EV19-10)……61

2.5.3 Albite-mica schist (sample EV19-17C)……62

2.6 $^{40}Ar/^{39}Ar$ geochronology……62

2.7 Zircon (U-Th)/He geochronology……67

2.8 Synthesis……..71

2.8.1 Cycladic Blueschist Unit……..71

2.8.2 Basal Unit……73

2.8.3 Evia Shear Zone……...77

2.9 Geodynamic implications……..…80

2.9.1 Exhumation of the Basal Unit…….…….……..80

2.9.2 Ductile thinning…….……82

2.9.3 Vergence of the Hellenic Subduction Zone……..……..84

2.9.4 Relevance to Cycladic geodynamics……..……85

2.10 Summary……90

2.11 Acknowledgments……..91

2.12 References……..92

Chapter 3: Strain partitioning in a flattening shear zone: re-evaluation of a Cycladic-style detachment system.....109

3.1 Abstract.....110

3.2 Introduction.....111

3.3 Tectonic setting.....112

3.3.1 Geology of southern Evia.....115

3.4 New field observations.....117

3.5 Analytical methods.....120

3.5.1 Quartz c-axis fabric analysis.....120

3.5.2 In situ $^{40}Ar/^{39}Ar$ *geochronology*.....122

3.5.3 In situ $^{87}Rb/^{87}Sr$ *geochronology*.....125

3.6 Quartz petrofabric analysis.....126

3.6.1 Sample descriptions.....126

3.6.2 Results.....130

3.7 Geochronology.....133

3.7.1 In situ $^{40}Ar/^{39}Ar$ *geochronology*.....133

3.7.2 In situ $^{87}Rb/^{87}Sr$ *geochronology*.....140

3.8 Discussion.....140

3.8.1 Vein microstructure and c-axis distributions.....143

3.8.2 In situ *white mica geochronology*.....147

3.8.3 Superimposed records of contraction and tension.....153

3.8.4 The Evia Shear Zone: a unique Cycladic exhumation structure?.....156

3.9 Conclusions.....161

3.10 Acknowledgments.....163

3.11 References.....163

Chapter 4: Syn-exhumation metasomatic glaucophane-phengite-quartz veins: exploring the control of *f*O2 and bulk composition on nominally HP metamorphic assemblages.....178

4.1 Abstract.....179

4.2 Introduction.....180

4.3 Cenozoic tectonics of the Cyclades.....182

4.4 Vein mineralogy and structure.....185

4.5 Analytical methods.....196

4.5.1 Scanning electron microscopy and electron microprobe analysis.....196

4.5.2 In situ $^{87}Rb/^{87}Sr$ *geochronology*.....197

4.5.3 $^{40}Ar/^{39}Ar$ *geochronology*.....198

4.5.4 Oxygen isotopes.....198

4.6 Mineral chemistry.....198

4.7 *In situ* $^{87}Rb/^{87}Sr$ geochronology.....201

4.8 $^{40}Ar/^{39}Ar$ geochronology.....202

4.9 Stable isotopes.....205

4.10 Discussion.....205

4.10.1 Fracturing and sealing mechanisms.....207

4.10.2 Temperatures of crystallization.....212

4.10.3 Timing of vein formation.....214

4.10.4 P-T-X controls on vein paragenesis.....216

4.10.5 Fluid source and modes of solute transport.....222

4.11 Conclusions.....226

4.12 Acknowledgments.....227

4.13 References.....228

Chapter 5: Conclusions.....246

5.1 Implications for regional tectonic models.....247

5.2 Strain localization and geometry during exhumation.....253

5.3 Practical applications of paired white mica $^{40}Ar/^{39}Ar$ and $^{87}Rb/^{87}Sr$ geochronology..256

5.4 Reactive transport in exhuming fossil subduction zones.....257

5.5 References.....263

Appendix A.....270

Appendix B.....298

Appendix C.....310

CHAPTER 1

INTRODUCTION

High-pressure, low-temperature (HP-LT) metamorphic rocks represent the material record of processes operating at depth within subduction zones. Exposures of HP-LT rocks are consequently an invaluable source of insight into the large-scale geodynamic processes that operate at destructive convergent margins (Behr and Burgmann, 2021). More than 250 such occurrences are known worldwide (Maruyama et al., 1996), and the unique pressure and temperature (PT) conditions generated within the cold down-going slab produce the distinctive and often visually striking minerals characteristic of the blueschist and eclogite metamorphic facies (Evans, 1990). The presence of certain minerals, particularly lawsonite, glaucophane, or omphacite, serve as markers that the rocks possessing these phases attained a particular corresponding depth along one of several characteristic geothermal gradients expected in subduction zones (Clarke et al., 2006; Tsujimori et al., 2006). This *a priori* constraint on metamorphic environment makes the coexisting structural records of HP-LT rocks exceptionally useful proxies for studying the mechanisms by which crustal rocks deform during subduction, and in turn implicates those mechanisms as drivers of potentially hazardous seismic activity at modern-day convergent margins. As the equivalent modern structures are inaccessible, the ancient rock record is one of very few ways to study subduction zone processes and seismogenic deformation (Behr and Burgmann, 2021).

However, the protracted and sometimes non-linear pathway from near-surface conditions to deep subduction and back again complicates the otherwise elegant use of HP-LT rocks described above. Both subduction and exhumation require immense forces to displace not only the rock volume of interest but also those situated above and below them. The subducting slab consequently undergoes considerable deformation, producing the penetrative metamorphic foliations and intricate folding visible in many exhumed subduction complexes (Cawood, 1982; Stöckhert, 2002;

Beaudoin et al., 2017). Identifying the stage of orogenesis at which a given structural feature developed is critical to reconstructing the paleotectonic history of an orogen, as well as for understanding the ability of different tectonic mechanisms to deform and reconfigure the affected crust. Correctly assigning structures to specific tectonic events becomes increasingly non-trivial with each successive episode of deformation, and later intervals of strain may obscure, or even outright erase, the structural record of earlier deformation. Even where there is a complete record of strain preserved in particularly well-studied HP-LT complexes, disentangling the relative timing, geometry, and tectonic significance of the structures often remains a major source of controversy (Huet et al., 2009; Jolivet and Brun, 2010; Ring et al., 2010; Beaudoin et al., 2017). Resultant uncertainties concerning the longevity, structural style, and overall geometry associated with the active subduction phase of orogenesis may significantly compromise the validity of models reliant on those underlying structural data.

By consequence, the study of exhumation mechanisms and their associated deformation styles is an integral part of understanding orogenic cycles and their products newly exposed again at the surface (Platt, 1993; Ring et al., 1999; Agard et al., 2009; Warren, 2013). As effectively all consolidated rock has at some point experienced appreciable burial, knowledge of exhumation processes has considerable interdisciplinary value. Foremost, exhumation typically produces strain geometries that readily preserve deformation generated during its earliest stages. Since exhuming rock progresses broadly from hotter to cooler temperatures, earlier-formed structural information is not lost to ductile overprint as is common during prograde burial (Reynolds and Lister, 1987; Lister and Davis, 1989; Jolivet et al., 2010; Grasemann et al., 2012). Exhumation-related structures are thus exceptional references for investigating fundamental questions regarding the strength of the crust, as associated deformation may evolve or migrate depending on the bulk rheology of the

affected crustal section. Accordingly, rocks that have localized deformation related to exhumation represent a unique, time-integrated record of strength variability for many abundant crustal rock types, representing deformation under a range of geologically common PT conditions.

For rock exhumed from deep or moderate depths, knowledge of the common geometries assumed by structures governing exhumation can help to predict the modern positioning of older features such as major crustal-scale shear zones or basal décollements (Doglioni, 1995; Reddy et al., 2002; Jolivet et al., 2004). Such geometric reconstructions also facilitate mineral exploration activities for mesozonal ore bodies, whose mineralization frequently exploits structures that may be related to exhumation or else has been dissected by them (Marchiev et al., 2005; Chambefort and Moritz, 2006; Menant et al., 2013; Liotta et al., 2015; Creus et al., 2023). At and above the brittle-ductile transition zone, the rates and geometries of exhumation inform models of basin evolution and coeval thermal regimes, factors critical to hydrocarbon exploration (Corcoran and Doré, 2005; Underdown and Redfern, 2007). The potential for complexity is of particular significance here, as the confluence of multiple generations of structures may serve as ideal traps for mineralizing fluids or hydrocarbons, and thus these resources may be controlled directly by relationships between contractional and tensional structures (e.g., Harding and Lowell, 1979; Forde and Bell, 1994; Pirajno, 2009; Edmundson et al., 2020; Zhou et al., 2021).

Fortunately, numerous analytical techniques have developed to circumvent the inherent structural complexity encountered in exhumed subduction complexes. Radiometric dating techniques are now refined such that diverse geological information may be ascertained by careful selection of geochronometer and analytical method (e.g., Cliff, 1985; Larson et al., 2023; Gyomlai et al., 2023). Numerical estimates for the timing of crystallization, cooling, and deformation are accessible from several rock-forming minerals that are often readily available in rocks formed

during HP-LT metamorphism. Among the most historically important include zircon U-Pb geochronology to date crystallization of igneous protoliths, timing of metamorphic rim growth, and determine sources of detrital populations (e.g., Rubatto et al., 1999; Trotet et al., 2001; Horton et al., 2010; Schneider et al., 2011; Seman et al., 2017); mica and amphibole $^{40}Ar/^{39}Ar$ geochronology to determine the timing of cooling below certain moderate temperatures (~400-600°C) or, for deformed specimens, the timing of shearing (Cossette et al., 2015; Dunlap et al., 1991; Laurent et al., 2021; Barnes et al., 2023); multi-mineral Rb-Sr geochronology, serving similar purposes to the $^{40}Ar/^{39}Ar$ system but with contrasting sensitivity to isotopic resetting and without the inconvenient potential addition of excess daughter isotope (Larson et al., 2023; Gyomlai et al., 2023); and low-temperature zircon and apatite (U-Th)/He and fission track thermochronometry, which date cooling of those minerals below a range of tectonically important temperatures of ~300°C. Still greater geochronological information is accessible using *in situ* techniques, allowing the spatial and microstructural contexts of the analyzed material to be fully retained (Laurent et al., 2021; Barnes et al., 2023). Consequently, the apparent age of specific (micro-)structures can now be defined, although natural samples do not always delineate the desired dates in a straightforward manner (Laurent et al., 2021; Di Vincenzo et al., 2022).

Historically, estimates of metamorphic pressure and temperature (PT) conditions to complement the timing constraints were obtained by empirical calculation using mineral equilibria for sets of two or more minerals (Evans, 1990). A critical volume of mineralogical thermodynamic data accrued over the last three decades now allows for precise estimation of the metamorphic PT conditions represented by a given mineral assemblage (Holland and Powell, 1998; White et al., 2014). If multiple samples with similar presumed tectonometamorphic histories are used, or relict phases or incipient reactions are observed within a sample, then a PT path can also be inferred

from the relative placement of individual estimates in PT space (e.g., Willner et al., 2004; Gasco et al., 2011; Massonne, 2014; Huet et al., 2015; Scheffer et al., 2016; Peillod et al., 2021). The combination of these methods with geochronology – for which several petrologically relevant mineral phases may serve as geochronometers – provides a powerful tool that, given appropriate interpretive scrutiny, can link a numerical age to a given point along the PT evolution within a region (e.g., Huet et al., 2015; Cruz-Uribe et al., 2015). Supporting data, in the form of stable isotopes, or simple mineral chemical geo-thermometers and -barometers can confirm or refine estimates for the same or different parts of the PT history to acquire a greater breadth of constraints at relatively low opportunity cost.

This thesis integrates many of the approaches outlined above to interrogate the exhumation history of the island of Evia, situated in the Aegean Sea. Evia occupies a critical position at the margin of the Cyclades, a world-class exposure of HP-LT metamorphic rocks, particularly Syros, the type locality of the blueschist facies index mineral glaucophane (Hausmann, 1845). The Cyclades have been the source of several fundamental concepts pertaining to both subduction and exhumation, and an excellent natural laboratory furthering their development since. The islands of Ios and Naxos have acted as the foundational model for metamorphic core complexes and an exemplar of its modern conception, respectively (Lister et al., 1984; Keay et al., 2001), whereas numerous Cycladic islands expose classical examples of exhumation-related low-angle detachments (Jolivet et al., 2010; Grasemann et al., 2012). Evia marks the northwesternmost limit for continuous exposure of the HP-LT unit. It should therefore be expected that the structural architecture facilitating exhumation terminates or otherwise changes on Evia, as recently demonstrated for the exposures to the southwest (Coleman et al., 2020). Nevertheless, prior to this thesis, Evia had been targeted mainly to understand the convergent stages of orogenesis in the

Cyclades, due in large part to the major nappe contact exposed there as the boundary to a tectonic window (Dubois and Bignot, 1979; Katsikatsos et al., 1982; Shaked et al., 2000). Both the footwall and hanging wall of the tectonic window, however, should have experienced exhumation comparable to that documented in the remainder of the Aegean region, and relevant structures and PTt data should be accessible in the records of strain and metamorphism in the rock record of Evia.

1.1. Exhumation mechanisms

The opening section of this chapter alluded to the diversity of mechanisms which may return deeply subducted rocks to the surface. Although certain mechanisms are responsible for an outsized proportion of the exhumation represented in the rock record, the potential for simultaneous operation of different mechanisms renders contributions from the less common processes non-trivial (Ring et al., 1999; Froitzheim et al., 2003). Each of the mechanisms functions to effectively remove overlying rock from atop the exhuming package (**Figure 1.1**). In most cases, unroofing is accomplished by displacing overlying rock, but the part of the crustal section that is attenuated and the driving mechanism, as well as the types of structures associated with the different exhumation styles, vary considerably.

Erosion is, at least from a purely geodynamic perspective, the simplest exhumation mechanism, requiring only passive removal of overburden via the ubiquitous processes of physical and chemical weathering and lateral transport as sediment. In active orogens however, erosion is frequently enhanced by tectonism, as regions of higher elevation are typically subject to higher rates of erosion (Burbank, 2002). Rates of erosion may also be enhanced by glacial action, and thus prolonged glaciations may drive periods of comparatively rapid exhumation (Zeitler et al., 2001; Fox et al., 2015). Intense erosion of overburden conveniently produces a conspicuous record

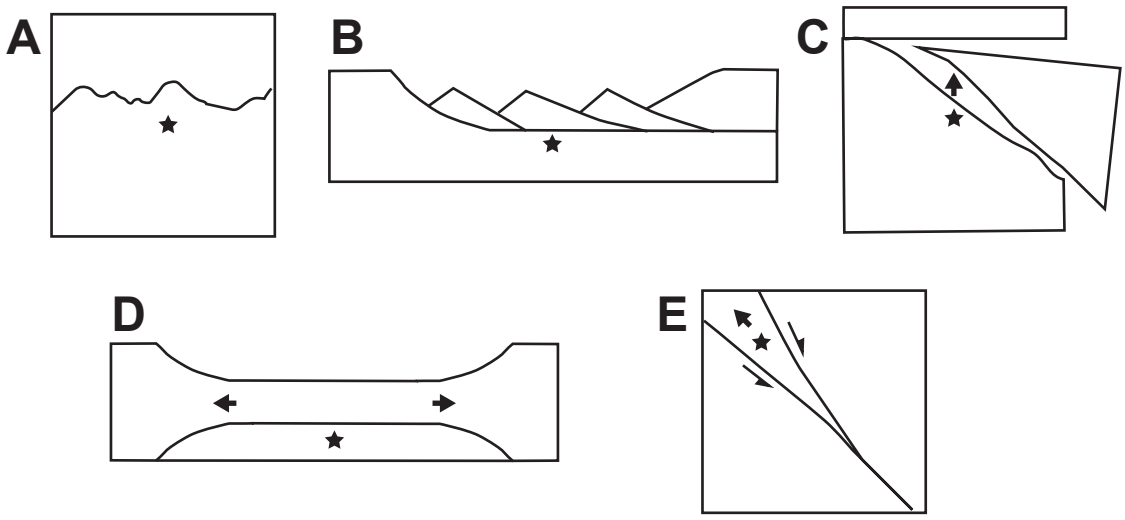

Figure 1.1. Cartoon diagrams depicting exhumation mechanisms discussed in the text. Black star indicates the exhuming rock; black arrows show displacement of material. (A) erosion; (B) low-angle normal faulting; (C) slab extraction; (D) ductile thinning; (E) wedge extrusion.

in the form of thick sedimentary successions of a similar age to the cooling experienced by the exhumed rock (e.g., Sanchez-Gomez et al., 2002). Despite its capacity for periodic tectonic or climatic enhancement, erosion in many cases operates at slower rates than its tectonic counterparts, and is most important for instances of particularly prolonged exhumation where more rapid tectonic processes were not co-active (Ring et al., 1999; Warren, 2013).

Perhaps the most famous among the tectonic drivers of exhumation are low-angle normal faults, also commonly known as detachments (**Figure 1.1B**). Detachment faults operate within tensional tectonic stress regimes (i.e., $\sigma_v = \sigma_1$). Their fault planes dip shallower than 30°, and displacement along them removes overburden (i.e., the hanging wall) from atop a large area because of these low dip angles (Lister and Davis, 1989; Axen, 2004; Collettini, 2014). Although sustained slip along such shallow faults was initially considered mechanically untenable, abundant field evidence now supports that detachment faults both initiated and operated at shallow dips (Lister and Davis, 1989; Axen, 2004; Jolivet et al., 2010; Grasemann et al., 2012; Biemiller et al., 2022). Most detachments originate in the ductile crust, and are mechanically linked to high-angle normal faults positioned structurally above them. Isostatic uplift of the footwall in response to the removal of the hangingwall results in upwarping (or 'doming') of the original low-angle plane, producing one side of the fault trace that displays an apparent reverse sense of displacement. Once the initial fault surface is no longer sufficiently planar to accommodate further strain, detachment faults characteristically initiate a new, structurally higher fault plane rooted in the original structure. Consequently, detachment faults also exhume themselves, and thus strain along them frequently exhibits a progression from ductile to brittle-ductile and finally brittle behaviour (i.e., 'ductile-then-brittle'). Exposed detachment planes commonly present this progression across a gradually narrowing zone of footwall deformation, featuring a wide zone of ductile mylonites

overprinted toward the hangingwall by cataclasites and terminated in one or more brittle, knife-sharp fault planes. Where detachment faulting has exhumed particularly deep structural levels, decompression melting may yield a footwall core dominated by migmatites and crustally-derived granitoids. Along with the diagnostic structural configuration here described, the deeply exhumed hot crust forms the titular 'core' of a metamorphic core complex. Although high-angle normal faults may also contribute to exhumation, their steeper dips mean they remove their hanging walls less efficiently per unit of fault-parallel displacement. High-angle faults therefore typically contribute modest magnitudes of upper crustal exhumation, late in the unroofing history of a given orogen.

In contrast to the types of exhumation discussed previously, ductile thinning (**Figure 1.1D**) typically drives unroofing at depth in a crustal section because rock accomplishing this style of exhumation must behave plastically (Ring and Brandon, 2008). A horizon undergoing ductile thinning exhumes subjacent rock by reducing the total thickness of the crustal section via a lateral redistribution of material (i.e., ductile strain). The amount of exhumation facilitated by thinning is proportional to the magnitude of thinning imposed on the deforming package of rock, and the requisite strain may be accommodated with or without an attendant volume change (Feehan and Brandon, 1999; Ring and Kumerics, 2008). In the former case, it is typically envisioned that thinning is accommodated by material transport in fluids, and there are fewer associated geometric constraints. An isovolumetric thinning, however, requires that strain compatibility be satisfied: material from the thinned horizon must extrude laterally in one or both other dimensions (Fossen and Cavalcante, 2017). Ductile thinning is associated with pure shear or flattening strains, and is essentially a horizontal form of transpression (Fossen and Cavalcante, 2017). Sufficient magnitudes of ductile thinning imposed upon an orogenic section may produce considerable lateral variation in preserved structural piles, with severe thinning resulting in the seemingly paradoxical

omission of parts of the tectonostratigraphy (e.g., Handy and Zingg, 1991). Ductile thinning is classically associated with convergent stages of orogeny, as overthickened crust may induce lateral ductile flow in the underlying lower crust (Rosenbaum et al., 2002; Long and Kohn, 2020); however, any tectonic process imposing pure shear or flattening strains onto a (sub-)horizontal plane may in principle result in ductile thinning.

Slab extraction (**Figure 1.1C**) also operates at depth by detaching a significant portion of a downgoing slab, leaving the underlying and overlying packages of rock to meet along an 'extraction fault' (Froitzheim et al., 2003, 2006). Extraction is most often implicated in the exhumation of ultrahigh pressure (UHP) metamorphic rocks. The mechanism was first described from the Alps, but has also been proposed in some other young orogens recording UHP metamorphism (e.g., Warren, 2013; Sandmann et al., 2015). A large missing section of metamorphic grade is a hallmark of this style of exhumation.

Finally, an extrusion wedge (**Figure 1.1E**) is the only mechanism currently documented where the exhuming body is displaced relative to the surrounding rock (Grujic et al., 1996). The 'wedge' generally comprises one or more slices detached from the subducting lower plate that have become attached to (underplated) the overriding lithosphere (Ring et al., 2007a; Peillod et al., 2023). Subduction continues uninterrupted, but the underplated material may begin to travel (extrude) back along the roof of the subduction channel in response to ongoing compression. The structural geometry of such an extruding wedge, where its base is in contact with the still-downgoing slab and its upper boundary touches the comparatively static upper plate lithosphere, is diagnostic of extrusion wedges: the wedge is a fault-bounded horse with a basal thrust and a roof fault showing apparent normal-sense displacement (Ring et al., 2007a). The scale of these structures, particularly after extensional deformation, is still somewhat contentious. Entire

extrusion wedges have been interpreted at times to be preserved across only several kilometers of stratigraphic thickness (e.g., Ring et al., 2007b), and at others to span much larger regional-scale (>100 km) intervals. Extrusion wedges are capable of effecting considerable magnitudes of exhumation, and at relatively fast rates. Rock within the wedge may survive relatively unmodified, with strain partitioning predominantly into the boundary shear zones, or else may undergo intense strain comparable to the earlier subduction phase (Allemand and Lardeaux, 1997; Jessup et al., 2006).

The preceding summaries provide only a short overview of some fundamental characteristics of each exhumation mechanism. Decades of integrated field study, numerical modelling, and theoretical treatment have demonstrated that each style of exhumation may vary in its presentation dependent on the rheological composition of the exhuming rock, the coexisting thermal regime, variability of far-field geodynamic parameters, and concurrent or sequential exhumation by one or more other unroofing mechanisms. For instance, an extruding wedge that undergoes transport-parallel elongation may have simultaneously exhumed its lower parts via ductile thinning, and record structural evidence consistent with both mechanisms (Vannay and Grasemann, 2001; Xypolias et al. 2010); or, a low-angle normal fault may experience multiple cycles of ductile-then-brittle behaviour if magmas intrude along the fault (Jolivet et al., 2010; Lecomte et al., 2010). As emphasized in the preceding section, the potential for complexity grows exponentially without careful and meticulous documentation of structures, their temporal relationships, and their geometric compatibility with the broader orogenic architecture.

1.2. Overview of Cycladic geology

The Cyclades are an archipelago located in the Aegean Sea, between mainland Greece and the island of Crete. The dominant lithological constituents of the Cycladic isles are known collectively as the Cycladic Blueschist Unit (CBU), which comprises both oceanic metavolcanic- and carbonate-dominated passive margin sequences (Jacobshagen, 1986; **Figure 1.2**). The CBU underwent blueschist to eclogite facies metamorphism that peaked in the early Eocene, though recent evidence suggests multiple protracted pulses are recorded between *c.* 50-40 Ma (Laurent et al., 2021; Uunk et al., 2022). The CBU is thought to represent subducted and metamorphosed equivalents of similar, oceanic-passive margin rocks belonging to the Pindos Unit exposed on continental Greece and the Peloponnese (Bonneau, 1984). Units less abundantly represented within the Cyclades include 1) a continental basement of disputed affinity ('Cycladic Basement') and 2) a second passive margin carbonate succession ('Basal Unit'), both structurally below the CBU; 3) klippen of the structurally higher Pelagonian Unit preserved in tectonic contact with the CBU; 4) early Miocene clastic sequences; 5) late Miocene granitoids intruding the various units; and 6) Pleistocene to recent volcanic successions (Jacobshagen, 1986; Ring et al., 2010). All pre-Miocene units, including the CBU, represent parts of the Hellenides segment of the broader Alpine orogen, and are composed of crystalline rock derived from rifted portions of Gondwana and their Triassic-Cretaceous depositional cover (Bonneau, 1984). The Hellenic orogen is essentially constructed of several discrete continental strands representing parts of the micro-continent Apulia, divided at different times in its history by arms of the Neotethys ocean, and accreted in a north-to-south direction along the southern margin of continental Europe (Papanikolaou, 2021).

The modern Aegean Sea is a back-arc environment that formed as a result of slab rollback since the early Miocene, as evinced by clastic sequences of similar age deposited in extensional

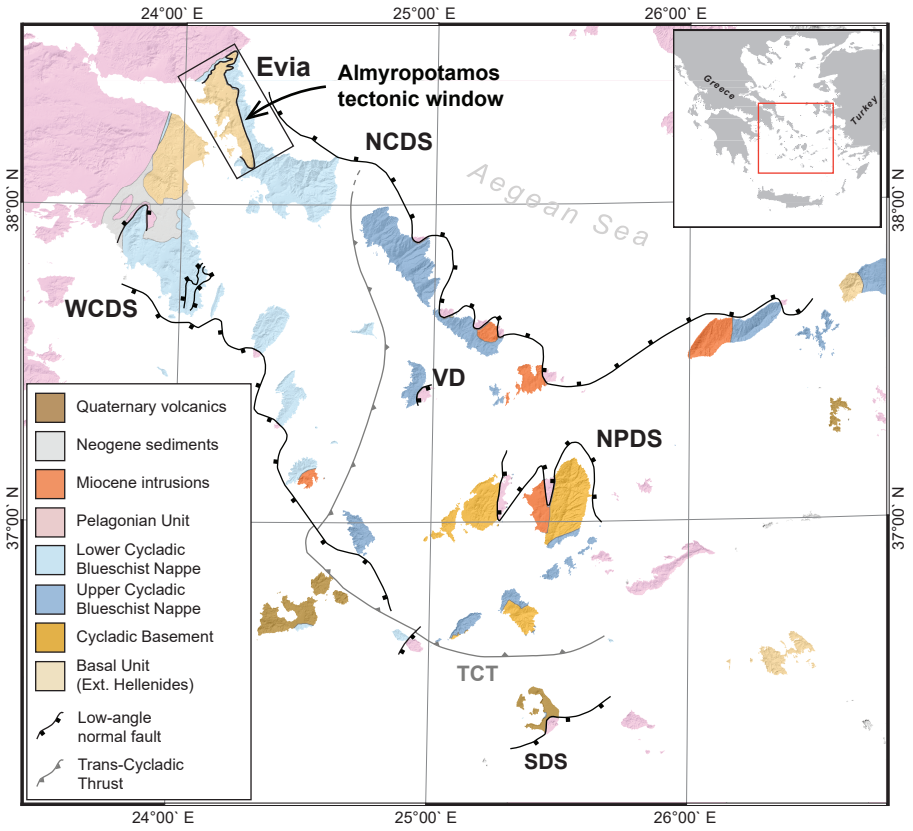

Figure 1.2. Simplified bedrock geology map of the Cyclades, Evia, and Attica. Modified after Coleman et al. (2020). NCDS: North Cycladic Detachment System; NPDS: Naxos-Paros Detachment System; SDS: Santorini Detachment System; TCT: Trans-Cycladic Thrust; VD: Vari Detachment; WCDS: West Cycladic Detachment System.

basins and radiometric dates from associated mylonites (Jolivet and Brun, 2010; Ring et al., 2010; **Figure 1.3**). Extension of Aegean crust drove the formation of regional-scale low-angle normal faults, which controlled the final stages of exhumation of the HP-LT rocks occupying their footwalls (Jolivet et al., 2010; Grasemann et al., 2012). Rocks in the footwall had likely already experienced considerable unroofing via syn-orogenic processes beginning in the late Eocene (e.g., Brichau et al., 2007). However, detachment faulting produced considerable segmentation of the Aegean crust and exerted a dominant control on the modern distribution of its major lithotectonic units (Jolivet et al., 2004, 2010). Whereas the island of Ios served as an important model for the conceptualization of detachment faulting, detachments are exposed on numerous other Cycladic islands, and the importance of this mechanism to exhumation in the region has been known for four decades (Lister et al., 1984; Gautier and Brun, 1994; Jolivet et al., 2004). Nevertheless, regional syntheses have only recently recognized the interconnectivity of two major groups: one spanning from Evia to at least as far as Ikaria, defining the North Cycladic Detachment System (NCDS; Jolivet et al., 2010); and another from Attica to Serifos, defining the West Cycladic Detachment System (WCDS; Grasemann et al., 2012). These two major structures, alongside several other less extensive fault systems, have accommodated extension of the Aegean with bivergent kinematics since the early Miocene. Consequent crustal thinning (to ~24 km; Cossette et al., 2016) has induced decompression melting, generating both the widespread Miocene intrusions and migmatites documented in the central Cyclades, where the deepest structural levels are exhumed.

1.3. Geology of Evia island

The geology of Evia will be described in greater detail in the relevant sections of Chapters 2, 3, and 4. This section intends mainly to provide a brief overview of the state of the geological literature on Evia at the time work on the thesis began.

Bedrock exposed on the southern parts of Evia has been correlated with the CBU at least since the late 1960s (Katsikatsos et al., 1969). However, the Almyropotamos tectonic window (**Figure 1.1**) that occupies half of the study area went unrecognized until a Lower Eocene nummulitic hard ground was documented at the top of the structurally lower marble sequence (Dubois and Bignot, 1979; Katsikatsos et al., 1987). Correlations between the lower marbles of Evia and their overlying flyschoid sediments were made with units exhibiting a similar tectonostratigraphic configuration, including those to the northwest on Mt. Olympos and Mt. Ossa (Schermer et al., 1990; Katsikatsos et al., 1991), as well as smaller local exposures on Tinos and Samos (Avigad and Garfunkel, 1989; Ring and Layer, 2003). These rocks together constitute the Basal Unit, a HP-LT unit structurally below the CBU recording an ostensibly younger peak of metamorphism (Shaked et al., 2000; Ring et al., 2007b; **Figure 1.3**). Due to its structural position, the Basal Unit is inferred to be the metamorphosed equivalent of the Gavrovo-Tripolitza Unit, a major lithotectonic unit that accreted outboard of the Pindos Unit and that also comprises a thick neritic carbonate succession (Papanikolaou, 2021). By direct extension, the inferred relationship implies the existence of a major nappe-bounding thrust fault, locally termed the 'Evia Thrust' but regionally designated the 'Basal Thrust.' The age of displacement along this structure, as well as the age of the HP-LT metamorphism recorded by the Basal Unit, is contentious (Shaked et al., 2000; Ring and Layer, 2003; Ring et al., 2007b; Tirel et al., 2009); Chapters 2 and 3 present new data that may resolve the disagreement.

The CBU exposed on Evia is subdivided into metavolcanic (Ochi Unit) and metacarbonate (Styra Unit) components. The two successions represent common subunits encountered throughout the CBU; however, the Ochi Unit has, in some interpretations, been correlated to the lithologically similar Makrotantalon Unit exposed nearby on NW Andros, which is of probable Pelagonian affinity (Huet et al., 2015; Bröcker, 2023). Some investigators also assign schists occupying an intermediate position between the Styra Unit and the Basal Unit to the base of the CBU. The most important implication of this disagreement is the resultant differences in placement of the tectonic contact – apparently representing a major subduction thrust situated at the roof of the subduction channel during underthrusting of the Basal Unit beneath the CBU – within the structural pile of southern Evia. Addressing the positioning of the tectonic contact is a central piece of the discussion in both Chapters 2 and 3.

Geochronology for the bedrock units of southern Evia has been performed primarily via the $^{40}Ar/^{39}Ar$ and $^{87}Rb/^{87}Sr$ methods (Maluski et al., 1981; Ring et al., 2001; Ring and Layer, 2003; Ring et al., 2007b). Limited supplemental zircon and apatite fission track thermochronology has also been conducted (Ring et al., 2007b). Despite the volume of available analytical data, dates have remained equivocal with respect to their tectonometamorphic significance, and apparently record a wide dispersal of dates with concentrations of dates in the late Eocene to early Miocene.

The southern boundary of the tectonic window lies immediately north of the broader, mountainous southernmost region of Evia. Here, the bedrock is composed almost entirely of the CBU (and, possibly, the Makrotantalon Unit; Katzir et al., 2000; Xypolias et al., 2012). This part of the island has been the subject of mainly structural study of both its ductile and brittle deformation (Nüchter and Stöckhert, 2007; Xypolias et al., 2012; Xypolias and Alsop, 2014). The unique glaucophane-bearing veins examined in Chapter 4 are located there, on southernmost Evia,

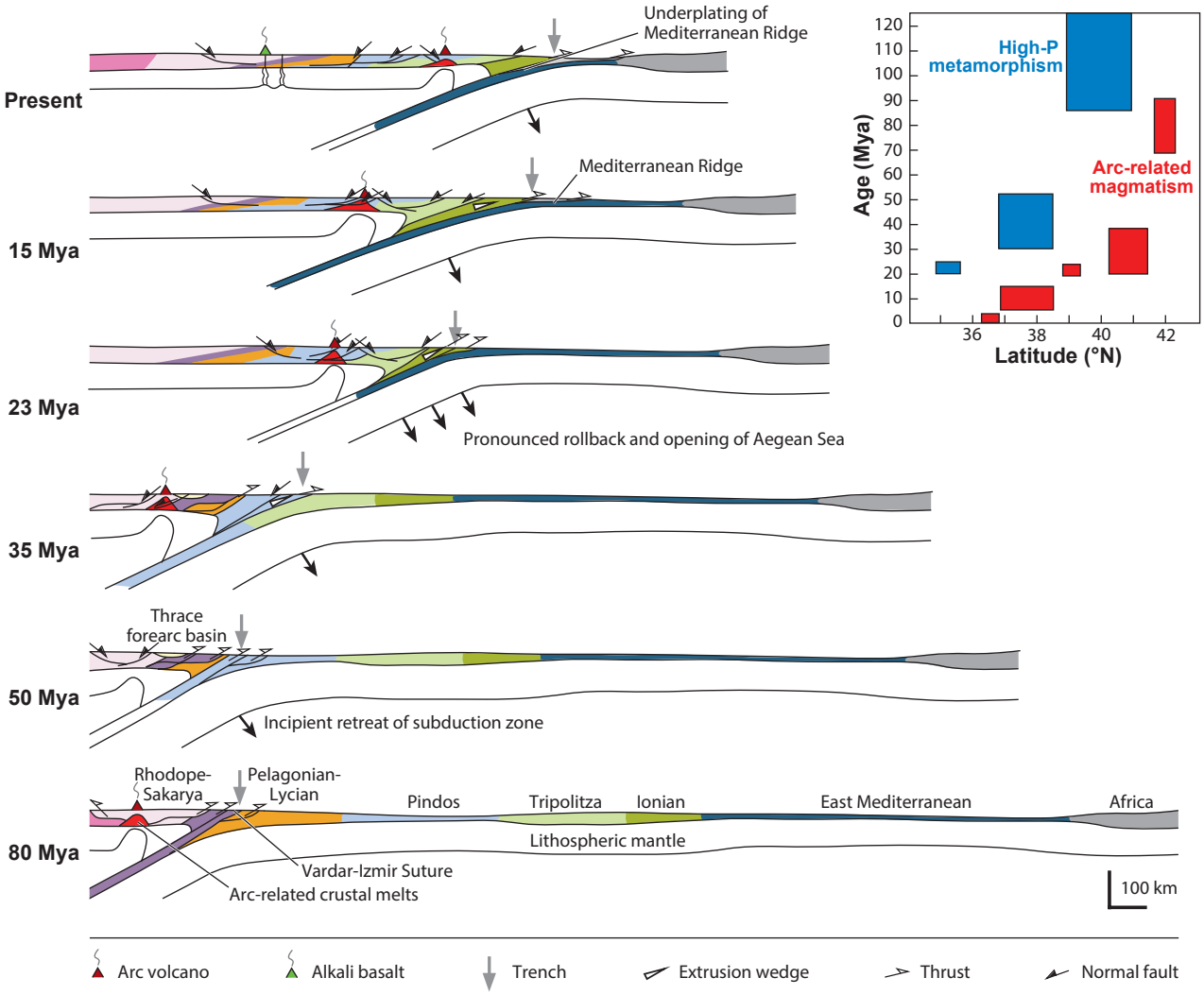

Figure 1.3. North-south cross sections across the central Aegean region since the Late Cretaceous highlighting geodynamic evolution of the subduction zone. Inset diagram shows the timing of important metamorphic events in the region. From Ring et al. (2010).

hosted in mafic metavolcanic rocks of the Ochi Unit. Irrespective of its affiliation to the CBU or Makrotantalon Unit, the Ochi Unit should retain an essentially identical tectonometamorphic history since the Eocene (Huet et al., 2015; Bröcker, 2023).

1.4. Thesis motivation and structure

This thesis intends to address the aforementioned gaps in the Cycladic literature pertaining to the exhumation of its HP-LT massif on Evia, while simultaneously investigating one of the few major reverse-sense tectonic contacts recognized in the region. Research in the Cyclades between the late 1990s and 2000s produced numerous island-scale syntheses of the local exhumation histories recorded by the HP-LT rocks there (Forster and Lister, 1999; Trotet et al., 2001; Ring et al., 2003; Mehl et al., 2005, 2007; Iglseder et al., 2006; Brichau et al., 2008; Huet et al., 2009; Thomson et al., 2009; Lecomte et al., 2010), following the initial identification of the major detachments controlling their exhumation (e.g., Lister et al., 1984; Gautier and Brun, 1994). Despite certain structures on southern Evia having been recognized prior to now as likely to be related to Cycladic exhumation (Jolivet et al., 2004; Ring et al., 2007b), Evia had not been the subject of a similar concerted study of its exhumation history. Because southern Evia exposes not only the CBU but also deeper structural levels, a more pronounced exhumation-related structural or geochronological signature may reasonably be expected on the island. From a different perspective, the recent recognition of the Trans-Cycladic Thrust (TCT; Grasemann et al., 2018), whose lateral extent was delineated by available thermodynamic data to at least Andros, also draws an enticing analogue to the tectonic relationship described on Evia astride the Basal Thrust (Katsikatsos et al., 1982; Shaked et al., 2000). Evidence sufficient to re-interpret the Basal Thrust as a continuation of the TCT would modify our understanding of the crustal structure and tectonic

relationships in the Cyclades to a significant degree. The products of the thesis would ultimately prove more fruitful with respect to the exhumation history of the Cyclades than to the convergent stages of its orogenesis.

Chapter 2 evaluates the premises of the above hypotheses using campaign-style geochronology alongside thermodynamic modelling and field-based structural documentation spanning the hanging wall and footwall of the Almyropotamos tectonic window. Chapter 2 improves the sampling density and spatial resolution of the geochronology to reassess the timing of crystallization, cooling, and deformation recorded by the white mica $^{40}Ar/^{39}Ar$ geochronometer in both the CBU and Basal Unit, and contributes an additional zircon (U-Th)/He (ZHe) dataset to the existing low-temperature thermochronology available for the Cyclades. The chapter complements the geochronology with a comprehensive assessment of the architecture of the structural pile defining the Almyropotamos window, contextualizing Evia among the significant advances in Aegean tectonics in the preceding decade and a half. A consistent, late Oligocene $^{40}Ar/^{39}Ar$ signature was obtained from white mica defining the dominant sub-horizontal metamorphic foliations near the contact between the Tsakei schists and the Basal Unit marble. Structures developed there require a component of ductile stretching parallel to the intermediate axis of the strain ellipsoid, as defined by the orientation of the stretching lineation and corroborated by the orthogonal orientation of co-occurring monoclinic kinematic indicators. Cooler brittle-ductile structures also implying *Y*-direction stretching suggest that flattening persisted during exhumation through the brittle-ductile transition, in which the ZHe data indicate occurred somewhat earlier than typical elsewhere in the Aegean. Thermodynamic modelling of the metamorphic assemblage coexisting in textural equilibrium with the micaceous foliation attests that the flattening structures formed under prehnite-pumpellyite to lower greenschist facies

conditions at moderately elevated pressures, whereas parts of the hanging wall retain assemblages consistent with peak HP-LT metamorphism. Chapter 2 concludes that the Basal Unit flysch succession, between two marble units belonging to the Basal Unit (footwall) and CBU (hanging wall), partitioned tensional strain in the late Oligocene – defining the Evia Shear Zone (ESZ) – that facilitated the exhumation of the underlying Basal Unit marbles. The oblate strain ellipsoid implied by the documented structures suggests that part of the flysch was attenuated by vertical thinning and lateral extrusion, providing insight into the tectonic mechanisms controlling the infrequent exposure of structural levels deeper than the CBU throughout the Aegean. Project conceptualization, field work, funding, and interpretation of the data were greatly assisted by David Schneider and Bernhard Grasemann, and Iwona Klonowska conducted sample processing and data acquisition to facilitate and perform thermodynamic modelling in PERPLE_X. Chapter 2 was published in *Tectonics* in December 2022, and was also fortunate to be awarded the Canadian Tectonics Group 2023 David Elliott Best Paper prize.

Chapter 3 serves as a direct continuation of the second chapter and further interrogates its central model. The Basal Unit flysch is compositionally heterogeneous, and comprises numerous blocks of locally or exotically derived lithotypes set within a schistose pelitic matrix. Its compositional heterogeneity should also produce rheological contrasts that influence the mechanical behavior of the flysch during partitioning of strain related to the ESZ. Among the heterogeneities encountered, boudinaged quartz veins serve as important strain markers recording flattening in the ESZ. Because, as shown in Chapter 2, the structural context of the veins attests to their deformation proceeding during the critical interval of exhumation, quartz within them has likely partitioned some of this strain. An automated fabric analyzer was used to measure quartz c-axis distributions from select veins showing microstructures typical of quartz that has undergone

dynamic recrystallization (i.e., bulging/serrated grain boundaries and subgrain development), with the goal of testing whether exhumation occurred within the flattening field of strain. Complementary *in situ* white mica geochronology ($^{40}Ar/^{39}Ar$ and $^{87}Rb/^{87}Sr$) was used to further investigate sample-scale disparities observed in the single-grain fusion $^{40}Ar/^{39}Ar$ data at contrasting structural levels within the newly proposed ESZ. Although both the vein quartz c-axis and *in situ* geochronology datasets proved more complex than that relatively simple hypothesis, the results highlight the preservation of two distinct deformation phases within the Basal Unit: one that likely captures the timing and conditions related to early Oligocene burial and HP-LT metamorphism, and the second capturing late Oligocene-early Miocene exhumation and (sub-)greenschist facies overprint. Chapter 3 provides the first robust geochronological evidence consigning HP-LT metamorphism of the Basal Unit to the Oligocene, and simultaneously strengthens arguments in Chapter 2 regarding the role of flattening, and commensurate lateral extrusion and thinning, in exhuming the Basal Unit on southern Evia. Chapter 3 features contributions from David Schneider, who facilitated fieldwork, provided funding, aided in study conceptualization, and in data interpretation and developing the tectonic model; Bernhard Grasemann, who guided the structural and c-axis texture interpretations; Alfredo Camacho, who assisted in sample preparation, data acquisition, and interpretation of *in situ* $^{40}Ar/^{39}Ar$ data; Kyle Larson, who processed the quartz petrofabric and *in situ* $^{87}Rb/^{87}Sr$ analyses and assisted in their interpretation; Victoria Scoging, who processed the petrofabric data as part of her Honours thesis; and Christina Bakowsky, who assisted with key structural observations and formulation of the tectonic model. Chapter 3 is currently under review, also in *Tectonics*.

The preceding two projects consider complications introduced to the orogenic record arising from partial overprint by later tectonic structures. Chapter 4 instead examines a

mineralogical variation on the overarching questions considered by this thesis, fostered by atypical *P-T-X* conditions that may nonetheless confuse the tectonic significance of a metamorphic mineral assemblage. Southernmost Evia exposes structural levels that have been correlated only with the CBU. On the southwestern slopes of Mt. Ochi, the highest point on southern Evia (1398 m), metabasaltic and quartzitic rocks assigned to the Ochi Unit preserve four variably-oriented quartz vein sets with dense selvages composed of glaucophane and phengitic white mica. Despite superficially resembling mineral assemblages anticipated to develop at peak HP-LT metamorphism, an aggregate of structural, geochronological, and geochemical data contradict such a straightforward – yet very common – *a priori* assumption. The data instead strongly favour an interpretation wherein the veins, along with their mineral infill, formed in the early Miocene when the region was already transitioning to back-arc extension. A wide and robust body of thermodynamic and geochronologic data from the region have established that the CBU had undergone significant unroofing and was likely at greenschist facies conditions at that time. Therefore, the glaucophane-bearing veins represent anomalous growth of minerals that are widely considered index minerals for peak HP-LT metamorphic conditions. Microstructural evidence suggests that fluid chemistry played a major role in permitting the apparent deviation in PT conditions. Critically, if similar fluid compositions are not uncommonly encountered during exhumation of HP-LT units, it would imply that some of the nominally blueschist facies rock may instead have equilibrated during exhumation. Such a conclusion would violate any connection made between those rocks and subduction zone processes on the basis of their ostensibly diagnostic mineral assemblages. David Schneider facilitated project conceptualization, data acquisition, funding, and interpretation; Bernhard Grasemann aided in the interpretation of the structural context and paragenetic model; Michał Bukała assisted with petrological interpretations;

Alfredo Camacho facilitated acquisition of the $^{40}Ar/^{39}Ar$ data and aided in their interpretation; and Kyle Larson provided *in situ* $^{87}Rb/^{87}Sr$ analyses and aided in their interpretation. As of March 2024, Chapter 4 is published in *Contributions to Mineralogy and Petrology*.

1.5. References

Agard, P., Yamato, P., Jolivet, L., & Burov, E. (2009). Exhumation of oceanic blueschists and eclogites in subduction zones: timing and mechanisms. Earth-Science Reviews, 92(1-2), 53-79.

Allemand, P., & Lardeaux, J. M. (1997). Strain partitioning and metamorphism in a deformable orogenic wedge: Application to the Alpine belt. Tectonophysics, 280(1-2), 157-169.

Avigad, D., & Garfunkel, Z. (1989). Low-angle faults above and below a blueschist belt—Tinos Island, Cyclades, Greece. Terra Nova, 1(2), 182-187.

Axen, G. J. (2004). Mechanics of low-angle normal faults. In Rheology and deformation of the lithosphere at continental margins (pp. 46-91). Columbia University Press.

Barnes, C. J., Schneider, D. A., Majka, J., Camacho, A., Bukała, M., & Włodek, A. (2023). $^{40}Ar/^{39}Ar$ dates controlled by white mica deformation and strain localization: Insights from comparing in situ laser ablation and single-grain fusion techniques. Journal of Metamorphic Geology, 41(9), 1143-1166.

Beaudoin, A., Augier, R., Jolivet, L., Jourdon, A., Raimbourg, H., Scaillet, S., & Cardello, G. L. (2017). Deformation behavior of continental crust during subduction and exhumation: Strain distribution over the Tenda massif (Alpine Corsica, France). Tectonophysics, 705, 12-32.

Behr, W. M., & Bürgmann, R. (2021). What's down there? The structures, materials and environment of deep-seated slow slip and tremor. Philosophical Transactions of the Royal Society A, 379(2193), 20200218.

Biemiller, J., Gabriel, A. A., & Ulrich, T. (2023). Dueling dynamics of low-angle normal fault rupture with splay faulting and off-fault damage. Nature Communications, 14(1), 2352.

Bonneau, M. (1984). Correlation of the Hellenide nappes in the south-east Aegean and their tectonic reconstruction. Geological Society, London, Special Publications, 17(1), 517-527.

Brichau, S., Ring, U., Carter, A., Monié, P., Bolhar, R., Stockli, D., & Brunel, M. (2007). Extensional faulting on Tinos island, Aegean sea, Greece: How many detachments?. Tectonics, 26(4).

Brichau, S., Ring, U., Carter, A., Bolhar, R., Monié, P., Stockli, D., & Brunel, M. (2008). Timing, slip rate, displacement and cooling history of the Mykonos detachment footwall, Cyclades, Greece, and implications for the opening of the Aegean Sea basin. Journal of the Geological Society, 165(1), 263-277.

Bröcker, M. (2023). The jadeitites from Syros and Tinos, Cycladic Blueschist Unit, Greece: field observations, mineralogical, geochemical and geochronological characteristics. Geological Magazine, 160(8), 1586-1606.

Burbank, D. W. (2002). Rates of erosion and their implications for exhumation. Mineralogical Magazine, 66(1), 25-52.

Cawood, P. A. (1982). Structural relations in the subduction complex of the Paleozoic New England Fold Belt, eastern Australia. The Journal of Geology, 90(4), 381-392.

Chambefort, I., & Moritz, R. (2006). Late Cretaceous structural control and Alpine overprint of the high-sulfidation Cu–Au epithermal Chelopech deposit, Srednogorie belt, Bulgaria. Mineralium Deposita, 41, 259-280.

Clarke, G. L., Powell, R., & Fitzherbert, J. A. (2006). The lawsonite paradox: a comparison of field evidence and mineral equilibria modelling. Journal of Metamorphic Geology, 24(8), 715-725.

Cliff, R. A. (1985). Isotopic dating in metamorphic belts. Journal of the Geological Society, 142(1), 97-110.

Coleman, M. J., Schneider, D. A., Grasemann, B., Soukis, K., Lozios, S., & Hollinetz, M. S. (2020). Lateral termination of a Cycladic-style detachment system (Hymittos, Greece). Tectonics, 39(9), e2020TC006128.

Collettini, C., Carpenter, B. M., Viti, C., Cruciani, F., Mollo, S., Tesei, T., ... & Chiaraluce, L. (2014). Fault structure and slip localization in carbonate-bearing normal faults: An example from the Northern Apennines of Italy. Journal of Structural Geology, 67, 154-166.

Corcoran, D. V., & Doré, A. G. (2005). A review of techniques for the estimation of magnitude and timing of exhumation in offshore basins. Earth-Science Reviews, 72(3-4), 129-168.

Cossette, É., Audet, P., Schneider, D., & Grasemann, B. (2016). Structure and anisotropy of the crust in the Cyclades, Greece, using receiver functions constrained by in situ rock textural data. Journal of Geophysical Research: Solid Earth, 121(4), 2661-2678.

Creus, P. K., Sanislav, I. V., Dirks, P. H., Jago, C. M., & Davis, B. K. (2023). The Dugald River-type, shear zone hosted, Zn-Pb-Ag mineralisation, Mount Isa Inlier, Australia. Ore Geology Reviews, 155, 105369.

Cruz-Uribe, A. M., Hoisch, T. D., Wells, M. L., Vervoort, J. D., & Mazdab, F. K. (2015). Linking thermodynamic modelling, Lu–Hf geochronology and trace elements in garnet: New P–T–t paths from the Sevier hinterland. Journal of Metamorphic Geology, 33(7), 763-781.

Di Vincenzo, G., Godard, G., & Molli, G. (2022). Dating Low-Grade Deformation: Role of Lithology and Strain Partitioning on Ar Isotope Records in the Alpi Apuane of Northern Apennines (Italy). Tectonics, 41(7), e2022TC007248.

Doglioni, C. (1995). Geological remarks on the relationships between extension and convergent geodynamic settings. Tectonophysics, 252(1-4), 253-267.

Dubois, R. & Bignot, G. (1979). Présence d'un ‘hardground’ nummulitique au de la série Cretacée d'Almyropotamos (Eubée méridionale, Grèce). Comptes Rendus de l'Académie des Sciences, Série II, 289, 993–995.

Dunlap, W. J., Teyssier, C., McDougall, I., & Baldwin, S. (1991). Ages of deformation from K/Ar and $^{40}Ar/^{39}Ar$ dating of white micas. Geology, 19(12), 1213-1216.

Edmundson, I., Rotevatn, A., Davies, R., Yielding, G., & Broberg, K. (2020). Key controls on hydrocarbon retention and leakage from structural traps in the Hammerfest Basin, SW

Barents Sea: implications for prospect analysis and risk assessment. Petroleum Geoscience, 26(4), 589-606.

Evans, B. W. (1990). Phase relations of epidote-blueschists. Lithos, 25(1-3), 3-23.

Forde, A., & Bell, T. H. (1994). Late structural control of mesothermal vein-hosted gold deposits in Central Victoria, Australia: Mineralization mechanisms and exploration potential. Ore Geology Reviews, 9(1), 33-59.

Forster, M. A., & Lister, G. S. (1999). Detachment faults in the Aegean core complex of Ios, Cyclades, Greece. Geological Society, London, Special Publications, 154(1), 305-323.

Fossen, H., & Cavalcante, G. C. G. (2017). Shear zones–A review. Earth-Science Reviews, 171, 434-455.

Fox, M., Herman, F., Kissling, E., & Willett, S. D. (2015). Rapid exhumation in the Western Alps driven by slab detachment and glacial erosion. Geology, 43(5), 379-382.

Froitzheim, N., Pleuger, J., Roller, S., & Nagel, T. (2003). Exhumation of high-and ultrahigh-pressure metamorphic rocks by slab extraction. Geology, 31(10), 925-928.

Froitzheim, N., Pleuger, J., & Nagel, T. J. (2006). Extraction faults. Journal of Structural Geology, 28(8), 1388-1395.

Gasco, I., Gattiglio, M., & Borghi, A. (2011). Lithostratigraphic setting and PT metamorphic evolution for the Dora Maira Massif along the Piedmont Zone boundary (middle Susa Valley, NW Alps). International Journal of Earth Sciences, 100, 1065-1085.

Gautier, P., & Brun, J. P. (1994). Ductile crust exhumation and extensional detachments in the central Aegean (Cyclades and Evvia Islands). Geodinamica Acta, 7(2), 57-85

Grasemann, B., Schneider, D. A., Stöckli, D. F., & Iglseder, C. (2012). Miocene bivergent crustal extension in the Aegean: Evidence from the western Cyclades (Greece). Lithosphere, 4(1), 23-39.

Gyomlai, T., Agard, P., Herviou, C., Jolivet, L., Monié, P., Mendes, K., & Iemmolo, A. (2023). In situ Rb–Sr and ^{40}Ar–^{39}Ar dating of distinct mica generations in the exhumed subduction complex of the Western Alps. Contributions to Mineralogy and Petrology, 178(9), 58.

Handy, M. R., & Zingg, A. (1991). The tectonic and rheological evolution of an attenuated cross section of the continental crust: Ivrea crustal section, southern Alps, northwestern Italy and southern Switzerland. Geological Society of America Bulletin, 103(2), 236-253.

Harding, T., & Lowell, J. D. (1979). Structural styles, their plate-tectonic habitats, and hydrocarbon traps in petroleum provinces. AAPG bulletin, 63(7), 1016-1058.

Hausmann, J.F.L. (1845). Beiträge zur Oryktographie von Syra, Journal für Praktische Chemie, 238–241.

Holland, T.J.B., & Powell, R. (1998). An internally consistent thermodynamic data set for phases of petrological interest. Journal of Metamorphic Geology, 16(3), 309-343.

Horton, B. K., Parra, M., Saylor, J. E., Nie, J., Mora, A., Torres, V., ... & Strecker, M. R. (2010). Resolving uplift of the northern Andes using detrital zircon age signatures. GSA Today, 20(7), 4-10.

Huet, B., Labrousse, L., & Jolivet, L. (2009). Thrust or detachment? Exhumation processes in the Aegean: Insight from a field study on Ios (Cyclades, Greece). Tectonics, 28(3).

Huet, B., Labrousse, L., Monie, P., Malvoisin, B., & Jolivet, L. (2015). Coupled phengite ^{40}Ar–^{39}Ar geochronology and thermobarometry: PTt evolution of Andros Island (Cyclades, Greece). Geological Magazine, 152(4), 711-727.

Jacobshagen, V. (1986). Geologie von Griechland. Borntraeger, Berlin-Stuttgart, p. 279.

Jessup, M. J., Law, R. D., Searle, M. P., & Hubbard, M. S. (2006). Structural evolution and vorticity of flow during extrusion and exhumation of the Greater Himalayan Slab, Mount Everest Massif, Tibet/Nepal: implications for orogen-scale flow partitioning. Geological Society, London, Special Publications, 268(1), 379-413.

Jolivet, L., & Brun, J. P. (2010). Cenozoic geodynamic evolution of the Aegean. International Journal of Earth Sciences, 99, 109-138.

Jolivet, L., Famin, V., Mehl, C., Parra, T., Aubourg, C., Hébert, R., et al. (2004). Strain localization during crustal-scale boudinage to form extensional metamorphic domes in the Aegean Sea. Geological Society of America, Special Papers, 185-210.

Jolivet, L., Lecomte, E., Huet, B., Denèle, Y., Lacombe, O., Labrousse, L., et al. (2010). The north cycladic detachment system. Earth and Planetary Science Letters, 289(1-2), 87-104.

Katsikatsos, G. (1991a). Geological map of Greece, Aliveri sheet. Institute of Geological Mining Research (IGME), Athens.

Katsikatsos, G., Mercier, J.-L., & Vergely, P. (1976). L'Eubée méridionale: une double fenêtre polyphasée dans les Hellénides internes (Grèce). Comptes Rendus de l'Académie des Sciences, Série D, 459-462.

Katzir, Y., Avigad, D., Matthews, A., Garfunkel, Z., & Evans, B. W. (2000). Origin, HP/LT metamorphism and cooling of ophiolitic mélanges in southern Evia (NW Cyclades), Greece. Journal of Metamorphic Geology, 18(6), 699-718.

Keay, S., Lister, G., & Buick, I. (2001). The timing of partial melting, Barrovian metamorphism and granite intrusion in the Naxos metamorphic core complex, Cyclades, Aegean Sea, Greece. Tectonophysics, 342(3-4), 275-312.

Larson, K. P., Button, M., Shrestha, S., & Camacho, A. (2023). A comparison of $^{87}Rb/^{87}Sr$ and $^{40}Ar/^{39}Ar$ dates: Evaluating the problem of excess ^{40}Ar in Himalayan mica. Earth and Planetary Science Letters, 609, 118058.

Laurent, V., Scaillet, S., Jolivet, L., Augier, R., & Roche, V. (2021). ^{40}Ar behaviour and exhumation dynamics in a subduction channel from multi-scale $^{40}Ar/^{39}Ar$ systematics in phengite. Geochimica et Cosmochimica Acta, 311, 141-173.

Lecomte, E., Jolivet, L., Lacombe, O., Denèle, Y., Labrousse, L., & Le Pourhiet, L. (2010). Geometry and kinematics of Mykonos detachment, Cyclades, Greece: Evidence for slip at shallow dip. Tectonics, 29(5).

Liotta, D., Brogi, A., Meccheri, M., Dini, A., Bianco, C., & Ruggieri, G. (2015). Coexistence of low-angle normal and high-angle strike-to oblique-slip faults during Late Miocene mineralization in eastern Elba Island (Italy). Tectonophysics, 660, 17-34.

Lister, G. S., Banga, G., & Feenstra, A. (1984). Metamorphic core complexes of Cordilleran type in the Cyclades, Aegean Sea, Greece. Geology, 12(4), 221-225.

Lister, G. S., & Davis, G. A. (1989). The origin of metamorphic core complexes and detachment faults formed during Tertiary continental extension in the northern Colorado River region, USA. Journal of Structural Geology, 11(1-2), 65-94.

Long, S. P., & Kohn, M. J. (2020). Distributed ductile thinning during thrust emplacement: A commonly overlooked exhumation mechanism. Geology, 48(4), 368-373.

Maluski, H., Vergely, P., Bavay, D., Bavay, P., & Katsikatsos, G. (1981). $^{39}Ar/^{40}$ Ar dating of glaucophanes and phengites in southern Euboa (Greece); geodynamic implications. Bulletin de la Société Géologique de France, 7(5), 469-476.

Marchev, P., Kaiser-Rohrmeier, M., Heinrich, C., Ovtcharova, M., von Quadt, A., & Raicheva, R. (2005). 2: Hydrothermal ore deposits related to post-orogenic extensional magmatism and core complex formation: The Rhodope Massif of Bulgaria and Greece. Ore Geology Reviews, 27(1-4), 53-89.

Maruyama, S., Liou, J. G., & Terabayashi, M. (1996). Blueschists and eclogites of the world and their exhumation. International Geology Review, 38(6), 485-594.

Massonne, H. J. (2014). Wealth of P–T–t information in medium-high grade metapelites: Example from the Jubrique Unit of the Betic Cordillera, S Spain. Lithos, 208, 137-157.

Mehl, C., Jolivet, L., & Lacombe, O. (2005). From ductile to brittle: Evolution and localization of deformation below a crustal detachment (Tinos, Cyclades, Greece). Tectonics, 24(4).

Mehl, C., Jolivet, L., Lacombe, O., Labrousse, L., & Rimmele, G. (2007). Structural evolution of Andros (Cyclades, Greece): a key to the behaviour of a (flat) detachment within an

extending continental crust. Geological Society, London, Special Publications, 291(1), 41-73.

Menant, A., Jolivet, L., Augier, R., & Skarpelis, N. (2013). The North Cycladic Detachment System and associated mineralization, Mykonos, Greece: Insights on the evolution of the Aegean domain. Tectonics, 32(3), 433-452.

Papanikolaou, D. (2021). Geology of Greece. Springer Nature.

Peillod, A., Majka, J., Ring, U., Drüppel, K., Patten, C., Karlsson, A., ... & Tehler, E. (2021). Differences in decompression of a high-pressure unit: A case study from the Cycladic Blueschist Unit on Naxos Island, Greece. Lithos, 386, 106043.

Platt, J. P. (1993). Exhumation of high-pressure rocks: A review of concepts and processes. Terra Nova, 5(2), 119-133.

Pirajno, F. (2008). Hydrothermal processes and mineral systems. Springer Science & Business Media.

Reddy, S., Wheeler, J., & Cliff, R. (1999). The geometry and timing of orogenic extension: An example from the western Italian Alps. Journal of Metamorphic Geology, 17(5), 573-590.

Reynolds, S. J., & Lister, G. S. (1987). Structural aspects of fluid-rock interactions in detachment zones. Geology, 15(4), 362-366.

Ring, U., & Reischmann, T. (2002). The weak and superfast Cretan detachment, Greece: exhumation at subduction rates in extruding wedges. Journal of the Geological Society, 159(3), 225-228.

Ring, U., & Layer, P. W. (2003). High-pressure metamorphism in the Aegean, eastern Mediterranean: Underplating and exhumation from the Late Cretaceous until the Miocene to Recent above the retreating Hellenic subduction zone. Tectonics, 22(3).

Ring, U., & Brandon, M. T. (2008). Exhumation settings, Part I: Relatively simple cases. International Geology Review, 50(2), 97-120.

Ring, U. W. E., & Kumerics, C. (2008). Vertical ductile thinning and its contribution to the exhumation of high-pressure rocks: the Cycladic blueschist unit in the Aegean. Journal of the Geological Society, 165(6), 1019-1030.

Ring, U., Brandon, M. T., Willett, S. D., & Lister, G. S. (1999). Exhumation processes. Geological Society, London, Special Publications, 154(1), 1-27.

Ring, U., Will, T., Glodny, J., Kumerics, C., Gessner, K., Thomson, S., ... & Drüppel, K. (2007a). Early exhumation of high-pressure rocks in extrusion wedges: Cycladic blueschist unit in the eastern Aegean, Greece, and Turkey. Tectonics, 26(2).

Ring, U., Glodny, J., Will, T., & Thomson, S. (2007b). An Oligocene extrusion wedge of blueschist-facies nappes on Evia, Aegean Sea, Greece: implications for the early exhumation of high-pressure rocks. Journal of the Geological Society, 164(3), 637-652.

Ring, U., Glodny, J., Will, T., & Thomson, S. (2010). The Hellenic subduction system: high-pressure metamorphism, exhumation, normal faulting, and large-scale extension. Annual Review of Earth and Planetary Sciences, 38, 45-76.

Rosenbaum, G., Avigad, D., & Sánchez-Gómez, M. (2002). Coaxial flattening at deep levels of orogenic belts: evidence from blueschists and eclogites on Syros and Sifnos (Cyclades, Greece). Journal of Structural Geology, 24(9), 1451-1462.

Rubatto, D., Gebauer, D., & Compagnoni, R. (1999). Dating of eclogite-facies zircons: the age of Alpine metamorphism in the Sesia–Lanzo Zone (Western Alps). Earth and Planetary Science Letters, 167(3-4), 141-158.

Sanchez-Gomez, M., Avigad, D. O. V., & Heimann, A. (2002). Geochronology of clasts in allochthonous Miocene sedimentary sequences on Mykonos and Paros Islands: implications for back-arc extension in the Aegean Sea. Journal of the Geological Society, 159(1), 45-60.

Sandmann, S., Nagel, T. J., Froitzheim, N., Ustaszewski, K., & Münker, C. (2015). Late Miocene to Early Pliocene blueschist from Taiwan and its exhumation via forearc extraction. Terra Nova, 27(4), 285-291.

Scheffer, C., Vanderhaeghe, O., Lanari, P., Tarantola, A., Ponthus, L., Photiades, A., & France, L. (2016). Syn-to post-orogenic exhumation of metamorphic nappes: Structure and thermobarometry of the western Attic-Cycladic metamorphic complex (Lavrion, Greece). Journal of Geodynamics, 96, 174-193.

Schermer, E. R., Lux, D. R., & Burchfiel, B. C. (1990). Temperature-time history of subducted continental crust, Mount Olympos Region, Greece. Tectonics, 9(5), 1165-1195.

Schneider, D. A., Senkowski, C., Vogel, H., Grasemann, B., Iglseder, C., & Schmitt, A. K. (2011). Eocene tectonometamorphism on Serifos (western Cyclades) deduced from

zircon depth-profiling geochronology and mica thermochronology. Lithos, 125(1-2), 151-172.

Seman, S., Stockli, D. F., & Soukis, K. (2017). The provenance and internal structure of the Cycladic Blueschist Unit revealed by detrital zircon geochronology, Western Cyclades, Greece. Tectonics, 36(7), 1407-1429.

Shaked, Y., Avigad, D., & Garfunkel, Z. (2000). Alpine high-pressure metamorphism at the Almyropotamos window (southern Evia, Greece). Geological Magazine, 137(4), 367-380.

Stöckhert, B. (2002). Stress and deformation in subduction zones: insight from the record of exhumed metamorphic rocks. Geological Society, London, Special Publications, 200(1), 255-274.

Thomson, S. N., Ring, U., Brichau, S., Glodny, J., & Will, T. M. (2009). Timing and nature of formation of the Ios metamorphic core complex, southern Cyclades, Greece. Geological Society, London, Special Publications, 321(1), 139-167.

Tirel, C., Gautier, P., Van Hinsbergen, D. J. J., & Wortel, M. J. R. (2009). Sequential development of interfering metamorphic core complexes: numerical experiments and comparison with the Cyclades, Greece. Geological Society, London, Special Publications, 311(1), 257-292.

Trotet, F., Jolivet, L., & Vidal, O. (2001). Tectono-metamorphic evolution of Syros and Sifnos islands (Cyclades, Greece). Tectonophysics, 338(2), 179-206.

Tsujimori, T., Sisson, V. B., Liou, J. G., Harlow, G. E., & Sorensen, S. S. (2006). Very-low-temperature record of the subduction process: A review of worldwide lawsonite eclogites. Lithos, 92(3-4), 609-624.

Underdown, R., & Redfern, J. (2007). The importance of constraining regional exhumation in basin modelling: a hydrocarbon maturation history of the Ghadames Basin, North Africa. Petroleum Geoscience, 13(3), 253-270.

Uunk, B., Brouwer, F., de Paz-Álvarez, M., van Zuilen, K., Huybens, R., van't Veer, R., & Wijbrans, J. (2022). Consistent detachment of supracrustal rocks from a fixed subduction depth in the Cyclades. Earth and Planetary Science Letters, 584, 117479.

Vannay, J. C., & Grasemann, B. (2001). Himalayan inverted metamorphism and syn-convergence extension as a consequence of a general shear extrusion. Geological Magazine, 138(3), 253-276.

Warren, C. J. (2013). Exhumation of (ultra-) high-pressure terranes: concepts and mechanisms. Solid Earth, 4(1), 75-92.

White, R. W., Powell, R. O. G. E. R., Holland, T. J. B., Johnson, T. E., & Green, E. C. R. (2014). New mineral activity–composition relations for thermodynamic calculations in metapelitic systems. Journal of Metamorphic Geology, 32(3), 261-286.

Willner, A. P., Glodny, J., Gerya, T. V., Godoy, E., & Massonne, H. J. (2004). A counterclockwise PTt path of high-pressure/low-temperature rocks from the Coastal Cordillera accretionary complex of south-central Chile: constraints for the earliest stage of subduction mass flow. Lithos, 75(3-4), 283-310.

Xypolias, P., & Alsop, G. I. (2014). Regional flow perturbation folding within an exhumation channel: A case study from the Cycladic Blueschists. Journal of Structural Geology, 62, 141-155.

Xypolias, P., Iliopoulos, I., Chatzaras, V., & Kokkalas, S. (2012). Subduction-and exhumation-related structures in the Cycladic Blueschists: Insights from south Evia Island (Aegean region, Greece). Tectonics, 31(2).

Zeitler, P.K., Koons, P.O., Bishop, M., Chamberlain, C.P., Craw, D., Edwards, M., Hamidullah, S., Jan, M.Q., Khan, M.A., Khattak, M.U.K., Kidd, W., Mackie, R., Meltzer, A., Park, S., Pecher, A., Poage, M., Sarker, G., Schneider, D.A., Seeber, L., Shroder, J. (2001). Crustal reworking at Nanga Parbat, Pakistan; Metamorphic consequences of thermal-mechanical coupling facilitated by erosion. Tectonics, 5, 712-728.

Zhou, Y., Xu, D., Dong, G., Chi, G., Deng, T., Cai, J., et. al (2021). The role of structural reactivation for gold mineralization in northeastern Hunan Province, South China. Journal of Structural Geology, 145, 104306.

CHAPTER 2

STRETCHED THIN: OLIGOCENE EXTRUSION AND DUCTILE THINNING OF THE BASAL UNIT ALONG THE EVIA SHEAR ZONE, NW CYCLADES, GREECE

2.1. Abstract

We present field-based structural, geochronological, and petrological evidence for a major new Oligocene extensional shear zone, the Evia Shear Zone (ESZ), on the island of Evia in the NW Aegean Sea. Strain related to this structure occurs in a diffuse zone structurally underlying the nappe contact between the Cycladic Blueschist Unit and Basal Unit, within rock previously attributed to the Tsakei Unit or Basal Unit metaflysch. Structures within the ESZ record stretching in both the X and Y directions under ductile and brittle-ductile conditions, indicative of a component of oblate coaxial strain during overall top-to-E general shear. New white mica $^{40}Ar/^{39}Ar$ geochronology from the ESZ shows that the structure was accommodating ductile deformation in the late Oligocene. Thermodynamic modelling shows that rock within the ESZ records greenschist facies retrogressive conditions of 310 ± 15°C and 7 ± 1 kbar. Zircon (U-Th)/He thermochronology demonstrates that both the CBU and Basal Unit had exhumed into the brittle crust by the middle Miocene, slightly earlier than indicated by low-temperature thermochronology for the HP-LT units throughout the Aegean. We interpret these data as evidence that the Basal Unit underwent rapid exhumation via syn-orogenic processes persisting until at least the early Miocene, facilitated in part by normal-sense displacement along the ESZ. The occurrence of structures representative of coaxial deformation in the shear zone alludes to a major role for ductile thinning in controlling exhumation of HP rocks in the Cyclades, perhaps influencing the relative rates of exhumation observed across the region.

2.2. Introduction

Exhumation of high-pressure, low-temperature (HP-LT) metamorphic rocks may be accomplished by a number of complementary or independent tectonic phenomena (e.g., Platt, 1993; Ring et al., 1999a; Agard et al., 2009). These processes may include erosion, eduction,

ductile thinning, low-angle detachment faulting, and high-angle normal faulting (Ring et al., 1999a; Froitzheim et al., 2003). Syn-orogenic processes may also accomplish considerable magnitudes of exhumation in the form of, for example, an extrusion wedge (e.g., Grujic et al., 1996; Ring et al., 2007a). Deconvolving the contribution from any one mechanism toward net exhumation is frequently complicated by structural interferences resulting from multiple such processes operating over the entire interval of burial and exhumation. Moreover, the scale and prominence of each process in the rock record is widely variable. Detachment faulting and erosion, for instance, produce spectacular and distinctive knife-sharp fault planes and thick basin-fill sequences (e.g., Lister and Davis, 1989; Avouac and Burov, 2009). Meanwhile, ductile thinning may be comparatively inconspicuous and require large quantities of structural data to resolve its nevertheless considerable modification of the crustal architecture in extended orogens (e.g., Feehan and Brandon, 1999; Ring et al., 1999a; Ring and Kassem, 2007; Long and Kohn, 2020).

The Cycladic Islands in Greece are the exhumed fragments of previously subducted crust, returned to the surface as a result of extension imposed on the Hellenic orogen (Lister et al., 1984; Jolivet and Brun, 2010). A large volume of research has sought to establish the tectonic mechanisms responsible for exhuming the HP-LT Attic-Cycladic Crystalline Massif , with particular focus on the Cycladic Blueschist Unit (CBU;Jacobshagen, 1986). Numerous island- and regional-scale studies have established a two-step exhumation history for the CBU, marked first by Eocene syn-orogenic wedge extrusion (e.g., Ring and Layer, 2003; Brichau et al., 2008) and then by Oligo-Miocene bivergent low-angle detachment faulting (Gautier and Brun, 1994; Jolivet and Patriat, 1999; Lecomte et al., 2010; Jolivet et al., 2010a; Grasemann et al., 2012). Despite being reported from a few localities in the Cyclades (e.g., Kumerics et al., 2005; Ring and Kumerics, 2008), ductile thinning remains poorly integrated into geodynamic models for

exhumation in the region, but may be an important mechanism governing the exhumation of units structurally below the CBU (e.g., Mizera and Behrmann, 2016) and perhaps even in determining the ultimate geometry of the major detachment systems (e.g., Ring and Glodny, 2021).

We present new pressure-temperature (PT) modelling results, structural observations, and white mica $^{40}Ar/^{39}Ar$ and zircon (U-Th)/He geochronology for the island of Evia in the northwestern Aegean Sea. Along with Ios and Sikinos, southern Evia is one of a select few localities where structural levels below the CBU are exposed (e.g., Avigad et al., 1997). Accordingly, Evia has frequently been targeted to understand the convergent phases of orogenesis related to nappe stacking (e.g., Ring et al., 2007b; Gerogiannis et al., 2021). The record of Oligo-Miocene exhumation on Evia has received comparatively little attention, despite the island occupying the footwall to the North Cycladic Detachment System (NCDS; Jolivet et al., 2010a; **Figure 2.1**). Our data show that mixed coaxial and non-coaxial extensional strain was accommodated within a wide zone immediately below the major nappe-bounding thrust at the base of the CBU. Shearing along this structure facilitated late Oligocene unroofing of the lower unit from its maximum burial depths, before ultimately assisting in exhuming its footwall into the brittle crust by the middle Miocene.

2.3. Tectonic Setting

The Hellenides in Greece comprise thickened crust resulting from Alpine convergence between the African and European plates during Mesozoic to early Cenozoic times (Papanikolaou, 1984; Doutsos et al., 1993; Papanikolaou, 2009). The geology of the Hellenides reflects the closure of multiple branches of the Neotethys and consequent accretion of exotic continental blocks (Jolivet and Brun, 2010). Extension and thinning of the orogen due to slab rollback of the African

plate since *c.* 30 Ma has exhumed subducted fragments of these accreted terranes to form HP-LT metamorphic core complexes (e.g., Lister et al., 1984; Jolivet and Brun, 2010).

The Attic-Cycladic Crystalline Massif is the most extensively studied of these core complexes and is best exposed in the Cycladic archipelago in the central Aegean Sea (**Figure 2.1**). The HP-LT rocks of the CBU constitute the bulk of the HP rocks exposed in the Cyclades, alongside the crystalline rocks situated structurally beneath them (Jacobshagen, 1986). The CBU comprises a thick Triassic-Jurassic carbonate succession intercalated with metaigneous and ophiolitic material recording early Eocene HP metamorphism (Tomaschek et al., 2003; Laurent et al., 2017), and is proposed to be the metamorphosed equivalent of the Pindos Unit (Bonneau, 1984). In the Aegean, the CBU tectonically overlies a pre-Alpine continental basement ("Cycladic Basement;" e.g., Ios, Huet et al., 2009; Sikinos, Augier et al., 2015) or the parautochthonous "Basal Unit" (e.g., Tinos, Avigad and Garfunkel, 1989; Evia, Avigad et al., 1997). The Basal Unit represents a Triassic-Upper Eocene carbonate platform capped by flysch, proposed to be a subducted fragment of the Gavrovo-Tripolitza Unit of the External Hellenides (e.g., Ring et al., 2001).

Exhumation of the CBU was likely initially facilitated by extrusion within the subduction channel, succeeded by systems of ductile-then-brittle low-angle detachment systems operating since the late Oligocene (Lister et al., 1984; Ring et al., 2007a; Jolivet et al., 2010a; Grasemann et al., 2012). At least three distinct phases of ductile deformation may therefore be discriminated within the CBU, relating respectively to subduction, syn-orogenic exhumation, and post-orogenic extension. The first two are represented largely by distributed ductile strain yielding complex isoclinal folds and mylonites, as well as subduction-related structures like the intra-CBU Trans-Cycladic Thrust (**Figure 2.1;** Grasemann et al., 2018; Wind et al., 2020) or the Basal

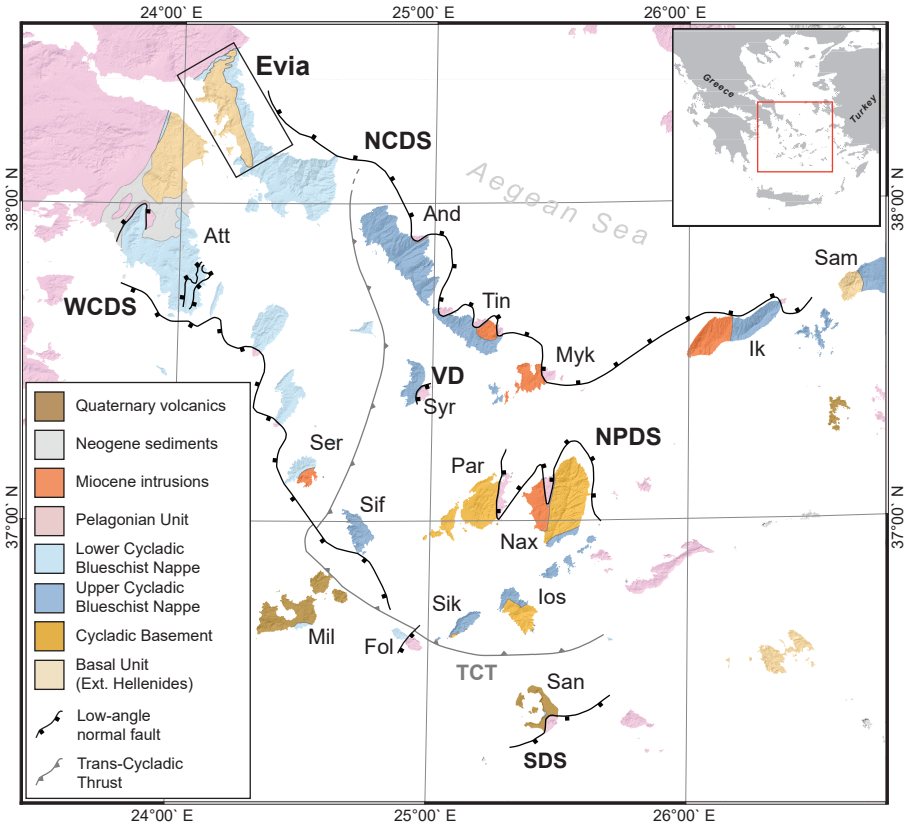

Figure 2.1. Simplified tectonic map of the Greek Cyclades with traces of major regional structures. Box shows location of the study area (Figure 2). Inset: Geographic map of the Aegean Sea. Box shows area of main map. Abbreviations: NCDS: North Cycladic Detachment System (Jolivet, Lecomte, et al., 2010); NPDS: Naxos-Paros Detachment System (Gautier et al., 1993); SDS: Santorini Detachment System (Schneider et al., 2018); TCT: Trans-Cycladic Thrust (Grasemann et al., 2018); VD: Vari Detachment (Trotet et al., 2001); WCDS: West Cycladic Detachment System (Grasemann et al., 2012). Modified after Grasemann et al. (2018) and Coleman et al. (2020).

Thrust/Cyclades-Menderes Thrust dividing the CBU and Basal Unit (Gessner et al., 2001; Gerogiannis et al., 2021). Although some central segments of the detachment systems record distributed deformation in the footwall (Jolivet et al., 2010a; Grasemann et al., 2012), deformation associated with post-orogenic extension was comparatively localized, controlled by low-angle detachments exposed on many Cycladic islands (e.g., Gautier and Brun, 1994; Jolivet et al., 2004). These low-angle structures place the CBU structurally below a hanging wall of Pelagonian Zone klippen (Dürr et al., 1978), which are affected by Cenozoic brittle deformation and fluid infiltration. The major detachment systems in the Cyclades accommodated bivergent extension characterized by ductile-then-brittle, top-to-N to -NE sense of shear along the North Cycladic Detachment System (NCDS; Jolivet et al., 2010a), and top-to-the-SW sense of shear along the West Cycladic Detachment System (Grasemann et al., 2012; **Figure 2.1**). Comparable detachments may also be found accommodating top-to-N extension on Naxos and Paros (Gautier et al., 1993), and top-to-S extension on Santorini and Folegandros (Schneider et al., 2018). The lifespan and structural position of these "Cycladic-style" detachments is locally related to late Miocene plutonism, which is observed to have arrested active detachments and promoted the formation of branches at higher structural levels (e.g., Lecomte et al., 2010; Denèle et al., 2011; Laurent et al., 2015).

The geodynamic history of the Basal Unit is comparatively poorly understood. Subduction of the paleogeographic precursor to the Basal Unit, the Gavrovo-Tripolitza Unit, is proposed to have initiated between 35-30 Ma (Sotiropoulos et al., 2003). The Basal Unit occupies tectonic windows in interior parts of the orogen, such as on Mt. Olympos, Evia, and Samos, and contains evidence for overprinted HP-LT metamorphic assemblages of alleged Oligocene to early Miocene age (Schermer, 1989; Shaked et al., 2000; Ring et al., 2001; Ring et al., 2007b; Gerogiannis et al.,

2021). Thrusting of the CBU atop the Basal Unit is inferred from paleogeographic correlations and the consistent tectonostratigraphic relationship between the units (e.g., Katsikatsos et al., 1982; Xypolias et al., 2003; Gerogiannis et al., 2021). Little is known directly of the conditions and timing of underthrusting and subsequent exhumation of the Basal Unit. Most studies consider the upper contact of the Basal Unit with the CBU to represent the original thrust, with or without later extensional reactivation (Schermer, 1989; Ring et al., 2007b).

2.3.1 Geological framework of Evia

Evia island is situated in the footwall of the NCDS, at the northwestern termination of this crustal-scale structure (Jolivet et al., 2010a; **Figure 2.1**). Southern Evia consists almost entirely of the CBU and underlying Basal Unit (**Figure 2.2**). In local nomenclature, the HP units of Evia are divided into the metacarbonate-dominated Styra Unit, and the primarily mafic metavolcanic Ochi Unit (Avigad et al., 1997). The Styra Unit is by consensus correlated with the CBU, though controversy exists as to whether the Ochi Unit shares this affiliation or is an extension of the Makrotantalon Unit of Andros (e.g., Papanikolaou, 1987; Xypolias and Alsop, 2014). The Basal Unit is situated structurally below these units in the Almyropotamos tectonic window (Katsikatsos, 1991a; Shaked et al., 2000). A purported nummulitic hard ground of Ypresian-Lutetian (Lower-Middle Eocene) age at the top of the Basal Unit marble sequence on Evia is the basis of the middle Eocene maximum depositional age imposed on the overlying metaflysch package (Dubois and Bignot, 1979).

A third unit, the Tsakei Unit, has been defined as occupying the intermediate structural levels between the CBU and Basal Unit, and its exposure is limited to the southern half of the tectonic window (Katsikatsos et al., 1991a; Shaked et al., 2000). The Tsakei Unit comprises predominantly pelitic schist interspersed with meter- to hundred meter-scale blocks of marble, metabasite, and

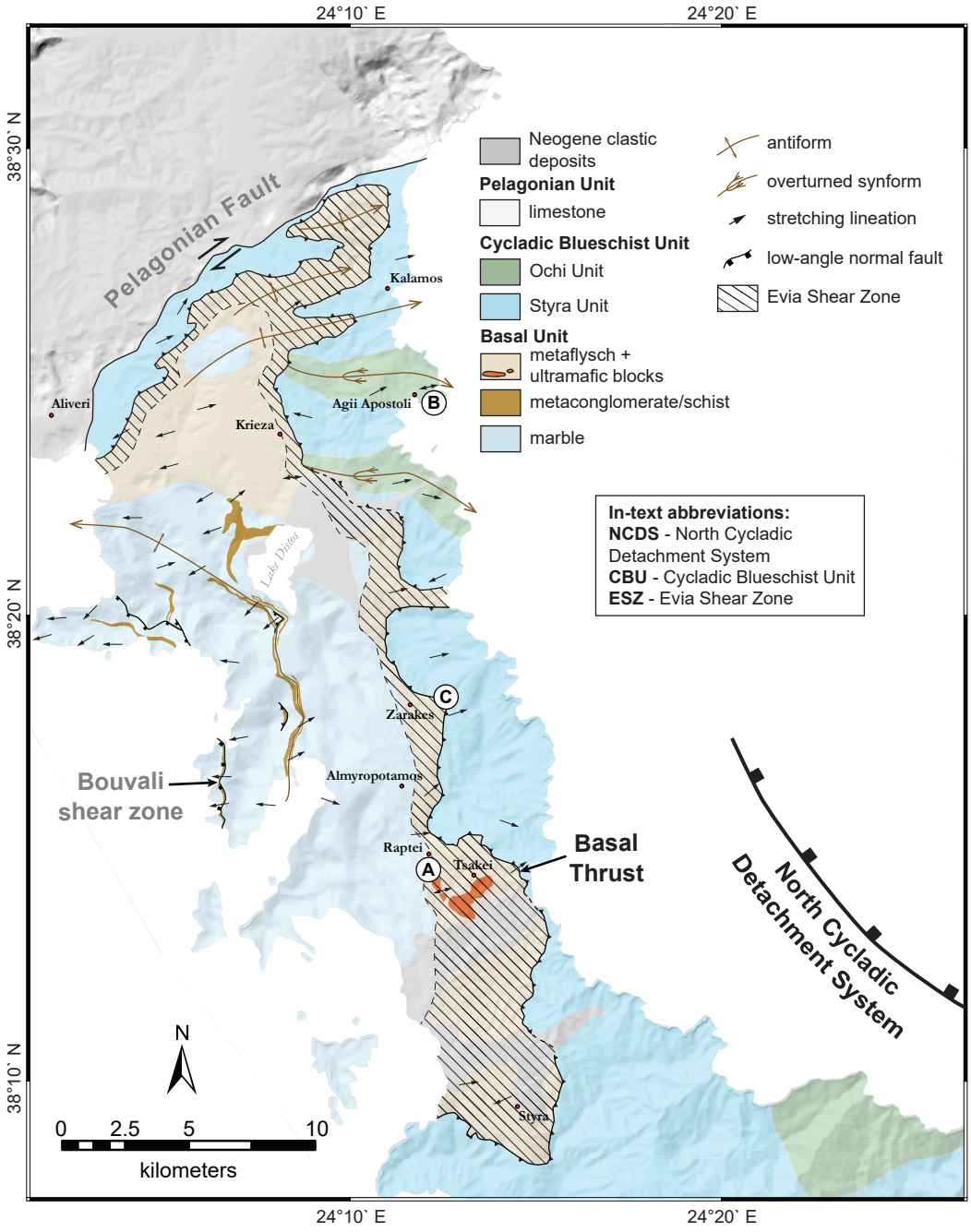

Figure 2.2. Geological map of southern Evia, Greece. Sampling locations for pressure-temperature modeling indicated: (a) albite-pumpelleyite schist (sample EV19-03); (b) glaucophane schist (sample EV19-10); (c) albite-mica schist (sample EV19-17C). Modified after Katsikatsos (1991a, 1991b).

serpentinite (Katsikatsos et al., 1991a). It has been variably interpreted as representing the base of the CBU (e.g., Ring et al., 2007b) or the top of the Basal Unit (e.g., Shaked et al., 2000). The former interpretation consequently places the Basal Thrust at the base of the Tsakei Unit toward the southern extent of the window, and at the base of the Styra Unit in the north, with the structure gradually cutting down-section into Basal Unit. Meanwhile, Shaked et al. (2000) considered the Tsakei Unit and Basal Unit metaflysch as a single unit, thereby placing the thrust contact consistently at the base of the Styra Unit.

As implied by the preceding discussion, for much of its length the Basal Thrust, and thus the first appearance of Basal Unit, is an inferred boundary. Xypolias et al. (2003) has reported the only structural description of the thrust on southern Evia, interpreting a 5 m thick mylonite to represent the structure along the northern boundary of the tectonic window. This description is consistent with that of corresponding structures elsewhere (e.g., Mt. Olympos; Schermer, 1989). Nevertheless, a comprehensive description of broader thrust-related structures developed peripheral to the Basal Thrust as exposed on Evia is not available. It has therefore generally been assumed that the island-scale configuration of both the hanging wall and footwall to the Basal Thrust reflect structures associated with thrusting. Subsequent extensional reactivation of the Basal Thrust was reported by Ring et al. (2007b), but data presented thus far seemingly indicate that this event contributed only marginally to the tectonic evolution of the island (Ring et al., 2007b; Gerogiannis et al., 2021).

In the footwall of the Basal Thrust, the internal architecture of the tectonic window has been the subject of extensive structural and bedrock mapping efforts. The Almyropotamos tectonic window is commonly depicted as a N-S trending, upright open antiform core, sometimes termed the 'Almyropotamos antiform' (Katsikatsos et al., 1991a; Xypolias et al., 2003; Gerogiannis et al.,

2021). Smaller km-scale folds with E-W trends have been interpreted either as continuous with similar structures in the hanging wall (**Section 2.3.1**; Katsikatsos et al., 1991a), or as having been rotated from an initial N-S orientation during dextral transpression along the Pelagonian Fault (**Figure 2.2**; Xypolias et al., 2003). Xypolias et al. (2003) and Gerogiannis et al. (2021) both viewed the Almyropotamos antiform as a fault-related fold generated by displacement along a major syn-orogenic ductile shear zone. Gerogiannis et al. (2021) furthermore delineated several normal-sense top-to-W shear zones (e.g., Bouvali shear zone) at upper structural levels of the western limb.

Pressure-temperature (PT) data available for Evia provide estimates of at least 10–12 kbar and 350–450°C for peak metamorphism across both the CBU and Basal Unit (Shaked et al., 2000; Katzir et al., 2000). Further evidence for HP-LT metamorphism of the Basal Unit includes high-Si white mica, glaucophane relics in albite porphyroblasts, and topotactic pseudomorphs of calcite after aragonite (Shaked et al., 2000; Gerogiannis et al., 2021). Limited white mica and biotite $^{40}Ar/^{39}Ar$ geochronology (Ring and Reischmann, 2002; Ring and Layer, 2003) and Rb-Sr amphibole and white mica isochron ages (Ring et al., 2001; Ring et al., 2007b) has led workers to propose that the CBU on Evia records Eocene syn-orogenic exhumation, whereas the Basal Unit preserves Oligo-Miocene dates recording its own HP-LT metamorphic event. Within this model, HP-LT metamorphism of the Basal Unit coincided with a greenschist facies overprint in the CBU. Lower-temperature cooling in the study area is constrained by a single zircon fission track age of 17.8 ± 0.9 Ma (Ring et al., 2007b).

2.4. Structure of southern Evia

We conducted new field mapping and structural analyses in, and adjacent to, the Almyropotamos tectonic window. The window forms an irregular curvilinear lithological and structural

discontinuity spanning the study area (**Figure 2.2**; Katsikatsos et al., 1991a,b; Shaked et al., 2000; Xypolias et al., 2003). The boundary of this tectonic contact is interpreted to correspond to the Basal Thrust, also known as the Evia Thrust (Xypolias et al., 2003). Hereafter, we adopt the interpretation of Shaked et al. (2000), as we likewise observe a broad compatibility in lithological composition and meso- to micro-scale structural features across the two units, and note multiple instances where schists mapped within the Tsakei Unit lie atop the Basal Unit marbles with no evidence of major tectonic discontinuity. Accordingly, in all following discussion, we consider the Tsakei Unit as part of the uppermost tectonostratigraphic unit of the footwall.

2.4.1. Hanging wall - Cycladic Blueschist Unit

The CBU forms the hanging wall of the tectonic window and is extensively exposed in the eastern half of the study area (**Figure 2.2**). Schistose and quartzitic lithologies of both the Styra and Ochi units commonly preserve pristine or minimally retrogressed HP-LT mineral assemblages, including euhedral glaucophane, epidote, and high-Si phengite. Retrogression in these rocks is generally represented by chlorite and post-kinematic albite porphyroblasts overgrowing mica-dominated microlithons (Shaked et al., 2000).

The internal structure of the CBU near the Almyropotamos window broadly adheres to that outlined by Xypolias et al. (2012) for southernmost Evia. Planar-foliated cipolin marbles sparsely interspersed with pelitic schist belonging to the Styra Unit compose the majority of the hanging wall exposure. Mesoscale, S- to SSW-vergent synformal folds with gentle easterly plunges control the distribution of the overlying Ochi Unit metabasic and psammitic lithologies (Katsikatsos et al., 1991a; **Figure 2.2**), which are complexly interwoven with Styra marbles and dominate coastal exposures in the east. Re-folding of initially upright folds about gently NE-dipping axial planes has resulted in type-III refolds with various interference patterns that are commonly visible at the

outcrop scale (Xypolias et al., 2012). Most coarse grained cipolin marbles (calcite grains up to 2 mm) of the Styra Unit are highly deformed and show the distinctive greenish-white metamorphic layering. Exclusively at the lowest structural levels of these marbles, quarter-folds and rotated and stretched quartz veins record top-to-WSW shear sense (**Figure 2.3a-b**). At higher structural levels the shear sense is reversed and records consistent top-to-ENE shear sense throughout the Styra Unit (**Figure 2.3c**). Mylonitic foliations in Styra Unit marbles and schists are pervasively overprinted by isolated shear bands up to several meters in length and penetrative S/C/C' fabrics recording a consistent top-to-E to -NE shear sense (**Figure 2.3d**).

2.4.2. Footwall – Basal Unit

The CBU is situated atop a footwall composed of pelitic schists belonging the uppermost metaflysch package of the Basal Unit, including the Tsakei Unit as previously defined (Katsikatsos et al., 1991a,b; **Figure 2.2**). Here we discriminate between two broad structural domains within the footwall. The first of these ('Upper Domain') is restricted to the uppermost structural levels of the Basal Unit, coinciding with the majority of the exposed thickness of the metaflysch package and only infrequently extending into the uppermost ~50 m of the Basal Unit marble. This zone comprises typical flyschoid lithologies, including pelitic schists and quartz-rich schists or metapsammites, as well as subordinate impure schistose marbles and localized phyllonites. Dispersed throughout this package are meter- to hundred meter-scale blocks of marble and a range of metabasic lithologies including metagabbro, metabasalt, talc-schist, and serpentinite. The metabasic suite is most prominently exposed near the village of Tsakei (**Figure 2.2;** Katsikatsos et al., 1991a). Foliation in these rocks is generally sub-horizontal, though at the scale of an outcrop may undulate to more moderate dips and sometimes includes flat-lying, intrafolial tight to isoclinal folds. More complex structures are locally observed, generally reflecting re-folding of earlier,

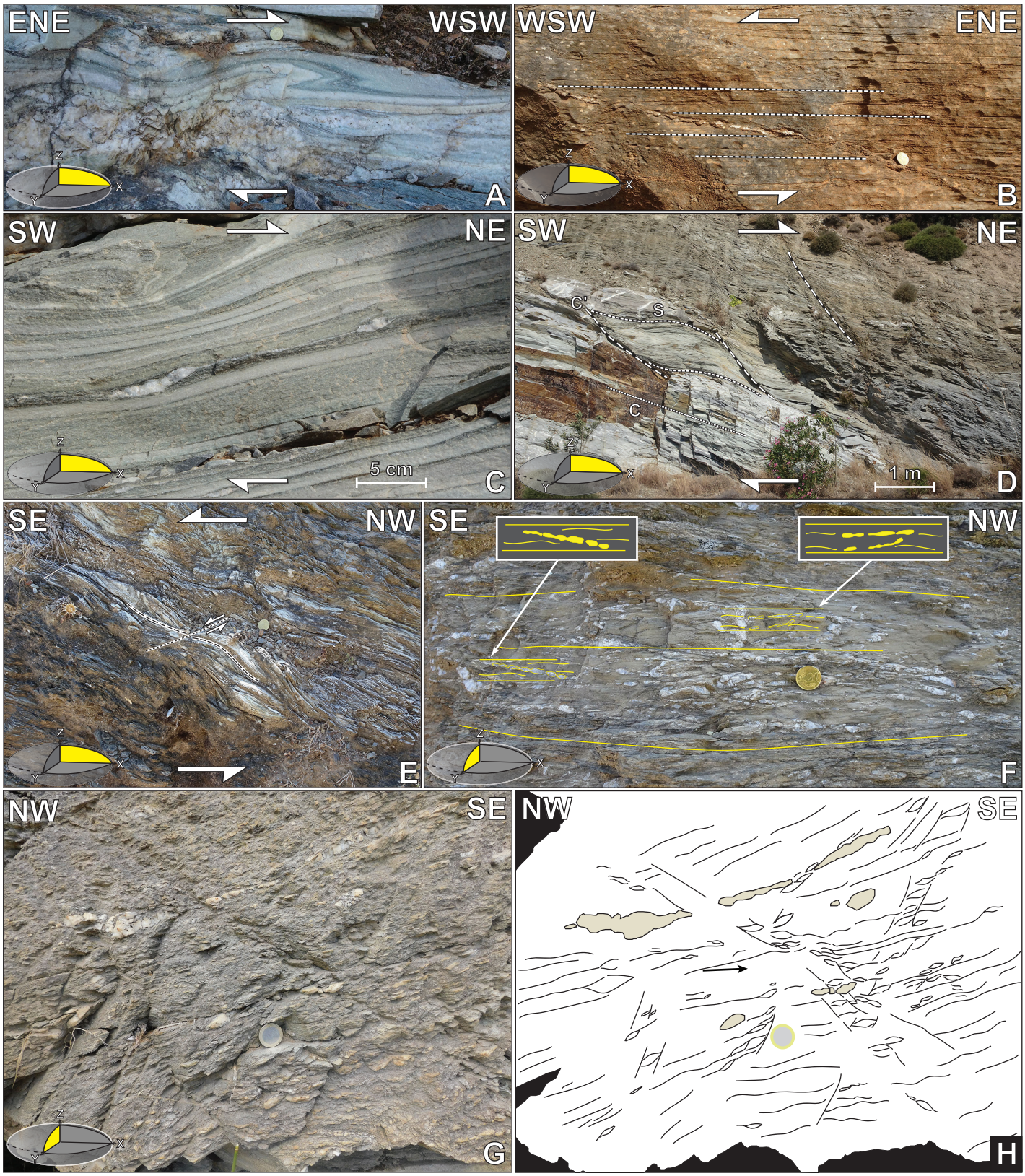
ENE
WSW
A
WSW
ENE
B
SW
NE
5 cm
C
SW
NE
C'
S
C
1 m
D
SE
NW
E
SE
NW
F
NW
SE
G
NW
SE
H

Figure 2.3. (previous page) Field photographs from the CBU and Upper Domain of the Basal Unit on Evia, Greece. (A) Quarter-fold in mylonitic marbles indicating top-to-WSW shear sense at lowermost structural levels of the Styra Unit (259110 E, 4224083 N). Main foliation dips toward 215°/15° recording a stretching lineation oriented 07°–246°. (B) Pinched-and-swelled quartz vein that has undergone ~200% stretching and been rotated into the shear direction, giving a top-to-WSW shear sense. Located at the basal parts of the Styra Unit (258533 E, 4223238 N). The foliation dips toward 180°/17° with a stretching lineation 07°–245°. (C) Highly stretched quartz sigmoid from upper structural levels of the Styra Unit. Shear sense here is consistently top-to-NE (259310 E, 4222016 N). The mylonitic foliation dips 253°/23° with a stretching lineation 24°–247°. (D) High-grade fabrics in Styra marbles and schists are pervasively overprinted by cooler ductile to brittle shear bands and S/C/C′ fabrics, deforming the mylonitic foliation into sigmoidal lenses (264761 E, 4218921 N). The main foliation (C-planes) dips toward 052°/19° with shear bands and C′-planes dipping toward 067°/46° and recording a top-to-ENE shear sense. (E) Shear band in talc-schists in metabasic blocks within the Basal Unit metaflysch (255061 E, 4236123 N). The foliation (C-plane) dips toward 320°/19° and the shear band (C′-plane) dips toward 015°/20° indicating top-to-E shear. (F) On an exposure perpendicular to the stretching lineation (YZ-section) pinch-and-swell stretched quartz veins parallel to the foliation indicate a strong elongation component parallel to the Y-direction. The oblate finite strain ellipsoid is confirmed by oblique pinch-and-swell quartz veins dipping at shallow angles toward the NW and SE, respectively (255022 E, 4236263 N). (G, H) Conjugate brittle/ductile high-angle faults overprinting phyllonitic foliation immediately below the boundary of the tectonic window at the NW extent of the study area (243193 E, 4254286 N). The conjugate fault set suggests NW-SE extension under brittle-ductile conditions. Note the pinch-and-swell stretching of quartz veins parallel to foliation (300°/26°) and perpendicular to the lineation. Scales: 20¢ coin (A, B, E, and F)—22.25 mm diameter; 1€ coin (G and H)—23.25 mm diameter.

more steeply inclined folds and veins about sub-horizontal axial planes, and an incipient to tightly-spaced sub-horizontal solution cleavage. The highly anisotropic phyllites and schists within this package commonly preserve shear bands, S/C, and S/C/C' fabrics demonstrating a general top-to-E or -NE shear sense (**Figure 2.3e**).

Dense quartz veining is a common structural feature of this domain. Individual veins are in large part parallel to the foliation and are locally affected by folding. Scattered exposures, with no obvious relationship to structural level within the metaflysch package, host veins that have pervasively accommodated stretching and form pinch-and-swell or boudinage structures that are oblique to the host foliation (**Figure 2.3f**). In exposures normal to the stretching lineation (i.e., YZ sections), vein sets are often observed 'climbing' the foliation at small angles in both directions, consistent with rotational transposition during overall flattening. Structures of this type are commonly developed alongside symmetrical foliation boudinage in lineation-parallel (XZ) sections. These extensional structures are widely distributed throughout the thickness of the metaflysch, and the obliquity of the stretched veins suggests that the foliations cross-cut by these structures are likewise associated with this horizontal stretching. Brittle-ductile to brittle conjugate high-angle faults in YZ planes (**Figure 2.3f-g**) indicate horizontal extension in the Y-direction under relatively cooler conditions (Platt and Vissers, 1980; Choukroune et al., 1987).

The second structural domain of the footwall ('Lower Domain') lies structurally below the metaflysch-dominated zone and encompasses the pure, medium to coarse crystalline calcite-dominated Basal Unit marble sequence and <100 m thin horizons of impure schistose marble, meta-sandstones, and meta-conglomerates. The apparent repetition of schist and metaconglomerate horizons within the marble, locally over widths of only hundreds of meters, suggests that these units are isoclinally folded within the marbles. Such a relationship is clearly

visible in satellite imagery (e.g., UTM zone 35S 248631E, 4247311N) and in isoclinal folds in the marbles and the metaconglomerates. The isoclinal folds have W-E to SW-NE trending fold axes, which are parallel to the stretching lineation of the highly sheared marbles, and axial planes parallel to the gently dipping mylonitic foliation (**Figure 2.4a-b**). A top-to-W to -SW shear sense is recorded by the mylonites (**Figure 2.4c-d**), with consistent shear sense maintained across both limbs. The sheared and isoclinally folded stack is further deformed into E-vergent, overturned tight folds with amplitudes and wavelengths of several hundreds of meters, which can be mapped following the metaconglomerate layers in satellite images (e.g., the hinge of an antiform visible at UTM zone 35S 250372E, 4242502N). At the outcrop-scale, the overprinting folds can be mapped by tracing the angle between a newly-developed axial plane cleavage and by S-, Z-, and M-folds (**Figure 2.4e-f**). These folds have subhorizontal fold axes trending N-S and gently to moderately W-dipping axial planes, which deform earlier isoclinal folds (with W-E trending axes) into outcrop- and map-scale type-II refold structures resulting, depending on the exposure, in mushroom, hook, and crescent interference patterns (**Figure 2.4g**).

During exhumation of the Basal Unit through the brittle-ductile transition, some of the W-to S-dipping schist and metaconglomerate layers have been reactivated as extensional top-W to top-S brittle-ductile shear zones. Deformation here manifests primarily in S/C/C' fabrics and shear bands (**Figure 2.4h**). Slickenfibres indicate that some shear bands acted as slip surfaces, which also indicate top-W extension (**Figure 2.4h inset**). The latest deformation is related to purely cataclastic top-E thrusting localized within the W-dipping metaconglomerate layers. Fault rocks in these structures are cohesionless ultracataclasites with internal clay gouge layers, which act as detachment horizons along which cataclastic lenses form duplex structures and antiformal stacks (**Figure 2.4i**).

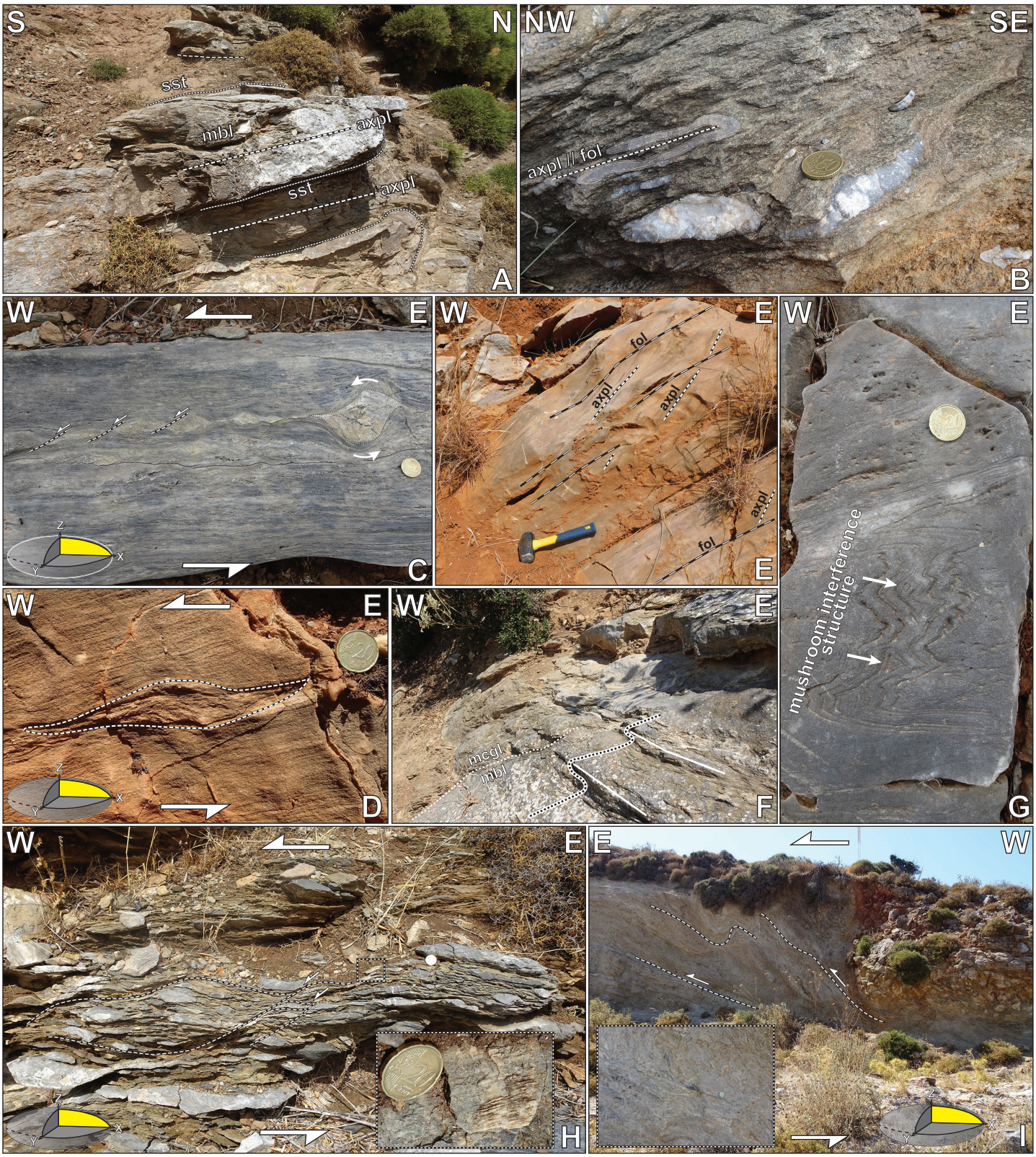
S
N
sst
mbl
axpl
sst
axpl
A
NW
SE
axpl // fol
B
W
E
C
W
E
fol
axpl
axpl
axpl
fol
E
W
E
mushroom interference structure
G
W
E
D
W
E
mcgl
mbl
F
W
E
H
E
W
I

Figure 2.4. (previous page) Field photographs from the Lower Domain of the Basal Unit on Evia, Greece. (A) Isoclinally folded marble and metasandstones (245240 E, 4247614 N) with fold axes (long dashed lines) parallel to the stretching lineation (09°–250°) and axial planes parallel to the general dip of the mylonitic foliation (240°/12°). (B) Isoclinal folding of a mm-scale marble layer within metaconglomerate (247279 E, 4238221 N). The fold axis is roughly parallel to the stretching lineation (21°–281°), and its axial plane is parallel to the general dip of the main foliation (302°/26°). (C) Shear band boudinage of dolomite in calcite marble mylonites indicating top-to-W ductile shearing (247106 E, 4239259 N). The rightmost boudin segment has developed into a winged inclusion confirming top-W ductile shearing. The mylonitic foliation dips 292°/38° and records a clear stretching lineation (28°–274°). (D) Sigmoidal carbonate schist layer in a mylonitic calcite marble recording top-to-W shear sense (249480 E, 4246369 N). The mylonitic foliation dips 228°/24° and records a stretching lineation oriented 21°–260°. (E) Penetrative axial planar cleavage (axpl) dipping at a steeper angle than the mylonitic foliation (fol) suggesting that this location occupies the upper limb of an E-vergent overturned fold (250608 E, 4242008 N). (F) Higher-order, S-shaped folds at the border between marbles and metaflysch in the overturned limb of an E-vergent antiform (250372 E, 4242502 N). The subhorizontal fold axis trends 05°–006° with an E-vergent axial plane dipping 284°/33°. (G) Type-II refold structure showing a mushroom interference pattern (248502 E, 4238591 N). The second fold axis trends 12°–345°and the M-shape suggest that this is a higher-order fold lying close to the hinge of an E-vergent overturned synform. (H) Ductile reactivation of metaconglomerate layers as top-to-W shear zones showing m-scale ductile shear bands dipping 280°/47° (247056 E, 4239251 N). Inset: Shear band reactivated as a brittle slip surface with slickenfibers trending 48°–282° recording top-to-W extension. (I) Cohesionless cataclasites localized in W-dipping schistose layers dipping 276°/24°. An E-vergent detachment fold is developed above a shallow-dipping detachment comprising clay gouge, demonstrating brittle top-to-E thrusting (249767 E, 4242663 N). Distance from base to top of outcrop is approximately 5m. Inset: Close-up of aforementioned gouge layer. Scale: 20¢ coin (A, C, D, G, H, I inset)—22 mm diameter; 50¢ coin (B)—24 mm diameter; hammer (E)—27 cm long; pen (F)—10 cm long.

2.5. Thermodynamic modelling

In order to evaluate existing PT estimates for Evia within the context of modern thermodynamic modelling techniques, we analyzed metamorphic rocks from different structural positions on the island. Three samples were selected after careful petrographic observation of mineral assemblages and their textural equilibrium to ensure the validity of the models (**Figure 2.2**). One from the base of the structural pile sample initially considered for modelling was discounted due to mineral disequilibrium and the absence of limiting assemblages. Detailed petrological and mineral chemical analyses were conducted for each sample using transmitted light petrography, scanning electron microscope backscatter electron (SEM-BSE) imaging, and electron microprobe (EMP) at the University of Uppsala (Uppsala, Sweden) and University of Ottawa (Ottawa, Canada). These data were used alongside whole-rock compositions acquired by X-ray fluorescence (XRF) to construct pseudosections for each sample using the thermodynamic modelling software Perple_X version 6.9.1 with the internally consistent thermodynamic dataset hp62ver.dat (Connolly, 2011; Holland and Powell, 2011). Models for all samples assumed H_2O saturation, with O_2 fugacity set to 0 for samples EV19-03 and EV19-17C due to the low abundance of Fe^{3+}-bearing phases in these samples. Meanwhile, models assumed an O_2 fugacity of 0.05 for sample EV19-10, as this optimally replicated both the measured mineral compositions and their abundance in the sample. Whole-rock geochemistry for each sample is reported in **Table S2.1** and mineral chemistry for the relevant phases is summarized in **Table S2.2**. Detailed pseudosections for each sample are presented in **Figure S2.1, S2.2,** and **S2.3**. Detailed analytical methodologies for bulk-rock geochemistry and EMP, as well as a list of solid solution models used, are presented in **Appendix A**.

2.5.1. Albite-pumpellyite schist (sample EV19-03)

Sample EV19-03 is an albite-pumpellyite schist from within metaflysch in the Upper Domain of the footwall near the Tsakei ultramafic blocks (**Figure 2.2**). The essential mineralogical constituents of the sample are white mica + quartz + albite + epidote + chlorite + pumpellyite + titanite + Ca-amphibole ± apatite (**Figure 2.5a**). Two generations of white mica are evident: the first defines foliation and has a high celadonite component (Si apfu: 3.32–3.53), whereas the second occurs as inclusions within epidote porphyroblasts and is muscovitic in composition (Si apfu: 3.13–3.24; **Figure 2.6a**). Porphyroblasts of pumpellyite, epidote, Ca-amphibole, and albite are dispersed throughout the groundmass. All of these phases preserve inclusions of relic lawsonite, and sodic amphibole is present in the cores of albite porphyroblasts (**Figure 2.5b**). Lawsonite inclusions are found primarily near the rims of the porphyroblasts, co-existing with inclusions of actinolite, chlorite, and titanite. Textural relationships suggest at least the latest stages of porphyroblast growth were post-kinematic. Pumpellyite forms equant rectangular porphyroblasts within the matrix, whereas epidote occurs as irregular relic grains generally near the margins of albite porphyroblasts. Epidote is compositionally homogeneous as zoisite or clinozoisite (Al apfu: 2.75–2.96; **Table S2.2**). Chlorite is present in small volumes and intergrown with the micaceous foliation, with compositions ranging from clinochlore to pycnochlorite (Si apfu: 5.61–5.94; X_{Mg}: 0.78–0.81; **Figure 2.6b**). Calcic amphibole is actinolite (X_{Na}: 0.03–0.11, X_{Mg} <0.2) and forms elongate prismatic crystals parallel to foliation (**Figure 2.6d**).

Sample EV19-03 was modelled in the Na_2O-MgO-Al_2O3-SiO_2-K_2O-CaO-TiO_2-MnO-FeO system, yielding results consistent with prehnite-actinolite to lower greenschist facies metamorphism under moderately elevated pressures of 310 ± 15°C and 7 ± 1 kbar. Mineral phases preserved as inclusions allude to an earlier, HP metamorphic paragenesis. Lawsonite relics support

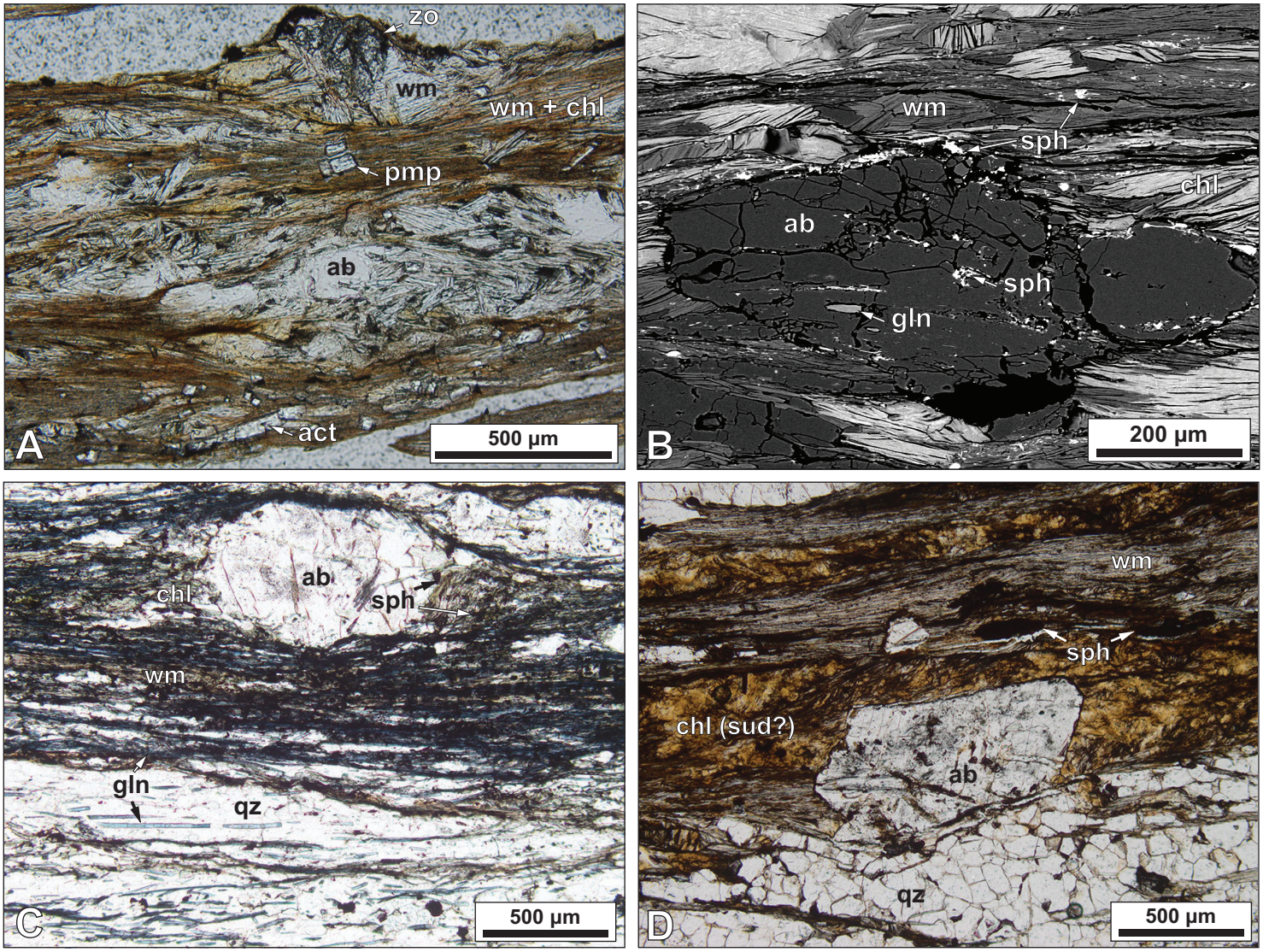

Figure 2.5. Photomicrographs showing the critical phase assemblages from rocks on Evia, Greece, considered for pressure-temperature calculations. (A; UTM: N 4236493, E 254695) Plane-polarized light (PPL) micrograph and (B) BSE image from sample EV19-03. (C; UTM: N 4254655, E 255728) PPL micrograph from sample EV19-10. (D; UTM: N 4242970, E 256031) PPL micrograph from sample EV19-17C. Refer to text for complete sample descriptions. Abbreviations: ab: albite; act: actinolite; chl: chlorite; gln: glaucophane; pmp: pumpellyite; sud: sudoite; ttn: titanite; qz: quartz; wm: white mica; zo: zoisite.

a range of plausible prograde paths for heating through lawsonite-bearing assemblages at lower temperatures, whereas glaucophane inclusions suggest that the rocks likely attained peak pressures in excess of ~8 kbar (**Figure 2.7a**; Holland, 1988).

2.5.2. Glaucophane schist (sample EV19-10)

Sample EV19-10 is a protomylonitic glaucophane schist from blueschist exposures near the town of Agii Apostoli, attributed to the Ochi Unit (**Figure 2.2;** Katsikatsos et al., 1991a). Surrounding rocks are dominated by intensely folded LS- and S-tectonites containing abundant glaucophane ± epidote (**Figure 2.5c**). Essential mineralogical constituents of the sample are glaucophane + white mica + albite + quartz + chlorite + titanite ± apatite ± biotite. The sample displays a penetrative foliation defined by mm-scale bands of acicular glaucophane, white mica and chlorite alternating with ribbons of quartz recrystallized by subgrain rotation (Passchier and Trouw, 2005). Accessory phases in the ferromagnesian-rich microlithons include albite, titanite, rutile, epidote, and apatite. Albite (An_{0-2}) forms small (<200 μm) porphyroblasts. Amphibole is sodic (Na_B: 1.70–1.95) with X_{Mg} <0.25 (0.14–0.24), and variable $Fe^{3+}/(Fe^{3+} + Al^{VI})$ between 0.13–0.80 (mean: 0.39). Most specimens plot around the ferroglaucophane-crossite division (0.13–0.5; mean: 0.29), but four analyses approach riebeckitic compositions (0.58–0.80; mean: 0.68). White mica in the sample is phengite (Si apfu: 3.52–3.60; X_{Mg}: 0.36–0.65; **Figure 2.6b**), and is sparsely overgrown by annitic biotite (X_{Mg}: 0.30–0.32; **Table S2.2**).

Sample 19-10 was modelled in the Na_2O-MgO-Al_2O_3-SiO_2-K_2O-CaO-TiO_2-FeO system. Models assumed an O_2 fugacity of 0.05, as this optimally replicated both the measured amphibole compositions and low observed abundances of jadeitic pyroxene in the sample. Manganese was omitted from the calculation because its inclusion over-stabilized garnet in initial models. An estimate of 460 ± 20°C and 12 ± 1 kbar is obtained using amphibole and white mica compositions,

further constrained by the restricted compositional range of albite and modal abundance isopleths determined for the sample. These conditions are consistent with the minimally retrogressed blueschist facies mineral assemblage, observed quartz microstructures, and previous estimates from southern Evia (Shaked et al., 2000; Katzir et al., 2000).

2.5.3. Albite-mica schist (sample 19-17C)

Sample 19-17C is an albite-mica schist collected 3 km east of the town of Zarakes (**Figure 2.2**). The sample mineralogy consists of white mica + albite + chlorite + quartz + titanite (**Figure 2.5d**). Whereas it is situated structurally below an exposure of Styra marble, we consider the sample to be within the Upper Domain metaflysch. The sample was modelled using thermodynamic properties for sudoite-group minerals after Lanari et al. (2014); a detailed description of the sample and modelling results are reported in **Appendix A**. The constructed pseudosection and calculated stability field are presented in **Figure 2.7c**.

The estimated PT conditions for this sample may be spurious, which we attribute to the poorly constrained behaviour of an unusual and abundant chlorite-like ('Na-bearing sudoite') phase. Independent of its tectonostratigraphic affinity, the PT conditions determined for the sample (520 ± 20°C, 10 ± 1 kbar) correspond to higher temperatures than any existing estimate for either unit on Evia. This, alongside a decoupling between predicted and experimentally determined mineral compositions and the presence of the aforementioned difficult-to-constrain chlorite specimen, prompts us to discount this sample from further discussion.

2.6. $^{40}Ar/^{39}Ar$ geochronology

In an attempt to expand the geochronological framework for southern Evia and better understand the timing of cooling and/or strain localization in the vicinity of the Almyropotamos

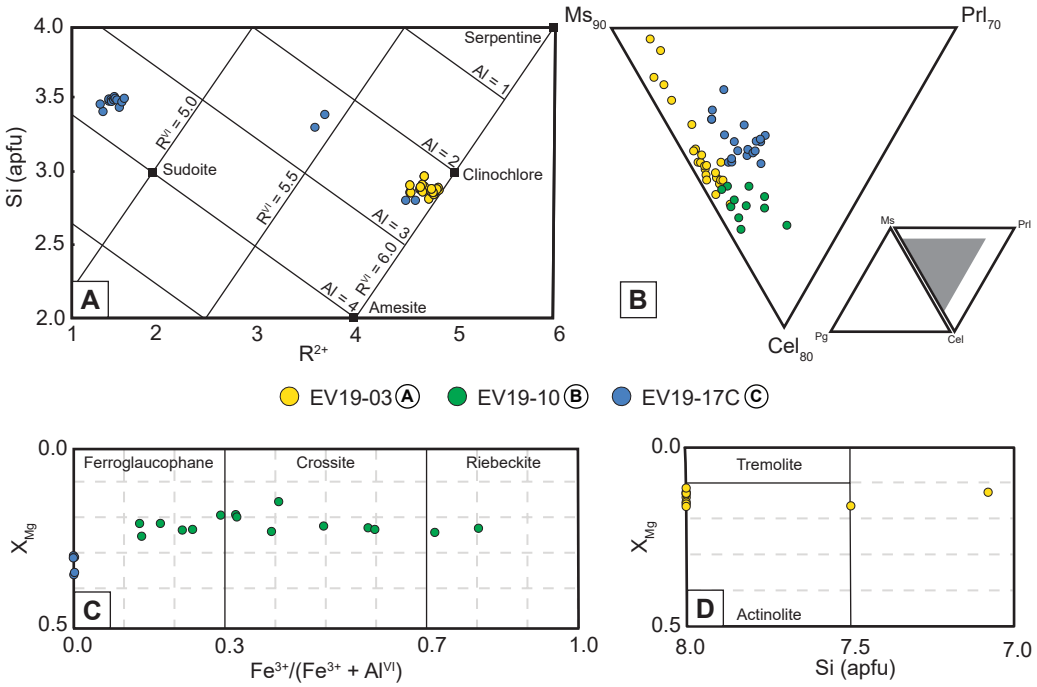

Figure 2.6. Compositional diagrams for mineral phases used in thermodynamic modeling. (A) Projected chlorite discrimination diagram using Si apfu versus divalent cation apfu after Wiewióra and Weiss (1990). (B) Abbreviated white mica ternary diagram. (C and D) Abbreviated sodic (C) and calcic (D) amphibole compositional diagrams after Hawthorne et al. (2012).

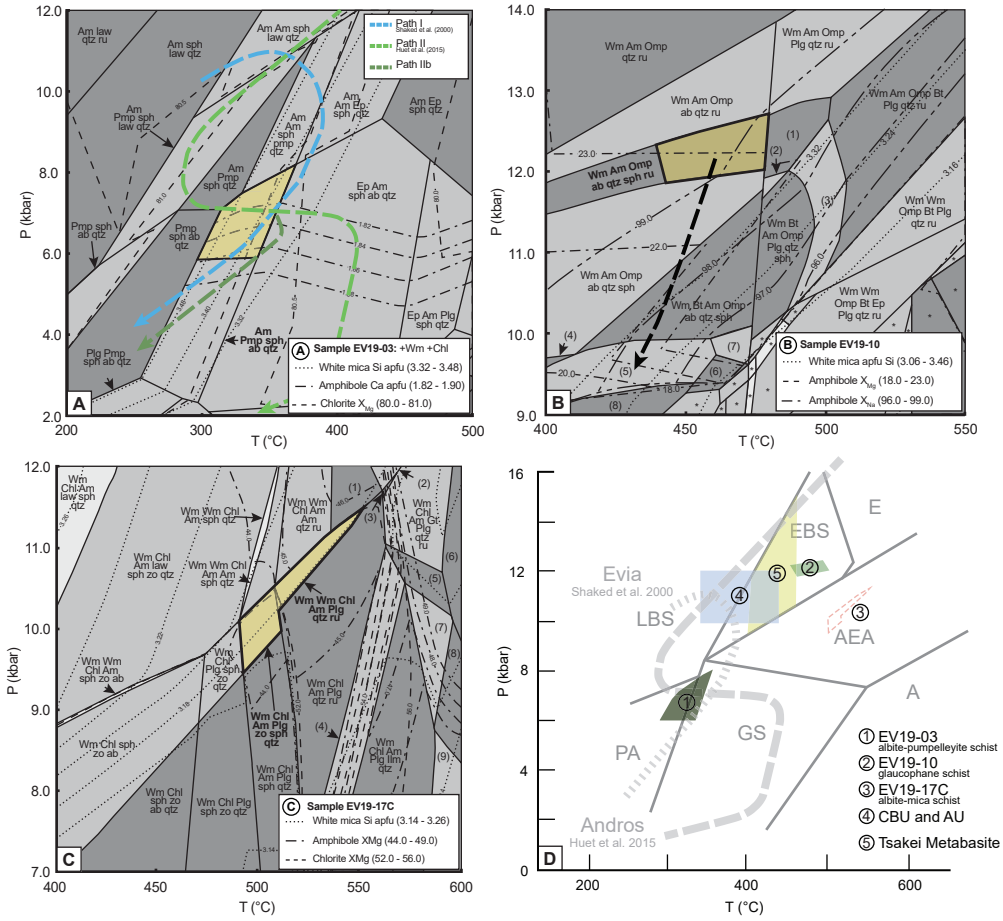

Figure 2.7. Thermodynamic modeling results for samples from southern Evia, Greece. (a) Pseudosection for sample EV19-03 (Basal Unit metaflysch). Superimposed arrows represent PT paths (Path I after Shaked et al. [2000]; Path II after Huet et al. [2015]) demonstrating that the present mineral assemblage may be consistent with either retrograde decompressive cooling or with isobaric heating. Path IIb shows an alternative path assuming the Basal Unit resumed decompressive cooling earlier into the phase of isobaric heating. See text for further discussion. (b) Pseudosection for sample EV19-10 (CBU). Mineral assemblages and compositions are consistent with conditions of 12 ± 1 kbar and 460 ± 20°C. (1) Wm-Am-Omp-Plg-ttn-q-ru; (2) Wm-Am-Omp-Plg-ttn-qtz; (3) Wm-Bt-Am-Omp-Plg-ttn-qtz-ru; (4) Wm-Stp-Am-Omp-ttn-ab-qtz; (5) Wm-Bt-Stp-Am-Omp-ttn-ab-qtz; (6) Wm-Bt-Stp-Ep-Am-Omp-ttn-ab-qtz; (7) Wm-Bt-Ep-Am-Omp-ttn-ab-qtz; (8) Wm-Bt-Stp-Ep-Omp-ttn-ab-qtz. (c) Pseudosection for sample EV19-17C (Basal Unit). Mineral assemblages and compositions indicate peak conditions of 10 ± 1 kbar and 520 ± 20°C. (d) Schematic diagram showing relative positions of new PT calculations with previously reported estimates (1–3, this study; 4, Shaked et al., 2000, 5, Katzir et al., 2000). Pressure-temperature-time (PTt) paths formulated for Andros (dashed line; Huet et al., 2015) and Evia (dotted line; Shaked et al., 2000) are superimposed. Mineral shorthands with capitalized first letter represents a modeled solid solution, whereas lowercase symbols represent a single phase. Abbreviations: PA: pumpellyite-actinolite facies; GS: greenschist facies; A: amphibolite facies; LBS: lawsonite blueschist facies; AEA: albite epidote amphibolite facies; EBS: epidote blueschist facies; E: eclogite facies. Facies boundaries after Evans (1990); note that the facies boundaries shown are intended for basaltic protoliths, but were used here to maintain consistency with previous PT syntheses. Complete pseudosections for each sample and field labels marked with (*) are reported in Figures S2.1–S2.3 of the appendix.

tectonic window, we analyzed white mica from nineteen samples spanning all structural levels of the Basal Unit and CBU using multiple single-grain total fusion $^{40}Ar/^{39}Ar$ geochronology (e.g., Schneider et al., 2018; Uunk et al., 2018; **Figure 2.8**, **Table 2.1**). Total fusion analyses were chosen as a broad survey approach to define the $^{40}Ar/^{39}Ar$ record of the CBU and Basal Unit, as well as detect systematic variations across structures mapped on the island. Samples were collected from the CBU (n: 6) and Basal Unit (n: 13), with emphasis placed on samples containing sufficiently coarse mica both within and distal to major structures. Eight samples from the Basal Unit were collected from the Upper Domain, and five from the Lower Domain. Total fusion dates were determined for 8-10 inclusion-free white mica grains per sample; we assigned a conservative 2σ error, rounded up to ±1 Ma for most analyses, except where propagated uncertainties already exceeded ±1 Ma. Mica separates were analyzed at the Manitoba Isotope Research Facility at the University of Manitoba (Winnipeg, Canada). Complete analytical procedures and $^{40}Ar/^{39}Ar$ data may be found in **Appendix A** and **Table S2.3**, respectively.

Samples selected for $^{40}Ar/^{39}Ar$ geochronology were primarily mica schists and schistose quartzites as well as marbles ranging in purity from low silicate content (>5 vol.%) to moderately or highly impure silicate-carbonate schists (**Figure 2.9; Figure S2.4**). No systematic first-order textural differences were observed among white mica populations from the CBU and Basal Unit. In pure silicate and silicate-carbonate schists from both units, white mica consistently defines the metamorphic fabric either as penetrative schistosity or mica-rich microlithons in more quartzose and calcareous lithologies (**Figure S2.4**). Across all units, micaceous foliation is locally dismembered by growth of late- to post-kinematic albite porphyroblasts. A tightly spaced solution cleavage is commonly observed in samples from the Upper Domain, and mica occupying cleavage domains may be oriented at high angles to the prevailing foliation. In the pure carbonate rocks,

mica occurs as isolated, euhedral rectangular grains up to 0.5 mm in diameter parallel to the shape-preferred orientation of calcite. One sample of Styra marble (19-17A) contained possibly neoblastic mica showing only weak alignment with the sample-scale foliation. White mica from all lithologies generally exceeds 50 μm in diameter, occurs in finer sizes only in phyllonites hosted within Upper Domain metaflysch, and is commonly associated with, but only rarely intergrown with, colourless to pale yellow magnesian chlorite.

White mica analyses from the CBU provide single-grain $^{40}Ar/^{39}Ar$ total fusion dates between 25 ± 1 Ma and 44 ± 1 Ma, with weighted mean sample ages between 29 ± 2 Ma and 42 ± 2 Ma (**Figure 2.9**). Single-grain dates are evenly distributed about a single peak at *c.* 36 Ma (n: 64), with a moderate skew toward older dates. Age dispersion within a single sample commonly spans 10 m.y. No obvious microstructural variations were identified as possible first-order controls on within-sample dispersion common to CBU samples.

Single-grain white mica $^{40}Ar/^{39}Ar$ dates from the Basal Unit range between 23 ± 1 Ma and 244 ± 3 Ma. Basal Unit data display wide age dispersion at both sample and map scale. As a whole, the single-grain age distribution for the Basal Unit spans a range of dates and lacks an obvious single peak (**Figure 2.9**). Most samples from the Lower Domain produce broadly coherent single-grain age populations, yielding weighted mean ages between 24 ± 1 Ma and 34 ± 2 Ma, with one older sample (19-06) providing a mean age of 46 ± 2 Ma. Comparatively, in the Upper Domain, we differentiate two groups with respect to $^{40}Ar/^{39}Ar$ systematics. The first group is situated nearest the upper tectonic contact with the Styra marbles, and yields youngest single-grain dates in the Eocene with infrequent Cretaceous to Triassic dates. Anomalously old dates in this group are associated with samples containing either single, elongate, subrounded white mica crystals much larger than the modal size of mica defining foliation, or with a spaced solution cleavage preserving

mica in microlithons at a high angle to foliation (**Figure S2.4**). The second group is concentrated at the internal contact between Basal Unit marble and metaflysch. Samples here include two mica schists and two impure schistose marbles, displaying uniform fabric-forming white mica populations, which yield internally consistent single-grain dates between 23 ± 1 and 28 ± 1 Ma (weighted mean ages: 23 ± 1 Ma to 26 ± 1 Ma).

2.7. Zircon (U-Th)/He geochronology

We utilized zircon (U-Th)/He (ZHe) geochronology to evaluate the relative timing of cooling to upper crustal temperatures (uppermost T_c of ~200°C; Reiners et al., 2004) between the CBU and Basal Unit. Seven samples were selected for ZHe analysis based on grain size, lithological suitability, and were obtained from a range of structural positions in an effort to capture a complete profile of the structural pile (**Table 2.1, Table S2.4**). Samples were collected from the Basal Unit (n: 5) and the CBU (n: 2), with three Basal Unit samples obtained from the Upper Domain (**Figure 2.8**). Selected lithologies comprise four coarse metapelitic albite-mica schists, one schistose quartzite, and one sample of pelitic matrix from the marble cobble metaconglomerate, from which 5-8 zircons of varying dimensions per sample were isolated for analysis. Analyses were performed at the Thermochronology Research and Instrumentation Laboratory at University of Colorado (Boulder, USA). Detailed analytical procedures may be found in **Appendix A**.

Samples consistently yielded colorless to slightly pink or pinkish-brown, euhedral prismatic zircon crystals between 90 and 200 μm in length with effective uranium (eU) between 192.3 and 2321.1 ppm (mean: 747.5 ppm) and effective spherical radii (ESR) between 23 and 52 μm (mean: 33 μm). Single zircon ZHe dates range between 12 ± 1 Ma and 21 ± 2 Ma, with weighted mean ages for individual samples between 15 ± 1 Ma and 18 ± 2 Ma (**Figure 2.9**). All samples produced weighted mean ages that are indistinguishable from one another within error, regardless of

Table 2.1. Summary of new white mica $^{40}Ar/^{39}Ar$ and zircon (U-Th)/He geochronology.

Sample	UTM (zone 35N)		Map Unit‡	Lithology	Mica $^{40}Ar/^{39}Ar$ age (Ma)†	2σ (Ma)	Zircon (U-Th)/He age (Ma)†	2σ (Ma)
19-01	N 4236420	E 254683	Basal Unit · metaflysch	carbonate-silicate schist	23	1	-	-
19-03*	N 4236179	E 254989	Basal Unit · metaflysch	pumpellyite-albite schist	26	1	-	-
19-04	N 4240399	E 249612	Basal Unit · metaconglomerate	impure schistose marble	34	2	-	-
19-06	N 4241927	E 249925	Basal Unit · metaconglomerate	albite-mica schist	46	2	-	-
19-08	N 4253851	E 251726	CBU · Styra Unit	schistose quartzite	35	2	-	-
19-09	N 4254648	E 255713	CBU · Styra Unit	albite-mica schist	35	2	-	-
19-10*	N 4254648	E 255713	CBU · Ochi Unit	glaucophane schist	30	2	-	-
19-16	N 4227638	E 256982	Basal Unit · metaflysch	carbonate-silicate schist	25	1	-	-
19-17A	N 4242963	E 256046	CBU · Styra Unit	marble	32	1	-	-
19-17C*	N 4242964	E 256047	Basal Unit · metaflysch	albite-mica schist	42	2	-	-
19-18	N 4247634	E 253894	Basal Unit · metaflysch	albite-mica schist	43-60	-	-	-
20-01	N 4236124	E 255082	Basal Unit · metaflysch	carbonate-silicate schist	-	-	15	1
20-02	N 4250127	E 249040	Basal Unit · metaconglomerate	impure schistose marble	27	2	-	-
20-03	N 4255556	E 246463	Basal Unit · metaflysch	albite-mica schist	29	1	17	1
20-04	N 4253784	E 250769	CBU · Styra Unit	schistose quartzite	29	2	15	1
20-08	N 4240399	E 249612	Basal Unit · metaconglomerate	impure schistose marble	-	-	17	1
20-10	N 4244237	E 249848	Basal Unit · metaconglomerate	impure schistose marble	24	1	-	-
20-13	N 4245327	E 253320	Basal Unit · metaflysch	albite-mica schist	36-244	-	15	1
20-14	N 4243187	E 253628	Basal Unit · marble	marble	26	1	-	-
20-18	N 4251120	E 254868	CBU · Styra Unit	glaucophane-albite-mica schist	-	-	18	2
20-19	N 4250585	E 255153	CBU · Ochi Unit	schistose quartzite	35	3	-	-
20-20	N 4236738	E 257239	Basal Unit · metaflysch	albite-mica schist	38	1	-	-
20-21	N 4259538	E 252168	Basal Unit · metaflysch	albite-mica schist	-	-	15	1

*Sample selected for petrological modelling

‡Entries correspond to lithological units in Figure 2.2

†Ages are weighted means of multiple single-grain analyses; see Figure 2.9. Samples reported as range yielded single grain ages too dispersed to calculate weighted mean age

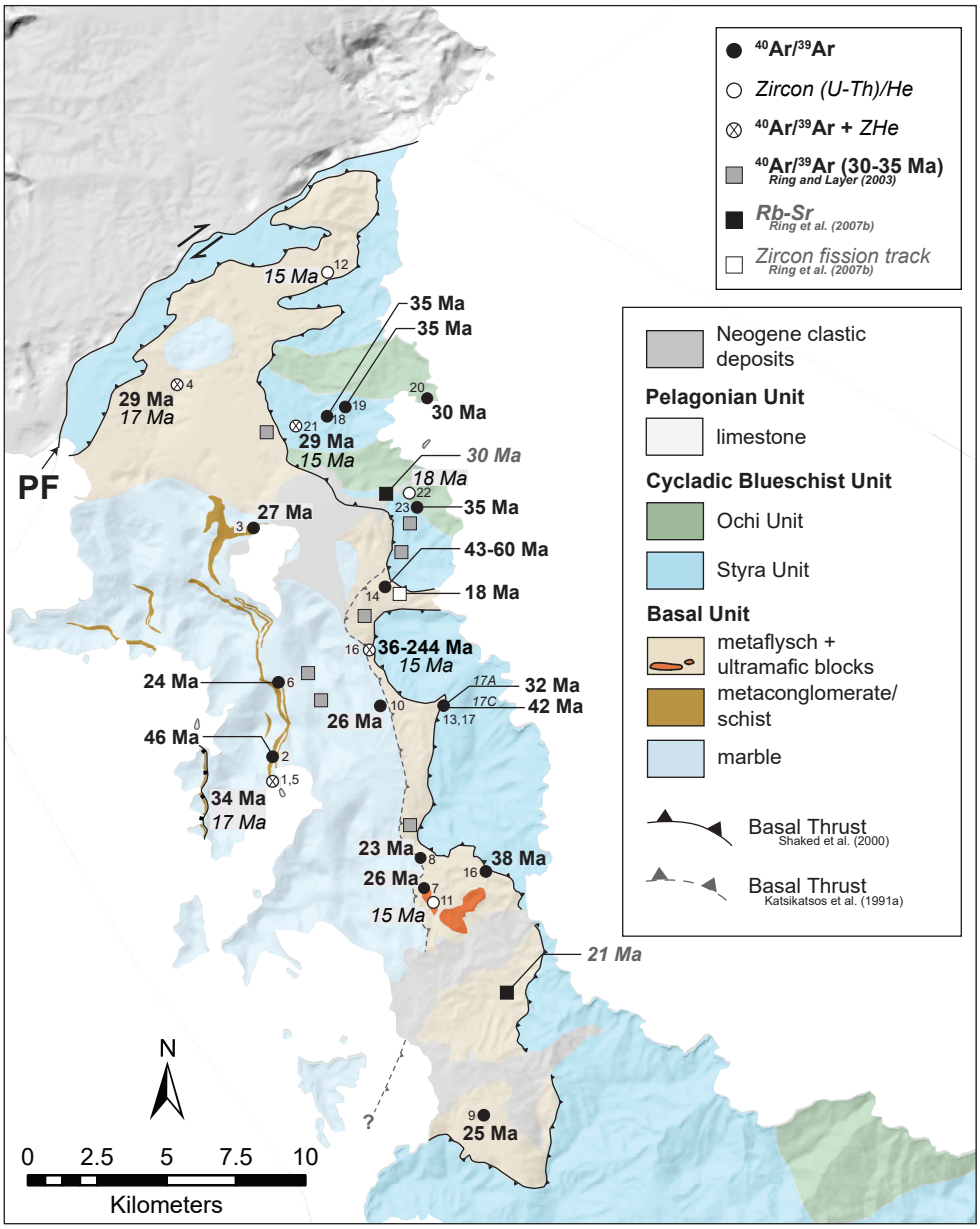

Figure 2.8. Simplified geologic map of southern Evia, Greece, showing sampling locations for new $^{40}Ar/^{39}Ar$ and zircon (U-Th)/He geochronology. Location of previous geochronologic data also shown. Small numbers beside each sample location correspond to Figure 2.9.

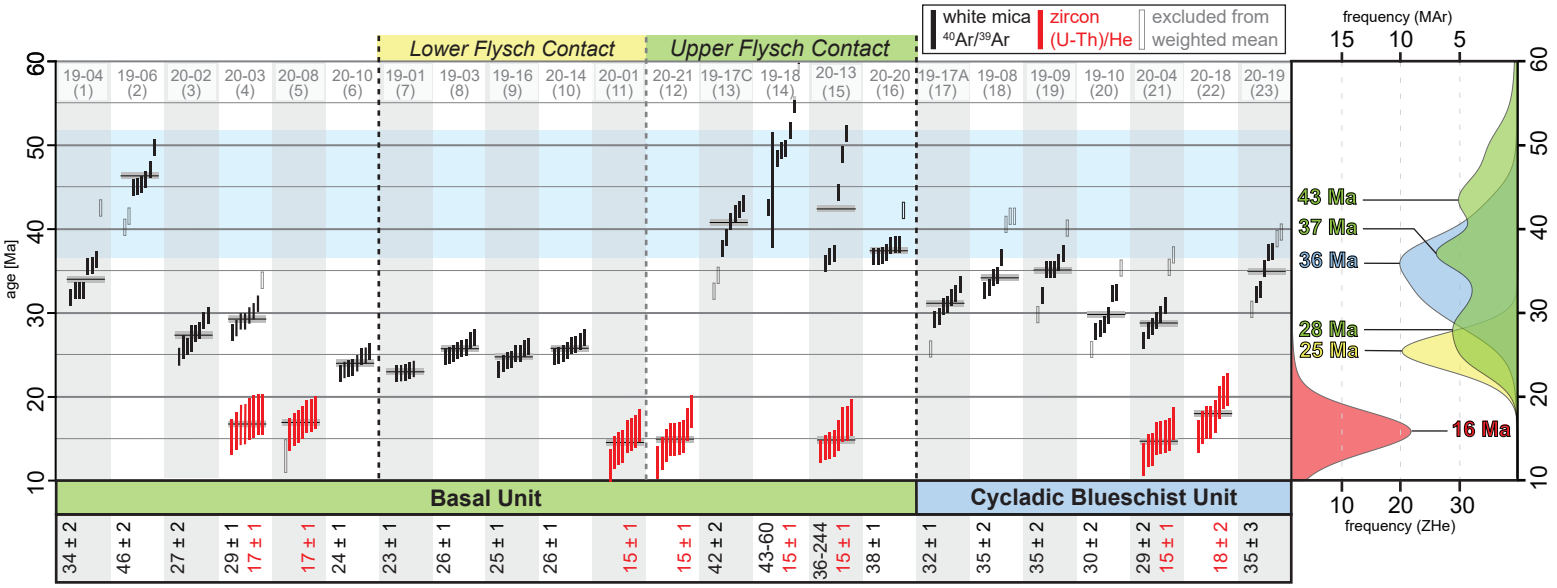

Figure 2.9. Summary of new multiple single-grain white mica total-fusion $^{40}Ar/^{39}Ar$ and zircon (U-Th)/He (ZHe) ages from southern Evia, Greece. Kernel density plot at right shows probability distribution for $^{40}Ar/^{39}Ar$ ages from the Basal Unit (green), CBU (blue), and from along the lower contact between the Basal Unit metaflysch and marble (yellow). Blue field marks proposed window of HP metamorphism of the CBU (e.g., Laurent et al., 2021). Data from all units were pooled to calculate the kernel density plot for ZHe ages (red). Numbers in parentheses below sample numbers indicate corresponding sample location on Figure 2.8.

structural position. The relatively young ZHe dates from all samples produced no observable correlation between grain age and eU or ESR (**Figure S2.5**).

2.8. Synthesis

2.8.1. Cycladic Blueschist Unit

Numerous island-scale petrogenetic, geochronological, and field-based structural studies have incrementally refined the regional tectonothermal history of the CBU (e.g., Dürr et al., 1978; Gautier et al., 1993; Parra et al., 2002; Huet et al., 2015; Grasemann et al., 2018). Earliest high-pressure metamorphism in the CBU has by now been resolved at *c.* 50-45 Ma (e.g., Tomaschek et al., 2003; Laurent et al., 2017; Uunk et al., 2022), and diverging tectonometamorphic histories have been recognized astride the Trans-Cycladic Thrust (Grasemann et al., 2018; Wind et al., 2020). The Trans-Cycladic Thrust dissects the CBU, placing higher-grade HP rocks (Upper Cycladic Blueschist Nappe; 'upper nappe' hereafter) over HP rocks that reached only comparatively shallow structural levels (Lower Cycladic Blueschist Nappe; 'lower nappe' hereafter). Available PT data suggest that the CBU on Andros belongs to the upper nappe (Huet et al., 2015), whereas the section exposed on the Attic Peninsula, directly east of Evia, attained peak conditions more compatible with the lower nappe (Scheffer et al., 2016; Coleman et al., 2020).

Peak pressure and temperature estimates obtained from our sample of glaucophane schist are within error of peak metamorphic conditions determined for the lower nappe (**Figure 2.7b**; Grasemann et al., 2018). Although the Ochi Nappe has alternatively been correlated with the Makrotantalon Unit of Andros (Papanikolaou, 1978; Xypolias and Alsop, 2014), existing PT estimates for the Makrotantalon Unit (18.5 kbar, 550°C; Huet et al., 2015) are significantly higher than those obtained for our sample. We therefore consider it likely that the CBU exposed on

southern Evia, including at least the northernmost mapped exposures of the Ochi Unit, belongs to the lower nappe. Consequently, we extend the trace of the Trans-Cycladic Thrust between Evia and Andros with a northerly strike (**Figure 2.1**).

The structural record of the CBU on Evia is broadly consistent with observations from throughout much the northern Cyclades. Penetrative mylonitic foliation and folding at a range of scales are commonly proposed to record prograde burial or early extrusion events. On Evia, these high-grade structures are associated with a predominant top-to-W shear sense near their basal tectonic contact (**Figure 2.3a-b**). A systematic reversal is observed at higher structural levels, where ductile structures record top-E to -NE shear sense **(Figure 2.3c**). Across all structural levels, these ductile features are overprinted by brittle-ductile shear bands and S/C/C' fabrics demonstrating top-to-E to -NE shear sense, relationships previously described from both Evia and the broader northern Cyclades (e.g., Gautier and Brun, 1994; Jolivet and Patriat, 1999; Xypolias et al., 2012). Strain geometries of this type are most commonly attributed to deformation sustained during continued cooling while the footwall of the NCDS is exhuming (e.g., Jolivet et al., 2010a).

Our $^{40}Ar/^{39}Ar$ data from the CBU contribute further to a dominantly late Eocene-early Oligocene age population on Evia (Maluski et al., 1981; Ring et al., 2001). Similar dates are documented throughout the Cyclades (e.g., Lister and Raouzaios, 1996; Bröcker and Franz, 1998; Schneider et al., 2011; Huyskens and Brocker, 2014; Cossette et al., 2015; Uunk et al., 2018), and have been interpreted as dating early ductile deformation below a nascent crustal-scale detachment (Jolivet et al., 2010a; Laurent et al., 2017) or the latest increments of syn-orogenic extrusion under blueschist facies conditions (Ring et al., 2010; Schneider et al., 2011; Cossette et al., 2015). Recent high-resolution $^{40}Ar/^{39}Ar$ geochronology from Syros has been used to argue that these dates may alternately represent partial resetting in sample-scale age populations encompassing the entire

range of HP metamorphism (*c.* 51-37 Ma) and dynamic recrystallization (*c.* 20-18 Ma; Laurent et al., 2021). These workers relate progressively younger apparent ages to intensity of greenschist-facies retrogression or to position within a strain gradient. Whereas the occurrence of minimally retrogressed blueschist facies assemblages among our CBU samples may favor the older *c.* 35 Ma dates as relating to the prograde HP metamorphic event, there is no systematic correlation in our samples between measured dates and degree of retrogression or structural position. The apparent absence of younger Oligo-Miocene ages in the CBU of southern Evia, commonly associated with strain imposed by deformation along the NCDS (e.g., Bröcker et al., 2004; Laurent et al., 2017), may either reflect the coarse sampling resolution of the total-fusion method capturing only the most populous intermediate ages, or may otherwise indicate that the section exposed in the study area represents middle structural levels of the CBU situated below the direct influence of the NCDS. The latter interpretation would be consistent with the inferred offshore trace of the structure (**Figure 2.1**; Jolivet et al., 2010a).

2.8.2. Basal Unit

The Basal Unit is widely recognized to record a HP metamorphic event (e.g., Schermer et al., 1990; Shaked et al., 2000; Gerogiannis et al., 2021), resulting from subduction of the Gavrovo-Tripolitza Unit in post-middle Eocene times (Dubois and Bignot, 1979; Thomson et al., 1998; Sotiropoulos et al., 2003). The HP assemblages have experienced near-total greenschist facies retrogradation, with the earlier metamorphic event evident only in relic glaucophane inclusions in albite (Schermer, 1989; Shaked et al., 2000; **Figure 2.5b**) and aragonite pseudomorphs in marble (Gerogiannis et al., 2021). The timing and tectonic significance of both metamorphic events remain somewhat controversial. Most existing models from the Aegean region propose that HP metamorphism of the Basal Unit initiated in, or at least persisted until, the early Miocene, coeval

with overthrusting and greenschist facies overprint of the CBU (e.g., Ring and Layer, 2003; Ring et al., 2007b; Gerogiannis et al., 2021). Others, meanwhile, have favored a late Eocene or early Oligocene event (e.g., Schermer, 1989; Shaked et al., 2000), or otherwise argue that early Miocene HP metamorphism is challenging to reconcile within broader regional geodynamic constraints (e.g., Tirel et al., 2009; Jolivet et al., 2013).

Of the two Basal Unit samples selected for thermodynamic modelling, only the albite-pumpellyite schist (19-03) yielded a geologically plausible PT estimate (**Figure 2.7a**). Phase assemblages in this sample capture the retrograde greenschist facies overprint, with only relics of lawsonite and sodic amphibole attesting to an earlier HP assemblage. Fabric-defining white mica compositions from this sample (Si apfu: 3.33–3.54; **Figure 2.6a, Table S2.2**) are indistinguishable from those previously reported from the Basal Unit (Si apfu <3.6, Shaked et al., 2000; 3.29–3.48, Ring et al., 2001), as are the relics of HP assemblages in the rock (Shaked et al., 2000; **Figure 2.5b**). Our nominal PT estimate for the sample (310 ± 15°C, 7 ± 1 kbar) is effectively identical to the M2 estimate of 325 ± 25°C and 7 ± 1 kbar obtained by Katzir et al. (2000) for the Tsakei metabasites, but suggests equilibration under marginally cooler temperatures than indicated by the retrograde segment of the PT path defined by Shaked et al. (2000).

Foliation-defining phengite grains from sample 19-03, which have apparently equilibrated under greenschist facies conditions, yield internally consistent late Oligocene $^{40}Ar/^{39}Ar$ dates. Moreover, our complete $^{40}Ar/^{39}Ar$ dataset from the Basal Unit does not define a dominantly Miocene and younger age trend as would be expected if the nappe had undergone comprehensive HP-LT metamorphism at that time (e.g., Laurent et al., 2021). Instead, $^{40}Ar/^{39}Ar$ dates from the Basal Unit broadly range from middle Eocene to late Oligocene, with many of these age populations showing minimal or acceptable scatter. Less common Paleocene to Triassic single-

grain dates are restricted to samples with petrographic evidence suggesting these dates are likely preserved in weakly strained mica-bearing microlithons or coarse detrital grains (**Figure S2.4**). The youngest, late Oligocene $^{40}Ar/^{39}Ar$ dates, including sample 19-03, consistently define well-behaved, internally consistent single-grain age populations – obtained predominantly from samples within the Upper Domain of the footwall (**Figure 2.8**). We accordingly interpret these late Oligocene $^{40}Ar/^{39}Ar$ dates as deformation ages recording recrystallization of foliation-defining white mica in response to the pronounced extensional strain imposed on this part of the structural pile (see discussion in **Section 2.7.3**). Whereas our geochronological data do not overwhelmingly favor a particular timing for HP metamorphism of the Basal Unit, they nevertheless do not strictly limit HP metamorphism to the early Miocene, and instead indicate that the Basal Unit was likely already undergoing greenschist facies overprint prior to that time.

In the Lower Domain, the map-scale pattern of schist and metaconglomerate exposures interwoven with the Basal Unit marble succession is consistent with a type-II fold interference pattern (**Figure 2.2**), a conclusion likewise supported by mushroom and crescent interference patterns visible in outcrop-scale folds (**Figure 2.4g**). This, in our view, renders both the outcrop-scale structure and map-scale distribution of metaconglomerate horizons more consistent with multi-generational, tight to isoclinal folding than with E-directed thrusting as previously proposed (Xypolias et al., 2003; Gerogiannis et al., 2021). Moreover, we did not encounter a ductile shear zone of sufficient magnitude to have been solely responsible for nappe-scale imbrication as has been suggested. The only shear zones encountered in the Lower Domain are those preferentially exploiting the metaconglomeratic intercalations within marble (e.g., Bouvali shear zone of Gerogiannis et al., 2021), which record deformation ranging from top-to-W to top-to-S. The structures and strain geometry associated with these shear zones indicate strain was accommodated

primarily by dissolution-precipitation creep over an interval of cooling from fully ductile to brittle-ductile conditions, suggesting the shear zones were active during exhumation of the Basal Unit.

Field observations reveal an early generation of W-E- to SW-NE-trending folds with axial planes (sub-)parallel to the prevailing mylonitic foliation (**Figure 2.4a-b**). In the Lower Domain, these folds were modified by W-dipping, close to tight, N-S trending folds (**Figure 2.4f-g; Figure 2.10**). Ductile shear sense indicators throughout the fold complex record consistent top-to-W shear (**Figure 2.4c-d**). The pervasive and highly ductile nature of early folding and associated W-directed shearing likely indicates that these structures roughly coincided with maximum burial of the Basal Unit, a conclusion reinforced by the synthetic top-W sense of shear observed at the base of the overlying Styra marbles (**Figure 2.4a-b;** see also **Section 2.8.3**). Assuming the aforementioned post-middle Eocene initiation of Basal Unit subduction, folding was likely contemporaneous with, or shortly post-dated, active syn-orogenic exhumation of the overriding CBU (Ring et al., 2007b; Jolivet et al., 2010a; Huet et al., 2015). Folding observed in the Lower Domain resembles structural relationships described from other Cycladic islands (e.g., Sifnos, Aravadinou et al., 2016; Roche et al., 2016; Milos, Grasemann et al., 2018). On Sifnos, refolding has been related to a transition from thrusting to syn-orogenic exhumation (Roche et al., 2016). We consider a similar interpretation for folding in the Basal Unit to be reasonable, given that strain localized top-to-W/top-to-S displacement along the metaconglomerate horizons, whose geometries require continuous strain as the rocks cooled through the brittle-ductile transition zone.

In summary, the Basal Unit sustained an early HP-LT metamorphic event that likely occurred earlier than the middle Miocene, contrary to previous interpretations. Peak burial roughly coincided with two distinct generations of pervasive folding at least discernable in the Lower Domain. The fold generations interact to define type-II refold structures visible across a range of

scales. The second, N-S trending folding event may represent the transition from subduction toward exhumation. Metaconglomerate and schist horizons, newly reoriented following this second folding event, localized minor top-to-W and -S shear zones that were active prior to, and during, exhumation through the brittle-ductile transition. Thermodynamic modelling results from metaflysch in the Upper Domain suggest that the greenschist facies overprint observed in the Basal Unit equilibrated under conditions (310 ± 15°C, 7 ± 1 kbar) coinciding with, or shortly preceding, the same interval of exhumation, revealing that the brittle-ductile transition was likely intersected shortly after unroofing from peak burial had begun.

2.8.3. Evia Shear Zone

The uppermost structural levels of the Basal Unit footwall, coinciding in large part with the metaflysch package, record a strain history distinct from that of the Lower Domain (**Figure 2.10**). Structures observed in outcrop here demonstrate a dominant top-to-E shear sense in lineation-parallel (XZ) sections (**Figure 2.3e**), alongside ductile and brittle-ductile structures indicative of pronounced horizontal stretching in orthogonal (YZ) sections. The strain is evident in structures including foliation-oblique pinched-and-swelled or boudinaged quartz veins, S/C/C' structures, and conjugate brittle-ductile fault sets (**Figure 2.3f-h**) – structural evidence consistent with the upper levels of the footwall having accommodated oblate coaxial flattening. Extensional inversion of the Basal Thrust, in a manner consistent with the structures we observe in the Upper Domain of the footwall, has been previously noted by Ring et al. (2007b) and Gerogiannis et al. (2021). Whereas these authors inferred a direct reactivation of the Basal Thrust itself, we hesitate to adopt this interpretation due to inconclusive evidence for direct overprinting of thrust-related structures. Instead, to avoid confusion with the Basal Thrust, hereafter we define the broad zone of oblate extensional strain described above as the 'Evia Shear Zone' (ESZ; **Figure 2.2**).

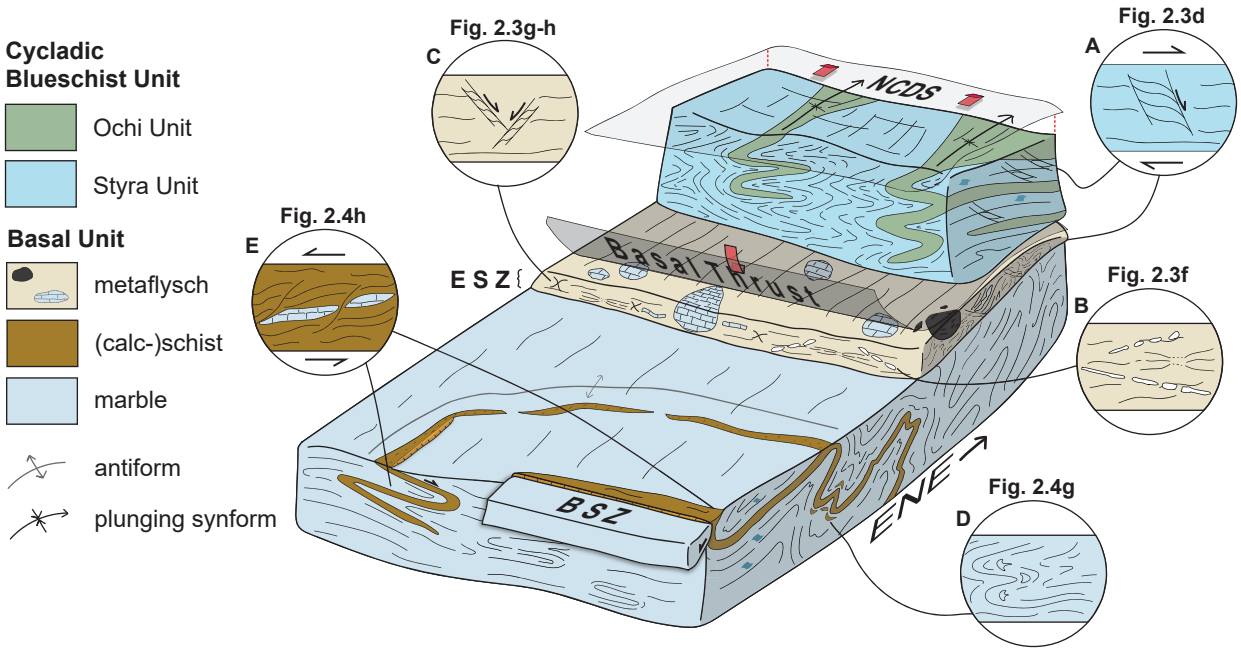

Figure 4.10. Synoptic diagram of important structural elements preserved by crystalline rocks exposed below the North Cycladic Detachment System (NCDS) on southern Evia, Greece. Important structural elements of the reconstruction are shown with references to corresponding field photographs, including: (A) Brittle-ductile top-to-E/NE shear bands in the CBU and metaflysch; (B) ductile and (C) brittle-ductile conjugate or otherwise symmetrical shear sense markers in YZ sections; (D) type-II fold interference patterns at deeper structural levels of the Basal Unit; and (E) brittle-ductile, top-to-W, -SW, and -S shear zones. Detailed descriptions of these structural elements are presented in Section 2.5.

White mica $^{40}Ar/^{39}Ar$ dates from several samples within the ESZ are among the youngest ages reported from Evia, and the data define minimally dispersed late Oligocene age populations (26-23 Ma, **Figure 2.8**; see also Maluski et al., 1981; Ring et al., 2001). Sample microstructure and the oblique cross-cutting relationships between boudinaged quartz veins and their host foliations in outcrop are consistent with both elements accommodating simultaneous stretching and transposition . Therefore, $^{40}Ar/^{39}Ar$ ages obtained for the micaceous foliation likely record deformation-induced recrystallization and resetting that coincides with accommodation of this ductile strain along the ESZ. The presence of analogous structures formed by oblate coaxial strain under comparatively cool brittle-ductile conditions implies that this style of deformation coincided with a protracted interval of exhumation since at least the late Oligocene. Furthermore, this interval of strain is bracketed by our ZHe data, which suggest that both the hangingwall and footwall of the tectonic window had cooled below 200–180°C by the middle Miocene (18-15 Ma). These geochronological constraints effectively date all ductile and brittle-ductile structures described here as pre-middle Miocene in age. Given its extensive mechanical influence and cold-over-hot strain geometry, we propose that the ESZ is a major Oligocene normal-sense shear zone (detachment, *sensu lato*) responsible in part for the modern juxtaposition of the CBU and Basal Unit, and for accomplishing exhumation of the latter into the shallow crust by the middle Miocene.

It is noteworthy that only white mica from the lowermost metaflysch and impure schistose marbles near the top of the marble sequence consistently records late Oligocene deformation (**Figure 2.8**). Samples located near the upper contact with the CBU, ostensibly the Basal Thrust as defined here, instead preserve a dispersion of Eocene dates, as well as infrequent Paleocene to Triassic dates associated with mica preserved as large detrital grains or occupying low strain microlithons (**Figure 2.9; Figure S2.4**). Although the total fusion approach used here does not

afford sufficient resolution necessary to assign a precise mechanism to this spatial distribution, it may allude to variable strain intensity recorded throughout the metaflysch package, with perhaps the most penetrative deformation localized along the lower intra-Basal Unit metaflysch-marble contact. Alternatively, strain distribution may be controlled by lithological heterogeneities inherent to the metaflysch, resulting in a differential geochronological record in more resistant lithologies (i.e., quartz-rich schists and metabasites). More comprehensive strain analysis or targeted geochronology would clarify the deformation profile through the thickness of the metaflysch and its relationship to the $^{40}Ar/^{39}Ar$ record, and by extension the time-integrated geometric evolution of the ESZ.

2.9. Geodynamic implications

2.9.1. Exhumation of the Basal Unit

Few existing models have directly explored the exhumation history of the Basal Unit. Xypolias et al. (2010) estimated vertical shortening of 20-50% along a proposed exposure of the Basal Thrust on nearby Attica, proposing that consequent syn-orogenic transport-parallel elongation of 30-90% could have been the primary mechanism of exhumation for the Basal Unit. Similarly, Gerogiannis et al. (2021) conceived of an E-directed, intra-Basal Unit thrust accomplishing syn-orogenic exhumation via a duplex-like structure, producing an overall geometry resembling an eastward extruding wedge. Workers in other tectonic windows farther afield (Schermer, 1989) considered low-angle normal faults integral to exhuming the Olympos-Ossa Unit (also proposed to correlate with the Gavrovo-Tripolitza Unit; Ring et al., 2010) under tectonic conditions analogous to conceptions of post-orogenic extension as commonly applied to the Aegean (e.g., Jolivet et al., 2010a).

New geochronology and structural data reveal that the Basal Unit on Evia underwent a period of exhumation and cooling spanning *c.* 10 m.y. between the late Oligocene and early Miocene, indicating the Basal Unit had started unroofing earlier than suggested by previous models (Ring et al., 2007b; Gerogiannis et al., 2021). Strain recorded in the ESZ indicates that it was a key structure in facilitating exhumation, doing so by combined vertical thinning and E-directed normal-sense displacement. The progression from fully ductile to brittle-ductile strain observed in the ESZ shows that the shear zone accommodated continuous strain over an extended depth interval while the structure itself also underwent progressive unroofing.

Considerable controversy in the Cyclades exists surrounding the timing with which post-orogenic extension replaced syn-orogenic extrusion as the primary driver of exhumation. Although displacement along the NCDS during post-orogenic extension was likely responsible for some exhumation of southern Evia (**Figure 2.1**), our data support at least a partially syn-orogenic unroofing history for the Basal Unit. Our PT results and $^{40}Ar/^{39}Ar$ geochronology show that greenschist facies overprint in the Basal Unit most likely overlapped with ductile deformation along the ESZ in the late Oligocene (*c.* 26-23 Ma), following as little as ~3-6 kbar (10-21 km) of exhumation (Shaked et al., 2000). Accepting *c.* 35-30 Ma as an upper bound for the timing of maximum burial of the Basal Unit (Thomson et al., 1998; Sotiropoulos et al., 2003), these rocks appear to have experienced a subduction and exhumation history considerably shorter than that inferred for the CBU (Ring et al., 2010). Rapid exhumation of the Basal Unit apparently commenced directly following peak burial, at depths too great to have feasibly been accommodated solely by detachment faulting.

We therefore consider it likely that, for at least part of its lifespan, the ESZ acted as the roof bounding normal-sense fault during syn-orogenic extrusion of the Basal Unit. Fully ductile

deformation within the ESZ ceased in the early Miocene, at which time brittle-ductile structures overprinted the earlier ductile structures. Although this timing would be in accord with the best-constrained evidence for active post-orogenic extension in the Cyclades (Avigad et al., 1997; Jolivet and Patriat, 1999; Ring et al., 2010; Grasemann et al., 2012), our data do not unequivocally demonstrate this transition on Evia. Instead, brittle-ductile structures in the ESZ appear to record cooler deformation with effectively identical strain components, suggesting that syn-orogenic exhumation of the Basal Unit may have persisted under cooler conditions into the early Miocene. Middle Miocene ZHe dates impose a lower bound on active syn-orogenic processes, as these would likely be arrested in the brittle crust; however, the transition from syn- to post-orogenic exhumation may have reasonably occurred at any point between 23-15 Ma. As the ESZ would theoretically have remained favorably oriented under post-orogenic extension, part of its strain history may have been accumulated following the transition. Nevertheless, the absence of a fully brittle low-angle detachment plane and consistent ZHe dates from both CBU and Basal Unit implies that final unroofing of southern Evia was accomplished as a coherent block in the footwall of the NCDS during the early Miocene.

2.9.2. Ductile thinning

Structural evidence for Oligo-Miocene coaxial deformation coeval with exhumation, like that described here for southern Evia, is gaining recognition across the Cyclades. Zones of coaxial strain developed during exhumation were predicted in several early tectonic models (e.g., Gautier and Brun, 1994; Jolivet et al., 2004), but were generally considered as byproducts of incipient, primarily detachment-driven unroofing near the lower crust. Attempts to quantify the contribution from ductile thinning toward overall exhumation in the Cyclades have yielded values of ~20%

vertical attenuation and equal values for attendant exhumation (Kumerics et al., 2005; Ring and Kumerics, 2008). A recent study from Ios has interpreted symmetrical N-S strain markers as a reflection of plane strain ductile thinning active under post-orogenic extension (Mizera and Behrmann, 2016). Ring and Glodny (2021) used the distribution of coaxial strain across the southern Cyclades to define a 'kinematic hinge zone,' a regional-scale feature that these authors speculate was either a byproduct of, or may even have directly controlled, bivergent extension in the Aegean.

Directly on Evia, Xypolias et al. (2010) reported vertical thinning on the order of ~20-50% using data from the northernmost parts of the tectonic window as well as its proposed extension on northeastern Attica (Xypolias et al., 2003; Xypolias et al., 2010). Our structural observations and geochronology are largely consistent with the tectonic interpretations put forward by these authors, though the transport-normal (i.e., Y-direction) stretching component documented here may mitigate total exhumation accomplished via transport-parallel elongation.

Whereas Xypolias et al. (2010, 2012) observe evidence for coaxial thinning throughout the CBU in the hanging wall of the Basal Thrust, the degree to which coaxial thinning has affected the Lower Domain of the Basal Unit in the footwall is not clear. Direct structural evidence like that found in the ESZ was not documented in the Lower Domain marbles and metaconglomerates. However, normal-sense shear zones developed within the interfolded metaconglomerates record continuous deformation from initially ductile through to brittle-ductile conditions, implying that they accommodated strain over essentially the same interval as the ESZ. These shear zones may accordingly have served to partition the coaxial strain recorded at higher structural levels along any favorably-oriented, rheologically-weak lithological discontinuities within an otherwise

rheologically homogeneous marble succession, explaining the coeval top-to-W and top-to-S deformation in the Lower Domain.

Parallels may be drawn between strain developed in the ESZ and modelled expectations of triclinic strain under inclined transpression (e.g., Dutton, 1997). Such shear zone geometries arise when non-coaxial shearing occurs in multiple directions, with a component of coaxial shortening across the shear zone (Jones et al., 2004). On Evia, the presence of a coaxial strain component operating orthogonally to the regional stretching lineation and inferred direction of transport closely resembles natural examples of such shear zones (e.g., Viola and Henderson, 2010). However, despite their mutually compatible influence on the resultant local crustal architecture (i.e., attenuation of shear zone thickness and structural geometry consistent with an oblate finite strain ellipsoid; Jones et al., 2004), structures within the Evia Shear Zone display excellent monoclinic symmetry similar to transpressional flow of Type C (Fossen and Tikoff, 1998), and we did not observe evidence for non-coaxial shearing in the Y-direction. Similarities between these models are nevertheless striking, and predict partial exhumation by transport-parallel elongation (i.e., ductile thinning; Jones et al., 2004; Viola and Henderson, 2010). Such a prediction was also made by Xypolias et al. (2010) for the Evia nappe stack that may account for part of the exhumation history of the Basal Unit.

2.9.3. Vergence of the Hellenic subduction zone

Orogenic models for the Hellenides commonly assume a long-lived, S- to SW-vergent subduction zone, and by consequence that all terranes accreted sequentially from oldest in northern Greece to youngest in eastern mainland Greece, the Peloponnese, and Crete (Jolivet and Brun, 2010; Ring et al., 2010; Papanikolaou, 2021). Alternative models have proposed that, for at least part of its

history, Hellenic subduction had a northeasterly vergence and resulted in subduction and accretion of material situated to the paleogeographic northeast of the Pelagonian Zone (e.g., Doutsos et al., 1993; Chatzaras et al., 2011; Gerogiannis et al., 2019, 2021). Data supporting this view include the top-to-NE kinematics commonly interpreted to represent syn-orogenic shear sense along the Evia Thrust, which appears to suggest the Basal Unit was thrust beneath the CBU from the northeast (Xypolias et al., 2012; Gerogiannis et al., 2021).

Here we document mylonitic fabrics that record top-to-W shear in both the Basal Unit and Styra marbles astride the Basal Thrust (**Figure 2.3a-b; Figure 2.4c-d**). We observe a distinct and systematic transition to top-to-E kinematics structurally up-section in both units (**Figure 2.3c-e**). The highly ductile nature of the structures recording top-to-W shear and their related metamorphic foliations indicates that these structures record strain that likely coincided with maximum burial. We interpret this to reflect the prevailing kinematics during nappe stacking, consistent with SW-vergent subduction, as top-to-E shear sense markers in either unit likely relate to younger structures: the ESZ in the footwall (this study), and either the NCDS (Jolivet and Patriat, 1999; Jolivet et al., 2010a) or the Styra-Ochi contact in the hanging wall (Xypolias et al., 2012).

2.9.4. Relevance to Cycladic geodynamics

Geodynamic models of the Aegean broadly agree that the CBU sustained HP metamorphism in the early Eocene (e.g., Tomaschek et al., 2003; Laurent et al., 2017). Thereafter, syn-orogenic wedge extrusion accomplished a significant fraction of total exhumation of the HP metamorphic rocks (**Figure 2.11a**), and the CBU was subject to greenschist facies metamorphic overprint by the end of this phase of its exhumation (Ring et al., 2007a,b; Ring and Kumerics, 2008; Huet et al., 2015; Grasemann et al., 2018). As previously discussed, the timing of this event is controversial, and tectonothermal models for the Cyclades diverge considerably from that point.

Some models consider the Aegean to be under post-orogenic extension as early as 35-30 Ma (e.g., Jolivet et al., 2010a; Huet et al., 2015; Laurent et al., 2017), whereas others argue that post-orogenic forces only became dominant in the early (e.g., Avigad et al., 1997; Ring et al., 2010; Grasemann et al., 2012; Cossette et al., 2015) or middle Miocene (e.g., Doutsos et al., 1993; Xypolias et al., 2012; Gerogiannis et al., 2021).

Our data provide strong evidence that the Basal Unit had begun to exhume no later than the late Oligocene, by which time it was recording greenschist facies retrogradation of earlier HP-LT assemblages. The restricted timeline this presents for subduction of the Basal Unit to ~10-12 kbar (35-30 Ma; Shaked et al., 2000; Sotiropoulos et al., 2003) and exhumation into the brittle crust thereafter (27-15 Ma; **Section 2.8.1**) appears more consistent with the magnitudes and rates of exhumation expected for syn-orogenic extrusion than for low-angle detachment faulting (e.g., Jolivet et al., 2003; Ring & Glodny, 2010; Balestrieri et al., 2011; Ryan et al., 2021; **Figure 2.11b**). Although a corresponding lower bounding thrust has not been found within the tectonic window on Evia, these deeper structural levels may be exposed among the proposed Basal Unit occurrences in northeastern Attica (Xypolias et al., 2010; **Figure 2.11c**). The exhumation history of the Basal Unit is comparable to that of the Phyllite-Quartzite Unit, another External Hellenic HP nappe that underwent a similarly condensed exhumation history (Jolivet et al., 2010b). This conclusion implies that Evia was experiencing compression until at least the early Miocene.

Ductile increments of strain along the major ductile-then-brittle detachments collectively defining the NCDS have been dated at *c.* 30-21 Ma on Tinos (Bröcker et al., 1993; Bröcker and Franz, 1998) and *c.* 29-25 Ma on Andros (Huyskens and Bröcker, 2014). As the structures yielding these dates grade into brittle detachment planes parallel to the earlier ductile shear zone fabric, they have been interpreted as post-orogenic structures that operated continuously since *c.* 30 Ma

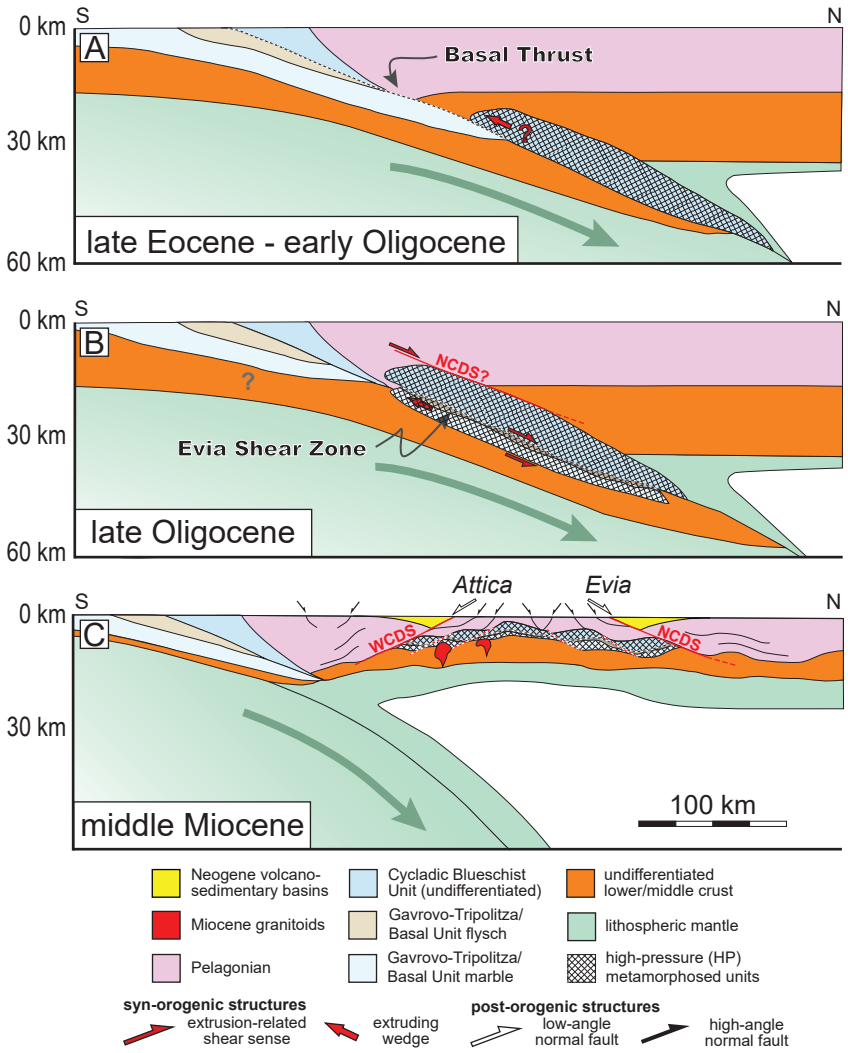

Figure 2.11. Schematic geodynamic evolution of a N-S transect (roughly E-W in modern coordinates) through Attica-Evia in the western Cyclades. (A) The continental platform of Apulia begins subducting by the early Oligocene. The Basal Thrust represents the fossilized subduction thrust along this interface as the proto-Basal Unit underthrusts the now partially exhumed Cycladic Blueschist Unit (CBU). (B) The Basal Unit begins exhuming as an extrusion wedge by the late Oligocene. The Evia Shear Zone develops between the extruding Basal Unit and overlying CBU, which may have stalled in the middle crust (see text). At this time, the Evia Shear Zone accommodates simultaneous top-to-N (top-to-E in modern coordinates) displacement and oblate coaxial flattening. The NCDS may already be active at the upper margin of the CBU. (C) Post-orogenic extension due to slab rollback significantly modifies the crust starting in the early Miocene. By the middle Miocene, the crust has undergone considerable extension accommodated by low- and high-angle normal faults, including the major North (NCDS) and West (WCDS) Cycladic Detachment Systems. By this time, the structural pile exposed on Evia has been exhumed into the upper crust (see also Jolivet et al., 2004; Grasemann et al., 2018).

(Jolivet et al., 2010a; Huet et al., 2015). Evidently, these structures were co-active with the ESZ, albeit at higher structural levels in the CBU (**Figure 2.11b**); however, the ESZ apparently did not accommodate significant brittle low-angle displacement.

Our observations further reinforce the proposal that low-angle detachments in the northern Cyclades formed initially as low-angle shear zones facilitating syn-orogenic extrusion of the CBU (Jolivet et al., 2010b; Philippon et al., 2012). Thereafter, these structures would theoretically remain favorably oriented for exploitation by N-S-directed bivergent extension (**Figure 2.11c**). The transition between syn-orogenic and post-orogenic tectonic regimes may appear continuous in the rock record and would reconcile the Oligocene deformation ages with arguments favoring continued convergence at that time (e.g., Avigad et al., 1997; Xypolias et al., 2010). However, this model is complicated somewhat by PT data obtained from both Andros and Tinos, which show that exhumation of the CBU may have stalled temporarily in the middle crust (Parra et al., 2002; Huet et al., 2015; **Figure 2.11b**). Furthermore, this model alone does little to account for the rapid low-temperature exhumation history of Evia relative to Andros and Tinos, which record a range of weighted mean ZHe dates from the CBU (Shin, 2014) between 14-9 Ma (Andros) and 12-10 Ma (Tinos) compared to consistent 18-15 Ma dates recorded throughout the structural pile of Evia (**Figure 2.9**).

The thermochronological record of Evia furthermore marks a deviation from a remarkably consistent regional dataset. Our ZHe data from Evia show that the island underwent an expedited cooling history relative to most of the CBU, even from localities where thermal effects of Miocene plutonism are absent (e.g., Brichau et al., 2006; Grasemann et al., 2012; Bargnesi et al., 2013; Berger et al., 2013; Soukis and Stockli, 2013; Schneider et al., 2018; Coleman et al., 2020). The cooling ages recorded on southern Evia instead overlap with those of the ostensibly structurally

higher Makrotantalon Unit (Andros; Shin, 2014) and Pelagonian Unit (Santorini; Schneider et al., 2018), suggesting that southern Evia followed an exhumation path that diverged considerably from the remainder of the Cyclades. A relatively early entry into the brittle crust may explain the lack of post-30 Ma $^{40}Ar/^{39}Ar$ dates in the CBU on Evia, as this unit may have already occupied a region of the crust too cool to accommodate ductile strain once the NCDS became active there.

The widespread record of coaxial strain and consequent ductile thinning on Evia, both within the ESZ and in the overlying CBU (Xypolias et al., 2010), provides an obvious mechanism to explain the differential timing of unroofing. Less easily rationalized is why ductile thinning would accelerate unroofing exclusively on Evia, particularly as estimates for net vertical attenuation there are no greater than estimates from elsewhere in the Cyclades (Ring and Kumerics, 2008; Xypolias et al., 2010), and coaxial strain more generally is not rare in the region (e.g., Gautier and Brun, 1994; Rosenbaum et al., 2002; Bond et al., 2007). It is possible that Evia is subjected to boundary effects arising from its position near the edge of the Aegean tectonic domain; however, documentation of these influences has thus far demonstrated what is likely only late and localized transpressional displacement (Xypolias et al., 2003). A resolvable strain component operating in the Y-direction is not unknown in the Cyclades, though has generally been reported to involve shortening rather than extension as observed on Evia (e.g., Avigad et al., 2001; Jolivet et al., 2004; Rabillard et al., 2015). Avigad et al. (2001) predicted that any such transport-normal shortening would necessarily be accompanied by compensatory extension toward the margins of the Cyclades, and it is therefore possible that this process is responsible for extension in the Y-direction on Evia. Alternatively, zones recording transport-normal shortening and extension may oscillate at regular intervals across the Aegean Sea, with extended zones accomplishing unroofing to greater structural depths.

It is conversely possible that the presence of the Basal Unit itself influenced the exhumation path of Evia. Basal Unit exposures across the Cyclades are both sparse and, in some instances, controversial (e.g., Bröcker and Franz, 2005). A conspicuous map-scale pattern or geological rationale for its distribution is not easy to distinguish, with proposed exposures found on Tinos (Avigad et al., 1989), Samos (Ring et al., 1999b), and mainland Greece (Schermer, 1989). Exposures of the Cycladic Basement, which occupies a lower structural position equivalent to the Basal Unit, are likewise documented on islands recognized to have accommodated significant ductile thinning in the Oligocene or Miocene (Mizera and Behrmann, 2016; Ring and Glodny, 2021). Whereas an intuitive understanding of this relationship would suggest that greater magnitudes of exhumation are responsible for greater depths of exposure, and not vice-versa, the irregular occurrence of windows to subjacent structural levels remains poorly understood and this theoretical causal link merits further investigation. Further detailed structural and geochronological investigations into these units and their tectonized boundaries would clarify the factors controlling their incidence, as well as their influence on the ultimate crustal-scale geometry of the Aegean region.

2.10. Summary

We present new geochronology, structural observations, and phase equilibrium modelling for southern Evia in the NW Aegean Sea. The data demonstrate that the Basal Unit, one of two major tectonostratigraphic units known to directly underlie the CBU in the Aegean region, was continuously exhuming since the late Oligocene. A broad zone of extensional strain, here named the Evia Shear Zone, was developed within the uppermost metaflysch package of the Basal Unit. Ductile and brittle-ductile structures preserved in the ESZ suggest that it accommodated coaxial stretching in both the X- and Y-directions in addition to top-to-E, non-coaxial strain, resulting in

an overall general shear with a component of oblate coaxial flattening. The ESZ was integral in unroofing the Basal Unit, accomplishing exhumation via a combination of top-to-E normal-sense displacement and vertical thinning, with the latter process resulting in as much as 20-50% vertical attenuation according to prior estimates (Xypolias et al., 2010). Exhumation was likely underway by the late Oligocene, as indicated by 26-23 Ma $^{40}Ar/^{39}Ar$ dates from recrystallized mica hosted within the ESZ, and had accomplished unroofing of the structural pile into the brittle crust by *c.* 18-15 Ma. Although the relative contribution from syn- and post-orogenic processes cannot be estimated from our data, we consider it likely that syn-orogenic processes would necessarily have played a significant role due to the considerable depth of peak burial estimated for the Basal Unit at ~10 kbar, corresponding to ~35 km depths (Shaked et al., 2000). This study contributes to a steadily growing body of evidence demonstrating a major role for coaxial strain in exhuming the HP-LT rocks. Evia presents another instance in which ductile thinning facilitated, or was perhaps even promoted by, the exposure of crustal material situated structurally beneath the CBU. Localities exposing these subjacent structural units are a promising target for future work in the Cyclades, representing a presently underutilized resource that will aid in refining models for the Cenozoic geodynamic evolution of the Aegean Sea.

2.11. Acknowledgments

Field work and analyses for this project were supported by an NSERC Discovery Grant awarded to D.A. Schneider and by an FWF grant I5399-N awarded to B. Grasemann. Thoughtful reviews were provided by S. Scaillet and G. Viola, whose input greatly improved the manuscript. L. Jolivet and F. Rossetti provided excellent editorial handling and feedback throughout the publication process. We thank A. Camacho (University of Manitoba), J. Metcalfe (University of Colorado Boulder), and G. Poirier (University of Ottawa) for their assistance with data acquisition

and interpretation. Insightful discussions regarding the regional geological context were provided by K. Soukis. Field work and sampling were assisted by S. Rzegocka, J. Spalding, and M. Kling.

2.12. References

Agard, P., Yamato, P., Jolivet, L., & Burov, E. (2009). Exhumation of oceanic blueschists and eclogites in subduction zones: timing and mechanisms. Earth-Science Reviews, 92(1-2), 53-79.

Aravadinou, E., Xypolias, P., Chatzaras, V., Iliopoulos, I., & Gerogiannis, N. (2016). Ductile nappe stacking and refolding in the Cycladic Blueschist Unit: insights from Sifnos Island (south Aegean Sea). International Journal of Earth Sciences, 105(7), 2075-2096.

Augier, R., Jolivet, L., Gadenne, L., Lahfid, A., & Driussi, O. (2015). Exhumation kinematics of the Cycladic Blueschists unit and back-arc extension, insight from the Southern Cyclades (Sikinos and Folegandros Islands, Greece). Tectonics, 34(1), 152-185.

Avigad, D., & Garfunkel, Z. (1989). Low-angle faults above and below a blueschist belt—Tinos Island, Cyclades, Greece. Terra Nova, 1(2), 182-187.

Avigad, D., Garfunkel, Z., Jolivet, L., & Azañón, J. M. (1997). Back arc extension and denudation of Mediterranean eclogites. Tectonics, 16(6), 924-941.

Avigad, D., Ziv, A., & Garfunkel, Z. (2001). Ductile and brittle shortening, extension-parallel folds and maintenance of crustal thickness in the central Aegean (Cyclades, Greece). Tectonics, 20(2), 277-287.

Avouac, J. P., & Burov, E. B. (1996). Erosion as a driving mechanism of intracontinental mountain growth. Journal of Geophysical Research: Solid Earth, 101(B8), 17747-17769.

Balestrieri, M. L., Pandeli, E., Bigazzi, G., Carosi, R., & Montomoli, C. (2011). Age and temperature constraints on metamorphism and exhumation of the syn-orogenic metamorphic complexes of Northern Apennines, Italy. Tectonophysics, 509(3-4), 254-271.

Bargnesi, E. A., Stockli, D. F., Mancktelow, N., & Soukis, K. (2013). Miocene core complex development and coeval supradetachment basin evolution of Paros, Greece, insights from (U–Th)/He thermochronometry. Tectonophysics, 595, 165-182.

Berger, A., Schneider, D. A., Grasemann, B., & Stockli, D. (2013). Footwall mineralization during Late Miocene extension along the West Cycladic Detachment System, Lavrion, Greece. Terra Nova, 25(3), 181-191.

Best, M., Christiansen, E., Deino, A., Grommé, C., Tingey, D., 1995. Correlation and emplacement of a large, zoned, discontinuously exposed ash flow sheet; the $^{40}Ar/^{39}Ar$ chronology, paleomagnetism, and petrology of the Pahranagat Formation, Nevada. Journal of Geophysical Research 100, 24593-24609.

Bond, C. E., Butler, R. W., & Dixon, J. E. (2007). Co-axial horizontal stretching within extending orogens: the exhumation of HP rocks on Syros (Cyclades) revisited. Geological Society, London, Special Publications, 272(1), 203-222.

Bonneau, M. (1984). Correlation of the Hellenide nappes in the south-east Aegean and their tectonic reconstruction. Geological Society, London, Special Publications, 17(1), 517-527.

Brichau, S., Ring, U., Carter, A., Bolhar, R., Monié, P., Stockli, D., & Brunel, M. (2008). Timing, slip rate, displacement and cooling history of the Mykonos detachment footwall, Cyclades, Greece, and implications for the opening of the Aegean Sea basin. Journal of the Geological Society, 165(1), 263-277.

Brichau, S., Ring, U., Ketcham, R. A., Carter, A., Stockli, D., & Brunel, M. (2006). Constraining the long-term evolution of the slip rate for a major extensional fault system in the central Aegean, Greece, using thermochronology. Earth and Planetary Science Letters, 241(1-2), 293-306.

Bröcker, M., & Franz, L. (1998). Rb–Sr isotope studies on Tinos Island (Cyclades, Greece): additional time constraints for metamorphism, extent of infiltration-controlled overprinting and deformational activity. Geological Magazine, 135(3), 369-382.

Bröcker, M., & Franz, L. (2005). The base of the Cycladic blueschist unit on Tinos Island (Greece) re-visited: Field relationships, phengite chemistry and Rb-Sr geochronology. Neues Jahrbuch fur Mineralogie-Abhandlungen, 181(1), 81-94.

Bröcker, M., Bieling, D., Hacker, P., & Gans, P. (2004). High-Si phengite records the time of greenschist facies overprinting: implications for models suggesting mega-detachments in the Aegean Sea. Journal of Metamorphic Petrology, 22(5), 427-442.

Bröcker, M., Kreuzer, H., Matthews, A., & Okrusch, M. (1993). $^{40}Ar/^{39}Ar$ and oxygen isotope studies of polymetamorphism from Tinos Island, Cycladic blueschist belt, Greece. Journal of Metamorphic Geology, 11(2), 223-240.

Choukroune, P., Gapais, D., & Merle, O. (1987). Shear criteria and structural symmetry. Journal of Structural Geology, 9(5-6), 525-530.

Coleman, M. J., Schneider, D. A., Grasemann, B., Soukis, K., Lozios, S., & Hollinetz, M. S. (2020). Lateral Termination of a Cycladic-Style Detachment System (Hymittos, Greece). Tectonics, 39(9), e2020TC006128.

Connolly, J. A. D. (2011). Perple_X [Software Package]. Pennsylvania, USA.

Cossette, É., Schneider, D. A., Warren, C. J., & Grasemann, B. (2015). Lithological, rheological, and fluid infiltration control on $^{40}Ar/^{39}Ar$ ages in polydeformed rocks from the West Cycladic detachment system, Greece. Lithosphere, 7(2), 189-205.

Dazé, A., Lee, J. K., & Villeneuve, M. (2003). An intercalibration study of the Fish Canyon sanidine and biotite $^{40}Ar/^{39}Ar$ standards and some comments on the age of the Fish Canyon Tuff. Chemical Geology, 199(1-2), 111-127.

Denèle, Y., Lecomte, E., Jolivet, L., Lacombe, O., Labrousse, L., Huet, B., & Le Pourhiet, L. (2011). Granite intrusion in a metamorphic core complex: the example of the Mykonos laccolith (Cyclades, Greece). Tectonophysics, 501(1-4), 52-70.

Diener, J. F. A., & Powell, R. (2012). Revised activity–composition models for clinopyroxene and amphibole. Journal of Metamorphic Geology, 30(2), 131-142.

Doutsos, T., Pe-Piper, G., Boronkay, K. T., & Koukouvelas, I. (1993). Kinematics of the central Hellenides. Tectonics, 12(4), 936-953.

Dubois, R. & Bignot, G. (1979). Présence d'un "hard ground" nummulitique au de la série cretacée d'Almyropotamos (Eubée meridionale, Grèce). Paris, Académie des Sciences Comptes Rendus, 289, 993–5.

Dürr, S. T., Altherr, R., Keller, J. O., & Okrusch, M. M. Seidel, E. 1978. The median Aegean crystalline belt: Stratigraphy, Structure, Metamorphism, Magmatism. Alps, Apennines, Hellenides, 455-477.

Evans, B. W. (1990). Phase relations of epidote-blueschists. Lithos, 25(1-3), 3-23.

Feehan, J. G., & Brandon, M. T. (1999). Contribution of ductile flow to exhumation of low-temperature, high-pressure metamorphic rocks: San Juan-Cascade nappes, NW Washington State. Journal of Geophysical Research: Solid Earth, 104(B5), 10883-10902.

Fossen, H. and Tikoff, B. (1998). Extended models of transpression and transtension, and application to tectonic settings. In: R. E. Holdsworth, R. A. Strachan and J. F. Dewey, Continental Transpressional and Transtensional Tectonics, The Geological Society of London. 135: 15-33.

Froitzheim, N., Pleuger, J., Roller, S., & Nagel, T. (2003). Exhumation of high-and ultrahigh-pressure metamorphic rocks by slab extraction. Geology, 31(10), 925-928.

Gautier, P., & Brun, J. P. (1994). Ductile crust exhumation and extensional detachments in the central Aegean (Cyclades and Evvia Islands). Geodinamica Acta, 7(2), 57-85.

Gautier, P., Brun, J. P., & Jolivet, L. (1993). Structure and kinematics of upper Cenozoic extensional detachment on Naxos and Paros (Cyclades Islands, Greece). Tectonics, 12(5), 1180-1194.

Gerogiannis, N., Aravadinou, E., Chatzaras, V., & Xypolias, P. (2021). Calcite pseudomorphs after aragonite: A tool to unravel the structural history of high-pressure marbles (Evia Island, Greece). Journal of Structural Geology, 148, 104373.

Gessner, K., Ring, U., Passchier, C. W., & Güngör, T. (2001). How to resist subduction: evidence for large-scale out-of-sequence thrusting during Eocene collision in western Turkey. Journal of the Geological Society, 158(5), 769-784.

Grasemann, B., Huet, B., Schneider, D. A., Rice, A. H. N., Lemonnier, N., & Tschegg, C. (2018). Miocene postorogenic extension of the Eocene synorogenic imbricated Hellenic subduction channel: New constraints from Milos (Cyclades, Greece). GSA Bulletin, 130(1-2), 238-262.

Grasemann, B., Schneider, D. A., Stöckli, D. F., & Iglseder, C. (2012). Miocene bivergent crustal extension in the Aegean: Evidence from the western Cyclades (Greece). Lithosphere, 4(1), 23-39.

Green, E., Holland, T., & Powell, R. (2007). An order-disorder model for omphacitic pyroxenes in the system jadeite-diopside-hedenbergite-acmite, with applications to eclogitic rocks. American Mineralogist, 92(7), 1181-1189.

Grujic, D., Casey, M., Davidson, C., Hollister, L. S., Kündig, R., Pavlis, T., & Schmid, S. (1996). Ductile extrusion of the Higher Himalayan Crystalline in Bhutan: evidence from quartz microfabrics. Tectonophysics, 260(1-3), 21-43.

Hawthorne, F. C., Oberti, R., Harlow, G. E., Maresch, W. V., Martin, R. F., Schumacher, J. C., & Welch, M. D. (2012). Nomenclature of the amphibole supergroup. American Mineralogist, 97(11-12), 2031-2048.

Holland, T. J. (1988). Preliminary phase relations involving glaucophane and applications to high pressure petrology: new heat capacity and thermodynamic data. Contributions to Mineralogy and Petrology, 99(1), 134-142.

Holland, T., & Powell, R. (2003). Activity–composition relations for phases in petrological calculations: an asymmetric multicomponent formulation. Contributions to Mineralogy and Petrology, 145(4), 492-501.

Holland, T. J. B., & Powell, R. (2011). An improved and extended internally consistent thermodynamic dataset for phases of petrological interest, involving a new equation of state for solids. Journal of Metamorphic Geology, 29(3), 333-383.

Holland, T. J., Green, E. C., & Powell, R. (2018). Melting of peridotites through to granites: a simple thermodynamic model in the system KNCFMASHTOCr. Journal of Petrology, 59(5), 881-900.

Huet, B., Labrousse, L., & Jolivet, L. (2009). Thrust or detachment? Exhumation processes in the Aegean: Insight from a field study on Ios (Cyclades, Greece). Tectonics, 28(3).

Huet, B., Labrousse, L., Monie, P., Malvoisin, B., & Jolivet, L. (2015). Coupled phengite ^{40}Ar–^{39}Ar geochronology and thermobarometry: PTt evolution of Andros Island (Cyclades, Greece). Geological Magazine, 152(4), 711-727.

Huyskens, M. H., & Bröcker, M. (2014). The status of the Makrotantalon Unit (Andros, Greece) within the structural framework of the Attic-Cycladic Crystalline Belt. Geological Magazine, 151(3), 430-446.

Jacobshagen, V. (1986). Geologie von Griechland. Borntraeger, Berlin-Stuttgart, p. 279.

Jolivet, L., & Brun, J. P. (2010). Cenozoic geodynamic evolution of the Aegean. International Journal of Earth Sciences, 99(1), 109-138.

Jolivet, L., & Patriat, M. (1999). Ductile extension and the formation of the Aegean Sea. Geological Society, London, Special Publications, 156(1), 427-456.

Jolivet, L., Faccenna, C., Huet, B., Labrousse, L., Le Pourhiet, L., Lacombe, O., ... & Driussi, O. (2013). Aegean tectonics: Strain localisation, slab tearing and trench retreat. Tectonophysics, 597, 1-33.

Jolivet, L., Faccenna, C., Goffé, B., Burov, E., & Agard, P. (2003). Subduction tectonics and exhumation of high-pressure metamorphic rocks in the Mediterranean orogens. American Journal of Science, 303(5), 353-409.

Jolivet, L., Famin, V., Mehl, C., Parra, T., Aubourg, C., Hébert, R., ... & Teyssier, C. (2004). Strain localization during crustal-scale boudinage to form extensional metamorphic domes in the Aegean Sea. Geological Society of America, Special Papers, 185-210.

Jolivet, L., Lecomte, E., Huet, B., Denèle, Y., Lacombe, O., Labrousse, L., ... & Mehl, C. (2010a). The north cycladic detachment system. Earth and Planetary Science Letters, 289(1-2), 87-104.

Jolivet, L., Trotet, F., Monié, P., Vidal, O., Goffé, B., Labrousse, L., & Agard, P. (2010b). Along-strike variations of P–T conditions in accretionary wedges and syn-orogenic extension, the HP–LT Phyllite–Quartzite Nappe in Crete and the Peloponnese. Tectonophysics, 480(1-4), 133-148.

Katsikatsos, G. (1991a). Geological map of Greece, Aliveri sheet. Institute of Geological Mining Research (IGME), Athens.

Katsikatsos, G. (1991b). Geological map of Greece, Rafina sheet. Institute of Geological Mining Research (IGME), Athens.

Katzir, Y., Avigad, D., Matthews, A., Garfunkel, Z., & Evans, B. W. (2000). Origin, HP/LT metamorphism and cooling of ophiolitic mélanges in southern Evia (NW Cyclades), Greece. Journal of Metamorphic Geology, 18(6), 699-718.

Krivovichev, S. V., Armbruster, T., Organova, N. I., Burns, P. C., Seredkin, M. V., & Chukanov, N. V. (2004). Incorporation of sodium into the chlorite structure: the crystal structure of glagolevite, $Na(Mg,Al)_6[Si_3AlO_{10}](OH,O)_8$. American Mineralogist, 89(7), 1138-1141.

Kuiper, K. F., Deino, A., Hilgen, F. J., Krijgsman, W., Renne, P. R., & Wijbrans, A. J. (2008). Synchronizing rock clocks of Earth history. Science, 320(5875), 500-504.

Kumerics, C., Ring, U., Brichau, S., Glodny, J., & Monié, P. (2005). The extensional Messaria shear zone and associated brittle detachment faults, Aegean Sea, Greece. Journal of the Geological Society, 162(4), 701-721.

Lanari, P., Wagner, T., & Vidal, O. (2014). A thermodynamic model for di-trioctahedral chlorite from experimental and natural data in the system $MgO–FeO–Al_2O_3–SiO_2–H_2O$: applications to P–T sections and geothermometry. Contributions to Mineralogy and Petrology, 167(2), 968.

Laurent, V., Beaudoin, A., Jolivet, L., Arbaret, L., Augier, R., Rabillard, A., & Menant, A. (2015). Interrelations between extensional shear zones and synkinematic intrusions: The example of Ikaria Island (NE Cyclades, Greece). Tectonophysics, 651, 152-171.

Laurent, V., Huet, B., Labrousse, L., Jolivet, L., Monie, P., & Augier, R. (2017). Extraneous argon in high-pressure metamorphic rocks: Distribution, origin and transport in the Cycladic Blueschist Unit (Greece). Lithos, 272, 315-335.

Laurent, V., Scaillet, S., Jolivet, L., Augier, R., & Roche, V. (2021). ^{40}Ar behaviour and exhumation dynamics in a subduction channel from multi-scale $^{40}Ar/^{39}Ar$ systematics in phengite. Geochimica et Cosmochimica Acta, 311, 141-173.

Lecomte, E., Jolivet, L., Lacombe, O., Denèle, Y., Labrousse, L., & Le Pourhiet, L. (2010). Geometry and kinematics of Mykonos detachment, Cyclades, Greece: Evidence for slip at shallow dip. Tectonics, 29(5).

Lister, G. S., & Davis, G. A. (1989). The origin of metamorphic core complexes and detachment faults formed during Tertiary continental extension in the northern Colorado River region, USA. Journal of Structural Geology, 11(1-2), 65-94.

Lister, G. S., & Raouzaios, A. (1996). The tectonic significance of a porphyroblastic blueschist facies overprint during Alpine orogenesis: Sifnos, Aegean Sea, Greece. Journal of Structural Geology, 18(12), 1417-1435.

Lister, G. S., Banga, G., & Feenstra, A. (1984). Metamorphic core complexes of Cordilleran type in the Cyclades, Aegean Sea, Greece. Geology, 12(4), 221-225.

Locock, A. J. (2014). An Excel spreadsheet to classify chemical analyses of amphiboles following the IMA 2012 recommendations. Computers & Geosciences, 62, 1-11.

Long, S. P., & Kohn, M. J. (2020). Distributed ductile thinning during thrust emplacement: A commonly overlooked exhumation mechanism. Geology, 48(4), 368-373.

Maluski, H., Vergely, P., Bavay, D., Bavay, P., & Katsikatsos, G. (1981). $^{39}Ar/^{40}$ Ar dating of glaucophanes and phengites in southern Euboa (Greece); geodynamic implications. Bulletin de la Société géologique de France, 7(5), 469-476.

Mizera, M., & Behrmann, J. H. (2016). Strain and flow in the metamorphic core complex of Ios Island (Cyclades, Greece). International Journal of Earth Sciences, 105(7), 2097-2110.

Papanikolaou, D. (1984). The three metamorphic belts of the Hellenides: a review and a kinematic interpretation. Geological Society, London, Special Publications, 17(1), 551-561.

Papanikolaou, D. (2009). Timing of tectonic emplacement of the ophiolites and terrane paleogeography in the Hellenides. Lithos, 108(1-4), 262-280.

Papanikolaou, D. (2021). Geology of Greece. Springer Nature.

Parra, T., Vidal, O., & Jolivet, L. (2002). Relation between the intensity of deformation and retrogression in blueschist metapelites of Tinos Island (Greece) evidenced by chlorite–mica local equilibria. Lithos, 63(1-2), 41-66.

Passchier, C. W., & Trouw, R. A. (2005). Microtectonics. Springer Science & Business Media.

Platt, J. P. (1993). Exhumation of high-pressure rocks: A review of concepts and processes. Terra Nova, 5(2), 119-133.

Platt, J. P., & Vissers, R. L. M. (1980). Extensional structures in anisotropic rocks. Journal of Structural Geology, 2(4), 397-410.

Rabillard, A., Arbaret, L., Jolivet, L., Le Breton, N., Gumiaux, C., Augier, R., & Grasemann, B. (2015). Interactions between plutonism and detachments during metamorphic core complex formation, Serifos Island (Cyclades, Greece). Tectonics, 34(6), 1080-1106.

Reiners, P. W., Spell, T. L., Nicolescu, S., & Zanetti, K. A. (2004). Zircon (U-Th)/He thermochronometry: He diffusion and comparisons with $^{40}Ar/^{39}Ar$ dating. Geochimica et Cosmochimica Acta, 68(8), 1857-1887.

Renne, P.R., Norman, E.B. (2001). Determination of the half-life of ^{37}Ar by mass spectrometry. Physical Review C, 63(4), 047302.

Renne, P. R., Swisher, C. C., Deino, A. L., Karner, D. B., Owens, T. L., & DePaolo, D. J. (1998). Intercalibration of standards, absolute ages and uncertainties in $^{40}Ar/^{39}Ar$ dating. Chemical Geology, 145(1-2), 117-152.

Ring, U., & Glodny, J. (2010). No need for lithospheric extension for exhuming (U) HP rocks by normal faulting. Journal of the Geological Society, 167(2), 225-228.

Ring, U., & Kassem, O. M. (2007). The nappe rule: why does it work?. Journal of the Geological Society, 164(6), 1109-1112.

Ring, U., & Kumerics, C. (2008). Vertical ductile thinning and its contribution to the exhumation of high-pressure rocks: the Cycladic blueschist unit in the Aegean. Journal of the Geological Society, 165(6), 1019-1030.

Ring, U., & Layer, P. W. (2003). High-pressure metamorphism in the Aegean, eastern Mediterranean: Underplating and exhumation from the Late Cretaceous until the Miocene to Recent above the retreating Hellenic subduction zone. Tectonics, 22(3).

Ring, U., & Reischmann, T. (2002). The weak and superfast Cretan detachment, Greece: exhumation at subduction rates in extruding wedges. Journal of the Geological Society, 159(3), 225-228.

Ring, U., Brandon, M. T., Willett, S. D., & Lister, G. S. (1999a). Exhumation processes. Geological Society, London, Special Publications, 154(1), 1-27.

Ring, U., Glodny, J., Will, T., & Thomson, S. (2007b). An Oligocene extrusion wedge of blueschist-facies nappes on Evia, Aegean Sea, Greece: implications for the early exhumation of high-pressure rocks. Journal of the Geological Society, 164(3), 637-652.

Ring, U., Glodny, J., Will, T., & Thomson, S. (2010). The Hellenic subduction system: high-pressure metamorphism, exhumation, normal faulting, and large-scale extension. Annual Review of Earth and Planetary Sciences, 38, 45-76.

Ring, U., Laws, S., & Bernet, M. (1999b). Structural analysis of a complex nappe sequence and late-orogenic basins from the Aegean Island of Samos, Greece. Journal of Structural Geology, 21(11), 1575-1601.

Ring, U., Layer, P. W., & Reischmann, T. (2001). Miocene high-pressure metamorphism in the Cyclades and Crete, Aegean Sea, Greece: Evidence for large-magnitude displacement on the Cretan detachment. Geology, 29(5), 395-398.

Ring, U., Will, T., Glodny, J., Kumerics, C., Gessner, K., Thomson, S., ... & Drüppel, K. (2007a). Early exhumation of high-pressure rocks in extrusion wedges: Cycladic blueschist unit in the eastern Aegean, Greece, and Turkey. Tectonics, 26(2).

Roche, V., Laurent, V., Cardello, G. L., Jolivet, L., & Scaillet, S. (2016). Anatomy of the Cycladic Blueschist Unit on Sifnos Island (Cyclades, Greece). Journal of Geodynamics, 97, 62-87.

Roddick, J. C. (1983). High precision intercalibration of ^{40}Ar-^{39}Ar standards. Geochimica et Cosmochimica Acta, 47(5), 887-898.

Rosenbaum, G., Avigad, D., & Sánchez-Gómez, M. (2002). Coaxial flattening at deep levels of orogenic belts: evidence from blueschists and eclogites on Syros and Sifnos (Cyclades, Greece). Journal of Structural Geology, 24(9), 1451-1462.

Ryan, E., Papeschi, S., Viola, G., Musumeci, G., Mazzarini, F., Torgersen, E., ... & Ganerød, M. (2021). Syn-orogenic exhumation of high-P units by upward extrusion in an accretionary wedge: Insights from the Eastern Elba nappe stack (Northern Apennines, Italy). Tectonics, 40(5), e2020TC006348.

Scheffer, C., Vanderhaeghe, O., Lanari, P., Tarantola, A., Ponthus, L., Photiades, A., & France, L. (2016). Syn-to post-orogenic exhumation of metamorphic nappes: Structure and thermobarometry of the western Attic-Cycladic metamorphic complex (Lavrion, Greece). Journal of Geodynamics, 96, 174-193.

Schermer, E.R. (1989). Tectonic evolution of the Mt. Olympos region, Greece (Doctoral dissertation).

Schermer, E. R., Lux, D. R., & Burchfiel, B. C. (1990). Temperature-time history of subducted continental crust, Mount Olympos Region, Greece. Tectonics, 9(5), 1165-1195.

Schneider, D. A., Grasemann, B., Lion, A., Soukis, K., & Draganits, E. (2018). Geodynamic significance of the Santorini detachment system (Cyclades, Greece). Terra Nova, 30(6), 414-422.

Schneider, D. A., Senkowski, C., Vogel, H., Grasemann, B., Iglseder, C., & Schmitt, A. K. (2011). Eocene tectonometamorphism on Serifos (western Cyclades) deduced from zircon depth-profiling geochronology and mica thermochronology. Lithos, 125(1-2), 151-172.

Shaked, Y., Avigad, D., & Garfunkel, Z. (2000). Alpine high-pressure metamorphism at the Almyropotamos window (southern Evia, Greece). Geological Magazine, 137(4), 367-380.

Shin, T.A. (2014). Tectonic evolution of Aegean metamorphic core complexes, Andros and Tinos islands, Greece (Doctoral dissertation).

Sotiropoulos, S., Kamberis, E., Triantaphyllou, M. V., & Doutsos, T. (2003). Thrust sequences in the central part of the External Hellenides. Geological Magazine, 140(6), 661-668.

Soukis, K., & Stockli, D. F. (2013). Structural and thermochronometric evidence for multi-stage exhumation of southern Syros, Cycladic islands, Greece. Tectonophysics, 595, 148-164.

Spell, T. L., & McDougall, I. (2003). Characterization and calibration of $^{40}Ar/^{39}Ar$ dating standards. Chemical Geology, 198(3-4), 189-211.

Steiger, R. H., & Jäger, E. (1977). Subcommission on geochronology: convention on the use of decay constants in geo-and cosmochronology. Earth and Planetary Science Letters, 36(3), 359-362.

Thomson, S. N., Stöckhert, B., Rauche, H., & Brix, M. R. (1998). Apatite fission-track thermochronology of the uppermost tectonic unit of Crete, Greece: implications for the post-Eocene tectonic evolution of the Hellenic subduction system. In Advances in Fission-Track Geochronology (pp. 187-205). Springer, Dordrecht.

Tirel, C., Gautier, P., Van Hinsbergen, D. J. J., & Wortel, M. J. R. (2009). Sequential development of interfering metamorphic core complexes: numerical experiments and comparison with the Cyclades, Greece. Geological Society, London, Special Publications, 311(1), 257-292.

Tomaschek, F., Kennedy, A. K., Villa, I. M., Lagos, M., & Ballhaus, C. (2003). Zircons from Syros, Cyclades, Greece—recrystallization and mobilization of zircon during high-pressure metamorphism. Journal of Petrology, 44(11), 1977-2002.

Uunk, B., Brouwer, F., de Paz-Álvarez, M., van Zuilen, K., Huybens, R., van't Veer, R., & Wijbrans, J. (2022). Consistent detachment of supracrustal rocks from a fixed subduction depth in the Cyclades. Earth and Planetary Science Letters, 584, 117479.

Uunk, B., Brouwer, F., ter Voorde, M., & Wijbrans, J. (2018). Understanding phengite argon closure using single grain fusion age distributions in the Cycladic Blueschist Unit on Syros, Greece. Earth and Planetary Science Letters, 484, 192-203.

Vidal, O., & Parra, T. (2000). Exhumation paths of high-pressure metapelites obtained from local equilibria for chlorite–phengite assemblages. Geological Journal, 35(3-4), 139-161.

Viola, G., & Henderson, I. C. (2010). Inclined transpression at the toe of an arcuate thrust: an example from the Precambrian 'Mylonite Zone'of the Sveconorwegian orogen. Geological Society, London, Special Publications, 335(1), 715-737.

White, R. W., Powell, R., Holland, T. J. B., Johnson, T. E., & Green, E. C. R. (2014). New mineral activity–composition relations for thermodynamic calculations in metapelitic systems. Journal of Metamorphic Geology, 32(3), 261-286.

White, R. W., Powell, R., Holland, T. J. B., & Worley, B. A. (2000). The effect of TiO_2 and Fe_2O_3 on metapelitic assemblages at greenschist and amphibolite facies conditions: mineral equilibria calculations in the system K_2O-FeO-MgO-Al_2O_3-SiO_2-H_2O-TiO_2-Fe_2O_3. Journal of Metamorphic Geology, 18(5), 497-511.

Wiewióra, A., & Weiss, Z. (1990). Crystallochemical classifications of phyllosilicates based on the unified system of projection of chemical composition: II. The chlorite group. Clay Minerals, 25(1), 83-92.

Wind, S. C., Schneider, D. A., Hannington, M. D., & McFarlane, C. R. (2020). Regional similarities in lead isotopes and trace elements in galena of the Cyclades Mineral District, Greece with implications for the underlying basement. Lithos, 366, 105559.

Xypolias, P., & Alsop, G. I. (2014). Regional flow perturbation folding within an exhumation channel: A case study from the Cycladic Blueschists. Journal of Structural Geology, 62, 141-155.

Xypolias, P., Iliopoulos, I., Chatzaras, V., & Kokkalas, S. (2012). Subduction-and exhumation-related structures in the Cycladic Blueschists: Insights from south Evia Island (Aegean region, Greece). Tectonics, 31(2).

Xypolias, P., Kokkalas, S., & Skourlis, K. (2003). Upward extrusion and subsequent transpression as a possible mechanism for the exhumation of HP/LT rocks in Evia Island (Aegean Sea, Greece). Journal of Geodynamics, 35(3), 303-332.

Xypolias, P., Spanos, D., Chatzaras, V., Kokkalas, S., & Koukouvelas, I. (2010). Vorticity of flow in ductile thrust zones: examples from the Attico-Cycladic Massif (Internal Hellenides, Greece). Geological Society, London, Special Publications, 335(1), 687-714.

CHAPTER 3

STRAIN PARTITIONING IN A FLATTENING SHEAR ZONE: RE-EVALUATION OF A CYCLADIC-STYLE DETACHMENT

3.1. Abstract

The Almyropotamos tectonic window on southern Evia island in the NW Aegean Sea subdivides two high pressure-low temperature metamorphic units, representing distinct thrust sheets juxtaposed during the Hellenic orogeny. Oligocene to recent extension accommodated by the Evia Shear Zone has obscured the original thrust contact by distributed ductile thinning of a metamorphosed flysch succession at the top of the structurally lower HP-LT unit, the Basal Unit. Ductile thinning has placed the lower Basal Unit marble sequence structurally adjacent to the overlying Styra marbles of the Cycladic Blueschist Unit. The partially attenuated flysch comprises a matrix dominated by pelitic schist, with dispersed cm- to hm-scale blocks of marble, carbonate schist, quartzite, and metabasite distributed throughout. Detailed structural investigation of the different constituent lithotypes in the flysch reveals that tectonic fabrics related to general flattening strain developed most strongly in the pelitic matrix, whereas the compositionally diverse blocks exhibit differential preservation of older foliations and structures. Quartz c-axis distributions from deformed quartz veins in carbonate and chlorite schists reflect an early, predominantly plane strain deformation at moderate temperatures, confirmed by ribbon porphyroclasts, and dynamic and static recrystallization microstructures in the vein quartz. A colder deformation is evident in some pelitic schists, capturing small circle Z-centered girdles consistent with the inferred oblate finite strain ellipsoid. New *in situ* $^{40}Ar/^{39}Ar$ and $^{87}Rb/^{87}Sr$ geochronology delineate the timing of the two deformation events and (micro-)structural associations corresponding to each. Geochronological data reaffirm the first-order observations of strain partitioning behaviour at the scale of the Evia Shear Zone, and confirm that the Basal Unit on Evia records two resolvable tectonometamorphic events: an early Oligocene HP-LT event, and a late Oligocene-early Miocene greenschist facies event that coincided with ductile thinning. The

diffuse and discontinuous style of deformation recorded within the ESZ is highly atypical of major structures facilitating exhumation in the Aegean Sea, and may represent an analogue to mélange-hosted shear zones that accommodate strain during subduction.

3.2. Introduction

From their first recognition in the rock record more than forty years ago, examination of low-angle normal faults (i.e., detachments) has revolutionized our understanding of the mechanics governing the return of deeply exhumed rocks to the surface (Wernicke, 1981; Lister et al., 1984; Wernicke and Axen, 1988; Lister and Davis, 1989; Scott and Lister, 1992). Detachment faulting is responsible for a significant magnitude of the unroofing observed in many young orogens, including the Basin and Range province, the Himalaya, and the Cyclades (Davis and Lister, 1988; Burchfiel et al., 1992; Gauthier and Brun, 1994; Carosi et al., 1998; Foster and John, 1999; Jolivet et al., 2010; Grasemann et al., 2012; Kellett et al., 2019). Regional-scale structures of this type often impart a conspicuous and visually striking strain signature well into their footwalls, and create predictable structural relationships that readily permit their identification in the field (Lister and Davis, 1989; Jolivet et al., 2010). Nevertheless, detachment faults may evolve in diverse ways that are controlled by the geological and mechanical conditions of their surroundings during their lifespans (e.g., Davis et al., 2002; Krohe and Mposkos, 2002; Braathen et al., 2004; Mehl et al., 2007; Lecomte et al., 2010; Kellett and Grujic, 2012; Coleman et al., 2020).

Detachment faults are rarely the sole determinants of exhumation, with several other processes often contributing to the exhumation history of a particular region (Ring et al., 1999; Froitzheim et al., 2003; Ring et al., 2010; Warren, 2013). For instance, wedge extrusion may be the process responsible for large magnitudes of exhumation at depth, whereas erosion, detachment

faulting, and ductile thinning may dominate at shallower levels and control the distribution and geometry of different crustal constituents (Ring et al., 1999; Ring and Layer, 2003; Brichau et al., 2006, 2008). Thus, accurately determining the exhumation mechanism(s) responsible for exhuming a particular package of rock is critical to reconstructing the evolution of an orogen, as unroofing histories involving multiple exhumation styles may result in highly complex geometric configurations of local- and regional-scale structural piles.

In a previous contribution, we discriminated among two structural domains within a tectonic window exposed on the island of Evia in the NW Aegean Sea (Ducharme et al., 2022). Deep structural levels of the lowermost thrust sheet (the Basal Unit), composed mainly of marbles, were interpreted as preserving structures reflecting the comprehensive deformational history of the unit, whereas its uppermost structural levels, coinciding largely with a package interpreted as metamorphosed Eocene flysch, were reported to exhibit a comparatively simpler structural record. A broadly sub-horizontal foliation in the latter domain was attributed to an extensional shear zone (the Evia Shear Zone; ESZ) operating with an oblate coaxial strain component, which produced ductile and brittle-ductile structures recording extension in the transport-normal (i.e., *Y*) direction during overall top-to-NE general flattening. The structure was proposed to have facilitated Oligo-Miocene unroofing of the Basal Unit via simultaneous operation as a low-angle normal fault and ductile thinning of the shear zone (Ducharme et al., 2022).

Our new work further interrogates the premises of the ductile thinning model on southern Evia using petrofabric analysis of deformed quartz veins and paired *in situ* $^{40}Ar/^{39}Ar$ and $^{87}Rb/^{87}Sr$ geochronology. Stretched quartz veins are important structures that record the oblate flattening strain component within the ESZ (cf. Fig. 3d of Ducharme et al., 2022), and may record, depending on the timing of their formation, distinct intervals of the strain history compared to previously

investigated quartzites of the region (Xypolias et al., 2003; Xypolias et al., 2010). The diverse lithological constituents of the Basal Unit flysch succession record differential strain, attesting to a complex bulk rheology. Thus, quartz veins hosted by different lithotypes may record c-axis distributions that do not all capture the same deformation conditions. Rheological heterogeneity may likewise influence the strain-sensitive white mica $^{40}Ar/^{39}Ar$ and $^{87}Rb/^{87}Sr$ geochronometers, which have been shown to record different dates depending on host rock competency and composition (Cossette et al., 2015; Laurent et al., 2021; Ribeiro et al., 2023; Barnes et al., 2023). Our data show that rheologically heterogeneous parts of an orogenic section, such as intercalated diverse sedimentary units and mélanges, may nevertheless localize structures that contribute significantly to exhumation, but that these structures may be obscured by an apparently incoherent strain record at the scale of the shear zone.

3.3. Tectonic setting

Southern parts of Evia island represent the northwestern limits of the Attic-Cycladic Crystalline Belt (ACCB), a high pressure-low temperature (HP-LT) metamorphic massif belonging to the greater Greek Hellenides. The ACCB is composed of metamorphosed equivalents to the Pindos and Gavrovo-Tripolitza units on mainland Greece, the Peloponnese, and Crete that were subducted below (and accreted outboard of) the Pelagonian Zone along the long-lived Hellenic subduction zone. Dominantly metabasic and metacarbonate rock of the Cycladic Blueschist Unit (CBU), interpreted to represent rock of Pindos affinity, constitutes the majority of the exposed ACCB (Bonneau, 1984). The CBU sustained early Eocene (*c.* 50 Ma) HP-LT metamorphism prior to its unroofing since the late Eocene (Jacobshagen, 1986; Jolivet et al., 2010). The CBU is underlain in the Cyclades either by a crystalline basement of disputed affinity

(Huet et al., 2009; Zlatkin et al., 2018), or by the Basal Unit, a Triassic-Eocene platform carbonate succession capped by Eocene flysch that has been correlated with the Gavrovo-Tripolitza unit (Katsikatsos et al., 1976; Dubois and Bignot, 1979; Schermer et al., 1990; Ring et al., 2010). The Basal Unit is exposed in tectonic windows across the Cyclades and in continental Greece, interpreted as representing fragments of the Gavrovo-Tripolitza that were subducted and tectonically juxtaposed below the CBU along the regional-scale Basal Thrust (Ring et al., 2010). The Basal Unit records relict mineralogical evidence of a separate HP-LT metamorphic episode (Shaked et al., 2000; Gerogiannis et al., 2021; Ducharme et al., 2022).

An outsized body of work on the ACCB has focused on the CBU, and thus the geodynamic evolution of the Cyclades is best understood with respect to this unit. The exhumation history of the CBU is broadly subdivided into two stages (Jolivet et al., 2010; Ring et al., 2010). The earliest increments of exhumation, commonly termed 'syn-orogenic' exhumation, were likely accomplished via wedge extrusion during continued contraction in the Aegean (Ring et al., 2007a; Jolivet et al., 2010; Uunk et al., 2022; Peillod et al., 2024). Syn-orogenic stages of exhumation were likely responsible for the majority of total unroofing experienced by the CBU, and may have produced internal imbrication by SW-vergent thrusting within the extruding wedge (Grasemann et al., 2018).

Later stages of exhumation, hereafter 'post-orogenic,' were dominated by bivergent extension along systems of ductile-then-brittle low-angle normal faults, including the North (NCDS) and West Cycladic Detachment Systems (WCDS; Jolivet et al., 2010; Grasemann et al., 2012; **Figure 3.1**). These structures developed in response to slab rollback and incipient back-arc formation since the early Miocene. Despite only facilitating the shallowest ~15 km of exhumation for most of the CBU (e.g., Ring and Layer, 2003; Ring and Kumerics, 2008), the major detachment

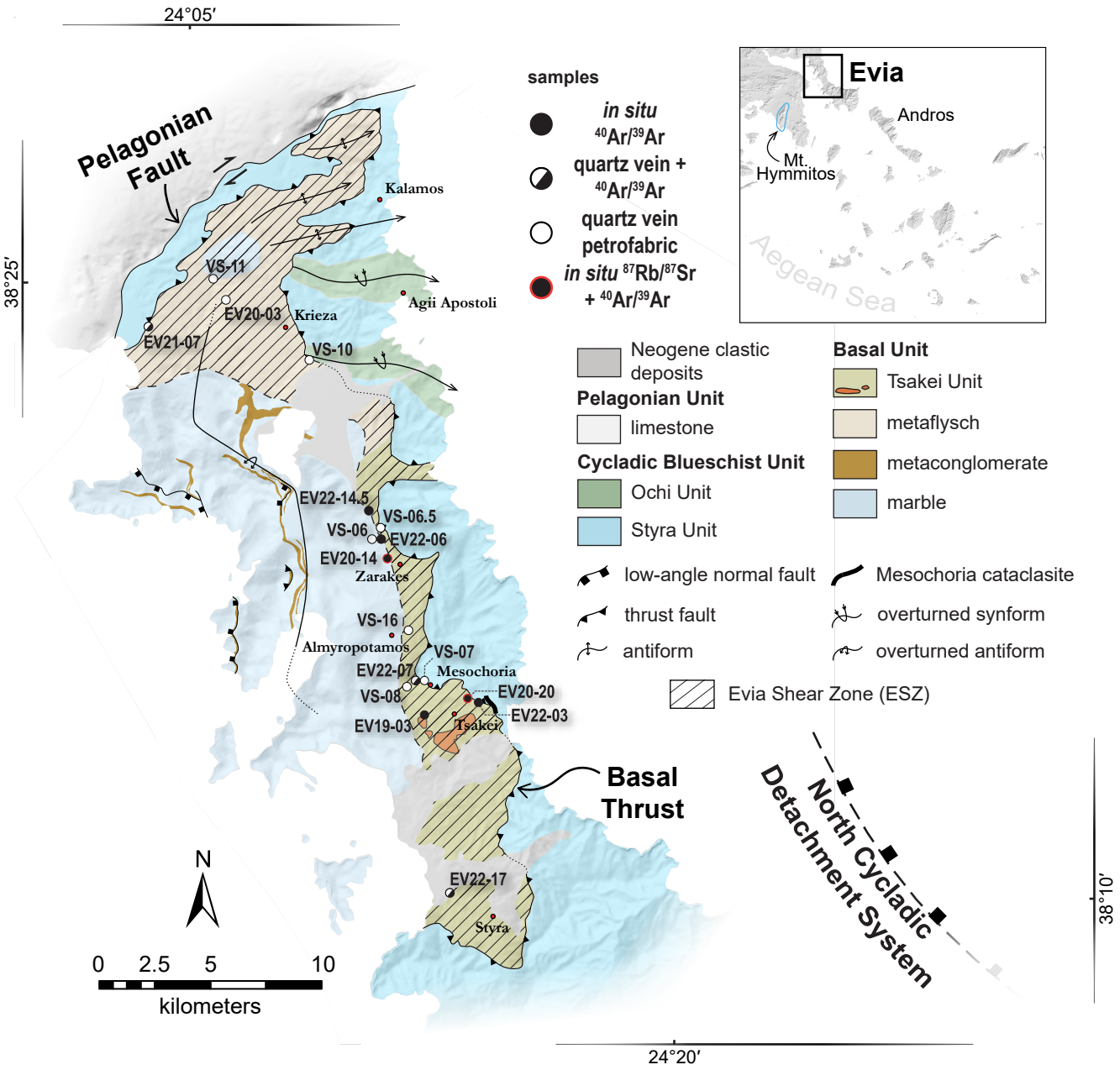

Figure 3.1. Geological map of southern Evia. Modified after Katsikatsos et al. (1991a,b) and Ducharme et al. (2022).

faults profoundly modified the geometry of the exhuming crust and exert a dominant control on the present-day exposures of the different lithostratigraphic units via ductile strain in their footwalls and segmentation of the ACCB into crustal-scale boudins (Jolivet et al., 2004, 2010).

3.3.1. Geology of southern Evia

The bedrock of southern Evia is composed primarily of the CBU and Basal Unit (**Figure 3.1**), where the CBU is subdivided into Styra and Ochi units, which are predominantly composed of marble and mafic metavolcanic rock, respectively (Papanikolaou, 1987). These rocks attained peak metamorphic conditions of ~400-460°C and ~12 kbar, with retrograde mineral assemblages suggesting greenschist facies overprinted at <350°C and <8 kbar (Shaked et al., 2000; Katzir et al., 2000; Ducharme et al., 2022). A third subdivision, the Tsakei Unit, has been applied in some interpretations to metapelitic schist underlying the Styra Unit (Katsikatsos et al., 1991a,b), but these rocks are assigned to the Basal Unit in some interpretations (Shaked et al., 2000; Ducharme et al., 2022). The Basal Unit is exposed in the Almyropotamos tectonic window, a major structural discontinuity occupying a significant portion of the island. The Almyropotamos window is, in principle, bounded by an exposure of the Basal Thrust (Ring et al., 2007b); however, the structure lacks comprehensive description, likely because it is either poorly exposed or has been obscured by reworking of the contact during exhumation (Ring et al., 2007b; Ducharme et al., 2022). Due to the aforementioned uncertainty regarding the Tsakei Unit, the tectonostratigraphic position of the tectonic contact is also disputed: it has been interpreted to lie either consistently at the base of the Styra Unit (Shaked et al. 2000; Ducharme et al., 2022), or is otherwise placed below the Tsakei Unit at the southern limits of the tectonic window (Katsikatsos et al., 1991a,b; Ring et al., 2007b). Although the presence of large (up to ~100 m scale) metabasic and serpentinitic blocks in the

Tsakei unit is the primary justification for its discrimination from the flysch succession, both units feature hallmarks of tectonic sedimentation like marble olistoliths and locally high densities of smaller scale lithological heterogeneities (Abbate et al., 1970; Katsikatsos et al., 1991a; Ring et al., 2007b).

Compared with that of the CBU, the geodynamic and metamorphic histories of the Basal Unit are poorly known. Evidence from the weakly to unmetamorphosed Gavrovo-Tripolitza exposures in the Peloponnese and Crete indicate it entered the Hellenic subduction zone between *c.* 35-30 Ma (Thomson et al., 1998; Sotiropoulos et al., 2003). Proposed timing for peak HP metamorphism recorded by the Basal Unit, meanwhile, span the Oligocene (Shaked et al., 2000; Ducharme et al., 2022) to early Miocene (Ring and Layer, 2003; Ring et al., 2007b; Gerogiannis et al., 2021), largely reflecting contrasting interpretations of early Miocene phengite $^{87}Rb/^{87}Sr$ and $^{40}Ar/^{39}Ar$ dates as capturing deformation or metamorphic events.

The Basal Unit on Evia attained maximum metamorphic conditions of ~11 kbar and ~400°C, prior to greenschist-facies overprint during unroofing that intersected conditions of ~7 kbar and ~310°C (Shaked et al., 2000; Ducharme et al., 2022). Zircon (U-Th)/He data show that the entire structural pile of southern Evia had exhumed into the brittle crust by the middle Miocene (*c.* 17-15 Ma), thus implying a rapid subduction and unroofing history relative to that of the CBU (Ducharme et al., 2022). To accommodate the short apparent interval between subduction, peak HP metamorphism, and exhumation, Ducharme et al. (2022) proposed a rapid transition from subduction to probable syn-orogenic exhumation of the Basal Unit, followed by post-orogenic exhumation that may have been synchronous with that of the CBU. Ductile thinning along major tectonic structures, accommodated either by pure shear (Xypolias et al., 2003, 2010) or flattening

(Ducharme et al., 2022) strain, may have partially facilitated the rapid exhumation of the Basal Unit on Evia and its neighboring exposures on the Attic Peninsula.

3.4. New field observations

The lithostratigraphic interval separating marbles belonging, respectively, to the Basal and Styra Units is dominated by pelitic, carbonate, and quartzose schists and quartzites, locally intercalated on the meter scale, with proportionally greater carbonate-rich schist toward its base. Several interpretations have been proposed; the schists are either divided between the Basal Unit metaflysch and Tsakei Unit (Katsikatsos et al., 1991a, b), or considered as belonging solely to the metaflysch unit (**Figure 3.1**). Independent of interpretation, the schists are overlain by massive to foliated marbles assigned to the Styra Unit of the CBU. These compositionally diverse schistose rocks were interpreted by Ducharme et al. (2022) to have localized ductile and brittle-ductile strain facilitating exhumation of structurally lower parts of the Basal Unit via ductile thinning and top-to-NE normal-sense displacement. To further explore this model, here we report new field observations focussed on the structural record of the schists.

The contact between the Styra marbles and the underlying schists is exposed along the road connecting the village of Mesochoria and the beach of the same name (**Figure 3.1**; **Figure 3.2A**). Multi-generational ultracataclasites occur below the marble, dipping ~30° toward the NE, with fragmented marble scree defining their upper limits (**Figure 3.2B**). Synthetic Riedel structures indicate the cataclasites accommodated top-to-NE brittle displacement (**Figure 3.2C**). Randomly oriented blocks of veined mafic and pelitic schist, up to a meter in diameter, are dispersed throughout the cataclasites. The upper contact with the marbles may be followed in exposures along opposing cliffs and in roadcuts to the north and south (**Figure 3.2D**). Marbles in the hanging

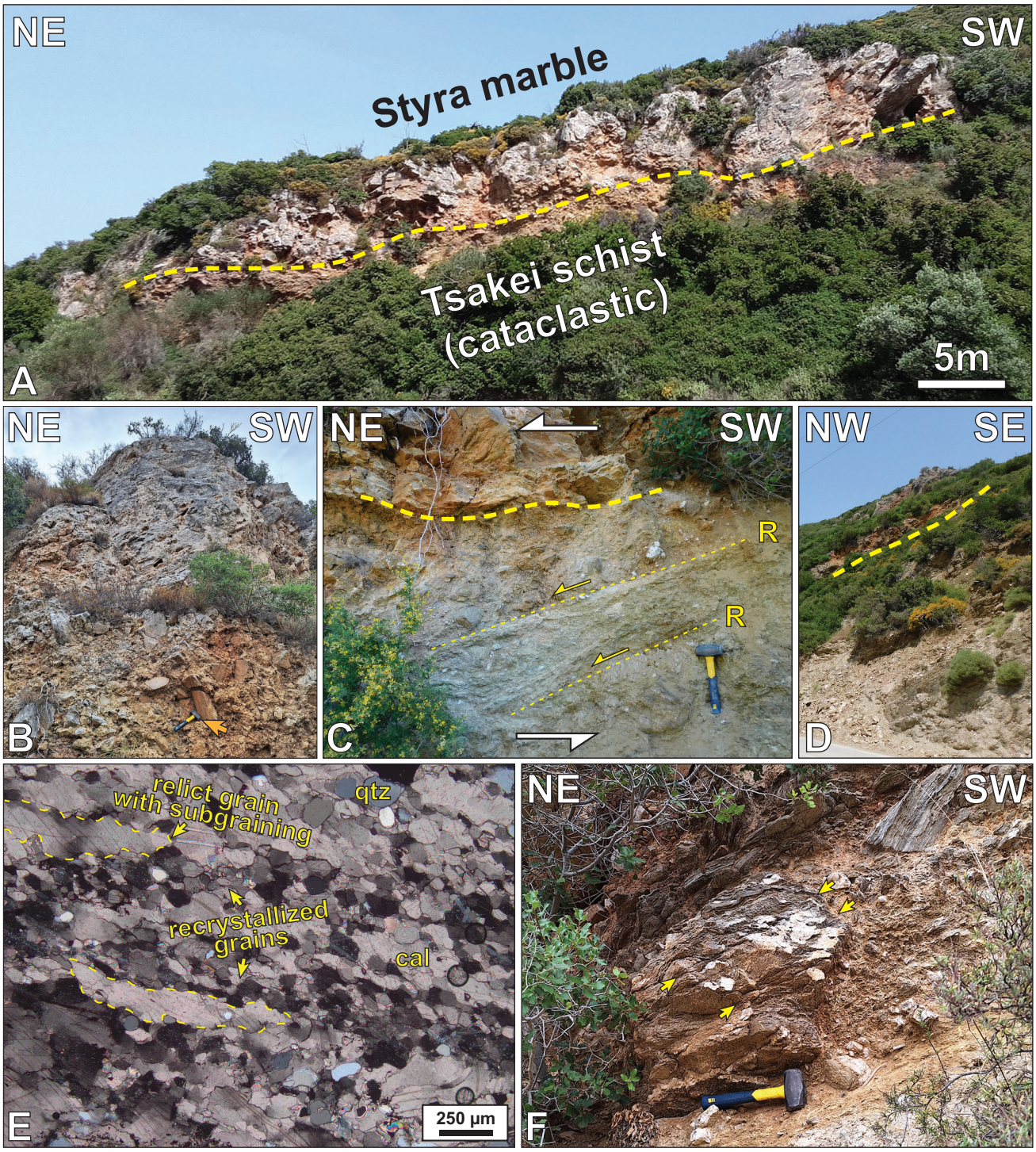

Figure 3.2. (A; UTM zone 35N, 258568E, 4236248N) Cliff face exposing Styra Unit marbles directly overlying cataclasized Tsakei schists. Same outcrop as B, C, E, and F. (B) Unconsolidated marble scree separates intact hanging wall from the underlying cataclastic horizon (arrow indicates scale). (C) Multi-generational cataclasite below little deformed Styra marble. Synthetic Riedel shears (R) indicate top-to-NE shear sense. (D; UTM zone 35N, 258370E, 4236244N) Along-strike continuation of the Styra-Tsakei contact. Schists in the bottom-right corner (same outcrop as Figure 3) underlie a poorly exposed section and show little evidence of brittle deformation. (E) Microstructure of marble from the hanging wall. Core-and-mantle structure and sutured grain boundaries indicate calcite has accommodated dynamic recrystallization. (F) Schist block structurally above the cataclasite horizon showing axial planar cleavage (arrows) at a high angle to foliation within the block. Scale: hammer: 27 cm long. Mineral abbreviations after Whitney and Evans (2010).

wall exhibit a microstructure characterized by a well-defined shape-preferred orientation (SPO) of calcite, with larger grains mantled by finer grains and exhibiting subgrain development and curved (type III) twins (**Figure 3.2E**).

Stratified pelitic and carbonate schists structurally below the cataclasites dip gently to the northwest and contain two discernible fold generations: (1) an earlier set of NE-trending, locally rootless intrafolial isoclinal folds; and (2) a NW-trending, close to isoclinal fold generation with axial planes dipping moderately or gently west. The latter folds are associated with a prominent W-dipping axial plane cleavage that cross-cuts the metamorphic foliation and earlier intrafolial folds (**Figure 3.3A; Figure 3.4C**). A similar axial plane cleavage is visible in blocks situated above the cataclasite (**Figure 3.2F**). Tiling and sigmoidal quartz vein boudins alongside a consistent NE-SW stretching lineation record consistent top-to-NE shear sense (**Figure 3.3B, C; Figure 3.4B**). Schists occupying the immediate footwall to the cataclastic horizon dip gently northwest (i.e., orthogonal to the dip of the cataclasite) and display well-preserved ductile and brittle-ductile structures, including multiple fold generations and the aforementioned axial plane cleavage.

Deeper structural levels, toward the lower contact with the Basal Unit marbles, are increasingly dominated by penetrative sub-horizontal foliations that lack evidence for the older multi-generational folding and associated axial plane cleavage (**Figure 3.4A, C**). Heterolithic rock exposures demonstrate a first-order control on the inconsistent occurrence of the older structures. Competent rock strata, when oriented at high angles to the incipient cleavage, are folded about axial planes parallel to the sub-horizontal crenulation cleavage developed in adjacent schists (**Figure 3.3D, 3.5A-B**). Competent rock units nevertheless commonly display a less prominent expression of the associated axial plane cleavage cross-cutting a relict, shallowly W-dipping older foliation (**Figure 3.5C**). Quartz veins oriented at high angles to the foliation are apparently

deformed only by the later of those two folds, and in outcrops showing a single continuous foliation, the later folds possess axial planes consistently parallel to the host rock foliation (**Figure 3.5D, Figure 3.6A, C**).

Other structures, such as shear bands and faults, localize preferentially in pelitic lithotypes along contacts with interspersed blocks of marble, quartzite, or metabasite (**Figure 3.5E**). A prominent example is the localization of normal faults along the metabasic blocks within the Tsakei Unit along the highway west of Raptei (**Figure 3.1; Figure 3.5F**).

3.5. Analytical Methods

3.5.1. Quartz c-axis fabric analysis

Twelve samples containing one or more quartz veins were selected for quartz petrofabric analysis. Oriented standard 30 μm polished thin sections of the samples were scanned with a Russell-Head Instruments G60+ automated fabric analyzer at the University of British Columbia, Okanagan (Kelowna, Canada). Analyzed sections are photographed from nine different angles using a range of polarizer and accessory plate orientations (Larson, 2018). The resulting images are processed together to develop a statistical rendering of the orientation of quartz c-axes, an achsenverteilungsanalyse diagram (Sander, 1950), with minimal detectable deviation from other c-axis determination techniques (Wilson et al., 2007; Peternell et al., 2010). Quartz c-axis orientations are stored at the pixel scale in the captured images, and c-axis orientations (one per quartz grain) are manually selected in the Investigator companion software. Between 609 and 5735 individual grain c-axis orientations were selected per sample from among quartz hosted in the veins. All distinguishable grains yielding a well-resolved c-axis orientation were included in the dataset, proceeding unidirectionally through a scan to minimize bias in the c-axis populations.

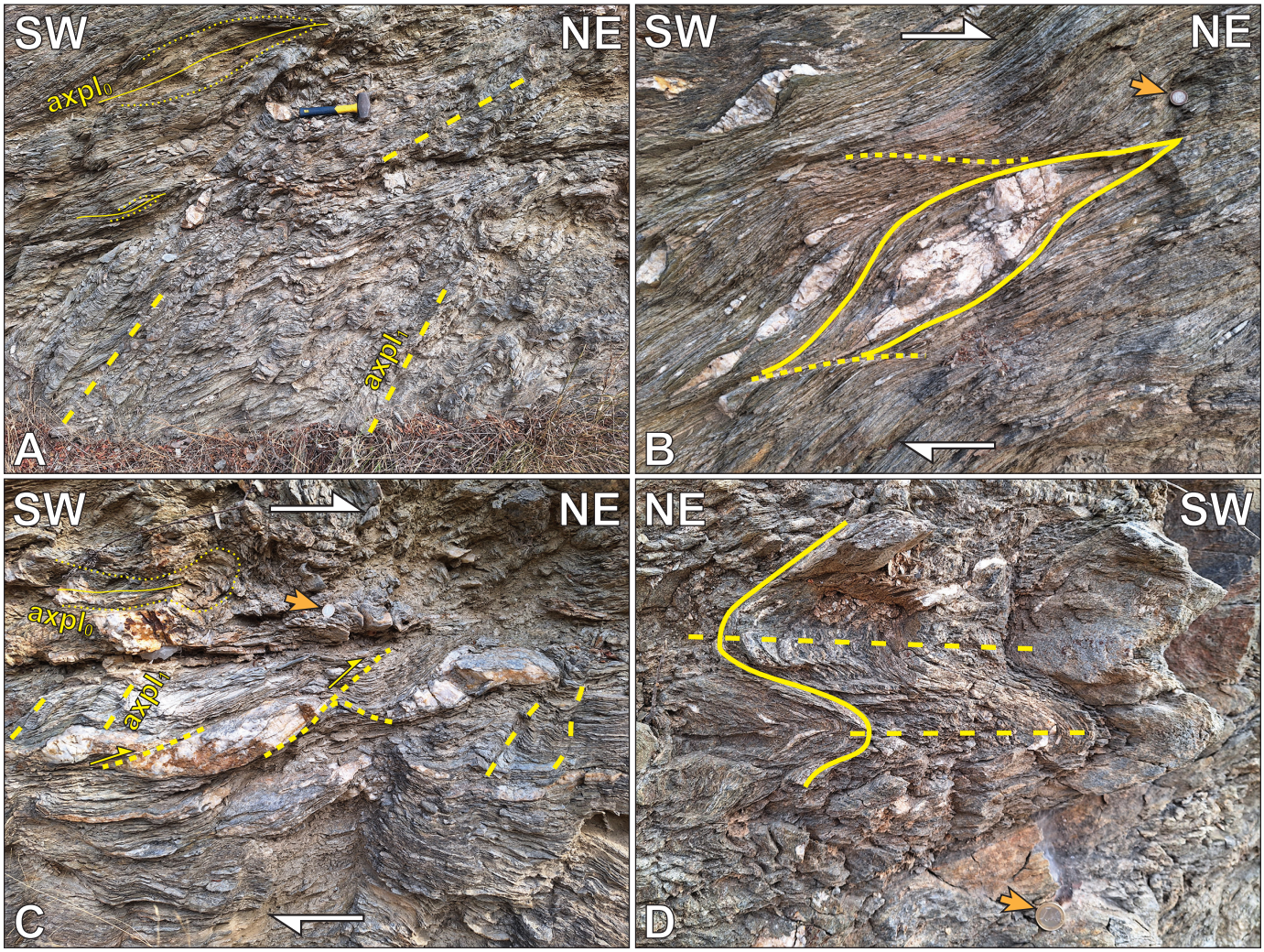

Figure 3.3. Field photographs of structures in schists in the footwall of cataclasites near Paralia Mesochoria (Figure 3.2). (A; UTM zone 35N, 257753E, 4236238N) A dominantly sub-horizontal foliation shows undulations related to NW-SE trending folds. A SW-dipping axial plane cleavage cross-cuts the foliation (thick dashed yellow line). Older, now rootless intrafolial isoclinal folds (thin dotted line: fold trace; thin solid line: axial plane) trend subparallel (NE-SW) to the exposed face. (B; UTM same as A) S/C-type shear bands (thick dotted line) showing top-to-NE shear sense. (C; UTM same as A) Tiling of imbricated quartz vein segments (thick dotted lines) indicating top-to-NE shear sense. The W-dipping axial plane cleavage (thick dashed line) resembles false antithetic C'-type shear bands. (D; UTM zone 35N, 254513E, 4239855N) Folded foliation (solid line) with NW-SE trending fold axes in a carbonate schist deeper into the footwall showing a subhorizontal axial plane cleavage (dashed line) and a more closely spaced axial plane cleavage. Orange arrows indicate location of scale. Scales: hammer: 27 cm long; 1€ coin: 23 mm diameter.

Selected c-axis orientations were processed using a custom script written in R (Larson, 2022). The script handles statistical analysis of the c-axis orientation data, including definitions of kernel widths and number of bins. These preferences are then used to generate scatter and contour plots on equal-area lower hemisphere stereonet projections. The script also calculates fabric strength parameters including multiples of uniform density (m.u.d.), the pole figure index J_{pf} of Mainprice et al. (2015), and fabric cylindricity parameters P, G, R, and B after Vollmer (1990).

3.5.2. In situ *$^{40}Ar/^{39}Ar$ geochronology*

A suite of standard 30 μm polished thin sections were prepared to examine the microstructures developed in mica from twenty samples. From among these, thirteen 150 μm polished thick sections were prepared with cyanoacrylate (i.e., super glue) from nine samples for *in situ* laser ablation $^{40}Ar/^{39}Ar$ geochronology. Thick sections were prepared using the same section of rock the thin sections were prepared from to maximize homology of visible microstructures.

Sections were thoroughly characterized and photographed using a combination of conventional transmitted and reflected light microscopy. Additional imaging was performed using a JEOL 6610LV scanning electron microscope (SEM) at the University of Ottawa to obtain backscatter electron (BSE) images, equipped with an energy dispersive spectrometry (EDS) detector for semi-quantitative mineral identification. Once regions containing a sufficient density of inclusion-free white mica were identified, regions of interest in the polished thick sections were isolated using a fine finishing saw and removed from their glass mount by dissolving the adhesive in acetone overnight. Isolated rock chips were then packaged into aluminum discs for irradiation.

Complementarily, white mica chemical compositions were determined from the counterpart thin sections via electron microprobe analysis at the University of Ottawa using a

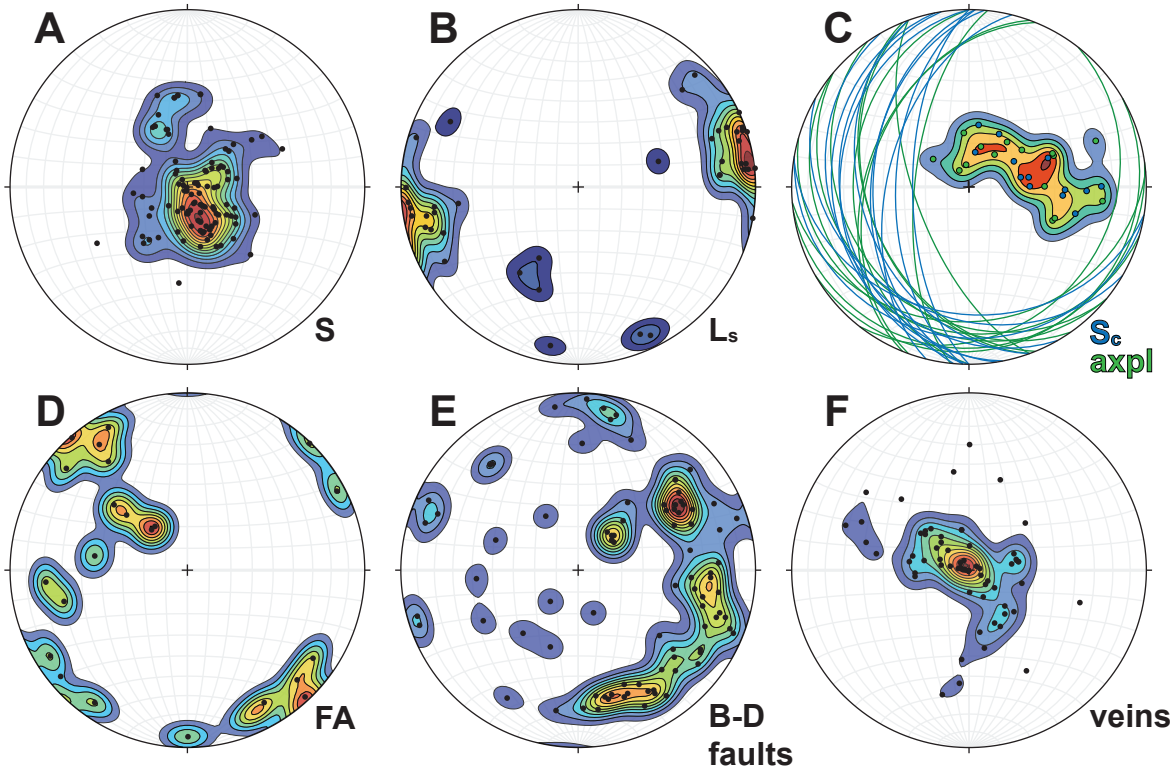

Figure 3.4. Equal area lower hemisphere stereonet plots of structural data from the schist unit of southern Evia. All planes are plotted as poles, except in C where both planes and poles are plotted. Abbreviations: S - foliation; Ls - stretching lineation; Sc - crenulation cleavage; axpl - axial plane cleavage; FA - fold axis; B-D - brittle-ductile.

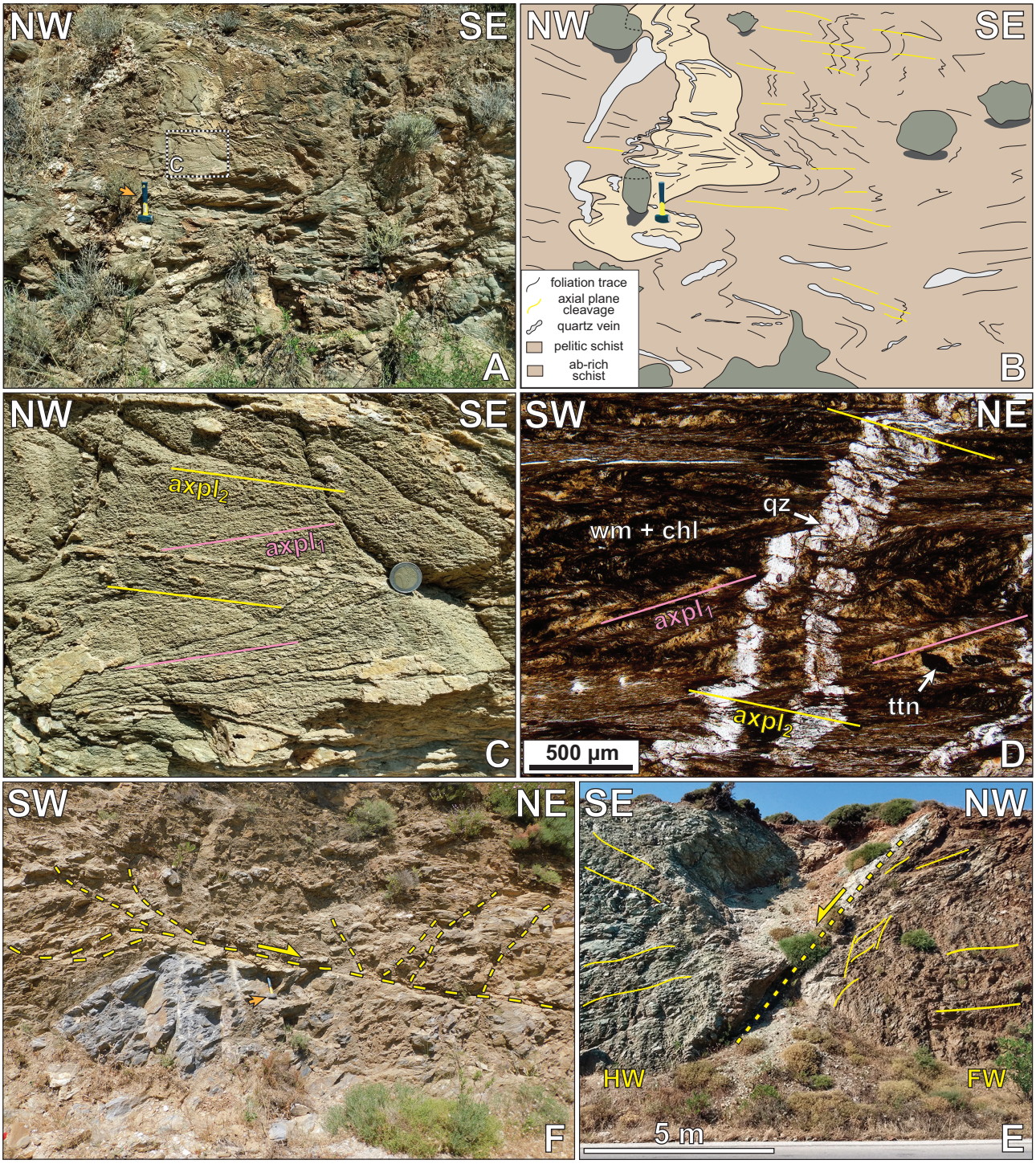

Figure 3.5. (A-D; UTM: 253314E, 4245312N) Photograph (C, E), interpretive sketch (D) and micrograph (F) of a competent subvertical semipelitic schist deformed within less competent chlorite schists. The matrix shows a gently E-dipping spaced crenulation cleavage that is axial planar to the dominant folds ($axpl_2$). The competent lens preserves an older, shallowly W-dipping axial plane cleavage ($axpl_1$) between a second fabric and quartz veins parallel to $axpl_2$. Thin section in D is cut parallel to NE-trending L_S, oblique to the outcrop face. (E; UTM: 254659E, 4237460N) Low-angle brittle-ductile normal fault and associated high-angle conjugate normal faults localized along the contact between pelitic schist and a marble block. (F; UTM: 254910E, 4236253N) High-angle, SE-dipping normal fault dividing a metabasic block (HW) from Tsakei schists (FW). Mineral abbreviations after Whitney and Evans (2010). Orange arrow indicates location of scale. Scale: hammer: 27 cm long; 2€ coin: 26 mm diameter.

JEOL 8230 SuperProbe. Major and minor elements were determined quantitatively using a 10 μm spot size. Spot selection prioritized white mica in the same microstructural contexts as were identified as targets for *in situ* $^{40}Ar/^{39}Ar$ analysis, as well as white mica defining the dominant metamorphic foliation.

Following a 60 day irradiation, sample chips were mounted using a ceramic adhesive (PELCO®) on a quartz slide placed in a stainless-steel chamber with a sapphire viewport attached to the stainless steel high vacuum extraction system and allowed to stabilize prior to analysis at the University of Manitoba (Winnipeg, Canada). Analyses were performed using a multi-collector Thermo Fisher Scientific ARUGS VI mass spectrometer connected to a Photon Machines (55W) Fusions 10.6 CO_2 laser to ablate target regions 200 μm x 50 μm in size. Comprehensive details of analytical methods for this stage are presented in **Appendix B**.

3.5.3. In situ $^{87}Rb/^{87}Sr$ geochronology

Two 150 μm thick polished sections were prepared for *in situ* $^{87}Rb/^{87}Sr$ geochronology using an Agilent 8900 triple-quadrupole inductively coupled plasma mass spectrometer equipped with a reaction cell (Zack and Hogmalm, 2016; Hogmalm et al. 2017) paired to an ESL 193 Excimer laser with a TwoVol3 ablation cell in the Fipke Laboratory for Trace Element Research at University of British Columbia, Okanagan (Kelowna, Canada). The analyses followed the basic procedures outlined in Larson et al. (2023) with white mica ablated using a 50 μm diameter spot, a repetition rate of 10 Hz and a laser fluence of 4 J/cm^2. Analyses of secondary reference materials, including the in-house white mica MA1 (c. 350 Ma, A. Camacho, unpubl. data) and the nano-powdered biotite Mica-Fe (310 ± 10 Ma, Govindaraju 1979; 305.4 ± 2.0 Ma, Rösel and Zack, 2022), yielded dates that overlap within error of those expected (347 ± 3 Ma and 306 ± 3 Ma,

respectively). Isochron calculations excluded analyses with high uncertainty, using a >30% (2 standard error of the mean) cut-off that resulted in the exclusion of one analysis per sample. Data processing and visualization were performed using the online version of the IsoPlotR package (Vermeesch, 2018).

3.6. Quartz petrofabric analysis

3.6.1. Sample descriptions

Veins exhibiting macroscopic evidence of deformation (i.e., rotation or stretching relative to the host foliation, or folding) were sampled from pelitic and carbonate schists of the Basal Unit metaflysch and Tsakei Unit to assess the presence of a crystallographic preferred orientation (CPO) in quartz (**Figure 3.1; Figure 3.7**). Veins exhibiting post-sealing deformation in quartz-rich lithotypes were comparatively rare, and thus these are unrepresented in our data. Chosen samples prioritized veins containing proportionally greater quartz than carbonate material, and which displayed microstructures consistent with dynamic recrystallization of quartz (e.g., subgrain formation, sutured/bulging grain boundaries, etc.).

Most quartz veins in the study area are oriented parallel or slightly oblique to the gently-dipping metamorphic foliation (**Figure 3.4F, Figure 3.6**). Veins displaying this relationship were either part of a continuous, laterally extensive pinch-and-swell quartz vein, or formed isolated boudin segments with lens-shaped geometries (**Figure 3.6E**). Two of the veins (VS-07B, VS-10J) are isoclinally folded about axial planes parallel to the penetrative foliation of their host rock (**Figure 3.6A, C**). Hinge sections of these veins cross-cut foliation at a high angle and may be ptygmatic or thickened (**Figure 3.6C, G**), whereas their limbs are foliation parallel or oblique and elongated parallel to foliation, like the isolated vein segments described above.

Vein fill consists of variable proportions of quartz and calcite, with some veins composed solely of quartz. Veins selected for quartz c-axis fabric analysis were dominantly coarse grained (average grain diameter >150 μm), frequently with a finer population (~40-250 μm) surrounding coarser (500-1000 μm) quartz ribbon porphyroclasts with abundant internal subgrains (**Figure 3.6D**). Ribbon porphyroclasts were observed in half the samples, whereas the remaining six (VS-08H, EV20-03, EV21-07, EV22-03, EV22-07, and EV22-17) contain comparatively equigranular polygonal aggregates exhibiting an SPO and serrated grain boundaries, with some (EV20-03, EV22-03) microstructures dominated by pinning of quartz by mica. Aspect ratios of the ribbon grains vary considerably, with some exhibiting nearly equant dimensions and others approaching aspect ratios of 10:1. Long axes of elongate subgrains are universally parallel to the long axis of their host ribbon. Quartz grains 'mantling' the ribbons exhibit low-amplitude grain boundary bulging and sutured grain boundaries and commonly display a shape preferred orientation (SPO), either with long axes approximately normal (**Figure 3.6D, H**) or oblique to the vein walls (**Figure 3.6B, F**). Oblique SPOs indicate a consistent top-to-NE or -ENE shear sense. Deformation lamellae of sub-basal type (with lamellae oriented between 70°-90° from the grain c-axis; e.g., White, 1973) and prismatic subgrains are commonly observed in both coarse older grains and finer new grains, although the latter are most prominently developed in relict grains. Grains surrounding relict grains are of approximately the same size as the subgrains therein, typically between 20-150 μm. Some, though not all, samples show an abundance of well-developed quartz triple junctions (**Figure 3.6D**).

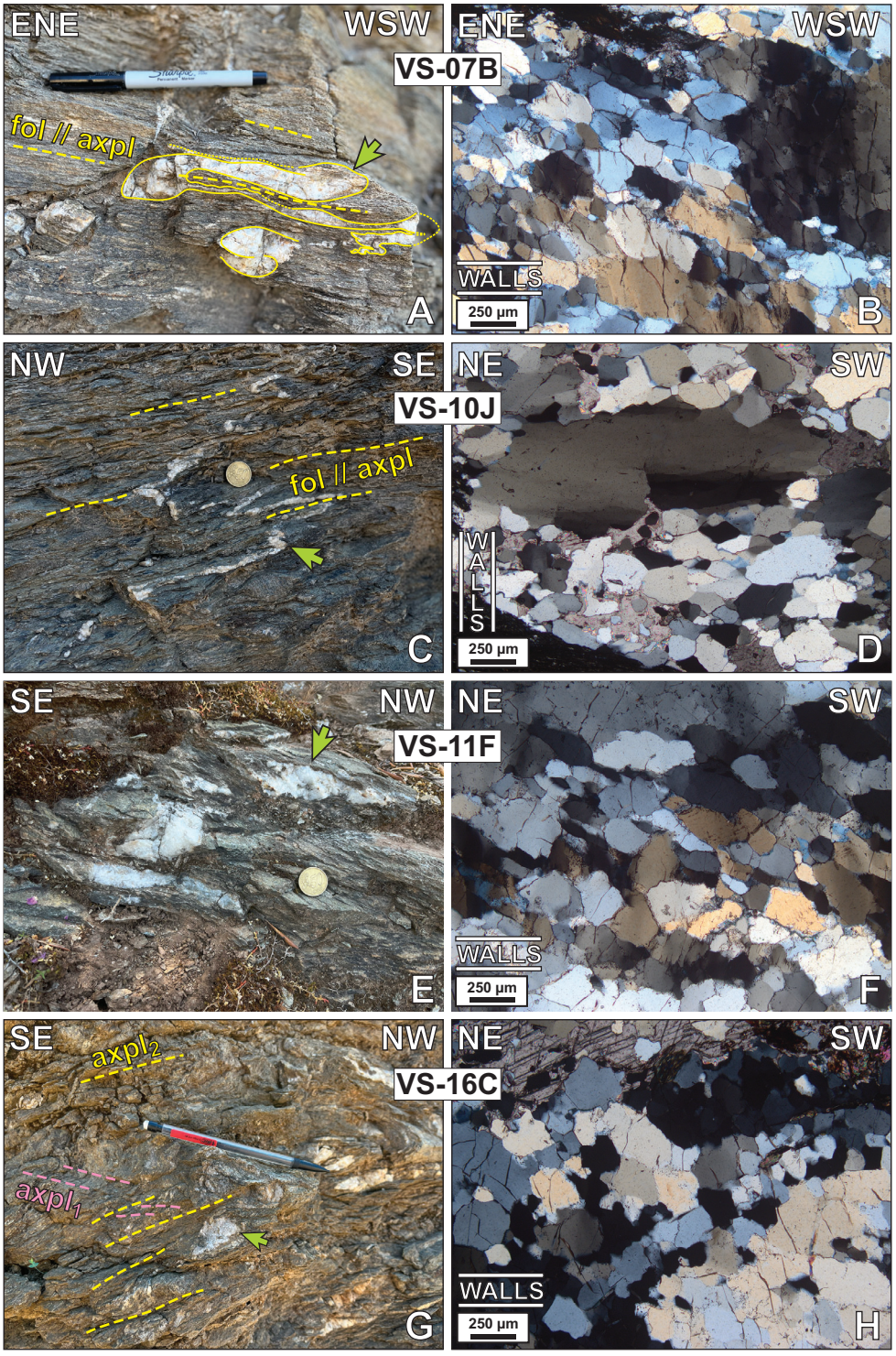
ENE
WSW
VS-07B
fol // axpl
A
ENE
WSW
WALLS
250 µm
B
NW
SE
VS-10J
fol // axpl
C
NE
SW
WALLS
250 µm
D
SE
NW
VS-11F
E
NE
SW
WALLS
250 µm
F
SE
NW
axpl2
axpl1
VS-16C
G
NE
SW
WALLS
250 µm
H

Figure 3.6. (previous page) Field photographs and micrographs of quartz veins used for petrofabric analysis. Lines lines labeled ′walls′ on micrographs indicate orientation of vein boundaries relative to photo. (A, B; UTM: 254783E, 4237525N) Vein sample VS-07B is isoclinally folded in outcrop with the gently W-dipping macroscopic host foliation parallel to the axial plane. Recrystallized quartz within the vein shows an oblique SPO indicating top-to-ENE shear sense. Note similar sizes of subgrains in the rightmost quartz ribbon and surrounding finer grains. (C, D; UTM: 250655E, 4252375N) Isoclinally folded vein sample VS-10J shows alternating pinch-and-swell of foliation-parallel limbs and isoclinal folding of foliation-normal hinges. Connecting segments of the vein are missing, perhaps due to pressure solution. Quartz shows an SPO parallel to the host foliation. Smaller grains show well-defined grain boundary triple junctions. (E, F; UTM: 245404Et, 4256238N) Sample VS-11F occurs as several disconnected segments. Quartz exhibits low-amplitude bulging at grain boundaries and an oblique SPO consistent with top-to-NE shear sense. (G, H; UTM: 254538E, 4239847N) Vein sample VS-16C is an isolated pocket of quartz occupying the hinge of a NE-SW trending fold in an outcrop preserving two axial plane cleavages. Quartz shows bulging and sutured grain boundaries. Green arrows indicate the approximate area shown in thin section. Scales sizes: A - 15 cm long; C, E - 24 mm diameter; G - 14.5 cm.

3.6.2. Results

Pole figures obtained from quartz veins deformed within the ESZ exhibit diverse c-axis distributions (**Figure 3.8**). Most pole figures display a prominent c-axis maximum or maxima close to Z (EV21-07; VS-07B; EV22-03; EV22-07; EV22-17) or Y (VS-10J; EV20-03B; VS-08H; VS-16C). One sample (VS-06.5A) shows a strong c-axis maximum ~30° from Y, defining the lower central segment of a girdle. Remaining samples possess two maxima of subequal c-axis concentrations separated by ~30° along a small circle (VS-06D) or along a great circle as part of a single girdle (VS-11F).

Four pole figures define distributions characterized by a small circle distribution centered on Z (EV21-07; EV22-03; EV22-07; EV22-17). The small circle segments of one such sample (EV21-07) are connected by an off-center girdle. Samples recording this type of distributions are mica schists that contain porphyroblasts of albite, and in one example (EV21-07), epidote. Carbonate constitutes a variable proportion of the veins, but in these mica schist samples is absent from the host rock. Samples defining Z-centered fabrics were collected at relatively high structural levels, near or immediately below the upper contact with the Styra marbles (**Figure 3.1, Figure 3.6**).

Three other samples, obtained largely from intermediate or lower structural levels of the Tsakei schists, yield pole figures defining asymmetric (VS-06.5A, VS-07B) or nearly symmetric (VS-11F) type-I cross-girdles (Lister, 1977). Girdle asymmetry, resolved relative to the oriented thin sections, top-to-WSW shear sense.

Other distributions are dominated by a single Y-axis maximum, with (VS-10J; VS-16C) or without (EV20-03B; VS-08H) the additional dispersion of c-axes along an adjoining small circle. Sample VS-16C displays a possible inclined, asymmetric type-II cross girdle (Lister, 1977) with

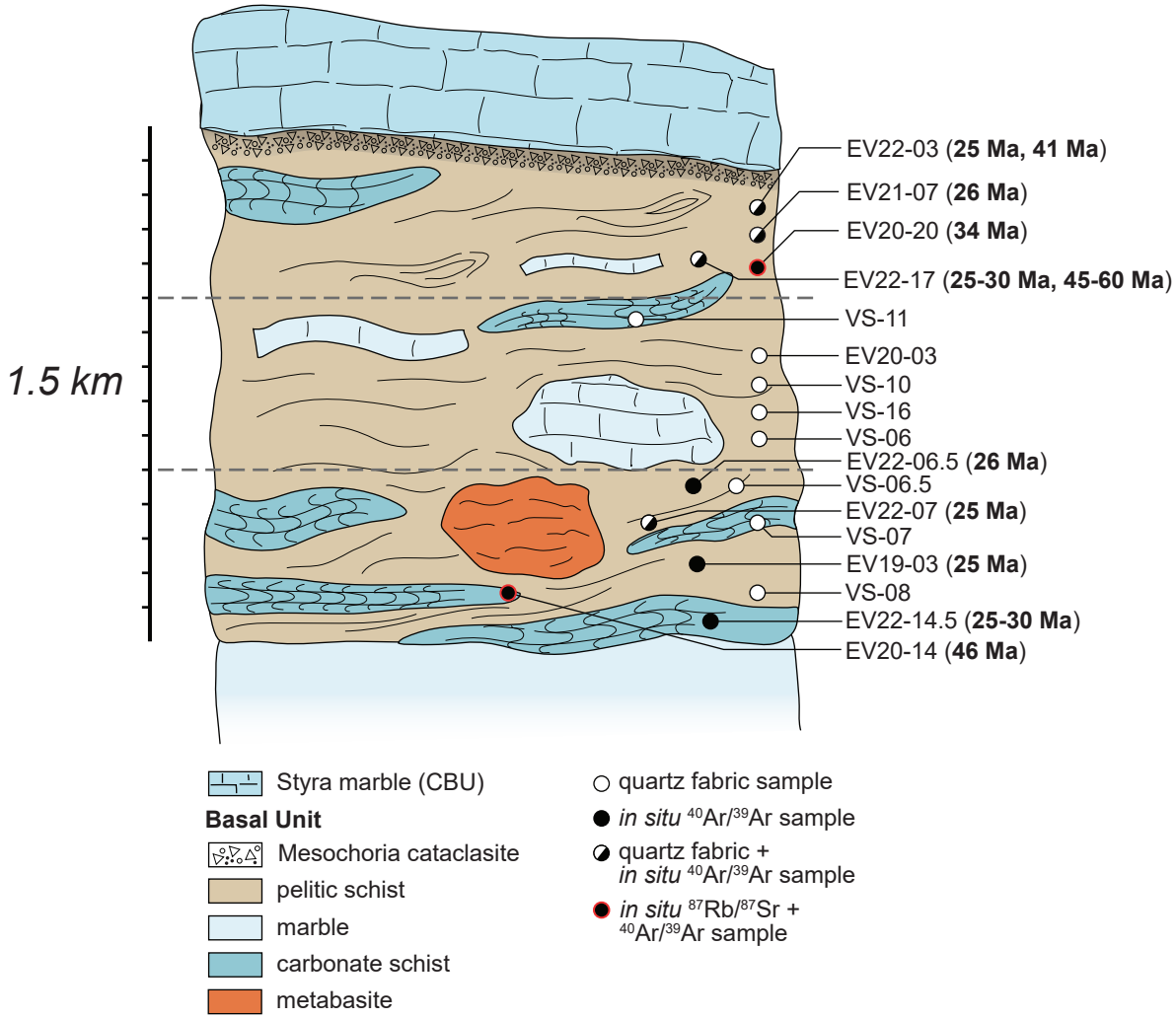

Figure 3.7. Schematic structural section of the schists on Evia showing approximate structural positions for each sample. The section considers the Tsakei Unit and Basal Unit flysch as a single continuous unit.

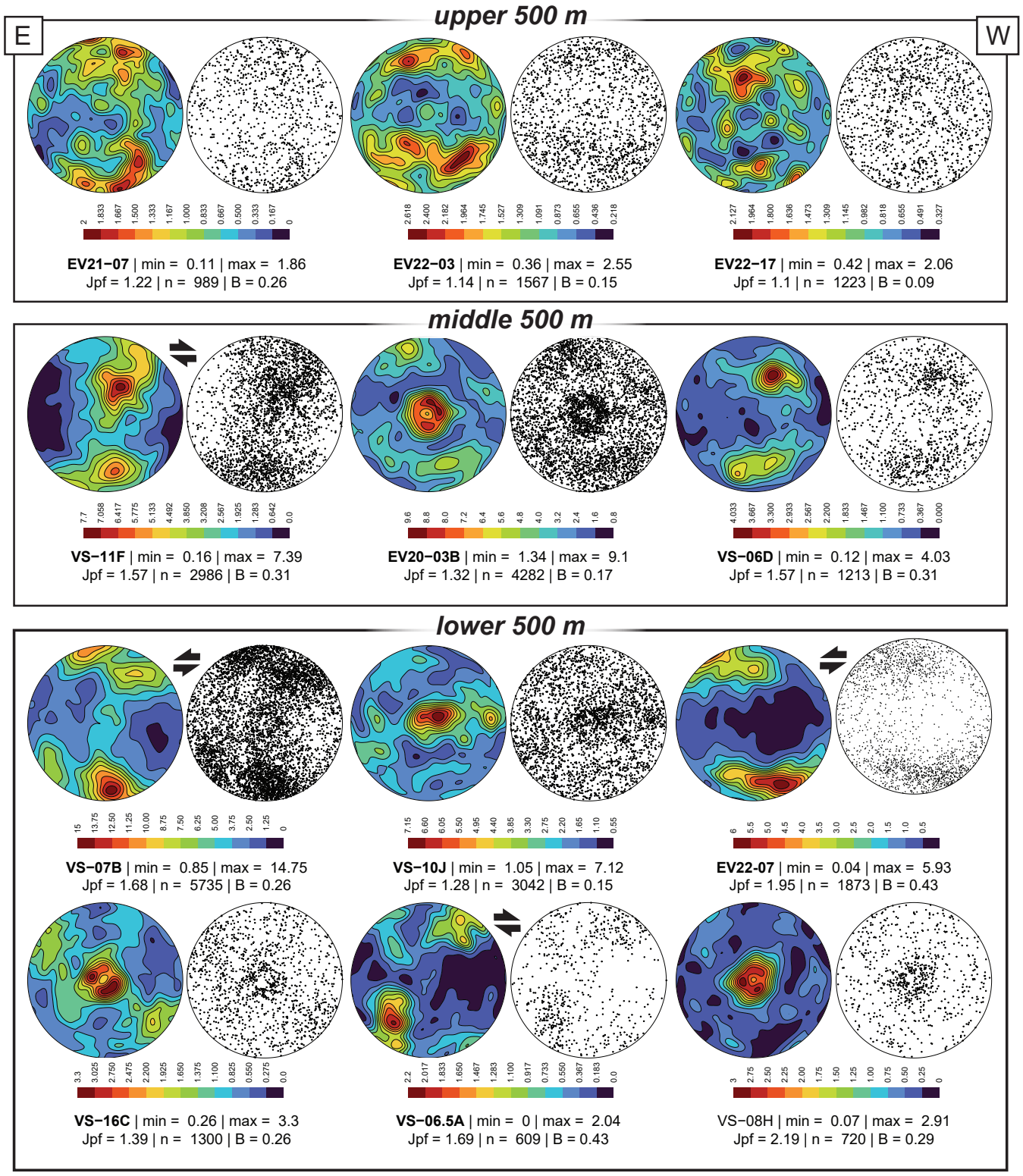

Figure 3.8. Lower hemisphere equal area projections showing contour (left) and scatter (right) plots of quartz c-axis orientations. Shear sense interpretations are included where applicable. All plots are oriented with the foliation (XY) plane oriented perpendicular and aligned E-W and the stretching lineation oriented parallel to the E-W direction. Samples are grouped according to structural position (see Figure 3.7).

one weaker limb. Finally, one sample (VS-06D) exhibits two subequal maxima symmetrically distributed about Y and oblique to both Z and X directions.

3.7. Geochronology

3.7.1. In situ *$^{40}Ar/^{39}Ar$ geochronology*

Nine samples from throughout the structural thickness of the Tsakei and flysch units were selected for *in situ* $^{40}Ar/^{39}Ar$ geochronology (**Figure 3.7**). Three among these – EV19-03, EV20-14, EV20-20 – were previously dated using the multiple single-grain total fusion method (Ducharme et al., 2022). Sample selection prioritized a variety of lithotypes dispersed throughout the purported width of the ESZ, with secondary preference applied to samples where mica-bearing microlithons exhibit distinct microstructures (e.g., shear bands, crenulation cleavage) to assess the correlation of microstructure with measured $^{40}Ar/^{39}Ar$ dates. White mica compositions were determined via EMPA on thin sections prepared from the same sample block as the dated thick sections, targeting white mica defining both metamorphic foliation and microstructures identified during initial sample characterization. Complete analytical results for the EMPA white mica chemistry and $^{40}Ar/^{39}Ar$ geochronology are presented in **Table S3.1** and **Table S3.2**, respectively.

In addition to recrystallized, foliation-concordant white mica, microstructures we targeted in the dated samples include: (1) coarser-grained, lens-shaped white mica 'fans' defining high or moderate angles to the foliation; (2) crenulated foliations with a spaced crenulation cleavage; (3) shear bands oriented at a high angle to the adjacent foliation; (4) isolated mono- or polycrystalline single grains appearing within veins and/or replacing or entrained within other mineral phases; and (5) mica occupying strain shadows to porphyroblasts of albite, epidote, or tourmaline (**Table 3.1**).

Table 3.1. Summary of new *in situ* $^{40}Ar/^{39}Ar$ geochronology.

Sample	Analysis	Microstructure	$^{40}Ar/^{39}Ar$ date (Ma)	±1σ	$\%^{40}Ar$	Mica Composition	
EV19-03: pumpellyite-albite schist (*n:* 11/12)						**Si (apfu)**	**X_{Mg}**
Chip 1	1	foliation	25.0	1.4	83.3	3.38 - 3.61 (mean: 3.45)	0.84 - 0.88 (mean: 0.85)
	2	foliation	25.7	1.0	88.5		
	3	foliation	24.7	1.1	83.8		
	4	foliation	23.3	1.0	74.4		
	5	foliation	26.5	0.9	89.8		
	6	foliation	26.5	0.9	90.3		
Chip 2	1	fan, high-angle	22.9	1.1	85.9		
	2	fan, high-angle	25.3	1.2	88.2		
	3	fan, high-angle	23.3	1.5	90.5		
	5	fan, high-angle	21.7	1.2	79.7		
	6	fan, low-angle, large single crystal	25.1	1.2	88.9		
EV20-14: impure schistose marble (*n:* 6/9)						**Si (apfu)**	**X_{Mg}**
Chip 1	1	foliation, micaceous microlithon	43.9	1.0	88.0	3.50 - 3.64 (mean: 3.54)	0.73 - 0.79 (mean: 0.76)
	2	foliation, micaceous microlithon	37.6	1.1	49.4		
	3	foliation, micaceous microlithon	38.6	1.0	57.1		
	4	foliation, micaceous microlithon	41.6	0.9	52.2		
	5	foliation, micaceous microlithon	42.0	1.1	58.3		
	6	*foliation, micaceous microlithon*	*40.6*	*1.4*	*38.8*		
Chip 2	*1*	*foliation, micaceous microlithon*	*47.0*	*1.4*	*48.1*		
	2	*foliation, micaceous microlithon*	*49.4*	*1.6*	*44.7*		
	3	foliation, micaceous microlithon	45.8	1.0	79.8		
EV20-20: albite-mica schist (*n:* 8/9)						**Si (apfu)**	**X_{Mg}**
Chip 1	1	foliation	34.9	1.3	81.7	3.35 - 3.46 (mean: 3.41)	0.67-0.73 (mean: 0.70)
Chip 2	*1*	-	*35.2*	*1.7*	*334.7*		
	2	foliation	29.8	2.2	63.2		
	3	fan	34.4	1.2	82.6		
	4	foliation	31.3	0.8	59.2		
Chip 4	1	foliation	35.9	1.0	93.6		
	2	foliation	29.3	1.6	69.9		
	3	fan	40.6	1.4	78.9		
	4	foliation/strain shadow	32.4	1.4	85.9		
EV21-07: epidote-albite schist (*n:* 8/8)						**Si (apfu)**	**X_{Mg}**
Chip 2	1	foliation	27.0	0.9	84.7	3.12 - 3.52 (mean: 3.36)	0.58 - 0.76 (mean: 0.69)
	2	foliation	23.7	0.9	81.5		
	3	fan	28.5	0.9	81.7		
	4	foliation	26.6	0.9	85.9		
Chip 3	1	foliation	27.1	0.7	73.9		
	2	foliation	23.4	0.7	80.7		
	3	strain shadow	36.6	0.8	85.0		
	4	strain shadow	27.0	0.7	85.1		
EV22-03: protocataclastic albite-mica schist (*n:* 12/14)						**Si (apfu)**	**X_{Mg}**
Chip 1	1	foliation	46.8	0.9	86.0	3.36 - 3.42 (mean: 3.39)	0.74 - 0.81 (mean: 0.79)
	2	foliation	36.8	1.0	74.6		
	3	strain shadow	42.4	0.9	79.1		
	4	-	*27.3*	*1.4*	*50.0*		
Chip 2	1	coarse, blocky, vein fill	22.9	0.9	65.8		
	2	coarse, after albite	24.3	1.0	73.6		
	3	coarse, blocky, vein fill	23.9	0.8	77.6		
	4	strain shadow	35.2	1.1	74.3		
Chip 3	1	strain shadow	37.8	0.9	72.4		
	2	-	*22.5*	*1.2*	*46.9*		
	3	coarse, after albite	28.2	0.8	71.9		
	4	foliation	44.7	0.7	82.0		
	5	foliation	38.1	0.8	79.3		
	6	coarse, high-angle fan	25.1	0.7	82.8		

Table 3.1 cont.

EV22-06B: epidote-albite-tourmaline schist (*n:* 8/9)						**Si (apfu)**	**X_{Mg}**
Chip 1	1	fan, high-angle	22.8	0.6	79.5		
	3	strain shadow	29.1	0.5	102.0		
	4	shear band	25.7	0.5	89.6		
Chip 2	1	strain shadow	23.0	0.6	98.4	3.30 - 3.47 (mean: 3.37)	0.54 - 0.65 (mean: 0.60)
	2	strain shadow	30.3	0.6	93.4		
	3	foliation	25.4	0.7	60.1		
	4	foliation	23.3	0.6	83.0		
	5	foliation	25.9	0.6	71.7		
EV22-07: paragonite-tourmaline schist (*n:* 11/13)			***paragonite**			**Si (apfu)**	**X_{Mg}**
Chip 2	1*	foliation	31.8	4.4	87.8	phengite: 3.24 - 3.39 (mean: 3.32)	phengite: 0.60-0.66 (mean: 0.65)
	2*	foliation	26.4	1.8	66.0		
	*3**	-	*25.8*	*1.5*	*40.2*		
	4	foliation	21.1	0.8	72.3		
	5*	fan	42.0	0.7	71.6		
	6	foliation	55.3	0.6	81.0		
Chip 4	1*	foliation	28.6	2.6	71.6	paragonite: 2.96 - 3.02	paragonite: N/A
	2	fan	39.5	0.6	89.2		
	3*	foliation	29.4	2.7	82.6		
	4	fan	35.2	0.7	77.4		
	*5**	-	*29.5*	*3.5*	*33.7*		
	6	foliation	22.5	0.8	75.4		
	7	foliation	23.7	0.7	82.0		
EV22-14.5: carbonate-silicate schist (*n:* 12/12)						**Si (apfu)**	**X_{Mg}**
Chip 1	1	foliation-parallel cleavage domain	27.5	0.6	89.0		
	2	crenulated relic foliation	31.4	0.6	83.6		
Chip 2	1	foliation-parallel cleavage domain	28.1	0.6	88.7	3.48 - 3.64 (mean: 3.57)	0.76 - 0.81 (mean: 0.79)
	2	crenulated relic foliation	26.7	0.5	80.2		
	3	isolated blocky crystal in chlorite	25.0	0.8	75.0		
	4	foliation	29.5	0.7	93.3		
	5	high-angle coarse blocky crystals	25.9	0.6	77.8		
	6	foliation-parallel cleavage domain	30.3	0.6	87.4		
	7	crenulated relic foliation	31.6	1.0	83.2		
Chip 3	1	foliation-parallel cleavage domain	31.5	0.7	62.3		
	2	crenulated relic foliation	31.4	0.6	69.6		
	3	foliation-parallel cleavage domain	31.8	0.7	76.4		
EV22-17: albite-mica schist (*n:* 11/12)						**Si (apfu)**	**X_{Mg}**
Chip 1	1	foliation	34.0	1.4	63.8		
Chip 2	1	coarse, blocky, vein fill	30.4	0.5	77.0		
	2	coarse, blocky, vein fill	24.5	1.2	55.2		
	3	coarse, blocky, vein fill	27.4	1.1	56.6		
	4	coarse, blocky, vein fill	30.1	0.6	74.9		
Chip 3	1	shear band	29.4	0.7	84.3	3.33 - 3.59 (mean: 3.46)	0.72 - 0.82 (mean: 0.77)
	2	shear band	40.0	0.6	89.6		
	3	foliation	61.2	3.9	58.2		
	4	shear band	46.5	0.7	86.9		
Chip 4	1	shear band	39.8	0.5	88.1		
	2	shear band	57.2	0.4	90.5		
	3	*foliation*	*35.2*	*0.9*	*50.9*		

Potassic white mica is overwhelmingly phengite, with limited spot analyses indicating muscovitic compositions with Si < 3.2 apfu (**Figure 3.9**). Mica chemistry within a sample does not vary systematically with microstructure. Carbonate-rich lithotypes contain mica with the highest Al-celadonite component, whereas phengite in pelitic samples contained overall higher Fe^{2+}. However, pelitic schist sample EV19-03 contained more magnesian phengite than even the carbonate-rich samples. Despite providing stoichiometrically reasonable microprobe data, most analyses from three samples (EV20-20, EV22-03, EV22-17) failed the recalculation exclusion criteria outlined by Vidal and Parra (2000), perhaps implying sub-microscopic intergrowths or inclusions of a chemically similar mineral (e.g., illite).

The aggregate *in situ* $^{40}Ar/^{39}Ar$ data display a prominent peak at *c.* 25 Ma, along with a shoulder defined by dates between *c.* 30-35 Ma (**Figure 3.10**). A limited number of older, middle Eocene to Paleocene dates are also measured in four samples, but represent the dominant age population in only one sample (EV20-14). Some samples show a correlation between microstructure and $^{40}Ar/^{39}Ar$ date. Common relationships of this type include: (1) coarse intrafolial mica 'fans' record alternately older or younger ages relative to a planar foliation (**Figure 3.11A, B**); (2) older dates infrequently recorded by mica occupying strain shadows of albite, epidote, or titanite porphyroblasts (**Figure 3.11C**); (3) coarse mica crystals in veins or replacing albite provide younger dates than mica within the foliation (**Figure 3.11D**); and (4) crenulated older foliation, including both the relic folded foliations and the spaced cleavage domains, record older dates relative to comparatively undeformed mica crystals defining high angles to the crenulation cleavage or intergrown with chlorite parallel to the cleavage (**Figure 3.11E, F**).

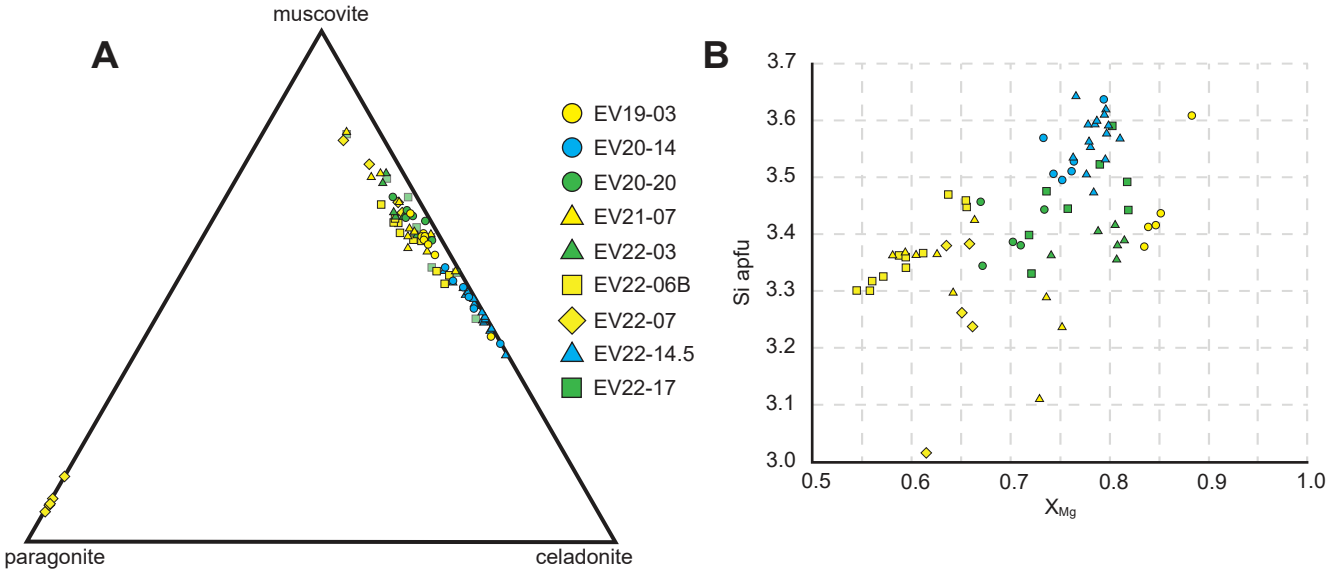

Figure 3.9. Compositional diagrams for white mica in samples selected for in situ $^{40}Ar/^{39}Ar$ and $^{87}Rb/^{87}Sr$ geochronology. (A) White mica ternary plot. (B) White mica Si apfu vs X_{Mg} plot.

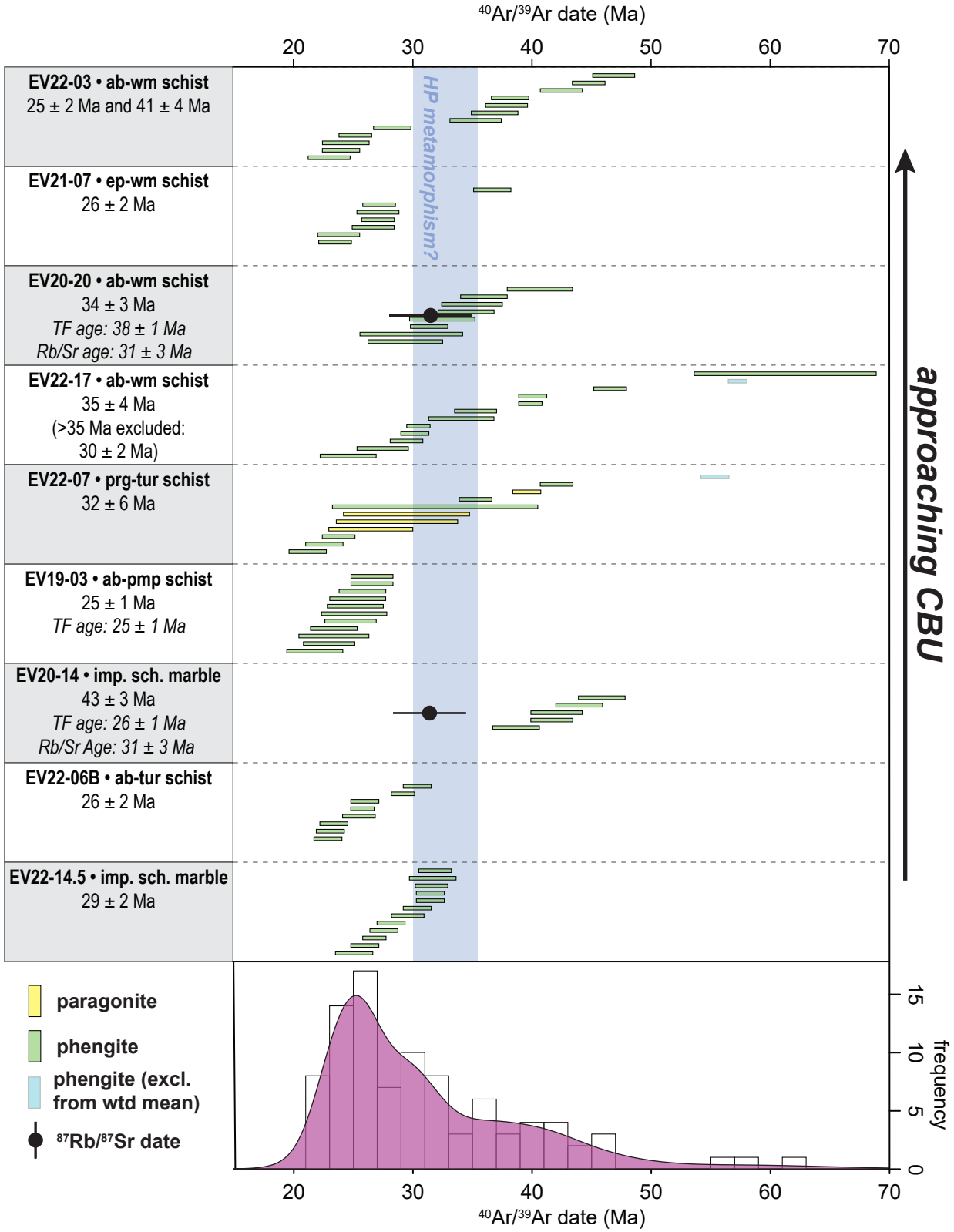

Figure 3.10. Summary of new in situ white mica $^{40}Ar/^{39}Ar$ geochronology from the Basal Unit and Tsakei schists of southern Evia. Samples are ordered from structurally lowest (bottom) to structurally highest (top). Bars indicate 1σ errors. TF age: single-grain total-fusion age (Ducharme et al., 2022). Blue bar indicates possible window of peak HP-LT metamorphism of the Basal Unit based on data from the Gavrovo-Tripolitza Zone (Thomson et al., 1999; Sotiropoulos et al., 2003). Refer to Table 3.1 for unabbreviated lithotype names.

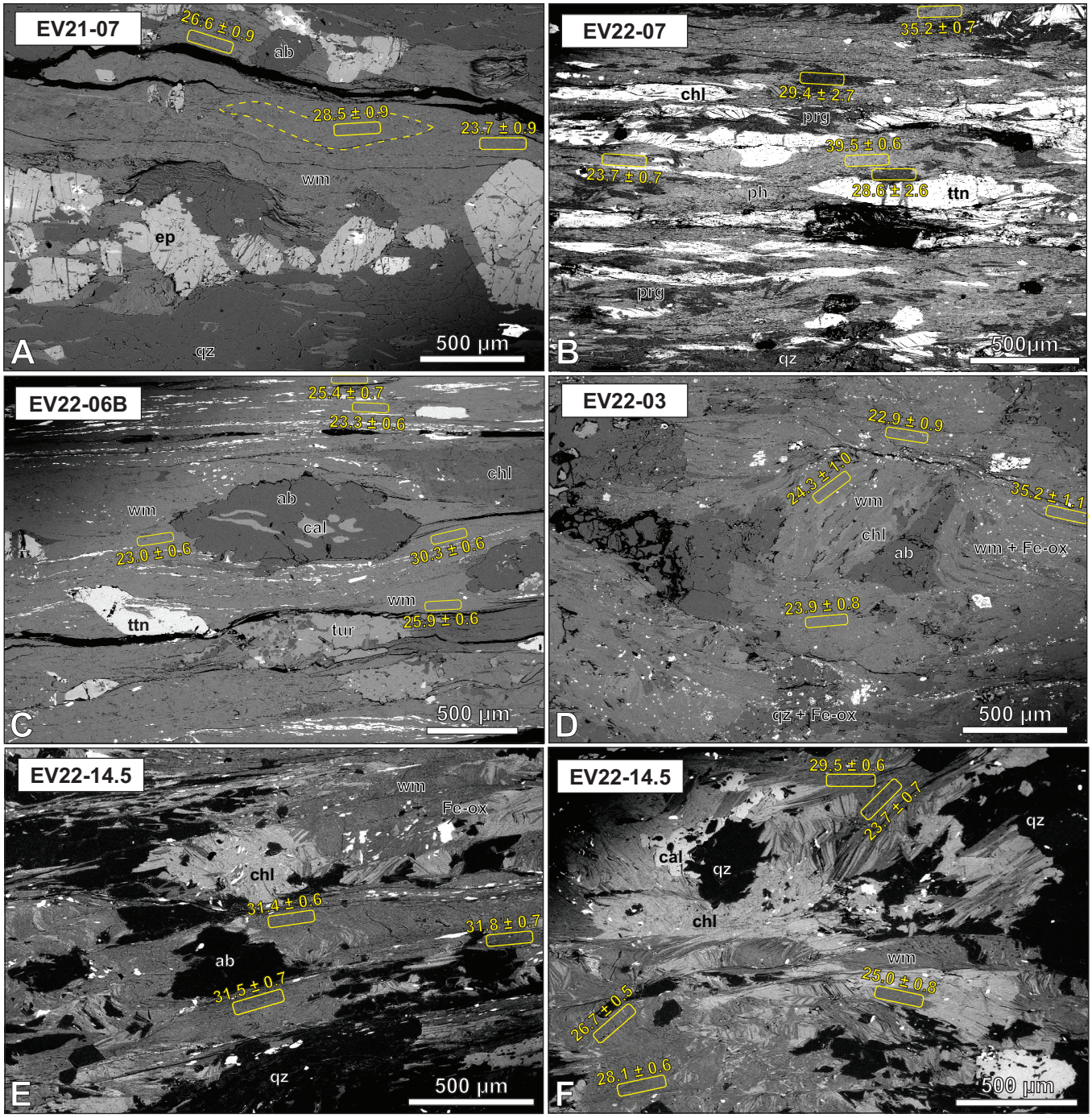

Figure 3.11. Backscatter electron images showing locations of in situ $^{40}Ar/^{39}Ar$ spot analyses. (A) High-angle white mica ′fans′ record late Oligocene dates, whereas foliation-defining mica records late Oligocene to early Miocene dates. (B) Discrete patches of phengite and paragonite in EV22-07 defining a single foliation yield late Oligocene dates within error of one another. Phengite in high-angle fans yields late Eocene dates. (C) Strain shadow preserving and early Oligocene date among foliation-defining white mica recording late Oligocene to early Miocene dates. (D) Coarse, blocky mica in EV22-03 overgrowing albite yield late Oligocene to early Miocene dates. Foliation in this sample has disseminated Fe-oxides and produces scattered late Eocene and older dates. (E and F) Sample EV22-14.5 exhibits mica microlithons with a spaced crenulation cleavage. Crenulated mica yields early to late Oligocene dates, whereas mica neoblasts intergrown with chlorite provided late Oligocene to early Miocene dates.

3.7.2. In situ $^{87}Rb/^{87}Sr$ *geochronology*

Two samples (EV20-14, EV20-20) from among those yielding Eocene and older *in situ* $^{40}Ar/^{39}Ar$ dates were selected for *in situ* $^{87}Rb/^{87}Sr$ geochronology. Sixty spot analyses were obtained from white mica in each sample. Supplemental analyses of low-Rb phases (calcite and albite) yielded poor analytical results and were excluded from isochron calculations. The complete analytical results are presented in **Table S3.3**. The data produce single population regressions that define overlapping isochrons of 31.1 ± 2.9 Ma (EV20-14; *n*: 59) and 31.4 ± 3.3 Ma (EV20-20; *n*: 59), respectively (**Figure 3.12**). Furthermore, the regressions define overlapping $^{87}Sr/^{86}Sr_i$ of 0.732 ± 0.007 and 0.722 ± 0.005.

3.8. Discussion

The field data reported here outline structural complexities not recognized by previous work on the tectonic contact of southern Evia (Shaked et al., 2000; Xypolias et al., 2003; Ring et al., 2007b; Gerogiannis et al., 2021; Ducharme et al., 2022). Most previous interpretations considered the CBU and Basal Unit, constituting the hanging wall and footwall of the Basal Thrust respectively, to have sustained an effectively identical strain history following thrusting (i.e., subduction of the Basal Unit). More recently, Ducharme et al. (2022) described dominantly planar foliated schists in the Tsakei Unit that they interpreted as relating to the so-called Evia Shear Zone (ESZ), a major structure assisting in unroofing the Basal Unit. Structures within the ESZ are consistent with top-to-NE general flattening, implying an oblate finite strain ellipsoid. Although our structural observations are broadly consistent with that finite strain geometry, the Tsakei and flysch units are not characterized solely by planar structures, but instead locally preserve two orthogonal fold generations and a related W-dipping axial plane cleavage. High angles between

both fold axes and axial planes of the two fold generations would, in principle, yield type-II refold structures. Along with the dominant easterly vergence of the later folds, the described structures strongly resemble the nappe-scale folding documented in the Basal Unit marbles at deeper structural levels of the Almyropotamos tectonic window (Ducharme et al., 2022).

Hence, the apparent structural continuity between the marbles in the footwall and the Tsakei unit near the tectonic contact with the CBU provides, in our view, compelling evidence that the Tsakei schists belong to the Basal Unit. This is also broadly in accordance with observed similarities in lithologic composition between the Tsakei schists and the Basal Unit flysch succession described both here and previously (Shaked et al., 2000; Ducharme et al., 2022). The complete suite of folds and the associated cleavage are not preserved comprehensively throughout the package of schists, with a subhorizontal planar foliation prevailing in many pelitic schist exposures (**Figure 3.4A**). (Micro-)structures in more carbonate- and quartz-rich lithotypes reveal a dominant foliation defined by a variably spaced crenulation cleavage that is axial planar to folded quartz veins in the same rocks (**Figure 3.5A-D; Figure 3.6A, C**). Vein segments in cleavage-parallel limbs exhibit boudinage and pinch-and-swell structure, whereas segments forming hinges and limbs at a high angle to cleavage exhibit ptygmatic folding. As the fold axes are parallel to the regional and local NE-SW stretching lineation (**Figure 3.4B**), the observed structures indicate the veins accommodated Y-direction stretching that likely also produced the flat-lying axial plane cleavage and the folds themselves.

Differential strain recorded by various flysch lithotypes implies the phyllosilicate-rich schists accommodated the bulk of the flattening strain. Pre-existing foliations and folds were fully transposed into a subhorizontal penetrative foliation in these mica and chlorite schists, whereas quartz- and carbonate-rich schists and marbles retain a partial or complete record of the older

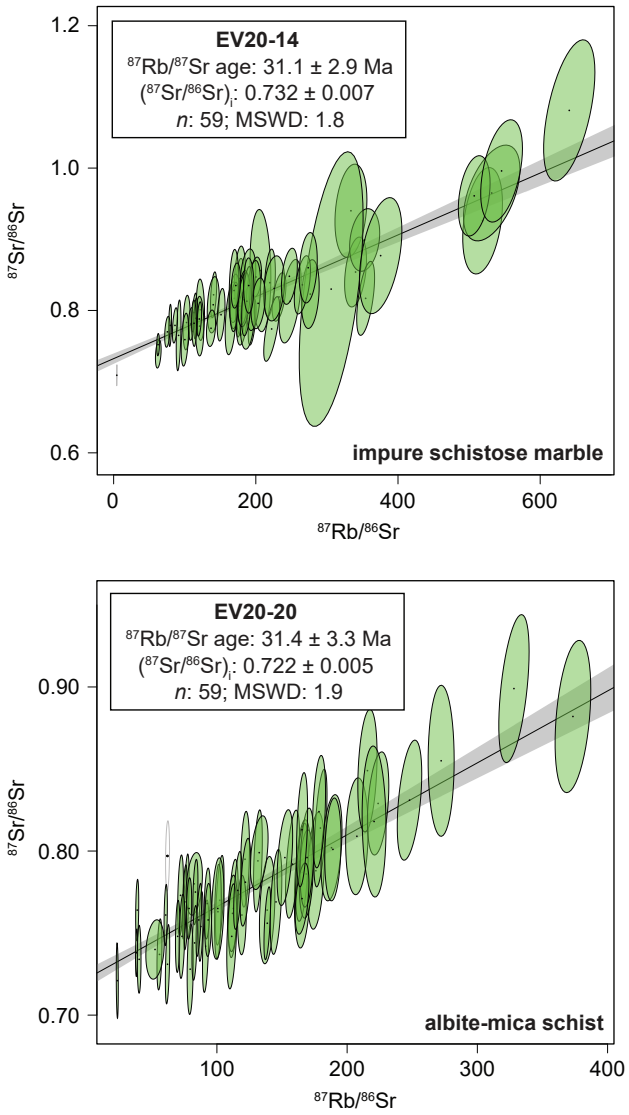

Figure 3.12. Isochron diagrams calculated using in situ white mica $^{87}Rb/^{87}Sr$ geochronology from samples EV20-14 and EV20-20. The two isochron dates are indistinguishable, despite the samples yielding contrasting ages via the in situ $^{40}Ar/^{39}Ar$ method (see Figure 3.10). Ellipses show 2σ errors. Empty ellipses are analyses that were excluded from the isochron regression.

structures. A consequential implication of this model is that, within the ESZ, strain acted diffusely, partitioning into numerous interconnecting shear zones within the pelitic lithotypes of the larger heterogeneous flysch succession. This style of deformation resembles that documented for block-in-matrix-type subduction zone mélanges (Fagereng and Sibson, 2010; Raimbourgh et al., 2019; Beall et al., 2019), rocks which are more commonly assumed to record syn-convergent deformation. Hereafter, we assess the compatibility of our new quartz petrofabric and geochronology datasets with this strain model.

3.8.1. Vein microstructure and c-axis distributions

Deformed veins on southern Evia exhibit quartz microstructures typical of deformation and recovery at moderate temperatures, with only modest local overprinting by lower-temperature microstructures (**Figure 3.7**). Half of the investigated vein samples (VS-06D, VS-06.5A, VS-07B, VS-10J, VS-11F, VS-16C) contain ribbon grains, some with aspect ratios as high as 10:1. These large (>0.5 mm) unrecrystallized quartz ribbons are mantled by finer grains (with long axes up to 200 μm) of equal size to subgrains developed within the ribbon porphryoclasts, indicative of dynamic recrystallization by subgrain rotation (SGR; Stipp et al., 2002) or Regime II of Hirth and Tullis (1992). Locally, these grains may exhibit planar grain boundary triple junctions. The relatively coarse recrystallized grain size (40-120 μm) implies that recrystallization proceeded at relatively low differential stress, whereas the recrystallization mechanism and triple junctions are consistent with temperatures of ~400-450°C. The latter microstructures imply a period at those temperatures wherein the veins did not accommodate significant strain. Sutured and bulging grain boundaries and deformation lamellae observed in recrystallized grains of some samples likely correspond to later, lower temperature deformation, at ~300°C (Stipp et al., 2002; Trepmann and

Stöckhert, 2003; Passchier and Trouw, 2005). A two-stage deformation history is consistent with the established tectonothermal framework of southern Evia. Most notably, the temperatures implied by vein quartz microstructures are in good agreement with temperature estimates coinciding respectively with peak (~400°C; Shaked et al., 2000) and retrograde (~310°C; Ducharme et al., 2022) metamorphism of the Basal Unit.

Quartz c-axis distributions from the veins capture a wide variance of textures (**Figure 3.8**). Five of the twelve pole figures (VS-07, EV21-07, EV22-03, EV22-07, EV22-17) exhibit c-axis maxima distributed about the Z axis. Quartz c-axis distributions of this type are interpreted to capture low-temperature deformation of quartz accommodated by basal <a> slip, though the role of this slip system is contested (Kilian and Heilbronner, 2017). Four samples (EV20-03B, VS-08H, VS-10J, VS-16C) define pole figures with prominent Y-maxima, distributions that are associated with higher temperature (>400°C) deformation (Schmid and Casey, 1986). One vein exhibiting a Y-maximum (VS-08H) comprises >50% calcite, with poor connectivity between quartz aggregates. Two other vein samples (VS-10J, VS-16C), both hosted in chlorite schist, exhibit a small circle c-axis girdle parallel or oblique to X in addition to the Y-maximum. Dispersion of quartz c-axes between X and Y typically develops during high-T (600-650°C) activation of prism <c> slip (Schmid and Casey, 1986); however, none of the units exposed on southern Evia have experienced such temperatures (Shaked et al., 2000; Katzir et al., 2000; Ducharme et al., 2022). Dispersion of c-axes toward X have alternatively been interpreted as the product of mechanical rotation of quartz crystals into the direction of maximum finite stretch (Larson et al., 2014), in rocks where quartz is not the dominant strain-bearing phase. Since both veins yielding this fabric contain a significant fraction of carbonate material, and their quartz aggregates show poor interconnectivity, rigid rotation of quartz aggregates within the weaker

calcitic vein fill or chloritic host rock appears plausible. Quartz in VS-10J is concentrated in the hinges of a ptygmatically folded vein, which may have further compounded the mechanical (rather than crystal-plastic) realignment of pre-existing quartz c-axis orientations. Some inheritance from initially wall-normal syntaxial growth of quartz crystals may also contribute (Ceccato et al., 2017). The final Y-maximum vein (EV20-03B) lacks monocrystalline quartz ribbons, like samples dominated by Z-maxima. Despite local bulging of grain boundaries, vein quartz in this sample instead dominantly shows planar 120° triple boundaries and pinning of thin quartz aggregates by mica. This sample may thus record a CPO related to crystal growth or deformation at the earlier set of metamorphic conditions, that were perhaps more favorable to prism <a> slip (e.g., Pennacchioni et al., 2010). Later quartz deformation may have been dominated by solution creep due to pinning by mica (e.g., Condit et al., 2022), causing minimal modification of the earlier CPO.

Two pole figures (VS-07B, VS-06.5A) define asymmetric type-I cross-girdles. Asymmetry in VS-06.5A clearly favors top-to-WSW shear sense, whereas VS-07B shows a somewhat ambiguous main girdle segment, apparently inclined consistent with top-to-WSW shear sense. Both pole figures comprise c-axes that are concentrated near the XZ plane, with less defined central girdle segments. One sample (VS-11F) defines an asymmetric pole figure resembling either a single girdle or type-I cross-girdle, with asymmetry consistent with a top-to-SW sense of shear. The shear sense in all three samples is at odds with top-to-ENE kinematics implied by oblique quartz SPOs in the veins (**Figure 3.7**), with the latter more consistent with (micro-)structural shear sense indicators (Xypolias et al., 2003; Ring et al., 2007b; Ducharme et al., 2022). Each of the discussed samples exhibits quartz microstructure indicative of predominant subgrain rotation recrystallization from coarse monocrystalline quartz ribbons, and thus its CPO may record earlier high-T deformation or else be inherited (Ceccato et al., 2017).

Notably, VS-07B and EV22-07 are separated in outcrop by only several meters. The two samples record distinct c-axis distributions: vein quartz in EV22-07, a pelitic schist, records a Z-centered small circle girdle distribution, whereas quartz in VS-07C, a silicate-carbonate schist, produces a type-I cross girdle. Both veins were apparently deformed in relation to the transposed, gently dipping foliation of their host rocks. Nevertheless, the veins record c-axis distributions consistent with (partly) non-coaxial plane strain (VS-07C) and coaxial flattening strain (EV22-07), respectively, and possibly indicate opposing shear senses. These observations can be rationalized in several ways: (1) more carbonate-rich host rocks may preserve older c-axis fabrics, either by accommodating less strain than the pelitic schists, or being less efficient at transmitting stress to the more competent quartz veins (Toy et al., 2008; Ceccato et al., 2017); (2) the CPO records antithetic slip prior to rotation of the veins through the instantaneous stretching axis (e.g., Grasemann et al., 2019); (3) an unmodified antithetic strain compartment developed within the partly coaxial strain regime; or (4) CPOs from compressed hinge and extended limb segments of the veins record different styles of deformation related to the same strain history. Our observations regarding preferential preservation of old structures in more carbonate- and quartz-rich lithotypes may favor the first interpretation, although conflicting shear sense indicated by vein quartz SPOs and limitations of our data mean we cannot discount a role for the other three explanations.

Quartz c-axis distributions consistent with predicted coaxial flattening are concentrated at the top of the structural pile (EV21-07, EV22-03, EV22-17), also occurring in one sample near its center (EV22-07; Schmid and Casey, 1986). Those from the uppermost ~500 m of the structural pile produced weakly defined fabrics (J_{pf}: 1.1-1.22; B: 0.09-0.26; **Figure 3.7, Figure 3.8**), with relatively low maximum c-axis densities of 1.86-2.55 m.u.d. The centrally located sample yielded a comparatively stronger fabric (J_{pf}: 1.95; B: 0.43; up to 5.93 m.u.d.). The apparent strengthening

of fabric intensity is likewise substantiated by the remaining pole figures (**Figure 3.8**). Petrofabric intensity may correlate with increasing finite strain, perhaps reflecting the downward-increasing strain gradient posited by Ducharme et al. (2022) and implied by our new field observations (e.g., Toy et al., 2008; Larson, 2018; Starnes et al., 2020). However, this may alternatively capture the earlier moderate temperature deformation conditions those c-axis distributions likely developed under. The weak fabrics may also be a consequence of the host mica schist partitioning strain only weakly into the quartz veins (e.g., Bhandari and Jiang, 2021), although this would seemingly contradict the behavior of EV22-07 discussed above. Quartz in the uppermost three samples exhibits pinning by adjacent phyllosilicates, which may promote dissolution creep over dislocation creep (Condit et al., 2022). As minor bulging is still observed in these samples, the weak c-axis textures may reflect the minor role of quartz dynamic recrystallization in those samples.

In summary, despite considerable variability among quartz c-axis distributions, quartz microstructures and c-axis distributions delineate an apparent two-stage deformation history like that proposed in previous work (Shaked et al., 2000; Katzir et al., 2000; Ducharme et al., 2022). Four of twelve quartz veins yield small circle Z distributions consistent with flattening strain predicted from macroscopic structures on southern Evia (Lister and Williams, 1979; Schmid and Casey, 1986). Similarly, pole figure asymmetry consistent with top-to-NE shearing seen in outcrop is only conclusively observed in the small-circle Z distribution of sample EV22-07 (Sullivan and Beane, 2010).

3.8.2. In situ *white mica geochronology*

Considerable geochronological data are now available for the Basal Unit on southern Evia (Maluski et al., 1981; Ring et al., 2001; Ring and Reischmann, 2002; Ring and Layer, 2003; Ring

et al., 2007b; Ducharme et al., 2022). Including data from the Tsakei Unit, most white mica $^{40}Ar/^{39}Ar$ and $^{87}Rb/^{87}Sr$ dates range between c. 35 Ma and c. 21 Ma. Data from Basal Unit exposures on Samos and Tinos yield comparatively restricted dates between c. 27-21 Ma (Bröcker and Franz, 1998; Ring and Reischmann, 2002; Ring and Layer, 2003). These results have been interpreted either to capture early Miocene underthrusting and HP-LT metamorphism of the Basal Unit (Ring and Layer, 2003; Ring et al., 2007b; Gerogiannis et al., 2021), or as recording an Oligocene HP event followed by Miocene greenschist facies metamorphism and extension (Shaked et al., 2000; Ducharme et al., 2022).

Our *in situ* analyses represent the first microstructurally resolved geochronology from the Basal Unit. *In situ* geochronology can clarify microstructurally controlled variance in regional $^{40}Ar/^{39}Ar$ datasets (e.g., Cossette et al., 2015; Laurent et al., 2021; Di Vincenzo et al., 2022; Barnes et al., 2023). Many studies highlight complexities inherent in the $^{40}Ar/^{39}Ar$ system attributed to (sub-)micron scale heterogeneity with respect to recorded $^{40}Ar/^{39}Ar$ date, that may result in discordance between the real or interpreted tectonic significance of certain microstructures and the $^{40}Ar/^{39}Ar$ date they record. For instance, *in situ* $^{40}Ar/^{39}Ar$ data from CBU on Syros and Sifnos record the complete Eocene to Miocene date interval spanning subduction to exhumation under greenschist facies conditions (Laurent et al., 2022). However, Laurent et al. (2021) note considerable within-sample variability that correlates more readily with sample petrology and degree of finite strain, implying an element of sample-scale equilibration of $^{40}Ar/^{39}Ar$ systematics. For the Basal Unit, which lacks pristine HP-LT assemblages, our new *in situ* data should in principle capture either exclusively the timing of retrograde metamorphism, or exhibit greater complexity corresponding to local finite strain. Despite being relatively understudied compared to the CBU, the regional framework afforded by data from the CBU and the limited existing data

from the Basal Unit and equivalent unmetamorphosed rocks permit certain assumptions for our own interpretations:

(1) Peak HP-LT metamorphism of the Basal Unit is younger than that of the CBU (*c.* 50 Ma; Laurent et al., 2021; Uunk et al., 2022), and loosely constrained by the early Eocene depositional age of the flysch unit (Dubois and Bignot, 1979);

(2) The Gavrovo-Tripolitza carbonate platform collided outboard of the Pindos oceanic suture occurred between *c.* 36 and 29 Ma (Thomson et al., 1998; Sotiropoulos et al., 2003); thus HP metamorphism of the Basal Unit likely coincided with, or shortly post-dated, this period (while also satisfying [1]);

(3) At least on Evia, zircon (U-Th)/He cooling ages require the Basal Unit exhumed into the brittle crust (T <200°C) before the middle Miocene (c. 17-15 Ma; Ducharme et al., 2022), synchronous with the CBU.

Overall, variability in our *in situ* $^{40}Ar/^{39}Ar$ data correlates with host lithotype, cm- to m-scale structures, and position within the structural pile. As expected, microstructural context of the ablated mica correlates inconsistently with the obtained date (**Table 3.1; Figure 3.11**). This may be partially attributable fine mica grains defining foliation in our samples, which can skew $^{40}Ar/^{39}Ar$ ages toward homogeneous younger dates (Di Vincenzo et al., 2022; Barnes et al., 2023). All samples, except for one, consist of phengitic white mica with average Si apfu >3.3, with the two carbonate-rich samples predictably containing the most aluminoceladonite-rich mica (>3.5 Si apfu; Cossette et al., 2015; Rogowitz et al., 2015; **Table 3.1, Figure 3.9**). Although the high-Si white mica records the oldest coherent date populations among our data, most samples show poor correlation between apparent $^{40}Ar/^{39}Ar$ age and white mica major element chemistry (e.g., Bröcker et al., 2004; Di Vincenzo et al., 2004; Laurent et al., 2021). Further, $^{40}Ar/^{39}Ar$ dates from the two

carbonate-rich samples differ by ~15 Myr; accordingly, sample structure, not mineral chemistry, offers a more compelling first-order control.

Perhaps unsurprisingly, broad similarities in both the age populations of our *in situ* data, and in their spatial distribution within the structural pile of Evia, direct us to similar conclusions as the single-grain fusion data (Ducharme et al., 2022). Unimodal, late Oligocene to early Miocene age populations dominate mica schist samples from lowermost structural levels of the Tsakei Unit, and in the Basal Unit flysch sample from directly below the tectonic contact with the CBU. Isolated older dates in these samples are obtained only from microstructures for which they are easily justified, like porphyroblast strain shadows (**Table 3.1; Figure 3.11**). The same microstructure may elsewhere yield dates indistinguishable from foliation-defining mica, affirming the inconsistent relationship between microstructure and $^{40}Ar/^{39}Ar$ systematics (e.g., Laurent et al., 2021).

Sample EV22-07 is unique in that it contains both phengite and paragonite (**Figure 3.9**). The two micas generally occur in distinct clusters. With one exception, phengite defining foliation yields young dates of 21.1 ± 0.8 to 23.7 ± 0.7 Ma, whereas paragonite records slightly older ages of 26.4 ± 1.8 to 31.8 ± 4.4 Ma (**Figure 3.11**). Large errors due to the low K of paragonite mean that even the older apparent ages are within 2σ error of the complete range of phengite dates (**Figure 3.10**), and thus their relative age is indeterminable from our data. However, three high-angle fans composed of phengite or mixed phengite-paragonite produced older dates between 35.2 ± 0.7 and 42.0 ± 0.7 Ma, distinctly older than dates obtained from foliation-defining phengite.

Carbonate-rich samples from similar structural depths as the samples discussed thus far yielded inconsistent results. One sample (EV20-14), previously dated as late Oligocene by the multiple single-grain fusion method, yielded by the *in situ* method a unimodal middle Eocene age

population (Ducharme et al., 2022). That discrepancy is discussed further below. The other carbonate schist sample (EV22-14.5) is from the base of the Tsakei schists, less than 50 m above the contact with the Basal Unit marble sequence. Micaceous microlithons in this sample are composed of crenulated phengite defining a spaced, subhorizontal cleavage dissecting an older foliation. Cleavage domains and relict foliation alike yield ages that define a continuous trend, preserving dates approximating the youngest dates in the mica schists (c. 26.7 ± 0.5 Ma), increasing toward a maximum captured by five analyses at c. 32 Ma (**Figure 3.10**).

The remaining three samples, all from near the structural top of the Tsakei schists, provided comparatively scattered $^{40}Ar/^{39}Ar$ dates. Uniquely among these, sample EV20-20 records a relatively unimodal late Eocene age population within error of its single-grain fusion dates (Ducharme et al., 2022). The other two samples retain the youngest late Oligocene dates (EV22-03, EV22-17), recorded by blocky white mica overgrowing albite porphyroblasts or in veins (**Figure 3.11**). The mica appears to post-date initial vein sealing, as the veins have been boudinaged and rotated into the foliation. Foliation-defining mica conversely record generally dispersed dates as old as Paleocene. Those analyses, as well as all data from sample EV20-14, provide dates older than the earliest proposed timing of metamorphism for the Basal Unit (c. 35-30 Ma). These either represent partially reset detrital mica grains, or signal the presence of excess ^{40}Ar.

The latter interpretation was tested using *in situ* $^{87}Rb/^{87}Sr$ dating of white mica in two samples yielding moderately scattered, late Eocene and older ages were measured. Although the $^{87}Rb/^{87}Sr$ system often behaves similarly to the $^{40}Ar/^{39}Ar$ systematics (Halama et al., 2018; Bosse and Villa, 2019), it is rarely subject to addition of daughter isotope and consequent obscuring of geologically meaningful dates (Gyomlai et al., 2023). This distinction is well illustrated by the two samples analyzed, which produced indistinguishable isochron ages of 31.1 ± 2.9 Ma and 31.4 ±

3.3 Ma (**Figure 3.12**). For EV20-20, three dating methods using two isotope systems (single-grain fusion $^{40}Ar/^{39}Ar$, *in situ* $^{40}Ar/^{39}Ar$, *in situ* $^{87}Rb/^{87}Sr$) now affirm that white mica in the sample records an event of late Eocene or early Oligocene age. Despite its $^{87}Rb/^{87}Sr$ isochron age not falling within error of the single-grain fusion weighted mean, both *in situ* methods allowed for deliberate avoidance of inclusions and other contaminants, and thus emphasize the reliability of the mutually overlapping *in situ* dates over the total fusion dates.

Conversely, EV20-14 has now provided three apparently distinct ages. With respect to the $^{40}Ar/^{39}Ar$ data, white mica analyzed by single-grain fusion produced better radiogenic ^{40}Ar yields than those analyzed *in situ* (**Table 3.1**; cf. **Table S2.3**), perhaps representing two distinct mica populations. Despite deliberately targeting the same mica populations, the $^{87}Rb/^{87}Sr$ and $^{40}Ar/^{39}Ar$ *in situ* datasets still produced different dates. This would appear to validate the inference that the older dates in this sample, and the dispersed old dates in EV22-03 and EV22-17, are products of excess Ar, and thus are not likely to be geologically meaningful. Moreover, excess Ar provides justification for some conflicting microstructure-date relationships, such as mm-thick brittle-ductile shear bands in EV22-17 that yielded dates ~20 Myr older than the foliation they cross-cut (**Table 3.1**).

In summary, our new *in situ* geochronology can be generalized as capturing two geologically significant dates. The first, of apparent early Oligocene age, is evident in $^{40}Ar/^{39}Ar$ data from samples EV20-20 and EV22-14.5, and captured by both $^{87}Rb/^{87}Sr$ isochrons. Isolated microstructural features, like albite strain shadows in EV22-06B, may also preserve this signal. A second, younger late Oligocene to early Miocene age signature is prevalent in samples exhibiting a coherent, planar foliation. The key distinction between samples preserving one population of $^{40}Ar/^{39}Ar$ dates appears to be of a structural nature. Samples preserving the older dates exhibit m-

to mm-scale structures that represent incomplete transposition of older folds and foliations, whereas those with an outwardly simple structure likely represent, as surmised in preceding discussions, tectonic fabrics newly transposed following late Oligocene flattening and exhumation. We interpret the early Oligocene dates as reflecting the timing of burial and HP-LT metamorphism of the Basal Unit, and the younger late Oligocene dates as dating deformation related to the ESZ and consequent exhumation. These conclusions are broadly aligned with previous models positing maximum burial of the Basal Unit in the late Oligocene (Maluski et al., 1981; Shaked et al., 2000; Ducharme et al., 2022).

3.8.3. Superimposed records of contraction and tension

The structural record of HP-LT units in the Cyclades represents a protracted interval of contraction followed by regional-scale tension. Contractional structures encompass those produced during subduction and subsequent syn-orogenic wedge extrusion, whereas tensional structures are dominantly those related to ductile-then-brittle low-angle detachment faulting and younger, brittle high-angle normal faults. All but the high-angle faults operated initially under ductile conditions, and have thus produced a complex array of structural relationships ranging from total obscuring of earlier structures to only partial overprinting or simple geometric modification (Ring et al., 2010). In the Cyclades, the spatial distribution of major post-orogenic structures subordinate to the NCDS and WCDS remains incompletely understood (Huet et al., 2009; Schneider et al., 2018; Coleman et al., 2020; Bakowsky et al., 2023). Without a clear and diagnostic strain signature, like the narrowing ductile-then-brittle strain typically found below knife-sharp brittle detachment planes, there are few methods by which to unequivocally distinguish a structure that operated during contraction from one that operated under tension. Several important structures

in the Cyclades exemplify such, oftentimes unresolved, controversies (e.g., Ios, Forster and Lister, 1999; Huet et al., 2009; Syros, Trotet et al., 2001; Philippon et al., 2011; Laurent et al., 2016).

The tectonic contact exposed on southern Evia now encapsulates yet another example of this debate. We contend that available geochronology all but requires that the Basal Unit flysch delineates an important tectonic boundary across which significant exhumation has occurred. Effectively indistinguishable ZHe dates measured throughout the structural pile demonstrate significant attenuation of intervening levels between the CBU and Basal Unit prior to their eventual exhumation into the brittle crust (Ducharme et al., 2022). The $^{40}Ar/^{39}Ar$ data point to much the same conclusion. White mica, defining foliations with a demonstrable relationship to stretched and transposed quartz veins, consistently yields the youngest $^{40}Ar/^{39}Ar$ dates yet documented on Evia (Maluski et al., 1981; Ring and Layer, 2003; Ring et al., 2007b; Ducharme et al., 2022). The coexisting structures suggest that the young dates capture ductile strain-induced reset of the $^{40}Ar/^{39}Ar$ systematics during ductile thinning of the flysch, providing a mechanism to directly explain the ZHe data.

Here, we have newly shown that this age signature is resolvable at all structural levels of the Basal Unit flysch. Furthermore, our *in situ* $^{40}Ar/^{39}Ar$ and $^{87}Rb/^{87}Sr$ data provide the first microstructurally resolved geochronology for the Basal Unit. The structural data and geochronology together yield an internally consistent, time-resolved strain history for the ESZ. Puzzlingly, despite considerable geochronological evidence that the ESZ accomplished significant exhumation of the Basal Unit, its strain geometry does not closely resemble any equivalent structure documented in the Cyclades. The mechanical influence of these major structures is attested to in most instances by a wide zone of intense mylonitization imposed upon their footwalls. On the other hand, a significant volume of material at any given structural position within the ESZ

shows little evidence for having accommodated the flattening strain observed in the pelitic lithotypes. The $^{40}Ar/^{39}Ar$ systematics of mica in the footwalls of most major detachments in the Cyclades are comprehensively reset, and now date the timing of mylonitization (Jolivet et al., 2010; Grasemann et al., 2012). Meanwhile, the ESZ, throughout its thickness, preserves blocks in which earlier portions of the strain history and corresponding age signature remain essentially intact.

The Mesochoria cataclasites (**Figure 3.2**) imply that the tectonic contact accommodated at least some terminal brittle deformation. Strain documented in the vicinity of the contact is, nonetheless, atypical in many ways compared to strain observed at major tectonic boundaries elsewhere in the Cyclades. First, although the Mesochoria cataclasites extend along several hundred meters of strike length, further lateral continuity was either not observed or else too poorly exposed, where predicted, for conclusive correlation. Accordingly, cataclasis of the contact may only be relatively localized. Second, mylonites are neither observed within nor structurally below the cataclasites, meaning the tectonic contact lacks part of the characteristic strain geometry classically associated with detachment faulting (Lister and Davis, 1989). Lastly, the non-mylonitic schists in the immediate footwall of the tectonic contact mark an abrupt ~90 degree change in strike. Both the cataclasites and the Styra marbles in the hanging wall dip to the northeast; meanwhile, rocks structurally below the cataclasites dip to the southwest. The latter two points attest further to the apparently limited mechanical influence of the cataclastic deformation.

Nevertheless, the width of the cataclastic damage zone (5-10 m) suggests accommodation of non-negligible, albeit localized, brittle strain. Moreover, the orientation of the cataclastic horizon, and shear sense indicators preserved within and structurally below it, show that cataclastic deformation acted with kinematics synthetic to those of both the ESZ and the NCDS, and parallel

to overall extension in the Aegean. Available geo- and thermochronology, compounded by the new geochronology presented here, requires that the cold, brittle cataclasites are no older than early or middle Miocene in age, redoubling the likelihood of a relationship to Aegean extension. Integrating this with the top-to-NE simple shear component observed in ductile and brittle-ductile strain related to the ESZ (Ducharme et al., 2022), it is tempting to conclude that the ESZ preserves some expression, however disparate, of the complete ductile-then-brittle strain history expected of a major detachment fault.

3.8.4. The Evia Shear Zone: a unique Cycladic exhumation structure?

Evia is situated in the footwall of the NCDS, one of two crustal-scale detachment systems facilitating post-orogenic exhumation in the Cyclades (Jolivet et al., 2010). Whereas the structure is projected offshore of Evia, the mechanical influence of the NCDS is evident in top-to-NE brittle-ductile shear bands developed in rocks correlated with the CBU on the island (Jolivet et al., 2004; Ducharme et al., 2022). The NCDS likely accomplished significant unroofing of southern Evia (Jolivet et al., 2010). Although southern Evia marks the northwestern limits of continuous exposure of the ACCB, it has been suggested that the NCDS extends along strike as far as the Pelion peninsula (Hinshaw et al., 2024). Conversely, the WCDS exhibits structural evidence consistent with that structure terminating in western Attica, at a similar along-strike position to where Evia lies along the NCDS (Coleman et al., 2020). At its proposed terminus on Mt. Hymmitos, the WCDS presents as a pair of co-active brittle-then-ductile detachments. Whereas the upper detachment divides Upper Unit (Pelagonian) above from CBU below, as is normally the situation, Coleman et al. (2020) interpreted the second detachment as juxtaposing two subdivisions of the CBU, structurally below the first.

Several compelling parallels may be drawn between the ESZ and the Mt. Hymmitos detachments. First, the ESZ developed structurally below the extensional contact between Upper Unit and CBU, in contrast to more classical examples from the Cyclades that branched structurally upward (Lister and Davis, 1989; Jolivet et al., 2010; Lecomte et al., 2010). Second, ductile strain was apparently accommodated synchronously along the ESZ and NCDS, as described for the Mt. Hymmitos detachments, also in contrast to other branched Cycladic detachments (Coleman et al., 2020). Thermochronology astride of the lower detachment of Hymmitos differs markedly from that across the ESZ, however: the Lower Unit on Attica yielded considerably younger ZHe dates than the Middle Unit, whereas ZHe dates from the Basal Unit and CBU on Evia are indistinguishable (Coleman et al., 2020; Ducharme et al., 2022). Additionally, the lower detachment of Hymmitos still exhibits the conventional strain geometry of a low-angle normal fault.

Notwithstanding the limited data constraining the geodynamic history of the Basal Unit, its participation within the broader evolution of the Aegean Sea can be inferred using the more established framework of the CBU. Estimates for peak HP metamorphism recorded by the Basal Unit indicate maximum PT conditions of ~10 kbar and ~400°C, slightly lower than peak metamorphism recorded by the CBU on Evia (Shaked et al., 2000). It can be assumed that these metamorphic maxima were achieved diachronously, as the CBU was likely undergoing syn-orogenic wedge extrusion as the Basal Unit was subducting in the late Eocene (Ring et al., 2007b; Jolivet et al., 2010; Huet et al., 2015; Laurent et al., 2016; Peillod et al., 2024). This interval of syn-orogenic unroofing of the CBU coincides with subduction of the Basal Unit, juxtaposing the two along the Basal Thrust (**Figure 3.13A**). Based on rapid inferred exhumation rates, Ducharme et al. (2022) proposed an interval of syn-orogenic unroofing of the Basal Unit. The timing of this

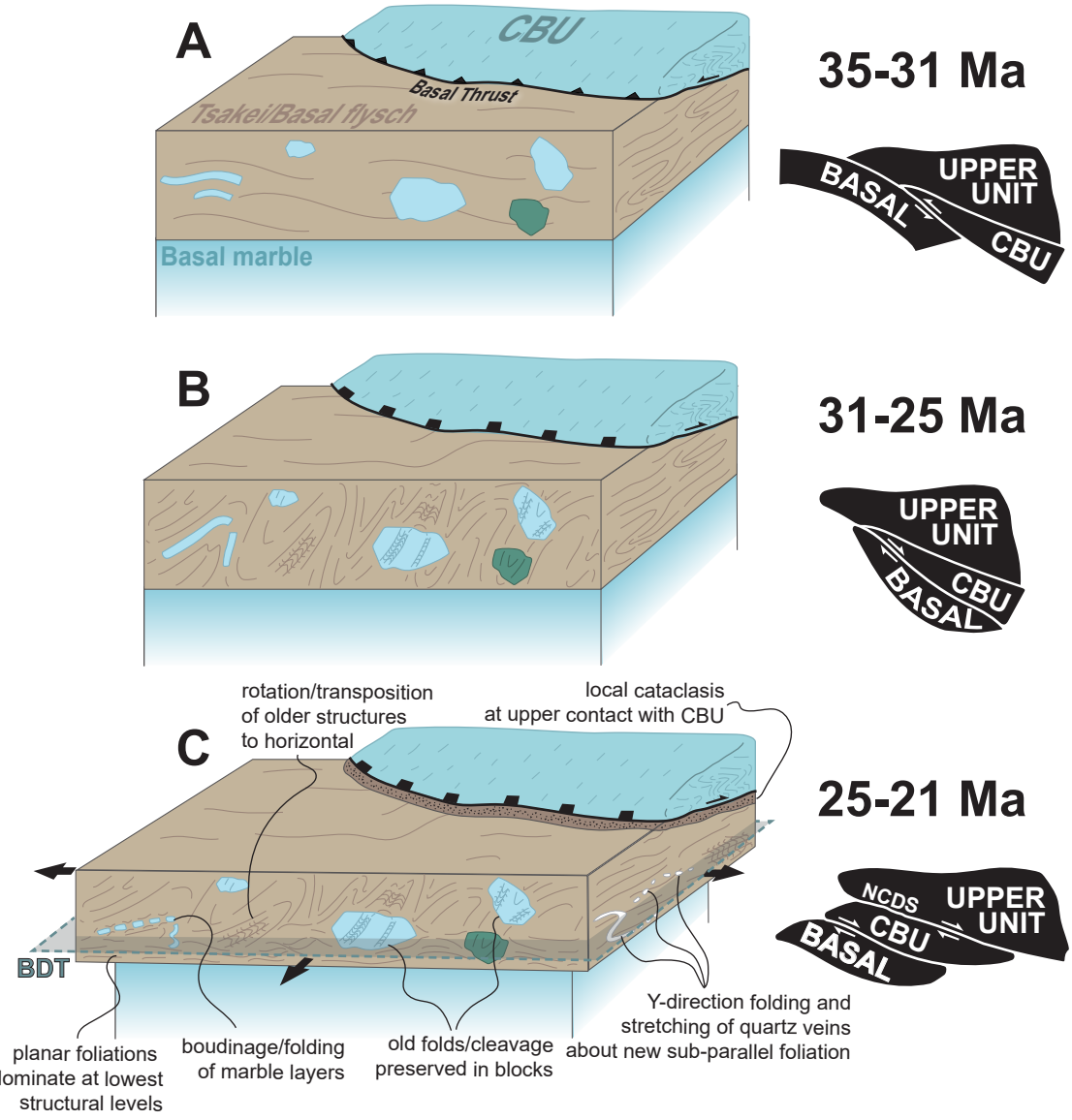

Figure 3.13. Schematic model for the tectonic evolution of the Basal Unit flysch succession from subduction of the Basal Unit (A), syn-orogenic extrusion (B), and post-orogenic unroofing and coaxial flattening (C). The Basal Unit flysch records syn-convergence fabrics and structures that were partially, or locally totally, overprinted during exhumation by structures related to flattening and consequent vertical ductile thinning. See text for details.

stage remains unclear, and syn-orogenic exhumation may have immediately followed peak metamorphism at c. 32 Ma, or else initiated at any time before c. 25 Ma (**Figure 3.13B**). By 25 Ma, pre-existing folding and related structures were being transposed and overprinted by a sub-horizontal cleavage of variable intensity related to vertical flattening (**Figure 3.13C**). At this time, metamorphic assemblages developed in rocks exhibiting penetrative sub-horizontal foliations and macroscopic structural evidence of flattening finite strain developed under lower greenschist facies conditions at elevated pressures (310 ± 15°C, 7 ± 1 kbar; Ducharme et al., 2022). Note that this estimate is obtained from the base of the schists. If the Basal Unit flysch and Tsakei schists are laterally equivalent – that is, they do not contribute cumulatively to the thickness of the structural pile as depicted in Katsikatsos et al. (1991a) – then the total measured thickness of the schists is ~1.5 km. Assuming modest attenuation of ~25% due to ductile thinning (e.g., Ring and Kumerics, 2008; Xypolias et al., 2010), and a moderately relaxed post-subduction regime geotherm of 20°C/km, this would yield a ~2 km thick restored section and a vertical temperature differential of ~40°C between structurally highest and lowest schists. At temperatures as low as those estimated, parts of the structural pile would be approaching the brittle-ductile transition for white mica (~250°C; Dunlap et al., 1991; White, 2001; Akker et al., 2021), whereas mica at lower structural levels would still be deforming via fully ductile mechanisms.

Such contrasts in strain partitioning behavior corresponding to lithology are documented elsewhere, with similar consequences for the $^{40}Ar/^{39}Ar$ record of white mica (Cossette et al., 2015; Beaudoin et al., 2020; Laurent et al., 2021). Conversely, the down-section intensification of strain observed in the schists implies a strain gradient not generally predicted for extensional structures, which produce footwall strain that intensifies up-section toward the detachment plane (Lister and Davis, 1989; Grasemann et al., 2012). It is also inconsistent with observations of shear zone

evolution more generally, which record the highest strain typically in their centers (Fossen and Cavalcante, 2017). In the Cyclades, mylonites developed in the footwall of the major detachments often deform coherent marbles and mica schists of the CBU, or the late Miocene granitoids that intrude them (Jolivet et al., 2010; Grasemann et al., 2012). In this way, the heterolithic composition of the Basal Unit flysch may differ significantly, and behave more similarly to a block-in-matrix mélange (Fagereng and Sibson, 2010; Beall et al., 2019). Bulk deformation of these rocks typically proceeds with strain partitioning strongly into the weak matrix, with the more competent clasts and blocks accommodating comparatively minor strain (Fagereng and Sibson, 2010). This prediction aligns well with our empirical field observations, in which overprinting of older structures is most severe in the weak pelitic matrix but comparatively minor in the other constituent lithotypes.

Detachment faults commonly localize along major pre-existing discontinuities, like nappe boundaries, but local geology may cause structures to deviate from this rule. On Tinos and Mykonos, intrusion of middle Miocene granitoid magmas upwarped the local geotherms, causing new detachment branches to form structurally above the main branch, but below the displaced brittle-ductile transition (Jolivet and Patriat, 1999; Jolivet et al., 2010; Lecomte et al., 2010). On Folegandros, strain localized at the center of the island shows a progression from ductile to brittle-ductile structures, but a brittle detachment plane is situated at higher structural levels in the hanging wall, with little related strain apparent at intervening levels (Bakowsky et al., 2023). A similar migration in the locus of deformation may explain the structures observed in the Basal Unit flysch on Evia. Strain remained localized near the basal contact with the Basal Unit marbles for as long as the structurally lowest schists were able to accommodate it via ductile mechanisms. More competent lithologies, like carbonate and quartzose schists and quartzites, sustained less intense

deformation, and at higher structural levels still preserve minimally reworked older subduction-related structures and foliations. Once the schistose package had fully exhumed above the brittle-ductile transition for micaceous rocks, distributed deformation became unfavorable, and strain instead localized as fully brittle cataclasis along the structurally higher tectonic contact with the CBU (**Figure 3.2, Figure 3.13C**). Mounting evidence, even in the Cyclades alone, indicates that detachment faults are highly sensitive to bulk rheology, as influenced by prevailing PT conditions and lithological context, during their activity. Low-angle normal faulting within the rock record may therefore be expected to exhibit a wide variability in expression that is intimately tied to its immediate geological context. Despite potentially facilitating considerable magnitudes of exhumation, some of these structures may be obscured by meter-scale heterogeneities that display an apparently incoherent record of extensional deformation.

3.9. Conclusions

The uppermost structural levels of the Basal Unit on southern Evia comprise a lithologically heterogeneous schistose metasedimentary succession, interpreted as a flysch package, that experienced Cenozoic HP-LT metamorphism. This interval of rock divides two marble-dominated units that represent two distinct thrust sheets in the broader Hellenic orogen, the Basal Unit and the Cycladic Blueschist Unit. The modern exposure of this earlier syn-convergent thrust has been re-exploited or overprinted by diffuse extensional strain accommodated primarily by the intervening package of flysch. The resultant structure, the Evia Shear Zone, drove exhumation of the underlying Basal Unit marbles, unroofing them into the brittle crust simultaneously with the CBU hanging wall.

New *in situ* white mica $^{40}Ar/^{39}Ar$ and $^{87}Rb/^{87}Sr$ geochronology highlight similar predominant age signatures as documented previously from the Basal Unit flysch. Dominant microstructure-resolved trends indicate the younger late Oligocene age population is recorded predominantly by schists displaying a single planar metamorphic foliation, whereas those preserving a spaced secondary cleavage and older foliation record the older late Eocene dates. Host lithotype exerts a major first-order control on the differential preservation of relict structural features, a trend which is corroborated by the macroscopic structural record observed in more carbonate- and quartz-rich schists, and in quartz microstructures and c-axis distributions. The distinct age populations are interpreted to reflect late Eocene-early Oligocene subduction and HP-LT metamorphism, followed by recrystallization of mica during ductile strain related to exhumation in the late Oligocene.

Exhumation of the Basal Unit was accomplished in part by general shear localized in the flysch, manifesting with a top-to-NE non-coaxial component, alongside superimposed coaxial flattening. The resulting oblate finite strain ellipsoid is captured in outcrop by structures which demonstrate extension operating parallel to the intermediate stretching (Y-) axis, such as boudinaged quartz veins. Quartz in the deformed veins yields variable c-axis distributions, but several nonetheless record *Z*-centered distributions, including small-circle girdles, consistent with the flattening strain inferred from macroscopic structures.

Rather than a single continuous ductile-then-brittle detachment as is common in the Cyclades, strain in the ESZ partitioned diffusely into more mica-rich lithotypes, preserving older structures in more competent blocks. The situation described on Evia attests to the diversity of deformation styles capable of facilitating exhumation of HP-LT rocks. Moreover, the differential record of strain produced in the highly rheologically heterogeneous flysch succession parallels

observations from similar block-in-matrix mélanges commonly found in exhumed subduction zones (Fagereng and Sibson, 2010; Beall et al., 2019). The apparently discontinuous strain had effectively obscured the presence of an exhumation-related structure, and thus a potential role for similar rocks should be re-evaluated in terranes where magnitudes of unroofing appear to exceed the capacity of previously identified structures.

3.10 Acknowledgments

Funding for this project was provided by an NSERC Discovery grant awarded to Schneider. We are grateful to G. Poirier (University of Ottawa) for his assistance with data acquisition on the scanning electron microscope and electron microprobe. We thank J. Spalding for excellently assisting in the field.

3.11 References

Abbate, E., Bortolotti, V., & Passerini, P. (1970). Olistostromes and olistoliths. Sedimentary Geology, 4(3-4), 521-557.

Akker, I. V., Berger, A., Zwingmann, H., Todd, A., Schrank, C. E., Jones, M. W., ... & Herwegh, M. (2021). Structural and chemical resetting processes in white mica and their effect on K-Ar data during low temperature metamorphism. Tectonophysics, 800, 228708.

Bakowsky, C., Schneider, D. A., Grasemann, B., & Soukis, K. (2023). Miocene ductile thinning below the Folegandros Detachment System, Cyclades, Greece. Terra Nova, 35(3), 220-229.

Barnes, C. J., Schneider, D. A., Majka, J., Camacho, A., Bukała, M., & Włodek, A. (2023). $^{40}Ar/^{39}Ar$ dates controlled by white mica deformation and strain localization: Insights

from comparing in situ laser ablation and single-grain fusion techniques. Journal of Metamorphic Geology, 41(9), 1143-1166.

Beall, A., Fagereng, Å., & Ellis, S. (2019). Strength of strained two-phase mixtures: Application to rapid creep and stress amplification in subduction zone mélange. Geophysical Research Letters, 46(1), 169-178.

Beaudoin, A., Scaillet, S., Mora, N., Jolivet, L., & Augier, R. (2020). In situ and step-heating $^{40}Ar/^{39}Ar$ dating of white mica in low-temperature shear zones (Tenda massif, Alpine Corsica, France). Tectonics, 39(12), e2020TC006246.

Bhandari, A., & Jiang, D. (2021). A multiscale numerical modeling investigation on the significance of flow partitioning for the development of quartz c-axis fabrics. Journal of Geophysical Research: Solid Earth, 126(2), e2020JB021040.

Bonneau, M. (1984). Correlation of the Hellenide nappes in the south-east Aegean and their tectonic reconstruction. Geological Society, London, Special Publications, 17(1), 517-527.

Bosse, V., & Villa, I. M. (2019). Petrochronology and hygrochronology of tectono-metamorphic events. Gondwana Research, 71, 76-90.

Braathen, A., Osmundsen, P. T., & Gabrielsen, R. H. (2004). Dynamic development of fault rocks in a crustal-scale detachment: An example from western Norway. Tectonics, 23(4).

Brichau, S., Ring, U., Ketcham, R. A., Carter, A., Stockli, D., & Brunel, M. (2006). Constraining the long-term evolution of the slip rate for a major extensional fault system in the central

Aegean, Greece, using thermochronology. Earth and Planetary Science Letters, 241(1-2), 293-306.

Brichau, S., Ring, U., Carter, A., Bolhar, R., Monié, P., Stockli, D., & Brunel, M. (2008). Timing, slip rate, displacement and cooling history of the Mykonos detachment footwall, Cyclades, Greece, and implications for the opening of the Aegean Sea basin. Journal of the Geological Society, 165(1), 263-277.

Bröcker, M., & Franz, L. (1998). Rb–Sr isotope studies on Tinos Island (Cyclades, Greece): additional time constraints for metamorphism, extent of infiltration-controlled overprinting and deformational activity. Geological Magazine, 135(3), 369-382.

Bröcker, M., Bieling, D., Hacker, B., & Gans, P. (2004). High-Si phengite records the time of greenschist facies overprinting: Implications for models suggesting mega-detachments in the Aegean Sea. Journal of Metamorphic Geology, 22(5), 427-442.

Burchfiel, B. C., Zhiliang, C., Hodges, K. V., Yuping, L., Royde, L. H., Changrong, D., & Jiene, X. (1992). The South Tibetan detachment system, Himalayan Orogen: Extension contemporaneous with and parallel to shortening in a Collisional mountain belt. Special Paper of the Geological Society of America, 269, 1-41.

Carosi, R., Lombardo, B., Molli, G., Musumeci, G., Pertusati, P. C. (1998). The South Tibetan detachment system in the Rongbuk valley, Everest region. Deformation features and geological implications. Journal of Asian Earth Sciences, 16(2-3), 299-311.

Ceccato, A., Pennacchioni, G., Menegon, L., & Bestmann, M. (2017). Crystallographic control and texture inheritance during mylonitization of coarse grained quartz veins. Lithos, 290, 210-227.

Coleman, M. J., Schneider, D. A., Grasemann, B., Soukis, K., Lozios, S., & Hollinetz, M. S. (2020). Lateral termination of a Cycladic-style detachment system (Hymittos, Greece). Tectonics, 39(9), e2020TC006128.

Condit, C. B., French, M. E., Hayles, J. A., Yeung, L. Y., Chin, E. J., & Lee, C. T. A. (2022). Rheology of metasedimentary rocks at the base of the subduction seismogenic zone. Geochemistry, Geophysics, Geosystems, 23(2), e2021GC010194.

Cossette, É., Schneider, D. A., Warren, C. J., & Grasemann, B. (2015). Lithological, rheological, and fluid infiltration control on $^{40}Ar/^{39}Ar$ ages in polydeformed rocks from the West Cycladic detachment system, Greece. Lithosphere, 7(2), 189-205.

Davis, G. A., & Lister, G. S. (1988). Detachment faulting in continental extension; Perspectives from the Southwestern US Cordillera. Processes in Continental Lithospheric Deformation, 218, 133.

Davis, G. A., Darby, B. J., Yadong, Z., & Spell, T. L. (2002). Geometric and temporal evolution of an extensional detachment fault, Hohhot metamorphic core complex, Inner Mongolia, China. Geology, 30(11), 1003-1006.

Di Vincenzo, G., Carosi, R., & Palmeri, R. (2004). The relationship between tectono-metamorphic evolution and argon isotope records in white mica: constraints from in situ $^{40}Ar–^{39}Ar$ laser analysis of the Variscan basement of Sardinia. Journal of Petrology, 45(5), 1013-1043.

Di Vincenzo, G., Godard, G., & Molli, G. (2022). Dating Low-Grade Deformation: Role of Lithology and Strain Partitioning on Ar Isotope Records in the Alpi Apuane of Northern Apennines (Italy). Tectonics, 41(7), e2022TC007248.

Dubois, R. & Bignot, G. (1979). Présence d'un "hard ground" nummulitique au de la série cretacée d'Almyropotamos (Eubée meridionale, Grèce). Paris, Académie des Sciences Comptes Rendus, 289, 993–5.

Ducharme, T. A., Schneider, D. A., Grasemann, B., & Klonowska, I. (2022). Stretched thin: Oligocene extrusion and ductile thinning of the Basal Unit along the Evia Shear Zone, NW Cyclades, Greece. Tectonics, 41(12), e2022TC007561.

Dunlap, W. J., Teyssier, C., McDougall, I., & Baldwin, S. (1991). Ages of deformation from K/Ar and $^{40}Ar/^{39}Ar$ dating of white micas. Geology, 19(12), 1213-1216.

Fagereng, Å., & Sibson, R. H. (2010). Mélange rheology and seismic style. Geology, 38(8), 751-754.

Forster, M. A., & Lister, G. S. (1999). Detachment faults in the Aegean core complex of Ios, Cyclades, Greece. Geological Society, London, Special Publications, 154(1), 305-323.

Fossen, H., & Cavalcante, G. C. G. (2017). Shear zones–A review. Earth-Science Reviews, 171, 434-455.

Foster, D. A., John, B. E. (1999). Quantifying tectonic exhumation in an extensional orogen with thermochronology: examples from the southern Basin and Range Province. Geological Society, London, Special Publications, 154(1), 343-364.

Froitzheim, N., Pleuger, J., Roller, S., & Nagel, T. (2003). Exhumation of high-and ultrahigh-pressure metamorphic rocks by slab extraction. Geology, 31(10), 925-928.

Gautier, P., & Brun, J. P. (1994). Crustal-scale geometry and kinematics of late-orogenic extension in the central Aegean (Cyclades and Evia Island). Tectonophysics, 238(1-4), 399-424.

Gerogiannis, N., Aravadinou, E., Chatzaras, V., & Xypolias, P. (2021). Calcite pseudomorphs after aragonite: A tool to unravel the structural history of high-pressure marbles (Evia Island, Greece). Journal of Structural Geology, 148, 104373.

Govindaraju, K. (1979). Report (1968–1978) on two mica reference samples: biotite Mica-Fe and phlogopite Mica-Mg. Geostandards Newsletter, 3(1), 3-24.

Grasemann, B., Schneider, D. A., Stöckli, D. F., & Iglseder, C. (2012). Miocene bivergent crustal extension in the Aegean: Evidence from the western Cyclades (Greece). Lithosphere, 4(1), 23-39.

Grasemann, B., Huet, B., Schneider, D. A., Rice, A. H. N., Lemonnier, N., & Tschegg, C. (2018). Miocene postorogenic extension of the Eocene synorogenic imbricated Hellenic subduction channel: New constraints from Milos (Cyclades, Greece). GSA Bulletin, 130(1-2), 238-262.

Grasemann, B., Dabrowski, M., & Schöpfer, M. P. (2019). Sense and non-sense of shear reloaded. Journal of Structural Geology, 125, 20-28.

Gyomlai, T., Agard, P., Herviou, C., Jolivet, L., Monié, P., Mendes, K., & Iemmolo, A. (2023). In situ Rb–Sr and ^{40}Ar–^{39}Ar dating of distinct mica generations in the exhumed subduction complex of the Western Alps. Contributions to Mineralogy and Petrology, 178(9), 58.

Halama, R., Glodny, J., Konrad-Schmolke, M., & Sudo, M. (2018). Rb-Sr and in situ $^{40}Ar/^{39}Ar$ dating of exhumation-related shearing and fluid-induced recrystallization in the Sesia zone (Western Alps, Italy). Geosphere, 14(4), 1425-1450.

Hinshaw, E. R., Stockli, D. F., & Soukis, K. (2024). Coherent underplating of HP-LT blueschist packages and basement during Hellenic subduction recorded by zircon U-Pb data, Pelion, Greece. Journal of the Geological Society, jgs2023-147.

Hirth, G., & Tullis, J. (1992). Dislocation creep regimes in quartz aggregates. Journal of Structural Geology, 14(2), 145-159.

Huet, B., Labrousse, L., & Jolivet, L. (2009). Thrust or detachment? Exhumation processes in the Aegean: Insight from a field study on Ios (Cyclades, Greece). Tectonics, 28(3).

Jacobshagen, V. (1986). Geologie von Griechland. Borntraeger, Berlin-Stuttgart, p. 279.

Jolivet, L., & Patriat, M. (1999). Ductile extension and the formation of the Aegean Sea. Geological Society, London, Special Publications, 156(1), 427-456.

Jolivet, L., Famin, V., Mehl, C., Parra, T., Aubourg, C., Hébert, R., & Philippot, P. (2004). Strain localization during crustal-scale boudinage to form extensional metamorphic domes in the Aegean Sea. Geological Society of America Special Paper, 380, 185-210.

Jolivet, L., Lecomte, E., Huet, B., Denèle, Y., Lacombe, O., Labrousse, L., ... & Mehl, C. (2010). The north cycladic detachment system. Earth and Planetary Science Letters, 289(1-2), 87-104.

Katsikatsos, G. (1991a). Geological map of Greece, Aliveri sheet. Institute of Geological Mining Research (IGME), Athens.

Katsikatsos, G. (1991b). Geological map of Greece, Rafina sheet. Institute of Geological Mining Research (IGME), Athens.

Katsikatsos, G., Mercier, J.-L., & Vergely, P. (1976). L'Eubée méridionale: une double fenêtre polyphasée dans les Hellénides internes (Grèce). Comptes Rendus de l'Académie des Sciences, Série D, 459-462.

Katzir, Y., Avigad, D., Matthews, A., Garfunkel, Z., & Evans, B. W. (2000). Origin, HP/LT metamorphism and cooling of ophiolitic mélanges in southern Evia (NW Cyclades), Greece. Journal of Metamorphic Geology, 18(6), 699-718.

Kellett, D. A., & Grujic, D. (2012). New insight into the South Tibetan detachment system: Not a single progressive deformation. Tectonics, 31(2).

Kellett, D. A., Cottle, J. M., & Larson, K. P. (2019). The South Tibetan Detachment System: history, advances, definition and future directions. Geological Society, London, Special Publications, 483(1), 377-400.

Kilian, R., & Heilbronner, R. (2017). Analysis of crystallographic preferred orientations of experimentally deformed Black Hills Quartzite. Solid Earth, 8(5), 1095-1117.

Krohe, A., & Mposkos, E. (2002). Multiple generations of extensional detachments in the Rhodope Mountains (northern Greece): evidence of episodic exhumation of high-pressure rocks. Geological Society, London, Special Publications, 204(1), 151-178.

Larson, K. P. (2018). Refining the structural framework of the Khimti Khola region, east-central Nepal Himalaya, using quartz textures and c-axis fabrics. Journal of Structural Geology, 107, 142-152.

Larson, K. P. (2023). FabricPlotR. https://doi.org/10.17605/OSF.IO/MJTXV

Larson, K. P., Lamming, J. L., & Faisal, S. (2014). Microscale strain partitioning? Differential quartz crystallographic fabric development in Phyllite, Hindu Kush, Northwestern Pakistan. Solid Earth, 5(2), 1319-1327.

Laurent, V., Jolivet, L., Roche, V., Augier, R., Scaillet, S., & Cardello, G. L. (2016). Strain localization in a fossilized subduction channel: Insights from the Cycladic Blueschist Unit (Syros, Greece). Tectonophysics, 672, 150-169.

Laurent, V., Scaillet, S., Jolivet, L., Augier, R., & Roche, V. (2021). ^{40}Ar behaviour and exhumation dynamics in a subduction channel from multi-scale ^{40}Ar/^{39}Ar systematics in phengite. Geochimica et Cosmochimica Acta, 311, 141-173.

Lecomte, E., Jolivet, L., Lacombe, O., Denèle, Y., Labrousse, L., & Le Pourhiet, L. (2010). Geometry and kinematics of Mykonos detachment, Cyclades, Greece: Evidence for slip at shallow dip. Tectonics, 29(5).

Lister, G. S., & Davis, G. A. (1989). The origin of metamorphic core complexes and detachment faults formed during Tertiary continental extension in the northern Colorado River region, USA. Journal of Structural Geology, 11(1-2), 65-94.

Lister, G. S., & Williams, P. F. (1979). Fabric development in shear zones: theoretical controls and observed phenomena. Journal of Structural Geology, 1(4), 283-297.

Lister, G. S., Banga, G., & Feenstra, A. (1984). Metamorphic core complexes of Cordilleran type in the Cyclades, Aegean Sea, Greece. Geology, 12(4), 221-225.

Mainprice, D., Bachmann, F., Hielscher, R., & Schaeben, H. (2015). Descriptive tools for the analysis of texture projects with large datasets using MTEX: strength, symmetry and components. Geological Society, London, Special Publications, 409(1), 251-271.

Maluski, H., Vergely, P., Bavay, D., Bavay, P., & Katsikatsos, G. (1981). $^{39}Ar/^{40}$ Ar dating of glaucophanes and phengites in southern Euboa (Greece); geodynamic implications. Bulletin de la Société Géologique de France, 7(5), 469-476.

Mehl, C., Jolivet, L., Lacombe, O., Labrousse, L., & Rimmele, G. (2007). Structural evolution of Andros (Cyclades, Greece): a key to the behaviour of a (flat) detachment within an extending continental crust. Geological Society, London, Special Publications, 291(1), 41-73.

Passchier, C. W., & Trouw, R. A. (2005). Microtectonics. Springer Science & Business Media.

Peillod, A., Patten, C. G., Drüppel, K., Beranoaguirre, A., Zeh, A., Gudelius, D., ... & Kolb, J. (2024). Disruption of a high-pressure unit during exhumation: Example of the Cycladic Blueschist unit (Thera, Ios and Naxos islands, Greece). Journal of Metamorphic Geology, 42(2), 225-255.

Pennacchioni, G., Menegon, L., Leiss, B., Nestola, F., & Bromiley, G. (2010). Development of crystallographic preferred orientation and microstructure during plastic deformation of natural coarse-grained quartz veins. Journal of Geophysical Research: Solid Earth, 115(B12).

Peternell, M., Hasalová, P., Wilson, C. J., Piazolo, S., & Schulmann, K. (2010). Evaluating quartz crystallographic preferred orientations and the role of deformation partitioning

using EBSD and fabric analyser techniques. Journal of Structural Geology, 32(6), 803-817.

Philippon, M., Brun, J. P., & Gueydan, F. (2011). Tectonics of the Syros blueschists (Cyclades, Greece): From subduction to Aegean extension. Tectonics, 30(4).

Raimbourg, H., Famin, V., Palazzin, G., Yamaguchi, A., Augier, R., Kitamura, Y., & Sakaguchi, A. (2019). Distributed deformation along the subduction plate interface: The role of tectonic mélanges. Lithos, 334, 69-87.

Ribeiro, B. V., Kirkland, C. L., Kelsey, D. E., Reddy, S. M., Hartnady, M. I., Faleiros, F. M., ... & Clark, C. (2023). Time-strain evolution of shear zones from petrographically constrained Rb–Sr muscovite analysis. Earth and Planetary Science Letters, 602, 117969.

Ring, U., & Kumerics, C. (2008). Vertical ductile thinning and its contribution to the exhumation of high-pressure rocks: the Cycladic blueschist unit in the Aegean. Journal of the Geological Society, 165, 1019.

Ring, U., & Layer, P. W. (2003). High-pressure metamorphism in the Aegean, eastern Mediterranean: Underplating and exhumation from the Late Cretaceous until the Miocene to Recent above the retreating Hellenic subduction zone. Tectonics, 22(3).

Ring, U., & Reischmann, T. (2002). The weak and superfast Cretan detachment, Greece: exhumation at subduction rates in extruding wedges. Journal of the Geological Society, 159(3), 225-228.

Ring, U., Brandon, M. T., Willett, S. D., & Lister, G. S. (1999). Exhumation processes. Geological Society, London, Special Publications, 154(1), 1-27.

Ring, U., Glodny, J., Will, T., & Thomson, S. (2007b). An Oligocene extrusion wedge of blueschist-facies nappes on Evia, Aegean Sea, Greece: implications for the early exhumation of high-pressure rocks. Journal of the Geological Society, 164(3), 637-652.

Ring, U., Glodny, J., Will, T., & Thomson, S. (2010). The Hellenic subduction system: high-pressure metamorphism, exhumation, normal faulting, and large-scale extension. Annual Review of Earth and Planetary Sciences, 38, 45-76.

Ring, U., Layer, P. W., & Reischmann, T. (2001). Miocene high-pressure metamorphism in the Cyclades and Crete, Aegean Sea, Greece: Evidence for large-magnitude displacement on the Cretan detachment. Geology, 29(5), 395-398.

Ring, U., Will, T., Glodny, J., Kumerics, C., Gessner, K., Thomson, S., ... & Drüppel, K. (2007a). Early exhumation of high-pressure rocks in extrusion wedges: Cycladic blueschist unit in the eastern Aegean, Greece, and Turkey. Tectonics, 26(2).

Rogowitz, A., Huet, B., Schneider, D., & Grasemann, B. (2015). Influence of high strain rate deformation on $^{40}Ar/^{39}Ar$ mica ages from marble mylonites (Syros, Greece). Lithosphere, 7(5), 535-540.

Rösel, D., & Zack, T. (2022). LA-ICP-MS/MS Single-Spot Rb-Sr Dating. Geostandards and Geoanalytical Research, 46(2), 143-168.

Sander, B. (1950), Einführung in die Gefügekunde der Geologischen Körper, Zweiter Teil, Die Korngefuege, Springer-Verlag, Wein-Inssbruck.

Schermer, E. R., Lux, D. R., & Burchfiel, B. C. (1990). Temperature-time history of subducted continental crust, Mount Olympos Region, Greece. Tectonics, 9(5), 1165-1195.

Schmid, S. M., & Casey, M. (1986). Complete fabric analysis of some commonly observed quartz c-axis patterns. Mineral and Rock Deformation: Laboratory Studies, 36, 263-286.

Schneider, D. A., Grasemann, B., Lion, A., Soukis, K., & Draganits, E. (2018). Geodynamic significance of the Santorini detachment system (Cyclades, Greece). Terra Nova, 30(6), 414-422.

Scott, R. J., & Lister, G. S. (1992). Detachment faults: Evidence for a low-angle origin. Geology, 20(9), 833-836.

Shaked, Y., Avigad, D., & Garfunkel, Z. (2000). Alpine high-pressure metamorphism at the Almyropotamos window (southern Evia, Greece). Geological Magazine, 137(4), 367-380.

Sotiropoulos, S., Kamberis, E., Triantaphyllou, M. V., & Doutsos, T. (2003). Thrust sequences in the central part of the External Hellenides. Geological Magazine, 140(6), 661-668.

Starnes, J. K., Long, S. P., Gordon, S. M., Zhang, J., & Soignard, E. (2020). Using quartz fabric intensity parameters to delineate strain patterns across the Himalayan Main Central thrust. Journal of Structural Geology, 131, 103941.

Stipp, M., StuÈnitz, H., Heilbronner, R., & Schmid, S. M. (2002). The eastern Tonale fault zone: a 'natural laboratory'for crystal plastic deformation of quartz over a temperature range from 250 to 700 C. Journal of structural geology, 24(12), 1861-1884.

Sullivan, W. A., & Beane, R. J. (2010). Asymmetrical quartz crystallographic fabrics formed during constrictional deformation. Journal of Structural Geology, 32(10), 1430-1443.

Thomson, S. N., Stöckhert, B., Rauche, H., & Brix, M. R. (1998). Apatite fission-track thermochronology of the uppermost tectonic unit of Crete, Greece: implications for the post-Eocene tectonic evolution of the Hellenic subduction system. In Advances in Fission-Track Geochronology: A selection of papers presented at the International Workshop on Fission-Track Dating, Ghent, Belgium, 1996 (pp. 187-205). Springer Netherlands.

Toy, V.G., Prior, D.J. & Norris, R.J. 2008. Quartz fabrics in the Alpine Fault mylonites: Influence of pre-existing preferred orientations on fabric development during progressive uplift. Journal of Structural Geology 30(5), 602–621.

Trepmann, C. A., & Stöckhert, B. (2003). Quartz microstructures developed during non-steady state plastic flow at rapidly decaying stress and strain rate. Journal of Structural Geology, 25(12), 2035-2051.

Trotet, F., Jolivet, L., & Vidal, O. (2001). Tectono-metamorphic evolution of Syros and Sifnos islands (Cyclades, Greece). Tectonophysics, 338(2), 179-206.

Uunk, B., Brouwer, F., de Paz-Álvarez, M., van Zuilen, K., Huybens, R., van't Veer, R., & Wijbrans, J. (2022). Consistent detachment of supracrustal rocks from a fixed subduction depth in the Cyclades. Earth and Planetary Science Letters, 584, 117479.

Vermeesch, P. (2018). IsoplotR: A free and open toolbox for geochronology. Geoscience Frontiers, 9(5), 1479-1493.

Vidal, O., & Parra, T. (2000). Exhumation paths of high-pressure metapelites obtained from local equilibria for chlorite–phengite assemblages. Geological Journal, 35(3-4), 139-161.

Vollmer, F. W. (1990). An application of eigenvalue methods to structural domain analysis. Geological Society of America Bulletin, 102(6), 786-791.

Warren, C. J. (2013). Exhumation of (ultra-) high-pressure terranes: concepts and mechanisms. Solid Earth, 4(1), 75-92.

Wernicke, B. (1981). Low-angle normal faults in the Basin and Range Province: nappe tectonics in an extending orogen. Nature, 291(5817), 645-648.

Wernicke, B., & Axen, G. J. (1988). On the role of isostasy in the evolution of normal fault systems. Geology, 16(9), 848-851.

White, S. (2001). Textural and microstructural evidence for semi-brittle flow in natural fault rocks with varied mica contents. International Journal of Earth Sciences, 90, 14-27.

Wilson, C. J., Russell-Head, D. S., Kunze, K., & Viola, G. (2007). The analysis of quartz c-axis fabrics using a modified optical microscope. Journal of Microscopy, 227(1), 30-41.

Xypolias, P., Kokkalas, S., & Skourlis, K. (2003). Upward extrusion and subsequent transpression as a possible mechanism for the exhumation of HP/LT rocks in Evia Island (Aegean Sea, Greece). Journal of Geodynamics, 35(3), 303-332.

Xypolias, P., Spanos, D., Chatzaras, V., Kokkalas, S., & Koukouvelas, I. (2010). Vorticity of flow in ductile thrust zones: examples from the Attico-Cycladic Massif (Internal Hellenides, Greece). Geological Society, London, Special Publications, 335(1), 687-714.

Zlatkin, O., Avigad, D., & Gerdes, A. (2018). New detrital zircon geochronology from the Cycladic Basement (Greece): Implications for the Paleozoic accretion of peri-Gondwanan terranes to Laurussia. Tectonics, 37(12), 4679-4699.

CHAPTER 4

SYN-EXHUMATION METASOMATIC GLAUCOPHANE-PHENGITE-QUARTZ VEINS FORMED AT MODERATE PRESSURES: EXPLORING THE CONTROL OF fO_2 AND BULK COMPOSITION ON NOMINALLY HP METAMORPHIC ASSEMBLAGES

4.1. Abstract

Veins composed of glaucophane + phengite + quartz cross-cut the high pressure-low temperature (HP-LT) Cycladic Blueschist Unit (CBU) of southern Evia, Greece. The veins exhibit a rheology-dependent distribution within layered metamorphic rock comprising cm-scale intercalations of albite-clinopyroxene metabasalt and schistose quartzite. Strain was accommodated by ductile processes in the quartzite, whereas brittle deformation produced four sets of crack-seal syntaxial veins in the coarser grained metabasalt. All vein sets are subvertical to steeply-dipping and are oriented at high angles to one another. The geometry of the planar vein walls suggests the veins are mode-I (opening mode) fractures, whose sub-vertical orientations indicate formation during extension. Oxygen isotope thermometry using phengite-quartz pairs provides crystallization temperatures of 315-335°C. Combined $^{40}Ar/^{39}Ar$ and *in-situ* $^{87}Rb/^{87}Sr$ geochronology of vein-hosted phengite and glaucophane indicate crystallization and vein sealing at *c*. 22-23 Ma, when the CBU is predicted to be undergoing greenschist facies metamorphism coincident with regional extension. The structural and stable isotope data are likewise consistent with a syn-exhumation extensional setting, and easily reconciled with existing petrological data indicating the CBU sustained prolonged residence near the greenschist-blueschist facies boundary. We propose a model whereby phengite and glaucophane were stabilized at greenschist facies conditions by the elevated α_{SiO2} and fO_2 in the fluid parental to the veins. Our data provide strong new evidence for the sensitivity of nominally blueschist facies minerals to bulk system chemistry, supported by thermodynamic modelling evidence from other orogens that such HP-LT minerals may exhibit stabilities that span multiple stages of orogenesis.

4.2. Introduction

Hydrothermal veins are preserved throughout the rock record and appear in nearly all geological contexts. Veins are the structural record of open space created by brittle fracturing or ductile dilation, fluid infiltration, and sealing by mineral precipitation (Ramsay and Huber 1983; Bons et al. 2012). Evidence from natural examples and from numerical and analogue modelling indicates a range of opening mechanisms reflecting the tectonic framework of vein formation, and several endmember styles of crystallization during vein sealing controlled by physicochemical properties of the parental fluids (Ramsay 1980; Urai et al. 1991; Bons 2001; Bons et al. 2012). Veins accordingly represent a valuable record of stress conditions and fluid regimes coeval with their formation. These aqueous fluids may moreover act as conduits for advective mass transfer, driving metasomatic alteration that may extend to the km-scale (Bebout and Barton 1993; Harlov and Austrheim 2013). Whereas veins in the rock record are disproportionately composed of carbonate minerals or quartz, the unique chemical environment of some hydrothermal systems may produce more complex metamorphic mineral assemblages that offer insight into contemporaneous pressure and temperature (PT) conditions.

Rare examples of veins hosted within exhumed high-pressure, low-temperature (HP-LT) terranes may exhibit structural or mineralogical evidence suggesting the veins formed, or were metamorphosed at, blueschist to eclogite facies conditions (e.g., Gao and Klemd 2001; Widmer and Thompson 2001; Behr and Bürgmann 2021; Muñoz-Montecinos et al. 2020; Giuntoli and Viola 2022). High-pressure veins frequently display strain elements indicative of opening, at least partially, via brittle fracturing, despite having apparently formed below the brittle-ductile transition zone (e.g., Philippot and Selverstone 1991; Castelli et al. 1998; Spandler and Hermann 2006; Bukała et al. 2020). Veins from these settings provide insight into the fluid compositions and

hydrothermal regimes characteristic of subduction zone systems, and represent candidates for a geologic record of deep-seated seismological phenomena like slow slip and non-volcanic tremor (e.g., Behr and Bürgmann 2021; Menegon and Fagereng 2021; Giuntoli and Viola 2022). Correctly interpreting structures as relating to sub-arc volatile flux or deep seismogenic processes requires deconvolution of successive metamorphic mineral assemblages and (micro)structures. Despite significant recent advancements, however, thermodynamic modelling of fluid-rock interactions in metamorphic systems remains a challenging task (e.g., Huang and Sverjensky 2019; Menzel et al. 2020), due to the largely unexplored solubility of major elements in aqueous fluids and mismatch between thermodynamically- and empirically-derived solubilities (Tiraboshi et al. 2018; Macris et al. 2020). Consequently, conclusions drawn from such systems often rely on the validity of *a priori* inferences of contemporaneous PT conditions using minerals in the veins or surrounding host rock.

Herein, we describe syntaxial glaucophane-phengite-quartz veins in the Cycladic Blueschist Unit (CBU) of southern Evia (NW Cyclades, Greece). We utilize a multi-analytical approach incorporating mineral chemistry, geochronology, and stable isotope thermometry to develop a conceptual model for the paragenesis of the veins. In our model, fractures preferentially formed in metabasaltic rock of a complexly folded quartzite and metabasalt of a metaophiolitic sequence. Although they contain dense selvages of glaucophane and phengite – minerals considered diagnostic of HP-LT conditions – the veins exhibit undeformed planar geometries and are oriented uniformly within their tectonized and rheologically stratified host rock package. The data collectively reveal that vein formation likely coincided with regional retrograde greenschist facies metamorphism, and that the nominally HP minerals crystallized by consequence of the local bulk composition imposed, in part, by the throughgoing fluids. We argue that the mineral assemblage in the veins developed under elevated pressures in the greenschist facies during

exhumation, despite superficially resembling a blueschist facies assemblage. Our conclusions underscore recent evidence from thermodynamic models demonstrating that rock exhumed from the subduction channel may exhibit coeval, ostensibly greenschist or blueschist facies mineral assemblages dependent primarily on the bulk chemistry of a local reacting volume (e.g., Manzotti et al. 2020; Muñoz-Montecinos et al. 2020).

4.3. Cenozoic tectonics of the Cyclades

The Cycladic archipelago and parts of the Attic peninsula in the Aegean Sea are composed predominantly of the CBU, a HP-LT metamorphic nappe (Dürr et al. 1978; Jacobshagen 1986). The CBU underwent Eocene HP-LT metamorphism at *c.* 50 Ma and likely remained at HP conditions until at least the middle or late Eocene (Tomaschek et al. 2003; Schneider et al. 2011; Huet et al. 2015; Laurent et al. 2021; Uunk et al. 2022). The CBU experienced syn-orogenic wedge extrusion in the late Eocene prior to unroofing into the upper crust along a series of regional-scale, low-angle detachment faults active since the early Miocene (Tomaschek et al. 2003; Ring et al. 2007a; Jolivet et al. 2010; Grasemann et al. 2012; Laurent et al. 2017). The CBU sustained a greenschist facies overprint of variable intensity during late syn-orogenic and post-orogenic exhumation (Schliestedt and Matthews 1987; Ring et al. 2010).

The southernmost region of Evia is occupied by two lithological units corresponding to the CBU: the predominantly metacarbonate Styra Unit, and the overlying, partly ophiolitic Ochi Unit, which comprises ultramafic, mafic, and felsic igneous rocks and quartzitic metasediments and ironstones (Katsikatsos et al.,1991a; Katzir et al. 2000; Xypolias et al. 2012; **Figure 4.1**). The Ochi Unit has alternatively been correlated with the Makrotantalon Unit situated at the top of the structural pile of Andros to the southeast (Papanikolaou 2009; Gerogiannis et al. 2019). The Ochi

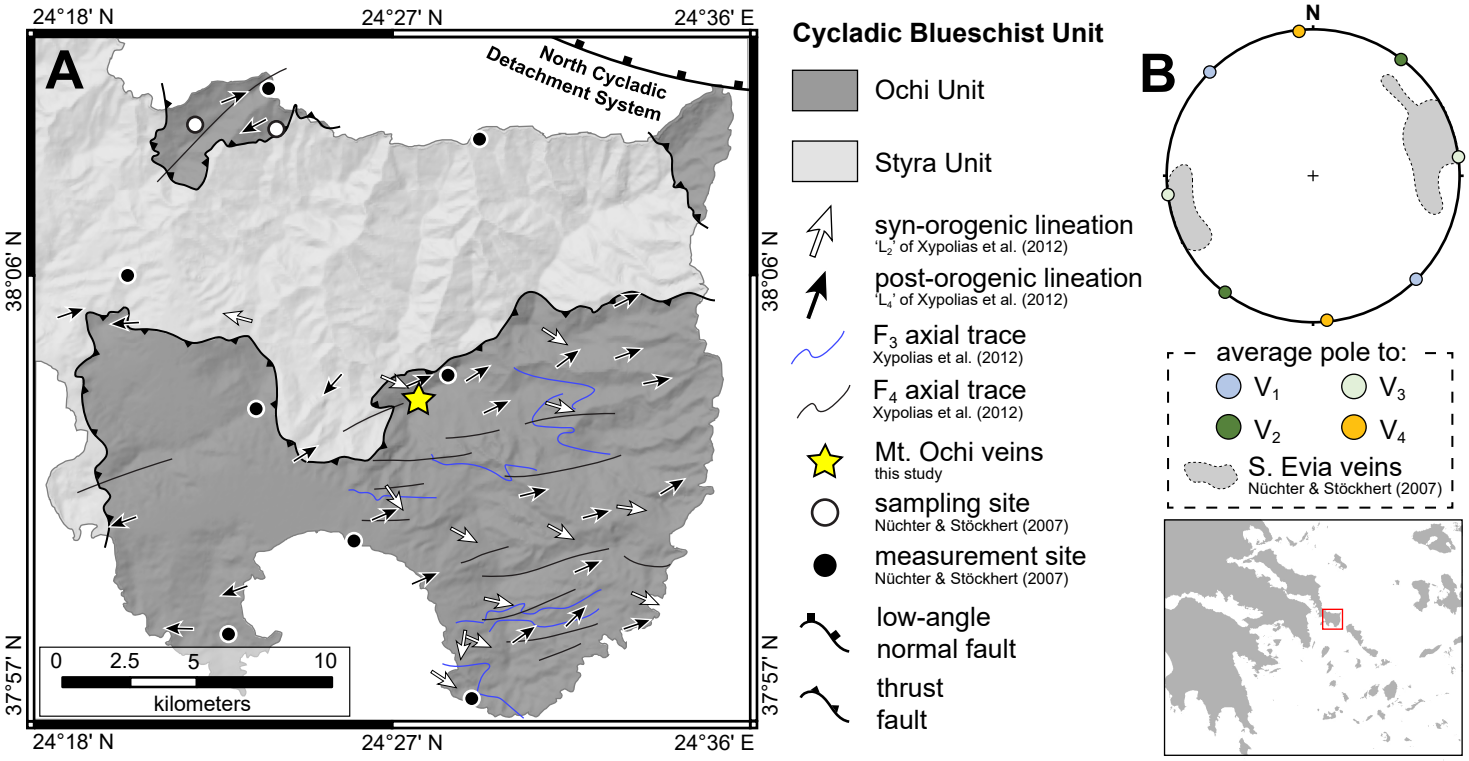

Figure 4.1. (A) Geologic map of southern Evia. Modified after Katsikatsos et al. (1991) and Xypolias et al. (2012). (B) Stereonet showing average poles to each vein set, and includes vein measurement data (shaded region) from Nüchter and Stöckhert (2007). Inset map shows the location of the study area NW of the Cyclades.

Unit is interpreted to have been thrust atop the Styra Unit in the subduction channel prior to pervasive reworking of the nappes by multiple generations of folds (Xypolias et al. 2012). The CBU-affiliated units structurally overlie a ~3 km thick parautochthonous platform carbonate and flysch sequence that is exposed in a tectonic window in south-central Evia (Katsikatsos et al. 1991b; Shaked et al. 2000; Ducharme et al. 2022). The entire structural pile of southern Evia is situated in the footwall of the North Cycladic Detachment System (NCDS), a fault network extending from Samos across the northern Cyclades to Evia (Jolivet et al. 2010). The NCDS was likely partly responsible for post-orogenic exhumation of southern Evia, and its influence is recorded by numerous top-to-N and top-to-NE kinematic indicators preserved up to 500 m below the detachment (e.g., Mehl et al. 2007; Jolivet et al. 2010; Menant et al. 2013; Laurent et al. 2015; Ducharme et al. 2022).

The CBU-equivalent units of southern Evia experienced peak HP-LT metamorphism of ~10-12 kbar and ~400-460°C (Shaked et al. 2000; Katzir et al. 2000; Ducharme et al. 2022). Whereas the timing of peak HP-LT metamorphism likely coincides with that of the broader CBU, relevant $^{40}Ar/^{39}Ar$ and $^{87}Rb/^{87}Sr$ geochronology from the Styra and Ochi units has yielded dates for phengitic white mica and glaucophane between *c.* 35-30 Ma (Maluski et al. 1981; Ring et al. 2007b; Ducharme et al. 2022). Similar dates obtained elsewhere in the Cyclades have been interpreted as capturing the timing of earliest greenschist or latest blueschist facies metamorphism, incipient strain related to the major detachments, or else a geologically meaningless mixture of contrasting age domains (Cossette et al. 2015; Laurent et al. 2022). Greenschist facies overprint of the CBU on Evia is considered to have begun by *c.* 25-21 Ma (Ring et al. 2007b; Ducharme et al. 2022), coeval with estimates for the remainder of the CBU to the south.

4.4. Vein mineralogy and structure

Distinct vein sets containing sodic amphibole (optically identified as predominantly glaucophane) + quartz ± white mica ± epidote locally occur in an exposure of the Ochi Unit directly west of Mt. Ochi (UTM Zone 35N, E277323, N4215232.; **Figure 4.1**, **Figure 4.2a**). The most prominent vein set cross-cuts all others and contains dense selvages of glaucophane oriented at high angles to the vein walls (**Figure 4.2b**). The veins are hosted within medium-grained metabasites and schistose quartzite tectonically intercalated at the cm-scale, but preferentially within the metabasic layers, pinching out or terminating abruptly near contacts between the two lithotypes. In plan view normal to the metamorphic layering, the coarser grained metabasites are dissected by four differently oriented vein sets, each of which contains variable modal proportions of the three main constituent minerals. Despite evidence of folding in the host rocks, veins retain a dominantly planar geometry (**Figure 4.2c-d**).

The metabasic lithology is orange-brown to green-brown in color and exhibits a granular appearance, lacking macroscopically identifiable minerals apart from a dominant prismatic phase locally defining an ENE-WSW trending mineral lineation. Intercalated quartzites are a pale buff or cream color with abundant blue prismatic glaucophane crystals, up to 3 mm long, distributed throughout a fine-grained matrix. The glaucophane defines a weak mineral lineation oriented at a small angle to the lineation in the metabasites, and subparallel to the most prominent vein set. Thin (~1 mm) seams of almost exclusively glaucophane are parallel to this vein set, apparently concentrated along contacts between the two dominant host lithologies.

Four samples (EV19-15A, B, C, D; **Table 4.1**) of the veined rocks were collected for laboratory investigation; additional micrograph documentation is provided in the supplementary information file (**Figure S4.1, S4.2**). Petrographic study reveals that the metabasites are composed

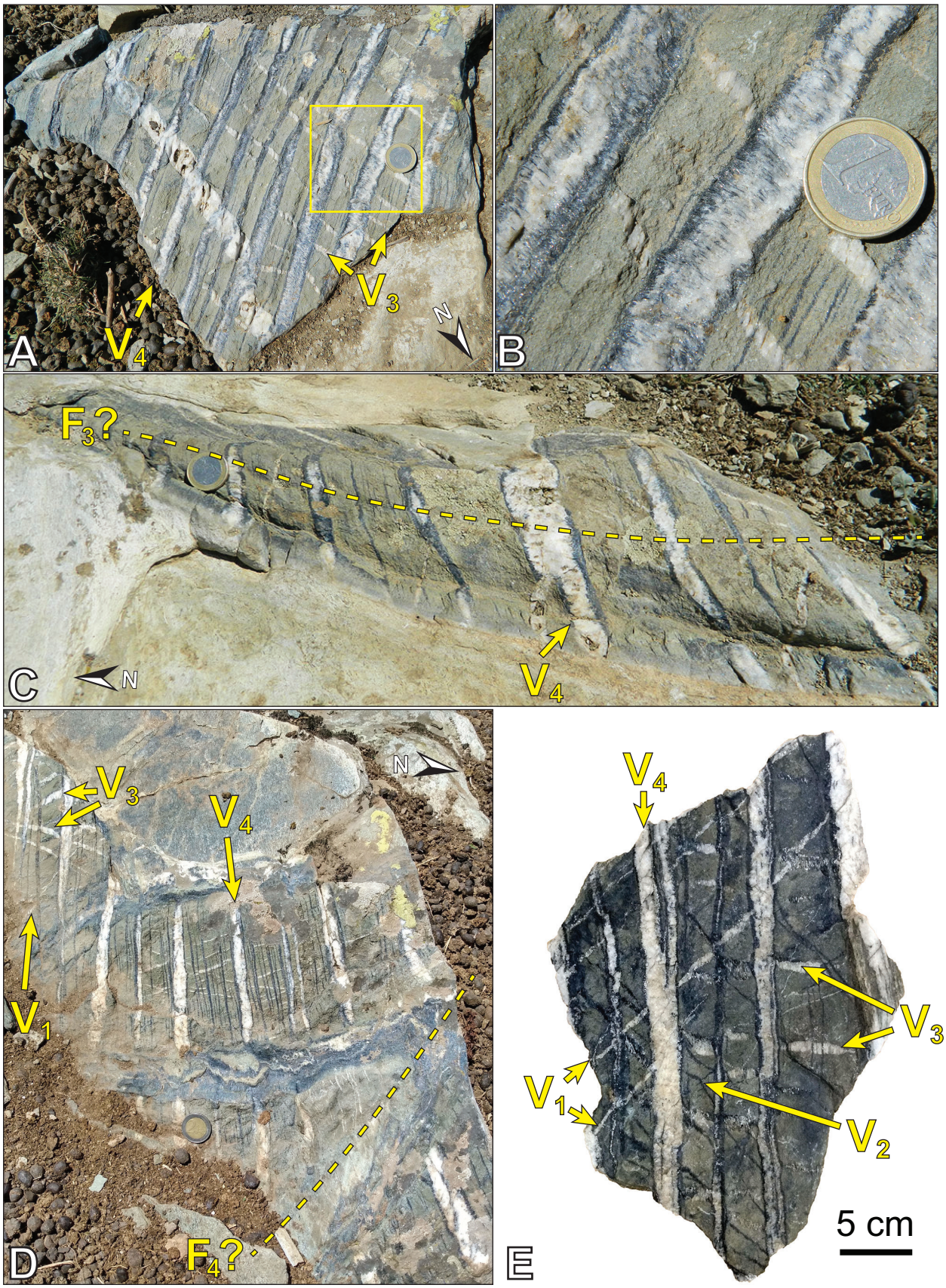
A
V4
V3
N
B
C
F3?
V4
N
D
V3
V4
V1
N
F4?
E
V4
V3
V1
V2
5 cm

Figure 4.2. (previous page) Outcrop photographs of the Mt. Ochi glaucophane-bearing veins. (A) Representative photo showing prominent, evenly-spaced V_4 veins hosting dense glaucophane + quartz. The prominent veins cross-cut and offset numerous V_3 veins of varying widths containing mostly quartz. Box shows location of figure 4.2B. (B) Close-up photo showing the distribution of glaucophane within the V_4 veins and the cross-cutting relationship of V_3 veins by narrow glaucophane-rich seams. (C) V_4 veins of variable width transecting an upright folded (F_3) metabasalt horizon. The metabasalt is overlain on either side by quartzite with a mineral lineation defined by glaucophane. (D) Evenly-spaced V_4 veins cross-cutting smaller V_1 and V_3 veins. A tight flat-lying fold (F_4?) outlined by glaucophane crystals appears to cross-cut the V_4 veins, but veins reappear apparently undisturbed on the opposite side. (E) Sample EV19-15C indicating the structures used to define the vein set nomenclature. Fold nomenclature after Xypolias et al. (2012).

mostly of moderately (2nd order) birefringent, elongate prismatic clinopyroxene (70-75%) and interstitial anhedral albite (10-15%; **Figure 4.3a**). Euhedral aggregates of albite are the dominant phase in several thin layers where partial relicts of prismatic clinopyroxene occur as inclusions. Other minerals include euhedral crystals of glaucophane, phengite, and epidote, the latter of which forms abundant euhedral inclusions in albite. Chlorite is locally predominant over albite and occupies the interstices of clinopyroxene grains, and appears as a major phase alongside glaucophane and minor biotite in some albite-dominated layers (**Figure 4.3b**).

Clinopyroxene is preserved in various states of alteration. In places, clinopyroxene crystals retain a clear prismatic morphology and individual crystals may still be discerned in transmitted light. Backscatter electron imaging in these regions nevertheless reveals that clinopyroxene is occluded by dense subrounded quartz inclusions <10 μm in diameter (**Figure 4.4a**). Quartz inclusions are seldom distinguishable in transmitted light. Where quartz is visible in transmitted light, it occurs alongside euhedral crystals of glaucophane, phengite, and epidote, and clinopyroxene takes on a fuzzy appearance due to skeletal intergrowth with either quartz (**Figure 4.4b**) or albite (**Figure 4.4c**).

The schistose quartzite comprises aggregates of quartz (60-70%) with dispersed white mica (15%), glaucophane (15%), hematite, and minor albite (**Figure 4.3c**). Quartz forms fine-grained granoblastic recrystallized aggregates with grain dimensions limited by the surrounding fine-grained phyllosilicates. Preferred orientations of the long axes of glaucophane and white mica, as well as a subtle shape preferred orientation (SPO) of quartz, collectively define a planar foliation.

Each vein set hosts variable proportions of sodic amphibole + quartz ± white mica ± epidote. Glaucophane displays a conspicuous compositional zonation in nearly all occurrences

(**Figure 4.5a**); mica, in contrast, is not zoned (**Figure 4.5b**). Quartz, epidote, and infrequent titanite are common inclusions in glaucophane cores (**Figure 4.5c**). Glaucophane and phengite form large, pristine crystals displaying elongate prismatic or tabular habits. Both minerals are found primarily in systematic orientations along vein walls, but also occur sparsely in the vein cores. Host rock fragments are commonly included within veins, most often as elongate wall-parallel inclusions (**Figure 4.5d**). Hereafter we briefly describe each vein set that we have discriminated, the nomenclature for which was developed using a sample (EV19-15C) containing most of the vein sets observed across the exposure (**Figure 4.2e**).

V_1 veins. The oldest vein population (V_1) strikes NE-SSW, and are commonly <5 mm wide with parallel walls and a planar geometry. Quartz is the predominant constituent of V_1 veins, the margins of which are lined with dispersed, dense clusters of phengite and glaucophane, with phengite generally present in greater size and abundance (**Figure 4.3d**). The long axes of these minerals are either sub-perpendicular, or else at an angle of ~40-50°, to the vein walls. Quartz shows a well-developed SPO parallel to the inclined mica and amphibole, except in some vein cores, where large grains exhibit only undulatory extinction (**Figure 4.5e**). Quartz grain boundaries are ubiquitously serrated and exhibit low-amplitude bulging with dispersed small grains distributed along grain boundaries.

V_2 veins. V_2 veins strike NW-SE, are few in number, and composed almost entirely of interlocking glaucophane crystals with some vein cores of mica, minimal quartz, and rare epidote. Glaucophane crystals line the walls of V_2 veins at an oblique angle to the vein walls with a moderately distorted prismatic morphology. Mutually impinging glaucophane crystals in these veins display regular alternation between two nearly orthogonal crystallographic orientations (**Figure 4.3e**).

Table 4.1. Summary of samples of the Mt. Ochi veins.

Sample ID	Vein sets	Host rock contacts	$^{87}Rb/^{87}Sr$	$^{40}Ar/^{39}Ar$	^{18}O
EV19-15A	V_3, V_4	planar			
EV19-15B	V_3, V_4	undulose, isoclinally folded			
EV19-15C	V_1, V_2, V_3, V_4	planar	x	x	x
EV19-15D	V_2, V_3, V_4	isoclinally folded	x	x	

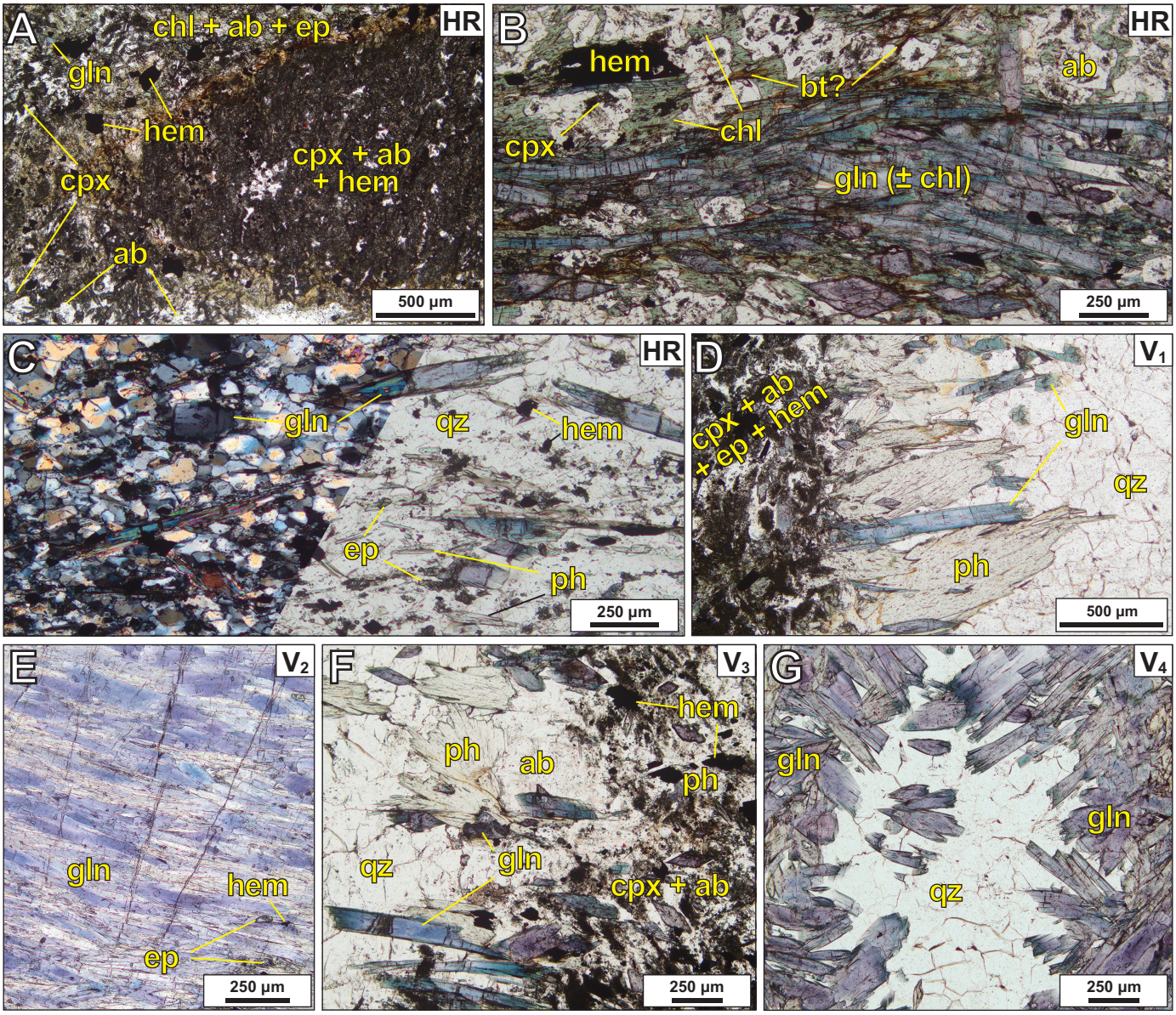

Figure 4.3. Micrographs of major vein sets and their host rocks (HR). (A) Fragment of minimally altered metabasaltic host rock surrounded by a more typical albite + epidote + clinopyroxene + chlorite assemblage. (Plane-polarized light; PPL). (B) Seam of glaucophane intergrown with chlorite in an albite-dominated host rock layer (PPL). (C) Typical schistose quartzitic host rock layer. Micrograph divided into cross-polarized light (XPL, left) and PPL (right) to illustrate the crystalline structure of quartz. (D) Margin of a V_1 vein showing inward growth of phengite and glaucophane from the metabasaltic wall rock. YZ plane of the vein is shown (PPL). (E) Interlocking glaucophane crystals from a V_2 vein. Note the alternation between pleochroic extremes (colorless to violet). YZ plane of the vein is shown (PPL). (F) Margin of a V_3 vein showing wall rock at the margin that has undergone significant alteration to albite. YZ plane of the vein is shown (PPL). (G) Centre of a V_4 vein shows a seam of quartz transecting glaucophane oriented at a high angle to the vein walls (parallel to the vertical of the photo). XY plane of the vein is shown (PPL). ab albite, bt biotite; chl chlorite; cpx clinopyroxene; ep epidote; hem hematite; ph phengite; qz quartz.

V_3 veins. This vein generation strikes NNW-SSE (**Figure 4.2a**), or locally defines a conjugate set with small angles at ~30° from this trend (**Figure 4.2d**). V_3 veins frequently exhibit a lenticular shape with the highest aperture ratios of all veins studied. The prevalence of nominal HP minerals in V_3 veins is variable, ranging from quartz-dominated veins with few phengite and glaucophane crystals, to comprising almost exclusively the latter two minerals. Phengite and glaucophane are oriented at moderate or high angles to the vein walls (**Figure 4.3f**) and are often colinear with another nominal HP mineral grain on the opposing vein wall. Quartz defines a well-developed SPO parallel to the long axes of glaucophane and phengite with predominantly lobate to serrated grain boundaries.

V_4 veins. The youngest, largest and most consistently developed vein set, V_4 veins are planar, spaced at regular intervals of 5-10 cm, and strike consistently ENE-WSW (**Figure 4.1b**). Veins are up to 30 mm in width, with dense selvages of glaucophane oriented at high angles to the vein walls with a central quartz seam (**Figure 4.3g**). Approximately 30-40% of V_4 veins within a given rock volume are <1 mm wide and are dominated by elongate single glaucophane crystals spanning the full width of the fractures, with only minor interstitial quartz (**Figure 4.5c**). Cores of V_4 veins and vertical extensions toward bounding ductily deformed layers are conversely composed of quartz with dispersed euhedral glaucophane and phengite. Quartz in V_4 veins locally exhibits low-amplitude grain boundary bulging and serrated boundaries, but notably less pervasively than in other veins.

Solid inclusion trails comprising small amphibole crystals are a common feature of V_4 veins (**Figure 4.5d**). In intermediate-width veins, inclusion trails may span from one glaucophane-rich selvage to the other. Toward the vein core, these features are isolated within one or more quartz grains. Some narrow fractures parallel to V_4 are predominantly filled either by quartz or

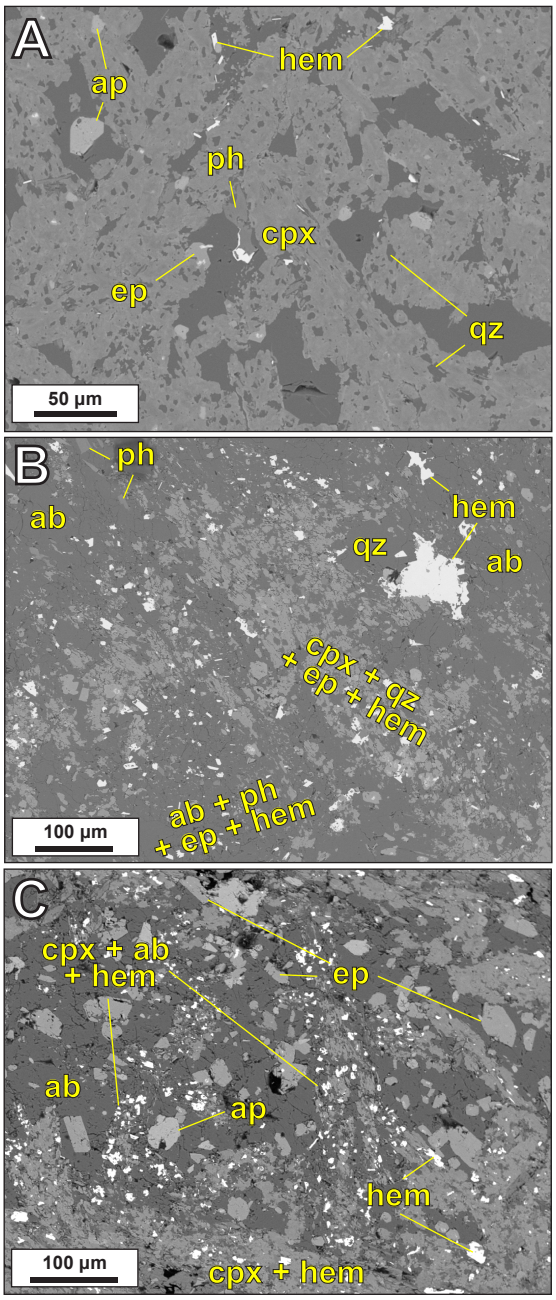

Figure 4.4. Backscatter electron images of host rock clinopyroxene in various stages of alteration. (A) Poikiloblastic clinopyroxene envelops numerous inclusions of quartz. (B) Skeletal clinopyroxene exhibiting partial replacement by quartz and hematite. (C) Skeletal clinopyroxene exhibiting comprehensive replacement by albite and hematite. Mineral abbreviations: ab: albite; ap: apatite; cpx: clinopyroxene; ep: epidote; hem: hematite; ph: phengite; qz: quartz.

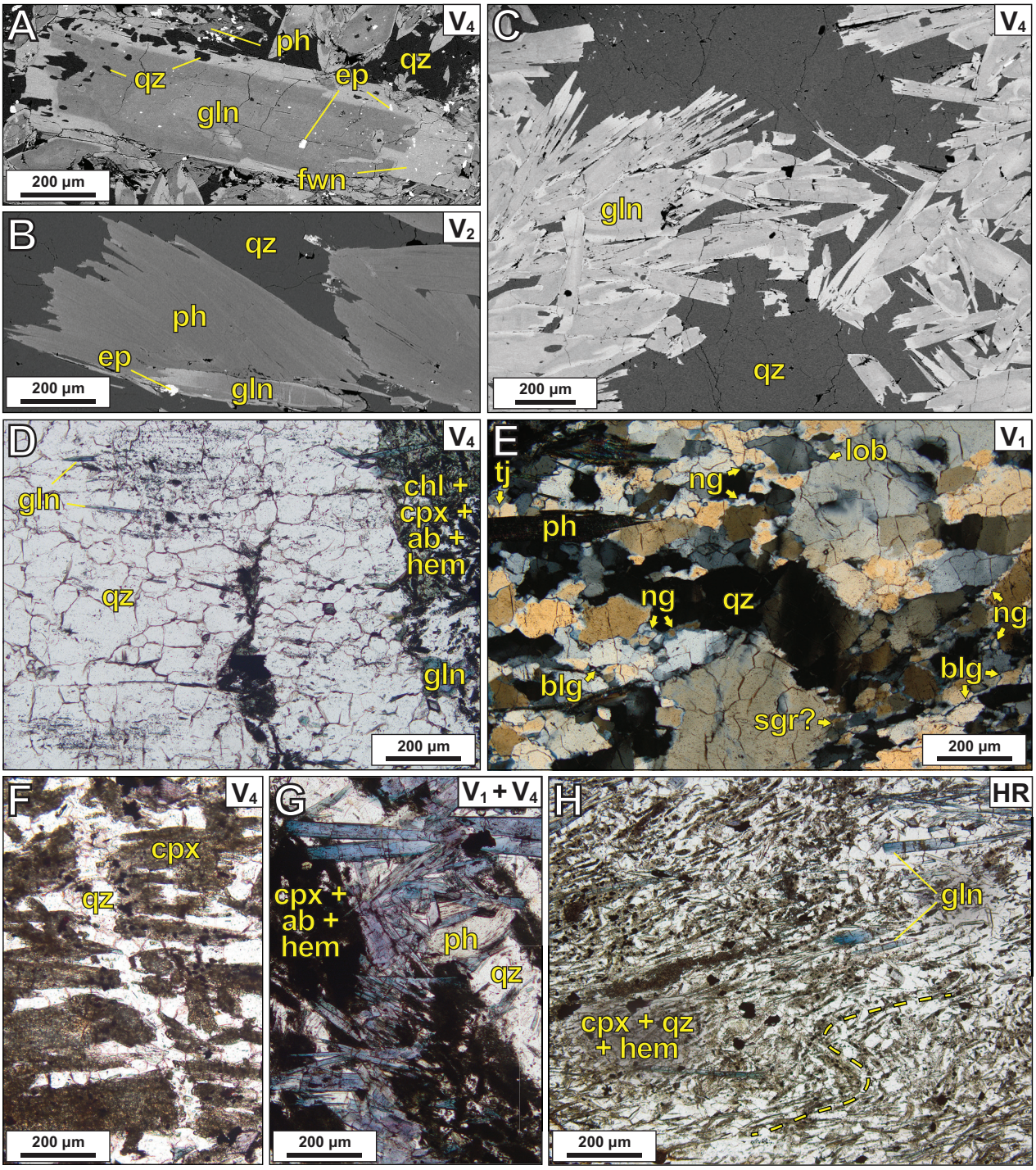
A
V4
ph
qz
qz
ep
gln
fwn
200 µm
B
V2
qz
ph
ep
gln
200 µm
C
V4
gln
qz
200 µm
D
V4
gln
chl +
cpx +
ab +
hem
qz
gln
200 µm
E
V1
lob
tj
ng
ph
ng
qz
ng
blg
blg
sgr?
200 µm
F
V4
cpx
qz
200 µm
G
V1 + V4
cpx +
ab +
hem
ph
qz
200 µm
H
HR
gln
cpx + qz
+ hem
200 µm

Figure 4.5. (previous page) Micrographs and electron backscatter images of structural and mineralogical features of the Mt. Ochi veins. (A) Backscatter electron image of a large glaucophane grain exhibiting typical core-to-rim zoning. (B) Backscatter electron image of a phengite grain showing relative compositional homogeneity. (C) Photomicrograph of an XY (foliation-parallel) section of a V_4 vein. Note the common inclusions of quartz in glaucophane cores. (D) Photomicrograph from a V_4 vein showing mineral inclusion trails in the vein quartz and a solid inclusion band of entrained host rock. YZ plane of the vein is shown (PPL). (E) Core of a V_1 vein showing typical vein quartz textures. Elongate quartz grains with interlobate and bulging grain boundaries at the margins of the micrograph are truncated by large quartz crystals showing undulatory extinction and incipient subgrain development. XY plane of the vein is shown (XPL). (F) Narrow quartz vein infilling a transgranular fracture which cross-cut clinopyroxene grains in metabasaltic host rock. YZ plane shown (PPL). (G) Narrow V_3 vein sealed by elongate glaucophane spanning the width of the fracture. XY plane shown (PPL). (H) Shear zone within a quartz-flooded section of a host metabasalt. Elongate clinopyroxene crystals trace the outline of tight folds with sub-horizontal axial planes (PPL). Mineral abbreviations: ab: albite; chl: chlorite; cpx: clinopyroxene; ep: epidote; fwin: ferriwinchite; hem: hematite; ph: phengite; qz: quartz. Microstructure abbreviations: blg: grain boundary bulging; lob: lobate grain boundary; ng: new recrystallized grain; sgr: subgrain rotation recrystallization; tj: grain boundary triple junction

glaucophane. The former veins show puzzle-like geometry of transected clinopyroxene grains, suggesting sealing of transgranular fractures (**Figure 4.5f**). In the latter, glaucophane crystals span the full width of the fractures (**Figure 4.5g**).

Other structures. Several additional structures occur either too infrequently or too isolated from larger structures to place within the relative age hierarchy of the more abundant vein sets. Numerous small curvilinear veinlets filled with glaucophane + quartz occur in an orientation subparallel or slightly oblique to V_4 veins, but these are typically isolated from other structures within intact host rock. One thin (>0.5 mm) foliation-parallel seam comprising coarse epidote + glaucophane + hematite (sample EV19-15D) cross-cuts all earlier structures but is transected by a later (V_4?) vein generation. Several small sub-horizontal shear zones are developed within both the metabasic and schistose layers, where the prismatic ferromagnesian mineral aggregates outline kinks or tight folds, but individual crystals retain largely intact euhedral crystal shapes (**Figure 4.5h**). These shear zones are cross-cut by V_4 veins, with no evidence of phengite or quartz within the transecting vein material having accommodated greater shear relative to other parts of the vein.

4.5. Analytical Methods

4.5.1. Scanning Electron Microscopy and Electron Microprobe Analysis

Four standard 30 μm thick polished sections (one from EV19-15A and three from EV19-15C) were selected for analysis as these samples permitted straightforward discrimination between vein sets. Cores, mantles, and rims of white mica and amphibole specimens were analyzed using a 10 μm diameter spot size to determine any compositional zoning. Preliminary reconnaissance and mineral identification on the scanning electron microscope (SEM) by electron dispersive spectroscopy (EDS) was performed at the University of Ottawa (Ottawa, Canada) using a JEOL

6610LV SEM. Quantitative wavelength-dispersive spectroscopy (WDS) microprobe analyses were conducted at the University of Ottawa using a JEOL JXA-8230 SuperProbe. Full analytical details can be found in the data repository.

4.5.2. In-situ $^{87}Rb/^{87}Sr$ geochronology

Three 100 µm thick polished sections were prepared from samples EV19-15C and EV19-15D for *in-situ* $^{87}Rb/^{87}Sr$ geochronology using an Agilent 8900 triple-quadrupole inductively coupled plasma mass spectrometer equipped with a reaction cell (Zack and Hogmalm 2016; Hogmalm et al. 2017) paired to an ESL 193 Excimer laser with a TwoVol3 ablation cell in the Fipke Laboratory for Trace Element Research at University of British Columbia, Okanagan (Kelowna, Canada). The analyses followed the basic procedures outlined in Larson et al. (2023) with both phengite and sodic amphibole ablated using a 50 µm diameter spot, a repetition rate of 10 Hz and a laser fluence of 4 J/cm^2. Analyses of secondary reference materials, including the in-house white mica MA1 (*c.* 350 Ma, A. Camacho, unpubl. data) and the nano-powdered biotite Mica-Fe (310 ± 10 Ma, Govindaraju 1979; 305.4 ± 2.0 Ma, Rösel and Zack 2021), yielded dates that overlap within error of those expected (347 ± 3 Ma and 306 ± 3 Ma, respectively). Isochron calculations excluded analyses with high uncertainty, using a >30% (2 standard error of the mean) cut-off that resulted in the exclusion of twelve glaucophane analyses from EV19-15D and zero phengite analyses. Data processing and visualization were performed using the online version of the IsoPlotR package (Vermeesch 2018).

4.5.3. $^{40}Ar/^{39}Ar$ geochronology

Material belonging to V_3 and V_4 veins and the schistose quartzite host rock from EV19-15C and EV19-15D was isolated with a finishing saw and lightly crushed in a mortar and pestle. The crushed material was then sieved to obtain the 256-512 μm and 128-256 μm size fractions, from which 50-60 grains of both white mica and glaucophane were hand-picked for $^{40}Ar/^{39}Ar$ geochronology. $^{40}Ar/^{39}Ar$ analytical work was performed at the University of Manitoba (Winnipeg, Canada) using a multi-collector Thermo Fisher Scientific ARGUS VI mass spectrometer, linked to a stainless steel Thermo Fisher Scientific extraction/purification line and Photon Machines (55 W) Fusions 10.6 CO_2 laser. Full analytical details can be found in the data repository.

4.5.4. Oxygen isotopes

Vein material belonging to V_1, V_3, and V_4 veins from EV19-15C was isolated with a finishing saw and lightly crushed in a mortar and pestle. The crushed material was then sieved to obtain the 256-512 μm and 128-256 μm size fractions, from which 15-20 mg each of inclusion-free quartz and mica was hand-picked. The material was analyzed at the Queens Facility for Isotope Research at Queens University (Kingston, Canada) via boron pentafluoride digestion using a Thermo Scientific MAT 253 stable isotope ratio mass spectrometer. Analytical errors are 0.4‰ and are reported relative to Vienna Standard Mean Ocean Water (VSMOW).

4.6. Mineral chemistry

Electron microprobe (EMP) analyses were used to define white mica and amphibole chemistry and investigate compositional variations across and within the vein sets. Full data tables

can be found in **Table S4.1**. White mica compositions from all veins and the host rock plot in a restricted range between muscovite and celadonite (i.e., phengite) with elevated Si content (Si apfu: 3.43-3.53, mean: 3.46; **Figure 4.6a**) and uniform intermediate X_{Mg} (0.45-0.61; **Figure 4.6b**). Variations were neither observed from core to rim within single crystals, nor among populations occupying different vein sets, although biotite present along cleavage planes affected some excluded EMP analyses. Pyrophyllite and paragonite consistently comprise <0.05 mole fraction of each analysis.

Amphibole recalculations were performed using the formula of Locock (2014), and hereafter we employ the nomenclature of Hawthorne (2012). Amphibole displays concentric zonation visible in transmitted light and backscatter images (**Figure 4.5a**). Cores and mantles are glaucophane, with compositions slightly below the glaucophane-ferroglaucophane divide (X_{Mg}: ~0.5; **Figure 4.6c**). Mantles are comparatively Al enriched relative to the cores. The outermost rims appear bright in backscatter images and display a deep green-blue pleochroism in transmitted light. Rim Ca contents commonly exceed 0.5 apfu and exhibit wider compositional variability, ranging from glaucophane to magnesioriebeckite to (ferri-)winchite (**Figure 4.6c-d**). Similar to white mica, sodic amphibole compositions display no resolvable systematic variation across both the vein sets and host rock, including in their core-to-rim chemistry. In addition to the large, zoned specimens of sodic amphibole, several isolated and unzoned euhedral crystals were observed in the ductily deformed groundmass as well as in V_3 veins. Analysis of these isolated grains by EDS indicates these are either ferri-winchite or, less frequently, actinolite.

Microprobe analyses were also conducted on host rock feldspar, clinopyroxene, epidote, and chlorite. Feldspar is consistently endmember albite (An_{0-2}) regardless of host lithology. Epidote and chlorite are relatively invariant in composition. Epidote group phases exhibit

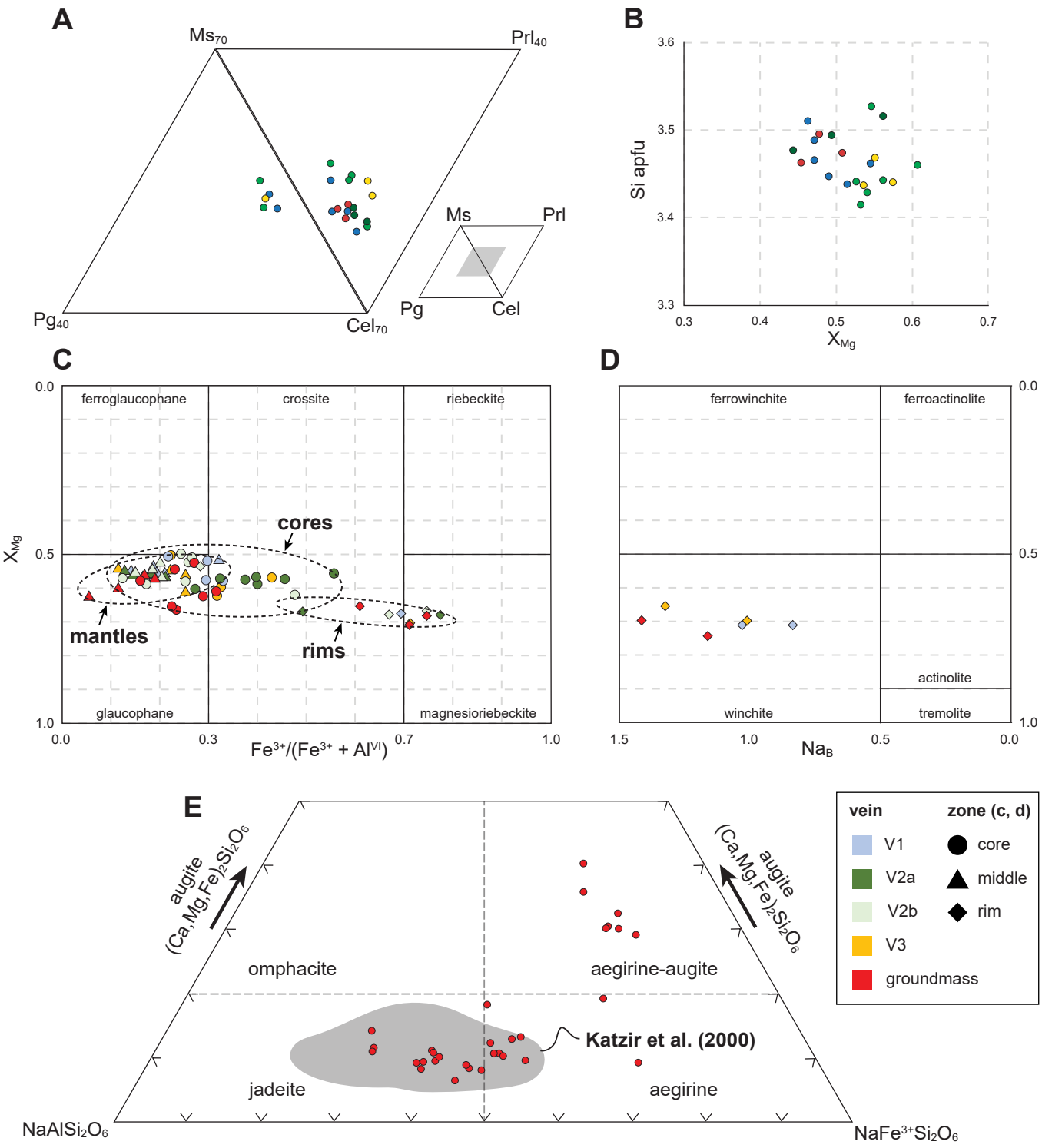

Figure 4.6. Mineral chemistry plots for HP minerals in the Mt. Ochi veins and their host lithotypes. (A) Abbreviated dual mica ternary diagrams. (B) White mica Si apfu vs X_{Mg} plot. (C) Sodic and (D) sodic-calcic amphibole X_{Mg} vs $Fe^{3+}/(Fe^{3+} + Al)$ plot after Hawthorne et al. (2012). (E) Abbreviated pyroxene jadeite-aegirine-augite ternary plot. Shaded region summarizes data from Katzir et al. (2000).

$Fe^{3+}/(Fe^{3+} + Al) = 0.28\text{-}0.32$, classified as epidote following the nomenclature of Armbruster et al. (2006). Chlorite is close to ideal clinochlore and generally exhibits full octahedral site occupancy, with $X_{Fe} = 0.45\text{-}0.52$.

Notably, clinopyroxene compositions varied across samples. Clinopyroxene formulae were recalculated following Cawthorne and Collerson (1974), with Fe^{3+} (i.e., aegirine) assumed to be in equal molar abundance to molar Na in excess of Al (i.e., jadeite). In EV19-15A and EV19-15B, clinopyroxene defines a wide array spanning the jadeite-aegirine join, from $Jd_{60}Aeg_{30}Di_{10}$ at the jadeite-rich extreme and up to $Jd_{40}Aeg_{50}Di_{10}$ at the aegirine-rich extreme, consistent with earlier data from Ochi metabasalt (Katzir et al. 2000). A segment of the host rock relatively poor in glaucophane and white mica locally displayed irregular but distinguishable cores and rims within prismatic clinopyroxene grains. Cores here were among the most jadeite-rich specimens measured, whereas rims showed a marked increase in aegirine component. Clinopyroxene from sample EV19-15C exhibited comparatively high Ca and low Al, plotting as aegirine-augite with average composition $Jd_{19}Aeg_{53}Di_{29}$.

4.7. *In-situ* $^{87}Rb/^{87}Sr$ geochronology

Phengite and glaucophane were dated *in situ* from specimens hosted in V_1-V_4 in EV19-15C, and V_2-V_4 in EV19-15D. Phengite analyses define a linear array, forming a low-dispersion isochron. Glaucophane analyses were comparatively Rb-poor and accordingly the data clusters near the $^{87}Sr/^{86}Sr$ (Y-) axis. Analyses of glaucophane display a high degree of scatter about the Y-axis consistent with low Sr concentrations (**Table S4.2**). The higher precision glaucophane analyses, however, plot along the same isochron as the phengite. A single glaucophane analysis from EV19-15C yielded an $^{87}Rb/^{86}Sr$ ratio >50 (**Figure 4.7a**). Discrete chemical zones in

glaucophane were narrower than the diameter of the laser ablation pit and thus could not be targeted. Accordingly, glaucophane data represent analysis of material from the cores and mantles.

Two isochrons constructed using *in-situ* phengite and glaucophane $^{87}Rb/^{87}Sr$ spot analyses from EV19-15C and EV19-15D define mutually indistinguishable isochron ages of 21 ± 5 Ma (n_{wm}: 27, n_{gln}: 7; MSWD: 1.1) and 24 ± 5 Ma (n_{wm}: 19, n_{gln}: 20; MSWD: 1.8), respectively (**Figure 4.7**). Each sample produced mutually indistinguishable $(^{87}Sr/^{86}Sr)_I$ intercepts of 0.712 ± 0.007 and 0.709 ± 0.004, respectively.

4.8. $^{40}Ar/^{39}Ar$ geochronology

We also performed multiple single-grain, total-fusion $^{40}Ar/^{39}Ar$ geochronology on phengite and glaucophane from the youngest two vein sets (V_3, V_4), which were selected due to the abundance of the target phases within them. Seven to eight pristine white mica crystals (n: 22) analyzed from one V_3 vein in sample EV19-15C, and from two V_4 veins – one each from sample EV19-15C and EV19-15D – yielded total-fusion $^{40}Ar/^{39}Ar$ dates between 21.4 ± 0.6 and 23.0 ± 0.7 Ma (weighted mean: 22.2 Ma ± 0.3 Ma; MSWD: 0.62; **Figure 4.8; Table S4.3**). One step-heating experiment yielded a plateau age of 22.6 ± 0.2 Ma (MSWD: 1.49; **Figure S4.3a; Table S4.3**).

Vein-hosted glaucophane included both elongate prismatic single crystals and radial polycrystalline aggregates. Most specimens were opaque to weakly translucent, making it difficult to select against the presence of inclusions. Ductily deformed groundmass from sample EV19-15D yielded mostly single translucent crystals, smaller than those obtained from the veins. Glaucophane yielded comparatively dispersed results relative to phengite, as well as numerous systematically implausible analyses. High Ca/K values (>5) and routinely low $^{40}Ar^*$ yields

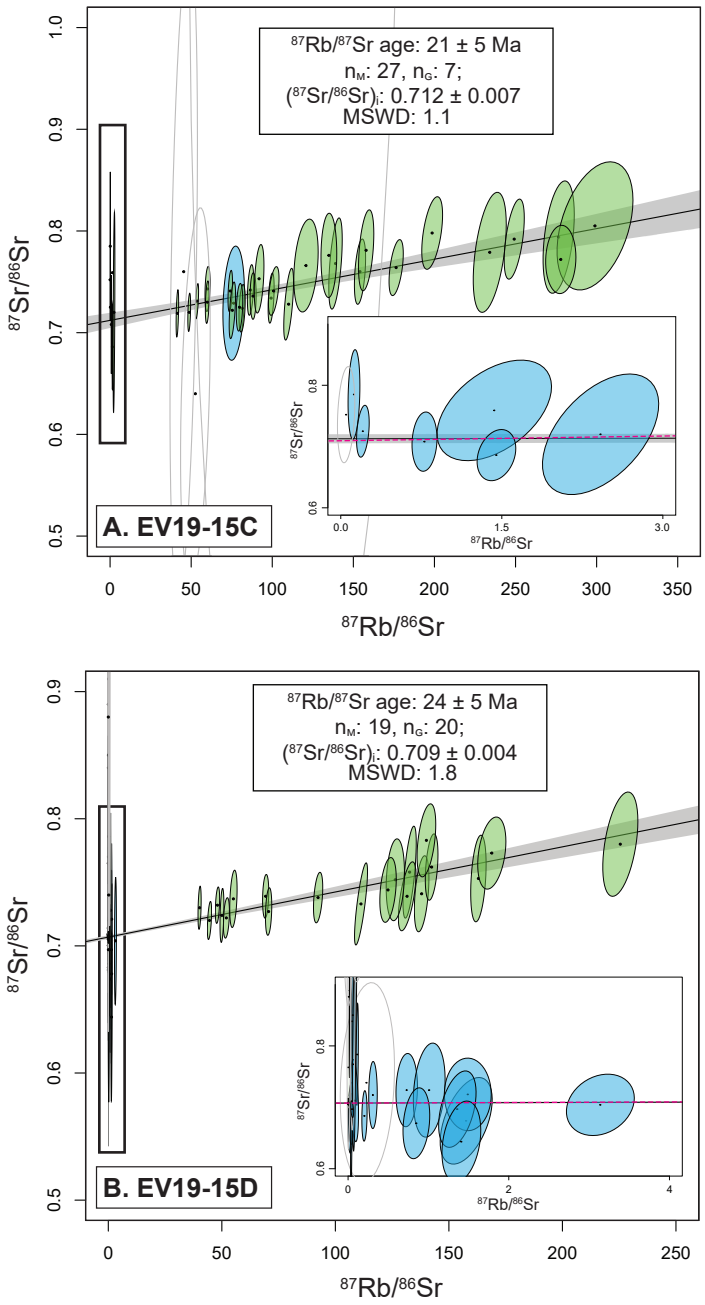

Figure 4.7. Isochron diagrams for in-situ $^{87}Rb/^{87}Sr$ analyses of glaucophane (blue ellipses) and phengite (green ellipses) hosted in the Mt. Ochi veins for (A) EV19-15C and (B) EV19-15D. Inset plot shows details of the glaucophane analyses, which cluster near the $^{87}Sr/^{86}Sr$ (low-Rb) axis. Magenta dashed line corresponds to an isochron calculated using only phengite data, showing minimal deviation from the complete two-mineral isochron. Ellipses are 2σ.

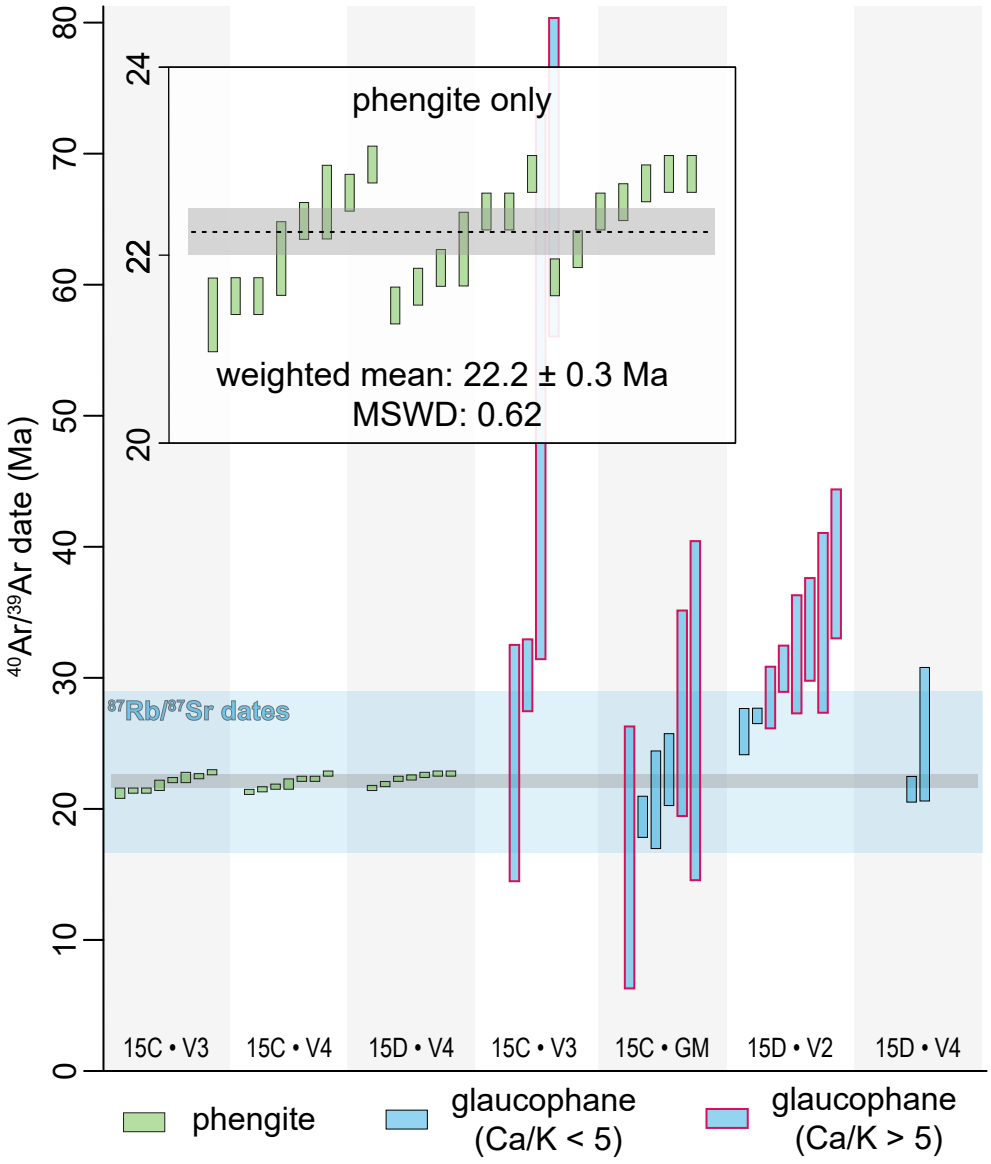

Figure 4.8. Summary of new multiple, single-grain total fusion $^{40}Ar/^{39}Ar$ data for phengite (green bars) and glaucophane (blue bars) from different vein sets and the groundmass (GM) of the Mt. Ochi veins. Black line and grey error bar indicate the weighted mean age calculated using the phengite data (see text for discussion). Range of calculated $^{87}Rb/^{87}Sr$ isochron dates is indicated by the blue field. Errors are 1σ.

produced high analytical uncertainties for most total fusion dates. Grains deemed to return acceptable or only moderately disturbed analytical results provide $^{40}Ar/^{39}Ar$ dates between 18 and 39 Ma, which together provide a weighted mean age of 26 ± 3 Ma (MSWD: 14). These grains commonly exhibit Ca/K <5, which coupled with mineral chemical data (**Figure 4.6**) indicate minimal contribution from sodic-calcic rims to the analyses. A single step-heating experiment on V_4 glaucophane yielded a disturbed saddle-shaped spectrum with apparent age steps between *c.* 25 Ma and 0 Ma and an integrated age of 15.2 ± 1 Ma (**Figure S4.3b; Table S4.3**). Due to these analytical challenges, we emphasize the phengite data as the most reliable measure of the $^{40}Ar/^{39}Ar$ systematics in the veins.

4.9. Stable isotopes

In order to determine the temperature of vein formation, we conducted ^{18}O isotopic analyses of vein-hosted white mica and quartz. Quartz from V_1, V_3, and V_4 veins yielded $\delta^{18}O$ values of 14.9‰, 18.5‰, and 15.9‰, respectively, whereas phengite from the same veins yielded $\delta^{18}O$ of 10.7‰, 11.9‰, and 11.5‰. Quartz-phengite pairs provided $\Delta^{18}O$ values of 4.2‰, 6.6‰, and 4.4‰. Calculations using the quartz-phengite isotope fractionation calibration of Zheng (1993) indicate equilibration temperatures of 334°C for V_1 veins, 172°C for V_3 veins, and 315°C for V_4 veins, with 2σ errors of ± 40°C (**Table 4.2**).

4.10. Discussion

Data outlined in the preceding sections attest to broad similarities among the mineralogical, geochronological, and (micro-)structural features of the Mt. Ochi veins, independent of their apparent relative ages. The contrasting fracture orientations nevertheless require that different vein

Table 4.2. Summary of oxygen isotope data from the Mt. Ochi veins.

Sample	Quartz (‰)[a]	2σ	Phengite (‰)[a]	2σ	Δqz-phg (‰)[a]	$T_{qz\text{-}phg}$ (°C)[b]	±	Fluid (‰)[c]
V_1	14.9	0.4	10.7	0.4	4.2	335	40	10.3
V_3	18.5	0.4	11.9	0.4	6.6	172	40	5
V_4	15.9	0.4	11.5	0.4	4.4	315	40	9.6

[a]Values reported relative to Vienna Standard Mean Ocean Water (VSMOW)

[b]Calculations performed using the quartz-phengite calibration of Zheng (1993)

[c]Calculations performed using the quartz-water calibration of Matsuhisa et al. (1979)

generations formed under an apparently transient local stress field. Consequently, whereas we did not observe mutually cross-cutting relationships among the Mt. Ochi vein sets, we assume that each vein set formed over a single interval of cyclic crack-sealing, prior to the development of any successive fracture set(s). This suggests that repeated crack-sealing crossed a critical volume threshold upon which brittle failure exploiting the pre-existing fracture planes became unfavorable. Our second assumption is that sealing in all fractures was facilitated by an aqueous fluid whose composition and PT conditions favored the precipitation of a consistent mineral assemblage, albeit with variable modal proportions. This indicates that veins formed over a restricted interval during which a fluid exhibiting relatively invariant chemistry readily infiltrated newly-formed fractures at reasonably constant PT conditions, a proposal underscored further by our geochronologic data. In the following discussion, we regard the Mt. Ochi veins as essentially monogenetic features and explore the implications of this hypothesis for their paragenesis.

4.10.1. Fracturing and sealing mechanisms

Structural evidence from a range of scales supports the Mt. Ochi veins as having formed as opening-mode fractures. Most vein sets exhibit parallel planar walls with lenticular cross-sections and correlative features indicating opening by lateral translation of the vein walls (**Figure 4.2a-b**, **Figure 4.5f**). Inclusion trails within the veins (**Figure 4.5d**) track at least part of the opening history as having proceeded at a high angle to the vein walls (Bons et al. 2012). An exception may be highlighted for V_3 veins, which display lenticular morphologies and excessively high aperture ratios (Vermilye and Scholz 1995), but whose wall geometries nevertheless favor a tensile opening mechanism.

The systematic orientation of elongate vein-hosted minerals at high angles to the vein walls indicates a syntaxial sealing mechanism, with crystal growth proceeding inward from the wall rock (Bons et al. 2012). Glaucophane and phengite exhibit well-developed crystal facets and euhdral morphologies, with phengite occasionally growing radially from the host rock, features consistent with crystallization into an open fracture (**Figure 4.3f**). In wider veins, wall-parallel host rock inclusion trails and discontinuous mineral inclusion bands have been identified (**Figure 4.5d**), microstructures that are commonly associated with crack-seal veins (Ramsay et al. 1980; Uysal et al. 2011; Bons et al. 2012). However, the Mt. Ochi veins show no direct microstructural evidence for incremental brittle failure and sealing. On the contrary, solid inclusion trails are generally isolated occurrences, and moreover the concentric zonation of glaucophane implies an uninterrupted interval of growth. Wall-parallel fluid inclusion trails are likewise systematically absent from the Mt. Ochi veins, having perhaps been obscured during partial recrystallization of the vein quartz.

Natural fractures exhibit a power-law size distribution, whose apertures increase with their length (Vermilye and Scholz 1995; Olson 2003; Alzayer et al. 2015). Whereas narrow veins (<2 mm) are represented among the Mt. Ochi veins, the highly regular spacing of V_4 veins of similar widths seemingly violates common fracture size distributions. Veins of this width are also frequently assumed to develop from an amalgamation of crack-seal cycles, a conclusion that is elsewhere supported by vein microstructure (Alzayer et al. 2015). As summarized above, several lines of evidence favor a single-seal origin for the Mt. Ochi veins, despite clear support for an initial tensile failure event (i.e., uniform growth of glaucophane along vein walls). The considerable widths of the veins (up to 30 mm) are thus somewhat problematic, particularly given our data which suggest a paragenesis in the middle or lower crust (see below), where elevated

confining pressures should limit wall-normal displacement. The extremely high aperture ratios of V_3 veins further complicate matters, with aperture ratios in some veins approaching 1.

The Mt. Ochi veins do, however, exhibit some properties consistent with mechanisms for single-stage vein sealing. 'Contact growth' sealing of Wilson (1994) describes dynamic recrystallization of vein fill due to stresses imposed by mutual impingement of precipitating crystals during sealing. This may explain, with some limitations, the appearance of strain partitioned entirely into quartz within the veins (see below). Nearby on southern Evia, Nüchter and Stöckhert (2007) interpreted high aperture ratio quartz veins as recording prolonged opening via ductile creep following brittle fracturing linked to seismicity along a structurally higher extensional fault. The veins display evidence for syntaxial sealing, with finer, dynamically recrystallized quartz along vein margins surrounding a progressively coarsening central vein fill. Subsequent numerical modelling of the same veins indicates that the post-seismic widening was accommodated by buckling of the vein walls, with more pronounced widening predicted for vein fill that is more viscous than the surrounding host rock (Nüchter 2017).

Wider Mt. Ochi veins similarly show an increase in grain size from margins to cores; however, the contrast is neither as pronounced nor as consistently developed as the examples described by Nüchter and Stöckhert (2007). Although entire veins appear minimally deformed, quartz in the Mt. Ochi veins exhibits evidence for incipient dynamic recrystallization, in contrast to the undeformed glaucophane and phengite (**Figure S4.1**). Quartz grain boundaries are commonly serrated and interlobate, with low-amplitude bulging and some small new grains formed along grain boundaries (**Figure S4.2**). There is an apparent decrease in recrystallized volume fraction from earliest (V_1) to latest (V_4) veins, although recrystallized volume fraction is known to be sensitive to parameters of probable relevance to the Mt. Ochi veins, including water

content and co-active dissolution-precipitation creep (Stipp and Kunze 2008). The textures described are largely consistent with low-temperature grain boundary migration (i.e., bulging of Stipp et al. 2002), with or without minor subgrain rotation, likely at temperatures below ~400°C. Interpreting the unusual single-increment sealing widths and high apertures via sequential brittle fracture and ductile creep may explain, in part, the recrystallized quartz textures. However, widening of many parallel veins by ductile mechanisms implies complementary strain should be found in the host rock, for which we observe no evidence. Furthermore, the quartz-dominated veins are predicted to be less viscous relative to the pyroxene-albite host rock, which should be unfavorable to creep-mediated widening according to the models of Nüchter (2017). We accordingly hesitate to comprehensively interpret the opening and sealing mechanisms of the Mt. Ochi veins, but find sufficient microstructural evidence supporting inward-directed crystal growth indicative of a syntaxial sealing mechanism.

The broader structural context of the Mt. Ochi veins alludes to a major rheological control on fracturing. Moreover, the coexistence of mineralogically identical vein sets in several contrasting orientations implies short-term variability of the local stress field. Cyclic redistribution of crustal fluids along pathways created by viscously deforming rock and consequent local pore fluid pressure (P_f) variability commonly governs localization of brittle strain at or below the brittle-ductile transition (e.g., Sibson 1994, 2000; Hayman and Lavier 2014; Behr and Bürgmann 2021; Menegon and Fagereng 2021). As P_f approaches lithostatic conditions, transient changes in the local stress field are also more likely to occur (Faulkner et al. 2006; Ujiie et al. 2018). These stress changes may manifest either as a rotation of the principal stress orientations, or a modified stress ellipsoid (e.g., Scott 1996; Healy 2009).

The Mt. Ochi vein sets define an orthorhombic symmetry (**Figure 4.1b**). The first veins to open, V_1 and V_2, and some V_3 veins, define conjugate sets bisected by the orientations of the more abundant, NNW-SSE striking V_3 veins (**Figure 4.2a, d**). This distribution of vein orientations, seemingly forming relatively quickly, implies instantaneous shortening along the vertical axis with $\sigma_2 \approx \sigma_3$, allowing for instantaneous stretching in a range of directions within the horizontal plane, consistent with an overall oblate stress regime where $\sigma_v = \sigma_1$ (compressive stresses are negative). The latest vein set, V_4, occurs in a comparatively restricted ENE-WSW orientation and cross-cuts all previously formed veins, indicative of a transition to a more prolate stress field. Without a substantial contribution from P_f, this arrangement would require unrealistic tectonic stresses with tensional σ_3 and σ_2. These successive stress states can be attained, however, if P_f varied during vein formation (e.g., Sharma et al. 2023). The earlier vein sets (V_1-V_3) likely formed under a stress regime characterized by $\sigma_1 > P_f >> \sigma_2$, creating an oblate effective stress field. Later, V_4 veins opened and sealed following a reduction of P_f such that $\sigma_2 > P_f > \sigma_3$, with V_4 veins consequently opening exclusively perpendicular to σ_3. Since the implied local σ_3 is oriented perpendicular to the ENE-WSW trending mineral lineation (and associated regional stretching lineation; Xypolias et al. 2012), it appears likely that the stress field that produced the Mt. Ochi veins was restricted to the local scale and controlled mainly by P_f fluctuations. High vein concentrations (**Figure 4.2**) may imply that fracture saturation was achieved, perhaps due to enhanced fracture density induced by the rheological relationship of the viscous quartzitic matrix enveloping tabular metabasalt bodies (e.g., Reches 1998). Local saturation of V_3 veins – which are appropriately oriented perpendicular to the regional stretching lineation – may have caused any subsequent fractures to open orthogonal to V_3, matching the observed relationship with V_4 veins (Zulauf et al. 2014).

The quartzites, when ductile, likely acted as fluid conduits, with episodic fracturing in the metabasalt coinciding with fluid redistribution and corresponding P_f changes in the surrounding quartzites. An extensional setting, as implied by the hypothesized stress field described here, is also consistent with our new geochronology (see below). Whereas fluid-mediated hydrofracturing during ductile deformation is most often invoked for veins formed in subduction zones (Hayman and Lavier 2014; Behr and Bürgmann 2021; Menegon and Fagereng 2021), it has also been described from extensional regimes (Nüchter and Ellis 2011; Kassaras et al. 2022). Veins elsewhere on southern Evia have been interpreted as the products of distributed brittle-ductile strain beneath a major detachment fault (Nüchter and Stöckhert 2007), presumably the post-orogenic NCDS. Applying the latter correlation to the Mt. Ochi veins is sensible, given the broad structural similarities between the veins and apparent temporal coincidence with the NCDS (Jolivet et al. 2010). A crucial difference between the Mt. Ochi veins and the apparently coeval veins of Nüchter and Stöckhert (2007) are the absence of glaucophane and high-Si phengite from the latter. Such strikingly contrasting parageneses, despite effectively forming simultaneously, merit additional scrutiny.

4.10.2. Temperatures of crystallization

Quartz and phengite from the Mt. Ochi veins yield consistently positive $\delta^{18}O$ values relative to VSMOW. Phengite data occupy a narrow range between 10.7-11.9‰, whereas quartz spans a comparatively wider range between 14.9-18.5‰ (**Table 4.2**). Quartz-phengite pairs from V_1 and V_4 yield similar *T* estimates of 335 ± 40°C and 315 ± 40°C, respectively, whereas the V_3 quartz-phengite pair returns a significantly lower temperature of 172 ± 40°C (Zheng, 1993). We attribute this discrepancy mainly to the V_3 quartz, as $\delta^{18}O$ of V_3 phengite is within error of that of

V_4 phengite. The elevated $\delta^{18}O$ value obtained for the V_3 quartz aliquot may be due to contamination by quartz that was not in equilibrium with the broader vein system, that is, quartz material inadvertently sampled from the groundmass or from late increments of vein fill. Notably, V_3 exhibits the greatest density of fluid inclusions among the vein generations; however, quartz preferentially incorporates heavy oxygen isotopes relative to aqueous fluids, and contamination by the primary fluid $\delta^{18}O$ is unlikely to produce anomalously high values (**Table 4.2**). Thus, solid phase contamination appears to be the more likely explanation. Due to a lack of petrographic evidence to support later incursion of fluids and associated mineral growth in V_3 veins, we consider it more likely that these high values represent those of the host rocks, which have previously yielded comparably high $\delta^{18}O$ values for quartz (16.6‰; Katzir et al. 2000).

We consider the underlying assumption of isotopic equilibrium between vein-hosted quartz and phengite to be reasonable given the common presence of quartz as inclusions in early marginal glaucophane coexisting with phengite and its presence in the interstices between phengite crystals (**Figure 4.3d, f, 4.5a-c**). The validity of this assumption is further supported by the consistency between two of the calculated temperatures and those temperatures inferred to have accompanied nascent recrystallization of the vein quartz (<400°C) based on microstructures. Quartz-water fractionation calculations after Matsuhisa et al. (1979), using the *T* determined by quartz-phengite thermometry, indicate the parental fluid had a moderate positive $\delta^{18}O$ signature typical of igneous or metamorphic fluids. Although partial incorporation of a meteoric water signature cannot be discounted outright, any such contribution was likely relatively small and would not have significantly altered fluid chemistry or *T*. Since magmatism in the Cyclades is broadly late Miocene in age, and thus younger than the veins (see below), we consider the parental fluid to the Mt. Ochi veins to have most likely been of metamorphic origin.

4.10.3. Timing of vein formation

Mt. Ochi vein-hosted phengite and glaucophane yield $^{87}Rb/^{87}Sr$ and $^{40}Ar/^{39}Ar$ dates within error of one another (**Figure 4.7, 4.8**). *In-situ* $^{87}Rb/^{87}Sr$ data, pooled from all vein sets within each sample (**Table 4.1**), define single isochrons providing late Oligocene to earliest Miocene dates. Whereas glaucophanes are overwhelmingly Rb-poor and cluster near the $^{87}Sr/^{86}Sr$ axis, they nevertheless fall along isochrons defined by the phengite data alone (**Figure 4.7 inset**). This implies that – at minimum with respect to $^{87}Rb/^{87}Sr$ systematics – phengite and glaucophane across all vein sets effectively crystallized coevally, and given their apparent textural equilibrium and co-orientation are likely in isotopic equilibrium, as well. Whether or not the geochronology captures the timing of this crystallization requires assessment of whether (1) the geochronometers have sustained strain or fluid interaction resulting in recrystallization, and (2) the system experienced *T* in excess of the nominal closure temperature of either isotope system following vein sealing.

Both the $^{40}Ar/^{39}Ar$ and $^{87}Rb/^{87}Sr$ systems can exhibit strain sensitive resetting that has been extensively documented, particularly for white mica (e.g., Dunlap et al., 1991; Freeman et al., 1997; Kellett et al., 2016; Barnes et al., 2023; Larson et al., 2023; Ribeiro et al., 2023). In the Cyclades, this often accounts for the young exhumation-related ages recorded by ostensibly HP phengite (e.g., Wijbrans et al., 1990; Bröcker et al., 2004). However, we discount this interpretation for the Mt. Ochi veins for two reasons. The first is that, due to the orthorhombic symmetry of the vein sets, a stress field of any orientation would impose a resolved shear stress on at least one of the vein orientations. Consequently, if the Mt. Ochi veins recorded any significant strain following sealing, at least one vein set should exhibit evidence of non-coaxial strain such as vein rotation, development of flanking structures, or development of an internal foliation due to

transposition of the elongate vein minerals in response to shearing. Only endmember coaxial deformation would not produce such structures, and structures observed in the area show mainly monoclinic symmetries, with strain analysis yielding nonzero W_k, as expected of a strain regime influenced by major regional detachments (Jolivet et al. 2004; Ring et al. 2007b; Xypolias et al. 2010, 2012). Second, the $^{87}Rb/^{87}Sr$ system in phengite has shown greater retentivity, even in strained crystals, compared with corresponding $^{40}Ar/^{39}Ar$ dates (Larson et al. 2023; Ribeiro et al. 2023). Thus, the fact that both geochronometers record the same dates and exhibit no obvious microstructural evidence of recrystallization or significant post-crystallization dissolution-reprecipitation (**Figure 4.5a-c; Figure S4.1**) strongly disfavors strain-induced resetting.

Single-grain total fusion $^{40}Ar/^{39}Ar$ dating of vein-hosted phengite provided minimally scattered early Miocene $^{40}Ar/^{39}Ar$ dates that offer the most precise and internally consistent geochronologic constraints (**Figure 4.8 inset**). Glaucophane total fusion data are comparatively scattered and exhibit poor $^{40}Ar/^{39}Ar$ systematics (low $^{40}Ar^*$ yields), although many dates are within error of the phengite data, and any interpretation using these dates is equivocal. As previously mentioned, high Ca/K ratios obtained from glaucophane may reflect analysis of an outsized proportion of sodic-calcic rim material, or may signal the presence of fluid or solid inclusions (e.g., epidote, titanite). Inclusions commonly act as sinks for Ar, and their presence during analysis results in spurious 'old' apparent ages (Kelley 2002), which likely explains the dispersion in the glaucophane $^{40}Ar/^{39}Ar$ data. Excellent agreement between the phengite $^{40}Ar/^{39}Ar$ data and the $^{87}Rb/^{87}Sr$ isochron dates suggest that these provide a reasonable minimum age for the veins. Textural criteria within the veins combined with quartz-phengite oxygen isotope thermometry support crystallization temperatures of ~315-335°C, below even the minimum closure temperature estimates for either isotope system in phengite (e.g., Bosse et al. 2005; Warren et al. 2012; Laurent

et al. 2017). Moreover, peak *T* estimates for the Ochi Unit (≤460°C; Katzir et al. 2000; Ducharme et al. 2022) likewise approximate or fall below realistic estimates for these closure temperature values. We therefore consider it unlikely that the geochronology reflects cooling, and thus conclude that the dates capture the timing of primary crystallization during vein sealing. The phengite $^{40}Ar/^{39}Ar$ data provide the most robust estimates of this timing at *c.* 22-23 Ma. As previously noted, this timing coincides with similar dates throughout the Cyclades that are interpreted to record localized ductile strain below the major detachment systems, and imply a genetic relationship between the veins and the NCDS structurally above.

4.10.4. P-T-X controls on vein paragenesis

Our structural data and geochronology imply that glaucophane and high-Si phengite in the Mt. Ochi veins crystallized in the early Miocene, likely as the rock package was transiting the brittle-ductile transition. Prevailing models for the geodynamic evolution of the eastern Mediterranean suggest that by the early Miocene, the effects of slab rollback had begun influencing the upper crust, creating an incipient back-arc environment and signalling the transition toward the modern, fully extensional tectonic regime (Jolivet and Brun 2010; Ring et al. 2010; van Hinsbergen and Schmid 2012; Jolivet et al. 2013). In the Cyclades, this transition produced deformation below major detachments associated with greenschist to amphibolite facies retrogression of peak HP-LT assemblages, alongside coeval supradetachment basin fill sequences and decompression melting in the central Cyclades (Sanchez-Gomez et al. 2002; Vanderhaeghe et al. 2004; Jolivet et al. 2010; Ring et al. 2010; Grasemann et al. 2012). Accordingly, our data present compelling evidence that glaucophane and phengite in the Mt. Ochi veins crystallized under

tectonometamorphic conditions at odds with the HP-LT parageneses conventionally assigned to those minerals.

Although it is tempting to interpret the disparity between expected and apparent metamorphic conditions as reflecting local excursions in *P* or *T*, both are precluded by our new data. Positive pressure anomalies induced by, for example, non-hydrostatic stress states yield equilibrium shifts too modest to account for the assemblages present in the Mt. Ochi veins (e.g., Wheeler 2014; Hess et al. 2022). Competent materials undergoing strain within a rheologically heterogeneous package are moreover expected to behave as compartments of *low* relative pressure (Mancktelow 2008), as are the tensile fractures which here host the HP minerals. Meanwhile, locally cooler *T* may be achieved within a fracture if a cool (i.e., presumably meteoric) throughgoing fluid achieves saturation before thermally equilibrating with its surroundings, but our oxygen isotope data indicate fluid $\delta^{18}O$ signatures more aligned with a metamorphic or magmatic fluid (**Table 4.2**). Whereas some influence from small departures in *P* and *T* cannot be precluded, this was likely limited to a complementary role.

Conversely, abundant data have demonstrated that bulk system composition is a critical determinant of whether a blueschist or greenschist facies assemblage develops at particular PT conditions (Guiraud 1982; Maruyama et al. 1986; Massonne and Willmer 2008; Ukar and Cloos 2014; Manzotti et al. 2020; Muñoz-Montecinos et al. 2020). The stability of Na-amphibole and Na-clinopyroxene extends to considerably lower *P* if these minerals incorporate sufficient proportions of the Fe^{3+}-rich endmembers (magnesio-)riebeckite and aegirine, respectively (Maruyama et al. 1986; Liu and Bohlen 1995). Amphibole cores and rims as well as clinopyroxene in the metabasaltic host at Mt. Ochi all incorporate >0.4 mole fraction of their respective ferric endmembers, as well as ferriwinchite in amphibole rims (**Figure 6c-e**). Tschermak substitution in

white mica is likewise sensitive to elevated fO_2, provided there is concomitant high α_{SiO2} (Wang et al. 2017), a condition that was undoubtedly satisfied given the large volumes of quartz precipitated alongside the mica. Hematite is abundant in the host lithologies as the sole oxide phase, further attesting to elevated systemic fO_2 above the hematite-magnetite buffer.

The validity of this assumption may be tested using certain compositional geobarometers. Sections of the basaltic host rock which exhibit minimal veining and lack glaucophane comprise predominantly fuzzy clinopyroxene occluded by fine grained quartz inclusions (**Figure 4.4**). These textures may preserve the earlier prograde conversion of albite to jadeite, for example, in an oceanic plagiogranite protolith (e.g., Miyazaki et al. 1998; Tsujimori and Harlow 2012). Alternately, the inclusions may represent incongruent dissolution of jadeite within an already Si-saturated fluid (e.g., Wohlers et al. 2011). Nevertheless, textural evidence from visibly altered parts of the rock indicates that host rock-fluid interactions locally drove the retrograde conversion of clinopyroxene to albite via the reaction jadeite + quartz → albite (**Figure 4.3a-b, f**), producing also residual hematite from the aegirine component (**Figure 4.4c**). Liu and Bohlen (1995) demonstrated the pressure-dependence of the jadeite + quartz → albite equilibrium on the Fe^{3+} content of clinopyroxene. They calculated, to a lower bound of 10 kbar and 400°C, the stability of clinopyroxene with $X_{jd} = 0.5$. Assuming continuous linear behaviour at still lower T and X_{jd}, the equilibrium extrapolates to ~8 kbar at 300°C and perhaps lower still for X_{jd} of 0.4 as encountered in the Mt. Ochi metabasalts. Maruyama et al. (1986) described an alternative geobarometer using Al_2O_3 contents of Na-amphibole for systems with coexisting chlorite having X_{Fe} of 0.4-0.5, similar to the chlorite described here. A graphical estimate of core, mantle, and rim P estimates for the vein-hosted glaucophane vary from ~5.5-6 kbar (6-8 wt.% Al_2O_3), ~6-7 kbar (7-9 wt.% Al_2O_3), and ~4 kbar (2-3 wt.% Al_2O_3), respectively. The relatively low pressures indicated by these

estimates are supported by high X_{Ps} epidote compositions (with $Fe^{3+}/(Fe^{3+}+Al)$ corresponding to X_{Ps} of 0.28-0.32; Maruyama et al. 1986), which are in textural equilibrium with the glaucophane, phengite, and albite.

Notably, even the Na-amphibole species closest to endmember glaucophane in the Mt. Ochi veins is predicted to be stable at conditions generally associated with greenschist facies assemblages in the Cyclades. Such high-P greenschist facies parageneses are widely documented along retrograde segments of the clockwise PT paths in the region (e.g., Parra et al. 2002; Huet et al. 2015; Scheffer et al. 2016; Ducharme et al. 2022). Aggregation of petrogenetic modelling data has led to a proposal that the CBU had a protracted residence near the blueschist-greenschist facies transition resulting in isobaric heating during a pause in its unroofing history (Parra et al. 2002; Huet et al. 2015; Laurent et al. 2018; Peillod et al. 2021). This cessation occurred at greater apparent depths toward the central Cyclades, commensurate with the deeper structural levels exhumed there. Evia is proximal to Andros, which Huet et al. (2015) suggested experienced this arrest at 7 ± 1 kbar, in agreement with the P estimates calculated above. Our estimates of PT conditions during vein formation are effectively identical to those previously determined for retrograde assemblages in the CBU and structurally lower units on southern Evia (Katzir et al. 2000; Ducharme et al. 2022; **Figure 4.9, Table 4.3**), and to those interpreted to record the end of syn-orogenic exhumation on Andros (Huet et al., 2015). The new data imply a crustal geothermal gradient between 11 and 17°C/km at *c.* 22-23 Ma, comparable to the 16-17°C/km gradient inferred from the essentially synchronous (*c.* 21 Ma) onset of post-orogenic extension on Tinos (Parra et al. 2002; Tirel et al. 2009). Therefore, although the empirical geobarometers applied above yield some apparent inconsistency with the assumption of a single increment of vein sealing, the consistency with existing regional data strongly suggests the *P* and *T* estimates are reasonable. The

Table 4.3. Summary of existing pressure-temperature data from the vicinity of southern Evia

Locality	Unit	Lithology	Method	Temperature	Pressure	Interpretation	Age	Reference
Southern Evia	Tsakei and Ochi Units (CBU)	metabasite	Thermocalc v2.5, oxygen isotope thermometry	425 ± 25°C	>11 kbar	M1 (peak, HP)	Eocene	Katzir et al. (2000)
				<350°C	<8 kbar	M2 (retrograde)	early Miocene	
	Styra and Ochi Units (CBU)	not specified	Thermocalc v2.3, Si-in-phengite, empirical calculations	400 ± 50°C	11 ± 1 kbar	M1 (peak, HP)	post-middle Eocene	Shaked et al. (2000)
				380 ± 50°C	6 ± 1 kbar	M2 (retrograde)	not reported	
	Ochi Unit (CBU)	glaucophane schist	PERPLE_X	460 ± 20°C	12 ± 1 kbar	peak, HP	~50 Ma (peak), 30 ± 2 Ma (sample)	Ducharme et al. (2022)
	Basal Unit	pumpellyite-albite schist		310 ± 15 °C	7 ± 1 kbar	retrograde	26 ± 1 Ma	
Lavrion (SE Attica)	Lavrion schists (CBU)	mica schist	white mica-chlorite thermobarometry	311 ± 34°C	11 ± 2 kbar	M1 (peak, HP)	32-23 Ma	Scheffer et al. (2016); geochronology from Coleman et al. (2019)
				311 ± 34°C	7.5 ± 1.5 kbar	M3 (retrograde)		
	Kamariza schists (CBU)			298 ± 38°C	9.5 ± 1.5 kbar	M1 (peak, HP)	22-8 Ma	
				345 ± 40°C	6.75 ± 1.75 kbar	M3 (retrograde)		
Andros	Cycladic Blueschist Unit	mica schist	white mica-chlorite thermobarometry	260-400°C	8-14 kbar	syn-orogenic exhumation	pre-37 Ma	Huet et al. (2015)
				260-460°C	7 ± 1 kbar	isobaric heating	pre-30 Ma	
				410 ± 20°C	4-8 kbar	post-orogenic exhumation	pre-21 Ma	
	Makrotantalon Unit	garnet-glaucophane schist	Theriak-Domino	550°C	18.5 kbar	peak, HP	50-40 Ma	

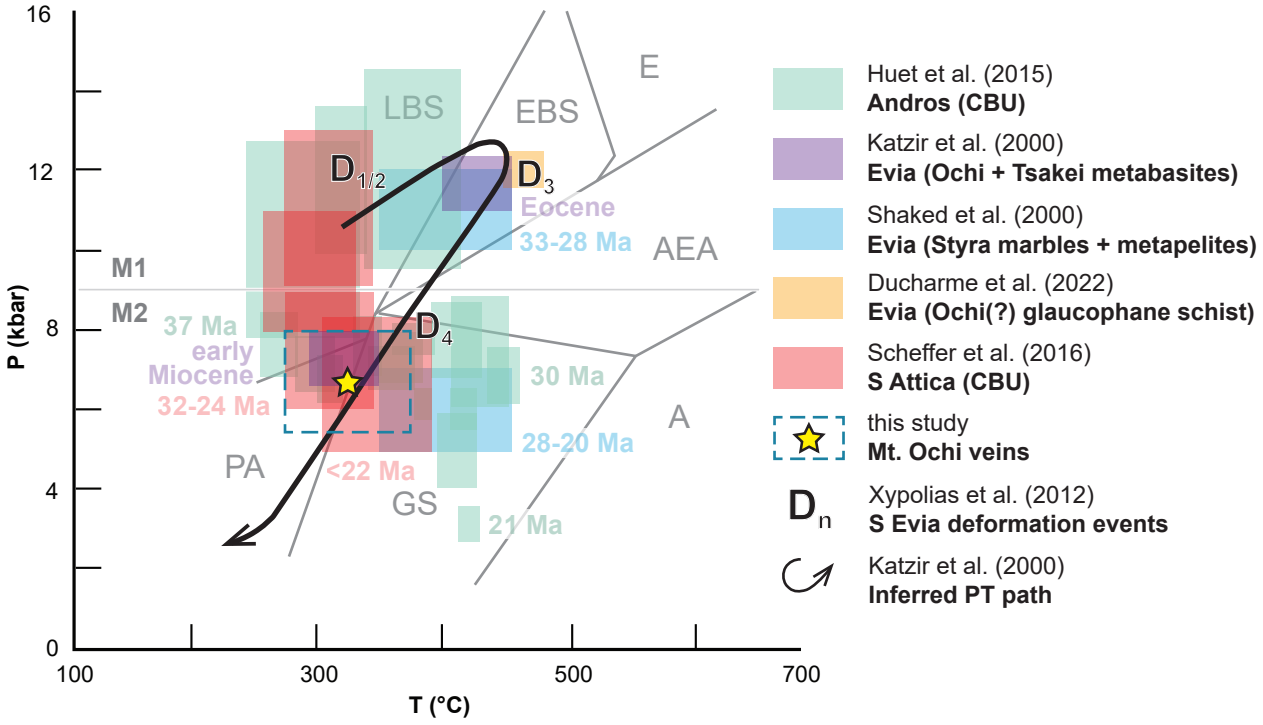

Figure 4.9. Pressure–temperature (PT) diagram summarizing previous estimates for metamorphic conditions and their approximate timing from the vicinity of southern Evia. Metamorphism recorded by the Cycladic Blueschist Unit (CBU) can be broadly subdivided into M1 (high pressure-low temperature) and M2 (retrograde greenschist facies), which fall approximately to either side of ~ 9 kbar. Further details for each PT estimate are provided in Table 3. Facies boundaries after Evans (1990).

apparent and abrupt shifts in *P* implied by Al_2O_3 contents may allude to rapid fluctuations in bulk composition during vein sealing, perhaps by consequence of sluggish kinetics of jadeite-fluid reactions at these relatively low temperatures, or due to fractionation of a stagnant fluid (e.g., Oliver and Bons 2001; Schott et al. 2009).

In summary, the Mt. Ochi veins likely developed at PT conditions more commonly associated with greenschist facies, rather than blueschist facies, assemblages throughout the CBU. Bulk composition of the system was likely primarily responsible for the favored crystallization of nominally 'blueschist facies' minerals. A direct control on the mineral assemblage was exerted by high Na contents (mediated by host rock clinopyroxene) and fO_2 (mediated by the throughgoing fluid) and the resultant predominance of ferric iron within the system, as demonstrated for rock subducted only to near the greenschist-blueschist facies boundary (Manzotti et al. 2020; Muñoz-Montecinos et al. 2020). Contrasting with those previous examples, the Mt. Ochi veins apparently developed some ~20-30 Myr following peak HP metamorphism, after substantial unroofing of the Ochi Unit had already occurred. This conclusion implies that certain mineral assemblages routinely used to empirically validate data as relating to subduction zone geodynamics may conversely capture conditions coinciding with exhumation. Additional caution should be exerted when designing projects to study subduction-related tectonic processes, particularly heeding the Fe^{3+} content of HP clinopyroxene and amphibole species in rocks selected for these purposes.

4.10.5. Fluid source and modes of solute transport

Models for atypical silicate veins commonly invoke either local diffusive mass transfer from adjacent host rock or advection from an external source (e.g., Kerrich 1990; Beitter 2008). Local diffusion is often favored due to physical limitations on establishing hydrothermal

circulation at a regional scale. Metamorphic vein minerals typically co-occur as host rock porphyroblasts in these systems, offering petrological evidence supporting the same conclusion (Kerrich 1990). Advective transport implies significant fluid volumes exploiting an extensive permeability network, affording a short interval over which a fluid may deposit its solutes. The local volumetric density and limited extent of the Mt. Ochi veins, as well as the occurrence of chemically indistinguishable phengite and amphibole in the host rock, favor a proximal source.

Glaucophane and phengite in the veins, however, exhibit essentially proportional Fe and Mg (X_{Mg}: 0.50-0.74 and 0.45-0.61, respectively), whereas clinopyroxene in the host rock contains little or no Mg (<5 wt.%; mean: 1.8 wt.%). Similarly, no primary sources of Ca or K were identified in either host lithotype. Compositional homogeneity of vein and host rock minerals suggests a shared genesis related to the vein-forming fluid. Other phases in textural equilibrium with glaucophane and phengite, including chlorite and epidote, likewise incorporated these components and are likely, therefore, hydrothermal. Thus, the only hydrous minerals observed in either host lithotype are apparently part of a metasomatic assemblage that includes glaucophane + phengite + epidote + chlorite + hematite + quartz. The fluid was accordingly either generated by primary hydrous minerals that are now entirely obscured, or else was externally derived. We consider the latter option more compelling, and accordingly conclude that the Mt. Ochi veins are most likely the products of coupled short-range diffusion and long-range advection.

Katzir et al. (2000) attributed geochemical features of the Ochi metabasalts and gabbros to seafloor alteration of primary alkalic petrogenetic features, including elevated Na, K, and Fe, depleted Ca, and the presence of aegirine-rich Na-clinopyroxene. These authors also invoked a nappe-scale hydrothermal system during peak HP metamorphism to account for enriched $\delta^{18}O$ signatures of the glaucophane in these rocks. The geochemical features proposed to be fingerprints

of a seafloor hydrothermal system bear a striking resemblance to the fluid components implicated here in producing the Mt. Ochi glaucophane-phengite veins. Vein-hosted quartz and phengite also exhibit elevated $\delta^{18}O$ signatures like those Katzir et al. (2000) associate with peak HP-LT conditions, which they concluded were derived from a fluid in equilibrium with Ochi Unit metasediments. Because our conclusions broadly align with those of Katzir et al. (2000), we propose that their inferred large-scale hydrothermal system was the same system responsible for the Mt. Ochi veins. Rather than operating at peak burial, however, these fluids produced far-reaching metasomatic alteration of the metabasites during syn-exhumation metamorphism near the blueschist-greenschist facies transition (**Figure 4.9**). Whereas Katzir et al. (2000) considered the aegirine-rich clinopyroxene to be a primary magmatic artifact, our documentation of increasing aegirine component toward clinopyroxene rims in the metasomatized host rock argues instead that initially jadeitic clinopyroxene was converted to more aegirine-rich compositions with greater degrees of fluid interaction.

The paragenesis of a single vein set can be summarized as follows. Initially small volumes of a Si-saturated, oxidized K- and Mg-bearing aqueous fluid infiltrate the metabasite, perhaps channelized by adjacent viscously deforming quartzite (**Figure 4.10a**). Vein minerals preferentially nucleate on, and crystallize inward from, the wall rock, while reactions between the Si-rich fluids and jadeite in the host rock may liberate additional components to drive crystallization of glaucophane and phengite. The positive ΔV of the jadeite + quartz $\rightarrow$ albite reaction, once proceeding in a sufficient volume of the rock, may promote further fracturing (**Figure 4.10b**). Later sealing increments of a given vein are dominated by quartz with comparatively sparse phengite and glaucophane (**Figure 4.10c**).

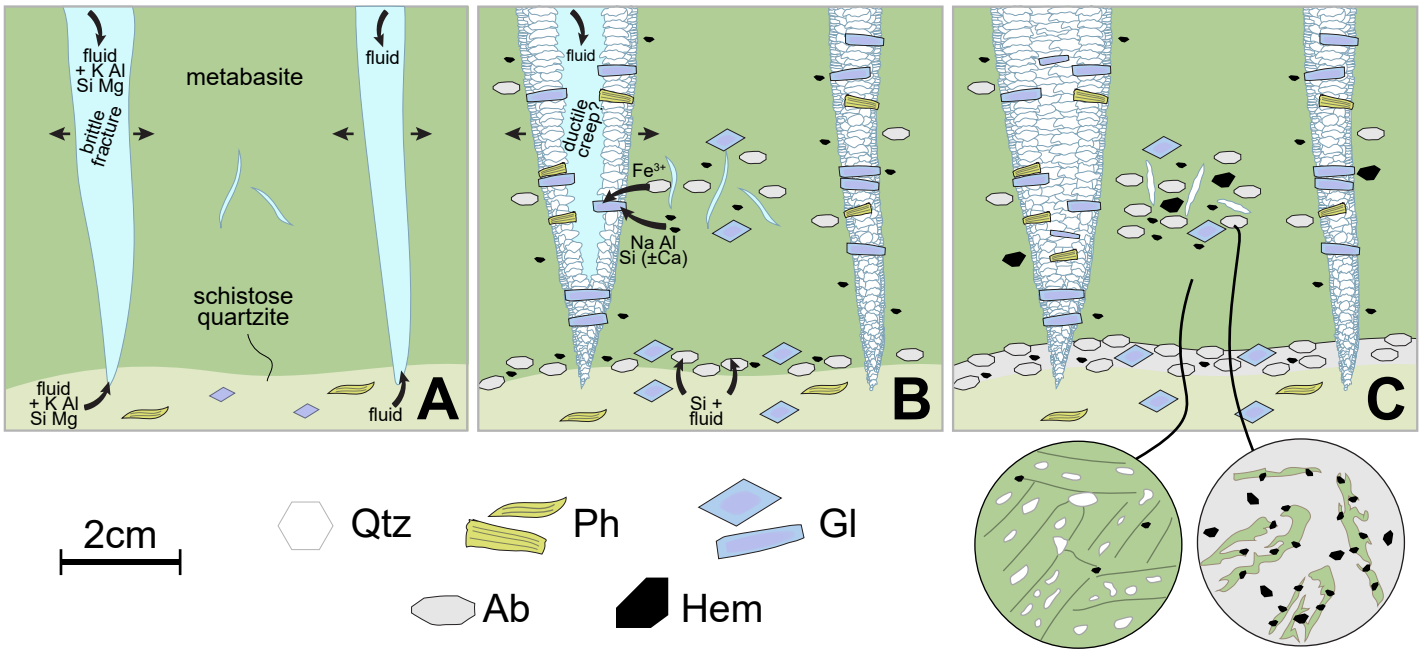

Figure 4.10. Schematic diagram depicting the development of a single Mt. Ochi vein set. (A) Initial fracture formation. Fluids infiltrate metabasaltic layers following channeling in ductily deforming schistose quartzite, infilling fractures and pre-existing pore space in the host rock. (B) The modified bulk composition introduced by the fluids promotes the growth of glaucophane, phengite, and hematite, as well as the conversion of jadeite to albite. A subset of the veins are selected to widen, possibly via ductile creep mechanisms. Later increments of sealing are comparatively dominated by quartz, with lower modal proportions of the ferromagnesian phases observed along the vein walls. (C) The second (or later) increment of vein fill, comprising comparatively quartz-rich, glaucophane- and phengite-poor precipitates, yields the final sealed state of the vein(s). Albite-rich layers form at interfaces between the metabasalt and schistose quartz, due to greater proximity of fluid, shorter diffusion length-scales for reaction with silica, or both. Callout bubbles in (C) show the detail of well-preserved clinopyroxene domains (poikiloblasts) compared with fluidized albite-bearing domains (skeletal with hematite overgrowths).

Limited available thermodynamic data for aqueous solubilities, speciation, and activities of silicate minerals as well as computational demands currently prohibit comprehensive modeling of the paragenesis of the Mt. Ochi veins (Tiraboshi et al. 2018; Macris et al. 2020; Menzel et al. 2020). Microstructures observed in jadeite, along with its high aqueous solubility among silicates (Azimov and Burin 2007), implicate dissolution and reactive conversion to albite as possible mechanisms for local contributions to vein mineral growth. Structurally and chemically simple minerals (e.g., Al_2SiO_5 polymorphs) predominate as vein fill in metamorphic veins (e.g., Kerrick 1990; Beitter et al. 2008; Bucholz and Ague 2010), suggesting that these are thermodynamically favored over comparatively complex minerals like glaucophane and phengite.

Whether the relevant control on the precipitation of these minerals in the Mt. Ochi veins has bearing on apparently disparate *P* recorded in zoned amphibole (**Figure 4.9**), which in a single-sealing model has grown continuously without variations in ambient metamorphic conditions, relies on more data than presently available for the governing thermodynamic mechanisms. The Mt. Ochi veins nonetheless provide an exceptional snapshot of reactive transport processes in operation and may serve as ideal natural analogues with which to test the conclusions of future theoretical and experimental predictions.

4.11. Conclusions

Glaucophane- and phengite-bearing quartz veins from Mt. Ochi on southernmost Evia island record (micro-)structural, geochronological, and stable isotope evidence that mutually support crystallization during vein sealing at lower pressures than typically predicted for nominally HP minerals. Fracturing styles and the consistent subvertical orientation of σ_1 indicate opening and single-increment sealing within an extensional stress field. Miocene $^{87}Rb/^{87}Sr$ and $^{40}Ar/^{39}Ar$ dates

corroborate the structural data, demonstrating that the nominally HP minerals crystallized at a time widely perceived to coincide with back-arc extension and greenschist facies retrograde metamorphism throughout the Aegean. Oxidizing fluids accomplished advective redistribution of material from relatively local sources, likely within the same structural unit, alongside diffusion from the host rock.

The structural alignment of HP minerals, like glaucophane, is widely used to assign an early, syn-convergence timing to associated structures and fabrics within the overall tectonometamorphic evolution of an orogen (e.g., Inger and Cliff 1994; Wintsch et al. 1999; Rosenbaum et al. 2002; Xypolias et al. 2012; Augier et al. 2015; Corti et al. 2017). These inferences are predicated on the paradigm that blueschist and eclogite facies assemblages survive only where the influence of post-peak, syn-exhumation strain and fluidization is minimal (e.g., Fitzherbert et al. 2005; Halama and Konrad-Schmolke 2015; Roche et al. 2016), or where fluid compositions favor their preservation (Kleine et al. 2014). Our data reinforce observations that natural mineral assemblages widely associated with HP-LT conditions may in fact have formed at relatively shallow depths (Manzotti et al. 2020; Muñoz-Montecinos et al. 2020), and newly extend these observations to the retrograde path. Accordingly, inferences based only on the presence of minerals like glaucophane in the field may be meaningless in the context of syn-convergent tectonics.

4.12. Acknowledgments

Field and analytical work for this project were supported by an NSERC Discovery grant awarded to Schneider and by a GSA Graduate Student Research Grant awarded to Ducharme. Bukała acknowledges 'Juan de la Cierva' Fellowship number JFJC2021-047505-I funded by

MCIN/AEI/10.13039/501100011033 and CSIC. We thank E. Poulaki and an anonymous reviewer for thoughtful critiques which greatly improved the manuscript, and thank D. Canil for excellent editorial handling. We thank G. Poirier (Ottawa) and M. Button (UBCO) for their help with data collection, and are grateful to K. Hattori, C. Barnes, B. O'Driscoll, B. Hess, and J. Ague for insightful discussions into the origins of the veins.

4.13. References

Alzayer, Y., Eichhubl, P., & Laubach, S. E. (2015). Non-linear growth kinematics of opening-mode fractures. Journal of Structural Geology, 74, 31-44.

Armbruster, T., Bonazzi, P., Akasaka, M., Bermanec, V., Chopin, C., Gieré, R., ... & Pasero, M. (2006). Recommended nomenclature of epidote-group minerals. European Journal of Mineralogy, 18(5), 551-567.

Augier, R., Jolivet, L., Gadenne, L., Lahfid, A., & Driussi, O. (2015). Exhumation kinematics of the Cycladic Blueschists unit and back-arc extension, insight from the Southern Cyclades (Sikinos and Folegandros Islands, Greece). Tectonics, 34(1), 152-185.

Azimov, P. Y., & Bushmin, S. A. (2007). Solubility of minerals of metamorphic and metasomatic rocks in hydrothermal solutions of varying acidity: thermodynamic modeling at 400–800 C and 1–5 kbar. Geochemistry International, 45, 1210-1234.

Barnes, C. J., Schneider, D. A., Majka, J., Camacho, A., Bukała, M., & Włodek, A. (2023). $^{40}Ar/^{39}Ar$ dates controlled by white mica deformation and strain localization: Insights from comparing in situ laser ablation and single-grain fusion techniques. Journal of Metamorphic Geology, 41(9), 1143-1166.

Bebout, G. E., & Barton, M. D. (1993). Metasomatism during subduction: products and possible paths in the Catalina Schist, California. Chemical Geology, 108(1-4), 61-92.

Behr, W. M., & Bürgmann, R. (2021). What's down there? The structures, materials and environment of deep-seated slow slip and tremor. Philosophical Transactions of the Royal Society A, 379(2193), 20200218.

Beitter, T., Wagner, T., & Markl, G. (2008). Formation of kyanite–quartz veins of the Alpe Sponda, Central Alps, Switzerland: implications for Al transport during regional metamorphism. Contributions to Mineralogy and Petrology, 156(6), 689-707.

Bons, P. D. (2001). The formation of large quartz veins by rapid ascent of fluids in mobile hydrofractures. Tectonophysics, 336(1-4), 1-17.

Bons, P. D., Elburg, M. A., & Gomez-Rivas, E. (2012). A review of the formation of tectonic veins and their microstructures. Journal of Structural Geology, 43, 33-62.

Bosse, V., Féraud, G., Ballèvre, M., Peucat, J. J., & Corsini, M. (2005). Rb–Sr and $^{40}Ar/^{39}Ar$ ages in blueschists from the Ile de Groix (Armorican Massif, France): Implications for closure mechanisms in isotopic systems. Chemical Geology, 220(1-2), 21-45.

Bröcker, M., Bieling, D., Hacker, B., & Gans, P. (2004). High-Si phengite records the time of greenschist facies overprinting: Implications for models suggesting mega-detachments in the Aegean Sea. Journal of Metamorphic Geology, 22(5), 427-442.

Bucholz, C. E., & Ague, J. J. (2010). Fluid flow and Al transport during quartz-kyanite vein formation, Unst, Shetland Islands, Scotland. Journal of Metamorphic Geology, 28(1), 19-39.

Bukała, M., Barnes, C. J., Jeanneret, P., Hidas, K., Mazur, S., Almqvist, B. S., ... & Majka, J. (2020). Brittle deformation during eclogitization of early Paleozoic blueschist. Frontiers in Earth Science, 8, 594453.

Castelli, D., Rolfo, F., Compagnoni, R., & Xu, S. (1998). Metamorphic veins with kyanite, zoisite and quartz in the Zhu-Jia-Chong eclogite, Dabie Shan, China. Island Arc, 7(1-2), 159-173.

Cawthorn, R. G., & Collerson, K. D. (1974). The recalculation of pyroxene end-member parameters and the estimation of ferrous and ferric iron content from electron microprobe analyses. American Mineralogist: Journal of Earth and Planetary Materials, 59(11-12), 1203-1208.

Cossette, É., Schneider, D. A., Warren, C. J., & Grasemann, B. (2015). Lithological, rheological, and fluid infiltration control on $^{40}Ar/^{39}Ar$ ages in polydeformed rocks from the West Cycladic detachment system, Greece. Lithosphere, 7(2), 189-205.

Ducharme, T. A., Schneider, D. A., Grasemann, B., & Klonowska, I. (2022). Stretched thin: Oligocene extrusion and ductile thinning of the Basal Unit along the Evia Shear Zone, NW Cyclades, Greece. Tectonics, 41(12), e2022TC007561.

Dunlap, W.J., Teyssier. C., McDougall, I., & Baldwin, S. (1991). Ages of deformation from K/Ar and $^{40}Ar/^{39}Ar$ dating of white micas. Geology, 19(12), 1213-1216.

Dürr, S.T., Altherr, R., Keller, J.O., Okrusch, M.M., Seidel, E. (1978). The median Aegean crystalline belt: Stratigraphy, structure, metamorphism, magmatism. In: Cloos H, Roeder D, Schmidt K (eds) Alps, Apennines, Hellenides 38, Stuttgart, Schweizerbart, 455-477.

Evans, B. W. (1990). Phase relations of epidote-blueschists. Lithos, 25(1-3), 3-23.

Faulkner, D. R., Mitchell, T. M., Healy, D., & Heap, M. J. (2006). Slip on'weak'faults by the rotation of regional stress in the fracture damage zone. Nature, 444(7121), 922-925.

Fitzherbert, J. A., Clarke, G. L., & Powell, R. (2005). Preferential retrogression of high-P metasediments and the preservation of blueschist to eclogite facies metabasite during exhumation, Diahot terrane, NE New Caledonia. Lithos, 83(1-2), 67-96.

Freeman, S. R., Inger, S., Butler, R. W. H., & Cliff, R. A. (1997). Dating deformation using Rb-Sr in white mica: Greenschist facies deformation ages from the Entrelor shear zone, Italian Alps. Tectonics, 16(1), 57-76.

Gao, J., & Klemd, R. (2001). Primary fluids entrapped at blueschist to eclogite transition: evidence from the Tianshan meta-subduction complex in northwestern China. Contributions to Mineralogy and Petrology, 142(1), 1-14.

Gerogiannis, N., Xypolias, P., Chatzaras, V., Aravadinou, E., & Papapavlou, K. (2019). Deformation within the Cycladic subduction–exhumation channel: new insights from the enigmatic Makrotantalo nappe (Andros, Aegean). International Journal of Earth Sciences, 108, 817-843.

Giuntoli, F., & Viola, G. (2022). A likely geological record of deep tremor and slow slip events from a subducted continental broken formation. Scientific Reports, 12(1), 4506.

Govindaraju, K. (1979). Report (1968–1978) on two mica reference samples: biotite Mica-Fe and phlogopite Mica-Mg. Geostandards Newsletter, 3(1), 3-24.

Grasemann, B., Schneider, D. A., Stöckli, D. F., & Iglseder, C. (2012). Miocene bivergent crustal extension in the Aegean: Evidence from the western Cyclades (Greece). Lithosphere, 4(1), 23-39.

Guiraud, M. (1982). Géothermobarométrie du faciès schiste vert à glaucophane: modélisation et applications (Afghanistan, Pakistan, Corse, Bohême). Dissertation, University of Montpellier.

Halama, R., & Konrad-Schmolke, M. (2015). Retrograde metasomatic effects on phase assemblages in an interlayered blueschist–greenschist sequence (Coastal Cordillera, Chile). Lithos, 216, 31-47.

Harlov, D.E., Austrheim, H. (2013). Metasomatism and the chemical transformation of rock: rock-mineral-fluid interaction in terrestrial and extraterrestrial environments. In: Harlov, D.E., Austrheim, H. (eds.) Metasomatism and the Chemical Transformation of Rock. Lecture Notes in Earth System Sciences, Springer Berlin Heidelberg, pp 1-16.

Hawthorne, F. C., Oberti, R., Harlow, G. E., Maresch, W. V., Martin, R. F., Schumacher, J. C., & Welch, M. D. (2012). Nomenclature of the amphibole supergroup. American Mineralogist, 97(11-12), 2031-2048.

Hayman, N. W., & Lavier, L. L. (2014). The geologic record of deep episodic tremor and slip. Geology, 42(3), 195-198.

Healy, D. (2009). Anisotropy, pore fluid pressure and low angle normal faults. Journal of Structural Geology, 31(6), 561-574.

Hess, B. L., Ague, J. J., & Voorhees, P. W. (2022). Quantifying the Effects of Non-Hydrostatic Stress on Multi-Component Minerals. Journal of Geophysical Research: Solid Earth, 127(9), e2022JB025201.

Hogmalm, K.J., Zack, T., Karlsson, A.K.O., Sjöqvist, A.S., Garbe-Schönberg, D. (2017). In situ Rb–Sr and K–Ca dating by LA-ICP-MS/MS: an evaluation of N_2O and SF_6 as reaction gases. Journal of Analytical Atomic Spectrometry, 32(2), 305-313.

Huang, F., & Sverjensky, D. A. (2019). Extended Deep Earth Water Model for predicting major element mantle metasomatism. Geochimica et Cosmochimica Acta, 254, 192-230.

Huet, B., Labrousse, L., Monie, P., Malvoisin, B., & Jolivet, L. (2015). Coupled phengite ^{40}Ar–^{39}Ar geochronology and thermobarometry: PTt evolution of Andros Island (Cyclades, Greece). Geological Magazine, 152(4), 711-727.

Inger, S., & Cliff, R. A. (1994). Timing of metamorphism in the Tauern Window, Eastern Alps: Rb-Sr ages and fabric formation. Journal of Metamorphic Geology, 12(5), 695-707.

Jacobshagen, V. (1986). Geologie von Griechland. Borntraeger, Berlin-Stuttgart.

Jolivet, L., Famin, V., Mehl, C., Parra, T., Aubourg, C., Hébert, R., et al. (2004). Strain localization during crustal-scale boudinage to form extensional metamorphic domes in the Aegean Sea. Special papers-Geological Society of America, 185-210.

Jolivet, L., & Brun, J. P. (2010). Cenozoic geodynamic evolution of the Aegean. International Journal of Earth Sciences, 99, 109-138.

Jolivet, L., Lecomte, E., Huet, B., Denèle, Y., Lacombe, O., Labrousse, L., ... & Mehl, C. (2010). The north cycladic detachment system. Earth and Planetary Science Letters, 289(1-2), 87-104.

Jolivet, L., Faccenna, C., Huet, B., Labrousse, L., Le Pourhiet, L., Lacombe, O., ... & Driussi, O. (2013). Aegean tectonics: Strain localisation, slab tearing and trench retreat. Tectonophysics, 597, 1-33.

Kassaras, I., Kapetanidis, V., Ganas, A., Karakonstantis, A., Papadimitriou, P., Kaviris, G., ... & Voulgaris, N. (2022). Seismotectonic analysis of the 2021 Damasi-Tyrnavos (Thessaly, Central Greece) earthquake sequence and implications on the stress field rotations. Journal of Geodynamics, 150, 101898.

Katsikatsos, G. (1991a). Geological map of Greece, Karystos sheet. Institute of Geological Mining Research (IGME), Athens.

Katsikatsos, G. (1991b). Geological map of Greece, Aliveri sheet. Institute of Geological Mining Research (IGME), Athens.

Katzir, Y., Avigad, D., Matthews, A., Garfunkel, Z., & Evans, B. W. (2000). Origin, HP/LT metamorphism and cooling of ophiolitic mélanges in southern Evia (NW Cyclades), Greece. Journal of Metamorphic Geology, 18(6), 699-718.

Kerrick, D.M. (1990). Aluminum metasomatism. In: Ribbe, P.H. (ed.) The Al_2SiO_5 polymorphs. Reviews in Mineralogy, 22, 311-352.

Kellett, D. A., Warren, C., Larson, K. P., Zwingmann, H., van Staal, C. R., & Rogers, N. (2016). Influence of deformation and fluids on Ar retention in white mica: Dating the Dover Fault, Newfoundland Appalachians. Lithos, 254, 1-17.

Kelley, S. (2002). Excess argon in K-Ar and Ar-Ar geochronology. Chemical Geology, 188(1-2), 1-22.

Kleine, B. I., Skelton, A. D., Huet, B., & Pitcairn, I. K. (2014). Preservation of blueschist-facies minerals along a shear zone by coupled metasomatism and fast-flowing CO2-bearing fluids. Journal of Petrology, 55(10), 1905-1939.

Larson, K. P., Button, M., Shrestha, S., & Camacho, A. (2023). A comparison of $^{87}Rb/^{87}Sr$ and $^{40}Ar/^{39}Ar$ dates: Evaluating the problem of excess ^{40}Ar in Himalayan mica. Earth and planetary science letters, 609, 118058.

Laurent, V., Beaudoin, A., Jolivet, L., Arbaret, L., Augier, R., Rabillard, A., & Menant, A. (2015). Interrelations between extensional shear zones and synkinematic intrusions: The example of Ikaria Island (NE Cyclades, Greece). Tectonophysics, 651, 152-171.

Laurent, V., Huet, B., Labrousse, L., Jolivet, L., Monie, P., & Augier, R. (2017). Extraneous argon in high-pressure metamorphic rocks: Distribution, origin and transport in the Cycladic Blueschist Unit (Greece). Lithos, 272, 315-335.

Laurent, V., Lanari, P., Naïr, I., Augier, R., Lahfid, A., & Jolivet, L. (2018). Exhumation of eclogite and blueschist (Cyclades, Greece): Pressure–temperature evolution determined by thermobarometry and garnet equilibrium modelling. Journal of Metamorphic Geology, 36(6), 769-798.

Laurent, V., Scaillet, S., Jolivet, L., Augier, R., & Roche, V. (2021). ^{40}Ar behaviour and exhumation dynamics in a subduction channel from multi-scale $^{40}Ar/^{39}Ar$ systematics in phengite. Geochimica et Cosmochimica Acta, 311, 141-173.

Liu, J., & Bohlen, S. R. (1995). Mixing properties and stability of jadeite-acmite pyroxene in the presence of albite and quartz. Contributions to Mineralogy and Petrology, 119, 433-440.

Locock, A.J. (2014). An Excel spreadsheet to classify chemical analyses of amphiboles following the IMA 2012 recommendations. Computers & Geosciences, 62, 1-11.

Macris, C. A., Newton, R. C., Wykes, J., Pan, R., & Manning, C. E. (2020). Diopside, enstatite and forsterite solubilities in H2O and H2O-NaCl solutions at lower crustal and upper mantle conditions. Geochimica et Cosmochimica Acta, 279, 119-142.

Maluski, H., Vergely, P., Bavay, D., Bavay, P., Katsikatsos, G. (1981). $^{39}Ar/^{40}Ar$ dating of glaucophanes and phengites in southern Euboa (Greece); geodynamic implications. Bulletin of the Geological Society of France 7(5), 469-476.

Mancktelow, N. S. (2008). Tectonic pressure: Theoretical concepts and modelled examples. Lithos, 103(1-2), 149-177.

Manzotti, P., Ballèvre, M., Pitra, P., Putlitz, B., Robyr, M., & Müntener, O. (2020). The growth of sodic amphibole at the greenschist-to blueschist-facies transition (Dent Blanche, Western Alps): bulk-rock chemical control and thermodynamic modelling. Journal of Petrology, 61(4), egaa044.

Maruyama, S., Cho, M., & Liou, J. G. (1986). Experimental investigations of blueschist-greenschist transition equilibria: Pressure dependence ofAl2O3 contents in sodic amphiboles—A new geobarometer. Geological Society of America Memoirs, 164, 1-16.

Massonne, H. J., & Willner, A. P. (2008). Phase relations and dehydration behaviour of psammopelite and mid-ocean ridge basalt at very-low-grade to low-grade metamorphic conditions. European Journal of Mineralogy, 20(5), 867-879.

Mehl, C., Jolivet, L., Lacombe, O., Labrousse, L., & Rimmele, G. (2007). Structural evolution of Andros (Cyclades, Greece): a key to the behaviour of a (flat) detachment within an extending continental crust. Geological Society, London, Special Publications, 291(1), 41-73.

Menant, A., Jolivet, L., Augier, R., & Skarpelis, N. (2013). The North Cycladic Detachment System and associated mineralization, Mykonos, Greece: Insights on the evolution of the Aegean domain. Tectonics, 32(3), 433-452.

Menegon, L., & Fagereng, Å. (2021). Tectonic pressure gradients during viscous creep drive fluid flow and brittle failure at the base of the seismogenic zone. Geology, 49(10), 1255-1259.

Menzel, M. D., Garrido, C. J., & Sánchez-Vizcaíno, V. L. (2020). Fluid-mediated carbon release from serpentinite-hosted carbonates during dehydration of antigorite-serpentinite in subduction zones. Earth and Planetary Science Letters, 531, 115964.

Miyazaki, K., Sopaheluwakan, J., Zulkarnain, I., & Wakita, K. (1998). A jadeite–quartz–glaucophane rock from Karangsambung, central Java, Indonesia. Island Arc, 7(1-2), 223-230.

Muñoz-Montecinos, J., Angiboust, S., Cambeses, A., & García-Casco, A. (2020). Multiple veining in a paleo–accretionary wedge: The metamorphic rock record of prograde dehydration and transient high pore-fluid pressures along the subduction interface (Western Series, central Chile). Geosphere, 16(3), 765-786.

Nüchter, J. A. (2017). How vein sealing boosts fracture widening rates–The buckling-enhanced aperture growth mechanism for syn-tectonic veins. Tectonophysics, 694, 69-86.

Nüchter, J. A., & Ellis, S. (2010). Complex states of stress during the normal faulting seismic cycle: Role of midcrustal postseismic creep. Journal of Geophysical Research: Solid Earth, 115(B12).

Nüchter, J. A., & Stöckhert, B. (2007). Vein quartz microfabrics indicating progressive evolution of fractures into cavities during postseismic creep in the middle crust. Journal of Structural Geology, 29(9), 1445-1462.

Olson, J. E. (2003). Sublinear scaling of fracture aperture versus length: an exception or the rule?. Journal of Geophysical Research: Solid Earth, 108(B9).

Oliver, N. H., & Bons, P. D. (2001). Mechanisms of fluid flow and fluid–rock interaction in fossil metamorphic hydrothermal systems inferred from vein–wallrock patterns, geometry and microstructure. Geofluids, 1(2), 137-162.

Papanikolaou, D. (2009). Timing of tectonic emplacement of the ophiolites and terrane paleogeography in the Hellenides. Lithos, 108(1-4), 262-280.

Parra, T., Vidal, O., & Jolivet, L. (2002). Relation between the intensity of deformation and retrogression in blueschist metapelites of Tinos Island (Greece) evidenced by chlorite–mica local equilibria. Lithos, 63(1-2), 41-66.

Peillod, A., Majka, J., Ring, U., Drüppel, K., Patten, C., Karlsson, A., ... & Tehler, E. (2021). Differences in decompression of a high-pressure unit: A case study from the Cycladic Blueschist Unit on Naxos Island, Greece. Lithos, 386, 106043.

Philippot, P., & Selverstone, J. (1991). Trace-element-rich brines in eclogitic veins: implications for fluid composition and transport during subduction. Contributions to Mineralogy and Petrology, 106, 417-430.

Ramsay, J.G., Huber, M.I. (1983). The techniques of modern structural geology, Vol 1: strain analysis. Academic Press, Cambridge.

Ramsay, J.G. (1980). The crack–seal mechanism of rock deformation. Nature, 284(5752), 135-139. https://doi.org/10.1016/0191-8141(80)90038-3

Reches, Z. E. (1998). Tensile fracturing of stiff rock layers under triaxial compressive stress states. International Journal of Rock Mechanics and Mining Sciences, 35(4-5), 456-457.

Ribeiro, B. V., Kirkland, C. L., Kelsey, D. E., Reddy, S. M., Hartnady, M. I., Faleiros, F. M., ... & Clark, C. (2023). Time-strain evolution of shear zones from petrographically constrained Rb–Sr muscovite analysis. Earth and Planetary Science Letters, 602, 117969.

Ring, U., Will, T., Glodny, J., Kumerics, C., Gessner, K., Thomson, S., Güngör, T., Monié, P., Okrusch, M., Drüppel, K. (2007a). Early exhumation of high-pressure rocks in extrusion wedges: Cycladic blueschist unit in the eastern Aegean, Greece, and Turkey. Tectonics, 26(2).

Ring, U., Glodny, J., Will, T., & Thomson, S. (2007). An Oligocene extrusion wedge of blueschist-facies nappes on Evia, Aegean Sea, Greece: implications for the early exhumation of high-pressure rocks. Journal of the Geological Society, 164(3), 637-652.

Ring, U., Glodny, J., Will, T., & Thomson, S. (2010). The Hellenic subduction system: high-pressure metamorphism, exhumation, normal faulting, and large-scale extension. Annual Review of Earth and Planetary Sciences, 38, 45-76.

Roche, V., Laurent, V., Cardello, G. L., Jolivet, L., & Scaillet, S. (2016). Anatomy of the Cycladic Blueschist Unit on Sifnos Island (Cyclades, Greece). Journal of Geodynamics, 97, 62-87.

Rösel, D., & Zack, T. (2022). LA-ICP-MS/MS Single-Spot Rb-Sr Dating. Geostandards and Geoanalytical Research, 46(2), 143-168.

Rosenbaum, G., Avigad, D., & Sánchez-Gómez, M. (2002). Coaxial flattening at deep levels of orogenic belts: evidence from blueschists and eclogites on Syros and Sifnos (Cyclades, Greece). Journal of Structural Geology, 24(9), 1451-1462.

Sanchez-Gomez, M., Avigad, D. O. V., & Heimann, A. (2002). Geochronology of clasts in allochthonous Miocene sedimentary sequences on Mykonos and Paros Islands: implications for back-arc extension in the Aegean Sea. Journal of the Geological Society, 159(1), 45-60.

Scheffer, C., Vanderhaeghe, O., Lanari, P., Tarantola, A., Ponthus, L., Photiades, A., & France, L. (2016). Syn-to post-orogenic exhumation of metamorphic nappes: Structure and thermobarometry of the western Attic-Cycladic metamorphic complex (Lavrion, Greece). Journal of Geodynamics, 96, 174-193.

Schliestedt, M., & Matthews, A. (1987). Transformation of blueschist to greenschist facies rocks as a consequence of fluid infiltration, Sifnos (Cyclades), Greece. Contributions to Mineralogy and Petrology, 97(2), 237-250.

Schott, J., Pokrovsky, O. S., & Oelkers, E. H. (2009). The link between mineral dissolution/precipitation kinetics and solution chemistry. Reviews in mineralogy and geochemistry, 70(1), 207-258.

Schneider, D. A., Senkowski, C., Vogel, H., Grasemann, B., Iglseder, C., & Schmitt, A. K. (2011). Eocene tectonometamorphism on Serifos (western Cyclades) deduced from zircon depth-profiling geochronology and mica thermochronology. Lithos, 125(1-2), 151-172.

Scott, D. R. (1996). Seismicity and stress rotation in a granular model of the brittle crust. Nature, 381(6583), 592-595.

Shaked, Y., Avigad, D., & Garfunkel, Z. (2000). Alpine high-pressure metamorphism at the Almyropotamos window (southern Evia, Greece). Geological Magazine, 137(4), 367-380.

Sharma, N. K., Biswal, T. K., & Chinnasamy, S. S. (2023). Structural implications of paleofluid pressure and paleostress estimates of the quartz veins from sulfide deposits of the Ambaji-Deri region, Neoproterozoic South Delhi Terrane, Aravalli-Delhi Mobile Belt, North-West India. Journal of Asian Earth Sciences, 245, 105552.

Sibson, R. H. (1994). Crustal stress, faulting and fluid flow. Geological Society, London, Special Publications, 78(1), 69-84.

Sibson, R. H. (2000). Tectonic controls on maximum sustainable overpressure: fluid redistribution from stress transitions. Journal of Geochemical Exploration, 69, 471-475.

Spandler, C., & Hermann, J. (2006). High-pressure veins in eclogite from New Caledonia and their significance for fluid migration in subduction zones. Lithos, 89(1-2), 135-153.

Stipp, M., & Kunze, K. (2008). Dynamic recrystallization near the brittle-plastic transition in naturally and experimentally deformed quartz aggregates. Tectonophysics, 448(1-4), 77-97.

Stipp, M., StuÈnitz, H., Heilbronner, R., & Schmid, S. M. (2002). The eastern Tonale fault zone: a 'natural laboratory'for crystal plastic deformation of quartz over a temperature range from 250 to 700 C. Journal of structural geology, 24(12), 1861-1884.

Tiraboschi, C., Tumiati, S., Sverjensky, D., Pettke, T., Ulmer, P., & Poli, S. (2018). Experimental determination of magnesia and silica solubilities in graphite-saturated and redox-buffered high-pressure COH fluids in equilibrium with forsterite+ enstatite and magnesite+ enstatite. Contributions to Mineralogy and Petrology, 173, 1-17.

Tirel, C., Gautier, P., Van Hinsbergen, D. J. J., & Wortel, M. J. R. (2009). Sequential development of interfering metamorphic core complexes: numerical experiments and

comparison with the Cyclades, Greece. Geological Society, London, Special Publications, 311(1), 257-292.

Tomaschek, F., Kennedy, A. K., Villa, I. M., Lagos, M., & Ballhaus, C. (2003). Zircons from Syros, Cyclades, Greece—recrystallization and mobilization of zircon during high-pressure metamorphism. Journal of Petrology, 44(11), 1977-2002.

Tsujimori, T., & Harlow, G. E. (2012). Petrogenetic relationships between jadeitite and associated high-pressure and low-temperature metamorphic rocks in worldwide jadeitite localities: a review. European Journal of Mineralogy, 24(2), 371-390.

Ujiie, K., Saishu, H., Fagereng, Å., Nishiyama, N., Otsubo, M., Masuyama, H., & Kagi, H. (2018). An explanation of episodic tremor and slow slip constrained by crack-seal veins and viscous shear in subduction mélange. Geophysical Research Letters, 45(11), 5371-5379.

Ukar, E., & Cloos, M. (2014). Low-temperature blueschist-facies mafic blocks in the Franciscan mélange, San Simeon, California: Field relations, petrology, and counterclockwise P-T paths. Bulletin, 126(5-6), 831-856.

Urai, J. L., Williams, P. F., & Van Roermund, H. L. M. (1991). Kinematics of crystal growth in syntectonic fibrous veins. Journal of Structural Geology, 13(7), 823-836.

Uunk, B., Brouwer, F., de Paz-Álvarez, M., van Zuilen, K., Huybens, R., van't Veer, R., & Wijbrans, J. (2022). Consistent detachment of supracrustal rocks from a fixed subduction depth in the Cyclades. Earth and Planetary Science Letters, 584, 117479.

Uysal, I. T., Feng, Y. X., Zhao, J. X., Bolhar, R., Işik, V., Baublys, K. A., ... & Golding, S. D. (2011). Seismic cycles recorded in late Quaternary calcite veins: geochronological,

geochemical and microstructural evidence. Earth and Planetary Science Letters, 303(1-2), 84-96.

van Hinsbergen, D. J., & Schmid, S. M. (2012). Map view restoration of Aegean–West Anatolian accretion and extension since the Eocene. Tectonics, 31(5).

Vanderhaeghe, O., Whitney, D. L., Teyssier, C., & Siddoway, C. S. (2004). Structural development of the Naxos migmatite dome. Geological Society of America, Special Papers, 211-228.

Vermeesch, P. (2018). IsoplotR: A free and open toolbox for geochronology. Geoscience Frontiers, 9(5), 1479-1493.

Vermilye, J. M., & Scholz, C. H. (1995). Relation between vein length and aperture. Journal of structural geology, 17(3), 423-434.

Wang, R., Cudahy, T., Laukamp, C., Walshe, J. L., Bath, A., Mei, Y., ... & Laird, J. (2017). White mica as a hyperspectral tool in exploration for the Sunrise Dam and Kanowna Belle gold deposits, Western Australia. Economic Geology, 112(5), 1153-1176.

Warren, C.J., Hanke, F., Kelley, S.P. (2012). When can muscovite $^{40}Ar/^{39}Ar$ dating constrain the timing of metamorphic exhumation? Chemical Geology, 291, 79-86.

Wheeler, J. (2014). Dramatic effects of stress on metamorphic reactions. Geology, 42(8), 647-650.

Widmer, T., Thompson, A.B. (2001). Local origin of high pressure vein material in eclogite facies rocks of the Zermatt-Saas Zone, Switzerland. Americal Journal of Science, 301(7), 627-656.

Wijbrans, J. R., Schliestedt, M., & York, D. (1990). Single grain argon laser probe dating of phengites from the blueschist to greenschist transition on Sifnos (Cyclades, Greece). Contributions to Mineralogy and Petrology, 104, 582-593.

Wilson, C. J. L. (1994). Crystal growth during a single-stage opening event and its implications for syntectonic veins. Journal of structural geology, 16(9), 1283-1296.

Wintsch, R. P., Byrne, T., & Toriumi, M. (1999). Exhumation of the Sanbagawa blueschist belt, SW Japan, by lateral flow and extrusion: evidence from structural kinematics and retrograde PTt paths. Geological Society, London, Special Publications, 154(1), 129-155.

Wohlers, A., Manning, C. E., & Thompson, A. B. (2011). Experimental investigation of the solubility of albite and jadeite in H_2O, with paragonite+ quartz at 500 and 600 C, and 1–2.25 GPa. Geochimica et Cosmochimica Acta, 75(10), 2924-2939.

Xypolias, P., Spanos, D., Chatzaras, V., Kokkalas, S., & Koukouvelas, I. (2010). Vorticity of flow in ductile thrust zones: examples from the Attico-Cycladic Massif (Internal Hellenides, Greece). Geological Society, London, Special Publications, 335(1), 687-714.

Xypolias, P., Iliopoulos, I., Chatzaras, V., & Kokkalas, S. (2012). Subduction-and exhumation-related structures in the Cycladic Blueschists: Insights from south Evia Island (Aegean region, Greece). Tectonics, 31(2).

Zack, T., & Hogmalm, K. J. (2016). Laser ablation Rb/Sr dating by online chemical separation of Rb and Sr in an oxygen-filled reaction cell. Chemical Geology, 437, 120-133.

Zheng, Y. F. (1993). Calculation of oxygen isotope fractionation in hydroxyl-bearing silicates. Earth and Planetary Science Letters, 120(3-4), 247-263.

Zulauf, J., Zulauf, G., Göttlich, J., & Peinl, M. (2014). Formation of chocolate-tablet boudins: Results from scaled analogue models. Journal of Structural Geology, 68, 97-111.

CHAPTER 5

CONCLUSIONS

5.1. Implications for regional tectonic models

This thesis presents a significant revision to the tectonic framework of the Almyropotamos window, and of southern Evia more generally, compared with existing models. When research for this thesis began, most models considered the Basal Thrust on Evia to be a major thrust fault facilitating nappe stacking during Hellenic convergence (Shaked et al., 2000; Xypolias et al., 2003; Ring and Layer, 2003; Ring et al., 2007; Gerogiannis et al., 2021). Although structures likely related to exhumation had been previously reported from the island (Jolivet and Patriat, 1999; Jolivet et al., 2004; Ring et al., 2007), their importance within the overall tectonic evolution of Evia remained underexplored. The major conclusions of the thesis regarding the tectonic evolution of the Basal Unit, and its relationship to the overlying CBU, differ significantly from those of previous models (Bröcker and Franz, 1998; Ring et al., 1999; Ring et al., 2001; Bröcker et al., 2005), but resemble models for equivalent rocks from Mt. Olympos (Schermer, 1989).

Chapter 2 highlighted the strain geometry developed in the vicinity of the previously mapped tectonic contact (Katsikatsos et al., 1991a,b). New observations presented herein indicate the strain associated with the tectonic contact developed most prominently within pelitic schists assigned to either the Basal Unit flysch succession or the similarly flyschoid Tsakei Unit. Critically, relevant structures exhibit apparent stretching in both directions within the horizontal plane, indicating that the maximum principal stress, σ_1, was oriented vertically at the time those structures developed. If the tectonic contact on southern Evia were a thrust, particularly a segment of one responsible for orogen-scale nappe stacking, then preserved structures should instead reflect crustal thickening. By contrast, shear sense synthetic to that expected to coincide with extension in the north Aegean Sea, and overprinting relationships between progressively cooler structures, instead show that deformation coincided with exhumation during regional extension (Jolivet et al.,

2010). This inference was further supported by the results of campaign-style white mica $^{40}Ar/^{39}Ar$ and zircon (U-Th)/He (ZHe) geochronology also presented in Chapter 2. A significant quantity of multiple, single-grain total fusion data from the vicinity of the tectonic window attests to a record of dominantly Eocene to early Oligocene $^{40}Ar/^{39}Ar$ dates in both the hanging wall and footwall. Along the tectonic contact, however, a consistent unimodal late Oligocene $^{40}Ar/^{39}Ar$ age record is preserved. Those Oligocene dates closely resemble existing white mica geochronology from elsewhere in the Cyclades, interpreted to capture the timing of mylonitic deformation in the footwalls of the major regional detachment systems (Jolivet et al., 2010; Grasemann et al., 2012). Although the analytical methodology used in Chapter 2 allowed only implicit correlations of dates to microstructures documented in mica within the sample, *in situ* geochronology employed in Chapter 3 effectively confirmed the inferences of Chapter 2: simple, planar, flat-lying foliation represent pervasive transposition of older structures during extension, and mica defining those foliations record the younger late Oligocene dates. By contrast, *in situ* $^{40}Ar/^{39}Ar$ data from Chapter 3 also indicate that samples displaying composite foliations, i.e., samples whose mica exhibit a spaced crenulation cleavage or that apparently preserve multiple fold generations, yield early Oligocene and older $^{40}Ar/^{39}Ar$ dates like those obtained from the hanging wall and footwall of the tectonic contact by the total-fusion method. All of this is underscored by the ZHe data, which provide identical 17-15 Ma cooling ages across the tectonic contact. Thus, the progressive cooling of both the CBU and Basal Unit occurred synchronously, implying both that there was significant attenuation of intervening levels dividing the two, and that the NCDS exerted a strong control on the unroofing of both units.

Thus, interpretations of the data outlined in this thesis favour the tectonic contact between the Basal Unit and CBU on Evia as a late Oligocene structure that was active during and following

the transition to tension in the Aegean region. Earlier, syn-convergent strain affecting the HP-LT units is widely considered to have operated during south-vergent subduction, yielding a top-to-SW shear sense in modern coordinates in the western Aegean. As the Basal Thrust represents a fossilized subduction thrust, it should share those characteristics. Structural observations presented in Chapters 2 and 3 indicate that preservation of the syn-subduction record of strain (in the form of, e.g., m- to km-scale imbrication via multi-generational folding, top-to-SW ductile shear sense) may be limited to internal parts of the two nappes (Chapter 2), and to low-strain blocks or domains within the shear zone (Chapter 3). Judging by its state of preservation on Evia, any initially pervasive record of syn-subduction deformation along the Basal Thrust was either entirely overprinted by exhumation-related strain, or else was excised from the structural pile exposed on Evia due to the local geometry of the extensional fault systems.

Investigating the nappe-scale continuity of observations presented in this thesis constitutes an enticing avenue for future research. The equivalent tectonic contacts exposed on Tinos and Samos (e.g., Ring et al., 1999; Bröcker et al., 2005) have received little attention, but corroboration – or contradiction – of the structural features reported from Evia at those localities is key to establishing whether ductile thinning along the orogen-scale CBU-Basal Unit contact was of regional importance. Although extrapolating observations from Evia across the entire Cyclades appears the more vindicating premise, if equivalent exposures preserve contrasting tectonic modes of deformation and exhumation, then it would caution the use of relatively small-scale (i.e., m- to km-scale) data to impose far-reaching modifications to orogen-scale (i.e., hundreds of km) models, which is at present a generally permissible convention.

Unequivocally demonstrating that Tinos and Samos still expose the same structure, however, would present a significant challenge. A simpler rationale, if distinct strain records are

documented, would be to conclude that the exposures are unrelated, or were otherwise misinterpreted. Whether the Almyropotamos window is necessarily a tectonic contact between two major thrust sheets, or simply a structure causing internal imbrication within the CBU, was a question entertained at several points during this thesis. Although Chapter 3 highlights structural differences that strengthen the argument that the window divides two discrete nappes, contrasting structural geometries alone do not strictly require that they developed in two separate nappes. Absent such exclusionary evidence, it remains possible that the structural pile of Evia consists of a pair of imbricated thrust sheets of CBU affinity that experienced distinct deformation histories. Such an interpretation is consistent, albeit in a different fashion, with the lack of an age break in the ZHe data, but does not explain the relative absence of dates capturing peak HP metamorphism (*c.* 50-40 Ma for CBU; Laurent et al., 2021) in either the hanging wall or footwall of the Evia Shear Zone. The existence of the Almyropotamos tectonic window altogether is itself predicated largely on fossil evidence from Evia that has not been reproduced since (Dubois and Bignot, 1979). Therefore, future work on the Basal Unit should prioritize not only meticulous field documentation of structures both parallel and perpendicular to the local stretching lineation, high spatial resolution geochronology, and detailed thermodynamic modelling, but also attempt to document evidence, paleontological or otherwise, that reaffirms its distinction from the CBU.

Independent of the ultimate resolution to the above, there are several outstanding questions concerning structural levels below the CBU in the Cyclades that remain underdeveloped. Primary among these is the relationship between the pre-Alpine Cycladic Basement and the Basal Unit, which occupy equivalent structural levels but are nowhere documented together. The Cycladic Basement has been posited to represent the original crystalline basement to either the CBU (Pindos) or Basal Unit (Gavrovo-Tripolitza). Whereas the former is more easily reconciled with

the observed field relationships, the contact between the CBU and Cycladic Basement is frequently tectonic in nature (Forster and Lister, 1999; Huet et al., 2009; Augier et al., 2015), although the timing of displacement along it is disputed (Poulaki et al., 2019). A shared affinity with the Basal Unit is still tenable if, for instance, pronounced ductile thinning of the Basal Unit has locally completely attenuated it and placed the CBU in direct contact with its crystalline basement. Notably, ductile thinning has also been documented between the CBU and Cycladic Basement on Ios (Mizera and Behrmann, 2016).

Most large-scale tectonic syntheses of the geodynamic evolution in the Aegean emphasize the behaviour of the metamorphic belt in its overall direction of tectonic transport, i.e., north-south to northeast-southwest in modern coordinates (**Figure 1.3**; Jolivet et al., 2004; Jolivet and Brun, 2010; Ring et al., 2010). This thesis documents structures indicating material redistribution also locally occurred perpendicular to the transport direction, an important tectonic consideration that receives only infrequent attention in the Cyclades. Contrary to the general flattening and lateral extrusion implied around the Almyropotamos tectonic window, most prior instances of three-dimensional coaxial deformation support contraction on southernmost Evia, Naxos, Andros, and Serifos, producing syn-extensional upright folds whose axes parallel the transport direction (Avigad et al., 2001; Tschegg and Grasemann, 2009; Ziv et al., 2010; Xypolias et al., 2012). Each of these lies southeast of the Almyropotamos window, along a vector parallel to the intermediate axis of strain documented there. As discussed in Chapter 2, Avigad et al. (2001) argued that transport-normal contraction was responsible for the maintenance of Aegean crustal thickness despite the overall extension imposed upon the region. Those authors note that their model implies an influx of material from outside of the observed region of contraction, a role which southern Evia, near the tectonic window, is ideally positioned to serve. The validity of this model can be

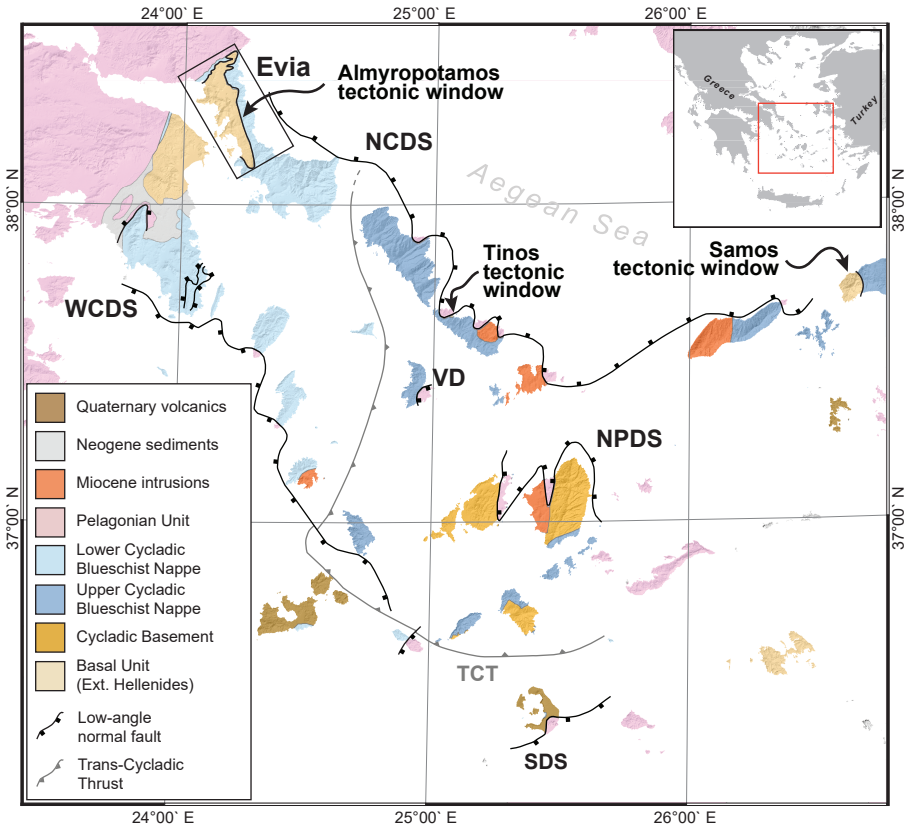

Figure 5.1. Simplified bedrock geology map of the Cyclades, Evia, and Attica. Modified after Coleman et al. (2020). NCDS: North Cycladic Detachment System; NPDS: Naxos-Paros Detachment System; SDS: Santorini Detachment System; TCT: Trans-Cycladic Thrust; VD: Vari Detachment; WCDS: West Cycladic Detachment System.

further tested by investigating whether flattening strains are preserved elsewhere at the margins of the Aegean, such as on Attica, Samos, or still farther afield to the east, potentially on the flanks of the Menderes Massif in western Turkey.

Finally, Chapter 1 mentioned the two motivating hypotheses for studying the tectonic window on Evia: investigating whether the Basal Thrust may be an extension of the Trans-Cycladic Thrust (TCT), which would require that the structure was active during syn-orogenic wedge extrusion of the CBU (Grasemann et al., 2018); and to document the nature of the exhumation-related strain and geochronology on Evia. Whereas the two objectives were not mutually exclusive, and the Basal Thrust had been implicated in prior models invoking wedge extrusion (Ring et al., 2007), available PT estimates from the tectonic window do not show a significant difference in peak PT conditions like those used to delineate the TCT (see Chapter 2; Shaked et al., 2000; Katzir et al., 2000). Furthermore, although underthrusting of the Basal Unit below the CBU would, in effect, place the Basal Thrust at the base of the CBU extrusion wedge, subduction of the Basal Unit may have post-dated extrusion of the CBU (see discussion in Chapters 2 and 3; Huet et al., 2015). Conversely, the data better illustrate the exhumation architecture of the Basal Unit; the consequences of this conclusion are discussed in detail in the following section.

5.2. Strain localization and geometry during exhumation

The major detachment systems of the Cyclades are responsible for segmentation and geometric reconfiguration of the Aegean crust (Gautier and Brun, 1994; Jolivet et al., 2004; Jolivet et al., 2010; Grasemann et al., 2012). Structures developed on each of the islands where segments of the detachments are exposed evolve in a broadly consistent and predictable manner up-section toward the detachment (Jolivet et al., 2010; Grasemann et al., 2012). However, certain detachments

do not show the same straightforward progression from a wide ductile strain corridor through progressive narrowing and embrittlement toward the detachment plane. Some Cycladic detachments are deflected structurally upwards and return to ductile strain due to arrest of the old detachment plane and synchronous heating by an intrusion (e.g., Jolivet et al., 2010; Lecomte et al., 2011; Schneider et al., 2011). Others may capture only part of the strain evolution, with the more brittle stages of deformation apparently absent or occurring at higher structural levels (e.g., Huet et al., 2009; Bakowsky et al., 2023). Finally, multiple coeval detachment branches may exhume the crust in tandem near the along-strike termination of the detachment system (Coleman et al., 2020).

Intrusive rocks are not documented on Evia, but the Evia Shear Zone (ESZ) exhibits an atypical strain gradient and was likely active at the same time as the North Cycladic Detachment System (NCDS). Mt. Hymmitos, occupying roughly the same position along strike of the West Cycladic Detachment System (WCDS) as the Almyropotamos window is along strike of the NCDS, exposes multiple detachment branches that were co-active since the early Miocene (Coleman et al., 2020). Although the NCDS and WCDS, in principle, place a hanging wall of Pelagonian affinity (Upper Unit) in contact with a footwall composed of CBU (Jacobshagen, 1986; Jolivet et al., 2010), certain branches do not adhere to this strict definition. Some branches instead juxtapose early Miocene clastic rock or late Miocene plutons against Pelagonian (Gautier et al., 1993; Jolivet et al., 2010; Lecomte et al., 2011); Pelagonian against Pelagonian (Bakowsky et al., 2023); or CBU against CBU (Coleman et al., 2020).

It is therefore not unreasonable to consider the ESZ, despite its unique position between the CBU and Basal Unit, as a potential co-active branch of the NCDS. Like other branches of the major detachments, the ESZ represents an extensional structure effecting top-to-NE displacement,

synthetic with that of the NCDS (Jolivet et al., 2010). Moreover, $^{40}Ar/^{39}Ar$ data interpreted in Chapters 2 and 3 as dating deformation along the ESZ overlap with the timing of activity for the NCDS (Jolivet et al., 2010), and new ZHe dates from Chapter 2 suggest the Basal Unit and CBU on Evia underwent essentially simultaneous unroofing into the upper crust. Whereas the similar ZHe dates suggest much of that exhumation was facilitated by the NCDS, the ESZ must have contributed a non-negligible magnitude of unroofing to the Basal Unit to position it at such similar structural levels as the CBU. The already tectonized nappe contact may have simply provided a convenient weak plane to localize the branch. An equivalent major contact is not exposed on Mt. Hymmitos, which is composed exclusively of CBU (Coleman et al., 2020); however, the validity of this interpretation can be tested using the mapped Basal Unit exposures on northeast Attica (Katsikatsos et al., 1991b; Xypolias et al., 2010).

The ESZ is nevertheless unique among previously documented Cycladic detachments. In terms of strain geometry, it is the first major structure accomplishing exhumation in the Aegean exhibiting a general flattening mode of deformation. Additionally, no other detachment has yet been reported to show the relatively discontinuous deformation style as described for the ESZ in Chapter 3. Discussion therein compares the strain observed in the ESZ to that reported from mélange shear zones, which are characterized by anastomosing shear zones exploiting a weak, dominantly pelitic matrix with relatively low strain or brittlely deformed competent phacoids dispersed throughout (Fagereng and Sibson, 2010; Fagereng, 2013). However, mélange shear zones are generally interpreted to have formed during subduction (Fagereng and Sibson, 2010; Leah et al., 2022; Tulley et al., 2022), a conclusion that would be inconsistent with the geochronologic and structural evidence preserved within the ESZ. A major implication of this thesis is therefore that these mélange structures may also record strain related to exhumation, rather

than solely that related to burial as has been the common view. Re-evaluation of such structures, facilitated in large part by geochronology, may yield considerable insight into the exhumation histories and mechanisms of the localities where those rocks reside.

5.3. Practical applications of paired white mica $^{40}Ar/^{39}Ar$ and $^{87}Rb/^{87}Sr$ geochronology

Integration of multiple geochronometers is increasingly the preferred approach to answer complex questions pertaining to tectonics and metamorphism. The contrasting behaviour of different isotopic systems and their respective mineral chronometers carries the potential to impose much stronger constraints than any single geochronologic technique alone (Johnson et al., 2018; Glorie et al., 2022; Gyomlai et al., 2023; Larson et al., 2023). Two systems of particular importance to the study of low- and moderate-temperature orogenic events are the $^{40}Ar/^{39}Ar$ (and K/Ar) and $^{87}Rb/^{87}Sr$ systems, particularly in white mica, which both exhibit closure to volume diffusion processes at moderate temperatures and are sensitive to strain-induced resetting (Gyomlai et al., 2023). Key distinctions between the two chronometers include the inert and gaseous nature of Ar, which may render it more sensitive to strain-induced resetting, and the potential for externally sourced excess ^{40}Ar to skew measured dates to older, geologically meaningless values (Gyomlai et al., 2023; Larson et al., 2023). Despite the high mobility of Rb in crustal fluids, the two chronometers nonetheless appear to maintain distinct yet geologically meaningful age information in many cases (Villa et al., 2016; Larson et al., 2023).

Thus far, research intended to evaluate the co-applicability of the two geochronometers has been designed to interrogate the relationship between their recorded ages across a spectrum of geological contexts (Armstrong et al., 1966; Sherlock et al., 1999; Bosse et al, 2005; Schneider et al., 2008). Chapters 3 and 4 apply the concepts developed in those studies, particularly via *in situ*

$^{87}Rb/^{87}Sr$ techniques (Rösel and Zack, 2022; Gyomlai et al., 2023; Larson et al., 2023), to test certain assumptions regarding the $^{40}Ar/^{39}Ar$ results. In Chapter 3, the assumption tested was that the most dispersed of the *in situ* $^{40}Ar/^{39}Ar$ dates were due to the presence of excess Ar. The $^{87}Rb/^{87}Sr$ chronometer yielded indistinguishable ages from the two samples analyzed with this method, both of which agreed with the younger (and more geologically plausible) dates. In Chapter 4, the *in situ* $^{87}Rb/^{87}Sr$ data were used to validate the inference made from sample-scale structure that the dated phengite were not significantly deformed, as this may have produced a disparity in the dates obtained from each geochronometer. The $^{40}Ar/^{39}Ar$ and $^{87}Rb/^{87}Sr$ systems here produced dates which are indistinguishable from one another within error, considerably strengthening the central argument that the dates capture the timing of vein sealing. The combined use of white mica $^{40}Ar/^{39}Ar$ and $^{87}Rb/^{87}Sr$ dating, particularly for *in situ* applications of the isotope systems, is a powerful and cost-effective tool for bolstering tectonic models generated from either geochronometer individually.

5.4. Reactive transport in exhuming subduction terranes

Chapter 4 describes, for the first time, an occurrence of glaucophane- and phengite-bearing quartz veins hosted in metabasaltic rock of the Ochi Unit on southernmost Evia. Structural and isotopic data presented in that chapter support the rapid sequential formation of each of the four vein sets during post-orogenic exhumation, apparently at odds with the typical prograde or early retrograde settings typically expected to produce the nominally high-pressure minerals. Microstructures and mineral chemistry documented in the host rock indicate it is composed predominantly of ferric iron-enriched sodic clinopyroxene that has experienced variable degrees of retrogradation following the reaction jadeite + quartz → albite (Holland, 1980).

In addition to the aegirinitic-jadeitic composition of the clinopyroxene, high modal abundances of secondary hematite, and mineral chemical data from glaucophane and epidote in the veins and host rock, provide evidence that the hydrothermal system was enriched in ferric iron. The influence of Fe^{3+} component on lowering the pressures at which glaucophane and jadeite are stable is well-documented (e.g., Maruyama et al., 1986; Liu and Bohlen, 1995; Manzotti et al., 2020; Muñoz-Montecinos et al., 2020) and discussed at length in Chapter 4. The documented effects of fluid on the clinopyroxene, presumed also to be the parental fluid to the veins, suggests an increase in Fe^{3+} content near clinopyroxene rims, and the liberation of elements fundamental to the crystallization of glaucophane during conversion to albite.

The empirical geobarometers used to estimate equilibrium pressure contemporaneous with vein crystallization in Chapter 4 yield disparate results between approximately 4 and 8 kbar. Microstructural evidence conversely favours a single stage of sealing, indicating this does not reflect real variance in ambient PT conditions. The implication of the observed disparity is therefore that stabilization of different amphibole species during core-to-rim growth was facilitated, at least in part, by shifts in bulk composition (i.e., PTX space). Modelling of the system in PERPLE_X was attempted, but the model was unable to reconcile the documented vein assemblage with thermodynamic predictions: either multiple co-existing species of calcic and sodic amphiboles or chlorite were predicted, or the model failed at higher fO_2 values.

The key factor underlying the uncertainties in Chapter 4 is a lack of data to constrain the thermodynamics of solubility for minerals. Hydrothermal solutions are both of critical importance in many geologic systems, but are also intensely complex with respect to thermodynamics (Azimov and Burin, 2007; Menzel et al., 2020). What few data are available for speciation of geologically important dissolved components for different pressures, temperatures, and fluid

compositions severely limit predictions of mineral will be favoured for crystallization. Of note for the Mt. Ochi veins discussed in Chapter 4 is the small number of crystallized species. Only three to four minerals are observed (glaucophane, phengite, quartz, epidote), despite the system being described at minimum by eight components (K_2O-Na_2O-CaO-FeO-MgO-Al_2O_3-SiO_2-H_2O). Even treating the three amphibole species as distinct phases, the Gibbs phase rule suggests that the system had multiple unutilized degrees of freedom (8 – 7 + 2 = 3). Accordingly, there may be as yet unrecognized thermodynamic controls on the development of the Mt. Ochi veins that restricted the veins from crystallizing a more diverse mineral speciation. Possible mechanisms may include a favourable interfacial energy for crystallization on the clinopyroxene-dominated vein substrate, or factors imposing a crystallization regime strongly limited by growth-favoured crystallization (Carlson, 2010). Further, a poor understanding of mobility and diffusion parameters for Al, an element of direct significance to the crystallizing phases in the Mt. Ochi veins, may pose an additional barrier to understanding the mechanisms governing that system (e.g., Manning, 2006; Kelly et al., 2013). Determining experimental mineral solubility data are a critical next step in progressing our understanding of metamorphic systems, in both HP-LT settings and more broadly.

The principal implication of Chapter 4 is that there may be other cryptic occurrences of apparently blueschist facies rocks whose mineral assemblages have been mediated by processes like those inferred to have produced the Mt. Ochi veins. However, the Mt. Ochi veins are an especially conspicuous example. Differential interaction with retrogressive fluids is often invoked to explain the otherwise inscrutable contrast between zones of strong greenschist facies overprint and those with well-preserved HP-LT parageneses. If retrogressive fluid systems are established episodically at different stages of exhumation, then they may produce both blueschist and greenschist facies retrograde parageneses, depending on fluid chemistry. A better understanding of

the underlying processes, particularly if reactive transport and fluid chemistry routinely meaningfully alter the stable PT window for the blueschist facies index minerals, would allow for more accurate estimation of the geometries of post-peak retrogradation in exhuming HP-LT terranes.

5.5. References

Armstrong, R. L., Jäger, E., & Eberhardt, P. (1966). A comparison of K-Ar and Rb-Sr ages on Alpine biotites. Earth and Planetary Science Letters, 1(1), 13-19.

Augier, R., Jolivet, L., Gadenne, L., Lahfid, A., & Driussi, O. (2015). Exhumation kinematics of the Cycladic Blueschists unit and back-arc extension, insight from the Southern Cyclades (Sikinos and Folegandros Islands, Greece). Tectonics, 34(1), 152-185.

Avigad, D., Ziv, A., & Garfunkel, Z. (2001). Ductile and brittle shortening, extension-parallel folds and maintenance of crustal thickness in the central Aegean (Cyclades, Greece). Tectonics, 20(2), 277-287.

Azimov, P. Y., & Bushmin, S. A. (2007). Solubility of minerals of metamorphic and metasomatic rocks in hydrothermal solutions of varying acidity: thermodynamic modeling at 400–800 C and 1–5 kbar. Geochemistry International, 45, 1210-1234.

Bakowsky, C., Schneider, D. A., Grasemann, B., & Soukis, K. (2023). Miocene ductile thinning below the Folegandros Detachment System, Cyclades, Greece. Terra Nova, 35(3), 220-229.

Bosse, V., Féraud, G., Ballèvre, M., Peucat, J. J., & Corsini, M. (2005). Rb–Sr and $^{40}Ar/^{39}Ar$ ages in blueschists from the Ile de Groix (Armorican Massif, France): Implications for closure mechanisms in isotopic systems. Chemical Geology, 220(1-2), 21-45.

Bröcker, M., & Franz, L. (1998). Rb–Sr isotope studies on Tinos Island (Cyclades, Greece): additional time constraints for metamorphism, extent of infiltration-controlled overprinting and deformational activity. Geological Magazine, 135(3), 369-382.

Brocker, M., & Franz, L. (2005). The base of the Cycladic blueschist unit on Tinos Island (Greece) re-visited: Field relationships, phengite chemistry and Rb-Sr geochronology. Neues Jahrbuch fur Mineralogie-Abhandlungen, 181(1), 81-94.

Carlson, W. D. (2011). Porphyroblast crystallization: linking processes, kinetics, and microstructures. International Geology Review, 53(3-4), 406-445.

Coleman, M. J., Schneider, D. A., Grasemann, B., Soukis, K., Lozios, S., & Hollinetz, M. S. (2020). Lateral termination of a Cycladic-style detachment system (Hymittos, Greece). Tectonics, 39(9), e2020TC006128.

Dubois, R. & Bignot, G. (1979). Présence d'un ‘hardground’ nummulitique au de la série Cretacée d'Almyropotamos (Eubée méridionale, Grèce). Comptes Rendus de l'Académie des Sciences, Série II, 289, 993–995.

Fagereng, Å. (2013). On stress and strain in a continuous-discontinuous shear zone undergoing simple shear and volume loss. Journal of Structural Geology, 50, 44-53.

Fagereng, Å., & Sibson, R. H. (2010). Mélange rheology and seismic style. Geology, 38(8), 751-754.

Forster, M. A., & Lister, G. S. (1999). Detachment faults in the Aegean core complex of Ios, Cyclades, Greece. Geological Society, London, Special Publications, 154(1), 305-323.

Gautier, P., & Brun, J. P. (1994). Ductile crust exhumation and extensional detachments in the central Aegean (Cyclades and Evvia Islands). Geodinamica Acta, 7(2), 57-85

Gerogiannis, N., Aravadinou, E., Chatzaras, V., & Xypolias, P. (2021). Calcite pseudomorphs after aragonite: A tool to unravel the structural history of high-pressure marbles (Evia Island, Greece). Journal of Structural Geology, 148, 104373.

Glorie, S., Gillespie, J., Simpson, A., Gilbert, S., Khudoley, A., Priyatkina, N., ... & Kirkland, C. L. (2022). Detrital apatite Lu–Hf and U–Pb geochronology applied to the southwestern Siberian margin. Terra Nova, 34(3), 201-209.

Grasemann, B., Schneider, D. A., Stöckli, D. F., & Iglseder, C. (2012). Miocene bivergent crustal extension in the Aegean: Evidence from the western Cyclades (Greece). Lithosphere, 4(1), 23-39.

Grasemann, B., Huet, B., Schneider, D. A., Rice, A. H. N., Lemonnier, N., & Tschegg, C. (2018). Miocene postorogenic extension of the Eocene synorogenic imbricated Hellenic subduction channel: New constraints from Milos (Cyclades, Greece). GSA Bulletin, 130(1-2), 238-262.

Gyomlai, T., Agard, P., Herviou, C., Jolivet, L., Monié, P., Mendes, K., & Iemmolo, A. (2023). In situ Rb–Sr and ^{40}Ar–^{39}Ar dating of distinct mica generations in the exhumed subduction complex of the Western Alps. Contributions to Mineralogy and Petrology, 178(9), 58.

Holland, T. J. (1980). The reaction albite= jadeite+ quartz determined experimentally in the range 600–1200 C. American Mineralogist, 65(1-2), 129-134.

Huet, B., Labrousse, L., & Jolivet, L. (2009). Thrust or detachment? Exhumation processes in the Aegean: Insight from a field study on Ios (Cyclades, Greece). Tectonics, 28(3).

Huet, B., Labrousse, L., Monie, P., Malvoisin, B., & Jolivet, L. (2015). Coupled phengite ^{40}Ar–^{39}Ar geochronology and thermobarometry: PTt evolution of Andros Island (Cyclades, Greece). Geological Magazine, 152(4), 711-727.

Jacobshagen, V. (1986). Geologie von Griechland. Borntraeger, Berlin-Stuttgart, p. 279.

Johnson, T. A., Vervoort, J. D., Ramsey, M. J., Aleinikoff, J. N., & Southworth, S. (2018). Constraints on the timing and duration of orogenic events by combined Lu–Hf and Sm–Nd geochronology: an example from the Grenville orogeny. Earth and Planetary Science Letters, 501, 152-164.

Jolivet, L., & Patriat, M. (1999). Ductile extension and the formation of the Aegean Sea. Geological Society, London, Special Publications, 156(1), 427-456.

Jolivet, L., & Brun, J. P. (2010). Cenozoic geodynamic evolution of the Aegean. International Journal of Earth Sciences, 99, 109-138.

Jolivet, L., Famin, V., Mehl, C., Parra, T., Aubourg, C., Hébert, R., et al. (2004). Strain localization during crustal-scale boudinage to form extensional metamorphic domes in the Aegean Sea. Geological Society of America, Special Papers, 185-210.

Jolivet, L., Lecomte, E., Huet, B., Denèle, Y., Lacombe, O., Labrousse, L., et al. (2010). The north cycladic detachment system. Earth and Planetary Science Letters, 289(1-2), 87-104.

Katsikatsos, G. (1991a). Geological map of Greece, Aliveri sheet. Institute of Geological Mining Research (IGME), Athens.

Katsikatsos, G. (1991b). Geological map of Greece, Rafina sheet. Institute of Geological Mining Research (IGME), Athens.

Katzir, Y., Avigad, D., Matthews, A., Garfunkel, Z., & Evans, B. W. (2000). Origin, HP/LT metamorphism and cooling of ophiolitic mélanges in southern Evia (NW Cyclades), Greece. Journal of Metamorphic Geology, 18(6), 699-718.

Kelly, E. D., Carlson, W. D., & Ketcham, R. A. (2013). Crystallization kinetics during regional metamorphism of porphyroblastic rocks. Journal of Metamorphic Geology, 31(9), 963-979.

Larson, K. P., Button, M., Shrestha, S., & Camacho, A. (2023). A comparison of $^{87}Rb/^{87}Sr$ and $^{40}Ar/^{39}Ar$ dates: Evaluating the problem of excess ^{40}Ar in Himalayan mica. Earth and Planetary Science Letters, 609, 118058.

Leah, H., Fagereng, Å., Groome, N., Buchs, D., Eijsink, A., & Niemeijer, A. (2022). Heterogeneous subgreenschist deformation in an exhumed sediment-poor mélange. Journal of Geophysical Research: Solid Earth, 127(8), e2022JB024353.

Lecomte, E., Jolivet, L., Lacombe, O., Denèle, Y., Labrousse, L., & Le Pourhiet, L. (2010). Geometry and kinematics of Mykonos detachment, Cyclades, Greece: Evidence for slip at shallow dip. Tectonics, 29(5).

Liu, J., & Bohlen, S. R. (1995). Mixing properties and stability of jadeite-acmite pyroxene in the presence of albite and quartz. Contributions to Mineralogy and Petrology, 119, 433-440.

Manning, C. E. (2006). Mobilizing aluminum in crustal and mantle fluids. Journal of Geochemical Exploration, 89(1-3), 251-253.

Manzotti, P., Ballèvre, M., Pitra, P., Putlitz, B., Robyr, M., & Müntener, O. (2020). The growth of sodic amphibole at the greenschist-to blueschist-facies transition (Dent Blanche, Western Alps): bulk-rock chemical control and thermodynamic modelling. Journal of Petrology, 61(4), egaa044.

Maruyama, S., Liou, J. G., & Terabayashi, M. (1996). Blueschists and eclogites of the world and their exhumation. International Geology Review, 38(6), 485-594.

Menzel, M. D., Garrido, C. J., & Sánchez-Vizcaíno, V. L. (2020). Fluid-mediated carbon release from serpentinite-hosted carbonates during dehydration of antigorite-serpentinite in subduction zones. Earth and Planetary Science Letters, 531, 115964.

Mizera, M., & Behrmann, J. H. (2016). Strain and flow in the metamorphic core complex of Ios Island (Cyclades, Greece). International Journal of Earth Sciences, 105, 2097-2110.

Muñoz-Montecinos, J., Angiboust, S., Cambeses, A., & García-Casco, A. (2020). Multiple veining in a paleo–accretionary wedge: The metamorphic rock record of prograde dehydration and transient high pore-fluid pressures along the subduction interface (Western Series, central Chile). Geosphere, 16(3), 765-786.

Poulaki, E. M., Stockli, D. F., Flansburg, M. E., & Soukis, K. (2019). Zircon U-Pb chronostratigraphy and provenance of the Cycladic Blueschist Unit and the nature of the contact with the Cycladic Basement on Sikinos and Ios Islands, Greece. Tectonics, 38(10), 3586-3613.

Ring, U., & Reischmann, T. (2002). The weak and superfast Cretan detachment, Greece: exhumation at subduction rates in extruding wedges. Journal of the Geological Society, 159(3), 225-228.

Ring, U., & Layer, P. W. (2003). High-pressure metamorphism in the Aegean, eastern Mediterranean: Underplating and exhumation from the Late Cretaceous until the Miocene to Recent above the retreating Hellenic subduction zone. Tectonics, 22(3)

Ring, U., Brandon, M. T., Willett, S. D., & Lister, G. S. (1999). Exhumation processes. Geological Society, London, Special Publications, 154(1), 1-27.

Ring, U., Glodny, J., Will, T., & Thomson, S. (2007). An Oligocene extrusion wedge of blueschist-facies nappes on Evia, Aegean Sea, Greece: implications for the early exhumation of high-pressure rocks. Journal of the Geological Society, 164(3), 637-652.

Rösel, D., & Zack, T. (2022). LA-ICP-MS/MS Single-Spot Rb-Sr Dating. Geostandards and Geoanalytical Research, 46(2), 143-168.

Schermer, E. R., Lux, D. R., & Burchfiel, B. C. (1990). Temperature-time history of subducted continental crust, Mount Olympos Region, Greece. Tectonics, 9(5), 1165-1195.

Schneider, J., Bosch, D., & Monie, P. (2008). Individualization of textural and reactional microdomains in eclogites from the Bergen Arcs (Norway): Consequences for Rb/Sr and Ar/Ar radiochronometer behavior during polymetamorphism. Geochemistry, Geophysics, Geosystems, 9(12).

Schneider, D. A., Senkowski, C., Vogel, H., Grasemann, B., Iglseder, C., & Schmitt, A. K. (2011). Eocene tectonometamorphism on Serifos (western Cyclades) deduced from

zircon depth-profiling geochronology and mica thermochronology. Lithos, 125(1-2), 151-172.

Shaked, Y., Avigad, D., & Garfunkel, Z. (2000). Alpine high-pressure metamorphism at the Almyropotamos window (southern Evia, Greece). Geological Magazine, 137(4), 367-380.

Sherlock, S., Kelley, S., Inger, S., Harris, N., & Okay, A. (1999). ^{40}Ar-^{39}Ar and Rb-Sr geochronology of high-pressure metamorphism and exhumation history of the Tavsanli Zone, NW Turkey. Contributions to Mineralogy and Petrology, 137, 46-58.

Tschegg, C., & Grasemann, B. (2009). Deformation and alteration of a granodiorite during low-angle normal faulting (Serifos, Greece). Lithosphere, 1(3), 139-154.

Tulley, C. J., Fagereng, Å., Ujiie, K., Diener, J. F. A., & Harris, C. (2022). Embrittlement within viscous shear zones across the base of the subduction thrust seismogenic zone. Geochemistry, Geophysics, Geosystems, 23(9), e2021GC010208.

Xypolias, P., Kokkalas, S., & Skourlis, K. (2003). Upward extrusion and subsequent transpression as a possible mechanism for the exhumation of HP/LT rocks in Evia Island (Aegean Sea, Greece). Journal of Geodynamics, 35(3), 303-332.

Xypolias, P., Spanos, D., Chatzaras, V., Kokkalas, S., & Koukouvelas, I. (2010). Vorticity of flow in ductile thrust zones: examples from the Attico-Cycladic Massif (Internal Hellenides, Greece). Geological Society, London, Special Publications, 335(1), 687-714.

Xypolias, P., Iliopoulos, I., Chatzaras, V., & Kokkalas, S. (2012). Subduction-and exhumation-related structures in the Cycladic Blueschists: Insights from south Evia Island (Aegean region, Greece). Tectonics, 31(2).

Ziv, A., Katzir, Y., Avigad, D., & Garfunkel, Z. (2010). Strain development and kinematic significance of the Alpine folding on Andros (western Cyclades, Greece). Tectonophysics, 488(1-4), 248-255.

APPENDICES

APPENDIX A. Supporting Information for Chapter 2

Introduction

The supplementary file contains detailed analytical methodologies and unabridged pseudosections (**Figures S1-S3** below). Additional supporting figures provide photomicrographs of white mica textures from samples dated using $^{40}Ar/^{39}Ar$ geochronology (**Figure S4**), and plots of zircon (U-Th)/He (ZHe) date vs. effective uranium (eU) and effective spherical radius (ESR) for all dated zircon grains (**Figure S5**). Tabulated data files for the whole-rock geochemistry (**Table S1**) and mineral chemical analyses (**Table S2**) used for thermodynamic modelling, $^{40}Ar/^{39}Ar$ analytical data (**Table S3**), and ZHe analytical data (**Table S4**) are available in the appendix below.

Text S2.1. Sample preparation

Conventional procedures were used to extract and select the most appropriate minerals from rock samples in preparation for (U-Th)/He and $^{40}Ar/^{39}Ar$ dating. Each sample was cleaned with a wire brush and water to remove any surface contamination. The sample was allowed to air dry and was then crushed to a size fraction of ≤1 cm with the use of a standard jaw crusher. The material was then passed through a series of sieves to obtain grain size fractions >250 µm, 63-250 µm and <63 µm. The 63-250 µm fraction was then rinsed through a decantation process to remove any remaining fine powder adhering to the grains and dried for 24 h at a temperature of 30°C using a heat lamp. Heavy mineral separation was then conducted using methylene iodide (SG: 3.3 g/cm^3) in order to obtain a more concentrated fraction of zircon. White mica was obtained from the >250 µm size fraction using a mortar and pestle to further crush the sample while preserving the integrity of the mica. Samples were sieved to obtain a 150 µm-250 µm size fraction. In the case of white mica and zircon grains were then picked using tweezers under a binocular microscope.

Text S2.2. Thermodynamic modelling

S2.2.1. Whole-rock geochemistry

Major element geochemistry was determined for three samples by X-ray fluorescence (XRF) spectrometry at the X-ray Core Facility at the University of Ottawa. Finely powdered rock samples were mixed with an in-house lithium borate flux (78.5/20.5 $Li_2B_4O_7/LiBO_2$). Samples were then fused in a Claisse M4 Gas Fusion Fluxer to produce compositionally homogeneous glass beads. Resultant materials were then analyzed using a Rigaku SuperMini200 WDXRF. A set of 12 reference materials were used for the analyses and included UB-N, UM-2, MRG-1, PM-s, BCR-2, WS-E, SY-3, BHVO-2, BM, AN-G, BCR-032, PC-1016.

S2.2.2. Scanning Electron Microscopy (SEM)

Scanning electron microscopy was performed at the University of Ottawa using a JEOL 6610LV SEM. Backscatter electron imaging and exploratory electron dispersive spectroscopy (EDS) were carried out with an accelerating voltage of 15 kV and a working distance of 11 mm on standard 30 µm thick polished thin sections.

S2.2.3. Electron Microprobe (EMPA)

Mineral chemistry of petrologically significant phases was analyzed via electron microprobe (EMPA). Analyses were performed at University of Ottawa using a JEOL JXA-8230 SuperProbe, and at Uppsala University using a JEOL JXA-8530F Hyperprobe Field Emission Electron EPMA. Mineral phases of interest, including amphibole, white mica, plagioclase, pumpellyite, biotite, lawsonite, and epidote were quantitatively analyzed using a beam diameter ranging from 1 to 10 µm with an accelerating voltage of 15 keV and beam current of 20 nA. Dwell times of 10 s were used for X-ray peak positions and 5 s for background positions. Wavelength dispersive spectroscopy (WDS) acquired quantitative chemical data for the major and minor elements Si, Al, Ca, Mg, Fe, K, Na, Ti, Cr, and Mn. The laboratory standards used at University of Ottawa were sanidine (Si, Al, K), diopside (Ca, Mg), hematite (Fe), albite

(Na), rutile (Ti), chromite (Cr), and tephroite (Mn); and at Uppsala University were pyrope (Si, Mg), wollastonite (Si, Ca), Al_2O_3 (Al), MgO (Mg), fayalite (Fe), orthoclase (K), albite (Na), pyrophanite (Ti, Mn), Cr_2O_3 (Cr), apatite (P, F), and vanadinite (F, Cl).

Mineral formulae were recalculated using the AX software (Holland, 2018) for each phase on the basis of stoichiometric oxygen contents of 8 O for plagioclase and lawsonite, 11 O for biotite, 14 O for chlorite, and 24.5 O for pumpellyite, and 12.5 O for epidote. White mica compositions were recalculated manually on the basis of 11 O, following the methodology of Vidal & Parra (2000) and Parra et al. (2002), accepting only analyses with weight percent oxide sums between 92-96% and with < 0.5 wt.% TiO_2 + MnO + CaO. Recalculations assumed 11 oxygens and calculated molar fractions for seven end-members (Mg- and Fe-Al-celadonite, muscovite, annite, phlogopite, paragonite, pyrophyllite). Amphibole recalculations were performed using the methodology of Locock (2014), assuming 22 O excluding the W site, and following the IMA 2012 nomenclature for the amphibole supergroup (Hawthorne et al., 2012). All recalculations yielded best results using assumptions of Σ13eCa and Σ15eNK for determination of ferric and ferrous iron content. All mineral chemical data and associated formula recalculations may be found in **Table S2**.

S2.2.4. Solution Models

Pseudosection modelling was conducted using Perple_X version 6.9.1, with the internally consistent thermodynamic dataset hp62ver.dat (Holland and Powell, 2011). Solid solution models used in the calculation of all pseudosections included:

i) white mica, chlorite, garnet, and chloritoid after White et al. (2014);
ii) biotite after White et al. (2014), modified by Holland et al. (2018);
iii) amphibole after Diener and Powell (2011) for EV19-03 and EV19-10 and after Green et al. (2016) for EV19-17 (the solution models were chosen based on amphibole composition);
iv) plagioclase, ternary feldspar, and epidote after Holland and Powell (1998);
v) ilmenite after White et al. (2000), modified by White et al. (2014);
vi) omphacite after Green et al. (2007);
vii) pumpellyite and stilpnomelane *ad-hoc* model after Holland and Powell (2011).

S2.2.5. Sample EV19-10

The P-T pseudosection for glaucophane schist Sample EV19-10 was calculated in the Na_2O-MgO-Al_2O_3-SiO_2-K_2O-CaO-TiO_2-FeO-O_2 system with saturated H_2O. An O_2 fugacity of 0.05 was chosen for the modelling, as this amount of O_2 best stabilized the mineral assemblage observed in the thin section and the chemical composition of the major mineral phases. The O_2 estimation was based initially on a P-O_2 pseudosection (not presented here). Larger quantities of O_2 stabilized clinopyroxene (omphacite/jadeite), which was not observed in the sample. In the final calculated PT pseudosection (**Figure S2**) with O_2 = 0.05, the stability field most accurately representing the mineral assemblage of Sample EV19-10 contains omphacite/jadeite at very low modal abundance (<2 vol. %). Two possibilities for this discrepancy could be either that Jadeite was broken down to albite + quartz (major minerals in the sample), or was present but not detected in the rock or studied thin section.

S2.2.6. Sample EV19-17C

Sample 19-17C is an albite-mica schist collected 3 km east of the town of Zarakes (**Figure 2**). The sample mineralogy consists of white mica + albite + chlorite + quartz + titanite (**Figure 5d**). Sparse inclusions of ferroglaucophane (X_{Mg}: 0.44–0.49) and rutile in albite porphyroblasts allude to an earlier HP paragenesis. White mica and subordinate chlorite define a penetrative foliation with local intrafolial folding. Porphyroblasts of titanite and albite (An_{0-2}) are common. Foliation-concordant bands of an unidentified fine-grained, dark blue to black material are preserved inside albite and are locally continuous with folding preserved in the groundmass, indicating albite was stabilized during or shortly following ductile deformation. White mica defining foliation is phengitic (Si apfu: 3.42–3.50; XMg:

0.67–0.70), whereas an early muscovitic generation (Si apfu: 3.14–3.30; XMg: 0.53–0.68) is preserved in albite. Two varieties of chlorite were observed. The first is represented by more ordinary compositions ranging from brunsvigite to pycnochlorite. The second is an Al- and Si-rich species resembling sudoite (Wiewióra & Weiss, 1990; Lanari et al., 2014) that is present both as large grains within the foliation and as inclusions in quartz and albite (**Figure 6b, Table S2**).

Modelling in the Na_2O-MgO-Al_2O3-SiO_2-K_2O-CaO-TiO_2-FeO system yields a peak pressure of 10 ± 1 kbar and peak temperatures of 520 ± 20°C. Models were hindered by the unconstrained thermodynamic properties of the sudoite-like phase. The chlorite group mineral in sample EV19-17C has approximately equal proportions of Al and Si (3.29–3.61 apfu Al, 3.42–3.52 apfu Si), with a dominance of Mg over Fe^{2+} in the octahedral sites (0.81–1.24 apfu Mg vs. 0.42–0.67 apfu Fe^{2+}; total octahedral site occupancy: 1.41–1.65). The approximate formula $Al_3(Mg,Fe^{2+})_{1.5}\square(Si_{3.5}Al_{0.5})O_{10}(OH)_8$ does not satisfy electroneutrality, but its Na content (0.32–0.52 apfu) may plausibly offset this. The mineral most closely resembles sudoite (ideal formula: $Al_3(Mg,Fe^{2+})_2\square(Si_3Al)O_{10}(OH)_8$; Wiewióra & Weiss, 1990); however, Na substitution into chlorite is observed elsewhere only in alkaline intrusions (Krivovichev et al., 2004). Inclusions rich in Al were not observed during petrographic characterization, but contamination remains a petrologically plausible explanation. The thermodynamic properties for the sudoite subgroup of Lanari et al. (2014) were applied during modelling, but the calculated stability field nevertheless indicates implausibly high temperatures for the geologic context and assemblages observed.

Text S2.3. $^{40}Ar/^{39}Ar$ geochronology

Once samples were picked and characterized, $^{40}Ar/^{39}Ar$ analytical work was performed at the University of Manitoba (Winnipeg, Canada) using a multi-collector Thermo Fisher Scientific ARGUS VI mass spectrometer, linked to a stainless steel Thermo Fisher Scientific extraction/purification line and Photon Machines (55 W) Fusions 10.6 CO_2 laser. Argon isotopes (from mass 40 to 37) were measured using Faraday detectors with low noise 1 x 10^{13} Ω resistors and mass 36 was measured using a compact discrete dynode detector. The sensitivity for argon measurements is ~6.312 x 10^{17} moles/fA as determined from measured aliquots of Fish Canyon Sanidine (Dazé et al., 2003; Kuiper et al., 2008).

Standards and unknowns were placed in 2 mm deep wells in 18 mm diameter aluminum disks, with standards placed strategically so that the lateral neutron flux gradients across the disk could be evaluated. Planar regressions were fit to the standard data, and the $^{40}Ar/^{39}Ar$ neutron fluence parameter, J, interpolated for the unknowns. Uncertainties in J are estimated at 0.1-0.2% (1s), based on Monte Carlo error analysis of the planar regressions (Best et al., 1995). All specimens were irradiated in the cadmium-lined, in-core CLICIT facility of the Oregon State University TRIGA reactor. The duration of irradiation was 12 h and using the Fish Canyon sanidine (Kuiper et al., 2008) and GA1550 biotite (Spell and McDougall, 2003) standards.

Irradiated samples were placed in a Cu sample tray, with a KBr cover slip, in a stainless steel high vacuum extraction line and baked with an infrared lamp for 24 h. Single crystals were either fused or step-heated using the laser, and reactive gases were removed, after ~3 min, by three GP-50 SAES getters (two at room temperature and one at 450°C) prior to being admitted to an ARGUS VI mass spectrometer by expansion. Five argon isotopes were measured simultaneously over a period of 6 min. Measured isotope abundances were corrected for extraction-line blanks, which were determined before every sample analysis. Line blanks averaged ~5 fA for mass 40 and ~0.022 fA for mass 36.

Mass discrimination was monitored by online analysis of air pipettes, which gave during two separate sessions mean of D: 1.0063 ± 0.0001 and D: 1.0089 ± 0.0005 per amu, based on 67 aliquots interspersed with the unknowns. A value of 295.5 was used for the atmospheric $^{40}Ar/^{36}Ar$ ratio (Steiger and Jäger, 1977) for the purposes of routine measurement of mass spectrometer discrimination using air aliquots, and correction for atmospheric argon in the $^{40}Ar/^{39}Ar$ age calculation. Corrections are made for neutron-induced ^{40}Ar from potassium, ^{39}Ar and ^{36}Ar from calcium, and ^{36}Ar from chlorine (Roddick, 1983; Renne et al., 1998; Renne and Norman, 2001). Results are reported in **Table S1**.

S2.4. (U-Th)/He geochronology

The analytical portion of the (U-Th)/He experiments was conducted at the TRaIL (Thermochronology Research and Instrumentation Laboratory) facility at the University of Colorado (Boulder, USA). Individual mineral grains are handpicked using a Leica M165 binocular microscope equipped with a calibrated digital camera and capable of both reflected and transmitted, polarized light. The grains are screened for quality, including crystal shape and the presence of inclusions. The dimensions of the crystals are measured and converted to equivalent spherical radius (ESR) as this value is more readily incorporated into the equations that govern the diffusion of He throughout the grain; from this point forward in the paper references to grain size are measurements of ESR. After characterization, grains are placed into small Nb tubes that are then crimped on both ends. This Nb packet is then loaded into an ASI Alphachron He extraction and measurement line. The packet is placed in the UHV extraction line (~$3x10^{-8}$ torr) and heated with a diode laser to ~800-1100°C for 5 to 10 m to extract the radiogenic ^{4}He. The degassed ^{4}He is then spiked with approximately 13 ncc of pure ^{3}He, cleaned via interaction with two SAES getters, and analyzed on a Balzers PrismaPlus QME 220 quadrupole mass spectrometer. Degassed grains are then removed from the line, and taken to a Class 10 clean lab for dissolution. Zircon are dissolved using Parr large-capacity dissolution vessels in a multi-step acid-vapor dissolution process. Grains (including the Nb tube) are placed in Ludwig-style Savillex vials, spiked with a ^{235}U-^{230}Th tracer, and mixed with 200 µl of Optima grade HF. The vials are then capped, stacked in a 125 mL Teflon liner, placed in a Parr dissolution vessel, and baked at 220°C for 72 h. After cooling, the vials are uncapped and dried down on a 90°C hot plate until dry. The vials then undergo a second round of acid-vapor dissolution, this time with 200 µl of Optima grade HCl in each vial that is baked at 200°C for 24 h. Vials are then dried down a second time on a hot plate. Once dry, 200 µl of a 7:1 HNO_3:HF mixture is added to each vial, the vial is capped, and cooked on the hot plate at 90°C for 4 h. Once the minerals are dissolved, regardless of the dissolution process, they are diluted with 1 to 3 mL of doubly-deionized water, and taken to the ICP-MS lab for analysis. Mineral standards of Durango apatite (31.5 Ma) and Fish Canyon Tuff zircon (28.2 Ma) are routinely analyzed (degassed and dissolved) in conjunction with the samples with each run to ensure data integrity. Sample solutions, along with standards and blanks, are analyzed for U, Th, and Sm content using a Thermo Element 2 magnetic sector mass spectrometer. Once the U, Th, and Sm contents have been measured, He dates and all associated data are calculated on a custom spreadsheet made by TRaIL staff. Results are presented in **Table 1** of the manuscript, with detailed analytical data reported in **Table S4**.

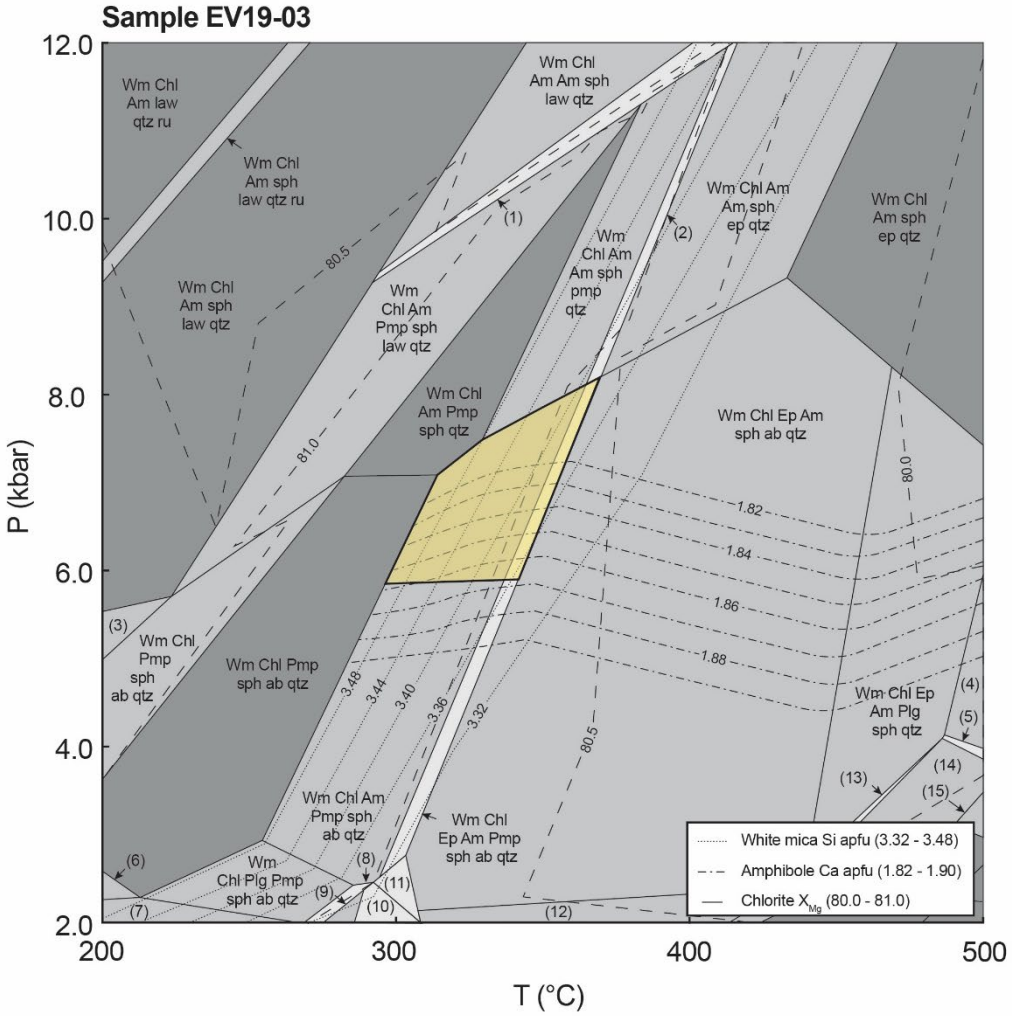

(1) Wm Chl Am Am law sph qtz
(2) Wm Chl Ep Am Am Pmp sph qtz
(3) Wm Chl Am law sph ab q
(4) Wm Chl Am Am Plg sph qtz
(5) Wm Chl Am Am Plg Plg sph qtz
(6) Wm Chl Pmp sph ab qtz heu
(7) Wm Chl Pmp sph ab heu
(8) Wm Chl Pmp Plg sph prh ab qtz
(9) Wm Chl Plg sph prh ab qtz
(10) Wm Chl Ep Plg sph prh ab qtz
(11) Wm Chl Ep Am sph prh ab qtz
(12) Wm Chl Ep Am Plg sph ab qtz
(13) Wm Chl Ep Am Plg Plg sph qtz
(14) Wm Chl Am Plg Plg sph qtz
(15) Wm Chl Plg Plg sph phl qtz

Figure S2.1.
Complete pseudosection calculated for Sample EV19-03, an albite-pumpellyite schist modeled in the Na_2O-MgO-Al_2O3-SiO_2-K_2O-CaO-TiO_2-MnO-FeO system, calculated under water-saturated conditions.

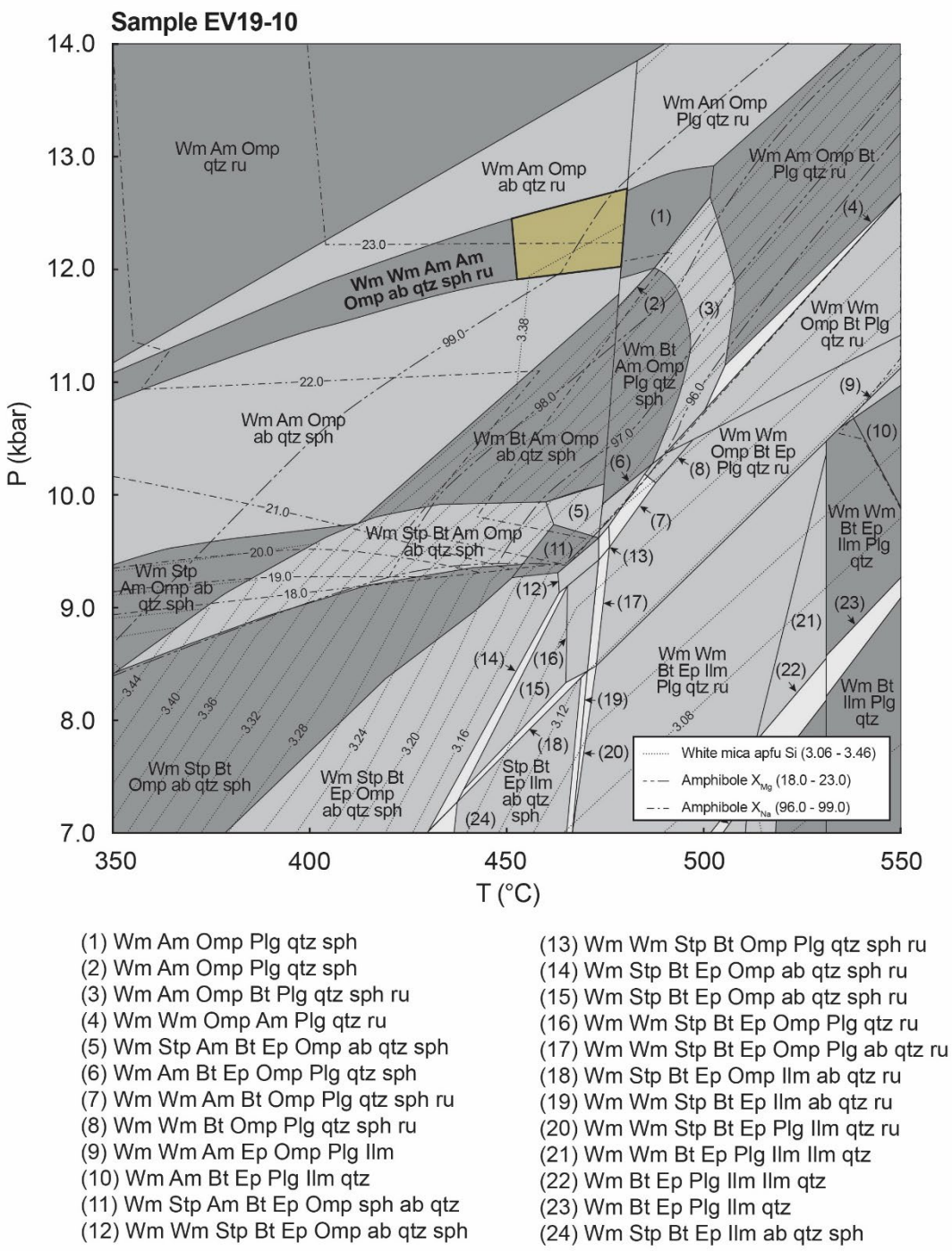

(1) Wm Am Omp Plg qtz sph
(2) Wm Am Omp Plg qtz sph
(3) Wm Am Omp Bt Plg qtz sph ru
(4) Wm Wm Omp Am Plg qtz ru
(5) Wm Stp Am Bt Ep Omp ab qtz sph
(6) Wm Am Bt Ep Omp Plg qtz sph
(7) Wm Wm Am Bt Omp Plg qtz sph ru
(8) Wm Wm Bt Omp Plg qtz sph ru
(9) Wm Wm Am Ep Omp Plg Ilm
(10) Wm Am Bt Ep Plg Ilm qtz
(11) Wm Stp Am Bt Ep Omp sph ab qtz
(12) Wm Wm Stp Bt Ep Omp ab qtz sph
(13) Wm Wm Stp Bt Omp Plg qtz sph ru
(14) Wm Stp Bt Ep Omp ab qtz sph ru
(15) Wm Stp Bt Ep Omp ab qtz sph ru
(16) Wm Wm Stp Bt Ep Omp Plg qtz ru
(17) Wm Wm Stp Bt Ep Omp Plg ab qtz ru
(18) Wm Stp Bt Ep Omp Ilm ab qtz ru
(19) Wm Wm Stp Bt Ep Ilm ab qtz ru
(20) Wm Wm Stp Bt Ep Plg Ilm qtz ru
(21) Wm Wm Bt Ep Plg Ilm Ilm qtz
(22) Wm Bt Ep Plg Ilm Ilm qtz
(23) Wm Bt Ep Plg Ilm qtz
(24) Wm Stp Bt Ep Ilm ab qtz sph

Figure S2.2.
Complete pseudosection calculated for Sample EV19-10, a glaucophane schist modeled in the Na_2O-MgO-Al_2O3-SiO_2-K_2O-CaO-TiO_2-FeO-O_2 system, calculated under water-saturated conditions.

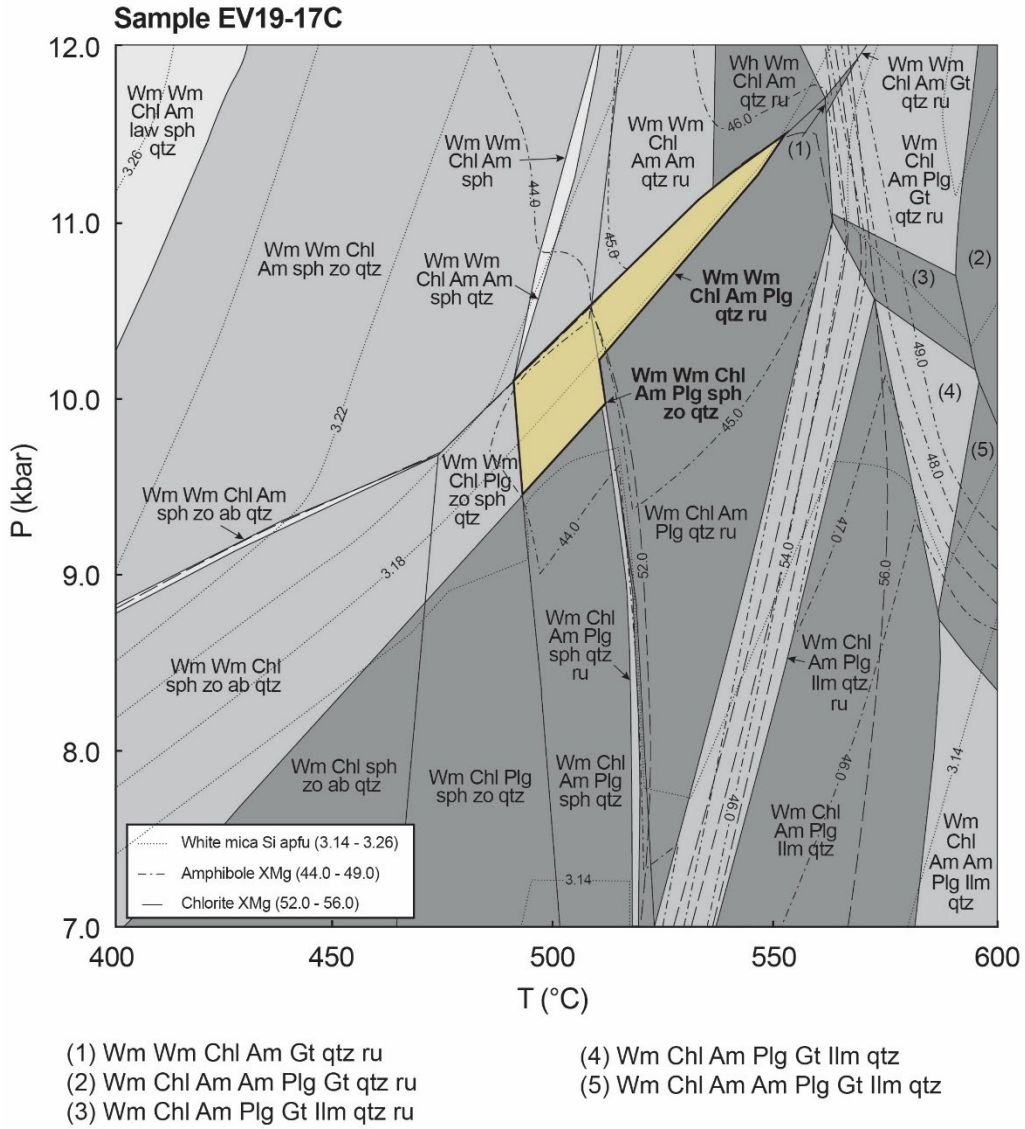

(1) Wm Wm Chl Am Gt qtz ru
(2) Wm Chl Am Am Plg Gt qtz ru
(3) Wm Chl Am Plg Gt Ilm qtz ru
(4) Wm Chl Am Plg Gt Ilm qtz
(5) Wm Chl Am Am Plg Gt Ilm qtz

Figure S2.3.
Complete pseudosection calculated for Sample EV19-17C, an albite-mica schist modeled in the Na_2O-MgO-Al_2O3-SiO_2-K_2O-CaO-TiO_2-MnO-FeO system, calculated under water-saturated conditions.

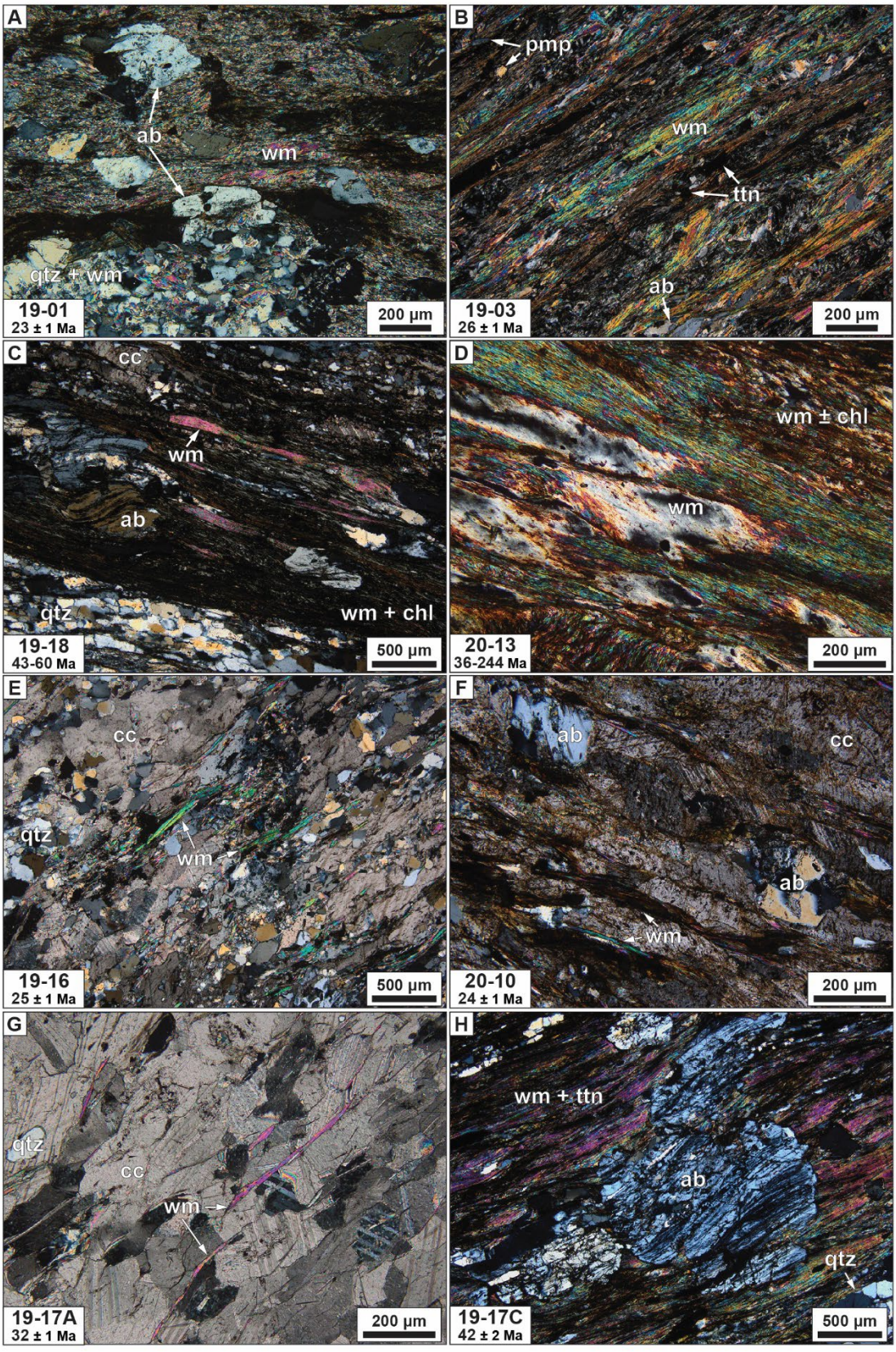
A
ab
wm
qtz + wm
19-01
23 ± 1 Ma
200 µm
B
pmp
wm
ttn
ab
19-03
26 ± 1 Ma
200 µm
C
cc
wm
ab
qtz
wm + chl
19-18
43-60 Ma
500 µm
D
wm ± chl
wm
20-13
36-244 Ma
200 µm
E
cc
qtz
wm
19-16
25 ± 1 Ma
500 µm
F
ab
cc
ab
wm
20-10
24 ± 1 Ma
200 µm
G
qtz
cc
wm
19-17A
32 ± 1 Ma
200 µm
H
wm + ttn
ab
qtz
19-17C
42 ± 2 Ma
500 µm

Figure S2.4.
(Previous page) Representative photomicrographs of white mica from select samples analyzed using white mica $^{40}Ar/^{39}Ar$ geochronology. (A, B) Phyllonitic (A) and schistose (B) samples from the boundary of the tectonic window. White mica from both samples record late Oligocene to early Miocene $^{40}Ar/^{39}Ar$ ages with minimal dispersion. (C, D) Samples from the uppermost exposed levels of Basal Unit near the eastern limits tectonic window. Both samples preserve scattered single-grain age populations with anomalously old ages. (C) Large optically continuous single grains align with the fine-grained micaceous foliation but show minimal evidence for recrystallization. These may represent undeformed detrital grains. (D) A spaced crenulation cleavage divides two domains with contrasting optical orientation. White mica occupying the hinges of foliation-parallel folds may have experienced comparatively low strain and accordingly preserves inherited ages. (E) Single white mica crystals dispersed within the carbonate matrix of an impure schistose marble from the Basal Unit south of Nea Styra. White mica is oriented parallel to a weak shape preferred orientation (SPO) developed in the carbonate minerals. (F) Seams of fine-grained white mica defining foliation within an impure schistose marble sampled from an intercalated marble cobble conglomerate horizon. Carbonate minerals display a more strongly developed SPO than in E. (G, H) Marble and albite-mica schist sampled from an outcrop exposing a contact between the two lithologies. Despite the comparatively greater extent of recrystallization of white mica in the schist, white mica in the marble records younger $^{40}Ar/^{39}Ar$ ages. Mineral abbreviations after Whitney and Evans (2010).

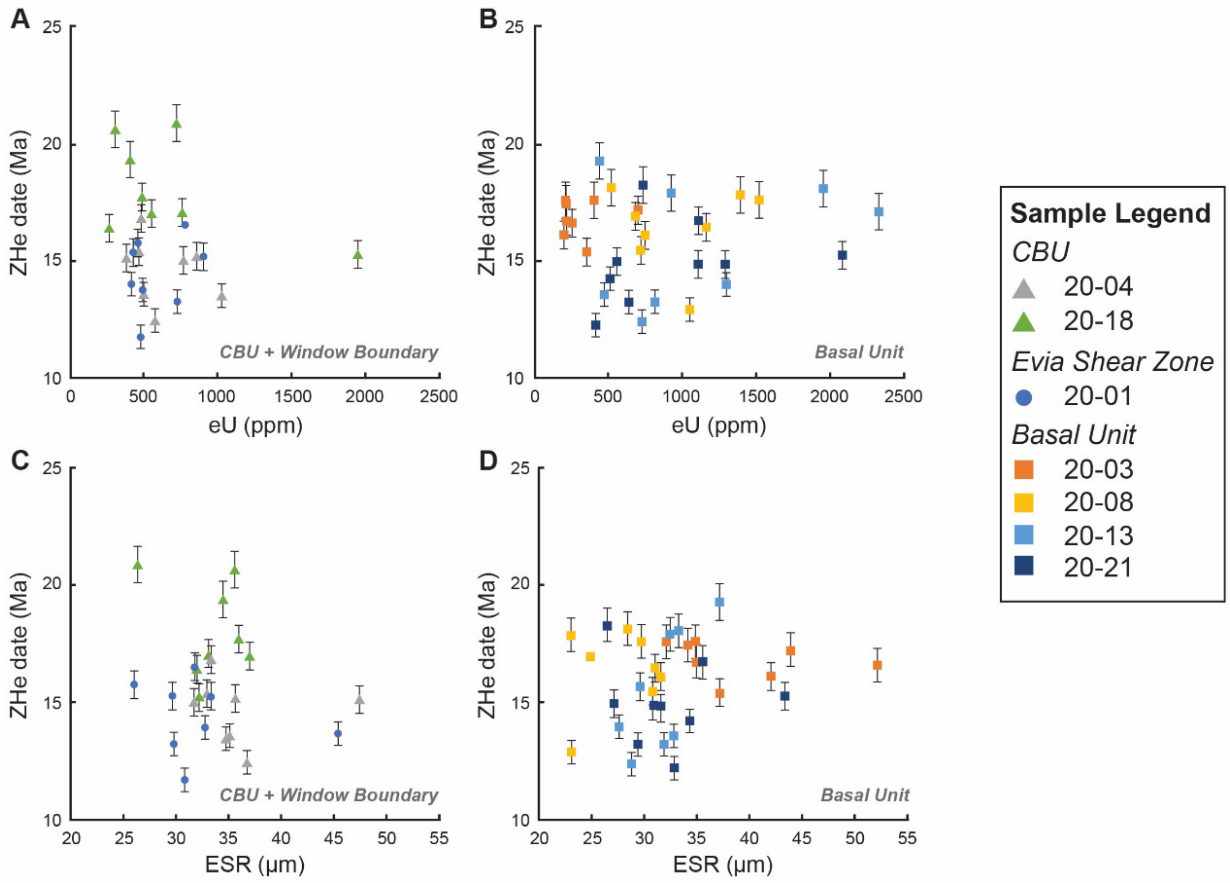

Figure S2.5.
Zircon (U-Th)/He (ZHe) date vs eU (A, B) and vs effective spherical radius (ESR; C, D) plots for samples analyzed from the CBU, Basal Unit, and the Evia Shear Zone. Neither eU nor grain size exerts a discernible control on ZHe ages recorded at the sample scale. Sample locations may be found in **Figure 8** of the manuscript.

Table S2.1.
Whole-rock geochemical data from samples from southern Evia (Greece) used for thermodynamic modelling.

Table S2.2.
Electron microprobe mineral chemistry analyses from samples from southern Evia (Greece) used for thermodynamic modelling.

Table S2.3.
Analytical results for white mica total fusion $^{40}Ar/^{39}Ar$ geochronology for samples from southern Evia (Greece).

Table S2.4.
Analytical results for zircon (U-Th)/He geochronology for samples from from southern Evia (Greece).

Table S2.1. Whole-rock geochemical data from samples from southern Evia (Greece) used for thermodynamic modelling.

Element (wt.% oxide)	**EV19-03** albite-pumpelleyite schist **Basal Unit** (Tsakei Unit)	**EV19-10** glaucophane schist **CBU** (Ochi Unit)	**EV19-17C** albite-mica schist **Basal Unit** (Tsakei Unit)
SiO_2	43.68	74.49	51.69
TiO_2	0.19	0.26	0.90
Al_2O_3	20.23	12.57	17.57
Fe_2O_3	0.10	n.a.	n.a.
FeO	5.93	3.31	6.43
MnO	0.15	0.00	0.00
MgO	13.57	0.62	3.76
CaO	2.91	0.26	0.78
Na_2O	0.39	6.22	1.34
K_2O	4.32	1.10	3.59
P_2O_5	0.00	0.00	0.00
H_2O	7.50	0.68	4.04
Total	98.96	99.51	90.10

Table S2.2a. Electron microprobe results and formula recalculations for white micafrom southern Evia (Greece) used for thermodynamic modelling.

EV19-03 albite-pumpellyite schist																							
Analysis	1	2	3	4	5	6	7	8	9	10	11	12	13	14	15	16	17	18	19	20	21	22	23
Min	mu	mu	mu	mu	mu	mu	mu	mu	mu	mu	mu	mu	mu	mu	mu	mu	mu	mu	mu	mu	mu	mu	mu
Facility	University of Ottawa																			Uppsala University			
SiO_2	52.87	51.79	51.44	51.72	51.71	51.35	52.43	50.71	48.72	50.23	52.42	50.91	51.87	52.66	53.36	47.95	51.36	51.21	50.89	50.77	51.66	47.67	52.21
TiO_2	0.04	0.04	0.03	0.04	0.06	0.03	0.05	0.02	0.18	0.04	0.03	0.05	0.03	0.04	0.06	0.03	0.03	0.02	0.08	0.00	0.00	0.07	0.03
Al_2O_3	26.01	27.72	28.13	27.54	26.45	28.72	25.60	27.58	31.75	29.13	26.31	29.00	27.16	26.53	24.78	33.25	27.43	27.80	29.43	28.42	25.95	35.48	27.08
Cr_2O_3	0.02	0.13	0.01	0.03	0.02	0.00	0.00	0.16	0.00	0.00	0.05	0.00	0.19	0.02	0.00	0.02	0.00	0.00	0.01	0.07	0.14	0.07	0.05
FeO	1.26	1.19	1.06	1.27	1.34	1.03	1.15	1.21	0.89	1.14	1.27	0.94	1.13	1.30	1.31	0.68	1.16	1.08	0.84	1.17	1.16	0.48	0.85
MnO	0.01	0.02	0.02	0.01	0.03	0.00	0.02	0.01	0.00	0.00	0.01	0.01	0.03	0.02	0.04	0.01	0.01	0.02	0.00	0.01	0.03	0.03	0.04
MgO	4.48	3.94	3.79	4.02	4.11	3.58	4.51	4.15	2.40	3.81	4.28	3.55	4.06	4.34	4.76	1.86	3.88	3.87	3.04	3.62	4.08	1.00	4.13
CaO	0.01	0.02	0.01	0.02	0.01	0.02	0.01	0.03	0.05	0.00	0.01	0.01	0.02	0.02	0.01	0.01	0.02	0.03	0.27	0.01	0.02	0.01	0.02
Na_2O	0.17	0.16	0.19	0.18	0.21	0.16	0.13	0.15	0.20	0.18	0.22	0.17	0.19	0.22	0.15	0.29	0.14	0.19	0.13	0.16	0.21	0.45	0.16
K_2O	10.92	10.95	11.05	10.95	10.92	10.99	10.88	11.07	10.77	11.06	10.87	10.88	10.84	10.63	10.97	10.77	10.99	11.01	10.67	11.04	10.20	10.45	10.55
Totals	95.79	95.96	95.73	95.78	94.86	95.88	94.78	95.09	94.96	95.65	95.47	95.52	95.52	95.78	95.44	94.87	95.02	95.23	95.35	95.28	93.44	95.71	95.12
Oxygens	11	11	11	11	11	11	11	11	11	11	11	11	11	11	11	11	11	11	11	11	11	11	11
Si	3.49	3.41	3.40	3.42	3.45	3.38	3.50	3.38	3.24	3.33	3.47	3.37	3.43	3.47	3.54	3.19	3.42	3.40	3.36	3.38	3.48	3.13	3.46
Ti	0.00	0.00	0.00	0.00	0.00	0.00	0.00	0.00	0.01	0.00	0.00	0.00	0.00	0.00	0.00	0.00	0.00	0.00	0.00	0.00	0.00	0.00	0.00
Al	2.02	2.15	2.19	2.14	2.08	2.23	2.01	2.17	2.49	2.28	2.05	2.26	2.12	2.06	1.94	2.61	2.15	2.18	2.29	2.23	2.06	2.75	2.11
Cr	0.00	0.01	0.00	0.00	0.00	0.00	0.00	0.01	0.00	0.00	0.00	0.00	0.01	0.00	0.00	0.00	0.00	0.00	0.00	0.00	0.01	0.00	0.00
Fe^{3+}	0.00	0.00	0.00	0.00	0.00	0.00	0.00	0.00	0.00	0.00	0.00	0.00	0.00	0.00	0.00	0.00	0.00	0.00	0.00	0.00	0.00	0.00	0.00
Fe^{2+}	0.07	0.07	0.06	0.07	0.07	0.06	0.06	0.07	0.05	0.06	0.07	0.05	0.06	0.07	0.07	0.04	0.06	0.06	0.05	0.07	0.07	0.03	0.05
Mn	0.00	0.00	0.00	0.00	0.00	0.00	0.00	0.00	0.00	0.00	0.00	0.00	0.00	0.00	0.00	0.00	0.00	0.00	0.00	0.00	0.00	0.00	0.00
Mg	0.44	0.39	0.37	0.40	0.41	0.35	0.45	0.41	0.24	0.38	0.42	0.35	0.40	0.43	0.47	0.18	0.39	0.38	0.30	0.36	0.41	0.10	0.41
Ca	0.00	0.00	0.00	0.00	0.00	0.00	0.00	0.00	0.00	0.00	0.00	0.00	0.00	0.00	0.00	0.00	0.00	0.00	0.02	0.00	0.00	0.00	0.00
Na	0.02	0.02	0.02	0.02	0.03	0.02	0.02	0.02	0.03	0.02	0.03	0.02	0.02	0.03	0.02	0.04	0.02	0.02	0.02	0.02	0.03	0.06	0.02
K	0.92	0.92	0.93	0.92	0.93	0.92	0.93	0.94	0.91	0.94	0.92	0.92	0.92	0.89	0.93	0.91	0.93	0.93	0.90	0.94	0.88	0.88	0.89
Si (T1+T2)	3.49	3.41	3.40	3.42	3.45	3.38	3.50	3.38	3.24	3.33	3.47	3.37	3.43	3.47	3.54	3.19	3.42	3.40	3.36	3.38	3.48	3.13	3.46
Ti (T2)	0.00	0.00	0.00	0.00	0.00	0.00	0.00	0.00	0.01	0.00	0.00	0.00	0.00	0.00	0.00	0.00	0.00	0.00	0.00	0.00	0.00	0.00	0.00
Al(IV) (T2)	0.51	0.58	0.60	0.58	0.54	0.61	0.50	0.62	0.75	0.67	0.53	0.63	0.56	0.53	0.46	0.81	0.58	0.60	0.63	0.62	0.52	0.86	0.54
Al(VI) (M2)	1.51	1.57	1.59	1.56	1.54	1.62	1.51	1.55	1.74	1.61	1.53	1.63	1.55	1.53	1.47	1.80	1.57	1.58	1.66	1.60	1.54	1.89	1.57
Mg (M2)	0.42	0.37	0.35	0.37	0.39	0.33	0.43	0.38	0.21	0.34	0.40	0.32	0.39	0.40	0.46	0.16	0.36	0.36	0.29	0.34	0.39	0.09	0.39
Fe (M2)	0.07	0.06	0.06	0.07	0.07	0.05	0.06	0.06	0.04	0.06	0.07	0.05	0.06	0.07	0.07	0.03	0.06	0.06	0.05	0.06	0.06	0.02	0.04
Fe + Mg (M2)	0.49	0.43	0.41	0.44	0.46	0.38	0.49	0.45	0.26	0.39	0.47	0.37	0.45	0.47	0.53	0.20	0.43	0.42	0.34	0.40	0.46	0.11	0.43
Mn (M2)	0.00	0.00	0.00	0.00	0.00	0.00	0.00	0.00	0.00	0.00	0.00	0.00	0.00	0.00	0.00	0.00	0.00	0.00	0.00	0.00	0.00	0.00	0.00
Mg (M1)	0.02	0.02	0.02	0.03	0.02	0.02	0.02	0.03	0.02	0.04	0.02	0.03	0.02	0.03	0.01	0.02	0.02	0.02	0.01	0.02	0.02	0.01	0.02
Fe (M1)	0.00	0.00	0.00	0.00	0.00	0.00	0.00	0.00	0.01	0.01	0.00	0.00	0.00	0.00	0.00	0.00	0.00	0.00	0.00	0.00	0.00	0.00	0.00
vac (M1)	0.98	0.98	0.98	0.97	0.98	0.97	0.98	0.97	0.97	0.95	0.98	0.97	0.98	0.97	0.98	0.98	0.98	0.98	0.99	0.97	0.98	0.99	0.98
K (A)	0.92	0.92	0.93	0.92	0.93	0.92	0.93	0.94	0.91	0.94	0.92	0.92	0.92	0.89	0.93	0.91	0.93	0.93	0.90	0.94	0.88	0.88	0.89
Na (A)	0.02	0.02	0.02	0.02	0.03	0.02	0.02	0.02	0.03	0.02	0.03	0.02	0.02	0.03	0.02	0.04	0.02	0.02	0.02	0.02	0.03	0.06	0.02
vac (A)	0.06	0.06	0.04	0.05	0.04	0.06	0.06	0.04	0.06	0.04	0.05	0.06	0.06	0.08	0.05	0.05	0.05	0.04	0.08	0.04	0.10	0.07	0.09
Paragonite	0.02	0.02	0.02	0.02	0.03	0.02	0.02	0.02	0.03	0.02	0.03	0.02	0.02	0.03	0.02	0.04	0.02	0.02	0.02	0.02	0.03	0.06	0.02
Phlogopite	0.02	0.02	0.02	0.03	0.02	0.02	0.02	0.03	0.02	0.04	0.02	0.03	0.02	0.03	0.01	0.02	0.02	0.02	0.01	0.02	0.02	0.01	0.02
Annite	0.00	0.00	0.00	0.00	0.00	0.00	0.00	0.00	0.01	0.01	0.00	0.00	0.00	0.00	0.00	0.00	0.00	0.00	0.00	0.00	0.00	0.00	0.00
Mg-Celadonite	0.40	0.33	0.33	0.33	0.37	0.31	0.41	0.31	0.18	0.27	0.38	0.29	0.35	0.37	0.44	0.14	0.34	0.33	0.28	0.30	0.38	0.08	0.37
Fe-Celadonite	0.06	0.06	0.05	0.06	0.07	0.05	0.06	0.05	0.04	0.04	0.06	0.04	0.05	0.06	0.07	0.03	0.06	0.05	0.04	0.05	0.06	0.02	0.04
Pyrophyllite	0.06	0.06	0.04	0.05	0.04	0.06	0.06	0.04	0.06	0.04	0.05	0.06	0.06	0.08	0.05	0.05	0.05	0.04	0.08	0.04	0.10	0.07	0.09
Muscovite	0.43	0.51	0.53	0.50	0.47	0.54	0.43	0.54	0.66	0.58	0.45	0.55	0.49	0.43	0.40	0.72	0.51	0.53	0.57	0.56	0.42	0.76	0.45
X_{Mg}	0.86	0.86	0.86	0.85	0.85	0.86	0.87	0.86	0.83	0.86	0.86	0.87	0.86	0.86	0.87	0.83	0.86	0.86	0.87	0.85	0.86	0.79	0.90

Table S2.2a cont.

EV19-10 - glaucophane schist											
Analysis	1	2	3	4	5	6	7	8	9	10	11
Min	mu	mu	mu	mu	mu	mu	mu	mu	mu	mu	mu
Facility	Ottawa	Uppsala University									
SiO_2	48.57	53.41	51.86	51.33	52.13	51.80	51.82	51.69	52.71	52.66	51.77
TiO_2	0.11	0.11	0.13	0.11	0.06	0.00	0.08	0.04	0.16	0.05	0.13
Al_2O_3	21.83	22.78	24.00	22.58	23.47	23.97	24.74	24.88	24.84	23.22	24.37
Cr_2O_3	0.00	0.00	0.00	0.00	0.00	0.00	0.00	0.01	0.04	0.02	0.04
FeO	8.09	6.03	5.75	7.34	5.59	5.71	4.98	4.00	5.10	6.09	5.44
MnO	0.23	0.29	0.26	0.25	0.25	0.28	0.28	0.23	0.24	0.29	0.23
MgO	2.29	2.49	2.34	2.49	2.54	2.36	2.45	2.60	2.59	2.54	2.44
CaO	0.09	0.00	0.06	0.08	0.01	0.04	0.05	0.06	0.08	0.06	0.00
Na_2O	0.06	0.09	0.12	0.11	0.11	0.07	0.07	0.03	0.15	0.08	0.10
K_2O	10.76	10.76	10.29	9.24	10.59	10.48	10.02	10.66	9.32	9.71	10.25
Totals	92.25	95.97	94.81	93.86	94.75	94.71	94.49	94.19	95.32	94.79	94.77
Oxygens	11	11	11	11	11	11	11	11	11	11	11
Si	3.47	3.60	3.53	3.53	3.55	3.53	3.52	3.52	3.52	3.57	3.52
Ti	0.01	0.01	0.01	0.01	0.00	0.00	0.00	0.00	0.01	0.00	0.01
Al	1.84	1.81	1.93	1.83	1.89	1.93	1.98	1.99	1.96	1.86	1.95
Cr	0.00	0.00	0.00	0.00	0.00	0.00	0.00	0.00	0.00	0.00	0.00
Fe^{3+}	0.12	0.00	0.00	0.18	0.00	0.00	0.00	0.00	0.05	0.04	0.00
Fe^{2+}	0.37	0.34	0.33	0.25	0.32	0.33	0.28	0.23	0.24	0.31	0.31
Mn	0.01	0.02	0.01	0.01	0.01	0.02	0.02	0.01	0.01	0.02	0.01
Mg	0.24	0.25	0.24	0.25	0.26	0.24	0.25	0.26	0.26	0.26	0.25
Ca	0.01	0.00	0.00	0.01	0.00	0.00	0.00	0.00	0.01	0.00	0.00
Na	0.01	0.01	0.02	0.01	0.01	0.01	0.01	0.00	0.02	0.01	0.01
K	0.98	0.93	0.89	0.81	0.92	0.91	0.87	0.92	0.80	0.84	0.89
Si (T1+T2)	3.47	3.60	3.53	3.53	3.55	3.53	3.52	3.52	3.52	3.57	3.52
Ti (T2)	0.01	0.01	0.01	0.01	0.00	0.00	0.00	0.00	0.01	0.00	0.01
Al(IV) (T2)	0.53	0.39	0.46	0.47	0.44	0.47	0.48	0.48	0.47	0.43	0.48
Al(VI) (M2)	1.31	1.41	1.46	1.36	1.44	1.46	1.50	1.51	1.49	1.43	1.48
Mg (M2)	0.24	0.25	0.23	0.25	0.25	0.23	0.23	0.26	0.26	0.26	0.23
Fe (M2)	0.37	0.34	0.31	0.25	0.31	0.31	0.27	0.23	0.24	0.31	0.29
Fe + Mg (M2)	0.69	0.59	0.54	0.64	0.56	0.54	0.50	0.49	0.51	0.57	0.52
Mn (M2)	0.01	0.02	0.01	0.01	0.01	0.02	0.02	0.01	0.01	0.02	0.01
Mg (M1)	0.00	0.00	0.01	0.00	0.01	0.01	0.01	0.00	0.00	0.00	0.01
Fe (M1)	0.00	0.00	0.02	0.00	0.01	0.01	0.02	0.00	0.00	0.00	0.02
vac (M1)	1.00	1.00	0.97	1.00	0.98	0.98	0.97	1.00	1.00	1.00	0.97
K (A)	0.98	0.93	0.89	0.81	0.92	0.91	0.87	0.92	0.80	0.84	0.89
Na (A)	0.01	0.01	0.02	0.01	0.01	0.01	0.01	0.00	0.02	0.01	0.01
v (A)	0.01	0.06	0.09	0.18	0.06	0.08	0.12	0.07	0.19	0.15	0.10
Paragonite	0.01	0.01	0.02	0.01	0.01	0.01	0.01	0.00	0.02	0.01	0.01
Phlogopite	0.00	0.00	0.01	0.00	0.01	0.01	0.01	0.00	0.00	0.00	0.01
Annite	0.00	0.00	0.02	0.00	0.01	0.01	0.02	0.00	0.00	0.00	0.02
Mg-Celadonite	0.19	0.24	0.21	0.23	0.23	0.21	0.21	0.26	0.23	0.23	0.21
Fe-Celadonite	0.28	0.33	0.28	0.22	0.29	0.28	0.24	0.22	0.21	0.27	0.26
Pyrophyllite	0.01	0.06	0.09	0.18	0.06	0.08	0.12	0.07	0.19	0.15	0.10
Muscovite	0.51	0.35	0.38	0.37	0.38	0.39	0.38	0.44	0.35	0.34	0.38
X_{Mg}	0.40	0.42	0.42	0.51	0.45	0.42	0.47	0.54	0.52	0.45	0.44

Table S2.2a cont.

EV19-17C - albite-mica schist																						
Analysis	1	2	3	4	5	6	7	8	9	10	11	12	13	14	15	16	17	18	19	20	21	22
Min	mu	mu	mu	mu	mu	mu	mu	mu	mu	mu	mu	mu	mu	mu	mu	mu	mu	mu	mu	mu	mu	mu
Facility					University of Ottawa											Uppsala University						
SiO_2	48.39	48.76	48.56	46.06	48.77	48.17	49.77	51.23	50.45	49.83	49.71	47.11	53.69	51.09	52.75	52.31	52.62	53.03	50.20	49.45	52.26	52.52
TiO_2	0.11	0.16	0.07	0.22	0.07	0.10	0.10	0.06	0.07	0.08	0.13	0.82	0.02	0.11	0.12	0.09	0.06	0.14	0.10	0.47	0.05	0.15
Al_2O_3	26.15	22.80	25.81	28.68	26.09	25.80	26.53	26.03	24.50	25.30	31.36	32.11	27.03	28.13	23.83	26.20	26.32	26.89	27.00	30.59	26.88	26.28
Cr_2O_3	0.02	0.04	0.06	-	0.02	0.03	0.01	0.07	0.05	0.06	0.10	-	0.03	0.04	0.01	0.04	0.07	0.04	0.09	0.01	0.02	0.03
FeO	2.37	4.17	3.58	3.13	2.31	2.85	2.30	2.45	2.60	2.55	1.80	3.73	2.44	2.02	3.37	2.31	2.48	2.32	1.96	2.96	2.41	2.57
MnO	0.02	0.03	0.04	0.02	0.01	0.08	0.03	0.03	-	0.03	0.01	0.02	0.01	0.03	0.04	0.00	0.00	0.04	-	0.03	0.05	0.03
MgO	3.10	4.71	4.05	1.94	2.99	3.02	3.07	3.31	3.51	3.36	1.93	1.29	3.43	2.81	3.98	3.35	3.32	3.21	2.78	1.91	3.34	3.35
CaO	0.04	0.33	0.53	0.25	0.32	0.25	0.19	0.42	0.33	0.27	0.10	-	0.49	0.28	0.41	0.01	0.17	0.27	0.04	0.05	0.50	0.30
Na_2O	0.24	0.09	0.12	0.56	0.17	0.12	0.14	0.14	0.11	0.13	0.27	0.61	0.19	0.19	0.24	0.13	0.11	0.13	0.14	0.18	0.26	0.07
K_2O	10.73	8.35	7.69	8.08	9.15	8.74	9.13	7.72	8.54	8.53	8.31	9.63	8.40	8.91	8.65	10.11	9.74	8.96	9.68	9.94	8.51	8.42
Totals	95.66	93.94	95.05	93.46	94.44	93.69	95.83	96.03	94.73	94.68	93.72	95.31	95.72	93.61	93.40	94.56	94.89	95.03	91.99	95.59	94.27	93.71
Oxygens	11	11	11	11	11	11	11	11	11	11	11	11	11	11	11	11	11	11	11	11	11	11
Si	3.39	3.47	3.39	3.28	3.43	3.42	3.44	3.50	3.52	3.48	3.31	3.16	3.51	3.42	3.56	3.49	3.50	3.50	3.44	3.28	3.48	3.51
Ti	0.01	0.01	0.00	0.01	0.00	0.01	0.01	0.00	0.00	0.00	0.01	0.04	0.00	0.01	0.01	0.00	0.00	0.01	0.01	0.02	0.00	0.01
Al	2.16	1.91	2.12	2.40	2.16	2.16	2.16	2.09	2.01	2.08	2.46	2.54	2.08	2.22	1.90	2.06	2.06	2.09	2.18	2.39	2.11	2.07
Cr	0.00	0.00	0.00	0.00	0.00	0.00	0.00	0.00	0.00	0.00	0.01	0.00	0.00	0.00	0.00	0.00	0.00	0.00	0.00	0.00	0.00	0.00
Fe^{3+}	0.00	0.00	0.00	0.00	0.00	0.00	0.00	0.00	0.00	0.00	0.00	0.00	0.00	0.00	0.00	0.00	0.00	0.00	0.00	0.00	0.00	0.00
Fe^{2+}	0.14	0.25	0.21	0.19	0.14	0.17	0.13	0.14	0.15	0.15	0.10	0.21	0.13	0.11	0.19	0.13	0.14	0.13	0.11	0.16	0.13	0.14
Mn	0.00	0.00	0.00	0.00	0.00	0.00	0.00	0.00	0.00	0.00	0.00	0.00	0.00	0.00	0.00	0.00	0.00	0.00	0.00	0.00	0.00	0.00
Mg	0.32	0.50	0.42	0.21	0.31	0.32	0.32	0.34	0.36	0.35	0.19	0.13	0.33	0.28	0.40	0.33	0.33	0.32	0.28	0.19	0.33	0.33
Ca	0.00	0.03	0.04	0.02	0.02	0.02	0.01	0.03	0.03	0.02	0.01	0.00	0.03	0.02	0.03	0.00	0.01	0.02	0.00	0.00	0.04	0.02
Na	0.03	0.01	0.02	0.08	0.02	0.02	0.02	0.02	0.01	0.02	0.04	0.08	0.02	0.03	0.03	0.02	0.01	0.02	0.02	0.02	0.03	0.01
K	0.96	0.76	0.68	0.73	0.82	0.79	0.80	0.67	0.76	0.76	0.71	0.82	0.70	0.76	0.75	0.86	0.83	0.75	0.85	0.84	0.72	0.72
Si (T1+T2)	3.39	3.47	3.39	3.28	3.43	3.42	3.44	3.50	3.52	3.48	3.31	3.16	3.51	3.42	3.56	3.49	3.50	3.50	3.44	3.28	3.48	3.51
Ti (T2)	0.01	0.01	0.00	0.01	0.00	0.01	0.01	0.00	0.00	0.00	0.01	0.04	0.00	0.01	0.01	0.00	0.00	0.01	0.01	0.02	0.00	0.01
Al(IV) (T2)	0.60	0.52	0.61	0.71	0.57	0.58	0.56	0.50	0.48	0.52	0.68	0.80	0.49	0.57	0.43	0.50	0.50	0.49	0.55	0.69	0.52	0.48
Al(VI) (M2)	1.56	1.40	1.52	1.69	1.59	1.58	1.60	1.59	1.54	1.56	1.78	1.74	1.59	1.65	1.47	1.56	1.56	1.60	1.63	1.70	1.59	1.58
Mg (M2)	0.31	0.40	0.32	0.16	0.28	0.27	0.28	0.29	0.33	0.31	0.15	0.10	0.30	0.25	0.36	0.32	0.31	0.29	0.27	0.16	0.30	0.29
Fe (M2)	0.13	0.20	0.16	0.15	0.12	0.15	0.12	0.12	0.14	0.13	0.08	0.16	0.12	0.10	0.17	0.12	0.13	0.12	0.11	0.14	0.12	0.12
Fe + Mg (M2)	0.44	0.60	0.48	0.31	0.41	0.42	0.40	0.41	0.46	0.44	0.22	0.26	0.41	0.35	0.53	0.44	0.44	0.40	0.37	0.30	0.41	0.42
Mn (M2)	0.00	0.00	0.00	0.00	0.00	0.00	0.00	0.00	0.00	0.00	0.00	0.00	0.00	0.00	0.00	0.00	0.00	0.00	0.00	0.00	0.00	0.00
Mg (M1)	0.01	0.10	0.10	0.04	0.03	0.04	0.04	0.05	0.04	0.04	0.04	0.03	0.04	0.03	0.04	0.02	0.02	0.03	0.02	0.03	0.04	0.04
Fe (M1)	0.01	0.05	0.05	0.04	0.01	0.02	0.01	0.02	0.02	0.02	0.02	0.05	0.02	0.01	0.02	0.01	0.01	0.01	0.01	0.03	0.01	0.02
vac (M1)	0.98	0.86	0.85	0.92	0.96	0.93	0.95	0.93	0.95	0.94	0.93	0.92	0.95	0.96	0.94	0.97	0.97	0.96	0.98	0.94	0.95	0.94
K (A)	0.96	0.76	0.68	0.73	0.82	0.79	0.80	0.67	0.76	0.76	0.71	0.82	0.70	0.76	0.75	0.86	0.83	0.75	0.85	0.84	0.72	0.72
Na (A)	0.03	0.01	0.02	0.08	0.02	0.02	0.02	0.02	0.01	0.02	0.04	0.08	0.02	0.03	0.03	0.02	0.01	0.02	0.02	0.02	0.03	0.01
v (A)	0.01	0.23	0.30	0.19	0.16	0.19	0.18	0.31	0.23	0.22	0.26	0.10	0.28	0.21	0.22	0.12	0.16	0.23	0.14	0.13	0.24	0.27
Paragonite	0.03	0.01	0.02	0.08	0.02	0.02	0.02	0.02	0.01	0.02	0.04	0.08	0.02	0.03	0.03	0.02	0.01	0.02	0.02	0.02	0.03	0.01
Phlogopite	0.01	0.10	0.10	0.04	0.03	0.04	0.04	0.05	0.04	0.04	0.04	0.03	0.04	0.03	0.04	0.02	0.02	0.03	0.02	0.03	0.04	0.04
Annite	0.01	0.05	0.05	0.04	0.01	0.02	0.01	0.02	0.02	0.02	0.02	0.05	0.02	0.01	0.02	0.01	0.01	0.01	0.01	0.03	0.01	0.02
Mg-Celadonite	0.28	0.25	0.16	0.10	0.25	0.21	0.25	0.24	0.29	0.26	0.12	0.06	0.26	0.23	0.31	0.32	0.30	0.28	0.27	0.13	0.25	0.26
Fe-Celadonite	0.12	0.12	0.08	0.09	0.11	0.11	0.10	0.10	0.12	0.11	0.06	0.09	0.11	0.09	0.15	0.12	0.12	0.11	0.11	0.11	0.10	0.11
Pyrophyllite	0.01	0.23	0.30	0.19	0.16	0.19	0.18	0.31	0.23	0.22	0.26	0.10	0.28	0.21	0.22	0.12	0.16	0.23	0.14	0.13	0.24	0.27
Muscovite	0.54	0.25	0.29	0.46	0.43	0.40	0.40	0.26	0.30	0.33	0.45	0.59	0.28	0.40	0.23	0.40	0.37	0.32	0.45	0.55	0.32	0.28
X_{Mg}	0.70	0.67	0.67	0.52	0.70	0.65	0.70	0.71	0.71	0.70	0.66	0.38	0.71	0.71	0.68	0.72	0.70	0.71	0.72	0.53	0.71	0.70

Table S2.2b. Electron microprobe results and formula recalculations for chlorite from southern Evia (Greece) used for thermodynamic modelling.

EV19-03 - albite-pumpellyite schist																					
Analysis	1	2	3	4	5	6	7	8	9	10	11	12	13	14	15	16	17	18	19	20	21
Min	chl	chl	chl	chl	chl	chl	chl	chl	chl	chl	chl	chl	chl	chl	chl	chl	chl	chl	chl	chl	chl
Facility	University of Ottawa																	Uppsala University			
SiO_2	30.07	28.64	28.38	28.72	28.68	29.03	29.07	28.24	28.75	28.71	28.45	29.11	28.74	28.83	28.25	28.98	29.43	29.68	29.98	29.87	29.88
TiO_2	0.02	0.01	0.01	0.01	0.02	0.01	0.01	0.01	0.00	0.00	0.01	0.00	0.01	0.01	0.00	0.01	0.00	0.02	0.06	0.02	0.06
Al_2O_3	18.88	19.42	19.90	20.19	20.33	19.53	19.89	20.76	20.54	19.90	19.99	19.30	19.77	19.38	19.65	19.76	21.61	21.62	20.98	20.22	20.63
Cr_2O_3	0.04	0.02	0.18	0.00	0.00	0.02	0.03	0.00	0.00	0.07	0.03	0.04	0.04	0.05	0.00	0.01	0.04	0.01	0.00	0.15	0.24
FeO	11.14	10.91	11.42	11.17	11.29	11.27	11.61	11.16	10.63	11.90	11.30	11.46	11.71	11.46	12.03	11.74	11.18	10.88	10.93	12.06	10.89
MnO	0.26	0.23	0.23	0.23	0.19	0.25	0.26	0.18	0.17	0.26	0.22	0.26	0.27	0.26	0.24	0.25	0.26	0.20	0.22	0.31	0.14
MgO	25.09	25.60	23.81	24.36	24.49	25.94	24.55	25.13	25.01	24.82	25.27	25.68	25.19	25.41	24.43	25.02	24.64	25.14	24.79	24.86	25.57
CaO	0.67	0.08	0.10	0.05	0.04	0.01	0.11	0.02	0.02	0.04	0.03	0.04	0.01	0.04	0.02	0.06	0.33	0.60	0.41	0.12	0.09
Na_2O	0.02	0.06	0.02	0.01	0.01	0.00	0.01	0.00	0.02	0.02	0.01	0.04	0.00	0.00	0.01	0.00	0.00	0.02	0.02	0.00	0.00
K_2O	0.02	0.03	0.02	0.01	0.02	0.00	0.01	0.01	0.00	0.03	0.01	0.01	0.00	0.00	0.01	0.01	0.00	0.02	0.01	0.01	0.02
Totals	86.21	85.00	84.07	84.75	85.07	86.06	85.55	85.51	85.14	85.75	85.32	85.94	85.74	85.44	84.64	85.84	87.50	88.19	87.40	87.61	87.51
Oxygens	14.00	14.00	14.00	14.00	14.00	14.00	14.00	14.00	14.00	14.00	14.00	14.00	14.00	14.00	14.00	14.00	14.00	14.00	14.00	14.00	14.00
Si	2.98	2.88	2.89	2.89	2.88	2.88	2.91	2.82	2.87	2.87	2.85	2.90	2.87	2.89	2.87	2.89	2.87	2.87	2.92	2.92	2.90
Ti	0.00	0.00	0.00	0.00	0.00	0.00	0.00	0.00	0.00	0.00	0.00	0.00	0.00	0.00	0.00	0.00	0.00	0.00	0.01	0.00	0.00
Al	2.21	2.30	2.39	2.40	2.41	2.29	2.35	2.44	2.42	2.35	2.36	2.27	2.33	2.29	2.35	2.32	2.48	2.46	2.41	2.33	2.36
Cr	0.00	0.00	0.01	0.00	0.00	0.00	0.00	0.00	0.00	0.01	0.00	0.00	0.00	0.00	0.00	0.00	0.00	0.00	0.00	0.01	0.02
Fe^{3+}	0.00	0.00	0.00	0.00	0.00	0.00	0.00	0.00	0.00	0.00	0.00	0.00	0.00	0.00	0.00	0.00	0.00	0.00	0.00	0.00	0.00
Fe^{2+}	0.92	0.92	0.97	0.94	0.95	0.94	0.97	0.93	0.89	1.00	0.95	0.96	0.98	0.96	1.02	0.98	0.91	0.88	0.89	0.99	0.89
Mn	0.02	0.02	0.02	0.02	0.02	0.02	0.02	0.02	0.01	0.02	0.02	0.02	0.02	0.02	0.02	0.02	0.02	0.02	0.02	0.03	0.01
Mg	3.71	3.84	3.61	3.66	3.66	3.84	3.66	3.74	3.72	3.70	3.78	3.81	3.75	3.79	3.70	3.72	3.58	3.62	3.60	3.62	3.70
Ca	0.07	0.01	0.01	0.01	0.00	0.00	0.01	0.00	0.00	0.00	0.00	0.00	0.00	0.00	0.00	0.01	0.04	0.06	0.04	0.01	0.01
Na	0.00	0.01	0.00	0.00	0.00	0.00	0.00	0.00	0.00	0.00	0.00	0.01	0.00	0.00	0.00	0.00	0.00	0.00	0.01	0.00	0.00
K	0.00	0.00	0.00	0.00	0.00	0.00	0.00	0.00	0.00	0.00	0.00	0.00	0.00	0.00	0.00	0.00	0.00	0.00	0.00	0.00	0.00
Sum	9.92	9.98	9.91	9.91	9.92	9.97	9.92	9.96	9.92	9.96	9.97	9.97	9.96	9.96	9.96	9.95	9.89	9.91	9.88	9.91	9.90
X_{Mg}	0.80	0.81	0.79	0.80	0.79	0.80	0.79	0.80	0.81	0.79	0.80	0.80	0.79	0.80	0.78	0.79	0.80	0.80	0.80	0.79	0.81

Table S2.2b cont.

EV19-17C - glaucophane schist																	
Analysis	1	2	3	4	5	6	7	8	9	10	11	12	13	14	15	16	17
Min	chl	chl	chl	chl	chl	chl	chl	chl	chl	chl	chl	chl	chl	chl	chl	chl	chl
Facility	Uppsala University																
SiO_2	37.28	36.80	27.00	37.71	37.90	38.30	37.92	37.43	37.49	33.27	27.20	37.51	37.97	33.30	37.84	38.41	37.98
TiO_2	0.24	2.47	0.11	0.66	0.19	0.41	0.18	0.61	0.46	0.00	0.04	0.35	0.43	0.01	1.37	0.29	0.15
Al_2O_3	31.75	29.49	20.85	31.17	31.86	31.53	31.82	33.41	30.88	18.44	20.71	33.10	31.11	20.56	30.43	31.03	32.06
Cr_2O_3	0.02	0.04	0.31	0.15	0.08	0.03	0.05	0.01	0.01	0.00	0.06	0.02	0.10	0.05	0.04	0.10	0.01
FeO	8.22	7.85	24.82	7.10	7.58	7.18	7.64	5.69	8.61	18.62	23.57	7.74	7.41	19.17	7.86	5.43	7.50
MnO	0.03	0.02	0.24	0.04	0.02	0.05	0.00	0.05	0.00	0.18	0.29	0.00	0.00	0.18	0.00	0.09	0.07
MgO	6.11	7.08	14.92	7.00	6.77	7.38	6.88	7.37	6.90	13.56	16.47	5.88	7.07	13.20	6.99	9.08	6.70
CaO	0.01	0.09	0.00	0.04	0.00	0.06	0.02	0.79	0.01	1.60	0.00	0.04	0.03	1.37	0.04	0.50	0.01
Na_2O	2.37	2.70	0.15	2.76	2.60	2.74	2.62	1.82	2.89	0.18	0.10	2.07	2.62	0.12	2.81	2.45	2.65
K_2O	0.00	0.01	0.02	0.01	0.00	0.02	0.03	0.04	0.03	0.17	0.01	0.00	0.03	0.36	0.02	0.01	0.00
Totals	86.03	86.54	88.41	86.65	87.00	87.69	87.16	87.20	87.28	86.02	88.44	86.71	86.77	88.33	87.41	87.38	87.13
Oxygens	14.00	14.00	14.00	14.00	14.00	14.00	14.00	14.00	14.00	14.00	14.00	14.00	14.00	14.00	14.00	14.00	14.00
Si	3.49	3.45	2.81	3.50	3.50	3.51	3.50	3.42	3.49	3.40	2.81	3.47	3.52	3.31	3.50	3.51	3.50
Ti	0.02	0.17	0.01	0.05	0.01	0.03	0.01	0.04	0.03	0.00	0.00	0.02	0.03	0.00	0.10	0.02	0.01
Al	3.51	3.26	2.55	3.41	3.47	3.41	3.46	3.60	3.38	2.22	2.52	3.61	3.40	2.41	3.32	3.34	3.49
Cr	0.00	0.00	0.03	0.01	0.01	0.00	0.00	0.00	0.00	0.00	0.00	0.00	0.01	0.00	0.00	0.01	0.00
Fe^{3+}	0.00	0.00	0.00	0.00	0.00	0.00	0.00	0.00	0.00	0.00	0.00	0.00	0.00	0.00	0.00	0.00	0.00
Fe^{2+}	0.64	0.62	2.16	0.55	0.59	0.55	0.59	0.44	0.67	1.59	2.03	0.60	0.57	1.60	0.61	0.42	0.58
Mn	0.00	0.00	0.02	0.00	0.00	0.00	0.00	0.00	0.00	0.02	0.03	0.00	0.00	0.02	0.00	0.01	0.01
Mg	0.85	0.99	2.31	0.97	0.93	1.01	0.95	1.00	0.96	2.06	2.53	0.81	0.98	1.96	0.96	1.24	0.92
Ca	0.00	0.01	0.00	0.00	0.00	0.01	0.00	0.08	0.00	0.18	0.00	0.00	0.00	0.15	0.00	0.05	0.00
Na	0.43	0.49	0.03	0.50	0.47	0.49	0.47	0.32	0.52	0.04	0.02	0.37	0.47	0.02	0.50	0.43	0.47
K	0.00	0.00	0.00	0.00	0.00	0.00	0.00	0.01	0.00	0.02	0.00	0.00	0.00	0.05	0.00	0.00	0.00
Sum	8.95	8.99	9.91	8.99	8.98	9.00	8.99	8.90	9.05	9.52	9.94	8.89	8.98	9.51	9.00	9.02	8.98
X_{Mg}	0.57	0.62	0.52	0.64	0.61	0.65	0.62	0.70	0.59	0.56	0.55	0.57	0.63	0.55	0.61	0.75	0.61

Table S2.2c. Electron microprobe results and formula recalculations for amphibole from southern Evia (Greece) used for thermodynamic modelling.

EV19-03 - albite-pumpellyite schist																										
Analysis	1	2	3	4	5	6	7	8	9	10	11	12	13	14	15	16	17	18	19	20	21	22	23	24	25	26
Facility							University of Ottawa													Uppsala University						
SiO_2	57.84	58.47	58.24	58.45	59.05	58.82	58.50	58.13	49.97	52.43	58.44	58.32	58.29	58.44	58.34	58.27	58.26	57.66	57.97	58.48	58.22	58.37	58.49	58.39	57.73	58.03
TiO_2	0.00	0.00	0.02	0.02	0.01	0.00	0.00	0.00	1.08	0.58	0.00	0.01	0.00	0.00	0.00	0.03	0.00	0.00	0.00	0.04	0.00	0.05	0.00	0.01	0.01	0.08
Al_2O_3	0.70	0.69	0.78	0.41	0.50	0.41	0.56	0.57	6.85	4.44	0.46	0.27	0.60	0.37	0.67	0.65	0.66	0.66	0.49	0.58	0.98	0.46	0.61	0.49	0.50	0.65
Cr_2O_3	0.00	0.00	0.00	0.00	0.00	0.00	0.00	0.04	0.69	0.37	0.01	0.00	0.01	0.00	0.04	0.05	0.05	0.09	0.00	0.02	0.01	0.00	0.06	0.04	0.00	0.03
FeO	5.54	4.88	5.35	4.82	4.60	5.15	5.42	5.16	6.04	6.53	5.26	5.54	5.55	5.07	5.22	5.51	5.25	5.15	5.39	4.86	5.33	5.39	5.30	4.95	7.93	7.50
MnO	0.23	0.22	0.25	0.22	0.22	0.27	0.29	0.27	0.09	0.19	0.27	0.31	0.25	0.25	0.26	0.33	0.25	0.27	0.25	0.22	0.23	0.28	0.23	0.20	0.12	0.13
MgO	20.26	20.68	20.55	21.02	21.25	20.77	20.48	20.63	18.41	18.02	20.57	20.43	20.48	20.76	21.00	20.30	20.57	20.49	20.64	20.89	20.61	20.79	20.55	21.01	19.01	18.75
CaO	12.77	12.36	12.39	12.94	12.58	12.23	12.08	12.38	12.47	11.86	12.27	12.43	12.31	12.55	12.93	12.57	12.44	12.25	12.43	12.63	12.67	12.66	12.36	12.83	12.52	12.68
Na_2O	0.37	0.62	0.45	0.32	0.54	0.76	0.80	0.53	1.26	1.16	0.62	0.53	0.62	0.53	0.35	0.53	0.72	0.67	0.51	0.39	0.55	0.48	0.55	0.42	0.31	0.47
K_2O	0.04	0.11	0.06	0.02	0.05	0.12	0.11	0.05	0.02	0.07	0.09	0.09	0.07	0.05	0.03	0.13	0.06	0.06	0.08	0.06	0.08	0.04	0.10	0.05	0.03	0.05
P_2O_5	0.10	0.06	0.09	0.10	0.11	0.09	0.08	0.10	0.11	0.10	0.08	0.10	0.09	0.09	n.a.	n.a.	n.a.	n.a.	n.a.	n.a.	n.a.	n.a.	n.a.	n.a.	n.a.	n.a.
H_2O	2.30	2.31	2.30	2.31	2.31	2.30	2.30	2.30	2.26	2.27	2.30	2.30	2.30	2.30	n.a.	n.a.	n.a.	n.a.	n.a.	n.a.	n.a.	n.a.	n.a.	n.a.	n.a.	n.a.
Initial Total	100.16	100.39	100.50	100.63	101.21	100.92	100.62	100.16	99.25	98.03	100.38	100.35	100.57	100.42	98.84	98.36	98.26	97.31	97.76	98.18	98.69	98.52	98.24	98.39	98.16	98.36
Formula Assignments																										
T (ideally 8 apfu)																										
Si	8.01	8.04	8.02	8.03	8.04	8.06	8.05	8.03	7.08	7.51	8.05	8.06	8.03	8.05	7.99	8.03	8.02	8.01	8.02	8.03	7.98	8.02	8.05	8.02	8.04	8.05
P	0.01	0.00	0.01	0.01	0.01	0.01	0.01	0.01	0.01	0.01	0.01	0.01	0.01	0.01	0.00	0.00	0.00	0.00	0.00	0.00	0.00	0.00	0.00	0.00	0.00	0.00
Al	0.00	0.00	0.00	0.00	0.00	0.00	0.00	0.00	0.91	0.49	0.00	0.00	0.00	0.00	0.02	0.00	0.00	0.00	0.00	0.00	0.02	0.00	0.00	0.00	0.00	0.00
T subtotal	8.01	8.05	8.02	8.03	8.05	8.06	8.05	8.03	8.00	8.00	8.06	8.06	8.03	8.05	8.00	8.03	8.02	8.01	8.02	8.03	8.00	8.02	8.05	8.02	8.04	8.05
C (ideally 5 apfu)																										
Ti	0.00	0.00	0.00	0.00	0.00	0.00	0.00	0.00	0.12	0.06	0.00	0.00	0.00	0.00	0.00	0.00	0.00	0.00	0.00	0.01	0.00	0.01	0.00	0.00	0.00	0.01
Al	0.12	0.11	0.13	0.07	0.08	0.07	0.09	0.09	0.23	0.26	0.08	0.05	0.10	0.06	0.09	0.11	0.11	0.11	0.08	0.09	0.14	0.07	0.10	0.08	0.08	0.11
Fe^{3+}	0.00	0.00	0.00	0.00	0.00	0.00	0.00	0.01	0.15	0.05	0.00	0.00	0.01	0.00	0.00	0.00	0.01	0.02	0.02	0.00	0.00	0.01	0.00	0.00	0.00	0.00
Mn^{2+}	0.03	0.03	0.03	0.03	0.03	0.03	0.03	0.03	0.00	0.01	0.03	0.04	0.03	0.03	0.02	0.04	0.03	0.03	0.03	0.03	0.03	0.03	0.03	0.02	0.01	0.02
Fe^{2+}	0.64	0.56	0.62	0.55	0.52	0.59	0.62	0.59	0.54	0.73	0.61	0.64	0.63	0.58	0.60	0.64	0.59	0.58	0.60	0.56	0.61	0.61	0.61	0.57	0.92	0.87
Mg	4.18	4.24	4.22	4.30	4.31	4.24	4.20	4.25	3.89	3.85	4.23	4.21	4.20	4.26	4.29	4.17	4.22	4.24	4.26	4.28	4.21	4.26	4.21	4.30	3.95	3.88
C subtotal	4.96	4.94	4.99	4.95	4.94	4.93	4.95	4.97	5.00	5.00	4.94	4.93	4.97	4.93	5.00	4.95	4.97	4.99	4.99	4.96	4.99	4.99	4.96	4.98	4.97	4.88
B (ideally 2 apfu)																										
Mn^{2+}	0.00	0.00	0.00	0.00	0.00	0.00	0.00	0.00	0.01	0.02	0.00	0.00	0.00	0.00	0.01	0.00	0.00	0.00	0.00	0.00	0.00	0.00	0.00	0.00	0.00	0.00
Ca	1.89	1.82	1.83	1.90	1.84	1.80	1.78	1.83	1.89	1.82	1.81	1.84	1.82	1.85	1.90	1.86	1.83	1.82	1.84	1.86	1.86	1.86	1.82	1.89	1.87	1.89
Na	0.10	0.17	0.12	0.08	0.14	0.20	0.21	0.14	0.07	0.17	0.17	0.14	0.17	0.14	0.09	0.14	0.17	0.18	0.14	0.11	0.14	0.13	0.15	0.11	0.08	0.12
B subtotal	1.99	1.99	1.95	1.99	1.98	2.00	1.99	1.97	2.00	2.00	1.98	1.98	1.98	1.99	2.00	2.00	2.00	2.00	1.98	1.96	2.00	1.99	1.97	2.00	1.95	2.00
A (from 0 to 1 apfu)																										
Na	0.00	0.00	0.00	0.00	0.00	0.00	0.00	0.00	0.28	0.16	0.00	0.00	0.00	0.00	0.00	0.00	0.03	0.00	0.00	0.00	0.01	0.00	0.00	0.00	0.00	0.00
K	0.01	0.02	0.01	0.00	0.01	0.02	0.02	0.01	0.00	0.01	0.02	0.02	0.01	0.01	0.01	0.02	0.01	0.01	0.01	0.01	0.01	0.01	0.02	0.01	0.01	0.01
A subtotal	0.01	0.02	0.01	0.00	0.01	0.02	0.02	0.01	0.28	0.17	0.02	0.02	0.01	0.01	0.01	0.02	0.04	0.02	0.01	0.01	0.02	0.01	0.02	0.01	0.01	0.02
O (non-W)	22.00	22.00	22.00	22.00	22.00	22.00	22.00	22.00	22.00	22.00	22.00	22.00	22.00	22.00	22.00	22.00	22.00	22.00	22.00	22.00	22.00	22.00	22.00	22.00	22.00	22.00
W (ideally 2 apfu)																										
OH	2.00	2.00	2.00	2.00	2.00	2.00	2.00	2.00	2.00	2.00	2.00	2.00	2.00	2.00	2.00	2.00	2.00	2.00	2.00	2.00	2.00	2.00	2.00	2.00	2.00	2.00
W subtotal	2.00	2.00	2.00	2.00	2.00	2.00	2.00	2.00	2.00	2.00	2.00	2.00	2.00	2.00	2.00	2.00	2.00	2.00	2.00	2.00	2.00	2.00	2.00	2.00	2.00	2.00
Sum T,C,B,A	14.98	14.99	14.97	14.97	14.98	15.01	15.01	14.99	15.28	15.17	14.99	14.99	15.00	14.99	15.01	15.00	15.02	15.02	15.00	14.97	15.02	15.00	14.99	15.00	14.96	14.95
X_{Mg}	0.87	0.88	0.87	0.89	0.89	0.88	0.87	0.88	0.88	0.84	0.87	0.87	0.87	0.88	0.88	0.87	0.88	0.88	0.88	0.88	0.87	0.87	0.87	0.88	0.81	0.82

Table S2.2c cont.

EV19-10 - glaucophane schist																									
Analysis	1	2	3	4	5	6	7	8	9	10	11	12	13	14	15	16	17	18	19	20	21	22	23	24	25
Facility	University of Ottawa																Uppsala University								
SiO_2	55.44	51.08	53.99	53.09	50.29	54.10	53.30	52.46	53.91	51.34	54.63	55.16	56.39	54.63	56.30	55.88	55.68	54.96	56.74	55.26	53.17	56.43	56.41	56.29	55.78
TiO_2	0.01	0.03	0.00	0.02	0.65	0.01	0.00	0.01	0.02	0.03	0.03	0.00	0.00	0.00	0.07	0.02	0.07	0.00	0.00	0.02	0.00	0.02	0.00	0.00	0.04
Al_2O_3	10.29	4.00	8.42	8.28	3.74	8.41	8.17	6.66	8.68	3.87	6.12	4.28	8.72	2.68	6.56	7.87	7.68	5.42	8.47	4.23	2.44	9.89	8.78	8.77	7.64
Cr_2O_3	0.00	0.00	0.00	0.00	0.00	0.00	0.00	0.00	0.00	0.00	0.02	0.02	0.01	0.00	0.01	0.04	0.00	0.00	0.00	0.00	0.00	0.00	0.00	0.02	0.00
FeO	0.64	0.86	0.62	0.70	0.78	0.64	0.71	0.89	0.66	0.73	1.04	0.62	0.60	0.55	0.74	0.85	0.68	0.88	0.76	0.74	0.76	0.67	0.78	0.58	0.74
MnO	18.24	27.47	21.19	21.74	27.26	20.98	21.42	23.35	20.06	27.02	26.31	26.17	22.93	26.82	23.93	23.79	24.13	25.14	22.24	26.88	28.70	20.14	21.83	22.53	24.13
MgO	3.59	3.71	3.36	3.41	3.92	3.51	3.42	3.35	3.93	4.02	2.45	4.17	3.29	4.49	3.95	2.94	2.97	3.78	3.58	4.17	4.50	3.58	3.47	3.24	3.10
CaO	0.01	1.17	0.11	0.22	1.25	0.06	0.13	0.50	0.01	1.28	0.53	0.22	0.17	0.52	0.11	0.19	0.18	0.38	0.38	0.41	1.91	0.09	0.10	0.11	0.22
Na_2O	7.13	6.49	7.11	6.91	6.37	7.15	7.02	6.80	7.12	6.34	6.46	6.87	6.77	6.65	7.17	6.92	6.79	6.88	6.91	6.63	6.08	6.77	6.79	6.70	7.11
K_2O	0.00	0.10	0.02	0.04	0.10	0.01	0.03	0.05	0.01	0.17	0.06	0.02	0.02	0.02	0.04	0.00	0.01	0.04	0.02	0.03	0.13	0.04	0.00	0.02	0.02
Formula Assignments																									
T (ideally 8 apfu)																									
Si	8.11	7.81	8.05	7.96	7.90	8.05	8.01	7.97	8.02	7.84	8.05	8.07	8.09	8.13	8.07	8.05	8.05	8.04	8.08	8.06	7.91	8.08	8.07	8.09	8.03
Al	0.00	0.19	0.00	0.04	0.10	0.00	0.00	0.03	0.00	0.16	0.00	0.00	0.00	0.00	0.00	0.00	0.00	0.00	0.00	0.00	0.09	0.00	0.00	0.00	0.00
T subtotal	8.11	8.00	8.05	8.00	8.00	8.05	8.01	8.00	8.02	8.00	8.05	8.07	8.09	8.13	8.07	8.05	8.05	8.04	8.08	8.06	8.00	8.08	8.07	8.09	8.03
C (ideally 5 apfu)																									
Ti	0.00	0.00	0.00	0.00	0.08	0.00	0.00	0.00	0.00	0.00	0.00	0.00	0.00	0.00	0.01	0.00	0.01	0.00	0.00	0.00	0.00	0.00	0.00	0.00	0.01
Al	1.77	0.53	1.48	1.42	0.59	1.48	1.45	1.16	1.52	0.54	1.06	0.74	1.47	0.47	1.11	1.34	1.31	0.94	1.42	0.73	0.34	1.67	1.48	1.49	1.30
Cr	0.00	0.00	0.00	0.00	0.00	0.00	0.00	0.00	0.00	0.00	0.00	0.00	0.00	0.00	0.00	0.01	0.00	0.00	0.00	0.00	0.00	0.00	0.00	0.00	0.00
Fe^{3+}	0.03	1.33	0.32	0.53	0.45	0.33	0.45	0.70	0.37	1.29	0.73	1.10	0.23	1.19	0.72	0.56	0.63	0.92	0.40	1.02	1.37	0.27	0.46	0.31	0.63
Mn^{2+}	0.08	0.11	0.08	0.09		0.08	0.09	0.11	0.08	0.09	0.13	0.08	0.07	0.07	0.09	0.10	0.08	0.11	0.09	0.09	0.10	0.08	0.10	0.07	0.09
Fe^{2+}	2.20	2.18	2.32	2.20	2.96	2.28	2.24	2.27	2.13	2.16	2.51	2.11	2.53	2.15	2.15	2.31	2.29	2.15	2.25	2.26	2.20	2.15	2.15	2.39	2.28
Mg	0.78	0.85	0.75	0.76	0.92	0.78	0.77	0.76	0.87	0.92	0.54	0.91	0.70	1.00	0.84	0.63	0.64	0.83	0.76	0.91	1.00	0.76	0.74	0.69	0.67
C subtotal	4.87	5.00	4.95	5.00	5.00	4.95	4.99	5.00	4.98	5.00	4.98	4.93	5.00	4.87	4.92	4.95	4.96	4.95	4.92	5.00	5.00	4.93	4.93	4.96	4.96
B (ideally 2 apfu)																									
Ca	0.00	0.19	0.02	0.04	0.21	0.01	0.02	0.08	0.00	0.21	0.08	0.03	0.03	0.08	0.02	0.03	0.03	0.06	0.06	0.06	0.30	0.01	0.02	0.02	0.03
Na	2.00	1.81	1.98	1.97	1.53	1.99	1.98	1.92	2.00	1.79	1.85	1.95	1.88	1.92	1.98	1.93	1.90	1.94	1.91	1.87	1.70	1.88	1.88	1.87	1.97
B subtotal	2.00	2.00	2.00	2.00	2.00	2.00	2.00	2.00	2.00	2.00	1.93	1.98	1.91	2.00	2.00	1.96	1.93	2.00	1.97	1.94	2.00	1.89	1.90	1.89	2.00
A (from 0 to 1 apfu)																									
Ca																									
Na	0.02	0.12	0.07	0.04	0.41	0.07	0.07	0.08	0.06	0.09	0.00	0.00	0.00	0.00	0.01	0.00	0.00	0.01	0.00	0.00	0.06	0.00	0.00	0.00	0.02
K	0.00	0.02	0.00	0.01	0.02	0.00	0.01	0.01	0.00	0.03	0.01	0.00	0.00	0.00	0.01	0.00	0.00	0.01	0.00	0.01	0.02	0.01	0.00	0.00	0.00
A subtotal	0.02	0.13	0.08	0.05	0.43	0.08	0.07	0.09	0.06	0.12	0.01	0.00	0.00	0.01	0.02	0.00	0.00	0.02	0.00	0.01	0.08	0.01	0.00	0.00	0.02
O (non-W)	22.00	22.00	22.00	22.00	22.00	22.00	22.00	22.00	22.00	22.00	22.00	22.00	22.00	22.00	22.00	22.00	22.00	22.00	22.00	22.00	22.00	22.00	22.00	22.00	22.00
W (ideally 2 apfu)																									
OH	2.00	2.00	2.00	2.00	2.00	2.00	2.00	2.00	2.00	2.00	2.00	2.00	1.99	2.00	2.00	2.00	1.99	2.00	2.00	2.00	2.00	1.98	2.00	2.00	2.00
F	0.00	0.00	0.00	0.00	0.00	0.00	0.00	0.00	0.00	0.00	0.00	0.00	0.01	0.00	0.00	0.00	0.01	0.00	0.00	0.00	0.00	0.02			
Cl	0.00	0.00	0.00	0.00	0.00	0.00	0.00	0.00	0.00	0.00	0.00	0.00	0.00	0.00	0.00	0.00	0.00	0.00	0.00	0.00	0.00	0.00	0.00	0.00	0.00
W subtotal	2.00	2.00	2.00	2.00	2.00	2.00	2.00	2.00	2.00	2.00	2.00	2.00	2.00	2.00	2.00	2.00	2.00	2.00	2.00	2.00	2.00	2.00	2.00	2.00	2.00
Sum T,C,B,A	15.00	15.13	15.08	15.05	15.43	15.07	15.07	15.09	15.06	15.12	14.97	14.99	15.00	15.01	15.01	14.96	14.93	15.01	14.97	15.01	15.08	14.90	14.90	14.94	15.01
X_{Mg}	0.36	0.39	0.32	0.35	0.31	0.34	0.34	0.33	0.41	0.42	0.21	0.43	0.28	0.46	0.39	0.27	0.28	0.38	0.34	0.40	0.45	0.36	0.34	0.29	0.29
$Fe^{3+}/(Fe^{3+} + Al^{VI})$	0.02	0.72	0.18	0.27	0.44	0.18	0.24	0.37	0.19	0.71	0.41	0.60	0.13	0.72	0.39	0.29	0.32	0.50	0.22	0.58	0.80	0.14	0.24	0.17	0.33

Table S2.2c cont.

EV19-17C - albite-mica schist					
Analysis	1	2	3	4	5
Facility	Uppsala University				
SiO_2	57.94	58.79	59.18	58.54	59.25
TiO_2	0.04	0.03	0.07	0.08	0.05
Al_2O_3	11.56	11.50	11.57	11.37	11.33
Cr_2O_3	0.04	0.00	0.00	0.06	0.00
FeO	0.00	0.07	0.06	0.06	0.02
MnO	14.50	13.46	13.66	14.48	14.60
MgO	6.48	7.26	7.12	6.41	6.65
CaO	0.02	0.06	0.01	0.10	0.05
Na_2O	7.08	6.93	6.88	6.89	7.22
K_2O	0.00	0.03	0.01	0.00	0.02
F	0.13	0.15	0.01	0.00	0.00
Cl	0.00	0.01	0.00	0.10	0.22
Formula Assignments					
T (ideally 8 apfu)					
Si	8.07	8.10	8.12	8.12	8.12
Al	0.00	0.00	0.00	0.00	0.00
T subtotal	8.07	8.10	8.12	8.12	8.12
C (ideally 5 apfu)					
Ti	0.00	0.00	0.01	0.01	0.01
Al	1.90	1.87	1.87	1.86	1.83
Mn^{2+}	0.00	0.01	0.01	0.01	0.00
Fe^{2+}	1.69	1.55	1.57	1.68	1.67
Mg	1.35	1.49	1.46	1.33	1.36
C subtotal	4.94	4.92	4.91	4.88	4.87
B (ideally 2 apfu)					
Ca	0.00	0.01	0.00	0.02	0.01
Na	1.91	1.85	1.83	1.85	1.92
B subtotal	1.92	1.86	1.83	1.87	1.93
A (from 0 to 1 apfu)					
K	0.00	0.01	0.00	0.00	0.00
A subtotal	0.00	0.01	0.00	0.00	0.00
O (non-W)	22.00	22.00	22.00	22.00	22.00
W (ideally 2 apfu)					
OH	1.94	1.93	2.00	1.98	1.95
F	0.06	0.07	0.00	0.00	0.00
Cl	0.00	0.00	0.00	0.02	0.05
W subtotal	2.00	2.00	2.00	2.00	2.00
Sum T,C,B,A	14.93	14.89	14.86	14.87	14.92
X_{Mg}	0.44	0.49	0.48	0.44	0.45
$Fe^{3+}/(Fe^{3+} + Al^{VI})$	0.00	0.00	0.00	0.00	0.00

Table S2.2d. Electron microprobe results and formula recalculations for lawsonite from southern Evia (Greece) used for thermodynamic modelling.

EV19-03 - albite-pumpellyite schist					
Analysis	1	2	3	4	5
Min	lws	lws	lws	lws	lws
Facility	Ottawa		Uppsala University		
SiO_2	39.70	40.31	39.15	39.78	38.93
TiO_2	0.24	0.02	0.46	0.25	0.20
Al_2O_3	33.61	31.85	31.62	31.87	31.80
Cr_2O_3	0.08	0.33	0.03	0.01	0.04
FeO	0.27	0.33	0.39	0.13	0.13
MnO	0.01	0.05	0.00	0.01	0.00
MgO	0.13	0.24	0.20	0.06	0.01
CaO	17.33	17.46	17.24	17.60	17.46
Na_2O	0.00	0.00	0.04	0.07	0.09
K_2O	0.01	0.00	0.05	0.00	0.00
Totals	91.41	90.63	89.21	89.79	88.66
Oxygens	8.00	8.00	8.00	8.00	8.00
Si	2.01	2.06	2.03	2.05	2.03
Ti	0.01	0.00	0.02	0.01	0.01
Al	2.00	1.92	1.93	1.93	1.96
Cr	0.00	0.01	0.00	0.00	0.00
Fe^{3+}	0.01	0.01	0.02	0.01	0.01
Fe^{2+}	0.00	0.00	0.00	0.00	0.00
Mn	0.00	0.00	0.00	0.00	0.00
Mg	0.01	0.02	0.02	0.00	0.00
Ca	0.94	0.95	0.96	0.97	0.98
Na	0.00	0.00	0.00	0.01	0.01
K	0.00	0.00	0.00	0.00	0.00
Sum	4.98	4.97	4.98	4.98	4.99

Table S2.2e. Electron microprobe results and formula recalculations for feldspar from southern Evia (Greece) used for thermodynamic modelling.

EV19-03 - albite-pumpellyite schist			
Analysis	1	2	3
Min	fsp	fsp	fsp
Facility	University of Ottawa		
SiO_2	69.57	69.78	69.85
TiO_2	0.00	0.00	0.00
Al_2O_3	19.38	19.23	19.58
Cr_2O_3	0.00	0.00	0.00
FeO	0.10	0.02	0.03
MnO	0.00	0.00	0.00
MgO	0.00	0.00	0.00
CaO	0.03	0.04	0.06
Na_2O	11.65	11.80	11.86
K_2O	0.04	0.02	0.02
Totals	100.78	100.89	101.40
Oxygens	8.00	8.00	8.00
Si	3.01	3.02	3.01
Ti	0.00	0.00	0.00
Al	0.99	0.98	0.99
Cr	0.00	0.00	0.00
Fe^{3+}	0.00	0.00	0.00
Fe^{2+}	0.00	0.00	0.00
Mn	0.00	0.00	0.00
Mg	0.00	0.00	0.00
Ca	0.00	0.00	0.00
Na	0.98	0.99	0.99
K	0.00	0.00	0.00
Sum	4.98	4.99	4.99
An	0.00	0.00	0.00
Ab	0.98	0.99	0.99
Or	0.00	0.00	0.00

EV19-17C - albite-mica schist					
Analysis	1	2	3	4	5
Min	fsp	fsp	fsp	fsp	fsp
Facility	University of Ottawa				
SiO_2	70.71	70.12	70.25	70.94	70.35
TiO_2	0.00	0.01	0.00	0.03	0.02
Al_2O_3	19.65	19.92	19.48	19.80	19.58
Cr_2O_3	0.00	0.08	0.00	0.00	0.00
FeO	0.04	0.03	0.19	0.04	0.09
MnO	0.00	0.01	0.00	0.00	0.03
MgO	0.00	0.02	0.01	0.03	0.00
CaO	0.02	0.06	0.04	0.05	0.06
Na_2O	11.17	11.26	11.04	11.02	10.99
K_2O	0.01	0.04	0.02	0.01	0.00
Totals	101.60	101.55	101.05	101.93	101.12
Oxygens	8.00	8.00	8.00	8.00	8.00
Si	3.02	3.01	3.02	3.02	3.02
Ti	0.00	0.00	0.00	0.00	0.00
Al	0.99	1.01	0.99	0.99	0.99
Cr	0.00	0.00	0.00	0.00	0.00
Fe^{3+}	0.00	0.00	0.01	0.00	0.00
Fe^{2+}	0.00	0.00	0.00	0.00	0.00
Mn	0.00	0.00	0.00	0.00	0.00
Mg	0.00	0.00	0.00	0.00	0.00
Ca	0.00	0.00	0.00	0.00	0.00
Na	0.93	0.94	0.92	0.91	0.92
K	0.00	0.00	0.00	0.00	0.00
Sum	4.94	4.96	4.94	4.93	4.94
An	0.0	0.0	0.0	0.0	0.0
Ab	1.0	1.0	1.0	1.0	1.0
Or	0.0	0.0	0.0	0.0	0.0

Table S2.2f. Electron microprobe results and formula recalculations for pumpellyite from southern Evia (Greece) used for thermodynamic modelling.

EV19-03 - albite-pumpellyite schist																		
Analysis	1	2	3	4	5	6	7	8	9	10	11	12	13	14	15	16	17	18
Min	pmp	pmp	pmp	pmp	pmp	pmp	pmp	pmp	pmp	pmp	pmp	pmp	pmp	pmp	pmp	pmp	pmp	pmp
Facility	University of Ottawa														Uppsala University			
SiO_2	38.27	38.16	38.16	38.23	38.00	38.14	38.42	38.18	38.45	38.93	38.68	38.42	39.02	40.94	38.64	38.37	38.44	38.44
TiO_2	0.06	0.06	0.07	0.05	0.05	0.04	0.06	0.04	0.03	0.07	0.17	0.09	0.11	0.07	0.12	0.01	0.04	0.03
Al_2O_3	25.33	25.64	25.20	26.10	25.56	25.57	25.47	25.56	25.75	28.15	30.93	29.39	26.78	25.50	26.01	25.85	25.82	26.17
Cr_2O_3	0.00	0.03	0.00	0.00	0.00	0.03	0.05	0.00	0.08	0.05	0.01	0.00	0.01	0.00	0.04	0.53	0.41	0.07
FeO	1.35	1.22	1.30	1.40	1.35	1.33	1.41	1.46	1.39	1.32	0.74	0.89	1.40	0.86	1.49	1.40	1.43	1.45
MnO	0.41	0.54	0.46	0.36	0.59	0.53	0.41	0.38	0.44	0.38	0.16	0.22	0.22	0.05	0.42	0.43	0.44	0.42
MgO	4.10	3.88	3.98	3.65	3.76	3.81	3.96	3.82	3.74	3.12	1.83	1.94	3.32	3.97	4.13	3.87	3.95	3.87
CaO	22.72	22.87	22.89	22.91	22.67	22.83	22.77	22.95	22.90	21.69	19.89	21.36	23.24	22.67	22.93	22.54	22.93	23.12
Na_2O	0.10	0.09	0.09	0.10	0.16	0.11	0.13	0.10	0.10	0.10	0.05	0.05	0.08	0.13	0.13	0.08	0.08	0.12
K_2O	0.10	0.08	0.01	0.01	0.01	0.04	0.02	0.02	0.00	0.01	0.02	0.03	0.00	0.01	0.00	0.04	0.02	0.00
Totals	92.59	92.71	92.30	92.97	92.30	92.58	92.86	92.67	93.03	93.97	92.56	92.49	94.24	94.28	94.07	93.21	93.69	93.80
Oxygens	24.50	24.50	24.50	24.50	24.50	24.50	24.50	24.50	24.50	24.50	24.50	24.50	24.50	24.50	24.50	24.50	24.50	24.50
Si	6.09	6.06	6.09	6.05	6.06	6.07	6.09	6.07	6.08	6.05	6.02	6.03	6.09	6.33	6.05	6.06	6.05	6.04
Ti	0.01	0.01	0.01	0.01	0.01	0.01	0.01	0.01	0.00	0.01	0.02	0.01	0.01	0.01	0.01	0.00	0.01	0.00
Al	4.75	4.80	4.74	4.87	4.81	4.80	4.76	4.79	4.80	5.15	5.67	5.44	4.93	4.65	4.80	4.82	4.79	4.85
Cr	0.00	0.00	0.00	0.00	0.00	0.00	0.01	0.00	0.01	0.01	0.00	0.00	0.00	0.00	0.01	0.07	0.05	0.01
Fe^{3+}	0.18	0.16	0.17	0.19	0.18	0.18	0.19	0.19	0.18	0.17	0.10	0.12	0.06	0.10	0.18	0.12	0.15	0.14
Fe^{2+}	0.00	0.00	0.00	0.00	0.00	0.00	0.00	0.00	0.00	0.00	0.00	0.00	0.12	0.01	0.02	0.07	0.03	0.05
Mn	0.06	0.07	0.06	0.05	0.08	0.07	0.06	0.05	0.06	0.05	0.02	0.03	0.03	0.01	0.06	0.06	0.06	0.06
Mg	0.97	0.92	0.95	0.86	0.89	0.90	0.94	0.91	0.88	0.72	0.42	0.45	0.77	0.92	0.96	0.91	0.93	0.91
Ca	3.87	3.89	3.91	3.88	3.88	3.89	3.87	3.91	3.88	3.61	3.32	3.59	3.89	3.76	3.85	3.82	3.87	3.89
Na	0.03	0.03	0.03	0.03	0.05	0.03	0.04	0.03	0.03	0.03	0.02	0.02	0.03	0.04	0.04	0.03	0.02	0.04
K	0.02	0.02	0.00	0.00	0.00	0.01	0.00	0.00	0.00	0.00	0.00	0.01	0.00	0.00	0.00	0.01	0.00	0.00
Sum	15.97	15.97	15.96	15.94	15.96	15.96	15.95	15.95	15.93	15.80	15.59	15.69	15.92	15.81	15.97	15.95	15.96	15.98

Table S2.2g. Electron microprobe results and formula recalculations for biotite from southern Evia (Greece) used for thermodynamic modelling.

EV19-10 - glaucophane schist					
Analysis	1	2	3	4	5
Min	bi	bi	bi	bi	bi
Facility	University of Ottawa				Uppsala
SiO_2	38.71	36.51	37.90	36.44	37.73
TiO_2	0.39	0.50	0.49	0.66	0.24
Al_2O_3	14.44	13.42	14.40	12.83	14.10
Cr_2O_3	0.00	0.00	0.00	0.01	0.00
FeO	22.62	25.12	23.01	26.02	26.31
MnO	0.62	0.74	0.72	0.72	0.80
MgO	5.71	6.36	6.02	6.40	6.42
CaO	0.04	0.09	0.05	0.06	0.15
Na_2O	0.03	0.05	0.08	0.06	0.11
K_2O	10.35	9.72	10.00	9.59	8.51
Totals	92.91	92.51	92.67	92.79	94.37
Oxygens	11.00	11.00	11.00	11.00	11.00
Si	3.08	2.98	3.04	2.98	2.99
Ti	0.02	0.03	0.03	0.04	0.01
Al	1.36	1.29	1.36	1.24	1.32
Cr	0.00	0.00	0.00	0.00	0.00
Fe^{3+}	0.00	0.00	0.00	0.00	0.00
Fe^{2+}	1.51	1.71	1.54	1.78	1.75
Mn	0.04	0.05	0.05	0.05	0.05
Mg	0.68	0.77	0.72	0.78	0.76
Ca	0.00	0.01	0.00	0.01	0.01
Na	0.01	0.01	0.01	0.01	0.02
K	1.05	1.01	1.02	1.00	0.86
Sum	7.75	7.86	7.77	7.87	7.77
X_{Mg}	0.31	0.31	0.32	0.30	0.30

Table S2.2h. Electron microprobe results and formula recalculations for epidote from southern Evia (Greece) used for thermodynamic modelling.

EV19-03 - albite-pumpellyite schist														
Sample	1	2	3	4	5	6	7	8	9	10	11	12	13	14
Min	ep	ep	ep	ep	ep	ep	ep	ep	ep	ep	ep	ep	ep	ep
Facility						University of Ottawa							Uppsala University	
SiO_2	39.99	39.73	40.00	39.87	39.43	38.94	38.87	38.84	39.64	40.17	39.98	39.16	40.24	40.43
TiO_2	0.07	0.09	0.15	0.07	0.04	0.05	0.11	0.02	0.07	0.05	0.07	0.02	0.08	0.03
Al_2O_3	32.32	32.30	33.42	32.90	31.18	30.19	31.57	30.37	32.41	33.18	33.55	31.25	31.73	33.43
Cr_2O_3	0.00	0.00	0.00	0.00	0.00	0.03	0.00	0.00	0.00	0.00	0.00	0.00	0.00	0.01
FeO	1.48	1.26	0.26	1.14	2.92	3.52	2.25	3.28	1.44	0.49	0.40	3.38	2.40	0.79
MnO	0.08	0.05	0.02	0.08	0.02	0.11	0.08	0.02	0.08	0.04	0.03	0.05	0.04	0.09
MgO	0.02	0.03	0.00	0.01	0.03	0.14	0.04	0.04	0.02	0.01	0.00	0.05	0.03	0.03
CaO	24.51	24.61	24.80	24.50	24.33	23.39	24.06	24.17	24.69	24.57	24.84	24.22	24.67	24.54
Na_2O	0.01	0.02	0.00	0.00	0.00	0.00	0.00	0.00	0.00	0.05	0.02	0.00	0.00	0.01
K_2O	0.01	0.03	0.01	0.01	0.01	0.03	0.01	0.04	0.04	0.03	0.01	0.00	0.01	0.01
Totals	98.66	98.26	98.69	98.71	98.29	96.79	97.24	97.14	98.55	98.65	98.94	98.51	99.46	99.45
Oxygens	12.5	12.5	12.5	12.5	12.5	12.5	12.5	12.5	12.5	12.5	12.5	12.5	12.5	12.5
Si	3.02	3.01	3.01	3.01	3.01	3.02	2.99	3.01	3.00	3.02	3.00	2.99	3.03	3.02
Ti	0.00	0.01	0.01	0.00	0.00	0.00	0.01	0.00	0.00	0.00	0.00	0.00	0.01	0.00
Al	2.88	2.89	2.96	2.92	2.80	2.76	2.86	2.77	2.89	2.94	2.97	2.81	2.81	2.94
Cr	0.00	0.00	0.00	0.00	0.00	0.00	0.00	0.00	0.00	0.00	0.00	0.00	0.00	0.00
Fe^{3+}	0.09	0.08	0.02	0.07	0.19	0.23	0.15	0.21	0.09	0.03	0.03	0.22	0.15	0.05
Fe^{2+}	0.00	0.00	0.00	0.00	0.00	0.00	0.00	0.00	0.00	0.00	0.00	0.00	0.00	0.00
Mn	0.01	0.00	0.00	0.01	0.00	0.01	0.01	0.00	0.01	0.00	0.00	0.00	0.00	0.01
Mg	0.00	0.00	0.00	0.00	0.00	0.02	0.01	0.01	0.00	0.00	0.00	0.01	0.00	0.00
Ca	1.98	2.00	2.00	1.98	1.99	1.94	1.98	2.00	2.00	1.98	2.00	1.98	1.99	1.96
Na	0.00	0.00	0.00	0.00	0.00	0.00	0.00	0.00	0.00	0.01	0.00	0.00	0.00	0.00
K	0.00	0.00	0.00	0.00	0.00	0.00	0.00	0.00	0.00	0.00	0.00	0.00	0.00	0.00
Sum	7.99	8	7.995	7.992	7.995	7.983	7.999	8.004	8.004	7.993	8.001	8.001	7.989	7.986

Table S2.3. Analytical results for white mica total fusion $^{40}Ar/^{39}Ar$ geochronology for samples from southern Evia (Greece).

	Sample *Grain*	Age (Ma)	±1σ	^{40}Ar (fA)	±1σ	^{39}Ar (fA)	±1σ	^{38}Ar (fA)	±1σ	^{37}Ar (fA)	±1σ	^{36}Ar (fA)	±1σ	Ca/K	±1σ	Cl/K	±1σ	$\%^{40}Ar^*$	$^{40}Ar^*/^{39}Ar_K$	±1σ
Basal Unit	**19-01**	carbonate-silicate schist																		
	Grain 1	22.82	0.06	39.108	0.031	27.153	0.017	0.311	0.017	0.603	0.012	0.011	0.000	0.187	0.004	bdl†	-	91.994	1.324	0.003
	*Grain 2**	391.90	16.88	14.878	0.032	0.295	0.013	0.012	0.016	1.344	0.014	0.027	0.000	38.949	1.755	0.033	0.157	49.377	25.210	1.206
	Grain 3	23.28	0.08	30.433	0.034	20.885	0.015	0.244	0.016	0.067	0.014	0.007	0.000	0.027	0.006	bdl	-	92.803	1.352	0.005
	Grain 4	22.88	0.07	34.541	0.035	24.136	0.015	0.284	0.016	0.288	0.014	0.008	0.000	0.100	0.005	bdl	-	92.844	1.328	0.004
	Grain 5	22.70	0.11	25.049	0.033	15.696	0.014	0.203	0.015	0.397	0.015	0.015	0.000	0.213	0.008	0.002	0.003	82.615	1.318	0.006
	*Grain 6**	12.05	48.24	1.176	0.030	0.031	0.013	0.007	0.015	0.149	0.015	0.004	0.000	41.846	17.950	0.547	1.488	1.793	0.698	2.801
	*Grain 7**	97.97	33.98	4.557	0.033	0.068	0.013	0.022	0.016	0.653	0.014	0.015	0.000	83.266	16.579	0.808	0.696	8.471	5.805	2.068
	Grain 8	23.08	0.07	36.117	0.035	24.648	0.015	0.281	0.015	0.128	0.014	0.010	0.000	0.043	0.005	bdl	-	91.480	1.340	0.004
	19-03	pumpelleyite-albite schist																		
	Grain 1	25.86	0.04	96.404	0.036	58.618	0.020	0.702	0.015	1.109	0.013	0.028	0.000	0.160	0.002	0.000	0.001	91.379	1.502	0.002
	Grain 2	27.09	0.13	33.879	0.038	17.578	0.015	0.216	0.016	0.858	0.015	0.022	0.000	0.415	0.007	0.000	0.003	81.724	1.574	0.007
	Grain 3	26.65	0.21	18.959	0.034	8.786	0.014	0.101	0.015	0.393	0.014	0.018	0.000	0.381	0.013	bdl	-	71.790	1.549	0.012
	Grain 4	25.74	0.20	25.857	0.034	12.283	0.015	0.163	0.017	1.046	0.014	0.026	0.000	0.726	0.010	0.003	0.004	71.043	1.495	0.011
	Grain 5	25.17	0.07	41.572	0.035	25.569	0.014	0.328	0.016	0.011	0.015	0.013	0.000	0.003	0.005	0.002	0.002	89.968	1.462	0.004
	Grain 6	24.91	0.18	20.602	0.031	11.003	0.014	0.139	0.014	0.226	0.013	0.016	0.000	0.175	0.010	0.001	0.004	77.318	1.447	0.010
	Grain 7	24.83	0.06	42.311	0.036	26.701	0.015	0.310	0.016	0.012	0.014	0.012	0.000	0.003	0.005	bdl	-	91.069	1.442	0.004
	Grain 8	25.46	0.12	25.982	0.034	15.158	0.014	0.178	0.016	0.009	0.014	0.012	0.000	0.005	0.008	bdl	-	86.313	1.479	0.007
	19-04	impure schistose marble																		
	Grain 1	35.85	0.11	430.289	0.051	112.815	0.023	1.440	0.017	0.953	0.014	0.651	0.002	0.072	0.001	bdl	-	55.195	2.104	0.007
	*Grain 2**	42.55	0.16	428.706	0.056	87.781	0.018	1.199	0.016	0.591	0.014	0.706	0.003	0.057	0.001	0.001	0.001	51.265	2.502	0.010
	Grain 3	32.79	0.19	235.076	0.051	55.005	0.018	0.754	0.015	0.353	0.013	0.436	0.002	0.055	0.002	0.001	0.001	45.027	1.923	0.011
	Grain 4	32.78	0.14	398.399	0.052	96.157	0.022	1.244	0.016	1.013	0.012	0.721	0.002	0.090	0.001	bdl	-	46.423	1.922	0.008
	Grain 5	32.82	0.10	472.744	0.053	135.329	0.025	1.744	0.016	1.306	0.013	0.716	0.003	0.083	0.001	0.000	0.000	55.127	1.925	0.006
	Grain 6	31.86	0.17	271.236	0.046	64.417	0.018	0.871	0.016	1.150	0.014	0.510	0.002	0.153	0.002	0.000	0.001	44.389	1.868	0.010
	Grain 7	35.64	0.17	181.480	0.041	47.500	0.019	0.622	0.015	0.414	0.015	0.277	0.002	0.075	0.003	0.000	0.001	54.783	2.092	0.010
	Grain 8	36.36	0.12	323.283	0.054	85.643	0.021	1.113	0.016	0.513	0.013	0.474	0.002	0.051	0.001	0.000	0.001	56.578	2.135	0.007
	19-06	albite-mica schist																		
	Grain 1	45.34	0.10	254.810	0.046	70.677	0.020	0.907	0.015	0.866	0.014	0.223	0.001	0.105	0.002	0.001	0.001	74.049	2.668	0.006
	Grain 2	45.14	0.07	434.103	0.053	120.170	0.021	1.503	0.016	0.730	0.014	0.386	0.002	0.052	0.001	0.000	0.000	73.575	2.656	0.004
	Grain 3	49.70	0.06	294.099	0.044	81.424	0.023	1.033	0.015	0.209	0.014	0.186	0.001	0.022	0.001	0.001	0.001	81.121	2.929	0.004
	Grain 4	47.06	0.05	663.473	0.062	189.754	0.028	2.357	0.015	0.510	0.014	0.461	0.002	0.023	0.001	0.000	0.000	79.293	2.771	0.003
	Grain 5	45.95	0.08	299.516	0.045	83.079	0.019	1.037	0.017	0.311	0.015	0.251	0.001	0.032	0.002	0.000	0.001	75.055	2.704	0.005
	Grain 6	44.88	0.06	455.011	0.053	138.865	0.020	1.725	0.016	0.378	0.015	0.295	0.002	0.023	0.001	0.000	0.000	80.641	2.641	0.003
	*Grain 7**	41.33	0.08	281.563	0.045	88.166	0.021	1.075	0.016	0.305	0.014	0.226	0.001	0.030	0.001	bdl	-	76.117	2.430	0.004
	*Grain 8**	39.87	0.07	243.068	0.043	81.288	0.020	0.987	0.014	0.332	0.013	0.176	0.001	0.035	0.001	bdl	-	78.400	2.343	0.004
	19-16	carbonate-silicate schist																		
	Grain 1	25.06	0.08	44.567	0.037	26.589	0.016	0.328	0.015	0.024	0.014	0.020	0.000	0.007	0.004	0.001	0.002	86.253	1.445	0.005
	Grain 2	24.03	0.04	77.371	0.037	52.502	0.017	0.627	0.015	0.006	0.014	0.014	0.000	0.001	0.002	0.000	0.001	94.074	1.386	0.002
	Grain 3	24.26	0.02	119.427	0.037	81.670	0.020	0.959	0.015	0.038	0.014	0.015	0.000	0.003	0.001	bdl	-	95.683	1.398	0.001
	Grain 4	25.96	0.06	51.195	0.035	31.316	0.016	0.393	0.015	0.038	0.013	0.014	0.000	0.009	0.003	0.001	0.001	91.660	1.498	0.003
	Grain 5	25.79	0.06	42.279	0.033	26.420	0.016	0.303	0.015	0.062	0.013	0.009	0.000	0.018	0.004	bdl	-	93.005	1.488	0.004
	Grain 6	24.35	0.05	53.243	0.037	35.000	0.018	0.431	0.016	0.016	0.013	0.013	0.000	0.003	0.003	0.001	0.001	92.341	1.404	0.003
	Grain 7	23.24	0.07	40.443	0.035	27.249	0.016	0.341	0.015	0.009	0.012	0.013	0.000	0.002	0.004	0.001	0.002	90.308	1.340	0.004
	Grain 8	25.20	0.07	36.236	0.034	23.438	0.016	0.262	0.015	-0.001	0.014	0.007	0.000	bdl	-	bdl	-	94.052	1.453	0.004
	19-17C	albite-mica schist																		
	Grain 1	42.48	0.07	194.312	0.046	65.650	0.017	0.795	0.015	0.041	0.014	0.108	0.001	0.005	0.002	0.000	0.001	83.289	2.464	0.004
	Grain 2	39.65	0.05	254.371	0.045	93.650	0.021	1.120	0.015	0.046	0.014	0.130	0.001	0.004	0.001	bdl	-	84.634	2.298	0.003
	Grain 3	43.74	0.03	794.838	0.064	276.964	0.036	3.373	0.016	0.181	0.014	0.303	0.001	0.005	0.000	0.000	0.000	88.470	2.538	0.002
	*Grain 4**	35.11	0.04	366.508	0.049	147.818	0.024	1.784	0.015	0.097	0.014	0.220	0.001	0.005	0.001	bdl	-	81.992	2.032	0.002
	Grain 5	43.01	0.06	169.013	0.038	59.923	0.018	0.757	0.016	0.052	0.014	0.064	0.001	0.007	0.002	0.001	0.001	88.495	2.495	0.003
	Grain 6	38.28	0.07	294.540	0.042	100.264	0.020	1.236	0.015	0.073	0.013	0.242	0.001	0.006	0.001	0.000	0.000	75.527	2.218	0.004
	Grain 7	41.62	0.04	362.001	0.047	133.963	0.021	1.602	0.015	0.047	0.014	0.127	0.001	0.002	0.001	bdl	-	89.362	2.414	0.002
	*Grain 8**	33.21	0.03	431.530	0.051	196.878	0.026	2.379	0.016	0.091	0.014	0.175	0.001	0.003	0.001	0.000	0.000	87.705	1.921	0.002
	19-18	albite-mica schist																		
	Grain 1	*44.64*	*3.47*	12.604	0.032	0.759	0.013	0.014	0.015	0.065	0.013	0.036	0.000	0.708	0.147	bdl	-	15.632	2.595	0.204
	Grain 2	*60.17*	*0.09*	246.676	0.048	57.401	0.017	0.725	0.016	1.292	0.014	0.152	0.001	0.186	0.002	0.001	0.001	81.770	3.512	0.005
	Grain 3	*48.37*	*0.19*	87.436	0.044	22.505	0.015	0.267	0.017	1.344	0.014	0.082	0.001	0.493	0.005	bdl	-	72.475	2.815	0.011
	Grain 4	*51.72*	*0.16*	99.321	0.041	24.213	0.015	0.254	0.016	0.572	0.015	0.089	0.001	0.195	0.005	bdl	-	73.474	3.013	0.010
	Grain 5	*49.62*	*0.25*	104.932	0.057	21.786	0.015	0.324	0.016	1.027	0.014	0.143	0.001	0.390	0.005	0.005	0.002	59.993	2.888	0.015
	Grain 6	*42.61*	*0.50*	23.290	0.042	5.585	0.014	0.065	0.015	0.040	0.015	0.032	0.001	0.059	0.022	bdl	-	59.387	2.475	0.029
	Grain 7	*54.93*	*0.16*	168.202	0.042	38.603	0.016	0.487	0.014	0.966	0.015	0.151	0.001	0.207	0.003	0.000	0.001	73.523	3.202	0.009
	Grain 8	*49.45*	*0.11*	240.701	0.049	62.629	0.018	0.783	0.015	0.600	0.013	0.203	0.001	0.079	0.002	0.000	0.001	74.925	2.878	0.007

*Grain rejected for calculation of weighted mean age
†bdl = below detection limit

Table S2.3 cont.

	Sample / Grain	Age (Ma)	±1σ	^{40}Ar (fA)	±1σ	^{39}Ar (fA)	±1σ	^{38}Ar (fA)	±1σ	^{37}Ar (fA)	±1σ	^{36}Ar (fA)	±1σ	Ca/K	±1σ	Cl/K	±1σ	%^{40}Ar*	^{40}Ar*/^{39}Ar$_K$	±1σ
Basal Unit	**20-02**	impure schistose marble																		
	Grain 1	26.02	0.14	96.039	0.040	34.406	0.015	0.441	0.015	5.266	0.014	0.155	0.001	1.034	0.003	0.000	0.001	53.644	1.497	0.008
	Grain 2	27.88	0.12	132.528	0.038	46.676	0.019	0.675	0.015	0.565	0.013	0.194	0.001	0.081	0.002	0.005	0.001	56.549	1.605	0.007
	Grain 3	27.57	0.08	243.807	0.042	95.555	0.020	1.316	0.015	1.005	0.014	0.310	0.001	0.071	0.001	0.003	0.000	62.220	1.587	0.004
	Grain 4	27.01	0.27	43.852	0.037	13.613	0.014	0.191	0.015	1.864	0.013	0.078	0.001	0.927	0.006	0.003	0.003	48.269	1.555	0.015
	Grain 5	29.66	0.13	153.762	0.037	47.922	0.018	0.680	0.016	0.883	0.014	0.243	0.001	0.124	0.002	0.004	0.001	53.272	1.709	0.008
	Grain 6	26.01	0.21	63.384	0.037	21.706	0.015	0.301	0.016	5.534	0.015	0.109	0.001	1.729	0.005	0.003	0.002	51.253	1.497	0.012
	Grain 7	24.67	0.13	76.660	0.032	33.388	0.016	0.449	0.016	5.613	0.014	0.104	0.001	1.142	0.003	0.003	0.001	61.802	1.419	0.007
	Grain 8	29.12	0.10	224.091	0.041	79.356	0.019	1.095	0.016	26.850	0.016	0.331	0.001	2.300	0.001	0.003	0.001	59.359	1.677	0.006
	20-03	albite-mica schist																		
	Grain 1	29.00	0.16	315.089	0.044	75.892	0.019	1.020	0.016	0.101	0.014	0.635	0.002	0.009	0.001	0.000	0.001	40.326	1.674	0.009
	Grain 2	30.20	0.20	297.981	0.050	63.163	0.018	0.894	0.015	0.046	0.014	0.634	0.002	0.005	0.001	0.001	0.001	36.965	1.743	0.011
	Grain 3	31.10	0.17	273.331	0.044	71.999	0.021	0.943	0.015	0.048	0.013	0.485	0.002	0.004	0.001	0.000	0.001	47.326	1.796	0.010
	*Grain 4**	33.89	0.30	168.550	0.038	32.961	0.016	0.460	0.016	0.075	0.013	0.351	0.002	0.015	0.003	0.000	0.001	38.311	1.958	0.018
	Grain 5	28.96	0.16	282.776	0.045	77.637	0.019	1.042	0.016	0.079	0.013	0.516	0.002	0.007	0.001	0.001	0.001	45.901	1.671	0.010
	Grain 6	29.70	0.22	344.154	0.047	77.019	0.019	1.059	0.014	0.075	0.015	0.716	0.003	0.006	0.001	0.000	0.001	38.373	1.714	0.013
	Grain 7	28.23	0.19	210.516	0.045	55.990	0.017	0.768	0.016	0.038	0.013	0.402	0.002	0.004	0.002	0.001	0.001	43.333	1.629	0.011
	Grain 8	27.70	0.12	260.335	0.047	90.014	0.020	1.154	0.016	0.053	0.013	0.392	0.002	0.004	0.001	0.000	0.001	55.278	1.598	0.007
	20-10	impure schistose marble																		
	Grain 1	23.21	0.21	107.576	0.039	33.327	0.016	0.467	0.015	0.560	0.015	0.213	0.001	0.116	0.003	0.002	0.001	41.521	1.340	0.012
	Grain 2	22.78	0.28	95.494	0.040	23.015	0.016	0.378	0.015	0.555	0.013	0.221	0.001	0.167	0.004	0.008	0.002	31.700	1.315	0.016
	Grain 3	23.45	0.16	91.676	0.040	34.617	0.016	0.495	0.015	0.556	0.013	0.151	0.001	0.111	0.003	0.004	0.001	51.132	1.354	0.009
	Grain 4	23.48	0.37	59.295	0.039	13.031	0.014	0.202	0.015	0.370	0.013	0.141	0.001	0.197	0.007	0.004	0.003	29.802	1.356	0.022
	Grain 5	23.96	0.18	99.566	0.037	31.799	0.016	0.440	0.016	0.762	0.014	0.188	0.001	0.166	0.003	0.002	0.001	44.204	1.384	0.010
	Grain 6	24.79	0.10	67.690	0.034	32.710	0.016	0.446	0.015	0.215	0.014	0.070	0.001	0.045	0.003	0.004	0.001	69.225	1.432	0.006
	Grain 7	25.37	0.19	51.283	0.035	18.453	0.016	0.260	0.017	0.443	0.013	0.082	0.001	0.167	0.005	0.004	0.003	52.760	1.466	0.011
	Grain 8	24.86	0.30	51.642	0.035	14.660	0.014	0.224	0.014	0.607	0.013	0.104	0.001	0.288	0.006	0.006	0.003	40.764	1.435	0.017
	20-13	albite-mica schist																		
	Grain 1	*36.32*	*0.06*	106.412	0.038	37.507	0.016	0.466	0.015	-0.005	0.013	0.091	0.001	bdl	-	0.000	0.001	74.467	2.111	0.006
	Grain 2	*37.10*	*0.12*	85.801	0.034	27.980	0.015	0.377	0.014	0.035	0.013	0.085	0.001	0.014	0.005	0.003	0.001	70.401	2.157	0.009
	Grain 3	*37.51*	*0.11*	128.301	0.038	43.442	0.016	0.576	0.015	0.038	0.014	0.112	0.001	0.009	0.004	0.002	0.001	73.916	2.182	0.006
	Grain 4	*44.84*	*0.11*	49.829	0.035	16.908	0.016	0.233	0.014	-0.024	0.014	0.019	0.000	bdl	-	0.005	0.002	88.725	2.613	0.007
	Grain 5	*49.31*	*0.25*	106.941	0.037	30.808	0.015	0.402	0.014	0.015	0.013	0.061	0.001	0.005	0.005	0.002	0.001	82.936	2.877	0.007
	Grain 6	*51.78*	*0.11*	231.499	0.044	68.044	0.018	0.847	0.015	0.064	0.014	0.085	0.001	0.010	0.002	0.001	0.001	88.914	3.023	0.003
	Grain 7	*241.43*	*0.22*	300.107	0.051	19.284	0.014	0.221	0.016	-0.003	0.014	0.045	0.001	bdl	-	bdl	-	95.513	14.855	0.014
	Grain 8	*243.65*	*0.15*	228.116	0.048	14.747	0.014	0.194	0.015	-0.032	0.014	0.022	0.000	bdl	-	0.003	0.003	97.036	15.001	0.017
	20-14	marble																		
	Grain 1	25.39	0.03	107.210	0.038	58.086	0.018	0.667	0.015	0.035	0.013	0.073	0.001	0.006	0.003	bdl	-	79.549	1.467	0.004
	Grain 2	25.49	0.04	36.702	0.033	21.876	0.014	0.260	0.015	0.003	0.014	0.015	0.000	0.001	0.007	bdl	-	87.836	1.473	0.005
	Grain 3	25.77	0.04	27.755	0.031	17.562	0.014	0.198	0.015	0.006	0.013	0.005	0.000	0.004	0.008	bdl	-	94.299	1.489	0.005
	Grain 4	26.07	0.09	125.522	0.041	75.734	0.020	0.904	0.014	0.034	0.013	0.037	0.001	0.005	0.002	0.000	0.001	90.958	1.507	0.002
	Grain 5	26.67	0.09	142.933	0.038	81.189	0.021	0.964	0.016	0.045	0.013	0.058	0.001	0.006	0.002	bdl	-	87.632	1.542	0.002
	Grain 6	26.83	0.08	166.243	0.040	99.394	0.021	1.201	0.015	0.025	0.013	0.038	0.001	0.002	0.001	0.000	0.000	92.796	1.551	0.002
	Grain 7	27.17	0.07	37.648	0.036	21.564	0.013	0.239	0.014	0.035	0.013	0.012	0.000	0.018	0.007	bdl	-	90.019	1.571	0.005
	Grain 8	27.74	0.15	23.743	0.035	12.365	0.015	0.129	0.015	0.014	0.014	0.013	0.000	0.012	0.013	bdl	-	83.582	1.604	0.009
	20-20	albite-mica schist																		
	Grain 1	36.90	0.22	166.897	0.039	35.668	0.017	0.492	0.015	0.030	0.014	0.306	0.002	0.009	0.004	0.001	0.001	45.692	2.137	0.016
	Grain 2	37.01	0.21	192.884	0.046	42.528	0.018	0.561	0.017	0.030	0.014	0.343	0.002	0.008	0.004	bdl	-	47.279	2.143	0.014
	Grain 3	37.08	0.13	103.930	0.037	26.644	0.016	0.387	0.014	0.045	0.014	0.157	0.001	0.019	0.006	0.004	0.002	55.072	2.147	0.013
	Grain 4	37.43	0.27	132.207	0.039	27.171	0.015	0.354	0.015	-0.012	0.014	0.247	0.002	bdl	-	bdl	-	44.570	2.167	0.017
	Grain 5	38.33	0.19	121.139	0.037	32.706	0.016	0.386	0.014	0.034	0.014	0.163	0.001	0.012	0.005	bdl	-	59.985	2.220	0.011
	Grain 6	38.36	0.29	194.213	0.042	46.762	0.017	0.638	0.015	0.097	0.013	0.304	0.002	0.023	0.003	0.001	0.001	53.527	2.222	0.012
	Grain 7	38.43	0.24	429.767	0.067	78.509	0.021	1.110	0.017	0.108	0.013	0.861	0.004	0.015	0.002	0.000	0.001	40.685	2.226	0.016
	*Grain 8**	42.51	0.28	208.808	0.045	58.277	0.019	0.720	0.016	0.044	0.014	0.219	0.001	0.008	0.003	bdl	-	68.848	2.465	0.007

*Grain rejected for calculation of weighted mean age
†bdl = below detection limit

Table S2.3 cont.

Sample / Grain	Age (Ma)	±1σ	^{40}Ar (fA)	±1σ	^{39}Ar (fA)	±1σ	^{38}Ar (fA)	±1σ	^{37}Ar (fA)	±1σ	^{36}Ar (fA)	±1σ	Ca/K	±1σ	Cl/K	±1σ	%^{40}Ar*	^{40}Ar*/^{39}Ar$_K$	±1σ
Cycladic Blueschist Unit																			
19-08	schistose quartzite																		
Grain 1	35.01	0.01	596.254	0.060	281.662	0.036	3.395	0.015	1.023	0.014	0.079	0.001	0.028	0.000	0.000	0.000	95.796	2.027	0.001
*Grain 2**	42.09	0.02	458.644	0.057	180.479	0.031	2.149	0.016	0.151	0.014	0.056	0.001	0.006	0.001	0.000	0.000	96.110	2.441	0.001
*Grain 3**	42.06	0.02	329.328	0.049	129.744	0.022	1.539	0.016	0.773	0.014	0.040	0.001	0.046	0.001	0.000	0.000	96.166	2.440	0.001
Grain 4	33.52	0.02	274.162	0.045	132.453	0.022	1.591	0.016	2.395	0.013	0.057	0.001	0.141	0.001	0.000	0.000	93.740	1.939	0.001
Grain 5	37.12	0.02	524.918	0.058	225.093	0.028	2.731	0.014	1.572	0.013	0.134	0.001	0.054	0.000	0.000	0.000	92.244	2.150	0.001
Grain 6	34.66	0.02	458.460	0.052	217.414	0.032	2.602	0.016	2.360	0.013	0.072	0.001	0.085	0.000	0.000	0.000	95.185	2.006	0.001
Grain 7	33.09	0.03	262.693	0.047	128.972	0.023	1.530	0.014	0.869	0.015	0.051	0.001	0.052	0.001	bdl	-	94.034	1.914	0.002
*Grain 8**	41.10	0.02	691.299	0.066	268.519	0.037	3.207	0.016	2.491	0.014	0.169	0.001	0.072	0.000	0.000	0.000	92.611	2.383	0.001
19-09	albite-mica schist																		
Grain 1	35.08	0.20	103.144	0.038	29.730	0.015	0.408	0.016	0.599	0.012	0.145	0.001	0.158	0.003	0.002	0.002	58.552	2.031	0.012
*Grain 2**	40.10	0.09	232.766	0.045	75.629	0.020	0.942	0.016	0.982	0.014	0.192	0.001	0.102	0.001	0.000	0.001	75.562	2.325	0.005
*Grain 3**	29.67	0.23	87.748	0.039	23.623	0.016	0.332	0.015	0.942	0.013	0.160	0.001	0.314	0.004	0.002	0.002	46.189	1.715	0.014
Grain 4	35.13	0.09	88.022	0.035	35.960	0.015	0.444	0.014	0.510	0.012	0.050	0.001	0.112	0.003	0.000	0.001	83.126	2.034	0.005
Grain 5	37.12	0.10	160.687	0.040	53.771	0.019	0.641	0.016	0.942	0.013	0.152	0.001	0.138	0.002	bdl	-	71.986	2.150	0.006
Grain 6	31.97	0.24	71.023	0.038	18.483	0.014	0.232	0.015	0.824	0.012	0.125	0.001	0.355	0.005	bdl	-	48.139	1.849	0.014
Grain 7	35.93	0.08	381.738	0.050	119.607	0.022	1.490	0.016	1.643	0.014	0.448	0.002	0.109	0.001	bdl	-	65.210	2.080	0.005
Grain 8	35.08	0.19	87.167	0.036	24.217	0.014	0.310	0.016	0.296	0.013	0.128	0.001	0.097	0.004	0.000	0.002	56.440	2.031	0.011
19-10	glaucophane schist																		
Grain 1	29.46	0.13	62.622	0.037	24.348	0.015	0.288	0.015	0.048	0.013	0.071	0.001	0.015	0.004	bdl	-	66.178	1.701	0.008
Grain 2	32.22	0.18	78.078	0.036	25.419	0.015	0.313	0.016	0.317	0.013	0.104	0.001	0.098	0.004	bdl	-	60.634	1.862	0.011
Grain 3	32.10	0.18	81.434	0.038	25.549	0.016	0.342	0.015	0.141	0.014	0.115	0.001	0.043	0.004	0.002	0.002	58.217	1.855	0.010
Grain 4	28.42	0.33	219.340	0.050	34.081	0.017	0.526	0.015	0.290	0.013	0.552	0.002	0.067	0.003	0.001	0.001	25.505	1.641	0.019
Grain 5	27.61	0.38	117.248	0.039	18.860	0.013	0.301	0.014	0.079	0.013	0.295	0.001	0.033	0.006	0.003	0.002	25.638	1.593	0.022
*Grain 6**	35.16	0.11	70.067	0.036	27.052	0.018	0.307	0.016	0.197	0.013	0.050	0.001	0.057	0.004	bdl	-	78.528	2.033	0.006
*Grain 7**	25.40	0.27	606.818	0.063	89.068	0.021	1.372	0.016	0.293	0.013	1.610	0.004	0.026	0.001	0.000	0.001	21.516	1.465	0.016
Grain 8	27.88	0.25	196.356	0.039	40.570	0.017	0.563	0.015	0.165	0.014	0.443	0.002	0.032	0.003	0.000	0.001	33.261	1.609	0.014
19-17A	marble																		
Grain 1	31.60	0.10	58.205	0.033	26.031	0.016	0.324	0.016	1.189	0.014	0.037	0.001	0.370	0.004	0.001	0.002	81.764	1.828	0.006
Grain 2	31.83	0.13	45.241	0.034	19.355	0.014	0.241	0.015	0.139	0.014	0.032	0.000	0.058	0.006	0.000	0.002	78.785	1.841	0.008
Grain 3	30.42	0.15	26.317	0.031	12.848	0.013	0.125	0.015	0.035	0.014	0.012	0.000	0.022	0.009	bdl	-	85.884	1.758	0.009
Grain 4	32.70	0.15	45.214	0.033	18.077	0.015	0.211	0.015	0.091	0.014	0.037	0.000	0.040	0.006	bdl	-	75.671	1.892	0.009
Grain 5	30.00	0.14	37.089	0.029	17.114	0.015	0.248	0.016	0.092	0.013	0.025	0.000	0.043	0.006	0.006	0.003	80.062	1.734	0.008
Grain 6	26.54	0.20	27.219	0.032	11.433	0.014	0.133	0.017	0.229	0.014	0.033	0.000	0.163	0.010	bdl	-	64.394	1.532	0.012
Grain 7	33.19	0.35	20.669	0.037	6.787	0.014	0.069	0.014	0.048	0.014	0.026	0.000	0.057	0.016	bdl	-	63.085	1.920	0.020
Grain 8	34.29	0.11	51.123	0.037	21.245	0.015	0.267	0.016	0.719	0.013	0.031	0.000	0.276	0.005	0.001	0.002	82.497	1.984	0.007
20-04	schistose quartzite																		
Grain 1	26.83	0.14	126.355	0.032	45.302	0.016	0.611	0.017	0.128	0.014	0.189	0.001	0.019	0.002	0.002	0.001	55.505	1.547	0.008
Grain 2	31.02	0.04	139.868	0.038	68.989	0.017	0.830	0.016	0.258	0.013	0.053	0.001	0.025	0.001	0.000	0.001	88.388	1.791	0.002
*Grain 3**	37.10	0.04	141.182	0.041	61.295	0.018	0.752	0.015	0.021	0.014	0.031	0.000	0.002	0.002	0.001	0.001	93.185	2.145	0.002
Grain 4	29.24	0.28	276.965	0.045	53.279	0.017	0.773	0.015	0.112	0.014	0.632	0.003	0.014	0.002	0.001	0.001	32.477	1.688	0.017
Grain 5	29.86	0.20	162.309	0.041	41.526	0.016	0.553	0.016	0.111	0.012	0.306	0.002	0.018	0.002	0.000	0.001	44.114	1.723	0.012
*Grain 6**	35.62	0.19	384.761	0.053	84.620	0.019	1.169	0.016	0.298	0.012	0.710	0.003	0.024	0.001	0.001	0.001	45.301	2.059	0.011
Grain 7	28.51	0.04	115.201	0.039	64.970	0.020	0.798	0.016	0.148	0.014	0.027	0.000	0.015	0.001	0.001	0.001	92.813	1.645	0.002
Grain 8	27.95	0.14	243.780	0.049	71.692	0.018	0.948	0.015	0.081	0.013	0.432	0.002	0.007	0.001	0.000	0.001	47.440	1.612	0.008
20-19	schistose quartzite																		
*Grain 1**	30.58	0.06	116.279	0.038	46.302	0.016	0.591	0.015	0.049	0.013	0.115	0.001	0.012	0.003	0.001	0.001	70.515	1.770	0.006
Grain 2	32.43	0.05	151.730	0.040	70.587	0.018	0.845	0.015	-0.006	0.013	0.063	0.001	bdl	-	0.000	0.001	87.399	1.878	0.003
Grain 3	33.01	0.23	58.947	0.035	24.549	0.013	0.298	0.016	0.028	0.013	0.040	0.001	0.012	0.006	0.000	0.002	79.648	1.911	0.006
Grain 4	35.48	0.06	68.780	0.034	26.006	0.015	0.306	0.016	0.014	0.015	0.051	0.001	0.005	0.006	bdl	-	77.792	2.056	0.006
Grain 5	37.44	0.11	102.757	0.039	42.474	0.016	0.517	0.016	-0.003	0.014	0.034	0.000	bdl	-	0.000	0.001	89.785	2.171	0.004
Grain 6	37.60	0.08	135.016	0.042	52.522	0.016	0.640	0.016	-0.012	0.014	0.068	0.001	bdl	-	0.000	0.001	84.845	2.180	0.005
*Grain 7**	39.15	0.11	103.003	0.037	25.291	0.015	0.320	0.016	-0.028	0.014	0.153	0.001	bdl	-	bdl	-	55.788	2.271	0.014
*Grain 8**	39.95	0.11	249.152	0.044	91.125	0.019	1.106	0.015	0.022	0.014	0.126	0.001	0.002	0.002	0.000	0.000	84.811	2.317	0.003

*Grain rejected for calculation of weighted mean age
†bdl = below detection limit

Table S2.4. Analytical results for zircon (U-Th)/He geochronology for samples from from southern Evia (Greece)

	Sample / *Grain*	Corrected date (Ma)	2σ	Length measurement 1 (μm)	Width measurement 1 (μm)	Length measurement 2 (μm)	Width measurement 2 (μm)	Ft	# of terminations	Mass (μg)	Effective spherical radius (μm)	Rs (μm)	^{4}He (nmol/g)	±	U (ppm)	±	Th (ppm)	±	Sm (ppm)	±	eU (ppm)	±	Uncorr date (Ma)	Uncorr date analytic unc. (Ma) 2σ
Basal Unit	**20-01**	carbonate-silicate schist																						
	Grain 1	13.3	0.5	109.9	55.9	115.6	55.7	0.67	2	1.1	30.8	34.8	34.250	0.282	674.040	13.110	183.381	1.008	n.m.	n.m.	717.68	107.65	8.86	0.17
	Grain 2	15.4	0.5	128.5	50.7	127.9	57.3	0.67	2	1.2	29.8	35.1	23.265	0.222	379.452	5.300	173.123	3.035	n.m.	n.m.	420.65	63.10	10.26	0.16
	Grain 3	13.8	0.5	144.7	91.7	145.4	85.0	0.77	1	4.2	45.4	52.3	27.796	0.189	445.746	8.088	157.311	1.957	n.m.	n.m.	483.19	72.48	10.67	0.19
	Grain 4	15.8	1.1	92.3	53.7	94.5	44.6	0.59	2	0.5	29.7	28.0	22.431	0.107	399.541	16.818	204.662	2.369	n.m.	n.m.	448.25	67.24	9.29	0.34
	Grain 5	11.7	0.3	138.3	53.9	133.9	57.9	0.68	2	1.4	26.0	36.6	20.356	0.127	454.719	5.177	66.246	1.002	n.m.	n.m.	470.49	70.57	8.03	0.10
	Grain 6	14.0	0.7	87.6	72.6	98.7	58.6	0.66	2	1.0	32.7	34.5	20.382	0.181	363.425	10.092	188.539	2.814	n.m.	n.m.	408.30	61.24	9.27	0.24
	Grain 7	15.2	0.5	104.3	61.0	105.5	68.9	0.68	2	1.1	33.3	36.4	49.968	0.375	804.096	12.179	392.216	8.677	n.m.	n.m.	897.44	134.62	10.33	0.16
	Grain 8	16.5	0.7	103.6	58.0	105.2	64.8	0.68	2	1.1	31.8	35.8	46.490	0.380	717.367	15.386	240.136	2.744	n.m.	n.m.	774.52	116.18	11.14	0.23
	20-03	albite-mica schist																						
	Grain 1	15.4	1.5	147.1	64.7	144.7	73.4	0.71	2	0.8	37.2	39.5	20.287	0.098	331.235	5.377	65.251	0.715	n.m.	n.m.	346.76	52.01	10.85	0.17
	Grain 2	17.2	1.7	187.6	79.6	180.9	81.3	0.77	2	4.4	42.1	51.2	49.763	0.422	659.367	9.117	153.281	2.176	n.m.	n.m.	695.85	104.38	13.27	0.20
	Grain 3	17.6	1.8	164.1	66.3	159.1	47.7	0.69	2	1.0	52.2	37.4	25.936	0.141	372.919	4.948	101.986	2.363	n.m.	n.m.	397.19	59.58	12.11	0.16
	Grain 4	17.5	1.7	150.6	63.4	154.8	60.4	0.68	2	0.4	35.0	36.9	13.258	0.067	178.416	4.700	118.397	2.102	n.m.	n.m.	206.59	30.99	11.91	0.27
	Grain 5	16.1	1.6	203.0	75.3	202.8	75.1	0.76	2	1.1	43.9	49.7	12.726	0.086	165.119	2.562	114.143	2.017	n.m.	n.m.	192.28	28.84	12.28	0.18
	Grain 6	17.6	1.8	147.0	66.2	153.6	60.9	0.72	2	0.6	34.2	41.1	13.813	0.128	189.946	3.634	56.523	1.465	n.m.	n.m.	203.40	30.51	12.60	0.25
	Grain 7	16.6	1.7	216.2	98.9	216.0	92.8	0.80	2	2.6	32.1	60.3	17.704	0.094	212.594	4.918	142.442	2.328	n.m.	n.m.	246.50	36.97	13.33	0.27
	Grain 8	16.7	1.7	158.9	63.9	157.9	62.6	0.71	2	0.7	34.9	41.4	13.701	0.052	181.308	2.648	133.004	1.094	n.m.	n.m.	212.96	31.94	11.94	0.15
	20-08	impure schistose marble																						
	Grain 1	16.4	0.6	101.0	60.6	102.9	59.4	0.66	2	0.9	31.1	34.0	67.659	0.446	1064.471	20.727	396.285	4.449	n.m.	n.m.	1158.79	173.82	10.83	0.20
	Grain 2	17.8	0.6	89.9	46.2	85.3	40.0	0.58	2	0.5	23.1	27.1	77.261	0.538	1293.317	23.612	408.949	6.576	n.m.	n.m.	1390.65	208.60	10.31	0.18
	Grain 3	15.5	0.4	111.2	61.6	105.6	55.7	0.67	2	1.1	30.9	35.4	39.950	0.251	651.881	8.383	262.517	3.304	n.m.	n.m.	714.36	107.15	10.38	0.14
	Grain 4	16.9	0.8	82.3	48.3	83.0	47.7	0.58	2	0.5	24.9	27.2	36.161	0.336	655.102	15.201	105.295	1.046	n.m.	n.m.	680.16	102.02	9.87	0.23
	Grain 5	12.9	0.4	79.5	43.6	85.8	44.0	0.59	1	0.6	23.1	28.0	43.219	0.301	1018.203	17.793	117.513	4.095	n.m.	n.m.	1046.17	156.93	7.67	0.14
	Grain 6	16.1	0.7	113.8	60.9	116.7	58.3	0.66	2	1.0	31.6	34.5	42.832	0.212	685.300	16.823	246.831	5.105	n.m.	n.m.	744.05	111.61	10.68	0.24
	Grain 7	18.1	0.7	121.7	55.1	122.1	48.7	0.66	2	1.1	28.5	33.7	33.100	0.254	490.557	9.000	101.902	2.104	n.m.	n.m.	514.81	77.22	11.93	0.22
	Grain 8	17.6	0.7	123.9	57.5	121.5	51.8	0.64	2	0.9	29.8	32.2	91.950	0.541	1368.054	29.197	621.550	8.833	n.m.	n.m.	1515.98	227.40	11.26	0.22
	20-13	albite-mica schist																						
	Grain 1	19.3	1.9	166.3	63.7	164.3	71.1	0.71	2	1.8	37.2	40.2	32.195	0.170	405.234	10.446	131.156	3.190	n.m.	n.m.	436.45	65.47	13.68	0.33
	Grain 2	15.7	1.6	113.5	57.7	127.8	51.7	0.67	2	1.2	29.7	34.9	130.611	0.445	2102.954	35.128	916.745	10.584	n.m.	n.m.	2321.14	348.17	10.44	0.16
	Grain 3	12.4	1.2	102.0	50.0	121.3	57.1	0.66	2	1.0	28.8	33.6	31.734	0.209	671.122	21.484	222.326	5.289	n.m.	n.m.	724.04	108.61	8.13	0.24
	Grain 4	17.9	1.8	80.8	66.9	98.5	65.0	0.66	2	0.9	32.5	34.3	58.996	0.327	877.206	16.978	191.221	4.496	n.m.	n.m.	922.72	138.41	11.86	0.22
	Grain 5	18.1	1.8	181.1	53.9	189.7	62.6	0.70	2	2.3	33.3	39.8	134.370	0.821	1720.643	28.793	986.569	10.204	n.m.	n.m.	1955.45	293.32	12.75	0.20
	Grain 6	13.6	1.4	113.6	63.3	116.3	61.6	0.69	2	1.3	32.8	37.6	23.777	0.135	438.228	8.161	135.249	2.562	n.m.	n.m.	470.42	70.56	9.38	0.17
	Grain 7	13.2	1.3	137.3	55.6	130.9	61.3	0.67	2	1.1	31.9	34.6	38.477	0.247	761.022	9.643	209.246	4.266	n.m.	n.m.	810.82	121.62	8.81	0.12
	Grain 8	14.0	1.4	111.7	54.9	112.1	47.0	0.62	2	0.7	27.6	29.8	60.230	0.391	1266.868	25.659	119.102	2.586	n.m.	n.m.	1295.21	194.28	8.63	0.17
	20-21	albite-mica schist																						
	Grain 1	13.2	0.5	120.0	53.0	117.6	55.8	0.64	2	0.9	29.5	32.1	29.037	0.175	607.576	11.188	114.213	2.533	n.m.	n.m.	634.76	95.21	8.49	0.15
	Grain 2	12.2	0.5	139.8	61.8	139.1	58.2	0.70	2	1.7	32.9	38.8	18.877	0.156	394.566	7.355	57.787	2.425	n.m.	n.m.	408.32	61.25	8.58	0.17
	Grain 3	15.3	0.3	156.0	91.9	157.9	71.9	0.76	2	3.1	43.4	48.7	130.879	0.781	2077.556	16.769	36.288	0.568	n.m.	n.m.	2086.19	312.93	11.64	0.11
	Grain 4	16.7	0.6	120.6	71.3	116.6	65.7	0.71	2	1.6	35.6	40.1	70.945	0.313	1042.064	18.794	278.825	3.559	n.m.	n.m.	1108.42	166.26	11.88	0.20
	Grain 5	14.9	0.6	126.3	51.7	123.4	62.5	0.66	2	1.0	31.0	33.4	58.065	0.362	1082.398	24.357	89.766	0.950	n.m.	n.m.	1103.76	165.56	9.76	0.22
	Grain 6	14.2	0.5	122.0	59.0	117.5	71.8	0.70	2	1.5	34.4	38.9	27.147	0.252	472.571	8.415	135.286	2.960	n.m.	n.m.	504.77	75.72	9.98	0.19
	Grain 7	14.9	0.7	120.7	58.1	122.3	59.6	0.67	2	1.0	31.6	34.5	68.604	0.341	1251.949	33.617	144.430	4.283	n.m.	n.m.	1286.32	192.95	9.90	0.26
	Grain 8	15.0	0.4	106.6	49.2	109.6	51.4	0.64	2	0.9	27.2	32.1	28.412	0.201	492.744	7.018	251.870	3.477	n.m.	n.m.	552.69	82.90	9.54	0.14
	Grain 9	18.3	0.5	94.0	48.2	99.4	51.9	0.62	2	0.7	26.6	30.8	44.677	0.181	613.991	10.629	489.484	8.122	n.m.	n.m.	730.49	109.57	11.35	0.17
Cycladic Blueschist Unit	**20-04**	schistose quartzite																						
	Grain 1	15.4	0.5	131.3	63.9	142.9	57.0	0.70	2	1.6	33.0	38.7	26.348	0.178	404.913	7.647	217.559	4.597	n.m.	n.m.	456.69	68.50	10.71	0.19
	Grain 2	15.1	0.8	167.0	84.5	182.5	93.9	0.78	1	5.3	47.4	55.2	23.784	0.257	323.845	9.110	204.210	3.391	n.m.	n.m.	372.45	55.87	11.85	0.31
	Grain 3	15.0	0.6	140.0	60.7	153.8	53.5	0.69	2	1.6	31.7	37.6	42.225	0.153	655.800	14.159	438.463	10.094	n.m.	n.m.	760.15	114.02	10.31	0.19
	Grain 4	15.2	0.5	141.5	65.9	134.1	66.6	0.71	2	1.9	35.6	41.3	49.529	0.295	693.076	10.016	659.980	42.966	n.m.	n.m.	850.15	127.52	10.81	0.19
	Grain 5	16.8	0.5	106.7	63.3	100.9	67.5	0.68	2	1.2	33.4	36.9	29.246	0.248	410.143	6.854	265.055	5.470	n.m.	n.m.	473.23	70.98	11.47	0.19
	Grain 6	13.5	0.3	163.6	70.8	158.6	54.3	0.71	2	2.1	34.8	40.5	52.579	0.257	920.270	11.219	415.229	9.714	n.m.	n.m.	1019.09	152.86	9.58	0.11
	Grain 7	13.6	0.4	188.5	63.2	176.2	60.9	0.72	2	2.5	35.1	42.0	25.615	0.113	429.852	6.164	241.444	14.985	n.m.	n.m.	487.32	73.10	9.76	0.15
	Grain 8	12.4	0.4	149.0	67.8	155.7	67.4	0.72	2	2.3	36.8	43.1	27.452	0.146	476.255	8.994	376.454	5.829	n.m.	n.m.	565.85	84.88	9.01	0.15
	20-18	glaucophane-albite-mica schist																						
	Grain 1	20.6	0.4	141.6	74.7	140.2	57.1	0.74	2	2.9	35.6	45.6	24.695	0.088	263.002	2.993	155.562	2.915	n.m.	n.m.	300.03	45.00	15.27	0.16
	Grain 2	19.3	0.9	123.0	62.0	125.2	68.3	0.69	2	1.3	34.5	37.7	28.744	0.247	378.993	9.112	86.875	2.683	n.m.	n.m.	399.67	59.95	13.34	0.32
	Grain 3	20.9	0.6	99.7	48.1	96.8	50.5	0.60	2	0.6	26.3	28.6	48.323	0.231	682.849	9.887	135.538	3.025	n.m.	n.m.	715.11	107.27	12.54	0.18
	Grain 4	17.0	0.6	154.1	65.8	167.7	68.6	0.72	2	2.4	37.0	41.8	36.036	0.236	509.900	9.409	150.964	5.181	n.m.	n.m.	545.83	81.87	12.25	0.22
	Grain 5	15.2	0.4	137.6	65.6	134.9	51.9	0.66	2	1.1	32.2	34.3	105.839	0.478	1816.693	23.799	537.428	11.528	n.m.	n.m.	1944.60	291.69	10.10	0.13
	Grain 6	17.7	0.5	137.3	66.4	129.7	68.6	0.72	1	2.2	36.0	41.3	32.391	0.279	440.252	6.378	136.988	1.964	n.m.	n.m.	472.86	70.93	12.71	0.20
	Grain 7	17.0	0.5	115.9	61.2	121.3	63.8	0.68	2	1.1	33.1	36.2	46.811	0.276	715.844	11.506	144.712	3.892	n.m.	n.m.	750.29	112.54	11.58	0.19
	Grain 8	16.4	0.6	146.7	58.6	129.7	58.3	0.69	2	1.6	32.1	38.0	15.596	0.085	233.580	4.634	89.889	2.198	n.m.	n.m.	254.97	38.25	11.35	0.21

APPENDIX B. Supporting Information for Chapter 3

Introduction

The following pages contain complete analytical data for the white mica electron microprobe data (**Table S3.1a-i** below), *in situ* $^{40}Ar/^{39}Ar$ results (**Table S3.2** below), and *in situ* $^{87}Rb/^{87}Sr$ results (**Table S3.3** below).

Text S3.1. Microanalytical methods

S2.1. Scanning Electron Microscopy (SEM)

Scanning electron microscopy was performed at the University of Ottawa using a JEOL 6610LV SEM. Backscatter electron imaging and exploratory electron dispersive spectroscopy (EDS) were carried out with an accelerating voltage of 15 kV and a working distance of 11 mm on standard 30 µm thick polished thin sections.

S2.2. Electron Microprobe Analysis (EMPA)

Mineral chemistry of petrologically significant phases was analyzed via electron microprobe (EMPA). Analyses were performed at University of Ottawa using a JEOL JXA-8230 SuperProbe. White mica was quantitatively analyzed using a beam diameter of 10 µm with an accelerating voltage of 15 keV and beam current of 20 nA. Dwell times of 10 s were used for X-ray peak positions and 5 s for background positions. Wavelength dispersive spectroscopy (WDS) acquired quantitative chemical data for the major and minor elements Si, Al, Ca, Mg, Fe, K, Na, Ti, Cr, and Mn. The laboratory standards used at University of Ottawa were sanidine (Si, Al, K), diopside (Ca, Mg), hematite (Fe), albite (Na), rutile (Ti), chromite (Cr), and tephroite (Mn); and at Uppsala University were pyrope (Si, Mg), wollastonite (Si, Ca), Al_2O_3 (Al), MgO (Mg), fayalite (Fe), orthoclase (K), albite (Na), pyrophanite (Ti, Mn), Cr_2O_3 (Cr), apatite (P, F), and vanadinite (F, Cl).

White mica compositions were recalculated manually on the basis of 11 O, following the methodology of Vidal & Parra (2000) and Parra et al. (2002), accepting only analyses with weight percent oxide sums between 92-96% and with < 0.5 wt.% TiO_2 + MnO + CaO. Recalculations assumed 11 oxygens and calculated molar fractions for seven end-members (Mg- and Fe-Al-celadonite, muscovite, annite, phlogopite, paragonite, pyrophyllite).

Table S3.1a. White mica geochemistry from sample EV19-03.

	EV19-03												
	1	2	3	4	5	6	7	8	9	10	11	12	13
Microstructure	foliation		high-angle fan			shear band				-			
SiO_2	51.88	51.47	51.68	54.57	51.02	50.88	42.25	49.84	49.61	51.03	46.40	48.87	49.56
TiO_2	0.08	0.03	0.07	0.07	0.02	0.05	0.03	0.04	0.04	0.03	0.13	0.05	0.07
Al_2O_3	26.39	27.51	27.00	22.84	26.91	26.39	24.40	25.35	26.63	22.05	23.31	25.73	25.46
Cr_2O_3	0.09	0.03	0.05	0.03	0.06	0.17	0.02	0.07	0.06	0.16	0.07	0.08	0.07
FeO	1.46	1.38	1.27	1.33	1.93	1.52	5.58	1.39	1.43	1.69	1.73	1.25	1.60
MnO	0.03	0.05	0.04	0.04	0.02	0.04	0.11	0.00	0.03	0.02	0.01	0.00	0.05
MgO	4.34	4.05	4.10	5.65	5.48	4.72	12.51	4.03	3.88	5.56	3.70	3.94	3.99
CaO	0.02	0.02	0.02	0.00	0.00	0.03	0.08	0.02	0.02	0.24	0.05	0.05	0.01
Na_2O	0.17	0.17	0.16	0.06	0.14	0.18	0.10	0.12	0.15	0.09	0.12	0.16	0.21
K_2O	10.55	10.55	10.50	11.00	10.03	10.29	5.92	9.88	9.94	9.59	8.50	9.28	9.98
Cl	0.00	0.00	0.00	0.00	0.00	0.00	0.01	0.00	0.00	0.00	0.02	0.01	0.00
F	0.00	0.00	0.00	0.00	0.00	0.00	0.00	0.00	0.00	0.00	0.06	0.00	0.00
TOTAL	95.01	95.25	94.90	95.58	95.60	94.29	91.00	90.74	91.80	90.46	84.10	89.42	91.00
SiO_2	0.86	0.86	0.86	0.91	0.85	0.85	0.70	0.83	0.83	0.85	0.77	0.81	0.82
TiO_2	0.00	0.00	0.00	0.00	0.00	0.00	0.00	0.00	0.00	0.00	0.00	0.00	0.00
Al_2O_3	0.26	0.27	0.26	0.22	0.26	0.26	0.24	0.25	0.26	0.22	0.23	0.25	0.25
Cr_2O_3	0.00	0.00	0.00	0.00	0.00	0.00	0.00	0.00	0.00	0.00	0.00	0.00	0.00
FeO	0.02	0.02	0.02	0.02	0.03	0.02	0.08	0.02	0.02	0.02	0.02	0.02	0.02
MnO	0.00	0.00	0.00	0.00	0.00	0.00	0.00	0.00	0.00	0.00	0.00	0.00	0.00
MgO	0.11	0.10	0.10	0.14	0.14	0.12	0.31	0.10	0.10	0.14	0.09	0.10	0.10
CaO	0.00	0.00	0.00	0.00	0.00	0.00	0.00	0.00	0.00	0.00	0.00	0.00	0.00
Na_2O	0.00	0.00	0.00	0.00	0.00	0.00	0.00	0.00	0.00	0.00	0.00	0.00	0.00
K_2O	0.11	0.11	0.11	0.12	0.11	0.11	0.06	0.10	0.11	0.10	0.09	0.10	0.11
O	2.75	2.76	2.75	2.77	2.76	2.73	2.58	2.63	2.66	2.62	2.44	2.60	2.63
Norm	0.25	0.25	0.25	0.25	0.25	0.25	0.23	0.24	0.24	0.24	0.22	0.24	0.24
Si	3.45	3.41	3.44	3.61	3.38	3.42	3.00	3.46	3.41	3.57	3.48	3.44	3.45
Ti	0.00	0.00	0.00	0.00	0.00	0.00	0.00	0.00	0.00	0.00	0.01	0.00	0.00
Al	2.07	2.15	2.12	1.78	2.10	2.09	2.04	2.08	2.16	1.82	2.06	2.13	2.09
Cr	0.00	0.00	0.00	0.00	0.00	0.01	0.00	0.00	0.00	0.01	0.00	0.00	0.00
Fe	0.08	0.08	0.07	0.07	0.11	0.09	0.33	0.08	0.08	0.10	0.11	0.07	0.09
Mn	0.00	0.00	0.00	0.00	0.00	0.00	0.01	0.00	0.00	0.00	0.00	0.00	0.00
Mg	0.43	0.40	0.41	0.56	0.54	0.47	1.32	0.42	0.40	0.58	0.41	0.41	0.41
Ca	0.00	0.00	0.00	0.00	0.00	0.00	0.01	0.00	0.00	0.02	0.00	0.00	0.00
Na	0.02	0.02	0.02	0.01	0.02	0.02	0.01	0.02	0.02	0.01	0.02	0.02	0.03
K	0.90	0.89	0.89	0.93	0.85	0.88	0.54	0.88	0.87	0.85	0.81	0.83	0.89
X_{Mg}	0.84	0.84	0.85	0.88	0.84	0.85	0.80	0.84	0.83	0.85	0.79	0.85	0.82
Si(T1+T2)	3.45	3.41	3.44	3.61	3.38	3.42	3.00	3.46	3.41	3.57	3.48	3.44	3.45
Ti(T2)	0.00	0.00	0.00	0.00	0.00	0.00	0.00	0.00	0.00	0.00	0.01	0.00	0.00
Al(IV) (T2)	0.55	0.59	0.57	0.39	0.62	0.59	1.00	0.54	0.59	0.44	0.53	0.57	0.56
Al(VI) (M2)	1.52	1.56	1.55	1.39	1.48	1.50	1.04	1.54	1.57	1.38	1.53	1.57	1.53
Mg (M2)	0.40	0.37	0.38	0.54	0.44	0.42	0.78	0.39	0.36	0.53	0.38	0.37	0.39
Fe (M2)	0.08	0.07	0.07	0.07	0.09	0.08	0.19	0.07	0.07	0.09	0.10	0.07	0.09
Fe + Mg (M2)	0.48	0.44	0.45	0.62	0.52	0.50	0.97	0.46	0.43	0.62	0.47	0.43	0.48
Mn (M2)	0.00	0.00	0.00	0.00	0.00	0.00	0.01	0.00	0.00	0.00	0.00	0.00	0.00
Mg (M1)	0.03	0.03	0.02	0.01	0.11	0.05	0.55	0.03	0.04	0.05	0.04	0.04	0.03
Fe (M1)	0.00	0.01	0.00	0.00	0.02	0.01	0.14	0.01	0.01	0.01	0.01	0.01	0.01
vac (M1)	0.97	0.96	0.97	0.98	0.87	0.94	0.32	0.96	0.95	0.94	0.95	0.95	0.97
K (A)	0.90	0.89	0.89	0.93	0.85	0.88	0.54	0.88	0.87	0.85	0.81	0.83	0.89
Na (A)	0.02	0.02	0.02	0.01	0.02	0.02	0.01	0.02	0.02	0.01	0.02	0.02	0.03
v (A)	0.08	0.09	0.09	0.06	0.13	0.09	0.45	0.11	0.11	0.13	0.17	0.15	0.09
Paragonite	0.02	0.02	0.02	0.01	0.02	0.02	0.01	0.02	0.02	0.01	0.02	0.02	0.03
Phlogopite	0.03	0.03	0.02	0.01	0.11	0.05	0.55	0.03	0.04	0.05	0.04	0.04	0.03
Annite	0.00	0.01	0.00	0.00	0.02	0.01	0.14	0.01	0.01	0.01	0.01	0.01	0.01
Mg-Celadonite	0.31	0.28	0.30	0.48	0.20	0.27	-0.36	0.30	0.25	0.37	0.24	0.24	0.29
Fe-Celadonite	0.06	0.05	0.05	0.06	0.04	0.05	-0.09	0.06	0.05	0.06	0.06	0.04	0.07
Pyrophyllite	0.08	0.09	0.09	0.06	0.13	0.09	0.45	0.11	0.11	0.13	0.17	0.15	0.09
Muscovite	0.50	0.53	0.52	0.37	0.48	0.50	0.31	0.49	0.52	0.37	0.47	0.49	0.50
CeladoniteTOT	0.37	0.33	0.35	0.54	0.24	0.32	-0.45	0.35	0.30	0.43	0.30	0.29	0.36
ms	0.56	0.60	0.58	0.40	0.64	0.59	-2.28	0.57	0.62	0.46	0.60	0.62	0.57
pg	0.02	0.02	0.02	0.01	0.03	0.03	-0.10	0.02	0.02	0.01	0.02	0.03	0.03
cel	0.41	0.37	0.39	0.59	0.33	0.38	3.39	0.41	0.36	0.53	0.38	0.36	0.40
Villa and Parra (2000)													
Mg+Fe	0.05	0.03	0.05	0.04	0.02	0.06	0.06	0.03	0.04	0.08	0.08	0.04	0.06
K	0.00	0.00	0.00	0.00	0.00	0.00	0.00	0.00	0.00	0.00	0.00	0.00	0.00
Si	0.00	0.00	0.00	0.00	0.00	0.00	0.00	0.00	0.00	0.00	0.01	0.00	0.00
Al(VI)	-0.05	-0.03	-0.05	-0.04	-0.02	-0.06	-0.05	-0.03	-0.04	-0.08	-0.08	-0.04	-0.06

Analyses highlighted in red fail major element criteria of Villa and Parra (2000).
Analyses highlighted in orange fail major element criteria of Villa and Parra (2000) by a small margin, but are plotted as representative.
† Sample rejected only for failing mica purity tests of Villa and Parra (2000).

Table S3.1b. White mica geochemistry from sample EV20-14.

	EV20-14									
	1	2	3	4	5	6	7†	8†	9†	10†
Microstructure	foliation						-			
SiO_2	54.25	52.66	52.74	52.78	51.58	53.55	51.07	54.74	53.03	52.81
TiO_2	0.06	0.12	0.11	0.12	0.09	0.12	0.20	0.12	0.15	0.20
Al_2O_3	22.22	25.70	25.21	23.53	23.24	23.50	26.92	22.49	24.89	22.99
Cr_2O_3	0.04	0.10	0.11	0.06	0.08	0.05	0.07	0.09	0.10	0.07
FeO	2.31	2.32	2.28	2.91	3.30	3.02	2.19	2.27	2.36	2.59
MnO	0.01	0.00	0.02	0.00	0.04	0.01	0.02	0.00	0.00	0.00
MgO	4.99	3.94	4.06	5.27	5.34	4.63	3.79	5.08	4.22	4.44
CaO	0.04	0.07	0.02	0.05	0.02	0.04	0.04	0.14	0.01	0.03
Na_2O	0.02	0.13	0.13	0.05	0.05	0.07	0.13	0.03	0.09	0.08
K_2O	10.48	10.31	10.50	10.47	10.07	10.22	10.81	10.38	10.66	10.66
Cl	0.00	0.00	0.00	0.00	0.01	0.00	0.02	0.00	0.00	0.00
F	0.04	0.03	0.00	0.03	0.00	0.02	0.00	0.21	0.00	0.04
TOTAL	94.42	95.34	95.18	95.25	93.80	95.21	95.24	95.33	95.50	93.86
SiO_2	0.90	0.88	0.88	0.88	0.86	0.89	0.85	0.91	0.88	0.88
TiO_2	0.00	0.00	0.00	0.00	0.00	0.00	0.00	0.00	0.00	0.00
Al_2O_3	0.22	0.25	0.25	0.23	0.23	0.23	0.26	0.22	0.24	0.23
Cr_2O_3	0.00	0.00	0.00	0.00	0.00	0.00	0.00	0.00	0.00	0.00
FeO	0.03	0.03	0.03	0.04	0.05	0.04	0.03	0.03	0.03	0.04
MnO	0.00	0.00	0.00	0.00	0.00	0.00	0.00	0.00	0.00	0.00
MgO	0.12	0.10	0.10	0.13	0.13	0.11	0.09	0.13	0.10	0.11
CaO	0.00	0.00	0.00	0.00	0.00	0.00	0.00	0.00	0.00	0.00
Na_2O	0.00	0.00	0.00	0.00	0.00	0.00	0.00	0.00	0.00	0.00
K_2O	0.11	0.11	0.11	0.11	0.11	0.11	0.11	0.11	0.11	0.11
O	2.73	2.76	2.75	2.74	2.69	2.75	2.74	2.76	2.76	2.70
Norm	0.25	0.25	0.25	0.25	0.24	0.25	0.25	0.25	0.25	0.25
Si	3.64	3.50	3.51	3.53	3.51	3.57	3.41	3.63	3.52	3.58
Ti	0.00	0.01	0.01	0.01	0.00	0.01	0.01	0.01	0.01	0.01
Al	1.76	2.01	1.98	1.85	1.86	1.85	2.12	1.76	1.95	1.84
Cr	0.00	0.01	0.01	0.00	0.00	0.00	0.00	0.00	0.00	0.00
Fe	0.13	0.13	0.13	0.16	0.19	0.17	0.12	0.13	0.13	0.15
Mn	0.00	0.00	0.00	0.00	0.00	0.00	0.00	0.00	0.00	0.00
Mg	0.50	0.39	0.40	0.53	0.54	0.46	0.38	0.50	0.42	0.45
Ca	0.00	0.00	0.00	0.00	0.00	0.00	0.00	0.01	0.00	0.00
Na	0.00	0.02	0.02	0.01	0.01	0.01	0.02	0.00	0.01	0.01
K	0.90	0.87	0.89	0.89	0.87	0.87	0.92	0.88	0.90	0.92
X_{Mg}	0.79	0.75	0.76	0.76	0.74	0.73	0.76	0.80	0.76	0.75
Si(T1+T2)	3.64	3.50	3.51	3.53	3.51	3.57	3.41	3.63	3.52	3.58
Ti(T2)	0.00	0.01	0.01	0.01	0.00	0.01	0.01	0.01	0.01	0.01
Al(IV) (T2)	0.37	0.51	0.49	0.48	0.50	0.43	0.60	0.37	0.48	0.43
Al(VI) (M2)	1.39	1.50	1.49	1.38	1.37	1.41	1.52	1.39	1.46	1.40
Mg (M2)	0.48	0.37	0.39	0.48	0.47	0.43	0.36	0.49	0.41	0.45
Fe (M2)	0.13	0.12	0.12	0.15	0.16	0.16	0.12	0.12	0.13	0.15
Fe + Mg (M2)	0.61	0.50	0.52	0.62	0.64	0.59	0.48	0.61	0.54	0.59
Mn (M2)	0.00	0.00	0.00	0.00	0.00	0.00	0.00	0.00	0.00	0.00
Mg (M1)	0.01	0.02	0.01	0.05	0.07	0.03	0.01	0.01	0.01	0.00
Fe (M1)	0.00	0.01	0.00	0.02	0.02	0.01	0.00	0.00	0.00	0.00
vac (M1)	0.98	0.98	0.99	0.93	0.91	0.96	0.98	0.99	0.99	1.00
K (A)	0.90	0.87	0.89	0.89	0.87	0.87	0.92	0.88	0.90	0.92
Na (A)	0.00	0.02	0.02	0.01	0.01	0.01	0.02	0.00	0.01	0.01
v (A)	0.10	0.11	0.09	0.10	0.12	0.12	0.06	0.12	0.09	0.07
Paragonite	0.00	0.02	0.02	0.01	0.01	0.01	0.02	0.00	0.01	0.01
Phlogopite	0.01	0.02	0.01	0.05	0.07	0.03	0.01	0.01	0.01	0.00
Annite	0.00	0.01	0.00	0.02	0.02	0.01	0.00	0.00	0.00	0.00
Mg-Celadonite	0.42	0.29	0.32	0.32	0.29	0.33	0.26	0.41	0.33	0.38
Fe-Celadonite	0.11	0.09	0.10	0.10	0.10	0.12	0.08	0.10	0.10	0.12
Pyrophyllite	0.10	0.11	0.09	0.10	0.12	0.12	0.06	0.12	0.09	0.07
Muscovite	0.34	0.47	0.46	0.40	0.40	0.38	0.56	0.36	0.46	0.42
CeladoniteTOT	0.53	0.38	0.42	0.42	0.38	0.44	0.34	0.51	0.43	0.50
ms	0.39	0.54	0.52	0.48	0.50	0.46	0.61	0.41	0.51	0.45
pg	0.00	0.02	0.02	0.01	0.01	0.01	0.02	0.00	0.01	0.01
cel	0.61	0.44	0.46	0.51	0.49	0.53	0.37	0.58	0.48	0.54
Villa and Parra (2000)										
Mg+Fe	0.04	0.07	0.07	0.07	0.06	0.06	0.10	0.08	0.08	0.09
K	0.00	0.00	0.00	0.00	0.00	0.00	0.00	0.00	0.00	0.00
Si	0.00	0.01	0.01	0.01	0.00	0.01	0.01	0.01	0.01	0.01
Al(VI)	-0.04	-0.07	-0.07	-0.07	-0.06	-0.06	-0.10	-0.08	-0.08	-0.09

Analyses highlighted in red fail major element criteria of Villa and Parra (2000).

Analyses highlighted in orange fail major element criteria of Villa and Parra (2000) by a small margin, but are plotted as representative.

†Sample rejected only for failing mica purity tests of Villa and Parra (2000).

Table S3.1c. White mica geochemistry from sample EV20-20.

	EV20-20											
	1	2	3	4	5	6	7	8	9	10	11	12
Microstructure	foliation			fan	single crystal	-						
SiO_2	51.01	50.96	50.08	51.53	50.51	49.68	48.21	22.38	49.37	49.31	48.85	48.31
TiO_2	0.13	0.14	0.14	0.13	0.18	0.26	0.23	0.27	0.25	0.25	0.92	0.16
Al_2O_3	27.68	25.69	28.11	26.41	27.71	27.10	28.30	28.56	27.46	26.14	27.34	25.23
Cr_2O_3	0.07	0.21	0.10	0.17	0.06	0.23	0.17	0.29	0.15	0.18	0.22	0.22
FeO	2.74	3.24	2.99	2.41	2.46	3.64	3.13	3.11	3.92	2.77	4.14	4.76
MnO	0.00	0.01	0.04	0.00	0.03	0.04	0.01	0.00	0.03	0.03	0.04	0.06
MgO	3.74	3.67	3.42	3.73	3.24	3.93	3.76	1.53	3.97	3.43	3.04	5.22
CaO	0.02	0.05	0.06	0.06	0.01	0.06	0.12	0.05	0.04	0.03	0.04	0.09
Na_2O	0.26	0.06	0.26	0.12	0.20	0.24	0.20	0.30	0.16	0.10	0.19	0.11
K_2O	10.12	9.37	10.07	10.38	10.08	9.84	9.37	8.94	9.79	9.91	9.71	8.49
Cl	0.00	0.01	0.00	0.01	0.01	0.00	0.00	0.01	0.00	0.00	0.01	0.00
F	0.15	0.17	0.13	0.16	0.11	0.14	0.14	0.04	0.14	0.16	0.11	0.14
TOTAL	95.78	93.40	95.27	94.94	94.49	95.02	93.50	65.42	95.14	92.14	94.51	92.63
SiO_2	0.85	0.85	0.83	0.86	0.84	0.83	0.80	0.37	0.82	0.82	0.81	0.80
TiO_2	0.00	0.00	0.00	0.00	0.00	0.00	0.00	0.00	0.00	0.00	0.01	0.00
Al_2O_3	0.27	0.25	0.28	0.26	0.27	0.27	0.28	0.28	0.27	0.26	0.27	0.25
Cr_2O_3	0.00	0.00	0.00	0.00	0.00	0.00	0.00	0.00	0.00	0.00	0.00	0.00
FeO	0.04	0.05	0.04	0.03	0.03	0.05	0.04	0.04	0.05	0.04	0.06	0.07
MnO	0.00	0.00	0.00	0.00	0.00	0.00	0.00	0.00	0.00	0.00	0.00	0.00
MgO	0.09	0.09	0.08	0.09	0.08	0.10	0.09	0.04	0.10	0.09	0.08	0.13
CaO	0.00	0.00	0.00	0.00	0.00	0.00	0.00	0.00	0.00	0.00	0.00	0.00
Na_2O	0.00	0.00	0.00	0.00	0.00	0.00	0.00	0.00	0.00	0.00	0.00	0.00
K_2O	0.11	0.10	0.11	0.11	0.11	0.10	0.10	0.09	0.10	0.11	0.10	0.09
O	2.76	2.70	2.74	2.74	2.73	2.72	2.69	1.78	2.72	2.65	2.70	2.65
Norm	0.25	0.25	0.25	0.25	0.25	0.25	0.24	0.16	0.25	0.24	0.25	0.24
Si	3.38	3.46	3.35	3.45	3.39	3.34	3.28	2.30	3.32	3.40	3.31	3.34
Ti	0.01	0.01	0.01	0.01	0.01	0.01	0.01	0.02	0.01	0.01	0.05	0.01
Al	2.16	2.05	2.21	2.08	2.19	2.15	2.27	3.46	2.18	2.13	2.19	2.06
Cr	0.00	0.01	0.01	0.01	0.00	0.01	0.01	0.02	0.01	0.01	0.01	0.01
Fe	0.15	0.18	0.17	0.13	0.14	0.20	0.18	0.27	0.22	0.16	0.24	0.28
Mn	0.00	0.00	0.00	0.00	0.00	0.00	0.00	0.00	0.00	0.00	0.00	0.00
Mg	0.37	0.37	0.34	0.37	0.32	0.39	0.38	0.23	0.40	0.35	0.31	0.54
Ca	0.00	0.00	0.00	0.00	0.00	0.00	0.01	0.01	0.00	0.00	0.00	0.01
Na	0.03	0.01	0.03	0.02	0.03	0.03	0.03	0.06	0.02	0.01	0.03	0.01
K	0.86	0.81	0.86	0.89	0.86	0.84	0.81	1.17	0.84	0.87	0.84	0.75
X_{Mg}	0.71	0.67	0.67	0.73	0.70	0.66	0.68	0.47	0.64	0.69	0.57	0.66
Si(T1+T2)	3.38	3.46	3.35	3.45	3.39	3.34	3.28	2.30	3.32	3.40	3.31	3.34
Ti(T2)	0.01	0.01	0.01	0.01	0.01	0.01	0.01	0.02	0.01	0.01	0.05	0.01
Al(IV) (T2)	0.62	0.55	0.66	0.56	0.62	0.67	0.73	1.72	0.69	0.61	0.73	0.67
Al(VI) (M2)	1.54	1.51	1.56	1.52	1.57	1.48	1.54	1.74	1.49	1.52	1.45	1.39
Mg (M2)	0.33	0.33	0.30	0.35	0.30	0.34	0.31	0.12	0.33	0.33	0.31	0.41
Fe (M2)	0.13	0.16	0.15	0.13	0.13	0.18	0.15	0.14	0.18	0.15	0.24	0.21
Fe + Mg (M2)	0.46	0.49	0.45	0.48	0.43	0.52	0.46	0.26	0.52	0.48	0.54	0.62
Mn (M2)	0.00	0.00	0.00	0.00	0.00	0.00	0.00	0.00	0.00	0.00	0.00	0.00
Mg (M1)	0.04	0.04	0.04	0.02	0.02	0.05	0.07	0.11	0.07	0.02	0.00	0.13
Fe (M1)	0.02	0.02	0.02	0.01	0.01	0.03	0.03	0.13	0.04	0.01	0.00	0.07
vac (M1)	0.94	0.94	0.94	0.97	0.97	0.92	0.90	0.75	0.90	0.97	1.00	0.80
K (A)	0.86	0.81	0.86	0.89	0.86	0.84	0.81	1.17	0.84	0.87	0.84	0.75
Na (A)	0.03	0.01	0.03	0.02	0.03	0.03	0.03	0.06	0.02	0.01	0.03	0.01
v (A)	0.11	0.18	0.11	0.10	0.11	0.12	0.16	-0.23	0.14	0.11	0.13	0.24
Paragonite	0.03	0.01	0.03	0.02	0.03	0.03	0.03	0.06	0.02	0.01	0.03	0.01
Phlogopite	0.04	0.04	0.04	0.02	0.02	0.05	0.07	0.11	0.07	0.02	0.00	0.13
Annite	0.02	0.02	0.02	0.01	0.01	0.03	0.03	0.13	0.04	0.01	0.00	0.07
Mg-Celadonite	0.19	0.18	0.16	0.25	0.19	0.14	0.08	-0.23	0.11	0.19	0.08	0.06
Fe-Celadonite	0.08	0.09	0.08	0.09	0.08	0.07	0.04	-0.26	0.06	0.09	0.06	0.03
Pyrophyllite	0.11	0.18	0.11	0.10	0.11	0.12	0.16	-0.23	0.14	0.11	0.13	0.24
Muscovite	0.53	0.48	0.56	0.52	0.56	0.56	0.60	1.41	0.57	0.57	0.71	0.46
CeladoniteTOT	0.27	0.27	0.23	0.34	0.27	0.21	0.11	-0.49	0.17	0.28	0.13	0.09
ms	0.64	0.63	0.68	0.59	0.65	0.70	0.81	1.43	0.75	0.66	0.82	0.81
pg	0.04	0.01	0.04	0.02	0.03	0.04	0.04	0.06	0.03	0.02	0.03	0.02
cel	0.32	0.36	0.28	0.39	0.32	0.26	0.15	-0.49	0.22	0.32	0.15	0.16
Villa and Parra (2000)												
Mg+Fe	0.068	0.100	0.092	0.087	0.092	0.162	0.144	0.249	0.140	0.146	0.410	0.133
K	0.000	0.000	0.000	0.000	0.000	0.000	0.000	0.000	0.000	0.000	0.000	0.000
Si	0.007	0.007	0.007	0.006	0.009	0.013	0.012	0.021	0.013	0.013	0.047	0.008
Al(VI)	-0.068	-0.100	-0.089	-0.087	-0.091	-0.159	-0.144	-0.249	-0.138	-0.144	-0.414	-0.130

Analyses highlighted in red fail major element criteria of Villa and Parra (2000).
Analyses highlighted in orange fail major element criteria of Villa and Parra (2000) by a small margin, but are plotted as representative.
†Sample rejected only for failing mica purity tests of Villa and Parra (2000).

Table S3.1d. White mica geochemistry from sample EV21-07.

	EV21-07																		
	1	2	3	4	5	6	7	8	9†	10†	11†	12†	13†	14	15	16	17	18	19	20
Microstructure	foliation					shear band		strain shadow	-											
SiO_2	48.10	48.73	50.31	50.14	50.08	47.40	50.53	51.18	52.05	46.16	51.26	49.53	51.66	28.76	28.94	47.30	45.37	41.55	48.80	44.56
TiO_2	0.06	0.12	0.12	0.11	0.08	0.05	0.06	0.08	0.14	0.84	0.14	0.15	0.11	0.00	0.00	0.04	0.08	0.06	0.05	0.08
Al_2O_3	25.03	26.90	27.30	27.35	27.27	25.37	27.71	26.24	24.63	30.73	24.53	25.12	21.68	20.41	20.02	25.70	24.07	24.70	25.77	21.57
Cr_2O_3	0.00	0.00	0.00	0.03	0.00	0.01	0.01	0.01	0.40	0.01	0.33	0.21	0.52	0.00	0.00	0.04	0.00	0.00	0.01	0.32
FeO	4.42	4.58	3.81	4.03	3.62	4.64	3.94	3.44	3.23	2.88	3.18	4.62	3.27	12.26	11.59	3.50	5.39	7.54	3.88	7.87
MnO	0.02	0.03	0.05	0.03	0.04	0.06	0.01	0.00	0.01	0.03	0.05	0.00	0.03	0.29	0.15	0.00	0.06	0.17	0.02	0.07
MgO	6.89	4.58	3.25	3.12	3.37	7.85	3.21	3.79	5.03	4.31	5.56	6.67	6.88	23.94	24.17	2.80	8.25	12.62	4.96	10.59
CaO	0.04	0.07	0.00	0.00	0.02	0.12	0.20	0.04	0.10	0.02	0.15	0.20	0.17	0.17	0.23	0.19	0.16	0.09	0.06	0.38
Na_2O	0.25	0.21	0.46	0.29	0.36	0.14	0.21	0.23	0.07	0.05	0.20	0.21	0.04	0.00	0.02	0.07	0.17	0.16	0.23	0.10
K_2O	9.23	9.80	10.64	10.53	10.39	8.20	9.86	10.29	9.32	9.65	9.08	8.35	8.80	0.21	0.13	9.73	7.86	5.74	9.18	5.92
Cl	0.00	0.01	0.01	0.00	0.00	0.02	0.00	0.01	0.01	0.00	0.00	0.00	0.00	0.00	0.00	0.01	0.00	0.00	0.01	0.01
F	0.09	0.04	0.03	0.03	0.07	0.10	0.06	0.09	0.00	0.00	0.00	0.01	0.02	0.09	0.11	0.05	0.09	0.09	0.09	0.01
TOTAL	94.03	95.02	95.95	95.63	95.22	93.85	95.74	95.30	94.97	94.68	94.47	95.07	93.17	86.04	85.25	89.38	91.41	92.62	92.95	91.46
SiO_2	0.80	0.81	0.84	0.83	0.83	0.79	0.84	0.85	0.87	0.77	0.85	0.82	0.86	0.48	0.48	0.79	0.76	0.69	0.81	0.74
TiO_2	0.00	0.00	0.00	0.00	0.00	0.00	0.00	0.00	0.00	0.01	0.00	0.00	0.00	0.00	0.00	0.00	0.00	0.00	0.00	0.00
Al_2O_3	0.25	0.26	0.27	0.27	0.27	0.25	0.27	0.26	0.24	0.30	0.24	0.25	0.21	0.20	0.20	0.25	0.24	0.24	0.25	0.21
Cr_2O_3	0.00	0.00	0.00	0.00	0.00	0.00	0.00	0.00	0.00	0.00	0.00	0.00	0.00	0.00	0.00	0.00	0.00	0.00	0.00	0.00
FeO	0.06	0.06	0.05	0.06	0.05	0.06	0.05	0.05	0.04	0.04	0.04	0.06	0.05	0.17	0.16	0.05	0.08	0.10	0.05	0.11
MnO	0.00	0.00	0.00	0.00	0.00	0.00	0.00	0.00	0.00	0.00	0.00	0.00	0.00	0.00	0.00	0.00	0.00	0.00	0.00	0.00
MgO	0.17	0.11	0.08	0.08	0.08	0.19	0.08	0.09	0.12	0.11	0.14	0.17	0.17	0.59	0.60	0.07	0.20	0.31	0.12	0.26
CaO	0.00	0.00	0.00	0.00	0.00	0.00	0.00	0.00	0.00	0.00	0.00	0.00	0.00	0.00	0.00	0.00	0.00	0.00	0.00	0.01
Na_2O	0.00	0.00	0.01	0.00	0.01	0.00	0.00	0.00	0.00	0.00	0.00	0.00	0.00	0.00	0.00	0.00	0.00	0.00	0.00	0.00
K_2O	0.10	0.10	0.11	0.11	0.11	0.09	0.10	0.11	0.10	0.10	0.10	0.09	0.09	0.00	0.00	0.10	0.08	0.06	0.10	0.06
O	2.67	2.70	2.74	2.73	2.72	2.68	2.75	2.73	2.74	2.71	2.72	2.72	2.68	2.33	2.32	2.56	2.59	2.60	2.66	2.57
Norm	0.24	0.25	0.25	0.25	0.25	0.24	0.25	0.25	0.25	0.25	0.25	0.25	0.24	0.21	0.21	0.23	0.24	0.24	0.24	0.23
Si	3.29	3.30	3.37	3.37	3.37	3.24	3.37	3.43	3.48	3.12	3.45	3.33	3.52	2.26	2.28	3.38	3.21	2.93	3.35	3.17
Ti	0.00	0.01	0.01	0.01	0.00	0.00	0.00	0.00	0.01	0.04	0.01	0.01	0.01	0.00	0.00	0.00	0.00	0.00	0.00	0.00
Al	2.02	2.15	2.15	2.16	2.16	2.04	2.18	2.07	1.94	2.44	1.94	1.99	1.74	1.89	1.86	2.17	2.00	2.05	2.09	1.81
Cr	0.00	0.00	0.00	0.00	0.00	0.00	0.00	0.00	0.02	0.00	0.02	0.01	0.03	0.00	0.00	0.00	0.00	0.00	0.00	0.02
Fe	0.25	0.26	0.21	0.23	0.20	0.27	0.22	0.19	0.18	0.16	0.18	0.26	0.19	0.81	0.76	0.21	0.32	0.44	0.22	0.47
Mn	0.00	0.00	0.00	0.00	0.00	0.00	0.00	0.00	0.00	0.00	0.00	0.00	0.00	0.02	0.01	0.00	0.00	0.01	0.00	0.00
Mg	0.70	0.46	0.32	0.31	0.34	0.80	0.32	0.38	0.50	0.43	0.56	0.67	0.70	2.80	2.84	0.30	0.87	1.33	0.51	1.12
Ca	0.00	0.01	0.00	0.00	0.00	0.01	0.01	0.00	0.01	0.00	0.01	0.01	0.01	0.01	0.02	0.01	0.01	0.01	0.00	0.03
Na	0.03	0.03	0.06	0.04	0.05	0.02	0.03	0.03	0.01	0.01	0.03	0.03	0.00	0.00	0.00	0.01	0.02	0.02	0.03	0.01
K	0.81	0.85	0.91	0.90	0.89	0.72	0.84	0.88	0.79	0.83	0.78	0.72	0.77	0.02	0.01	0.89	0.71	0.52	0.81	0.54
X_{Mg}	0.74	0.64	0.60	0.58	0.62	0.75	0.59	0.66	0.74	0.73	0.76	0.72	0.79	0.78	0.79	0.59	0.73	0.75	0.70	0.71
Si(T1+T2)	3.29	3.30	3.37	3.37	3.37	3.24	3.37	3.43	3.48	3.12	3.45	3.33	3.52	2.26	2.28	3.38	3.21	2.93	3.35	3.17
Ti(T2)	0.00	0.01	0.01	0.01	0.00	0.00	0.00	0.00	0.01	0.04	0.01	0.01	0.01	0.00	0.00	0.00	0.00	0.00	0.00	0.00
Al(IV) (T2)	0.71	0.71	0.64	0.64	0.64	0.76	0.63	0.58	0.53	0.93	0.56	0.68	0.48	1.74	1.72	0.62	0.80	1.07	0.65	0.83
Al(VI) (M2)	1.31	1.44	1.51	1.52	1.53	1.28	1.54	1.49	1.41	1.52	1.38	1.32	1.26	0.15	0.14	1.55	1.21	0.98	1.44	0.98
Mg (M2)	0.51	0.36	0.29	0.28	0.30	0.54	0.27	0.34	0.43	0.35	0.47	0.49	0.58	1.45	1.47	0.26	0.58	0.77	0.39	0.72
Fe (M2)	0.18	0.20	0.19	0.20	0.18	0.18	0.19	0.17	0.16	0.13	0.15	0.19	0.16	0.42	0.40	0.19	0.21	0.26	0.17	0.30
Fe + Mg (M2)	0.69	0.56	0.49	0.48	0.48	0.72	0.46	0.51	0.59	0.49	0.62	0.68	0.74	1.87	1.87	0.45	0.80	1.03	0.56	1.03
Mn (M2)	0.00	0.00	0.00	0.00	0.00	0.00	0.00	0.00	0.00	0.00	0.00	0.00	0.00	0.02	0.01	0.00	0.00	0.01	0.00	0.00
Mg (M1)	0.19	0.10	0.03	0.04	0.04	0.26	0.05	0.04	0.07	0.08	0.09	0.18	0.11	1.35	1.37	0.03	0.29	0.55	0.12	0.40
Fe (M1)	0.07	0.06	0.02	0.03	0.02	0.09	0.03	0.02	0.02	0.03	0.03	0.07	0.03	0.39	0.37	0.02	0.11	0.19	0.05	0.17
vac (M1)	0.74	0.84	0.95	0.94	0.94	0.65	0.92	0.93	0.91	0.89	0.88	0.76	0.85	-0.73	-0.74	0.94	0.61	0.26	0.83	0.43
K (A)	0.81	0.85	0.91	0.90	0.89	0.72	0.84	0.88	0.79	0.83	0.78	0.72	0.77	0.02	0.01	0.89	0.71	0.52	0.81	0.54
Na (A)	0.03	0.03	0.06	0.04	0.05	0.02	0.03	0.03	0.01	0.01	0.03	0.03	0.00	0.00	0.00	0.01	0.02	0.02	0.03	0.01
v (A)	0.16	0.13	0.03	0.06	0.06	0.27	0.13	0.09	0.20	0.16	0.20	0.26	0.23	0.98	0.98	0.10	0.27	0.46	0.16	0.45
Paragonite	0.03	0.03	0.06	0.04	0.05	0.02	0.03	0.03	0.01	0.01	0.03	0.03	0.00	0.00	0.00	0.01	0.02	0.02	0.03	0.01
Phlogopite	0.19	0.10	0.03	0.04	0.04	0.26	0.05	0.04	0.07	0.08	0.09	0.18	0.11	1.35	1.37	0.03	0.29	0.55	0.12	0.40
Annite	0.07	0.06	0.02	0.03	0.02	0.09	0.03	0.02	0.02	0.03	0.03	0.07	0.03	0.39	0.37	0.02	0.11	0.19	0.05	0.17
Mg-Celadonite	0.10	0.11	0.20	0.17	0.19	-0.02	0.14	0.22	0.20	-0.07	0.18	0.05	0.23	-1.34	-1.34	0.17	-0.05	-0.40	0.13	-0.20
Fe-Celadonite	0.03	0.06	0.13	0.13	0.11	-0.01	0.09	0.11	0.07	-0.02	0.06	0.02	0.06	-0.38	-0.36	0.12	-0.02	-0.13	0.06	-0.08
Pyrophyllite	0.16	0.13	0.03	0.06	0.06	0.27	0.13	0.09	0.20	0.16	0.20	0.26	0.23	0.98	0.98	0.10	0.27	0.46	0.16	0.45
Muscovite	0.41	0.52	0.53	0.54	0.53	0.40	0.52	0.48	0.43	0.81	0.42	0.40	0.33	0.01	-0.03	0.55	0.38	0.31	0.45	0.25
CeladoniteTOT	0.13	0.17	0.33	0.30	0.30	-0.03	0.23	0.33	0.27	-0.09	0.24	0.07	0.29	-1.72	-1.70	0.28	-0.07	-0.54	0.19	-0.28
ms	0.72	0.73	0.58	0.62	0.60	1.02	0.67	0.57	0.60	1.12	0.61	0.81	0.53	0.00	0.01	0.65	1.12	-1.55	0.67	-14.86
pg	0.06	0.04	0.06	0.04	0.05	0.05	0.03	0.04	0.01	0.01	0.04	0.05	0.01	0.00	0.00	0.01	0.07	-0.11	0.05	-0.79
cel	0.22	0.24	0.36	0.34	0.35	-0.07	0.30	0.39	0.38	-0.12	0.35	0.14	0.46	1.00	0.99	0.33	-0.19	2.66	0.28	16.65
Villa and Parra (2000)																				
Mg+Fe	0.035	0.068	0.062	0.056	0.046	0.057	0.059	0.041	0.136	0.355	0.145	0.124	0.162	0.125	0.088	0.053	0.077	0.088	0.035	0.170
K	0.000	0.000	0.000	0.000	0.000	0.000	0.000	0.000	0.000	0.000	0.000	0.000	0.000	0.000	0.000	0.000	0.000	0.000	0.000	0.000
Si	0.003	0.006	0.006	0.005	0.004	0.003	0.003	0.004	0.007	0.043	0.007	0.008	0.006	0.000	0.000	0.002	0.004	0.003	0.002	0.004
Al(VI)	-0.034	-0.066	-0.059	-0.055	-0.044	-0.054	-0.059	-0.041	-0.136	-0.353	-0.142	-0.124	-0.160	-0.106	-0.078	-0.053	-0.073	-0.078	-0.034	-0.165

Analyses highlighted in red fail major element criteria of Villa and Parra (2000).
Analyses highlighted in orange fail major element criteria of Villa and Parra (2000) by a small margin, but are plotted as representative.
†**Sample rejected only for failing mica purity tests of Villa and Parra (2000).**

Table S3.1e. White mica geochemistry from sample EV22-03.

	EV22-03														
	1	2	3	4	5	6	7†	8†	9†	10†	11†	12†	13	14	15
Microstructure	isolated grain	fan	vein fill								-				
SiO_2	51.37	51.07	51.68	51.59	49.98	51.81	51.90	51.84	49.55	51.81	50.73	51.05	46.61	42.37	47.76
TiO_2	0.09	0.11	0.14	0.21	0.11	0.18	0.14	0.76	0.13	0.28	0.22	0.59	0.11	0.18	1.19
Al_2O_3	29.56	28.47	28.58	28.60	26.30	27.67	28.22	25.45	26.24	28.08	28.03	27.70	24.28	24.44	25.04
Cr_2O_3	0.10	0.05	0.10	0.08	0.21	0.09	0.35	0.27	0.27	0.26	0.34	0.25	0.11	0.16	0.34
FeO	1.40	1.51	1.65	1.43	3.24	1.58	1.40	2.41	3.21	1.97	2.06	2.03	6.22	8.31	4.80
MnO	0.00	0.04	0.05	0.00	0.00	0.04	0.01	0.03	0.04	0.04	0.02	0.01	0.03	0.00	0.03
MgO	3.29	3.55	3.45	3.53	5.20	3.68	3.53	4.53	4.76	3.61	3.49	3.56	7.53	7.86	5.43
CaO	0.00	0.04	0.11	0.01	0.07	0.01	0.00	0.09	0.10	0.01	0.03	0.06	0.22	0.36	0.18
Na_2O	0.37	0.27	0.24	0.36	0.13	0.25	0.31	0.08	0.18	0.24	0.25	0.29	0.15	0.12	0.08
K_2O	10.27	10.17	8.90	9.88	9.06	10.44	9.98	9.84	9.28	10.00	9.32	10.16	6.78	6.00	7.95
Cl	0.00	0.01	0.00	0.00	0.00	0.00	0.00	0.00	0.00	0.00	0.01	0.01	0.01	0.00	0.00
F	0.00	0.01	0.01	0.00	0.00	0.03	0.00	0.00	0.00	0.02	0.02	0.01	0.02	0.00	0.04
TOTAL	96.46	95.26	94.89	95.70	94.30	95.76	95.83	95.30	93.77	96.32	94.49	95.71	92.04	89.80	92.81
SiO_2	0.85	0.85	0.86	0.86	0.83	0.86	0.86	0.86	0.82	0.86	0.84	0.85	0.78	0.71	0.79
TiO_2	0.00	0.00	0.00	0.00	0.00	0.00	0.00	0.01	0.00	0.00	0.00	0.01	0.00	0.00	0.01
Al_2O_3	0.29	0.28	0.28	0.28	0.26	0.27	0.28	0.25	0.26	0.28	0.27	0.27	0.24	0.24	0.25
Cr_2O_3	0.00	0.00	0.00	0.00	0.00	0.00	0.00	0.00	0.00	0.00	0.00	0.00	0.00	0.00	0.00
FeO	0.02	0.02	0.02	0.02	0.05	0.02	0.02	0.03	0.04	0.03	0.03	0.03	0.09	0.12	0.07
MnO	0.00	0.00	0.00	0.00	0.00	0.00	0.00	0.00	0.00	0.00	0.00	0.00	0.00	0.00	0.00
MgO	0.08	0.09	0.09	0.09	0.13	0.09	0.09	0.11	0.12	0.09	0.09	0.09	0.19	0.20	0.13
CaO	0.00	0.00	0.00	0.00	0.00	0.00	0.00	0.00	0.00	0.00	0.00	0.00	0.00	0.01	0.00
Na_2O	0.01	0.00	0.00	0.01	0.00	0.00	0.01	0.00	0.00	0.00	0.00	0.00	0.00	0.00	0.00
K_2O	0.11	0.11	0.09	0.10	0.10	0.11	0.11	0.10	0.10	0.11	0.10	0.11	0.07	0.06	0.08
O	2.80	2.76	2.78	2.78	2.72	2.77	2.79	2.75	2.70	2.79	2.74	2.76	2.62	2.52	2.65
Norm	0.25	0.25	0.25	0.25	0.25	0.25	0.25	0.25	0.25	0.25	0.25	0.25	0.24	0.23	0.24
Si	3.36	3.38	3.41	3.39	3.37	3.42	3.41	3.45	3.36	3.40	3.38	3.38	3.25	3.08	3.29
Ti	0.00	0.01	0.01	0.01	0.01	0.01	0.01	0.04	0.01	0.01	0.01	0.03	0.01	0.01	0.06
Al	2.28	2.22	2.22	2.22	2.09	2.15	2.19	2.00	2.10	2.17	2.20	2.16	2.00	2.09	2.04
Cr	0.01	0.00	0.00	0.00	0.01	0.00	0.02	0.01	0.01	0.01	0.02	0.01	0.01	0.01	0.02
Fe	0.08	0.08	0.09	0.08	0.18	0.09	0.08	0.13	0.18	0.11	0.11	0.11	0.36	0.51	0.28
Mn	0.00	0.00	0.00	0.00	0.00	0.00	0.00	0.00	0.00	0.00	0.00	0.00	0.00	0.00	0.00
Mg	0.32	0.35	0.34	0.35	0.52	0.36	0.35	0.45	0.48	0.35	0.35	0.35	0.78	0.85	0.56
Ca	0.00	0.00	0.01	0.00	0.00	0.00	0.00	0.01	0.01	0.00	0.00	0.00	0.02	0.03	0.01
Na	0.05	0.03	0.03	0.05	0.02	0.03	0.04	0.01	0.02	0.03	0.03	0.04	0.02	0.02	0.01
K	0.86	0.86	0.75	0.83	0.78	0.88	0.84	0.83	0.80	0.84	0.79	0.86	0.60	0.56	0.70
X_{Mg}	0.81	0.81	0.79	0.81	0.74	0.81	0.82	0.77	0.73	0.77	0.75	0.76	0.68	0.63	0.67
Si(T1+T2)	3.36	3.38	3.41	3.39	3.37	3.42	3.41	3.45	3.36	3.40	3.38	3.38	3.25	3.08	3.29
Ti(T2)	0.00	0.01	0.01	0.01	0.01	0.01	0.01	0.04	0.01	0.01	0.01	0.03	0.01	0.01	0.06
Al(IV) (T2)	0.65	0.62	0.60	0.62	0.64	0.59	0.60	0.59	0.64	0.62	0.63	0.65	0.75	0.93	0.77
Al(VI) (M2)	1.63	1.60	1.62	1.60	1.45	1.56	1.59	1.41	1.46	1.56	1.58	1.51	1.24	1.16	1.27
Mg (M2)	0.30	0.32	0.30	0.33	0.41	0.35	0.34	0.45	0.40	0.34	0.32	0.35	0.52	0.53	0.49
Fe (M2)	0.07	0.08	0.08	0.07	0.14	0.09	0.08	0.13	0.15	0.10	0.11	0.11	0.24	0.31	0.24
Fe + Mg (M2)	0.37	0.40	0.38	0.40	0.55	0.44	0.41	0.58	0.55	0.45	0.42	0.46	0.76	0.84	0.73
Mn (M2)	0.00	0.00	0.00	0.00	0.00	0.00	0.00	0.00	0.00	0.00	0.00	0.00	0.00	0.00	0.00
Mg (M1)	0.02	0.03	0.04	0.02	0.11	0.01	0.01	0.00	0.09	0.01	0.03	0.00	0.27	0.33	0.07
Fe (M1)	0.01	0.01	0.01	0.00	0.04	0.00	0.00	0.00	0.03	0.00	0.01	0.00	0.12	0.19	0.03
vac (M1)	0.97	0.97	0.95	0.98	0.85	0.99	0.99	1.00	0.88	0.98	0.96	1.00	0.61	0.48	0.90
K (A)	0.86	0.86	0.75	0.83	0.78	0.88	0.84	0.83	0.80	0.84	0.79	0.86	0.60	0.56	0.70
Na (A)	0.05	0.03	0.03	0.05	0.02	0.03	0.04	0.01	0.02	0.03	0.03	0.04	0.02	0.02	0.01
v (A)	0.10	0.11	0.22	0.13	0.20	0.09	0.12	0.15	0.17	0.13	0.17	0.10	0.38	0.43	0.29
Paragonite	0.05	0.03	0.03	0.05	0.02	0.03	0.04	0.01	0.02	0.03	0.03	0.04	0.02	0.02	0.01
Phlogopite	0.02	0.03	0.04	0.02	0.11	0.01	0.01	0.00	0.09	0.01	0.03	0.00	0.27	0.33	0.07
Annite	0.01	0.01	0.01	0.00	0.04	0.00	0.00	0.00	0.03	0.00	0.01	0.00	0.12	0.19	0.03
Mg-Celadonite	0.21	0.22	0.14	0.21	0.12	0.26	0.23	0.20	0.13	0.19	0.15	0.19	-0.09	-0.23	-0.04
Fe-Celadonite	0.05	0.05	0.04	0.05	0.04	0.06	0.05	0.06	0.05	0.06	0.05	0.06	-0.04	-0.13	-0.02
Pyrophyllite	0.10	0.11	0.22	0.13	0.20	0.09	0.12	0.15	0.17	0.13	0.17	0.10	0.38	0.43	0.29
Muscovite	0.57	0.56	0.52	0.55	0.47	0.55	0.55	0.58	0.50	0.57	0.56	0.61	0.34	0.40	0.65
CeladoniteTOT	0.26	0.27	0.18	0.26	0.16	0.32	0.28	0.26	0.19	0.25	0.20	0.25	-0.13	-0.36	-0.06
ms	0.65	0.65	0.71	0.64	0.73	0.61	0.63	0.69	0.70	0.67	0.71	0.68	1.46	7.24	1.07
pg	0.05	0.04	0.04	0.05	0.03	0.04	0.05	0.01	0.03	0.04	0.04	0.04	0.09	0.31	0.02
cel	0.29	0.32	0.25	0.30	0.24	0.36	0.32	0.30	0.26	0.30	0.25	0.28	-0.54	-6.55	-0.09
Villa and Parra (2000)															
Mg+Fe	0.051	0.066	0.100	0.097	0.090	0.101	0.113	0.328	0.122	0.164	0.153	0.217	0.107	0.162	0.586
K	0.000	0.000	0.000	0.000	0.000	0.000	0.000	0.000	0.000	0.000	0.000	0.000	0.000	0.000	0.000
Si	0.004	0.005	0.007	0.010	0.006	0.009	0.007	0.038	0.006	0.014	0.011	0.029	0.006	0.010	0.062
Al(VI)	-0.051	-0.064	-0.097	-0.097	-0.090	-0.098	-0.113	-0.339	-0.120	-0.162	-0.152	-0.240	-0.106	-0.162	-0.584

Analyses highlighted in red fail major element criteria of Villa and Parra (2000).
Analyses highlighted in orange fail major element criteria of Villa and Parra (2000) by a small margin, but are plotted as representative.
†Sample rejected only for failing mica purity tests of Villa and Parra (2000).

Table S3.2. Analytical results for in situ white mica 40Ar/39Ar analyses from the Basal Unit schists of southern Evia.

			Corrected unknown values																	Blank values										
Sample	Age (Ma)	±1σ	^{40}Ar (fA)	±1σ	^{39}Ar (fA)	±1σ	^{38}Ar (fA)	±1σ	^{37}Ar (fA)	±1σ	^{36}Ar (fA)	±1σ	Ca/K	±1σ	Cl/K	±1σ	%^{40}Ar*	^{40}Ar*/^{39}Ar$_K$	±1σ	^{40}Ar (fA)	±1σ	^{39}Ar (fA)	±1σ	^{38}Ar (fA)	±1σ	^{37}Ar (fA)	±1σ	^{36}Ar (fA)	±1σ	J	±1σ
EV19-03	***Chip 1; J: 0.01708581 ± 0.00000909***																													
	25.0	1.4	1.4636	0.0305	1.4911	0.0133	0.0069	0.0161	-0.0298	0.0132	0.0007	0.0002	-0.36	0.16	-0.02	0.03	83.29	0.816779	0.046970	0.8756	0.0213	0.0086	0.0100	0.0140	0.0113	0.0509	0.0091	0.0040	0.0001	0.017086	9.092E-06
	25.7	1.0	2.0834	0.0311	2.1910	0.0137	0.0148	0.0160	-0.0152	0.0127	0.0008	0.0002	-0.13	0.10	-0.02	0.02	88.48	0.840622	0.034378	1.0899	0.0210	0.0252	0.0098	-0.0052	0.0117	0.0395	0.0093	0.0051	0.0002	0.017086	9.092E-06
	24.7	1.1	2.3078	0.0346	2.3983	0.0133	0.0571	0.0143	-0.0012	0.0128	0.0013	0.0003	-0.01	0.10	0.03	0.02	83.75	0.805271	0.034920	1.0119	0.0240	0.0084	0.0099	-0.0013	0.0092	0.0237	0.0087	0.0046	0.0002	0.017086	9.092E-06
	23.3	1.0	2.6031	0.0329	2.5416	0.0120	0.0095	0.0144	-0.0177	0.0131	0.0022	0.0003	-0.13	0.09	-0.03	0.02	74.42	0.761561	0.032690	1.0500	0.0240	0.0098	0.0079	0.0089	0.0107	0.0294	0.0098	0.0046	0.0002	0.017086	9.092E-06
	26.5	0.9	2.4880	0.0323	2.5811	0.0136	0.0599	0.0168	-0.0062	0.0127	0.0008	0.0002	-0.04	0.09	0.03	0.02	89.84	0.865312	0.031253	1.0659	0.0215	0.0226	0.0095	0.0119	0.0114	0.0166	0.0087	0.0046	0.0002	0.017086	9.092E-06
	26.5	0.9	2.5203	0.0308	2.6309	0.0137	0.0660	0.0155	0.0155	0.0125	0.0009	0.0002	0.11	0.09	0.04	0.02	90.34	0.864740	0.029301	0.9990	0.0213	0.0162	0.0097	-0.0104	0.0110	0.0140	0.0086	0.0045	0.0002	0.017086	9.092E-06
	Chip 2; J: 0.01708581 ± 0.00000909																													
	22.9	1.1	1.8549	0.0303	2.1284	0.0135	0.0228	0.0159	-0.0058	0.0127	0.0009	0.0002	-0.05	0.11	0.00	0.02	85.91	0.748147	0.035032	1.0173	0.0233	0.0038	0.0097	0.0160	0.0109	0.0351	0.0088	0.0042	0.0002	0.017086	9.092E-06
	25.3	1.2	2.1276	0.0320	2.2687	0.0129	0.0161	0.0156	-0.0088	0.0131	0.0008	0.0003	-0.07	0.11	-0.02	0.02	88.22	0.826686	0.038451	1.0350	0.0248	0.0406	0.0088	0.0216	0.0098	0.0405	0.0090	0.0054	0.0002	0.017086	9.092E-06
	23.3	1.5	1.3393	0.0365	1.5956	0.0121	0.0187	0.0141	0.0146	0.0140	0.0005	0.0002	0.17	0.16	0.00	0.03	90.55	0.759488	0.050308	0.9805	0.0251	0.0362	0.0088	0.0148	0.0101	0.0304	0.0097	0.0052	0.0002	0.017086	9.092E-06
	21.7	1.2	1.7226	0.0298	1.9365	0.0130	0.0442	0.0177	-0.0070	0.0145	0.0012	0.0002	-0.07	0.14	0.03	0.03	79.66	0.708067	0.040156	0.9359	0.0222	0.0351	0.0090	0.0008	0.0125	0.0407	0.0094	0.0044	0.0002	0.017086	9.092E-06
	25.1	1.2	1.7488	0.0333	1.8957	0.0131	0.0340	0.0150	0.0010	0.0136	0.0007	0.0002	0.01	0.13	0.02	0.02	88.91	0.819550	0.039627	0.9349	0.0239	0.0291	0.0092	-0.0072	0.0116	0.0412	0.0105	0.0048	0.0001	0.017086	9.092E-06
EV20-14;	***Chip 1; J: 0.01708581 ± 0.00000909***																													
	43.9	1.0	4.3348	0.0334	2.6457	0.0123	0.0239	0.0155	0.0221	0.0138	0.0018	0.0003	0.15	0.10	-0.01	0.02	87.97	1.440237	0.031706	0.9497	0.0223	0.0286	0.0086	0.0127	0.0107	0.0187	0.0092	0.0050	0.0002	0.017086	9.092E-06
	37.6	*1.1*	*7.4850*	*0.0320*	*2.9980*	*0.0124*	*0.0444*	*0.0150*	*0.0151*	*0.0127*	*0.0128*	*0.0004*	*0.09*	*0.08*	*0.01*	*0.01*	*49.44*	*1.233364*	*0.037480*	*0.9083*	*0.0234*	*0.0211*	*0.0084*	*0.0072*	*0.0087*	*0.0248*	*0.0088*	*0.0043*	*0.0002*	*0.017086*	*9.09E-06*
	38.6	1.0	6.8667	0.0344	3.0985	0.0121	0.0282	0.0144	0.0115	0.0140	0.0100	0.0003	0.07	0.08	-0.01	0.01	57.10	1.264388	0.033276	0.9184	0.0254	0.0285	0.0079	0.0050	0.0108	0.0208	0.0092	0.0046	0.0002	0.017086	9.092E-06
	41.6	0.9	8.7541	0.0316	3.3458	0.0125	0.0193	0.0151	-0.0059	0.0137	0.0141	0.0003	-0.03	0.08	-0.02	0.01	52.19	1.364294	0.029705	0.9092	0.0223	0.0314	0.0089	0.0152	0.0104	0.0375	0.0093	0.0043	0.0001	0.017086	9.092E-06
	42.0	1.1	6.1087	0.0343	2.5856	0.0129	0.0419	0.0167	-0.0104	0.0140	0.0086	0.0003	-0.08	0.10	0.01	0.02	58.34	1.377168	0.037621	1.0522	0.0239	0.0050	0.0088	-0.0119	0.0124	0.0240	0.0103	0.0048	0.0002	0.017086	9.092E-06
	40.6	*1.4*	*9.3137*	*0.0350*	*2.7104*	*0.0135*	*0.0390*	*0.0167*	*-0.0076*	*0.0123*	*0.0193*	*0.0004*	*-0.05*	*0.08*	*0.00*	*0.02*	*38.76*	*1.330653*	*0.046157*	*0.9260*	*0.0239*	*0.0043*	*0.0088*	*0.0184*	*0.0120*	*0.0396*	*0.0087*	*0.0044*	*0.0002*	*0.017086*	*9.09E-06*
	Chip 2; J: 0.01708581 ± 0.00000909																													
	47.0	*1.4*	*7.1798*	*0.0314*	*2.2343*	*0.0131*	*0.0287*	*0.0158*	*0.0318*	*0.0140*	*0.0127*	*0.0003*	*0.27*	*0.12*	*0.00*	*0.02*	*48.13*	*1.545682*	*0.046602*	*0.9659*	*0.0228*	*0.0133*	*0.0088*	*0.0030*	*0.0113*	*0.0062*	*0.0100*	*0.0044*	*0.0002*	*0.017086*	*9.09E-06*
	49.4	*1.6*	*7.9068*	*0.0311*	*2.1774*	*0.0135*	*0.0148*	*0.0152*	*0.0407*	*0.0139*	*0.0149*	*0.0004*	*0.35*	*0.12*	*-0.02*	*0.02*	*44.74*	*1.623515*	*0.054099*	*0.9818*	*0.0209*	*0.0145*	*0.0096*	*0.0021*	*0.0114*	*0.0050*	*0.0101*	*0.0046*	*0.0002*	*0.017086*	*9.09E-06*
	45.8	1.0	4.3758	0.0320	2.3170	0.0134	0.0143	0.0140	-0.0146	0.0139	0.0029	0.0002	-0.12	0.11	-0.02	0.02	79.81	1.505987	0.034519	0.9712	0.0228	0.0137	0.0095	0.0038	0.0100	0.0497	0.0102	0.0045	0.0001	0.017086	9.092E-06
EV20-20	***Chip 1; J: 0.01708581 ± 0.00000909***																													
	34.9	1.3	2.3714	0.0316	1.6943	0.0133	0.0201	0.0151	0.0066	0.0133	0.0015	0.0002	0.07	0.15	0.00	0.03	81.70	1.142662	0.042533	0.9263	0.0187	0.0258	0.0093	0.0173	0.0107	0.0186	0.0090	0.0045	0.0001	0.017086	9.092E-06
	Chip 2; J: 0.01708581 ± 0.00000909																													
	35.2	*1.7*	*0.5635*	*0.0310*	*1.6328*	*0.0137*	*-0.0027*	*0.0168*	*-0.0197*	*0.0132*	*-0.0045*	*0.0003*	*-0.23*	*0.15*	*-0.04*	*0.03*	*334.71*	*1.154051*	*0.055279*	*2.5261*	*0.0212*	*0.0172*	*0.0099*	*0.0127*	*0.0118*	*0.0409*	*0.0099*	*0.0099*	*0.0002*	*0.017086*	*9.09E-06*
	29.8	2.2	1.5872	0.0315	1.0303	0.0128	0.0215	0.0156	-0.0014	0.0135	0.0020	0.0002	-0.03	0.25	0.02	0.04	63.25	0.973570	0.073186	0.9049	0.0223	0.0013	0.0092	0.0054	0.0111	0.0193	0.0095	0.0041	0.0002	0.017086	9.092E-06
	34.4	1.2	2.4236	0.0324	1.7787	0.0128	0.0224	0.0156	0.0020	0.0130	0.0014	0.0002	0.02	0.14	0.00	0.03	82.64	1.125161	0.040771	0.9065	0.0215	0.0231	0.0095	-0.0028	0.0106	0.0159	0.0099	0.0044	0.0001	0.017086	9.092E-06
	31.3	0.8	3.3373	0.0260	1.9293	0.0083	0.0278	0.0117	0.0187	0.0090	0.0047	0.0001	0.19	0.09	0.01	0.02	59.22	1.023611	0.026588	0.0000	0.0000	0.0000	0.0000	0.0000	0.0000	0.0000	0.0000	0.0000	0.0000	0.017086	9.092E-06
	Chip 4; 0.01701518 ± 0.00001430																													
	35.9	1.0	2.8705	0.0339	2.0581	0.0132	0.0215	0.0136	-0.0273	0.0133	0.0014	0.0002	-0.27	0.13	-0.01	0.02	84.69	1.180136	0.034202	0.5825	0.0226	0.0353	0.0094	-0.0156	0.0095	0.0372	0.0093	0.0029	0.0001	0.017015	1.43E-05
	29.3	1.6	1.5829	0.0321	1.3384	0.0125	-0.0098	0.0146	0.0120	0.0144	0.0010	0.0002	0.18	0.22	-0.06	0.03	81.46	0.962658	0.052978	0.5993	0.0239	0.0280	0.0096	0.0179	0.0099	0.0225	0.0101	0.0033	0.0001	0.017015	1.43E-05
	40.6	1.4	2.6306	0.0334	1.6062	0.0136	-0.0091	0.0150	-0.0022	0.0128	0.0016	0.0002	-0.03	0.16	-0.05	0.03	81.74	1.337627	0.046167	0.5672	0.0219	0.0106	0.0101	0.0259	0.0102	0.0386	0.0093	0.0031	0.0001	0.017015	1.43E-05
	32.4	1.4	1.9923	0.0329	1.6068	0.0133	-0.0048	0.0148	0.0096	0.0147	0.0010	0.0002	0.13	0.19	-0.04	0.03	85.86	1.063683	0.047934	0.7202	0.0240	0.0300	0.0087	0.0179	0.0100	0.0008	0.0105	0.0036	0.0002	0.017015	1.43E-05
EV21-07	***Chip 2; 0.01701518 ± 0.00001430***																													
	27.0	0.9	2.1931	0.0341	2.3132	0.0128	0.0394	0.0163	0.0028	0.0133	0.0005	0.0002	0.02	0.11	0.01	0.02	93.63	0.886986	0.030129	0.5402	0.0231	0.0200	0.0082	-0.0042	0.0116	0.0277	0.0089	0.0032	0.0001	0.017015	1.43E-05
	23.7	0.9	2.5546	0.0317	2.2996	0.0138	0.0316	0.0159	-0.0349	0.0131	0.0025	0.0002	-0.30	0.11	0.00	0.02	69.88	0.775576	0.029737	0.5215	0.0211	0.0242	0.0095	0.0037	0.0123	0.0459	0.0092	0.0029	0.0001	0.017015	1.43E-05
	28.5	0.9	3.0153	0.0345	2.5412	0.0131	0.0339	0.0157	0.0182	0.0140	0.0022	0.0002	0.15	0.12	0.00	0.02	78.85	0.934859	0.028928	0.7965	0.0258	0.0166	0.0087	-0.0019	0.0105	0.0109	0.0103	0.0036	0.0001	0.017015	1.43E-05
	26.6	0.9	2.3574	0.0337	2.3137	0.0128	0.0120	0.0155	0.0077	0.0153	0.0011	0.0002	0.07	0.13	-0.02	0.02	85.89	0.874426	0.030972	0.5583	0.0245	0.0010	0.0096	-0.0023	0.0106	0.0351	0.0105	0.0031	0.0001	0.017015	1.43E-05
	Chip 3; 0.01701518 ± 0.00001430																													
	27.1	0.7	3.7814	0.0338	3.1376	0.0135	0.0111	0.0156	0.0125	0.0139	0.0034	0.0002	0.08	0.09	-0.03	0.01	73.86	0.889466	0.024533	0.5659	0.0237	0.0168	0.0093	0.0170	0.0114	0.0167	0.0093	0.0030	0.0001	0.017015	1.43E-05
	23.4	0.7	2.7063	0.0331	2.8452	0.0120	0.0067	0.0147	-0.0213	0.0126	0.0017	0.0002	-0.15	0.09	-0.03	0.02	80.73	0.767199	0.024728	0.6509	0.0226	0.0156	0.0086	0.0240	0.0102	0.0335	0.0096	0.0030	0.0001	0.017015	1.43E-05
	36.6	0.8	4.1496	0.0310	2.9263	0.0140	0.0455	0.0141	-0.0070	0.0132	0.0021	0.0002	-0.05	0.09	0.01	0.01	85.01	1.204442	0.025397	0.5170	0.0213	0.0341	0.0094	0.0154	0.0094	0.0368	0.0092	0.0032	0.0001	0.017015	1.43E-05
	27.0	0.7	3.1080	0.0318	2.9808	0.0136	0.0379	0.0164	0.0139	0.0131	0.0016	0.0002	0.09	0.09	0.00	0.02	85.09	0.886503	0.024200	0.5935	0.0226	0.0375	0.0095	-0.0038	0.0117	0.0352	0.0092	0.0028	0.0002	0.017015	1.43E-05

Italicized analyses were rejected due to low % ^{40}Ar yields.

paragonite

Table S3.2 cont.

Sample Grain	Age (Ma)	±1σ	^{40}Ar (fA)	±1σ	^{39}Ar (fA)	±1σ	^{38}Ar (fA)	±1σ	^{37}Ar (fA)	±1σ	^{36}Ar (fA)	±1σ	Ca/K	±1σ	Cl/K	±1σ	%^{40}Ar*	^{40}Ar*/^{39}Ar$_K$	±1σ	Blank ^{40}Ar (fA)	±1σ	Blank ^{39}Ar (fA)	±1σ	Blank ^{38}Ar (fA)	±1σ	Blank ^{37}Ar (fA)	±1σ	Blank ^{36}Ar (fA)	±1σ	J	±σ
	Chip 1; J: 0.01699999 ± 0.00000484																													
	46.8	0.9	4.4009	0.0275	2.4451	0.0122	0.0634	0.0150	-0.0236	0.0140	0.0020	0.0002	-0.20	0.12	0.04	0.02	86.02	1.546746	0.030155	0.5284	0.0193	0.0069	0.0080	-0.0180	0.0106	0.0548	0.0100	0.0031	0.0001	0.017000	4.84E-06
	36.8	1.0	3.7525	0.0325	2.3066	0.0125	0.0238	0.0149	0.0142	0.0134	0.0033	0.0002	0.13	0.12	-0.01	0.02	74.61	1.212787	0.032475	0.6110	0.0224	-0.0042	0.0090	0.0045	0.0109	0.0188	0.0097	0.0027	0.0001	0.017000	4.84E-06
	42.4	0.9	4.1365	0.0341	2.3349	0.0130	0.0344	0.0166	-0.0129	0.0118	0.0029	0.0002	-0.11	0.10	0.01	0.02	79.09	1.399880	0.031551	0.5517	0.0217	0.0308	0.0087	0.0026	0.0116	0.0071	0.0088	0.0029	0.0001	0.017000	4.84E-06
	27.3	*1.4*	*3.1245*	*0.0317*	*1.7409*	*0.0119*	*0.0036*	*0.0156*	*-0.0056*	*0.0137*	*0.0053*	*0.0003*	*-0.07*	*0.16*	*-0.03*	*0.03*	*49.96*	*0.895827*	*0.047983*	*0.6293*	*0.0225*	*0.0082*	*0.0081*	*0.0030*	*0.0105*	*0.0211*	*0.0096*	*0.0030*	*0.0001*	*0.017000*	*4.84E-06*
	Chip 2; J: 0.01699999 ± 0.00000484																													
	22.9	0.9	2.7533	0.0301	2.4066	0.0121	0.0554	0.0147	0.0265	0.0130	0.0033	0.0002	0.22	0.11	0.03	0.02	65.80	0.752249	0.028551	0.5766	0.0214	0.0109	0.0079	0.0002	0.0105	0.0292	0.0084	0.0028	0.0001	0.017000	4.84E-06
	24.3	1.0	2.6332	0.0309	2.4303	0.0137	0.0304	0.0164	-0.0066	0.0133	0.0023	0.0002	-0.06	0.11	0.00	0.02	73.61	0.796924	0.032318	0.5325	0.0226	0.0081	0.0085	-0.0112	0.0118	0.0187	0.0089	0.0029	0.0001	0.017000	4.84E-06
EV22-03	23.9	0.8	2.7214	0.0295	2.6919	0.0144	0.0371	0.0177	-0.0002	0.0137	0.0021	0.0002	0.00	0.10	0.00	0.02	77.57	0.783501	0.026017	0.5736	0.0234	0.0198	0.0100	0.0136	0.0133	0.0194	0.0090	0.0028	0.0001	0.017000	4.84E-06
	35.2	1.1	3.5369	0.0316	2.2695	0.0136	0.0225	0.0160	0.0293	0.0135	0.0031	0.0002	0.26	0.12	-0.01	0.02	74.33	1.157509	0.035244	0.5260	0.0238	0.0084	0.0099	0.0196	0.0106	0.0182	0.0085	0.0029	0.0001	0.017000	4.84E-06
	Chip 3; J: 0.01699999 ± 0.00000484																													
	37.8	0.9	4.4043	0.0332	2.5558	0.0145	0.0317	0.0160	0.0221	0.0142	0.0042	0.0002	0.18	0.11	0.00	0.02	72.41	1.246756	0.030285	0.5527	0.0226	0.0226	0.0099	0.0211	0.0110	0.0220	0.0100	0.0027	0.0001	0.017000	4.84E-06
	22.5	*1.2*	*3.1280*	*0.0326*	*1.9855*	*0.0125*	*0.0550*	*0.0143*	*0.0316*	*0.0139*	*0.0057*	*0.0002*	*0.33*	*0.14*	*0.04*	*0.02*	*46.86*	*0.737680*	*0.040497*	*0.5522*	*0.0223*	*0.0107*	*0.0085*	*-0.0004*	*0.0101*	*0.0359*	*0.0106*	*0.0027*	*0.0001*	*0.017000*	*4.84E-06*
	28.2	0.8	3.4157	0.0313	2.6449	0.0121	0.0497	0.0159	-0.0251	0.0133	0.0032	0.0002	-0.20	0.10	0.02	0.02	71.94	0.928178	0.026546	0.5534	0.0224	0.0074	0.0085	-0.0208	0.0115	0.0554	0.0098	0.0027	0.0001	0.017000	4.84E-06
	44.7	0.7	5.6632	0.0317	3.1445	0.0130	0.0720	0.0141	0.0050	0.0127	0.0035	0.0002	0.03	0.08	0.03	0.01	82.02	1.475944	0.023970	0.4876	0.0224	0.0042	0.0091	-0.0244	0.0090	0.0033	0.0094	0.0026	0.0001	0.017000	4.84E-06
	38.1	0.8	4.5501	0.0307	2.8699	0.0125	0.0115	0.0146	-0.0322	0.0133	0.0031	0.0002	-0.23	0.10	-0.02	0.01	79.33	1.256603	0.027966	0.5736	0.0214	0.0178	0.0088	0.0090	0.0095	0.0390	0.0096	0.0033	0.0001	0.017000	4.84E-06
	25.1	0.7	3.0630	0.0289	3.0771	0.0133	0.0531	0.0152	-0.0174	0.0138	0.0017	0.0002	-0.12	0.09	0.01	0.01	82.75	0.822991	0.023947	0.7657	0.0204	0.0049	0.0085	0.0055	0.0104	0.0317	0.0093	0.0038	0.0001	0.017000	4.84E-06
	Chip 1; J: 0.01699999 ± 0.00000484																													
	22.8	0.6	3.5958	0.0316	3.8107	0.0138	0.0324	0.0155	-0.0363	0.0134	0.0024	0.0002	-0.20	0.07	-0.01	0.01	79.46	0.749082	0.019916	0.7477	0.0219	0.0096	0.0086	0.0100	0.0099	0.0444	0.0102	0.0039	0.0001	0.017000	4.84E-06
	29.1	0.5	3.8322	0.0303	4.0825	0.0142	0.0602	0.0148	0.0138	0.0122	-0.0002	0.0002	0.07	0.06	0.01	0.01	101.96	0.956359	0.017864	1.0221	0.0222	0.0141	0.0091	-0.0008	0.0104	0.0272	0.0077	0.0048	0.0002	0.017000	4.84E-06
	25.7	0.5	3.9556	0.0299	4.1934	0.0143	0.0680	0.0145	0.0074	0.0133	0.0014	0.0002	0.04	0.07	0.01	0.01	89.59	0.844423	0.017805	0.7304	0.0223	0.0045	0.0101	-0.0042	0.0103	0.0174	0.0100	0.0033	0.0001	0.017000	4.84E-06
EV22-06B	***Chip 2; J: 0.01699999 ± 0.00000484***																													
	23.0	0.6	2.9133	0.0326	3.7943	0.0134	0.0465	0.0152	-0.0145	0.0128	0.0001	0.0002	-0.08	0.07	0.00	0.01	98.41	0.754950	0.019060	0.8401	0.0237	-0.0009	0.0092	0.0102	0.0116	0.0167	0.0088	0.0041	0.0002	0.017000	4.84E-06
	30.3	0.6	4.3595	0.0322	4.0889	0.0118	0.0288	0.0160	-0.0148	0.0141	0.0009	0.0002	-0.08	0.07	-0.02	0.01	93.39	0.994813	0.019835	0.7751	0.0217	0.0232	0.0078	0.0181	0.0114	0.0161	0.0101	0.0041	0.0002	0.017000	4.84E-06
	25.4	0.7	5.5730	0.0339	4.0151	0.0132	0.0309	0.0158	-0.0013	0.0135	0.0075	0.0003	-0.01	0.07	-0.01	0.01	60.13	0.833904	0.024526	0.7339	0.0226	0.0107	0.0087	0.0173	0.0109	0.0130	0.0094	0.0033	0.0002	0.017000	4.84E-06
	23.3	0.6	3.4040	0.0309	3.6946	0.0122	0.0474	0.0143	0.0132	0.0133	0.0020	0.0002	0.07	0.08	0.00	0.01	82.96	0.763719	0.019751	0.8094	0.0204	0.0157	0.0082	0.0094	0.0100	0.0231	0.0088	0.0034	0.0002	0.017000	4.84E-06
	25.9	0.6	4.7247	0.0315	3.9848	0.0121	0.0332	0.0148	0.0136	0.0140	0.0045	0.0003	0.07	0.07	-0.01	0.01	71.72	0.849723	0.020557	0.7908	0.0210	0.0058	0.0089	0.0161	0.0104	0.0350	0.0102	0.0034	0.0001	0.017000	4.84E-06
	Chip 3; J: 0.01696434 ± 0.00001737																													
	31.8	4.4	0.5718	0.0310	0.4787	0.0121	-0.0139	0.0144	0.0088	0.0129	0.0003	0.0002	0.52	0.77	-0.12	0.09	87.76	1.047502	0.147631	0.6602	0.0226	0.0334	0.0086	0.0253	0.0109	0.0167	0.0091	0.0035	0.0001	0.016964	1.737E-05
	26.4	1.8	1.5262	0.0324	1.1595	0.0131	-0.0085	0.0153	-0.0411	0.0122	0.0016	0.0002	-1.01	0.30	-0.06	0.04	66.04	0.868129	0.059764	0.5705	0.0234	-0.0138	0.0087	0.0133	0.0112	0.0419	0.0090	0.0032	0.0001	0.016964	1.737E-05
	25.8	*1.5*	*3.5817*	*0.0314*	*1.6942*	*0.0141*	*0.0330*	*0.0163*	*-0.0003*	*0.0128*	*0.0073*	*0.0003*	*-0.01*	*0.21*	*0.02*	*0.03*	*40.15*	*0.848066*	*0.048807*	*0.6179*	*0.0213*	*-0.0101*	*0.0092*	*-0.0018*	*0.0103*	*0.0341*	*0.0085*	*0.0029*	*0.0001*	*0.016964*	*1.74E-05*
	21.1	0.8	2.6933	0.0319	2.8113	0.0122	0.0317	0.0142	-0.0097	0.0135	0.0025	0.0002	-0.10	0.14	0.00	0.01	72.35	0.692424	0.024800	0.6153	0.0223	-0.0023	0.0084	-0.0023	0.0105	0.0415	0.0096	0.0032	0.0001	0.016964	1.737E-05
	42.0	0.7	7.0707	0.0343	3.6432	0.0124	0.0168	0.0164	-0.0025	0.0125	0.0068	0.0003	-0.02	0.10	-0.02	0.01	71.62	1.388576	0.023905	0.5990	0.0233	0.0060	0.0086	0.0175	0.0111	0.0270	0.0092	0.0031	0.0001	0.016964	1.737E-05
EV22-07	55.3	0.6	9.2526	0.0320	4.0832	0.0133	0.0395	0.0138	-0.0062	0.0130	0.0059	0.0002	-0.04	0.09	-0.01	0.01	81.04	1.834686	0.020576	0.5836	0.0225	0.0290	0.0097	0.0079	0.0100	0.0258	0.0088	0.0028	0.0001	0.016964	1.737E-05
	Chip 4; J: 0.01696434 ± 0.00001737																													
	28.6	2.6	1.0704	0.0318	0.8121	0.0129	0.0303	0.0154	0.0130	0.0137	0.0011	0.0002	0.46	0.48	0.07	0.06	71.59	0.942737	0.085230	0.6090	0.0223	-0.0041	0.0090	-0.0042	0.0114	0.0202	0.0092	0.0030	0.0001	0.016964	1.737E-05
	39.5	0.6	4.6515	0.0301	3.1726	0.0124	0.0418	0.0156	0.0037	0.0131	0.0017	0.0002	0.03	0.12	0.00	0.01	89.15	1.305849	0.021284	0.5685	0.0207	0.0095	0.0085	-0.0033	0.0111	0.0076	0.0095	0.0027	0.0001	0.016964	1.737E-05
	29.4	2.7	0.7810	0.0326	0.6670	0.0123	0.0060	0.0160	0.0328	0.0130	0.0006	0.0002	1.41	0.56	-0.01	0.07	82.62	0.967020	0.091172	0.5507	0.0230	0.0081	0.0085	0.0025	0.0115	0.0190	0.0090	0.0030	0.0001	0.016964	1.737E-05
	35.2	0.7	4.8209	0.0306	3.2086	0.0127	0.0367	0.0159	0.0475	0.0131	0.0039	0.0002	0.42	0.12	0.00	0.01	77.44	1.162614	0.022119	0.6156	0.0211	0.0290	0.0093	0.0107	0.0120	0.0005	0.0094	0.0032	0.0001	0.016964	1.737E-05
	29.5	*3.5*	*2.0555*	*0.0347*	*0.7131*	*0.0137*	*-0.0023*	*0.0156*	*0.0354*	*0.0138*	*0.0047*	*0.0002*	*1.43*	*0.56*	*-0.05*	*0.06*	*33.71*	*0.971242*	*0.116365*	*0.5269*	*0.0242*	*0.0221*	*0.0098*	*0.0119*	*0.0107*	*0.0068*	*0.0098*	*0.0030*	*0.0001*	*0.016964*	*1.74E-05*
	22.5	0.8	2.6878	0.0323	2.7382	0.0129	0.0288	0.0158	0.0064	0.0133	0.0023	0.0002	0.07	0.14	-0.01	0.02	75.39	0.739366	0.026583	0.5906	0.0218	0.0236	0.0095	0.0113	0.0110	0.0375	0.0088	0.0028	0.0001	0.016964	1.737E-05
	23.7	0.7	3.1259	0.0308	3.2848	0.0132	0.0472	0.0149	-0.0154	0.0152	0.0018	0.0002	-0.14	0.13	0.01	0.01	81.99	0.779470	0.024770	0.6401	0.0210	0.0317	0.0090	-0.0008	0.0105	0.0300	0.0111	0.0032	0.0002	0.016964	1.737E-05
	Chip 1; J: 0.01696434 ± 0.00001737																													
	27.5	0.6	3.4412	0.0322	3.3792	0.0145	0.0416	0.0153	-0.0042	0.0134	0.0013	0.0002	-0.04	0.11	0.00	0.01	89.01	0.905541	0.020649	0.5750	0.0220	0.0167	0.0104	0.0078	0.0102	0.0160	0.0093	0.0029	0.0001	0.016964	1.737E-05
	31.4	0.6	4.9408	0.0317	3.9862	0.0135	0.0376	0.0146	-0.0199	0.0132	0.0027	0.0002	-0.14	0.10	-0.01	0.01	83.57	1.034782	0.018394	0.5630	0.0217	-0.0022	0.0089	0.0133	0.0101	0.0441	0.0090	0.0028	0.0001	0.016964	1.737E-05
	Chip 2; J: 0.01696434 ± 0.00001737																													
	28.1	0.6	3.7097	0.0310	3.5493	0.0134	0.0556	0.0145	0.0316	0.0143	0.0015	0.0002	0.26	0.12	0.01	0.01	88.70	0.926312	0.019980	0.6419	0.0223	0.0341	0.0089	-0.0296	0.0106	0.0146	0.0097	0.0033	0.0001	0.016964	1.737E-05
	26.7	0.5	4.7205	0.0333	4.3071	0.0131	0.0678	0.0157	0.0122	0.0138	0.0032	0.0002	0.08	0.09	0.01	0.01	80.21	0.878304	0.017579	0.5211	0.0233	0.0102	0.0095	0.0118	0.0113	0.0221	0.0104	0.0027	0.0001	0.016964	1.737E-05
	25.0	0.8	3.1827	0.0323	2.9013	0.0127	0.0363	0.0148	0.0206	0.0129	0.0028	0.0002	0.20	0.13	0.00	0.01	74.99	0.821922	0.025752	0.5895	0.0230	0.0451	0.0085	-0.0061	0.0114	-0.0005	0.0086	0.0030	0.0001	0.016964	1.737E-05
EV22-14.5	29.5	0.7	3.0823	0.0309	2.9589	0.0133	0.0064	0.0155	0.0260	0.0134	0.0008	0.0002	0.25	0.13	-0.03	0.02	93.33	0.971349	0.023630	0.6414	0.0231	0.0077	0.0096	0.0288	0.0097	0.0158	0.0095	0.0033	0.0001	0.016964	1.737E-05
	25.9	0.6	3.8875	0.0288	3.5381	0.0142	0.0844	0.0150	0.0028	0.0144	0.0029	0.0002	0.02	0.12	0.03	0.01	77.80	0.853963	0.020249	0.5394	0.0203	0.0338	0.0102	-0.0202	0.0101	0.0315	0.0092	0.0029	0.0001	0.016964	1.737E-05
	30.3	0.6	4.1751	0.0324	3.6495	0.0134	0.0321	0.0152	0.0070	0.0138	0.0018	0.0002	0.06	0.11	-0.01	0.01	87.43	0.999305	0.019853	0.5094	0.0244	0.0228	0.0085	0.0160	0.0100	0.0278	0.0095	0.0029	0.0001	0.016964	1.737E-05
	31.6	1.0	3.1853	0.0424	2.5429	0.0127	0.0093	0.0169	0.0196	0.0134	0.0019	0.0003	0.22	0.15	-0.03	0.02	83.17	1.040866	0.034644	0.6494	0.0216	0.0123	0.0095	0.0183	0.0114	0.0240	0.0090	0.0033	0.0001	0.016964	1.737E-05
	Chip 3; J: 0.01690337 ± 0.00001493																													
	31.5	0.7	5.8673	0.0304	3.5075	0.0137	0.0273	0.0145	0.0207	0.0137	0.0076	0.0003	0.17	0.11	-0.01	0.01	62.31	1.041360	0.025004	0.5392	0.0225	0.0390	0.0086	0.0220	0.0107	0.0049	0.0087	0.0028	0.0001	0.016903	1.493E-05
	31.4	0.6	5.8304	0.0337	3.9077	0.0126	0.0561	0.0160	0.0033	0.0134	0.0060	0.0003	0.02	0.10	0.01	0.01	69.62	1.037808	0.021592	0.5280	0.0239	0.0295	0.0084	0.0143	0.0112	0.0390	0.0099	0.0030	0.0001	0.016903	1.493E-05
	31.8	0.7	4.7701	0.0301	3.4576	0.0140	0.0364	0.0151	0.0025	0.0124	0.0038	0.0002	0.02	0.10	-0.01	0.01	76.43	1.053367	0.022865	0.6126	0.0214	0.0186	0.0096	0.0153	0.0113	0.0241	0.0078	0.0030	0.0001	0.016903	1.493E-05
	Chip 1; J: 0.01690337 ± 0.00001493																													
	34.0	1.4	2.7953	0.0326	1.5845	0.0121	0.0252	0.0143	0.0176	0.0133	0.0035	0.0002	0.32	0.24	0.01	0.03	63.79	1.124418	0.045303	0.5437	0.0225	0.0194	0.0084	0.0098	0.0102	0.0325	0.0100	0.0030	0.0001	0.016903	1.493E-05
	Chip 2; J: 0.01690337 ± 0.00001493																													
	30.4	0.5	6.1949	0.0300	4.7337	0.0144	0.0722	0.0158	0.0006	0.0141	0.0048	0.0003	0.00	0.09	0.01	0.01	76.97	1.006263	0.017986	0.5614	0.0220	-0.0010	0.0098	-0.0017	0.0099	0.0150	0.0101	0.0028	0.0001	0.016903	1.493E-05
	24.5	1.2	2.9839	0.0332	2.0372	0.0119	0.0164	0.0153	0.0179	0.0129	0.0046	0.0002	0.26	0.19	-0.01	0.02	55.19	0.807677	0.040361	0.5483	0.0236	0.0127	0.0083	0.0074	0.0110	0.0118	0.0086	0.0029	0.0001	0.016903	1.493E-05
	27.4	1.1	3.6211	0.0309	2.2582	0.0125	0.0254	0.0153	-0.0007	0.0137	0.0053	0.0002	-0.01	0.18	0.00	0.02	56.56	0.906088	0.035514	0.5794	0.0213	0.0170	0.0090	0.0087	0.0112	0.0255	0.0101	0.0030	0.0001	0.016903	1.493E-05
EV22-17	30.1	0.6	5.3505	0.0321	4.0258	0.0146	0.0424	0.0148	0.0177	0.0134	0.0046	0.0002	0.13	0.10	-0.01	0.01	74.90	0.994489	0.019419	0.5640	0.0205	0.0296	0.0096	0.0087	0.0097	0.0200	0.0085	0.0029	0.0001	0.016903	1.493E-05
	Chip 3; J: 0.01690337 ± 0.00001493																													
	29.4	0.7	3.5382	0.0306	3.0630	0.0131	0.0363	0.0159	0.0052	0.0121	0.0019	0.0002	0.05	0.12	0.00	0.02	84.28	0.972675	0.024582	0.6132	0.0222	0.0172	0.0087	0.0153	0.0113	0.0247	0.0085	0.0029	0.0002	0.016903	1.493E-05
	40.0	0.6	5.7967	0.0333	3.9146	0.0144	0.0211	0.0141	0.0011	0.0133	0.0020	0.0002	0.01	0.10	-0.02	0.01	89.60	1.325450	0.020538	0.5201	0.0253	0.0294	0.0098	0.0323	0.0104	0.0305	0.0090	0.0032	0.0002	0.016903	1.493E-05
	61.2	3.9	2.1449	0.0324	0.6114	0.0140	0.0330	0.0149	0.0026	0.0139	0.0031	0.0002	0.12	0.66	0.12	0.07	58.20	2.039805	0.131181	0.5128	0.0233	0.0247	0.0096	-0.0025	0.0103	0.0280	0.0101	0.0029	0.0001	0.016903	1.493E-05
	46.5	0.7	6.3785	0.0344	3.5862	0.0141	0.0784	0.0157	-0.0333	0.0132	0.0027	0.0002	-0.27	0.11	0.03	0.01	86.91	1.544163	0.022016	0.6020	0.0216	0.0172	0.0108	-0.0035	0.0112	0.0292	0.0089	0.0032	0.0002	0.016903	1.493E-05
	Chip 4; J: 0.01690337 ± 0.00001493																													
	39.8	0.5	6.9079	0.0311	4.6121	0.0132	0.0407	0.0153	-0.0095	0.0129	0.0027	0.0002	-0.06	0.08	-0.01	0.01	88.11	1.318420	0.017625	0.5557	0.0206	0.0212	0.0093	0.0126	0.0114	0.0240	0.0087	0.0030	0.0001	0.016903	1.493E-05
	57.2	0.4	11.4666	0.0338	5.4415	0.0129	0.0712	0.0155	-0.0518	0.0151	0.0035	0.0002	-0.28	0.08	0.00	0.01	90.48	1.904576	0.014878	0.5541	0.0241	0.0029	0.0088	-0.0033	0.0105	0.0543	0.0102	0.0030	0.0001	0.016903	1.493E-05
	35.2	*0.9*	*8.3556*	*0.0338*	*3.6416*	*0.0122*	*0.0598*	*0.0151*	*0.0272*	*0.0136*	*0.0140*	*0.0003*	*0.22*	*0.11*	*0.01*	*0.01*	*50.88*	*1.166449*	*0.028506*	*0.5226*	*0.0243*	*0.0251*	*0.0084*	*0.0017*	*0.0117*	*0.0124*	*0.0101*	*0.0030*	*0.0001*	*0.016903*	*1.49E-05*

Italicized analyses were rejected due to low % ^{40}Ar yields.

paragonite

Table S3.3a. Analytical results for in situ $^{87}Rb/^{87}Sr$ geochronology from the Basal Unit schists of southern Evia.

	Analysis	Rb (ppm)	Sr (ppm)	$^{87}Rb/^{87}Sr$	2σ (%)	$^{87}Rb/^{86}Sr$	2σ (%)	$^{87}Sr/^{86}Sr$	2σ (%)	rho
phengite	EV20-14-1	260.0	3.7	222.30	4.40	164.99	4.00	0.789	5.300	0.40
	EV20-14-2	263.0	5.2	161.60	4.40	121.98	3.90	0.801	4.400	-0.08
	EV20-14-3	258.0	6.0	138.50	4.10	102.61	4.00	0.783	4.000	0.22
	EV20-14-4	257.0	5.0	164.50	5.80	120.91	4.10	0.778	4.400	-0.01
	EV20-14-5	240.0	3.3	232.00	6.30	178.80	3.40	0.819	5.400	0.06
	EV20-14-6	247.0	5.4	145.90	2.20	109.03	2.90	0.781	2.400	0.21
	EV20-14-7	245.0	3.3	223.60	4.30	177.73	3.60	0.845	4.400	0.24
	EV20-14-8	261.0	6.7	126.70	4.40	91.38	3.00	0.765	5.300	0.37
	EV20-14-9	264.0	3.2	257.00	7.20	206.51	5.80	0.856	8.200	-0.11
	EV20-14-10	254.0	1.2	606.00	5.30	518.95	4.40	0.926	6.600	0.33
	EV20-14-11	257.0	1.2	584.00	4.90	531.79	6.10	0.965	5.700	0.50
	EV20-14-12	251.0	1.8	376.00	5.30	333.84	5.50	0.940	5.700	0.24
	EV20-14-13	251.0	3.5	220.50	3.90	169.81	3.50	0.817	3.400	0.27
	EV20-14-14	248.0	3.5	222.10	2.30	170.13	2.90	0.807	3.300	0.29
	EV20-14-15	251.0	3.4	234.60	3.40	177.73	2.50	0.806	4.400	0.51
	EV20-14-16	232.0	3.0	236.00	4.90	189.07	4.70	0.848	3.700	0.25
	EV20-14-17	237.0	3.4	218.00	4.70	169.38	3.30	0.828	5.700	0.14
	EV20-14-18	239.0	1.7	430.00	4.30	340.26	3.70	0.854	4.700	0.35
	EV20-14-19	262.0	1.3	564.00	3.70	507.18	3.60	0.961	4.800	0.32
	EV20-14-20	269.0	1.2	587.00	3.90	545.70	4.40	0.996	5.900	0.44
	EV20-14-21	250.0	7.4	108.90	2.50	79.39	2.10	0.779	3.100	0.26
	EV20-14-22	251.0	2.6	301.90	3.20	232.73	3.40	0.819	3.400	0.49
	EV20-14-23	261.0	1.8	417.00	4.60	353.10	4.90	0.899	4.000	0.22
	EV20-14-24	253.0	2.9	279.00	5.00	219.67	2.90	0.839	4.600	0.33
	EV20-14-25	197.0	2.4	263.50	2.80	194.85	2.30	0.784	3.400	0.54
	EV20-14-26	37.3	0.3	415.00	14.00	306.02	12.00	0.830	19.000	0.52
	EV20-14-27	232.0	2.5	307.00	4.80	222.35	4.10	0.774	4.800	0.70
	EV20-14-28	237.0	3.2	243.60	3.40	180.72	3.50	0.789	3.900	0.37
	EV20-14-29	263.0	2.6	326.00	5.20	248.24	5.10	0.813	5.900	0.51
	EV20-14-30	223.0	1.9	361.00	3.90	276.60	3.70	0.823	4.800	0.22
	EV20-14-31	159.0	2.0	251.80	3.70	188.21	4.40	0.789	4.500	0.23
	EV20-14-32	249.0	4.2	181.30	2.60	140.60	2.50	0.822	3.200	0.42
	EV20-14-33	198.0	1.8	337.00	4.00	265.47	3.50	0.836	4.000	0.51
	EV20-14-34	252.0	1.0	639.00	4.50	640.93	4.60	1.081	7.500	0.54
	EV20-14-35	176.0	4.1	139.60	4.50	100.15	4.20	0.759	4.000	0.37
	EV20-14-36	259.0	2.8	289.00	5.00	225.77	5.30	0.831	4.500	0.24
	EV20-14-37	236.0	1.5	468.00	4.10	354.49	2.90	0.817	5.200	0.56
	EV20-14-38	153.0	1.0	457.00	4.70	375.57	6.50	0.877	7.600	0.43
	EV20-14-39†	173.0	91.0	6.68	3.80	4.46	4.00	0.709	1.700	0.45
	EV20-14-40	250.0	2.4	309.00	3.70	247.17	3.70	0.848	3.800	0.37
	EV20-14-41	247.0	3.2	235.40	3.30	182.33	3.50	0.818	3.800	0.35
	EV20-14-42	239.0	2.9	248.40	3.40	200.20	3.20	0.847	2.700	0.21
	EV20-14-43	235.0	2.9	252.00	4.40	196.56	4.20	0.821	4.900	0.32
	EV20-14-44	243.0	3.2	236.80	3.20	183.51	3.80	0.815	3.800	0.33
	EV20-14-45	219.0	3.8	181.90	3.50	140.06	4.90	0.808	4.000	0.27
	EV20-14-46	241.0	3.4	216.70	3.20	171.95	3.10	0.835	3.100	0.27
	EV20-14-47	227.0	3.6	200.10	3.70	151.08	3.00	0.794	3.800	0.36
	EV20-14-48	262.0	2.3	336.00	4.70	273.71	3.80	0.860	4.700	0.23
	EV20-14-49	255.0	9.8	88.50	4.70	62.81	5.20	0.739	2.200	0.32
	EV20-14-50	257.0	7.1	116.20	2.90	86.35	3.40	0.779	2.600	0.44
	EV20-14-51	252.0	3.2	243.50	3.40	187.36	3.20	0.813	4.900	0.48
	EV20-14-52	247.0	7.9	103.20	3.50	75.65	4.10	0.770	2.300	0.34
	EV20-14-53	257.0	2.9	264.00	3.90	203.30	4.00	0.810	3.600	0.32
	EV20-14-54	258.0	5.4	149.90	2.40	113.31	2.40	0.797	2.800	0.60
	EV20-14-55	262.0	9.9	87.40	2.60	62.49	2.50	0.752	1.700	0.16
	EV20-14-56	248.0	4.8	162.30	2.40	120.48	2.20	0.788	2.500	0.41
	EV20-14-57	240.0	4.9	155.00	2.50	115.45	1.90	0.789	3.000	0.38
	EV20-14-58	243.0	5.1	152.90	3.40	113.10	2.50	0.782	3.400	-0.07
	EV20-14-59	225.0	2.9	242.10	3.50	190.03	3.10	0.835	3.800	-0.02
	EV20-14-60	218.0	3.8	187.20	4.40	136.96	3.80	0.775	2.700	0.24
calcite	EV20-14C-1†	0.0	1800.0	0.00	-160.00	0.00	170.00	0.708	1.600	-0.01
	EV20-14C-2†	0.0	1800.0	0.00	61.00	0.00	60.00	0.714	1.400	0.00
	EV20-14C-4†	0.0	2500.0	0.00	94.00	0.00	93.00	0.696	2.900	0.61
	EV20-14C-5†	0.0	2200.0	0.00	-53.00	0.00	54.00	0.7129	1.300	-0.01
	EV20-14C-6†	6.9	2200.0	0.01	22.00	0.01	23.00	0.706	1.600	0.08
	EV20-14C-7†	0.0	2200.0	0.00	350.00	0.00	370.00	0.7161	1.300	0.06
	EV20-14C-9†	22.4	1800.0	0.05	2.40	0.03	2.40	0.714	1.600	0.21
	EV20-14C-10†	0.0	2400.0	0.00	-34.00	0.00	34.00	0.703	2.000	0.16

†Analysis rejected from isochron regression

Table S3.3a cont.

	Analysis	Rb (ppm)	Sr (ppm)	$^{87}Rb/^{87}Sr$	2σ (%)	$^{87}Rb/^{86}Sr$	2σ (%)	$^{87}Sr/^{86}Sr$	2σ (%)	rho
phengite	EV20-20-1	245.0	7.5	105.10	2.60	76.51	2.30	0.769	3.100	0.53
	EV20-20-2	196.0	3.3	192.60	3.70	138.57	3.50	0.764	3.500	0.30
	EV20-20-3	136.0	4.0	115.70	3.20	79.50	2.40	0.728	3.100	0.17
	EV20-20-4	234.0	3.4	226.10	3.10	165.96	3.20	0.78	4.100	0.29
	EV20-20-5	262.0	5.1	162.10	3.00	121.55	2.30	0.795	3.000	0.25
	EV20-20-6	212.0	6.6	103.40	1.70	75.22	2.00	0.769	2.400	0.54
	EV20-20-7	260.0	3.6	237.50	3.60	176.02	3.10	0.788	3.700	0.30
	EV20-20-8	230.0	14.0	53.70	2.50	38.84	2.50	0.764	2.000	0.26
	EV20-20-9	264.0	3.5	234.50	2.40	179.55	2.30	0.814	3.600	0.57
	EV20-20-10	262.0	3.3	248.50	3.20	188.00	3.50	0.802	3.300	0.35
	EV20-20-11	220.0	5.1	140.50	2.00	102.19	2.60	0.77	2.900	0.56
	EV20-20-12	243.0	7.3	111.90	6.20	82.60	6.20	0.78	2.000	0.28
	EV20-20-13	248.0	3.7	211.80	2.50	158.15	2.80	0.792	3.400	0.51
	EV20-20-14	261.0	3.7	224.30	2.50	165.32	2.40	0.787	3.100	0.44
	EV20-20-15	266.0	3.8	227.30	2.50	168.63	2.60	0.786	2.800	0.23
	EV20-20-16	179.0	11.0	54.66	1.80	38.27	1.70	0.738	1.600	0.25
	EV20-20-17	192.0	6.4	98.80	2.50	72.12	2.50	0.773	2.600	0.32
	EV20-20-18	251.0	5.3	154.80	1.80	112.56	2.70	0.765	3.200	0.43
	EV20-20-19	237.0	7.1	108.80	2.30	78.65	2.10	0.765	2.000	0.24
	EV20-20-20	157.0	9.2	58.20	3.10	40.34	2.90	0.734	2.300	0.03
	EV20-20-21	262.0	7.4	113.80	2.00	83.46	1.90	0.775	2.100	0.38
	EV20-20-22	256.0	9.9	84.30	1.50	60.70	1.70	0.761	2.000	0.32
	EV20-20-23	265.0	3.6	229.70	2.40	178.37	2.30	0.824	3.400	0.34
	EV20-20-24	230.0	6.2	123.60	1.90	87.74	1.60	0.754	2.300	0.43
	EV20-20-25	273.0	2.4	341.00	4.00	272.21	3.00	0.855	4.400	0.01
	EV20-20-26	271.0	3.4	250.20	3.10	189.07	2.70	0.801	3.200	0.18
	EV20-20-27	265.0	3.7	225.30	2.70	169.17	2.60	0.796	3.100	0.30
	EV20-20-28	231.0	4.2	175.40	2.60	131.50	2.10	0.794	3.200	0.42
	EV20-20-29	260.0	4.4	194.70	1.80	138.67	1.50	0.756	2.400	0.56
	EV20-20-30	280.0	3.2	272.50	3.60	207.47	3.40	0.809	3.600	0.11
	EV20-20-31	236.0	4.6	165.20	2.30	119.20	2.30	0.761	2.600	0.08
	EV20-20-32	276.0	2.0	387.00	3.70	328.06	2.90	0.899	4.100	0.50
	EV20-20-33	286.0	3.2	269.00	3.40	215.61	2.80	0.849	3.600	0.26
	EV20-20-34	257.0	3.6	226.10	2.20	165.42	2.60	0.771	2.300	0.44
	EV20-20-35	244.0	5.2	154.90	2.80	112.03	2.70	0.762	2.500	0.21
	EV20-20-36	238.0	3.8	199.70	2.50	145.41	2.50	0.769	3.400	0.43
	EV20-20-37	248.0	4.5	174.10	3.40	132.47	4.20	0.799	2.300	0.40
	EV20-20-38	260.0	2.5	315.20	2.50	247.92	3.10	0.831	3.600	0.44
	EV20-20-39	257.0	4.0	201.60	2.70	152.15	3.20	0.796	3.000	0.45
	EV20-20-40	294.0	4.2	215.00	3.10	165.42	2.10	0.813	3.500	0.36
	EV20-20-41	200.0	5.2	130.10	2.60	91.38	2.20	0.742	3.100	0.43
	EV20-20-42	293.0	3.1	286.00	3.40	223.84	3.00	0.829	3.100	0.34
	EV20-20-43	267.0	6.8	127.40	2.50	92.56	2.10	0.768	2.300	0.29
	EV20-20-44	293.0	3.2	287.00	3.80	220.74	3.40	0.818	4.600	-0.08
	EV20-20-45	282.0	1.8	451.00	3.80	373.43	3.00	0.882	4.300	0.35
	EV20-20-46	194.0	4.0	157.90	2.50	111.39	2.80	0.748	3.500	0.38
	EV20-20-47	225.0	5.3	140.10	2.50	100.79	2.10	0.763	3.100	0.25
	EV20-20-48	240.0	6.0	130.20	2.50	93.30	2.30	0.758	2.400	0.15
	EV20-20-49	273.0	6.3	139.30	3.90	100.69	3.90	0.765	3.300	0.24
	EV20-20-50	250.0	6.8	120.30	1.80	86.14	2.10	0.758	2.400	0.62
	EV20-20-51	266.0	5.5	158.40	1.90	115.99	2.20	0.776	2.500	0.53
	EV20-20-52	226.0	6.2	118.90	2.50	82.93	2.00	0.744	2.500	0.41
	EV20-20-53	220.0	7.3	98.90	2.10	69.87	2.00	0.748	2.400	0.20
	EV20-20-54	216.0	9.0	80.20	2.30	55.85	2.80	0.737	2.400	0.34
	EV20-20-55	217.0	6.9	103.50	2.10	73.19	2.50	0.748	2.800	0.35
	EV20-20-56	82.4	8.3	34.48	2.70	23.50	2.70	0.721	2.600	-0.19
	EV20-20-57†	248.0	9.3	82.30	2.60	62.06	2.00	0.797	2.200	0.18
	EV20-20-58	195.0	7.4	89.90	2.30	62.06	2.20	0.731	2.700	0.43
	EV20-20-59	227.0	4.4	165.10	2.20	121.87	2.70	0.781	2.800	0.51
	EV20-20-60	213.0	11.0	75.30	11.00	52.54	11.00	0.74	2.000	0.20
albite	EV20-20-61†	0.0	3000.0	0.00	120.00	0.00	120.00	0.6121	1.600	0.22
	EV20-20-62†	0.0	3200.0	0.00	22.00	0.00	22.00	0.607	1.400	0.18
	EV20-20-63†	0.0	3300.0	0.00	20.00	0.00	20.00	0.6113	1.500	0.09
	EV20-20-65†	0.0	3600.0	0.00	-43.00	0.00	42.00	0.683	2.400	0.16
	EV20-20-66†	0.0	2400.0	0.00	-3500.00	0.00	2400.00	0.71	1.700	-0.09
	EV20-20-67†	0.0	2500.0	0.00	32.00	0.00	32.00	0.655	2.300	0.17
	EV20-20-68†	0.0	2900.0	0.00	89.00	0.00	90.00	0.6139	1.400	0.04
	EV20-20-69†	0.0	3200.0	0.00	130.00	0.00	120.00	0.6092	1.500	0.17
	EV20-20-70†	0.0	3400.0	0.00	380.00	0.00	410.00	0.619	2.000	-0.12
	EV20-20-71†	0.0	3700.0	0.00	-780.00	0.00	640.00	0.7	2.400	0.01

†Analysis rejected from isochron regression

Table S3.3b. Analytical standard data for $^{87}Rb/^{87}Sr$ analyses.

Analysis	Rb (ppm)	Sr (ppm)	$^{87}Rb/^{87}Sr$	2σ (%)	$^{87}Rb/^{86}Sr$	2σ (%)	$^{87}Sr/^{86}Sr$	2σ (%)	rho	
1B-1	390.0	6.2	63.38	1.60	170.00	2.20	3.027	2.400	0.61	***Phlogopite***
1B-2	339.0	7.5	54.90	2.00	124.87	2.20	2.401	2.900	0.49	***isochron = 992 ± 12 Ma; MSWD = 2.4 Ma***
1B-3	286.0	9.4	45.69	1.60	79.61	3.50	1.827	2.400	0.89	***expected = 990 ± 5 Ma (Camacho et al. 2012)***
1B-4	270.0	10.0	43.59	1.70	68.69	2.00	1.669	2.100	0.08	
1B-5	280.0	9.8	44.63	2.00	74.79	2.10	1.762	1.700	0.50	
1B-6	299.0	11.0	42.63	2.10	67.20	2.60	1.653	2.000	0.37	
1B-7	300.0	12.0	41.47	1.40	64.95	2.10	1.645	1.800	0.60	
1B-8	284.0	11.0	42.73	1.40	65.06	1.90	1.609	1.900	0.71	
1B-9	382.0	8.2	58.81	1.70	117.30	1.70	2.265	2.000	0.23	
1B-10	387.0	7.4	61.20	1.90	137.50	3.30	2.514	3.100	0.74	
1B-11	362.0	5.6	63.70	1.60	169.20	3.00	2.992	2.800	0.66	
1B-12	297.0	11.0	43.38	1.10	66.98	1.60	1.640	1.700	0.50	
1B-13	292.0	10.0	44.20	2.40	75.86	2.20	1.810	2.800	0.31	
1B-14	293.0	9.9	44.25	1.20	76.51	1.70	1.813	2.000	0.72	
1B-15	276.0	11.0	41.80	2.20	66.02	1.50	1.670	2.200	0.21	
1O-1	375.0	2.2	75.70	2.70	881.00	10.00	12.700	8.800	0.87	***Phlogopite***
1O-2	366.0	1.9	75.50	2.10	1000.00	4.30	14.960	5.100	0.85	***Primary Matrix Calibration***
1O-3	364.0	1.8	75.60	2.30	1261.00	6.90	18.800	6.100	0.86	
1O-4	349.0	1.8	74.80	2.00	1021.00	4.60	15.360	4.700	0.80	
1O-5	376.0	1.8	79.70	2.20	1255.00	4.80	17.710	4.700	0.87	
1O-6	377.0	1.7	78.90	2.70	1560.00	6.70	22.100	5.700	0.91	
1O-7	381.0	1.5	81.70	2.60	2360.00	5.30	32.600	4.900	0.94	
1O-8	357.0	1.7	76.10	2.20	1273.00	5.50	19.000	5.600	0.86	
1O-9	381.0	1.7	79.80	2.00	1439.00	6.40	20.400	6.500	0.87	
1O-10	346.0	1.7	76.00	2.20	1283.00	6.50	19.100	7.000	0.91	
1O-11	391.0	1.6	82.40	2.50	1670.00	9.00	22.700	7.700	0.92	
1O-12	399.0	1.6	82.20	2.00	1880.00	6.70	25.900	6.300	0.96	
1O-13	389.0	1.6	83.00	2.30	1660.00	7.20	22.600	7.400	0.93	
1O-14	390.0	1.5	83.10	2.40	2120.00	8.00	28.600	7.500	0.91	
1O-15	358.0	1.5	78.70	2.90	1880.00	6.50	27.100	6.700	0.89	
MA1-1	1050.0	4.5	194.80	1.40	688.00	2.60	3.980	2.500	0.58	***White Mica***
MA1-2	977.0	4.5	188.80	1.40	632.00	2.50	3.800	2.900	0.58	***isochron (with plag) = 346 ± 2 Ma; MSWD = 0.84 Ma***
MA1-3	987.0	4.4	188.40	1.20	656.00	2.30	3.928	2.300	0.58	***expected = ca. 350 (Camacho, pers. Comm.)***
MA1-4	1030.0	4.7	183.80	1.10	636.00	2.00	3.862	2.400	0.69	
MA1-5	1020.0	4.6	187.60	1.30	653.00	2.10	3.920	2.700	0.68	
MA1-6	1070.0	4.8	186.40	1.10	651.00	2.30	3.890	2.700	0.75	
MA1-7	1040.0	4.6	187.60	1.20	651.00	1.90	3.923	2.100	0.72	
MA1-8	1040.0	4.7	185.80	1.20	634.00	2.00	3.846	2.300	0.58	
MA1-9	1040.0	4.6	189.30	1.60	639.00	1.80	3.780	2.700	0.60	
MA1-10	1080.0	4.7	189.00	1.20	670.00	2.30	3.992	2.400	0.68	
MA1-11	978.0	4.3	192.30	1.60	667.00	2.60	3.900	2.700	0.61	
MA1-12	1050.0	4.5	187.70	1.30	657.00	2.20	3.951	2.200	0.74	
MA1-13	1070.0	4.9	183.50	1.20	618.00	2.10	3.761	2.100	0.55	
MA1-14	953.0	4.2	185.70	1.40	657.00	2.30	3.960	2.500	0.43	
MA1-15	952.0	4.2	187.90	1.10	655.00	2.60	3.920	2.600	0.74	
MAPlag-1	8.4	47.0	0.58	4.30	0.42	5.10	0.747	1.300	0.25	
MAPlag-2	4.5	55.0	0.26	2.00	0.19	2.10	0.744	1.300	0.20	
MAPlag-3	3.4	55.0	0.20	2.10	0.14	2.30	0.743	1.200	0.29	
MAPlag-4	6.9	48.0	0.48	2.80	0.34	2.80	0.745	1.400	0.34	
MAPlag-5	3.8	49.0	0.25	1.90	0.18	1.90	0.742	1.300	0.38	

Table S3.3b cont.

MA2-1	1090.0	4.2	199.90	1.50	788.00	3.50	4.480	4.100	0.79	***White Mica***
MA2-2	1040.0	4.4	189.10	1.50	694.00	2.70	4.150	3.000	0.77	***isochron (with plag) = 350 ± 2 Ma; MSWD = 2.4 Ma***
MA2-3	1010.0	4.5	185.90	1.40	668.00	2.30	4.010	3.000	0.48	***expected = ca. 350 (Camacho, pers. Comm.)***
MA2-4	1020.0	4.6	183.50	1.30	636.00	2.30	3.950	2.800	0.65	
MA2-5	898.0	4.1	184.50	1.40	648.00	2.70	3.920	3.400	0.66	
MA2-6	1000.0	4.3	190.70	1.30	678.00	2.20	4.000	2.300	0.63	
MA2-7	909.0	4.1	180.10	1.20	642.00	2.30	4.013	2.400	0.56	
MA2-8	1060.0	4.6	186.90	1.30	683.00	2.60	4.130	2.700	0.69	
MA2-9	1070.0	4.6	186.50	1.00	673.00	2.20	4.060	2.600	0.75	
MA2-10	1110.0	4.7	186.40	1.20	687.00	2.40	4.128	2.100	0.61	
MA2-11	1090.0	4.7	186.10	1.20	692.00	2.50	4.190	2.500	0.56	
MA2-12	1110.0	4.8	186.20	1.50	680.00	2.60	4.140	2.700	0.58	
MA2-13	1060.0	4.4	187.20	1.10	699.00	2.20	4.163	2.400	0.60	
MA2-14	1080.0	4.4	187.70	1.30	723.00	2.10	4.322	2.300	0.66	
MA2-15	1250.0	4.3	203.30	1.20	878.00	2.60	4.880	2.700	0.76	

610_30-1	88.8	99.0	3.13	1.40	2.13	1.30	0.719	1.400	0.64	***Primary Pulse Mode Calibration***
610_30-2	86.3	98.0	3.06	1.50	2.07	1.40	0.713	1.400	0.51	
610_30-3	84.9	98.0	3.01	1.30	2.03	1.40	0.713	1.500	0.53	
610_30-4	86.1	98.0	3.07	1.40	2.03	1.40	0.696	1.400	0.65	
610_30-5	86.8	99.0	3.06	1.30	2.03	1.60	0.695	1.300	0.62	
610_30-6	86.7	98.0	3.07	1.40	2.07	1.70	0.709	1.200	0.52	
610_30-7	84.9	97.0	3.05	1.20	2.05	1.40	0.711	1.400	0.73	
610_30-8	86.7	97.0	3.07	1.50	2.07	1.30	0.713	1.600	0.55	
610_30-9	85.1	97.0	3.06	1.40	2.05	1.40	0.705	1.300	0.58	
610_30-10	88.4	97.0	3.14	1.70	2.11	1.80	0.709	1.400	0.60	
610_30-11	85.9	95.0	3.11	1.50	2.08	1.60	0.707	1.500	0.65	
610_30-12	83.5	93.0	3.05	1.60	2.06	1.50	0.716	1.500	0.46	
610_30-13	80.1	90.0	3.05	1.70	2.04	1.60	0.702	1.700	0.43	
610_30-14	79.9	90.0	3.07	1.70	2.08	1.50	0.712	1.500	0.53	
610_30-15	86.9	99.0	3.07	1.40	2.05	1.40	0.701	1.100	0.63	

610_60-1	423.0	510.0	3.30	1.90	2.08	1.90	0.710	1.100	0.51	***Primary Analogue Mode Calibration***
610_60-2	429.0	520.0	3.27	1.20	2.06	1.30	0.711	1.200	0.63	
610_60-3	427.0	520.0	3.29	1.40	2.05	1.50	0.707	1.200	0.68	
610_60-4	424.0	510.0	3.27	1.30	2.07	1.60	0.713	1.200	0.62	
610_60-5	425.0	520.0	3.32	1.60	2.08	1.70	0.707	1.200	0.55	
610_60-6	428.0	520.0	3.28	1.00	2.07	1.40	0.711	1.200	0.67	
610_60-7	423.0	510.0	3.28	1.00	2.06	1.10	0.710	1.100	0.62	
610_60-8	428.0	520.0	3.29	0.90	2.07	1.10	0.709	0.980	0.68	
610_60-9	428.0	520.0	3.30	1.00	2.08	1.30	0.711	1.100	0.65	
610_60-10	422.0	510.0	3.26	1.20	2.05	1.10	0.709	1.300	0.32	
610_60-11	424.0	520.0	3.29	1.30	2.07	1.40	0.709	1.100	0.43	
610_60-12	431.0	520.0	3.29	1.20	2.09	1.20	0.711	1.200	0.50	
610_60-13	424.0	510.0	3.29	1.40	2.06	1.50	0.709	1.300	0.60	
610_60-14	426.0	520.0	3.31	1.10	2.06	1.30	0.704	1.200	0.44	
610_60-15	424.0	510.0	3.24	1.40	2.07	1.60	0.720	1.400	0.62	

GA1150-1	817.0	15.0	152.90	2.40	120.80	2.50	0.892	2.400	0.41	***Biotite***
GA1150-2	1100.0	8.1	306.70	2.20	310.20	2.90	1.141	3.200	0.59	***isochron (with intercept) = 103 ± 3 Ma; MSWD = 0.51***
GA1150-3	969.0	12.0	215.20	2.00	185.50	2.20	0.974	1.800	0.29	***expected = 98.7 ± 1.9 Ma; Li et al. 2008***
GA1150-4	995.0	13.0	203.90	2.90	172.10	2.30	0.957	2.400	0.45	
GA1150-5	949.0	12.0	208.30	1.70	179.10	2.10	0.968	2.600	0.59	
GA1150-6	950.0	10.0	236.00	4.50	215.00	6.10	1.012	2.800	0.76	
GA1150-7	1040.0	11.0	245.50	2.90	221.60	3.90	1.020	3.200	0.74	
GA1150-8	929.0	9.1	251.40	3.80	225.10	2.70	1.020	4.800	0.46	
GA1150-9	882.0	11.0	222.00	6.20	187.90	3.30	0.966	4.500	0.41	
GA1150-10	1100.0	7.9	306.90	1.40	320.50	1.70	1.176	2.200	0.37	
GA1150-11	994.0	11.0	225.00	3.80	202.00	5.80	1.012	4.000	0.43	
GA1150-12	753.0	7.7	251.00	5.30	220.10	3.40	1.002	3.900	0.61	
GA1150-13	1070.0	10.0	250.70	2.10	229.40	2.20	1.032	2.400	0.40	
GA1150-14	992.0	9.1	257.80	2.20	246.30	1.70	1.073	2.600	0.47	
GA1150-15	841.0	11.0	207.90	2.00	174.90	1.70	0.952	2.900	0.47	

Mica Fe-1	2350.0	5.0	252.20	1.40	1831.00	3.80	8.190	4.000	0.85	***nano-powdered pressed biotite***
Mica Fe-2	2500.0	5.2	247.80	1.30	1868.00	3.00	8.480	2.700	0.77	***isochron (w intercept) = 299 ± 2 Ma; MSWD = 1.8 Ma***
Mica Fe-3	2500.0	5.5	245.80	1.20	1692.00	3.20	7.770	2.900	0.94	***expected = 303 ± 2 Ma; Rösel and Zack, 2022***
Mica Fe-4	2680.0	5.8	244.70	1.50	1774.00	3.30	8.210	3.200	0.87	
Mica Fe-5	2630.0	5.9	242.50	1.40	1646.00	2.70	7.630	2.500	0.85	
Mica Fe-6	2590.0	5.4	245.90	1.30	1826.00	2.50	8.340	2.800	0.82	
Mica Fe-7	2500.0	5.4	246.30	1.10	1752.00	2.30	8.030	2.400	0.78	
Mica Fe-8	2310.0	5.1	245.90	1.90	1691.00	2.90	7.710	3.700	0.81	
Mica Fe-9	2390.0	5.4	239.50	1.40	1655.00	3.10	7.810	3.100	0.83	
Mica Fe-10	2550.0	5.6	245.20	1.40	1657.00	2.80	7.620	3.000	0.76	
Mica Fe-11	2740.0	5.8	247.60	1.50	1780.00	3.10	8.040	2.300	0.73	
Mica Fe-12	2190.0	4.5	251.40	3.20	1733.00	3.10	7.850	4.600	0.77	
Mica Fe-13	2630.0	5.7	240.20	1.30	1711.00	3.30	8.020	2.800	0.88	
Mica Fe-14	2380.0	5.0	243.70	1.80	1763.00	3.30	8.050	3.200	0.68	
Mica Fe-15	2550.0	5.6	242.20	1.70	1709.00	3.10	7.960	3.100	0.75	

APPENDIX C – Supporting information for Chapter 4

Contents

- **Text S1 to S3**
  - **Text S1. Sample preparation**
  - **Text S2. Microanalytical methods**
    - **S2.1. Scanning Electron Microscopy (SEM)**
    - **S2.2. Electron Microprobe Analysis (EMPA)**
  - **Text S3. $^{40}Ar/^{39}Ar$ geochronology**
- **Figure S1-S3**
  - **Figure S1:** Photomicrographs documenting microstructures in glaucophane and phengite from the Mt. Ochi veins.
  - **Figure S2:** Cross-polarized photomicrographs with and without the tint plate inserted showing microstructures in vein quartz of the Mt. Ochi veins.
  - **Figure S3:** $^{40}Ar/^{39}Ar$ step-heating spectra from glaucophane and phengite of the Mt. Ochi veins.

Additional Supporting Information

- **Tables S1 to S3**
  - **Table S1a-f:** Complete electron microprobe (EMP) mineral chemistry. (**S1a**) white mica; (**S1b**) amphibole; (**S1c**) clinopyroxene; (**S1d**) epidote; (**S1e**) chlorite; (**S1f**) feldspar
  - **Table S2a-c:** Complete Rb/Sr analytical data. (**S2a**) Analytical results for phengite and glaucophane from sample EV19-15C. (**S2b**) Analytical results for phengite and glaucophane from sample EV19-15D.
  - **Table S3:** Complete phengite and glaucophane $^{40}Ar/^{39}Ar$ single-grain total fusion and step-heating analytical data.

Text S1. Sample preparation

Conventional procedures were used to extract and select white mica and glaucophane from samples of vein and host rock material in preparation for $^{40}Ar/^{39}Ar$ dating. Each sample was cleaned with a wire brush and water to remove any surface contamination. The sample was allowed to air dry and was then crushed to a size fraction of ≤1 cm with the use of a mortar and pestle. The material was then passed through a series of sieves to obtain grain size fractions >250 µm, 63-250 µm and <63 µm. Samples were sieved to obtain a 150 µm-250 µm size fraction. White mica and glaucophane grains were then picked using tweezers under a binocular microscope.

Text S2. Microanalytical methods

S2.1. Scanning Electron Microscopy (SEM)

Scanning electron microscopy was performed at the University of Ottawa using a JEOL 6610LV SEM. Backscatter electron imaging and exploratory electron dispersive spectroscopy (EDS) were carried

out with an accelerating voltage of 15 kV and a working distance of 11 mm on standard 30 μm thick polished thin sections.

S2.2. Electron Microprobe Analysis (EMPA)

Mineral chemistry of petrologically significant phases was analyzed via electron microprobe (EMPA). Analyses were performed at University of Ottawa using a JEOL JXA-8230 SuperProbe. Mineral phases of interest, including amphibole, white mica, plagioclase, chlorite, clinopyroxene, and epidote were quantitatively analyzed using a beam diameter of 10 μm with an accelerating voltage of 15 keV and beam current of 20 nA. Dwell times of 10 s were used for X-ray peak positions and 5 s for background positions. Wavelength dispersive spectroscopy (WDS) acquired quantitative chemical data for the major and minor elements Si, Al, Ca, Mg, Fe, K, Na, Ti, Cr, and Mn. The laboratory standards used at University of Ottawa were sanidine (Si, Al, K), diopside (Ca, Mg), hematite (Fe), albite (Na), rutile (Ti), chromite (Cr), and tephroite (Mn); and at Uppsala University were pyrope (Si, Mg), wollastonite (Si, Ca), Al_2O_3 (Al), MgO (Mg), fayalite (Fe), orthoclase (K), albite (Na), pyrophanite (Ti, Mn), Cr_2O_3 (Cr), apatite (P, F), and vanadinite (F, Cl).

Mineral formulae were recalculated using the AX software (Holland, 2018) for each phase on the basis of stoichiometric oxygen contents of 8 O for plagioclase and lawsonite, 11 O for biotite, 14 O for chlorite, and 24.5 O for pumpellyite, and 12.5 O for epidote. White mica compositions were recalculated manually on the basis of 11 O, following the methodology of Vidal & Parra (2000) and Parra et al. (2002), accepting only analyses with weight percent oxide sums between 92-96% and with < 0.5 wt.% TiO_2 + MnO + CaO. Recalculations assumed 11 oxygens and calculated molar fractions for seven end-members (Mg- and Fe-Al-celadonite, muscovite, annite, phlogopite, paragonite, pyrophyllite). Amphibole recalculations were performed using the methodology of Locock (2014), assuming 22 O excluding the W site, and following the IMA 2012 nomenclature for the amphibole supergroup (Hawthorne et al., 2012). All recalculations yielded best results using assumptions of Σ13eCa and Σ15eNK for determination of ferric and ferrous iron content. All mineral chemical data and associated formula recalculations may be found in **Table S1**.

Text S3. $^{40}Ar/^{39}Ar$ geochronology

Once samples were picked and characterized, $^{40}Ar/^{39}Ar$ analytical work was performed at the University of Manitoba (Winnipeg, Canada) using a multi-collector Thermo Fisher Scientific ARGUS VI mass spectrometer, linked to a stainless steel Thermo Fisher Scientific extraction/purification line and Photon Machines (55 W) Fusions 10.6 CO_2 laser. Argon isotopes (from mass 40 to 37) were measured using Faraday detectors with low noise 1 x 10^{13} Ω resistors and mass 36 was measured using a compact discrete dynode detector. The sensitivity for argon measurements is ~6.312 x 10^{17} moles/fA as determined from measured aliquots of Fish Canyon Sanidine (Dazé et al., 2003; Kuiper et al., 2008).

Standards and unknowns were placed in 2 mm deep wells in 18 mm diameter aluminum disks, with standards placed strategically so that the lateral neutron flux gradients across the disk could be evaluated. Planar regressions were fit to the standard data, and the $^{40}Ar/^{39}Ar$ neutron fluence parameter, J, interpolated for the unknowns. Uncertainties in J are estimated at 0.1-0.2% (1s), based on Monte Carlo error analysis of the planar regressions (Best et al., 1995). All specimens were irradiated in the cadmium-lined, in-core CLICIT facility of the Oregon State University TRIGA reactor. The duration of irradiation was 12 h and using the Fish Canyon sanidine (Kuiper et al., 2008) and GA1550 biotite (Spell and McDougall, 2003) standards.

Irradiated samples were placed in a Cu sample tray, with a KBr cover slip, in a stainless steel high vacuum extraction line and baked with an infrared lamp for 24 h. Single crystals were either fused or step-heated using the laser, and reactive gases were removed, after ~3 min, by three GP-50 SAES getters (two at room temperature and one at 450°C) prior to being admitted to an ARGUS VI mass spectrometer by expansion. Five argon isotopes were measured simultaneously over a period of 6 min. Measured

isotope abundances were corrected for extraction-line blanks, which were determined before every sample analysis. Line blanks averaged ~5 fA for mass 40 and ~0.022 fA for mass 36.

Mass discrimination was monitored by online analysis of air pipettes, which gave during two separate sessions mean of D: 1.0063 ± 0.0001 and D: 1.0089 ± 0.0005 per amu, based on 67 aliquots interspersed with the unknowns. A value of 295.5 was used for the atmospheric $^{40}Ar/^{36}Ar$ ratio (Steiger and Jäger, 1977) for the purposes of routine measurement of mass spectrometer discrimination using air aliquots, and correction for atmospheric argon in the $^{40}Ar/^{39}Ar$ age calculation. Corrections are made for neutron-induced ^{40}Ar from potassium, ^{39}Ar and ^{36}Ar from calcium, and ^{36}Ar from chlorine (Roddick, 1983; Renne et al., 1998; Renne and Norman, 2001). Results are reported in **Table S3**.

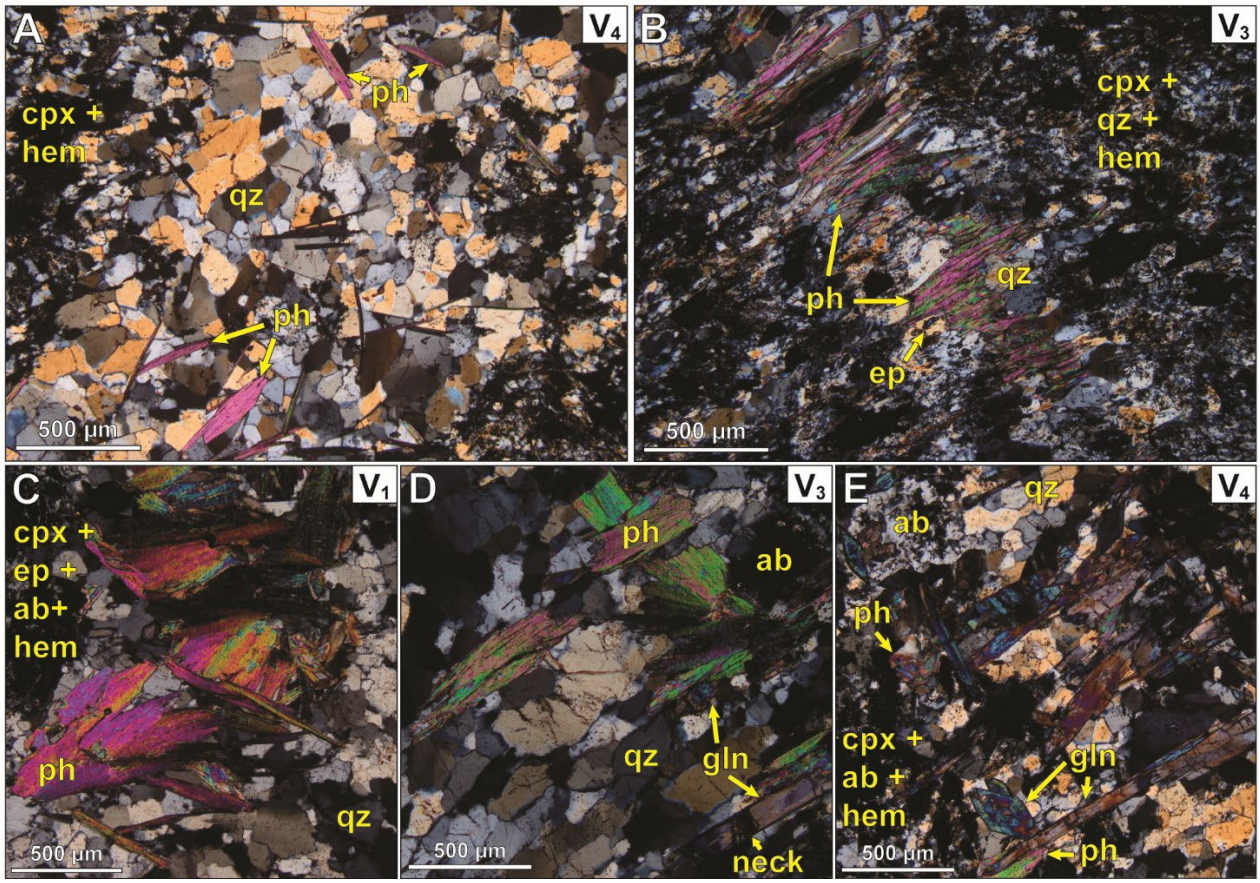

Figure S1. Photomicrographs documenting microstructures in glaucophane and phengite from the Mt. Ochi veins. (A) Euhedral phengite crystals within a V_4 vein. Mica forms euhedral blocky crystals situated along grain boundaries between quartz showing nascent dynamic recrystallization microstructures. (B) Phengite grown at the termination of a V_3 vein. Grain boundaries of the phengite are morphologically controlled by adjacent quartz grains and contact with the wall rock. (C) Coarse blocky and radial euhedral phengite crystals at the margin of a V_1 vein. Phengite grows both as euhedral elongate crystals at high angles to the vein wall, or at comparatively shallow angles with a radial morphology. Radial phengite exhibits a continuous, sweeping extinction. (D) Mutually impinging blocky and radial phengite crystals grown along the margin of a V_3 vein. Nearby glaucophane shows multiple concentric zones with optical continuity across them, and incipient extension (necking) parallel to its long axis. (E) Narrow V_4 vein with wall-normal glaucophane spanning the width of the vein. Quartz interstitial to the glaucophane shows well-developed grain boundary triple junctions. A subset of the glaucophane crystals are oriented parallel to the vein (i.e., normal to the plane of the photo). Mineral abbreviations: ab: albite; cpx: clinopyroxene; ep: epidote; gln: glaucophane; hem: hematite; ph: phengite; qz: quartz.

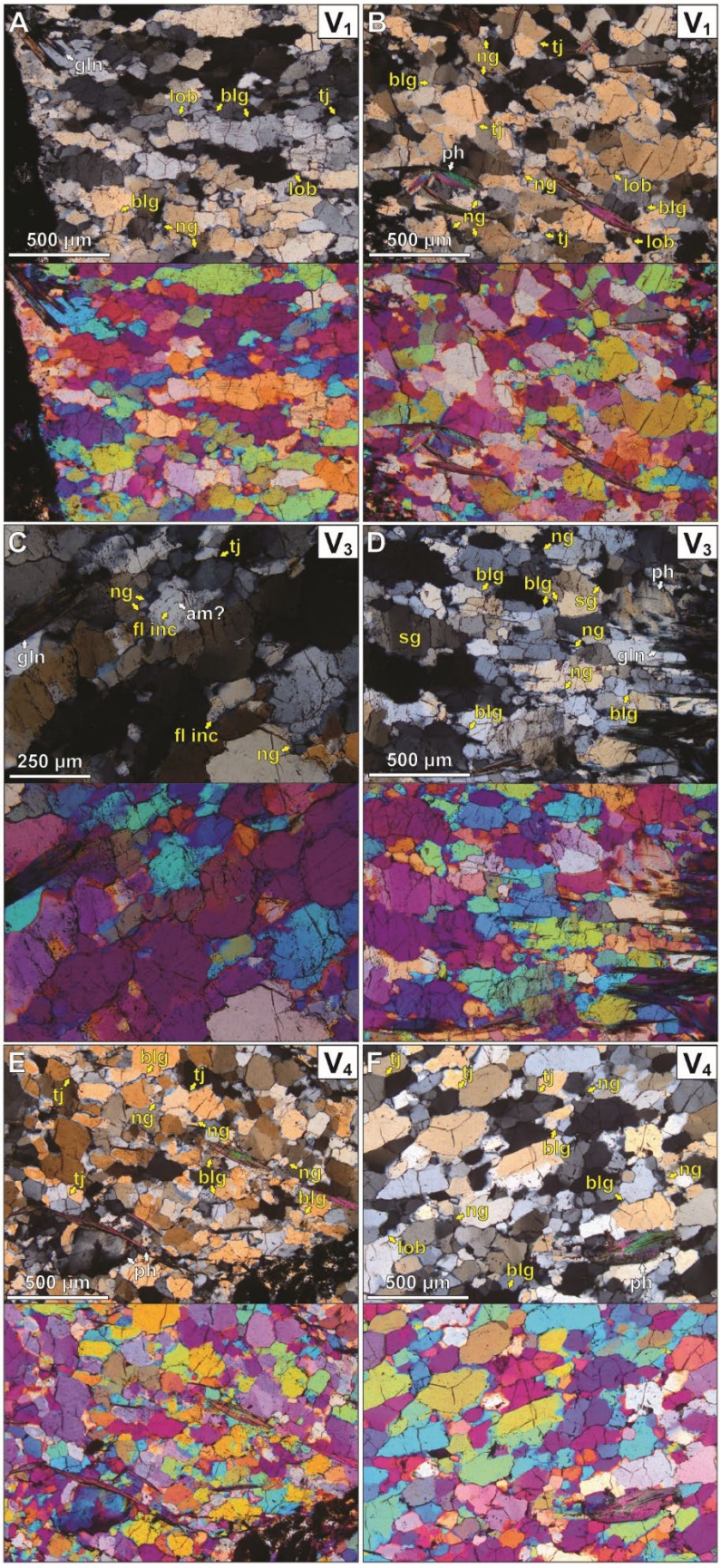
A
V1
gln
lob
blg
tj
lob
blg
ng
500 µm
B
V1
ng
tj
blg
tj
ph
ng
lob
blg
ng
tj
lob
500 µm
C
V3
tj
ng
am?
fl inc
gln
fl inc
ng
250 µm
D
V3
ng
blg
blg
ph
sg
sg
ng
gln
ng
blg
blg
500 µm
E
V4
blg
tj
tj
ng
ng
tj
blg
ng
blg
ph
500 µm
F
V4
tj
tj
tj
ng
blg
blg
ng
ng
lob
blg
ph
500 µm

Figure S2. (previous page) Cross-polarized photomicrographs without (top) and with (bottom) the tint plate inserted showing microstructures in vein quartz of the Mt. Ochi veins. (A, B) V_1 veins contain the greatest recrystallized volume fraction of the veins and some sparse triple junctions indicative of static recovery. Low-amplitude bulging and lobate grain boundaries are common. A moderately well-defined shape preferred orientation (SPO) is common. Several small new grains are observed and are as large as 30 μm in diameter. Quartz deformation microstructures in V_1 veins are largely consistent with recrystallization by grain boundary bulging recrystallization (BLG), with local evidence for minor subgrain rotation (SGR; Stipp et al., 2002). (C, D) V_3 veins exhibit a comparatively low recrystallized volume fraction, but display a more strongly developed SPO. Bulging is the predominant recrystallization mechanism, with larger prismatic quartz subgrains than V_1 veins. V_3 quartz is rich in fluid inclusions, although linear arrays of such inclusions are typically discontinuous beyond grain boundaries. Isolated large primary fluid inclusions imply that the cores of quartz crystals have not been subject to recrystallization, consistent with the dominance of low temperature grain boundary migration. (E, F) V_4 quartz exhibits nonhomogeneous strain distribution and dynamic recrystallization microstructures, with some regions of a given vein showing considerable low-amplitude bulging and formation of new grains <40 μm in diameter (E), whereas others show minimal evidence of dynamic recrystallization (F). Minor grain boundary bulging is usually present but occurs locally in roughly equal proportion to triple junctions representing static recovery. Mineral abbreviations: gln:glaucophane; ph: phengite. Microstructure abbreviations: blg: grain boundary bulging; fl inc: fluid inclusion; lob: lobate grain boundary; ng: new recrystallized grain; sg: subgraining; tj: grain boundary triple junction.

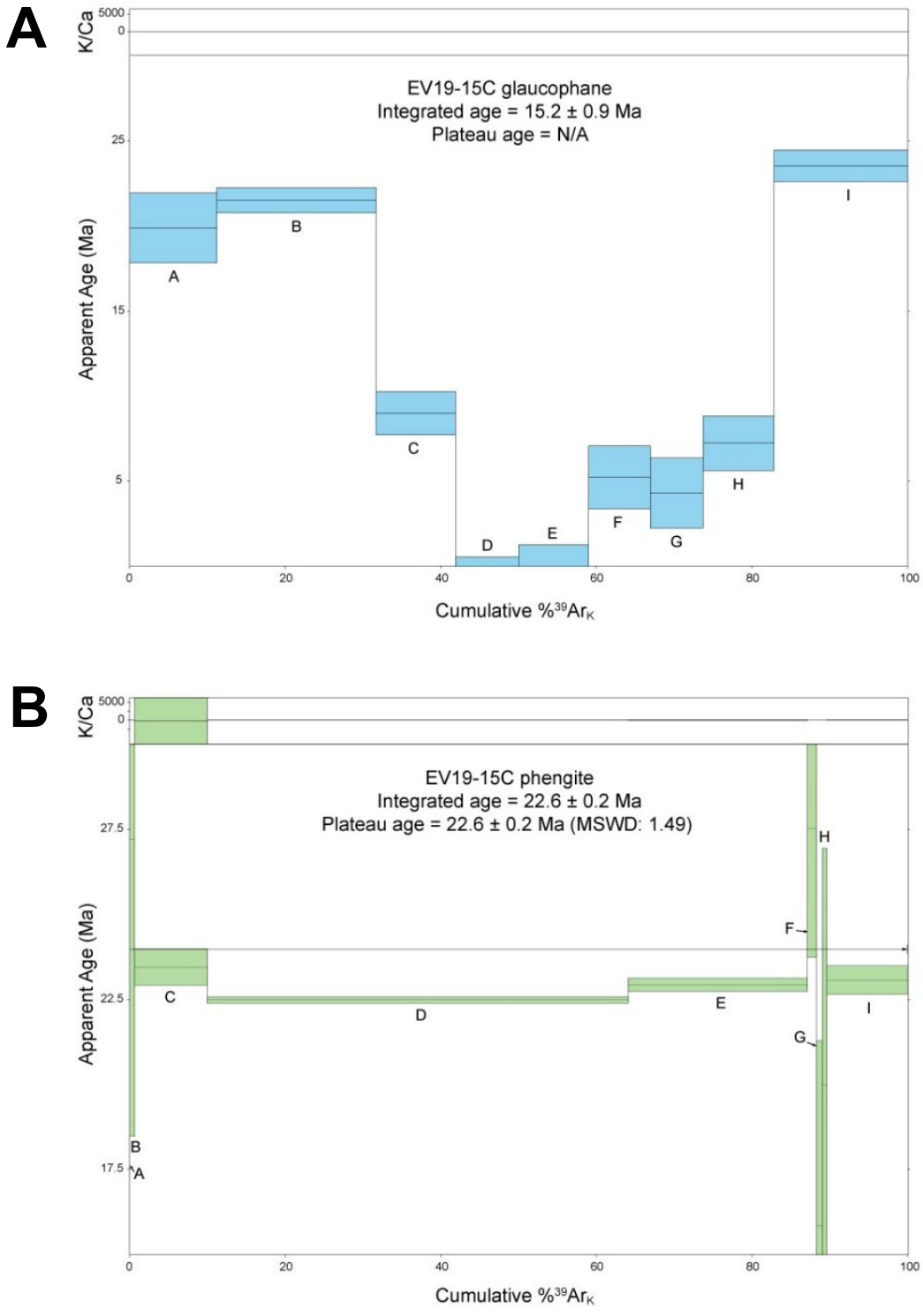

Figure S3. $^{40}Ar/^{39}Ar$ step-heating spectra from glaucophane and phengite of the Mt. Ochi veins. (A) Spectrum from a V_4 glaucophane from EV19-15C. (B) Spectrum from a V_4 phengite from EV19-15C.

Table S4.1a. Electron microprobe results for white mica from the Mt. Ochi veins and host rock, Evia, Greece

	WHITE MICA EV19-15C																					
	V_1						V_2						V_3			V_4				host rock		
Wt.%	**1**	**2**	**3**	**4**	**5**	**6**	**7**	**8**	**9**	**10**	**11**	**12**	**13**	**14**	**15**	**16**	**17**	**18**	**19**	**20**	**21**	**22**
SiO_2	51.35	50.76	50.53	50.60	49.82	51.04	50.53	50.91	51.55	51.11	51.16	52.43	52.51	51.12	50.25	47.42	50.88	50.91	50.02	51.61	50.56	50.90
TiO_2	0.01	0.02	0.08	0.08	0.09	0.08	0.08	0.03	0.01	0.01	0.03	0.01	n.d.	0.01	0.13	0.00	0.06	0.05	0.04	0.03	n.d.	n.d.
Al_2O_3	25.16	25.27	24.18	21.81	22.08	22.81	25.99	25.90	25.91	25.71	25.88	23.73	24.02	23.22	22.44	20.65	22.67	23.88	22.46	25.45	25.66	25.71
Cr_2O_3	n.d.	0.00	0.01	n.d.	n.d.	n.d.	0.01	0.01	0.02	n.d.	n.d.	0.02	n.d.	n.d.	n.d.	0.01	n.d.	0.01	0.02	0.02	0.01	0.02
FeO	4.70	5.15	6.08	7.43	7.64	7.14	4.78	4.59	3.65	4.91	4.22	5.21	5.03	6.37	7.66	8.73	6.90	5.84	7.78	4.57	4.13	4.64
MnO	0.07	0.02	0.18	0.08	0.09	0.04	0.05	0.02	0.04	0.06	0.03	0.03	0.03	0.02	0.05	0.16	0.04	0.05	0.04	0.05	0.06	0.04
MgO	3.18	3.07	3.30	3.63	3.86	3.60	3.07	3.04	3.18	3.07	3.05	3.53	3.66	3.51	3.45	7.31	3.58	3.40	3.66	3.16	3.15	3.03
CaO	n.d.	n.d.	n.d.	n.d.	0.03	0.02	0.00	0.01	0.01	n.d.	0.01	0.02	n.d.	0.01	n.d.	0.06	n.d.	n.d.	n.d.	0.01	0.04	0.00
Na_2O	0.30	0.29	0.16	0.08	0.06	0.07	0.31	0.31	0.32	0.26	0.39	0.19	0.14	0.10	0.12	0.14	0.05	0.14	0.08	0.31	0.35	0.35
K_2O	10.81	10.86	10.84	10.75	10.92	10.90	10.47	10.92	10.43	10.44	10.62	10.69	10.83	10.75	10.74	9.57	10.94	10.69	10.90	10.19	10.00	10.70
H_2O	4.37	4.36	4.33	4.30	4.29	4.31	4.37	4.37	4.41	4.38	4.39	4.37	4.37	4.33	4.30	4.26	4.31	4.35	4.29	2.19	2.19	2.18
TOTAL	99.96	99.79	99.68	98.76	98.88	100.01	99.65	100.10	99.53	99.95	99.77	100.24	100.58	99.43	99.14	98.30	99.44	99.32	99.29	97.59	96.16	97.58
	95.59	95.43	95.35	94.45	94.59	95.70	95.27	95.73	95.12	95.57	95.39	95.87	96.21	95.09	94.84	94.04	95.12	94.98	95.00	95.41	93.97	95.40
Molar																						
SiO_2	0.85	0.84	0.84	0.84	0.83	0.85	0.84	0.85	0.86	0.85	0.85	0.87	0.87	0.85	0.84	0.79	0.85	0.85	0.83	0.86	0.84	0.85
TiO_2	0.00	0.00	0.00	0.00	0.00	0.00	0.00	0.00	0.00	0.00	0.00	0.00	0.00	0.00	0.00	0.00	0.00	0.00	0.00	0.00	0.00	0.00
Al_2O_3	0.25	0.25	0.24	0.21	0.22	0.22	0.25	0.25	0.25	0.25	0.25	0.23	0.24	0.23	0.22	0.20	0.22	0.23	0.22	0.25	0.25	0.25
Cr_2O_3	0.00	0.00	0.00	0.00	0.00	0.00	0.00	0.00	0.00	0.00	0.00	0.00	0.00	0.00	0.00	0.00	0.00	0.00	0.00	0.00	0.00	0.00
FeO	0.07	0.07	0.08	0.10	0.11	0.10	0.07	0.06	0.05	0.07	0.06	0.07	0.07	0.09	0.11	0.12	0.10	0.08	0.11	0.06	0.06	0.06
MnO	0.00	0.00	0.00	0.00	0.00	0.00	0.00	0.00	0.00	0.00	0.00	0.00	0.00	0.00	0.00	0.00	0.00	0.00	0.00	0.00	0.00	0.00
MgO	0.08	0.08	0.08	0.09	0.10	0.09	0.08	0.08	0.08	0.08	0.08	0.09	0.09	0.09	0.09	0.18	0.09	0.08	0.09	0.08	0.08	0.08
CaO	0.00	0.00	0.00	0.00	0.00	0.00	0.00	0.00	0.00	0.00	0.00	0.00	0.00	0.00	0.00	0.00	0.00	0.00	0.00	0.00	0.00	0.00
Na_2O	0.00	0.00	0.00	0.00	0.00	0.00	0.01	0.01	0.01	0.00	0.01	0.00	0.00	0.00	0.00	0.00	0.00	0.00	0.00	0.01	0.01	0.01
K_2O	0.11	0.12	0.12	0.11	0.12	0.12	0.11	0.12	0.11	0.11	0.11	0.11	0.11	0.11	0.11	0.10	0.12	0.11	0.12	0.11	0.11	0.11
H_2O	0.24	0.24	0.24	0.24	0.24	0.24	0.24	0.24	0.24	0.24	0.24	0.24	0.24	0.24	0.24	0.24	0.24	0.24	0.24	0.12	0.12	0.12
O	2.72	2.70	2.68	2.64	2.63	2.68	2.71	2.72	2.73	2.72	2.72	2.72	2.73	2.68	2.65	2.60	2.66	2.68	2.64	2.72	2.69	2.71
apfu																						
Si	3.46	3.44	3.45	3.51	3.47	3.49	3.42	3.43	3.46	3.44	3.44	3.53	3.52	3.50	3.48	3.34	3.50	3.48	3.46	3.47	3.44	3.44
Ti	0.00	0.00	0.00	0.00	0.00	0.00	0.00	0.00	0.00	0.00	0.00	0.00	0.00	0.00	0.01	0.00	0.00	0.00	0.00	0.00	0.00	0.00
Al	2.00	2.02	1.95	1.78	1.81	1.84	2.07	2.06	2.05	2.04	2.05	1.88	1.90	1.87	1.83	1.72	1.84	1.92	1.83	2.02	2.06	2.05
Cr	0.00	0.00	0.00	0.00	0.00	0.00	0.00	0.00	0.00	0.00	0.00	0.00	0.00	0.00	0.00	0.00	0.00	0.00	0.00	0.00	0.00	0.00
Fe2+	0.27	0.29	0.35	0.43	0.44	0.41	0.27	0.26	0.21	0.28	0.24	0.29	0.28	0.36	0.44	0.51	0.40	0.33	0.45	0.26	0.24	0.26
Mn	0.00	0.00	0.01	0.00	0.01	0.00	0.00	0.00	0.00	0.00	0.00	0.00	0.00	0.00	0.00	0.01	0.00	0.00	0.00	0.00	0.00	0.00
Mg	0.32	0.31	0.34	0.38	0.40	0.37	0.31	0.31	0.32	0.31	0.31	0.35	0.37	0.36	0.36	0.77	0.37	0.35	0.38	0.32	0.32	0.30
Ca	0.00	0.00	0.00	0.00	0.00	0.00	0.00	0.00	0.00	0.00	0.00	0.00	0.00	0.00	0.00	0.00	0.00	0.00	0.00	0.00	0.00	0.00
Na	0.04	0.04	0.02	0.01	0.01	0.01	0.04	0.04	0.04	0.03	0.05	0.02	0.02	0.01	0.02	0.02	0.01	0.02	0.01	0.04	0.05	0.05
K	0.93	0.94	0.94	0.95	0.97	0.95	0.90	0.94	0.89	0.90	0.91	0.92	0.93	0.94	0.95	0.86	0.96	0.93	0.96	0.87	0.87	0.92
Site Assignment																						
Si (T1+T2)	3.46	3.44	3.45	3.51	3.47	3.49	3.42	3.43	3.46	3.44	3.44	3.53	3.52	3.50	3.48	3.34	3.50	3.48	3.46	3.47	3.44	3.44
Ti (T2)	0.00	0.00	0.00	0.00	0.00	0.00	0.00	0.00	0.00	0.00	0.00	0.00	0.00	0.00	0.01	0.00	0.00	0.00	0.00	0.00	0.00	0.00
Al(IV) (T2)	0.54	0.56	0.55	0.48	0.53	0.51	0.58	0.57	0.54	0.56	0.55	0.47	0.48	0.50	0.52	0.66	0.50	0.52	0.53	0.53	0.56	0.56
Al(VI) (M2)	1.46	1.46	1.40	1.30	1.28	1.33	1.49	1.49	1.51	1.48	1.50	1.41	1.41	1.37	1.32	1.06	1.33	1.40	1.30	1.49	1.51	1.48
Mg (M2)	0.29	0.28	0.30	0.33	0.34	0.32	0.27	0.28	0.30	0.27	0.28	0.32	0.33	0.31	0.31	0.56	0.32	0.30	0.32	0.28	0.28	0.28
Fe (M2)	0.24	0.26	0.31	0.37	0.38	0.35	0.24	0.24	0.19	0.24	0.22	0.27	0.26	0.32	0.38	0.38	0.35	0.29	0.38	0.23	0.21	0.24
Fe + Mg (M2)	0.54	0.54	0.60	0.70	0.72	0.67	0.51	0.51	0.49	0.52	0.50	0.59	0.59	0.63	0.68	0.94	0.67	0.60	0.70	0.51	0.49	0.52
Mn (M2)	0.00	0.00	0.01	0.00	0.01	0.00	0.00	0.00	0.00	0.00	0.00	0.00	0.00	0.00	0.00	0.01	0.00	0.00	0.00	0.00	0.00	0.00
Mg (M1)	0.03	0.03	0.04	0.05	0.06	0.05	0.04	0.03	0.02	0.04	0.02	0.03	0.03	0.04	0.05	0.21	0.05	0.04	0.06	0.03	0.03	0.03
Fe (M1)	0.02	0.03	0.04	0.06	0.07	0.06	0.03	0.02	0.02	0.03	0.02	0.03	0.03	0.05	0.06	0.14	0.05	0.04	0.07	0.03	0.03	0.02
vac (M1)	0.95	0.94	0.92	0.89	0.87	0.89	0.93	0.95	0.96	0.93	0.96	0.94	0.94	0.91	0.89	0.66	0.90	0.92	0.87	0.94	0.94	0.95
K (A)	0.93	0.94	0.94	0.95	0.97	0.95	0.90	0.94	0.89	0.90	0.91	0.92	0.93	0.94	0.95	0.86	0.96	0.93	0.96	0.87	0.87	0.92
Na (A)	0.04	0.04	0.02	0.01	0.01	0.01	0.04	0.04	0.04	0.03	0.05	0.02	0.02	0.01	0.02	0.02	0.01	0.02	0.01	0.04	0.05	0.05
v (A)	0.03	0.02	0.04	0.04	0.02	0.04	0.06	0.02	0.06	0.07	0.04	0.06	0.06	0.05	0.04	0.12	0.03	0.05	0.03	0.09	0.08	0.03
Paragonite	0.04	0.04	0.02	0.01	0.01	0.01	0.04	0.04	0.04	0.03	0.05	0.02	0.02	0.01	0.02	0.02	0.01	0.02	0.01	0.04	0.05	0.05
Phlogopite	0.03	0.03	0.04	0.05	0.06	0.05	0.04	0.03	0.02	0.04	0.02	0.03	0.03	0.04	0.05	0.21	0.05	0.04	0.06	0.03	0.03	0.03
Annite	0.02	0.03	0.04	0.06	0.07	0.06	0.03	0.02	0.02	0.03	0.02	0.03	0.03	0.05	0.06	0.14	0.05	0.04	0.07	0.03	0.03	0.02
Mg-Celadonite	0.25	0.23	0.22	0.24	0.22	0.23	0.22	0.23	0.28	0.23	0.25	0.29	0.29	0.25	0.22	0.21	0.24	0.24	0.21	0.26	0.26	0.24
Fe-Celadonite	0.21	0.21	0.23	0.28	0.25	0.26	0.20	0.20	0.18	0.21	0.20	0.24	0.23	0.25	0.27	0.14	0.26	0.24	0.25	0.21	0.19	0.20
Pyrophyllite	0.03	0.02	0.04	0.04	0.02	0.04	0.06	0.02	0.06	0.07	0.04	0.06	0.06	0.05	0.04	0.12	0.03	0.05	0.03	0.09	0.08	0.03
Muscovite	0.42	0.44	0.41	0.33	0.37	0.35	0.41	0.46	0.39	0.39	0.42	0.33	0.35	0.35	0.35	0.17	0.36	0.37	0.37	0.34	0.36	0.43
CeladoniteTOT	0.46	0.44	0.45	0.52	0.47	0.49	0.42	0.43	0.46	0.44	0.45	0.53	0.52	0.50	0.48	0.34	0.50	0.48	0.47	0.47	0.44	0.44
XMg	0.55	0.52	0.49	0.47	0.47	0.47	0.53	0.54	0.61	0.53	0.56	0.55	0.56	0.50	0.45	0.60	0.48	0.51	0.46	0.55	0.58	0.54
ms	0.44	0.47	0.45	0.37	0.42	0.39	0.44	0.48	0.41	0.41	0.44	0.35	0.37	0.39	0.39	0.26	0.40	0.40	0.42	0.37	0.39	0.46
pg	0.04	0.04	0.02	0.01	0.01	0.01	0.04	0.04	0.04	0.04	0.05	0.03	0.02	0.01	0.02	0.03	0.01	0.02	0.01	0.04	0.05	0.05
prl	0.03	0.02	0.04	0.04	0.03	0.04	0.06	0.02	0.07	0.08	0.04	0.06	0.06	0.05	0.04	0.18	0.04	0.05	0.03	0.09	0.09	0.03
cel	0.49	0.47	0.49	0.58	0.54	0.55	0.45	0.45	0.48	0.48	0.47	0.56	0.55	0.55	0.55	0.52	0.55	0.52	0.53	0.50	0.47	0.46

Table S4.1b. Electron microprobe results for amphibole from the Mt. Ochi veins and host rock, Evia, Greece.

	AMPHIBOLE CORES EV19-15C																											
	V_1				V_2							V_3							V_4				host rock						
Wt.%	**1**	**2**	**3**	**4**	**5**	**6**	**7**	**8**	**9**	**10**	**11**	**12**	**13**	**14**	**15**	**16**	**17**	**18**	**19**	**20**	**21**	**22**	**23**	**24**	**25**	**26**	**27**	**28**	**29**
SiO_2	58.61	57.75	57.46	57.87	56.78	58.70	57.36	57.37	58.30	57.93	58.47	57.82	58.41	59.43	58.02	59.50	57.67	58.65	57.46	57.58	58.96	58.35	58.84	59.00	57.09	59.02	58.05	59.11	58.98
TiO_2	0.20	0.12	0.08	0.01	0.06	n.d.	n.d.	0.14	0.02	n.d.	n.d.	0.10	0.10	n.d.	0.12	0.02	n.d.	0.01	0.05	0.02	0.01	n.d.	0.11	0.03	0.07	0.02	n.d.	0.05	0.02
Al_2O_3	7.82	7.92	7.92	8.19	6.01	7.38	4.84	6.45	7.53	6.71	6.32	8.18	7.82	9.38	8.10	8.90	6.17	7.92	6.81	7.16	7.61	7.62	8.34	8.88	7.31	7.81	7.84	8.53	8.65
Cr_2O_3	0.00	n.d.	n.d.	0.00	n.d.	0.00	n.d.	n.d.	0.01	0.00	n.d.	n.d.	0.00	n.d.	n.d.	n.d.	n.d.	n.d.	0.01	0.01	n.d.	n.d.	n.d.	n.d.	n.d.	0.01	n.d.	n.d.	0.00
FeO	16.19	16.92	16.11	15.68	18.28	14.47	19.95	17.37	16.13	16.78	16.60	16.84	16.68	13.61	16.33	13.30	17.45	14.91	18.13	17.46	14.85	15.50	15.55	13.55	17.23	15.42	14.39	12.67	12.67
MnO	0.23	0.28	0.27	0.26	0.37	0.18	0.27	0.18	0.22	0.19	0.28	0.32	0.28	0.21	0.22	0.25	0.25	0.30	0.24	0.22	0.18	0.22	0.28	0.24	0.23	0.19	0.22	0.20	0.23
MgO	7.55	7.42	8.22	8.37	8.52	9.06	8.06	8.41	8.38	8.40	8.56	7.38	7.34	8.73	7.61	8.63	8.79	8.67	8.18	8.11	9.14	8.64	8.08	8.59	8.37	9.06	9.28	9.88	9.99
CaO	0.11	0.13	0.21	0.29	0.92	0.05	0.23	0.26	0.13	0.15	0.17	0.09	0.08	0.01	0.07	0.03	0.21	0.26	0.15	0.18	0.12	0.11	0.12	0.22	1.37	0.18	0.27	0.23	0.24
Na_2O	6.97	6.84	6.92	7.00	6.73	7.18	6.97	7.19	7.05	7.00	6.76	7.13	6.97	7.25	7.03	7.17	6.84	7.09	7.16	6.66	6.99	6.93	7.15	6.91	7.14	7.22	7.22	7.19	7.31
K_2O	0.00	0.03	0.01	0.02	0.02	n.d.	0.01	0.00	n.d.	0.03	0.00	0.01	0.02	n.d.	n.d.	0.00	n.d.	n.d.	0.02	n.d.	0.02	0.01	n.d.	0.02	0.03	n.d.	n.d.	0.02	0.02
H_2O	2.13	2.12	2.13	2.13	2.09	2.15	2.08	2.11	2.13	2.12	2.12	2.12	2.13	2.16	2.13	2.16	2.11	2.14	2.10	2.11	2.14	2.14	2.14	2.16	2.10	2.13	2.14	2.16	2.16
TOTAL	99.79	99.54	99.32	99.82	99.77	99.17	99.76	99.48	99.90	99.31	99.28	99.98	99.81	100.77	99.63	99.96	99.49	99.96	100.32	99.51	100.03	99.51	100.61	99.60	100.92	101.07	99.40	100.05	100.27
Molar																													
SiO_2	0.98	0.96	0.96	0.96	0.95	0.98	0.95	0.95	0.97	0.96	0.97	0.96	0.97	0.99	0.97	0.99	0.96	0.98	0.96	0.96	0.98	0.97	0.98	0.98	0.95	0.98	0.97	0.98	0.98
TiO_2	0.00	0.00	0.00	0.00	0.00	0.00	0.00	0.00	0.00	0.00	0.00	0.00	0.00	0.00	0.00	0.00	0.00	0.00	0.00	0.00	0.00	0.00	0.00	0.00	0.00	0.00	0.00	0.00	0.00
Al_2O_3	0.15	0.16	0.16	0.16	0.12	0.14	0.09	0.13	0.15	0.13	0.12	0.16	0.15	0.18	0.16	0.17	0.12	0.16	0.13	0.14	0.15	0.15	0.16	0.17	0.14	0.15	0.15	0.17	0.17
Cr_2O_3	0.00	0.00	0.00	0.00	0.00	0.00	0.00	0.00	0.00	0.00	0.00	0.00	0.00	0.00	0.00	0.00	0.00	0.00	0.00	0.00	0.00	0.00	0.00	0.00	0.00	0.00	0.00	0.00	0.00
FeO	0.23	0.24	0.22	0.22	0.25	0.20	0.28	0.24	0.22	0.23	0.23	0.23	0.23	0.19	0.23	0.19	0.24	0.21	0.25	0.24	0.21	0.22	0.22	0.19	0.24	0.21	0.20	0.18	0.18
MnO	0.00	0.00	0.00	0.00	0.01	0.00	0.00	0.00	0.00	0.00	0.00	0.00	0.00	0.00	0.00	0.00	0.00	0.00	0.00	0.00	0.00	0.00	0.00	0.00	0.00	0.00	0.00	0.00	0.00
MgO	0.19	0.18	0.20	0.21	0.21	0.22	0.20	0.21	0.21	0.21	0.21	0.18	0.18	0.22	0.19	0.21	0.22	0.22	0.20	0.20	0.23	0.21	0.20	0.21	0.21	0.22	0.23	0.25	0.25
CaO	0.00	0.00	0.00	0.01	0.02	0.00	0.00	0.00	0.00	0.00	0.00	0.00	0.00	0.00	0.00	0.00	0.00	0.00	0.00	0.00	0.00	0.00	0.00	0.00	0.02	0.00	0.00	0.00	0.00
Na_2O	0.22	0.22	0.22	0.23	0.22	0.23	0.23	0.23	0.23	0.23	0.22	0.23	0.23	0.23	0.23	0.23	0.22	0.23	0.23	0.22	0.23	0.22	0.23	0.22	0.23	0.23	0.23	0.23	0.24
K_2O	0.00	0.00	0.00	0.00	0.00	0.00	0.00	0.00	0.00	0.00	0.00	0.00	0.00	0.00	0.00	0.00	0.00	0.00	0.00	0.00	0.00	0.00	0.00	0.00	0.00	0.00	0.00	0.00	0.00
H_2O	0.24	0.24	0.24	0.24	0.23	0.24	0.23	0.23	0.24	0.24	0.24	0.24	0.24	0.24	0.24	0.24	0.23	0.24	0.23	0.23	0.24	0.24	0.24	0.24	0.23	0.24	0.24	0.24	0.24
O	2.72	2.70	2.70	2.72	2.66	2.72	2.65	2.68	2.71	2.69	2.69	2.71	2.71	2.78	2.71	2.76	2.68	2.73	2.69	2.69	2.74	2.71	2.75	2.75	2.71	2.76	2.72	2.76	2.77
Formula Assignments																													
T (ideally 8 apfu)																													
Si	8.20	8.11	8.05	8.06	8.01	8.19	8.11	8.08	8.12	8.14	8.19	8.09	8.18	8.13	8.12	8.21	8.08	8.14	8.02	8.15	8.14	8.13	8.13	8.18	7.99	8.09	8.08	8.11	8.08
T subtotal	8.20	8.11	8.05	8.06	8.01	8.19	8.11	8.08	8.12	8.14	8.19	8.09	8.18	8.13	8.12	8.21	8.08	8.14	8.02	8.15	8.14	8.13	8.13	8.18	8.00	8.09	8.08	8.11	8.08
C (ideally 5 apfu)																													
Ti	0.02	0.01	0.01	0.00	0.01	0.00	0.00	0.02	0.00	0.00	0.00	0.01	0.01	0.00	0.01	0.00	0.00	0.00	0.01	0.00	0.00	0.00	0.01	0.00	0.01	0.00	0.00	0.01	0.00
Al	1.29	1.31	1.31	1.35	1.00	1.21	0.81	1.07	1.24	1.11	1.04	1.35	1.29	1.51	1.34	1.45	1.02	1.30	1.12	1.19	1.24	1.25	1.36	1.45	1.20	1.26	1.29	1.38	1.40
Cr	0.00	0.00	0.00	0.00	0.00	0.00	0.00	0.00	0.00	0.00	0.00	0.00	0.00	0.00	0.00	0.00	0.00	0.00	0.00	0.00	0.00	0.00	0.00	0.00	0.00	0.00	0.00	0.00	0.00
Fe^{3+}	0.35	0.55	0.63	0.55	0.83	0.45	1.00	0.70	0.58	0.66	0.69	0.48	0.41	0.31	0.46	0.20	0.91	0.43	0.83	0.34	0.57	0.60	0.40	0.27	0.44	0.58	0.52	0.39	0.42
Mn^{2+}	0.03	0.03	0.03	0.03	0.05	0.02	0.03	0.02	0.03	0.02	0.03	0.04	0.03	0.02	0.03	0.03	0.03	0.04	0.03	0.03	0.02	0.03	0.03	0.03	0.03	0.02	0.03	0.02	0.03
Fe^{2+}	1.54	1.44	1.26	1.27	1.33	1.24	1.36	1.35	1.30	1.31	1.26	1.49	1.55	1.25	1.45	1.33	1.13	1.30	1.29	1.73	1.15	1.21	1.40	1.30	1.58	1.19	1.16	1.06	1.03
Mg	1.57	1.55	1.72	1.74	1.79	1.88	1.70	1.77	1.74	1.76	1.79	1.54	1.53	1.78	1.59	1.78	1.83	1.79	1.70	1.71	1.88	1.79	1.67	1.78	1.75	1.85	1.93	2.02	2.04
C subtotal	4.80	4.90	4.95	4.94	5.00	4.81	4.90	4.92	4.88	4.86	4.81	4.91	4.82	4.87	4.88	4.79	4.93	4.86	4.98	5.00	4.86	4.88	4.87	4.83	5.00	4.91	4.92	4.89	4.92
B (ideally 2 apfu)																													
Ca	0.02	0.02	0.03	0.04	0.14	0.01	0.04	0.04	0.02	0.02	0.03	0.01	0.01	0.00	0.01	0.00	0.03	0.04	0.02	0.03	0.02	0.02	0.02	0.03	0.21	0.03	0.04	0.03	0.04
Na	1.89	1.86	1.88	1.89	1.84	1.94	1.91	1.96	1.90	1.91	1.84	1.93	1.89	1.92	1.91	1.92	1.86	1.91	1.94	1.83	1.87	1.87	1.92	1.86	1.80	1.92	1.95	1.91	1.94
B subtotal	1.91	1.88	1.91	1.94	1.98	1.95	1.95	2.00	1.92	1.93	1.86	1.95	1.91	1.92	1.92	1.92	1.89	1.95	1.96	1.86	1.89	1.89	1.94	1.89	2.00	1.95	1.99	1.95	1.98
A (0 to 1 apfu)																													
Na	0.00	0.00	0.00	0.00	0.00	0.00	0.00	0.00	0.00	0.00	0.00	0.00	0.00	0.00	0.00	0.00	0.00	0.00	0.00	0.00	0.00	0.00	0.00	0.00	0.14	0.00	0.00	0.00	0.00
K	0.00	0.01	0.00	0.00	0.00	0.00	0.00	0.00	0.00	0.01	0.00	0.00	0.00	0.00	0.00	0.00	0.00	0.00	0.00	0.00	0.00	0.00	0.00	0.00	0.01	0.00	0.00	0.00	0.00
A subtotal	0.00	0.01	0.00	0.00	0.00	0.00	0.00	0.00	0.00	0.01	0.00	0.00	0.00	0.00	0.00	0.00	0.00	0.00	0.00	0.00	0.00	0.00	0.00	0.00	0.15	0.00	0.00	0.00	0.00
O (non-W)	22.00	22.00	22.00	22.00	22.00	22.00	22.00	22.00	22.00	22.00	22.00	22.00	22.00	22.00	22.00	22.00	22.00	22.00	22.00	22.00	22.00	22.00	22.00	22.00	22.00	22.00	22.00	22.00	22.00
W (ideally 2 apfu)																													
OH	2.00	2.00	1.99	2.00	2.00	2.00	2.00	1.98	2.00	2.00	2.00	2.00	2.00	2.00	2.00	2.00	2.00	2.00	2.00	2.00	1.99	2.00	2.00	2.00	2.00	2.00	2.00	2.00	2.00
F	0.00	0.00	0.01	0.00	0.00	0.00	0.00	0.02	0.00	0.00	0.00	0.00	0.00	0.00	0.00	0.00	0.00	0.00	0.00	0.00	0.01	0.00	0.00	0.00	0.00	0.00	0.00	0.00	0.00
Cl	0.00	0.00	0.00	0.00	0.00	0.00	0.00	0.00	0.00	0.00	0.00	0.00	0.00	0.00	0.00	0.00	0.00	0.00	0.00	0.00	0.00	0.00	0.00	0.00	0.00	0.00	0.00	0.00	0.00
W subtotal	2.00	2.00	2.00	2.00	2.00	2.00	2.00	2.00	2.00	2.00	2.00	2.00	2.00	2.00	2.00	2.00	2.00	2.00	2.00	2.00	2.00	2.00	2.00	2.00	2.00	2.00	2.00	2.00	2.00
Sum T,C,B,A	14.91	14.89	14.91	14.94	14.99	14.95	14.95	15.00	14.92	14.93	14.86	14.95	14.91	14.92	14.92	14.92	14.89	14.95	14.97	15.00	14.89	14.89	14.94	14.89	15.15	14.95	14.99	14.95	14.98
$Fe^{3+}/(Al + Fe^{3+})$	0.21	0.29	0.33	0.29	0.45	0.27	0.55	0.40	0.32	0.37	0.40	0.26	0.24	0.17	0.26	0.12	0.47	0.25	0.43	0.22	0.31	0.32	0.23	0.16	0.27	0.31	0.29	0.22	0.23
$Mg/(Mg + Fe^{2+})$	0.51	0.52	0.58	0.58	0.57	0.60	0.56	0.57	0.57	0.57	0.59	0.51	0.50	0.59	0.52	0.57	0.62	0.58	0.57	0.50	0.62	0.60	0.54	0.58	0.53	0.61	0.62	0.66	0.66

Table S4.1b. cont.

AMPHIBOLE MANTLES
EV19-15C

	V_1						V_2					V_3					V_4					host rock			
Wt.%	**1**	**2**	**3**	**4**	**5**	**6**	**7**	**8**	**9**	**10**	**11**	**12**	**13**	**14**	**15**	**16**	**17**	**18**	**19**	**20**	**21**	**22**	**23**	**24**	**25**
SiO_2	58.61	58.66	58.44	59.04	58.68	58.86	59.48	59.41	59.76	58.92	58.52	59.39	58.73	58.73	58.60	34.88	58.22	58.20	59.21	58.82	58.99	59.97	58.19	59.74	59.71
TiO_2	0.08	0.01	n.d.	0.12	0.09	0.08	n.d.	n.d.	n.d.	0.01	n.d.	0.03	0.04	0.07	0.11	n.d.	n.d.	0.07	n.d.	n.d.	n.d.	n.d.	0.14	0.10	0.05
Al_2O_3	9.33	9.47	7.74	9.20	9.13	8.82	9.30	9.31	9.62	8.99	9.93	9.43	9.13	8.72	9.33	7.86	8.56	9.70	9.03	8.98	7.94	8.81	9.84	9.75	9.93
Cr_2O_3	0.01	0.01	n.d.	n.d.	n.d.	n.d.	0.01	0.01	n.d.	0.01	0.01	0.01	n.d.	n.d.	n.d.	n.d.	n.d.	n.d.	n.d.	n.d.	n.d.	n.d.	n.d.	n.d.	0.01
FeO	13.10	12.83	15.20	12.72	13.67	13.20	12.76	12.98	13.01	13.15	12.65	13.13	12.95	14.13	13.46	14.14	14.32	13.06	13.25	13.50	14.44	13.09	12.64	11.62	10.70
MnO	0.29	0.24	0.22	0.22	0.19	0.20	0.18	0.18	0.21	0.23	0.23	0.27	0.23	0.23	0.23	0.22	0.19	0.20	0.17	0.21	0.21	0.19	0.22	0.25	0.21
MgO	8.89	8.67	8.93	9.16	8.72	9.11	9.19	9.19	8.66	9.19	8.86	8.92	9.22	8.58	8.86	7.43	8.87	8.45	9.32	9.01	9.34	9.45	8.92	9.57	9.79
CaO	0.07	0.09	0.22	0.10	0.07	0.12	0.01	0.01	0.00	0.09	0.02	0.07	0.11	0.06	0.09	0.07	0.07	0.05	0.06	0.01	0.18	0.03	0.07	0.11	0.07
Na_2O	7.05	7.02	6.93	6.94	7.17	6.97	7.20	7.00	7.08	7.33	7.30	7.30	7.06	7.14	7.25	6.64	7.23	7.27	6.87	7.14	7.07	7.34	7.14	7.27	7.56
K_2O	0.02	0.02	0.01	0.03	0.00	0.02	n.d.	0.01	0.00	n.d.	n.d.	0.01	0.03	n.d.	n.d.	0.01	n.d.	0.02	0.00	n.d.	n.d.	0.01	n.d.	n.d.	n.d.
H_2O	2.16	2.17	2.14	2.17	2.16	2.16	2.17	2.17	2.17	2.16	2.17	2.16	2.16	2.15	2.16	2.05	2.15	2.16	2.16	2.16	2.15	2.16	2.17	2.18	2.19
TOTAL	99.61	99.19	99.84	99.70	99.87	99.53	100.30	100.26	100.51	100.09	99.69	100.74	99.67	99.80	100.08	73.31	99.62	99.18	100.07	99.84	100.32	101.05	99.33	100.59	100.22
Formula Assignments																									
T (ideally 8 apfu)																									
Si	8.08	8.102	8.105	8.108	8.094	8.138	8.102	8.126	8.106	8.132	8.142	8.122	8.172	8.112	8.076	8.123	8.097	8.135	8.075	6.851	8.159	8.053	8.132	8.149	8.113
T subtotal	8.08	8.102	8.105	8.108	8.094	8.138	8.102	8.126	8.106	8.132	8.142	8.122	8.172	8.112	8.076	8.123	8.097	8.135	8.075	8	8.159	8.053	8.132	8.149	8.113
C (ideally 5 apfu)																									
Ti	0.00	0.01	0.00	0.00	0.01	0.00	0.00	0.01	0.01	0.01	0.00	0.00	0.00	0.00	0.00	0.00	0.01	0.01	0.01	0.00	0.00	0.01	0.01	0.01	0.00
Al	1.40	1.59	1.46	1.46	1.52	1.55	1.27	1.49	1.49	1.44	1.50	1.50	1.55	1.46	1.62	1.52	1.48	1.42	1.52	0.67	1.41	1.60	1.57	1.60	1.29
Cr	0.00	0.00	0.00	0.00	0.00	0.00	0.00	0.00	0.00	0.00	0.00	0.00	0.00	0.00	0.00	0.00	0.00	0.00	0.00	0.00	0.00	0.00	0.00	0.00	0.00
Fe^{3+}	0.47	0.21	0.49	0.42	0.36	0.26	0.60	0.35	0.34	0.38	0.30	0.40	0.23	0.33	0.27	0.27	0.39	0.36	0.35	1.50	0.32	0.32	0.20	0.09	0.55
Mn^{2+}	0.02	0.02	0.02	0.03	0.03	0.03	0.03	0.03	0.02	0.02	0.02	0.02	0.02	0.03	0.03	0.03	0.03	0.03	0.03		0.02	0.03	0.03	0.02	0.03
Fe^{2+}	1.19	1.31	1.02	1.14	1.15	1.23	1.16	1.12	1.24	1.15	1.16	1.09	1.26	1.19	1.19	1.23	1.11	1.28	1.20	0.65	1.17	1.14	1.12	1.13	1.11
Mg	1.84	1.75	1.90	1.85	1.83	1.79	1.85	1.88	1.80	1.88	1.88	1.87	1.77	1.89	1.82	1.82	1.90	1.77	1.82	2.18	1.92	1.84	1.94	1.99	1.91
C subtotal	4.92	4.90	4.89	4.89	4.91	4.86	4.90	4.87	4.89	4.87	4.86	4.88	4.83	4.89	4.93	4.88	4.90	4.87	4.92	5.00	4.84	4.95	4.87	4.84	4.89
B (ideally 2 apfu)																									
Ca	0.01	0.01	0.01	0.00	0.01	0.01	0.03	0.02	0.01	0.02	0.00	0.00	0.00	0.01	0.00	0.01	0.02	0.01	0.01	0.02	0.00	0.01	0.02	0.01	0.03
Na	1.95	1.96	1.82	1.91	1.89	1.89	1.86	1.85	1.92	1.87	1.91	1.86	1.88	1.96	1.95	1.94	1.89	1.92	1.94	1.78	1.94	1.92	1.92	1.99	1.89
B subtotal	1.96	1.97	1.83	1.91	1.90	1.90	1.90	1.87	1.93	1.89	1.91	1.86	1.88	1.97	1.96	1.95	1.90	1.93	1.95	1.83	1.94	1.93	1.93	2.00	1.91
A (0 to 1 apfu)																									
Na	0.00	0.00	0.00	0.00	0.00	0.00	0.00	0.00	0.00	0.00	0.00	0.00	0.00	0.00	0.00	0.00	0.00	0.00	0.00	0.75	0.00	0.00	0.00	0.01	0.00
K	0.00	0.00	0.00	0.00	0.00	0.00	0.00	0.01	0.00	0.00	0.00	0.00	0.00	0.00	0.00	0.00	0.01	0.00	0.00	0.00	0.00	0.00	0.00	0.00	0.00
A subtotal	0.00	0.00	0.00	0.00	0.00	0.00	0.00	0.01	0.00	0.00	0.00	0.00	0.00	0.00	0.00	0.00	0.01	0.00	0.00	0.75	0.00	0.00	0.00	0.01	0.00
O (non-W)	22.00	22.00	22.00	22.00	22.00	22.00	22.00	22.00	22.00	22.00	22.00	22.00	22.00	22.00	22.00	22.00	22.00	22.00	22.00	22.00	22.00	22.00	22.00	22.00	22.00
W (ideally 2 apfu)																									
OH	2.00	2.00	1.99	2.00	2.00	2.00	1.99	2.00	2.00	2.00	2.00	1.98	2.00	2.00	2.00	2.00	2.00	2.00	2.00	2.00	2.00	2.00	2.00	2.00	2.00
F	0.00	0.00	0.01	0.00	0.00	0.00	0.01	0.00	0.00	0.00	0.00	0.02	0.00	0.00	0.00	0.00	0.00	0.00	0.00	0.00	0.00	0.00	0.00	0.00	0.00
Cl	0.00	0.00	0.00	0.00	0.00	0.00	0.00	0.00	0.00	0.00	0.00	0.00	0.00	0.00	0.00	0.00	0.00	0.00	0.00	0.00	0.00	0.00	0.00	0.00	0.00
W subtotal	2.00	2.00	2.00	2.00	2.00	2.00	2.00	2.00	2.00	2.00	2.00	2.00	2.00	2.00	2.00	2.00	2.00	2.00	2.00	2.00	2.00	2.00	2.00	2.00	2.00
Sum T,C,B,A	14.96	14.97	14.83	14.91	14.90	14.91	14.90	14.87	14.93	14.89	14.91	14.86	14.88	14.97	14.96	14.95	14.91	14.93	14.95	15.58	14.94	14.93	14.93	15.00	14.91
$Fe^{3+}/(Al + Fe^{3+})$	0.25	0.12	0.25	0.22	0.19	0.14	0.32	0.19	0.19	0.21	0.17	0.21	0.13	0.18	0.14	0.15	0.21	0.20	0.19	0.69	0.19	0.17	0.11	0.05	0.30
$Mg/(Mg + Fe^{2+})$	0.61	0.57	0.65	0.62	0.61	0.59	0.61	0.63	0.59	0.62	0.62	0.63	0.58	0.61	0.61	0.60	0.63	0.58	0.60	0.77	0.62	0.62	0.63	0.64	0.63

Table S4.1b. cont.

	AMPHIBOLE RIMS EV19-15C																		
	V_1				V_2		V_3			V_4						host rock			
SAMPLE	**1**	**2**	**3**	**4**	**5**	**6**	**7**	**8**	**9**	**10**	**11**	**12**	**13**	**14**	**15**	**16**	**17**	**18**	**19**
SiO_2	55.66	74.98	55.92	57.63	57.29	57.32	60.42	56.18	57.40	55.26	62.36	57.15	55.26	56.51	57.08	60.29	56.77	56.87	57.53
TiO_2	n.d.	n.d.	0.01	n.d.	n.d.	n.d.	n.d.	n.d.	n.d.	0.00	n.d.	n.d.	n.d.	n.d.	0.01	n.d.	0.01	n.d.	0.01
Al_2O_3	2.08	1.61	2.87	1.26	5.32	2.34	3.00	3.18	2.43	2.37	2.73	3.04	2.32	2.42	3.47	2.42	2.61	2.62	2.48
Cr_2O_3	0.01	n.d.	n.d.	n.d.	0.01	n.d.	n.d.	n.d.	n.d.	n.d.	0.01	0.01	n.d.	n.d.	0.00	0.01	0.00	0.00	0.01
FeO	15.75	11.84	18.18	14.47	16.23	19.93	19.02	18.05	19.38	17.46	17.54	18.53	16.36	18.93	17.45	16.68	17.81	17.60	14.45
MnO	0.46	0.23	0.33	0.57	0.29	0.28	0.29	0.29	0.29	0.39	0.32	0.23	0.51	0.41	0.35	0.38	0.43	0.41	0.53
MgO	13.01	6.40	10.94	14.62	10.12	10.16	11.20	10.60	10.41	11.25	8.74	10.44	12.61	11.02	10.36	9.51	11.87	11.49	13.34
CaO	6.37	1.32	2.83	6.87	1.13	1.22	1.23	2.31	1.49	3.85	1.75	1.13	6.47	2.68	2.37	4.86	3.36	2.72	5.38
Na_2O	3.88	3.41	5.89	3.06	6.60	6.29	5.28	5.87	6.42	4.68	5.39	6.31	3.70	5.99	5.65	4.65	5.17	5.66	4.27
K_2O	0.09	0.03	0.05	0.10	0.05	0.02	0.04	0.06	0.09	0.06	0.02	0.01	0.13	0.04	0.08	0.08	0.08	0.05	0.07
H_2O	2.08	2.26	2.07	2.10	2.11	2.07	2.10	2.08	2.07	2.08	2.12	2.09	2.07	2.07	2.09	2.10	2.08	2.08	2.11
TOTAL	99.39	102.08	99.09	100.69	99.17	99.63	102.59	98.62	99.97	97.41	100.98	98.93	99.43	100.07	98.90	100.99	100.19	99.52	100.18
Formula Assignments																			
T (ideally 8 apfu)																			
Si	7.95	9.73	7.98	8.09	8.05	8.09	8.36	8.02	8.09	8.05	8.67	8.08	7.90	7.99	8.11	8.50	8.00	8.03	8.05
Al	0.06	0.00	0.02	0.00	0.00	0.00	0.00	0.00	0.00	0.00	0.00	0.00	0.10	0.01	0.00	0.00	0.00	0.00	0.00
T subtotal	8.00	9.73	8.00	8.09	8.05	8.09	8.36	8.02	8.09	8.05	8.67	8.08	8.00	8.00	8.11	8.50	8.00	8.03	8.05
C (ideally 5 apfu)																			
Ti	0.00	0.00	0.00	0.00	0.00	0.00	0.00	0.00	0.00	0.00	0.00	0.00	0.00	0.00	0.00	0.00	0.00	0.00	0.00
Al	0.29	0.25	0.46	0.21	0.88	0.39	0.49	0.54	0.40	0.41	0.45	0.51	0.29	0.39	0.58	0.40	0.43	0.44	0.41
Cr	0.00	0.00	0.00	0.00	0.00	0.00	0.00	0.00	0.00	0.00	0.00	0.00	0.00	0.00	0.00	0.00	0.00	0.00	0.00
Fe^{3+}	0.72	0.00	1.05	0.42	0.86	1.34	0.19	1.09	1.19	0.80	0.25	1.27	0.77	1.16	0.91	0.00	0.96	1.08	0.70
Mn^{2+}	0.06	0.03	0.04	0.03	0.04	0.03	0.00	0.04	0.03	0.02	0.04	0.03	0.06	0.05	0.04	0.05	0.00	0.05	0.06
Fe^{2+}	1.16	1.29	1.12	1.28	1.05	1.01	2.00	1.07	1.09	1.32	1.79	0.92	1.19	1.08	1.16	1.97	1.11	1.00	0.99
Mg	2.77	1.24	2.33	3.06	2.12	2.14	2.31	2.26	2.19	2.44	1.81	2.20	2.69	2.32	2.19	2.00	2.49	2.42	2.78
C subtotal	5.00	2.80	5.00	5.00	4.95	4.91	5.00	4.98	4.91	5.00	4.34	4.92	5.00	5.00	4.89	4.42	5.00	4.98	4.95
B (ideally 2 apfu)																			
Mn^{2+}	0.00	0.00	0.00	0.04	0.00	0.00	0.03	0.00	0.00	0.03	0.00	0.00	0.00	0.00	0.00	0.00	0.05	0.00	0.00
Fe^{2+}	0.00	0.00	0.00	0.00	0.00	0.00	0.00	0.00	0.00	0.00	0.00	0.00	0.00	0.00	0.00	0.00	0.00	0.00	0.00
Ca	0.97	0.18	0.43	1.03	0.17	0.18	0.18	0.35	0.22	0.60	0.26	0.17	0.99	0.41	0.36	0.74	0.51	0.41	0.81
Na	1.03	0.86	1.57	0.83	1.80	1.72	1.42	1.62	1.76	1.32	1.45	1.73	1.01	1.59	1.56	1.27	1.41	1.55	1.16
B subtotal	2.00	1.04	2.00	1.91	1.97	1.90	1.64	1.98	1.98	1.95	1.71	1.90	2.00	2.00	1.92	2.00	1.97	1.96	1.97
A (from 0 to 1 apfu)																			
Na	0.05	0.00	0.06	0.00	0.00	0.00	0.00	0.00	0.00	0.00	0.00	0.00	0.02	0.05	0.00	0.01	0.00	0.00	0.00
K	0.02	0.01	0.01	0.02	0.01	0.00	0.01	0.01	0.02	0.01	0.00	0.00	0.02	0.01	0.01	0.01	0.01	0.01	0.01
A subtotal	0.06	0.01	0.07	0.02	0.01	0.00	0.01	0.01	0.02	0.01	0.00	0.00	0.04	0.06	0.01	0.02	0.01	0.01	0.01
O (non-W)	22.00	22.00	22.00	22.00	22.00	22.00	22.00	22.00	22.00	22.00	22.00	22.00	22.00	22.00	22.00	22.00	22.00	22.00	22.00
W (ideally 2 apfu)																			
OH	2.00	2.00	2.00	2.00	2.00	2.00	2.00	2.00	2.00	2.00	2.00	2.00	2.00	2.00	2.00	2.00	2.00	2.00	2.00
F	0.00	0.00	0.00	0.00	0.00	0.00	0.00	0.00	0.00	0.00	0.00	0.00	0.00	0.00	0.00	0.00	0.00	0.00	0.00
Cl	0.00	0.00	0.00	0.00	0.00	0.00	0.00	0.00	0.00	0.00	0.00	0.00	0.00	0.00	0.00	0.00	0.00	0.00	0.00
W subtotal	2.00	2.00	2.00	2.00	2.00	2.00	2.00	2.00	2.00	2.00	2.00	2.00	2.00	2.00	2.00	2.00	2.00	2.00	2.00
Sum T,C,B,A	15.06	13.58	15.07	15.02	14.98	14.91	15.01	14.99	15.00	15.01	14.72	14.90	15.04	15.06	14.93	14.94	14.99	14.99	14.98
$Fe^{3+}/(Al + Fe^{3+})$	0.71	0.00	0.69	0.67	0.49	0.78	0.28	0.67	0.75	0.66	0.36	0.71	0.72	0.75	0.61	0.00	0.69	0.71	0.63
$Mg/(Mg + Fe^{2+})$	0.71	0.49	0.68	0.70	0.67	0.68	0.54	0.68	0.67	0.65	0.50	0.70	0.69	0.68	0.65	0.50	0.69	0.71	0.74

Table S4.1c. Electron microprobe results for clinopyroxene from host rock to the Mt. Ochi veins, Evia, Greece.

	CLINOPYROXENE																														
	EV19-15A																			EV19-15B			EV19-15C								
Wt.%	**1**	**2**	**3**	**4**	**5**	**6**	**7**	**8**	**9**	**10**	**11**	**12**	**13**	**14**	**15**	**16**	**17**	**18**	**19**	**20**	**21**	**22**	**23**	**24**	**25**	**26**	**27**	**28**	**29**	**30**	**31**	**32**
SiO_2	58.33	56.94	57.88	57.73	57.27	55.98	55.77	56.36	54.99	55.84	56.91	55.52	54.47	55.78	53.53	53.56	55.63	54.99	55.00	55.32	54.46	55.46	58.79	53.53	53.64	53.83	50.70	52.29	52.70	53.74	52.62	52.45
TiO_2	0.17	0.26	0.09	0.19	0.12	0.32	0.38	0.16	0.30	0.09	0.15	0.47	0.16	0.25	0.29	0.27	0.26	0.15	0.27	0.31	0.27	0.31	0.27	0.03	0.03	0.02	0.07	0.10	0.11	0.06	0.36	0.16
Al_2O_3	13.10	9.16	9.82	13.32	12.47	12.91	12.17	14.07	9.40	13.90	14.60	10.28	9.95	12.80	10.84	9.20	12.14	10.01	10.06	11.17	10.09	11.15	11.14	4.07	3.50	3.71	3.78	3.32	4.26	4.13	5.70	5.52
Cr_2O_3	n.d.	n.d.	0.00	n.d.	0.00	0.01	0.02	n.d.	0.02	0.02	n.d.	0.02	n.d.	0.01	0.00	0.03	n.d.	0.00	n.d.	0.01	0.02	0.00	0.02	0.01	0.01	0.02	0.01	0.01	0.01	0.01	0.01	n.d.
FeO	14.39	17.68	16.37	12.85	13.84	15.42	15.84	14.49	20.73	13.83	13.76	19.18	18.97	15.77	17.96	20.05	16.42	18.54	19.93	17.37	18.85	17.20	15.93	21.34	20.81	20.44	21.28	22.37	19.74	20.41	25.07	24.65
MnO	0.09	0.08	0.06	0.03	0.06	0.06	0.10	0.07	0.09	0.09	0.08	0.08	0.11	0.08	0.10	0.07	0.05	0.09	0.08	0.05	0.02	0.02	0.03	0.16	0.22	0.21	0.30	0.22	0.27	0.24	0.08	0.03
MgO	0.94	0.92	1.10	0.59	0.83	0.77	0.92	0.70	0.89	0.62	0.86	0.97	1.05	0.82	0.86	0.90	0.77	0.99	0.81	0.85	1.08	0.87	0.52	4.00	4.55	4.34	4.54	3.80	4.83	4.19	1.44	1.02
CaO	1.17	1.34	1.69	1.34	1.10	1.38	1.45	1.41	0.91	1.50	1.13	1.10	1.19	1.37	1.06	1.22	1.51	1.39	1.12	0.95	0.95	0.86	0.61	6.87	7.71	7.09	7.26	6.73	7.46	6.94	1.46	1.72
Na_2O	13.77	12.69	11.81	13.49	13.26	13.25	12.92	12.64	13.07	12.65	13.26	12.89	12.70	13.19	13.10	12.00	12.75	12.55	12.98	12.98	12.49	12.89	12.51	9.61	9.23	9.46	8.28	9.66	8.91	9.52	11.55	12.46
K_2O	0.00	0.02	0.46	0.01	0.02	n.d.	0.01	0.01	0.01	0.01	n.d.	0.04	0.03	n.d.	0.01	0.39	0.01	0.01	0.02	0.06	0.08	n.d.	0.00	0.01	0.02	0.00	0.18	0.00	0.08	0.04	0.03	0.01
TOTAL	101.964	99.0975	99.2794	99.5448	98.9752	100.10	99.59	99.91	100.41	98.54	100.74	100.54	98.63	100.07	97.75	97.71	99.53	98.73	100.26	99.08	98.31	98.77	99.83	99.63	99.73	99.11	96.39	98.50	98.36	99.29	98.33	98.02
Molar																																
SiO_2	0.97	0.95	0.96	0.96	0.95	0.93	0.93	0.94	0.92	0.93	0.95	0.92	0.91	0.93	0.89	0.89	0.93	0.92	0.92	0.92	0.91	0.92	0.98	0.89	0.89	0.90	0.84	0.87	0.88	0.89	0.88	0.87
TiO_2	0.00	0.00	0.00	0.00	0.00	0.00	0.00	0.00	0.00	0.00	0.00	0.01	0.00	0.00	0.00	0.00	0.00	0.00	0.00	0.00	0.00	0.00	0.00	0.00	0.00	0.00	0.00	0.00	0.00	0.00	0.00	0.00
Al_2O_3	0.26	0.18	0.19	0.26	0.24	0.25	0.24	0.28	0.18	0.27	0.29	0.20	0.20	0.25	0.21	0.18	0.24	0.20	0.20	0.22	0.20	0.22	0.22	0.08	0.07	0.07	0.07	0.07	0.08	0.08	0.11	0.11
Cr_2O_3	0.00	0.00	0.00	0.00	0.00	0.00	0.00	0.00	0.00	0.00	0.00	0.00	0.00	0.00	0.00	0.00	0.00	0.00	0.00	0.00	0.00	0.00	0.00	0.00	0.00	0.00	0.00	0.00	0.00	0.00	0.00	0.00
FeO	0.20	0.25	0.23	0.18	0.19	0.43	0.44	0.40	0.58	0.39	0.38	0.53	0.53	0.44	0.50	0.56	0.46	0.52	0.55	0.48	0.52	0.48	0.44	0.59	0.58	0.57	0.59	0.62	0.55	0.57	0.70	0.69
MnO	0.00	0.00	0.00	0.00	0.00	0.00	0.00	0.00	0.00	0.00	0.00	0.00	0.00	0.00	0.00	0.00	0.00	0.00	0.00	0.00	0.00	0.00	0.00	0.00	0.00	0.00	0.00	0.00	0.00	0.00	0.00	0.00
MgO	0.02	0.02	0.03	0.01	0.02	0.02	0.02	0.02	0.02	0.02	0.02	0.02	0.03	0.02	0.02	0.02	0.02	0.02	0.02	0.02	0.03	0.02	0.01	0.10	0.11	0.11	0.11	0.09	0.12	0.10	0.04	0.03
CaO	0.02	0.02	0.03	0.02	0.02	0.02	0.03	0.03	0.02	0.03	0.02	0.02	0.02	0.02	0.02	0.02	0.03	0.02	0.02	0.02	0.02	0.02	0.01	0.12	0.14	0.13	0.13	0.12	0.13	0.12	0.03	0.03
Na_2O	0.44	0.41	0.38	0.44	0.43	0.43	0.42	0.41	0.42	0.41	0.43	0.42	0.41	0.43	0.42	0.39	0.41	0.41	0.42	0.42	0.40	0.42	0.40	0.31	0.30	0.31	0.27	0.31	0.29	0.31	0.37	0.40
K_2O	0.00	0.00	0.01	0.00	0.00	0.00	0.00	0.00	0.00	0.00	0.00	0.00	0.00	0.00	0.00	0.01	0.00	0.00	0.00	0.00	0.00	0.00	0.00	0.00	0.00	0.00	0.00	0.00	0.00	0.00	0.00	0.00
formula units																																
Si	2.08	2.13	2.14	2.09	2.10	2.00	2.00	2.00	1.99	2.01	2.00	2.00	2.00	1.99	1.98	2.00	2.00	2.01	1.99	2.01	2.00	2.01	2.08	1.99	2.00	2.01	1.96	1.98	1.98	2.00	1.98	1.99
Ti	0.00	0.01	0.00	0.01	0.00	0.01	0.01	0.00	0.01	0.00	0.00	0.01	0.00	0.01	0.01	0.01	0.01	0.00	0.01	0.01	0.01	0.01	0.01	0.00	0.00	0.00	0.00	0.00	0.00	0.00	0.01	0.00
Al	0.55	0.40	0.43	0.57	0.54	0.54	0.52	0.59	0.40	0.59	0.60	0.44	0.43	0.54	0.47	0.40	0.51	0.43	0.43	0.48	0.44	0.48	0.47	0.18	0.15	0.16	0.17	0.15	0.19	0.18	0.25	0.25
Cr	0.00	0.00	0.00	0.00	0.00	0.00	0.00	0.00	0.00	0.00	0.00	0.00	0.00	0.00	0.00	0.00	0.00	0.00	0.00	0.00	0.00	0.00	0.00	0.00	0.00	0.00	0.00	0.00	0.00	0.00	0.00	0.00
Fe	0.43	0.55	0.51	0.39	0.42	0.41	0.43	0.39	0.57	0.37	0.36	0.52	0.52	0.42	0.50	0.56	0.44	0.51	0.54	0.47	0.52	0.47	0.42	0.60	0.58	0.57	0.62	0.64	0.56	0.57	0.71	0.70
Mn	0.00	0.00	0.00	0.00	0.00	0.00	0.00	0.00	0.00	0.00	0.00	0.00	0.00	0.00	0.00	0.00	0.00	0.00	0.00	0.00	0.00	0.00	0.00	0.01	0.01	0.01	0.01	0.01	0.01	0.01	0.00	0.00
Mg	0.05	0.05	0.06	0.03	0.05	0.04	0.05	0.04	0.05	0.03	0.05	0.05	0.06	0.04	0.05	0.05	0.04	0.05	0.04	0.05	0.06	0.05	0.03	0.22	0.25	0.24	0.26	0.21	0.27	0.23	0.08	0.06
Ca	0.04	0.05	0.07	0.05	0.04	0.05	0.06	0.05	0.04	0.06	0.04	0.04	0.05	0.05	0.04	0.05	0.06	0.05	0.04	0.04	0.04	0.03	0.02	0.27	0.31	0.28	0.30	0.27	0.30	0.28	0.06	0.07
Na	0.95	0.92	0.85	0.95	0.94	0.92	0.90	0.87	0.92	0.88	0.90	0.90	0.90	0.91	0.94	0.87	0.89	0.89	0.91	0.91	0.89	0.91	0.86	0.69	0.67	0.68	0.62	0.71	0.65	0.69	0.84	0.92
K	0.00	0.00	0.02	0.00	0.00	0.00	0.00	0.00	0.00	0.00	0.00	0.00	0.00	0.00	0.00	0.02	0.00	0.00	0.00	0.00	0.00	0.00	0.00	0.00	0.00	0.00	0.01	0.00	0.00	0.00	0.00	0.00
Recalculations after Cawthorne and Collerson (1974)																																
Na + K	0.95	0.92	0.87	0.95	0.94	0.92	0.90	0.87	0.92	0.88	0.90	0.90	0.90	0.91	0.94	0.89	0.89	0.89	0.91	0.92	0.89	0.91	0.86	0.69	0.67	0.68	0.63	0.71	0.65	0.69	0.85	0.92
Al (jd)	0.55	0.40	0.43	0.57	0.54	0.54	0.52	0.59	0.40	0.59	0.60	0.44	0.43	0.54	0.47	0.40	0.51	0.43	0.43	0.48	0.44	0.48	0.47	0.18	0.15	0.16	0.17	0.15	0.19	0.18	0.25	0.25
Fe^{3+} (aeg)	0.40	0.52	0.44	0.38	0.41	0.37	0.38	0.28	0.52	0.29	0.30	0.46	0.47	0.37	0.47	0.48	0.38	0.46	0.48	0.44	0.46	0.43	0.39	0.52	0.51	0.52	0.46	0.56	0.46	0.51	0.59	0.67
Ti	0.00	0.01	0.00	0.01	0.00	0.01	0.01	0.00	0.01	0.00	0.00	0.01	0.00	0.01	0.01	0.01	0.01	0.00	0.01	0.01	0.01	0.01	0.01	0.00	0.00	0.00	0.00	0.00	0.00	0.00	0.01	0.00
Al	0.00	-0.01	0.00	-0.01	0.00	-0.01	-0.01	0.00	-0.01	0.00	0.00	-0.01	0.00	-0.01	-0.01	-0.01	-0.01	0.00	-0.01	-0.01	-0.01	-0.01	-0.01	0.00	0.00	0.00	0.00	0.00	0.00	0.00	-0.01	0.00
Ca (Wo)	0.04	0.05	0.07	0.05	0.04	0.05	0.06	0.05	0.04	0.06	0.04	0.04	0.05	0.05	0.04	0.05	0.06	0.05	0.04	0.04	0.04	0.03	0.02	0.27	0.31	0.28	0.30	0.27	0.30	0.28	0.06	0.07
Mg (En)	0.05	0.05	0.06	0.03	0.05	0.04	0.05	0.04	0.05	0.03	0.05	0.05	0.06	0.04	0.05	0.05	0.04	0.05	0.04	0.05	0.06	0.05	0.03	0.22	0.25	0.24	0.26	0.21	0.27	0.23	0.08	0.06
Fe^{2+} (Fs)	0.03	0.04	0.07	0.01	0.02	0.04	0.04	0.11	0.05	0.08	0.06	0.05	0.05	0.05	0.03	0.08	0.07	0.05	0.06	0.04	0.07	0.04	0.03	0.08	0.07	0.05	0.16	0.08	0.09	0.06	0.12	0.03
jadeite	0.55	0.4	0.43	0.57	0.54	0.54	0.52	0.59	0.40	0.59	0.60	0.44	0.43	0.54	0.47	0.40	0.51	0.43	0.43	0.48	0.44	0.48	0.47	0.18	0.15	0.16	0.17	0.15	0.19	0.18	0.25	0.25
aegirine	0.4	0.52	0.44	0.38	0.41	0.37	0.38	0.28	0.52	0.29	0.30	0.46	0.47	0.37	0.47	0.48	0.38	0.46	0.48	0.44	0.46	0.43	0.39	0.52	0.51	0.52	0.46	0.56	0.46	0.51	0.59	0.67
augite	0.12	0.14	0.2	0.09	0.11	0.08	0.09	0.14	0.10	0.11	0.11	0.11	0.11	0.09	0.08	0.13	0.11	0.10	0.10	0.08	0.12	0.09	0.06	0.30	0.32	0.29	0.42	0.29	0.36	0.30	0.20	0.09
total	1.07	1.06	1.07	1.04	1.06	1.00	0.99	1.01	1.02	1.00	1.01	1.01	1.01	1.01	1.02	1.02	1.00	1.00	1.02	1.00	1.02	0.99	0.92	1.00	0.99	0.98	1.05	1.00	1.02	0.99	1.05	1.01

Table S4.1d. Electron microprobe results for epidote from host rock to the Mt. Ochi veins, Evia, Greece.

	EPIDOTE								
	EV19-15A	EV19-15B			EV19-15C				
Wt.%	**1**	**2**	**3**	**4**	**5**	**6**	**7**	**8**	**9**
SiO_2	39.22	37.76	37.26	37.20	37.97	37.19	37.14	37.12	37.27
TiO_2	n.d.	0.06	0.02	n.d.	0.13	0.03	0.01	0.13	0.08
Al_2O_3	21.34	22.40	21.73	22.50	22.55	22.05	21.69	23.00	22.13
Cr_2O_3	0.02	0.03	0.04	0.02	0.02	n.d.	n.d.	n.d.	0.01
Fe_2O_3	14.82	15.09	15.09	15.20	14.74	15.24	15.93	13.92	15.07
MnO	0.61	0.59	0.89	0.59	0.68	0.98	0.74	1.00	1.37
MgO	0.04	0.05	0.04	0.03	0.03	0.02	0.02	0.02	0.03
CaO	21.41	22.57	22.09	22.20	22.86	22.11	22.17	22.04	21.58
Na_2O	0.05	n.d.	0.01	0.03	n.d.	n.d.	0.01	n.d.	0.01
K_2O	0.03	n.d.	n.d.	n.d.	n.d.	0.00	n.d.	0.03	0.01
H_2O	1.89	1.88	1.87	1.87	1.88	1.87	1.87	1.88	1.87
TOTAL	99.42	100.42	99.05	99.64	100.85	99.50	99.57	99.13	99.43
SiO_2	0.65	0.63	0.62	0.62	0.63	0.62	0.62	0.62	0.62
TiO_2	0.00	0.00	0.00	0.00	0.00	0.00	0.00	0.00	0.00
Al_2O_3	0.42	0.44	0.43	0.44	0.44	0.43	0.43	0.45	0.43
Cr_2O_3	0.00	0.00	0.00	0.00	0.00	0.00	0.00	0.00	0.00
Fe_2O_3	0.19	0.19	0.19	0.19	0.18	0.19	0.20	0.17	0.19
MnO	0.01	0.01	0.01	0.01	0.01	0.01	0.01	0.01	0.02
MgO	0.00	0.00	0.00	0.00	0.00	0.00	0.00	0.00	0.00
CaO	0.38	0.40	0.39	0.40	0.41	0.39	0.40	0.39	0.38
Na_2O	0.00	0.00	0.00	0.00	0.00	0.00	0.00	0.00	0.00
K_2O	0.00	0.00	0.00	0.00	0.00	0.00	0.00	0.00	0.00
H_2O	0.21	0.21	0.21	0.21	0.21	0.21	0.21	0.21	0.21
Formula Units	**all iron assumed ferric**								
Si	3.13	3.01	3.01	2.99	3.01	3.00	2.99	2.99	3.00
Ti	0.00	0.00	0.00	0.00	0.01	0.00	0.00	0.01	0.00
Al	2.01	2.10	2.07	2.13	2.11	2.09	2.06	2.18	2.10
Cr	0.00	0.00	0.00	0.00	0.00	0.00	0.00	0.00	0.00
Fe	0.89	0.90	0.92	0.92	0.88	0.92	0.97	0.84	0.91
Mn	0.04	0.04	0.06	0.04	0.05	0.07	0.05	0.07	0.09
Mg	0.00	0.01	0.00	0.00	0.00	0.00	0.00	0.00	0.00
Ca	1.83	1.93	1.91	1.91	1.94	1.91	1.91	1.90	1.86
Na	0.01	0.00	0.00	0.01	0.00	0.00	0.00	0.00	0.00
K	0.00	0.00	0.00	0.00	0.00	0.00	0.00	0.00	0.00
OH	1.01	1.00	1.01	1.00	0.99	1.01	1.00	1.01	1.01
X_{Ps}	0.31	0.30	0.31	0.30	0.29	0.31	0.32	0.28	0.30
X_{Cz}	0.69	0.70	0.69	0.70	0.71	0.69	0.68	0.72	0.70

Table S4.1e. Electron microprobe results for chlorite from host rock to the Mt. Ochi veins, Evia, Greece.

	CHLORITE							
	EV19-15A		EV19-15B		EV19-15C			
Wt.%	**1**	**2**	**3**	**4**	**5**	**6**	**7**	**8**
SiO_2	28.06	29.05	30.28	29.79	27.57	26.81	27.59	27.00
TiO_2	0.02	n.d.	0.02	n.d.	n.d.	n.d.	n.d.	0.03
Al_2O_3	19.70	20.61	23.87	21.23	19.26	19.75	19.58	19.49
Cr_2O_3	0.03	0.02	0.02	0.03	0.02	0.02	0.01	0.01
Fe_2O_3	16.61	17.44	14.28	15.81	18.34	18.56	19.03	18.75
MnO	0.80	0.92	0.53	0.60	0.92	0.96	0.90	0.90
MgO	20.86	19.81	16.10	18.79	20.48	20.20	20.62	20.58
CaO	0.04	0.01	0.15	0.09	0.14	0.09	0.04	0.10
Na_2O	n.d.	n.d.	0.05	n.d.	n.d.	n.d.	n.d.	n.d.
K_2O	0.25	0.86	0.12	0.16	0.06	n.d.	n.d.	0.02
H_2O	11.97	11.89	12.30	12.12	11.85	11.83	11.81	11.81
TOTAL	98.34	100.61	97.72	98.61	98.63	98.22	99.57	98.69
SiO_2	0.47	0.48	0.50	0.50	0.46	0.45	0.46	0.45
TiO_2	0.00	0.00	0.00	0.00	0.00	0.00	0.00	0.00
Al_2O_3	0.39	0.40	0.47	0.42	0.38	0.39	0.38	0.38
Cr_2O_3	0.00	0.00	0.00	0.00	0.00	0.00	0.00	0.00
Fe_2O_3	0.23	0.24	0.20	0.22	0.26	0.26	0.26	0.26
MnO	0.01	0.01	0.01	0.01	0.01	0.01	0.01	0.01
MgO	0.52	0.49	0.40	0.47	0.51	0.50	0.51	0.51
CaO	0.00	0.00	0.00	0.00	0.00	0.00	0.00	0.00
Na_2O	0.00	0.00	0.00	0.00	0.00	0.00	0.00	0.00
K_2O	0.01	0.02	0.00	0.00	0.00	0.00	0.00	0.00
H_2O	1.33	1.32	1.37	1.35	1.32	1.31	1.31	1.31
Si	2.86	2.91	3.02	2.99	2.83	2.76	2.81	2.77
Ti	0.00	0.00	0.00	0.00	0.00	0.00	0.00	0.00
Al	2.36	2.43	2.81	2.51	2.33	2.40	2.35	2.36
Cr	0.00	0.00	0.00	0.00	0.00	0.00	0.00	0.00
Fe	1.41	1.46	1.19	1.33	1.57	1.60	1.62	1.61
Mn	0.07	0.08	0.04	0.05	0.08	0.08	0.08	0.08
Mg	3.17	2.96	2.39	2.81	3.13	3.11	3.13	3.15
Ca	0.00	0.00	0.02	0.01	0.02	0.01	0.00	0.01
Na	0.00	0.00	0.01	0.00	0.00	0.00	0.00	0.00
K	0.03	0.11	0.01	0.02	0.01	0.00	0.00	0.00
OH	8.13	7.95	8.18	8.11	8.10	8.14	8.03	8.10
X_{Mg}	0.69	0.67	0.67	0.68	0.67	0.66	0.66	0.66

Table S4.1f. Electron microprobe results for feldspar from host rock to the Mt. Ochi veins, Evia, Greece.

	FELDSPAR					
	EV19-15A	EV19-15C				
Wt.%	1	2	3	4	5	6
SiO_2	68.47	69.22	68.82	68.99	68.99	68.99
TiO_2	n.d.	n.d.	n.d.	n.d.	n.d.	n.d.
Al_2O_3	20.02	19.91	19.95	19.84	19.76	19.96
Cr_2O_3	n.d.	n.d.	n.d.	n.d.	n.d.	n.d.
Fe_2O_3	0.19	0.18	0.24	0.12	0.34	0.01
MnO	n.d.	n.d.	n.d.	n.d.	n.d.	n.d.
MgO	n.d.	n.d.	0.01	0.01	n.d.	n.d.
CaO	0.04	0.09	0.05	0.02	0.04	0.00
Na_2O	11.97	11.77	12.02	12.06	11.66	11.96
K_2O	0.01	0.05	0.03	0.05	0.08	n.d.
Molar						
SiO_2	1.14	1.15	1.15	1.15	1.15	1.15
TiO_2	0.00	0.00	0.00	0.00	0.00	0.00
Al_2O_3	0.39	0.39	0.39	0.39	0.39	0.39
Cr_2O_3	0.00	0.00	0.00	0.00	0.00	0.00
Fe_2O_3	0.00	0.00	0.00	0.00	0.00	0.00
MnO	0.00	0.00	0.00	0.00	0.00	0.00
MgO	0.00	0.00	0.00	0.00	0.00	0.00
CaO	0.00	0.00	0.00	0.00	0.00	0.00
Na_2O	0.39	0.38	0.39	0.39	0.38	0.39
K_2O	0.00	0.00	0.00	0.00	0.00	0.00
Si	2.98	2.99	2.98	2.99	3.00	2.99
Ti	0.00	0.00	0.00	0.00	0.00	0.00
Al	1.03	1.01	1.02	1.01	1.01	1.02
Cr	0.00	0.00	0.00	0.00	0.00	0.00
Fe	0.00	0.00	0.00	0.00	0.01	0.00
Mn	0.00	0.00	0.00	0.00	0.00	0.00
Mg	0.00	0.00	0.00	0.00	0.00	0.00
Ca	0.00	0.00	0.00	0.00	0.00	0.00
Na	1.01	0.99	1.01	1.01	0.98	1.00
K	0.00	0.00	0.00	0.00	0.00	0.00
ab	1.00	0.99	1.00	1.00	1.00	1.00
an	0.00	0.00	0.00	0.00	0.00	0.00
or	0.00	0.00	0.00	0.00	0.00	0.00

Table S4.2a. $^{87}Rb/^{87}Sr$ analytical results for sample EV19-15C of the Mt. Ochi veins, Evia, Greece.

	EV19-15C							
	Analysis	Rb (ppm)	Sr (ppm)	$^{87}Rb/^{86}Sr$	2σ (%)	$^{87}Sr/^{86}Sr$	2σ (%)	rho
glaucophane	EV19-15C_G_V3-1	0.26	0.41	1.43	30.00	0.759	8.700	0.47
	EV19-15C_G_V3-2	0.04	0.77	0.12	36.00	0.785	7.500	0.19
	EV19-15C_G_V3-3	0.09	1.00	0.21	23.00	0.725	4.700	0.33
	EV19-15C_G_V3-4	0.31	0.94	0.78	12.00	0.708	5.500	0.11
	EV19-15C_G_V3-5	18.10	0.58	76.20	7.00	0.729	6.200	0.19
	EV19-15C_G_V3-6	0.37	0.56	1.45	10.00	0.686	4.900	0.26
	EV19-15C_G_V3-7	0.26	0.26	2.42	18.00	0.720	11.000	0.50
	EV19-15C_G_V3-8†	0.01	0.44	0.05	130.00	0.752	8.400	0.24
phengite	EV19-15C_M_V1-1	84.10	1.80	110.10	2.20	0.728	3.900	0.62
	EV19-15C_M_V1-10	87.50	2.60	81.40	1.90	0.724	2.600	0.34
	EV19-15C_M_V1-12	85.70	0.74	276.60	2.80	0.794	5.600	0.40
	EV19-15C_M_V1-13	80.70	1.30	154.10	1.80	0.760	3.400	0.41
	EV19-15C_M_V1-14	81.00	2.00	99.30	1.50	0.734	2.700	0.43
	EV19-15C_M_V1-15	84.30	2.70	74.10	1.50	0.741	2.200	0.42
	EV19-15C_M_V1-16	86.60	2.60	79.80	2.00	0.725	2.600	0.27
	EV19-15C_M_V1-17	86.20	0.69	299.00	6.30	0.805	6.300	0.40
	EV19-15C_M_V1-2	91.30	1.60	139.00	2.40	0.768	4.700	0.53
	EV19-15C_M_V1-3	86.20	2.40	86.60	1.80	0.742	2.700	0.38
	EV19-15C_M_V1-4	91.90	1.10	198.60	2.60	0.798	3.600	0.50
	EV19-15C_M_V1-5	86.50	3.80	53.57	1.50	0.731	1.900	0.58
	EV19-15C_M_V1-6	87.50	1.20	176.40	2.00	0.764	2.900	0.50
	EV19-15C_M_V1-7	90.20	3.60	60.10	2.10	0.743	2.400	0.27
	EV19-15C_M_V1-8	93.30	1.40	157.90	2.40	0.781	4.100	0.41
	EV19-15C_M_V1-9	84.20	3.40	59.94	1.60	0.730	2.300	0.33
	EV19-15C_M_V3-1	78.40	2.50	75.40	2.10	0.722	3.100	0.54
	EV19-15C_M_V3-10	90.60	0.95	234.10	3.50	0.779	6.100	0.46
	EV19-15C_M_V3-12	75.30	4.30	41.49	1.50	0.719	2.600	0.45
	EV19-15C_M_V3-13	80.50	2.20	88.20	1.70	0.736	2.500	0.04
	EV19-15C_M_V3-14	90.80	2.20	100.90	2.60	0.741	2.600	0.51
	EV19-15C_M_V3-15	95.20	0.92	249.20	2.00	0.792	4.000	0.53
	EV19-15C_M_V3-2	79.30	3.90	48.79	1.40	0.720	2.100	0.38
	EV19-15C_M_V3-3	84.30	2.30	91.90	2.60	0.753	3.600	0.38
	EV19-15C_M_V3-4	1.88	0.09	52.60	14.00	0.640	23.000	0.34
	EV19-15C_M_V3-5	0.57	0.02	114.00	46.00	1.260	73.000	0.12
	EV19-15C_M_V3-6	0.56	0.03	45.40	15.00	0.760	34.000	0.40
	EV19-15C_M_V3-7	94.00	0.83	277.90	2.70	0.772	3.500	0.06
	EV19-15C_M_V3-8	87.30	1.80	120.80	5.00	0.766	4.800	0.29
	EV19-15C_M_V3-9	88.80	1.60	134.90	2.90	0.776	4.300	0.04

†Analysis excluded from isochron calculation

Table S4.2b. $^{87}Rb/^{87}Sr$ analytical results for sample EV19-15D of the Mt. Ochi veins, Evia, Greece.

	EV19-15D							
	Analysis	Rb (ppm)	Sr (ppm)	$^{87}Rb/^{86}Sr$	2σ (%)	$^{87}Sr/^{86}Sr$	2σ (%)	rho
glaucophane	EV19-15D_G_Vha-1†	0.03	190.00	0.00	65.00	0.700	0.74	0.14
	EV19-15D_G_Vha-12	0.20	0.66	0.73	15.00	0.728	6.70	0.09
	EV19-15D_G_Vha-13	0.22	0.53	1.01	16.00	0.728	8.60	0.22
	EV19-15D_G_Vha-15	0.24	0.75	0.85	16.00	0.674	7.00	0.22
	EV19-15D_G_Vha-16	0.27	0.46	1.47	18.00	0.678	8.50	0.49
	EV19-15D_G_Vha-2†	0.02	2.00	0.04	83.00	0.683	6.90	0.20
	EV19-15D_G_Vha-3†	0.00	180.00	0.00	1200.00	0.709	1.10	0.08
	EV19-15D_G_Vha-4	0.54	0.42	3.14	11.00	0.704	5.80	0.22
	EV19-15D_G_Vha-5†	0.03	110.00	0.00	77.00	0.714	3.00	0.77
	EV19-15D_G_Vha-6†	0.03	1.60	0.04	58.00	0.681	5.00	-0.03
	EV19-15D_G_Vha-8	0.22	2.50	0.20	13.00	0.686	4.90	0.15
	EV19-15D_G_Vha-9	0.23	1.70	0.31	14.00	0.720	6.20	0.04
	EV19-15D_G_Vhb-1	0.60	0.98	1.49	16.00	0.721	6.70	0.00
	EV19-15D_G_Vhb-10†	0.02	2100.00	0.00	47.00	0.709	0.57	-0.03
	EV19-15D_G_Vhb-11	0.05	2200.00	0.00	36.00	0.709	0.70	0.03
	EV19-15D_G_Vhb-12†	0.03	1500.00	0.00	54.00	0.708	0.63	-0.08
	EV19-15D_G_Vhb-13†	0.00	1400.00	0.00	570.00	0.706	0.56	-0.10
	EV19-15D_G_Vhb-14	0.02	1600.00	0.00	49.00	0.709	0.56	0.06
	EV19-15D_G_Vhb-15†	0.00	34.00	0.00	850.00	0.765	9.20	-0.18
	EV19-15D_G_Vhb-16	0.08	9.20	0.02	29.00	0.890	13.00	0.55
	EV19-15D_G_Vhb-18	0.61	13.00	0.11	10.00	0.786	8.60	0.36
	EV19-15D_G_Vhb-19	0.26	7.40	0.09	15.00	0.910	13.00	0.50
	EV19-15D_G_Vhb-2†	0.02	0.53	0.08	51.00	0.711	7.70	-0.32
	EV19-15D_G_Vhb-20	0.21	6.80	0.07	22.00	0.770	15.00	0.21
	EV19-15D_G_Vhb-21	0.18	9.70	0.05	30.00	0.840	29.00	0.79
	EV19-15D_G_Vhb-22	0.07	2.90	0.06	38.00	0.850	18.00	0.31
	EV19-15D_G_Vhb-23	0.38	2.00	0.69	28.00	1.200	33.00	0.48
	EV19-15D_G_Vhb-24†	0.00	0.43	0.01	1800.00	1.480	34.00	0.02
	EV19-15D_G_Vhb-25	0.01	0.48	0.13	100.00	1.280	24.00	0.15
	EV19-15D_G_Vhb-26	0.00	1.90	0.01	190.00	0.880	23.00	0.25
	EV19-15D_G_Vhb-3	0.63	1.00	1.36	14.00	0.697	7.30	0.43
	EV19-15D_G_Vhb-4†	0.02	0.23	0.23	120.00	0.740	18.00	0.15
	EV19-15D_G_Vhb-5	0.18	0.32	1.41	14.00	0.644	8.40	0.28
	EV19-15D_G_Vhb-6†	0.00	1000.00	0.00	380.00	0.707	0.52	-0.03
	EV19-15D_G_Vhb-7	0.65	340.00	0.00	8.30	0.708	1.50	-0.07
	EV19-15D_G_Vhb-8	0.79	57.00	0.05	28.00	0.697	1.60	-0.37
	EV19-15D_G_Vhb-9†	0.02	1100.00	0.00	110.00	0.705	0.57	0.31
phengite	EV19-15D_M_V3-1	76.30	1.40	132.70	1.80	0.758	3.90	0.64
	EV19-15D_M_V3-10	77.80	3.40	55.10	2.40	0.737	2.50	0.33
	EV19-15D_M_V3-2	79.70	1.20	163.00	1.70	0.753	3.70	0.33
	EV19-15D_M_V3-3	81.00	1.50	131.60	2.40	0.739	3.00	0.62
	EV19-15D_M_V3-4	81.90	1.80	111.30	2.10	0.733	3.60	0.79
	EV19-15D_M_V3-5	79.30	3.80	50.05	1.40	0.724	2.40	0.34
	EV19-15D_M_V3-6	76.20	1.30	138.00	1.90	0.741	3.30	0.42
	EV19-15D_M_V3-7	76.50	1.50	126.40	2.60	0.752	3.50	0.19
	EV19-15D_M_V3-8	75.40	2.60	69.30	1.60	0.739	1.90	0.20
	EV19-15D_M_V3-9	73.10	3.70	48.08	1.60	0.732	1.60	0.37
	EV19-15D_M_Vha-1	82.90	1.40	142.40	1.60	0.762	2.80	0.38
	EV19-15D_M_Vha-10	93.90	1.40	168.90	3.00	0.773	3.00	0.32
	EV19-15D_M_Vha-2	79.40	2.80	70.60	1.60	0.727	2.10	0.25
	EV19-15D_M_Vha-3	78.80	4.30	44.56	1.70	0.720	1.70	0.48
	EV19-15D_M_Vha-4	78.70	4.80	40.20	1.40	0.730	1.90	0.35
	EV19-15D_M_Vha-5	91.50	2.40	92.40	1.80	0.738	2.20	0.40
	EV19-15D_M_Vha-6	84.00	3.90	52.00	2.10	0.722	1.80	0.32
	EV19-15D_M_Vha-7	85.90	0.93	225.50	2.80	0.780	4.30	0.44
	EV19-15D_M_Vha-8	93.30	1.80	123.20	2.40	0.744	2.80	0.34
	EV19-15D_M_Vha-9	77.40	1.30	140.10	2.40	0.783	3.00	0.44

†Analysis excluded from isochron calculation

Table S4.2c. $^{87}Rb/^{87}Sr$ analytical results for reference materials.

Analysis	Rb (ppm)	Sr (ppm)	$^{87}Rb/^{86}Sr$	2σ (%)	$^{87}Sr/^{86}Sr$	2σ (%)	rho	
M_MA1-1	806.0	4.1	630.40	1.50	3.812	1.300	0.73	***347 ± 3 Ma, MSWD = 1.2, n = 12***
M_MA1-10	780.0	3.8	638.50	1.50	3.846	1.600	0.70	***expected = ca. 350 Ma***
M_MA1-11	742.0	3.6	650.00	1.60	3.907	1.300	0.52	
M_MA1-12	739.0	3.6	654.00	1.60	3.960	1.500	0.72	
M_MA1-2	657.0	3.2	622.00	1.80	3.772	1.800	0.78	
M_MA1-3	648.0	3.1	659.00	1.50	3.898	1.700	0.73	
M_MA1-4	660.0	3.2	664.00	1.40	3.890	1.400	0.60	
M_MA1-5	692.0	3.4	633.00	1.60	3.827	1.600	0.53	
M_MA1-6	713.0	3.5	636.70	1.50	3.865	1.500	0.64	
M_MA1-7	727.0	3.5	647.90	1.50	3.933	1.500	0.62	
M_MA1-8	811.0	4.0	631.00	2.00	3.894	1.700	0.80	
M_MA1-9	745.0	3.7	629.10	1.60	3.817	1.500	0.67	
M_MicaFe-1	1780.0	4.7	1532.00	2.10	7.370	1.800	0.85	***306 ± 3 Ma, MSWD = 1.6, n = 12***
M_MicaFe-10	1770.0	4.5	1570.00	2.20	7.480	1.900	0.76	***expected = ca. 302-315 Ma, various***
M_MicaFe-11	1750.0	4.7	1476.00	3.00	7.140	2.600	0.88	
M_MicaFe-12	1780.0	4.7	1472.00	2.40	7.130	1.800	0.85	
M_MicaFe-2	1780.0	4.6	1465.00	2.30	7.170	2.100	0.87	
M_MicaFe-3	1680.0	4.2	1584.00	1.70	7.390	1.500	0.82	
M_MicaFe-4	1620.0	4.2	1595.00	2.60	7.290	2.400	0.92	
M_MicaFe-5	1600.0	4.0	1612.00	1.90	7.400	2.000	0.82	
M_MicaFe-6	1690.0	4.3	1567.00	1.50	7.460	1.700	0.84	
M_MicaFe-7	1640.0	4.1	1585.00	2.40	7.490	1.700	0.70	
M_MicaFe-8	1670.0	4.1	1651.00	2.50	7.830	2.000	0.89	
M_MicaFe-9	1740.0	4.4	1547.00	2.00	7.290	1.700	0.87	
M_MicaMg-1	1250.0	22.0	154.60	1.90	1.852	0.830	0.33	***Primary reference***
M_MicaMg-10	1050.0	18.0	155.30	1.40	1.859	0.810	0.18	
M_MicaMg-11	1090.0	19.0	154.70	1.50	1.853	0.890	0.04	
M_MicaMg-12	1130.0	19.0	156.30	1.60	1.861	0.670	0.37	
M_MicaMg-2	1330.0	22.0	155.20	1.80	1.860	1.200	0.45	
M_MicaMg-3	1130.0	19.0	155.60	1.30	1.867	0.890	0.35	
M_MicaMg-4	1070.0	19.0	154.30	1.40	1.846	0.730	0.16	
M_MicaMg-5	1070.0	18.0	156.40	1.60	1.856	0.840	0.25	
M_MicaMg-6	1100.0	19.0	154.70	1.60	1.863	0.780	0.45	
M_MicaMg-7	1050.0	18.0	155.60	1.70	1.851	0.840	0.32	
M_MicaMg-8	1070.0	18.0	155.20	1.50	1.863	0.760	0.16	
M_MicaMg-9	1120.0	19.0	155.40	1.60	1.854	0.790	0.28	
G_610-1	426.0	520.0	2.17	0.87	0.713	0.530	0.50	***Dispersion assessment***
G_610-10	428.0	520.0	2.13	0.85	0.710	0.520	0.45	
G_610-11	424.0	510.0	2.17	0.95	0.714	0.510	0.60	
G_610-12	426.0	520.0	2.16	0.90	0.714	0.560	0.61	
G_610-2	426.0	520.0	2.06	0.95	0.708	0.640	0.43	
G_610-3	425.0	510.0	2.12	0.82	0.710	0.640	0.51	
G_610-4	427.0	520.0	2.15	0.94	0.708	0.640	0.38	
G_610-5	425.0	510.0	2.15	0.86	0.707	0.540	0.56	
G_610-6	425.0	510.0	2.16	0.84	0.709	0.530	0.53	
G_610-7	427.0	520.0	2.15	0.88	0.712	0.570	0.52	
G_610-8	426.0	520.0	2.14	0.92	0.711	0.530	0.41	
G_610-9	425.0	510.0	2.13	0.89	0.711	0.530	0.58	
G_BCR2G-1	37.2	240.0	0.38	0.90	0.708	0.500	0.48	
G_BCR2G-10	37.1	240.0	0.37	1.20	0.710	0.590	0.87	
G_BCR2G-11	38.0	240.0	0.38	1.10	0.707	0.650	0.53	
G_BCR2G-12	38.9	250.0	0.38	1.00	0.707	0.650	0.87	
G_BCR2G-2	36.3	220.0	0.38	1.10	0.704	0.660	0.47	
G_BCR2G-3	34.8	220.0	0.38	1.10	0.703	0.660	0.59	
G_BCR2G-4	33.8	210.0	0.39	1.00	0.707	0.590	0.27	
G_BCR2G-5	35.1	220.0	0.38	1.20	0.707	0.530	0.33	
G_BCR2G-6	36.6	240.0	0.38	1.10	0.705	0.690	0.85	
G_BCR2G-7	35.6	220.0	0.38	1.10	0.706	0.580	0.59	
G_BCR2G-8	37.2	230.0	0.37	1.10	0.705	0.720	0.74	
G_BCR2G-9	38.5	250.0	0.37	0.97	0.708	0.630	0.90	

Table S4.3. Analytical results for white mica total fusion and step heating $^{40}Ar/^{39}Ar$ geochronology for samples from the Mt Ochi veins, southern Evia (Greece).

				Corrected unknown values																Blank values									
	Sample	Grain	Age (Ma)	±1σ	^{40}Ar (fA)	±1σ	^{39}Ar (fA)	±1σ	^{38}Ar (fA)	±1σ	^{37}Ar (fA)	±1σ	^{36}Ar (fA)	±1σ	Ca/K	±1σ	Cl/K	±1σ	%^{40}Ar*	$^{40}Ar^*/^{39}Ar_K$	±1σ	^{40}Ar (fA)	±1σ	^{39}Ar (fA)	±1σ	^{38}Ar (fA)	±1σ	^{37}Ar (fA)	±1σ	^{36}Ar (fA)	±1σ	J	±1σ
	Total Fusion																															
phengite	**EV19-15D V_3; J: 0.0117042 ± 0.0000968**																															
		Grain 1	22.44	0.06	79.097	0.071	64.380	0.048	0.797	0.015	0.017	0.014	0.036	0.001	0.008	0.007	0.001	0.001	85.868	1.054	0.003	0.537	0.022	0.128	0.009	0.041	0.011	0.032	0.010	0.012	0.000	0.011704	9.677E-05
		Grain 2	22.69	0.09	35.508	0.044	29.093	0.022	0.367	0.014	-0.005	0.014	0.014	0.000	-0.006	0.015	0.002	0.001	87.421	1.066	0.004	0.583	0.025	0.152	0.009	0.028	0.010	0.056	0.010	0.012	0.000	0.011704	9.677E-05
		Grain 3	22.03	0.19	21.191	0.033	15.575	0.016	0.205	0.016	0.020	0.014	0.017	0.000	0.039	0.028	0.003	0.003	76.088	1.034	0.009	0.574	0.022	0.133	0.009	0.035	0.012	0.049	0.010	0.011	0.000	0.011704	9.677E-05
		Grain 4	21.39	0.22	14.800	0.034	12.349	0.015	0.133	0.016	-0.009	0.014	0.008	0.000	-0.022	0.034	-0.004	0.004	83.874	1.004	0.010	0.550	0.025	0.123	0.010	0.055	0.011	0.057	0.010	0.011	0.000	0.011704	9.677E-05
		Grain 5	23.03	0.08	61.831	0.067	48.132	0.049	0.596	0.015	-0.008	0.014	0.032	0.001	-0.006	0.009	0.001	0.001	84.290	1.082	0.004	0.610	0.025	0.146	0.009	0.041	0.010	0.051	0.010	0.011	0.000	0.011704	9.677E-05
		Grain 6	22.57	0.15	23.484	0.033	17.767	0.018	0.218	0.016	-0.011	0.013	0.015	0.000	-0.020	0.023	0.000	0.003	80.269	1.060	0.007	0.567	0.022	0.155	0.009	0.047	0.011	0.055	0.010	0.011	0.000	0.011704	9.677E-05
		Grain 7	21.59	0.14	23.856	0.034	19.877	0.018	0.271	0.014	-0.010	0.014	0.012	0.000	-0.016	0.022	0.005	0.002	84.560	1.014	0.007	0.577	0.022	0.124	0.008	0.040	0.010	0.057	0.010	0.011	0.000	0.011704	9.677E-05
		Grain 8	21.57	0.07	51.514	0.051	46.023	0.042	0.582	0.015	0.011	0.014	0.015	0.000	0.007	0.010	0.002	0.001	90.553	1.013	0.003	0.516	0.024	0.151	0.010	0.032	0.010	0.038	0.009	0.011	0.000	0.011704	9.677E-05
	EV19-15C V_3; J: 0.0117042 ± 0.0000968																															
		Grain 1	22.50	0.11	94.700	0.107	54.765	0.059	0.686	0.015	0.016	0.015	0.123	0.001	0.009	0.008	0.000	0.001	61.180	1.057	0.005	0.530	0.024	0.150	0.009	0.054	0.010	0.043	0.011	0.011	0.000	0.011704	9.677E-05
		Grain 2	22.91	0.08	112.835	0.158	81.902	0.119	1.053	0.016	0.008	0.015	0.081	0.001	0.003	0.006	0.002	0.001	78.189	1.076	0.004	0.666	0.024	0.166	0.011	0.045	0.011	0.047	0.010	0.012	0.000	0.011704	9.677E-05
		Grain 3	22.47	0.07	141.978	0.196	111.409	0.157	1.438	0.016	0.043	0.013	0.080	0.001	0.012	0.004	0.002	0.000	82.898	1.055	0.003	0.551	0.022	0.163	0.009	0.025	0.011	0.049	0.010	0.014	0.000	0.011704	9.677E-05
		Grain 4	22.09	0.21	45.264	0.038	23.244	0.020	0.351	0.016	0.002	0.013	0.071	0.001	0.002	0.018	0.007	0.002	53.323	1.037	0.010	0.554	0.022	0.162	0.009	0.032	0.011	0.069	0.009	0.013	0.000	0.011704	9.677E-05
		Grain 5	21.92	0.14	35.448	0.039	25.683	0.019	0.348	0.015	-0.014	0.013	0.030	0.001	-0.017	0.016	0.004	0.002	74.642	1.029	0.007	0.645	0.025	0.205	0.009	0.037	0.010	0.066	0.010	0.013	0.000	0.011704	9.677E-05
		Grain 6	21.68	0.08	42.315	0.042	35.832	0.028	0.483	0.016	0.078	0.013	0.019	0.000	0.067	0.011	0.004	0.001	86.269	1.018	0.004	0.567	0.021	0.144	0.010	0.040	0.011	0.023	0.009	0.013	0.000	0.011704	9.677E-05
		Grain 7	21.49	0.12	35.856	0.039	27.806	0.023	0.360	0.014	0.016	0.014	0.026	0.001	0.018	0.016	0.002	0.001	78.308	1.009	0.006	0.532	0.021	0.147	0.009	0.040	0.010	0.055	0.011	0.012	0.000	0.011704	9.677E-05
	EV19-15C V_{2b}; J: 0.0117973 ± 0.00009677																															
		Grain 1	22.60	0.08	73.021	0.063	55.802	0.048	0.739	0.017	0.009	0.014	0.047	0.001	0.005	0.008	0.003	0.001	80.535	1.053	0.004	0.574	0.021	0.137	0.009	0.028	0.012	0.053	0.010	0.012	0.000	0.011797	9.677E-05
		Grain 2	21.84	0.06	88.813	0.094	74.495	0.076	0.954	0.015	0.018	0.013	0.042	0.001	0.007	0.005	0.002	0.001	85.442	1.018	0.003	0.534	0.024	0.145	0.011	0.036	0.011	0.053	0.008	0.012	0.000	0.011797	9.677E-05
		Grain 3	22.09	0.07	185.596	0.264	143.551	0.199	1.800	0.016	0.045	0.013	0.124	0.001	0.009	0.003	0.001	0.000	79.682	1.029	0.003	0.591	0.023	0.152	0.009	0.033	0.011	0.028	0.010	0.012	0.000	0.011797	9.677E-05
		Grain 4	22.90	0.06	85.386	0.073	69.868	0.054	0.896	0.015	-0.001	0.014	0.035	0.001	-0.001	0.006	0.002	0.001	87.413	1.067	0.003	0.587	0.020	0.142	0.009	0.025	0.011	0.048	0.009	0.011	0.000	0.011797	9.677E-05
		Grain 5	22.78	0.08	62.860	0.049	48.916	0.035	0.650	0.016	-0.041	0.014	0.035	0.001	-0.027	0.009	0.003	0.001	82.700	1.062	0.004	0.493	0.024	0.118	0.010	0.009	0.012	0.081	0.011	0.011	0.000	0.011797	9.677E-05
		Grain 6	22.47	0.06	135.225	0.147	107.980	0.117	1.332	0.016	0.048	0.013	0.072	0.001	0.014	0.004	0.001	0.000	83.673	1.047	0.003	0.544	0.024	0.128	0.008	0.040	0.011	0.029	0.010	0.011	0.000	0.011797	9.677E-05
		Grain 7	22.92	0.08	104.867	0.090	72.551	0.057	0.937	0.015	-0.014	0.013	0.091	0.001	-0.007	0.006	0.002	0.001	73.956	1.068	0.004	1.233	0.022	0.143	0.008	0.005	0.011	0.056	0.010	0.013	0.000	0.011797	9.677E-05
glaucophane	**EV19-15D V_3; J: 0.0117423 ± 0.00009677**																															
		Grain 1	32.00	2.27	4.608	0.031	1.096	0.013	-0.006	0.017	0.229	0.013	0.011	0.000	6.871	0.409	-0.054	0.045	35.664	1.502	0.107	0.477	0.023	0.128	0.009	0.053	0.012	0.022	0.010	0.011	0.000	0.011742	9.686E-05
		Grain 2	34.40	3.54	3.264	0.032	0.698	0.014	-0.001	0.016	0.115	0.014	0.008	0.000	5.438	0.679	-0.046	0.069	34.506	1.616	0.168	0.459	0.023	0.121	0.010	0.037	0.011	0.051	0.010	0.010	0.000	0.011742	9.686E-05
		Grain 3	33.89	1.99	6.500	0.032	1.466	0.013	0.040	0.015	0.290	0.014	0.015	0.000	6.521	0.314	0.039	0.030	35.859	1.592	0.095	0.558	0.020	0.114	0.009	0.023	0.010	0.014	0.009	0.010	0.000	0.011742	9.686E-05
		Grain 4	26.08	0.92	9.077	0.032	3.114	0.012	0.042	0.015	0.337	0.014	0.019	0.000	3.566	0.144	0.002	0.014	41.915	1.222	0.043	0.488	0.020	0.119	0.008	0.042	0.011	0.033	0.010	0.010	0.000	0.011742	9.686E-05
		Grain 5	38.91	2.91	6.133	0.032	1.000	0.013	0.030	0.016	0.317	0.013	0.016	0.000	10.488	0.466	0.044	0.046	29.755	1.830	0.138	0.560	0.022	0.127	0.009	0.043	0.012	0.037	0.010	0.010	0.000	0.011742	9.686E-05
		Grain 6	27.30	0.34	26.819	0.044	11.654	0.017	0.142	0.016	0.327	0.014	0.041	0.001	0.925	0.041	-0.001	0.004	55.640	1.280	0.016	0.546	0.020	0.118	0.008	0.046	0.011	0.046	0.010	0.010	0.000	0.011742	9.686E-05
		Grain 7	30.94	0.90	14.905	0.037	3.702	0.013	0.044	0.016	0.561	0.014	0.035	0.001	5.010	0.129	-0.005	0.012	36.026	1.451	0.042	0.484	0.023	0.117	0.009	0.040	0.012	0.050	0.010	0.010	0.000	0.011742	9.686E-05
		Grain 8	28.69	1.17	10.129	0.031	2.848	0.013	0.069	0.016	0.430	0.013	0.023	0.001	5.016	0.159	0.031	0.016	37.798	1.345	0.055	0.503	0.021	0.126	0.008	0.025	0.011	0.052	0.009	0.010	0.000	0.011742	9.686E-05
	EV19-15C V_3; J: 0.0116148 ± 0.00009677																															
		Grain 1	30.11	9.43	1.520	0.032	0.264	0.012	-0.007	0.015	0.074	0.013	0.004	0.000	9.337	1.730	-0.122	0.167	24.705	1.428	0.451	1.066	0.022	0.121	0.008	0.045	0.011	0.019	0.009	0.013	0.000	0.011615	9.686E-05
		Grain 2	25.36	5.08	2.925	0.032	0.489	0.014	-0.018	0.016	0.170	0.014	0.009	0.000	11.598	1.044	-0.150	0.095	20.006	1.201	0.242	0.456	0.023	0.119	0.010	0.046	0.012	0.046	0.010	0.010	0.000	0.011615	9.686E-05
		Grain 3	20.28	36.88	0.837	0.029	0.058	0.013	0.025	0.016	0.021	0.014	0.003	0.000	12.279	8.575	1.198	0.851	6.656	0.959	1.754	0.514	0.021	0.123	0.009	0.021	0.011	0.050	0.011	0.010	0.000	0.011615	9.686E-05
		Grain 4	43.75	12.98	1.268	0.031	0.193	0.013	0.034	0.015	0.041	0.014	0.003	0.000	7.179	2.476	0.467	0.228	31.568	2.083	0.625	0.506	0.022	0.098	0.009	0.029	0.009	0.052	0.010	0.010	0.000	0.011615	9.686E-05
		Grain 5	25.90	2.55	2.610	0.032	0.976	0.013	0.003	0.015	0.086	0.013	0.005	0.000	2.929	0.458	-0.028	0.046	45.861	1.227	0.122	0.556	0.021	0.131	0.009	0.047	0.010	0.034	0.009	0.011	0.000	0.011615	9.686E-05
		Grain 6	37.76	9.51	1.146	0.033	0.236	0.013	0.029	0.014	0.055	0.014	0.003	0.000	7.884	2.017	0.314	0.172	36.802	1.795	0.457	0.540	0.022	0.122	0.009	0.019	0.010	0.032	0.010	0.010	0.000	0.011615	9.686E-05
		Grain 7	29.89	6.86	0.867	0.033	0.354	0.013	0.035	0.016	0.053	0.014	0.001	0.000	4.978	1.373	0.251	0.130	57.842	1.417	0.328	0.734	0.022	0.123	0.009	0.028	0.011	0.061	0.009	0.011	0.000	0.011615	9.686E-05
		Grain 8	21.65	0.47	13.676	0.030	6.505	0.014	0.059	0.015	0.339	0.014	0.025	0.000	1.745	0.073	-0.010	0.007	48.755	1.025	0.022	0.563	0.021	0.120	0.008	0.036	0.011	0.021	0.010	0.011	0.000	0.011615	9.686E-05
	EV19-15C V_{2b}; J: 0.0117972 ± 0.00009677																															
		Grain 1	68.37	6.16	6.572	0.034	0.520	0.013	0.007	0.016	0.106	0.014	0.017	0.000	6.475	0.861	-0.011	0.087	25.490	3.226	0.296	0.579	0.025	0.135	0.009	0.049	0.011	0.026	0.009	0.012	0.000	0.011797	9.677E-05
		Grain 2	27.89	11.94	1.875	0.032	0.215	0.014	-0.020	0.015	0.086	0.013	0.006	0.000	12.622	2.110	-0.323	0.208	14.905	1.301	0.561	0.553	0.023	0.114	0.010	0.028	0.010	0.017	0.009	0.011	0.000	0.011797	9.677E-05
		Grain 3	30.43	1.38	8.875	0.031	2.125	0.013	0.016	0.017	0.361	0.014	0.021	0.000	5.395	0.207	-0.019	0.023	33.978	1.421	0.065	0.544	0.020	0.127	0.009	0.045	0.012	0.030	0.009	0.011	0.000	0.011797	9.677E-05
		Grain 4	52.35	10.62	3.096	0.032	0.249	0.013	0.034	0.015	0.133	0.013	0.009	0.000	17.008	1.950	0.350	0.183	19.656	2.459	0.506	0.481	0.020	0.122	0.009	0.004	0.011	0.061	0.009	0.011	0.000	0.011797	9.677E-05
		Grain 5	23.72	4.63	2.184	0.029	0.506	0.013	0.022	0.016	0.120	0.013	0.006	0.000	7.537	0.825	0.087	0.095	25.578	1.105	0.217	0.516	0.021	0.118	0.010	0.031	0.012	0.057	0.010	0.011	0.000	0.011797	9.677E-05
		Grain 6	-206.65	416.86	-0.026	0.034	-0.009	0.013	0.015	0.016	-0.006	0.014	0.000	0.000	23.179	62.775	-4.994	9.043	-307.823	-9.049	17.243	0.534	0.023	0.120	0.010	0.015	0.011	0.052	0.011	0.010	0.000	0.011797	9.677E-05
		Grain 7	142.78	171.21	-0.019	0.033	0.016	0.013	-0.028	0.015	0.010	0.013	0.000	0.000	21.900	33.737	-5.235	5.310	-562.657	6.876	8.571	0.484	0.024	0.114	0.010	0.045	0.010	0.031	0.010	0.010	0.000	0.011797	9.677E-05
		Grain 8	-255.69	241.20	1.097	0.034	0.018	0.011	-0.014	0.016	0.024	0.014	0.004	0.000	44.573	39.579	-2.461	3.043	-17.692	-11.050	9.713	0.477	0.023	0.135	0.008	0.040	0.011	0.043	0.010	0.009	0.000	0.011797	9.677E-05
		Grain 9	18.40	10.45	1.965	0.032	0.235	0.012	0.001	0.016	0.130	0.015	0.007	0.000	17.909	2.282	-0.031	0.193	10.194	0.856	0.489	0.616	0.022	0.098	0.009	0.036	0.011	0.042	0.010	0.010	0.000	0.011797	9.677E-05
	EV19-15C Groundmass; J: 0.0117423 ± 0.00009677																															
		Grain 1	12.38	13.29	0.928	0.034	0.168	0.012	-0.009	0.015	0.077	0.015	0.003	0.000	14.991	3.041	-0.192	0.269	10.392	0.578	0.62270666	0.527	0.024	0.122	0.009	0.031	0.011	0.042	0.010	0.010	0.000	0.011742	9.686E-05
		Grain 2	23.19	1.38	9.129	0.031	2.188	0.013	0.007	0.014	0.150	0.015	0.023	0.000	2.217	0.216	-0.031	0.018	26.024	1.086	0.0649833	0.548	0.022	0.113	0.009	0.040	0.009	0.051	0.010	0.011	0.000	0.011742	9.686E-05
		Grain 3	27.53	4.03	3.052	0.032	0.616	0.012	0.012	0.016	0.277	0.012	0.009	0.000	14.712	0.717	0.015	0.075	25.927	1.290	0.1901958	0.552	0.022	0.122	0.009	0.027	0.011	0.045	0.009	0.010	0.000	0.011742	9.686E-05
		Grain 4	16.49	5.09	1.583	0.033	0.452	0.013	0.023	0.015	0.087	0.013	0.005	0.000	6.284	0.951	0.109	0.095	21.945	0.770	0.23915397	0.504	0.025	0.117	0.008	0.026	0.009	0.056	0.009	0.010	0.000	0.011742	9.686E-05
		Grain 5	20.88	1.89	12.187	0.034	1.810	0.014	0.034	0.017	0.150	0.013	0.036	0.001	2.709	0.229	0.009	0.027	14.512	0.977	0.08915502	0.470	0.022	0.120	0.010	0.032	0.012	0.044	0.009	0.010	0.000	0.011742	9.686E-05
		Grain 6	19.63	0.78	11.416	0.031	3.738	0.013	0.054	0.016	0.189	0.013	0.028	0.000	1.658	0.114	0.003	0.013	30.077	0.918	0.03661091	0.562	0.023	0.125	0.009	0.040	0.012	0.050	0.009	0.010	0.000	0.011742	9.686E-05
		Grain 7	27.68	6.57	3.690	0.032	0.446	0.012	0.005	0.016	0.136	0.014	0.011	0.000	10.013	1.037	-0.013	0.102	15.638	1.298	0.31036512	0.485	0.020	0.132	0.010	0.032	0.010	0.026	0.009	0.010	0.000	0.011742	9.686E-05
		Grain 8	24.51	15.90	1.490	0.033	0.149	0.014	0.012	0.015	0.054	0.014	0.005	0.000	12.095	3.270	0.178	0.303	11.411	1.148	0.750	0.478	0.022	0.112	0.010	0.044	0.011	0.045	0.009	0.010	0.000	0.011742	9.686E-05
	Step Heating Experiments																															
Power	**Phengite**				*Plateau age: 22.6 ± 0.2 Ma (MSWD: 1.49)*				*Integrated age: 22.6 ± 0.2 Ma (MSWD: 0.23)*																									
0.2		*Step A*	-272.70	485.98	0.103	0.033	-0.009	0.013	0.024	0.015	0.000	0.014	0.000	0.000	-1.029	62.079	-7.539	11.501	108.484	-11.835	19.559	0.472	0.024	0.116	0.008	0.014	0.011	0.057	0.009	0.010	0.000	0.011700	5.511E-05
0.5		*Step B*	9.26	13.51	0.980	0.034	0.165	0.013	-0.012	0.014	-0.007	0.013	0.003	0.000	-1.810	3.304	-0.261	0.253	7.308	0.434	0.634	0.523	0.022	0.123	0.009	0.057	0.009	0.056	0.009	0.010	0.000	0.011700	5.511E-05
1.0		*Step C†*	22.91	2.25	2.527	0.032	1.045	0.014	-0.007	0.016	-0.008	0.015	0.005	0.000	-0.337	0.602	-0.055	0.043	44.569	1.077	0.106	0.467	0.025	0.103	0.010	0.041	0.011	0.041	0.010	0.009	0.000	0.011700	5.511E-05
1.5		*Step D†*	22.39	0.26	11.490	0.031	9.688	0.015	0.104	0.016	-0.023	0.014	0.004	0.000	-0.099	0.060	-0.004	0.005	88.819	1.052	0.012	0.470	0.021	0.093	0.011	0.033	0.012	0.069	0.009	0.010	0.000	0.011700	5.511E-05
1.8		*Step E†*	22.40	0.27	9.640	0.034	8.358	0.013	0.106	0.016	-0.010	0.014	0.003	0.000	-0.053	0.070	0.002	0.006	91.366	1.053	0.013	0.442	0.023	0.117	0.008	0.036	0.011	0.035	0.009	0.010	0.000	0.011700	5.511E-05
2.0		*Step F†*	22.33	0.13	19.470	0.033	17.721	0.015	0.231	0.015	0.018	0.013	0.003	0.000	0.043	0.032	0.003	0.002	95.614	1.049	0.006	0.466	0.020	0.128	0.008	0.033	0.011	0.036	0.009	0.010	0.000	0.011700	5.511E-05
2.5		*Step G†*	22.34	0.49	4.655	0.029	4.165	0.012	0.044	0.015	-0.003	0.014	0.001	0.000	-0.035	0.143	-0.004	0.011	94.040	1.050	0.023	0.523	0.018	0.101	0.008	0.030	0.010	0.047	0.009	0.010	0.000	0.011700	5.511E-05
3.0		*Step H†*	25.00	4.64	0.581	0.030	0.487	0.013	-0.017	0.015	-0.014	0.014	0.000	0.000	-1.244	1.173	-0.139	0.091	98.731	1.176	0.220	0.483	0.021	0.123	0.010	0.048	0.011	0.048	0.010	0.010	0.000	0.011700	5.511E-05
5.0		*Step I†*	22.17	3.59	0.729	0.032	0.577	0.013	-0.022	0.016	-0.026	0.013	0.000	0.000	-1.871	0.980	-0.147	0.079	82.709	1.042	0.170	0.440	0.024	0.129	0.009	0.056	0.011	0.058	0.010	0.010	0.000	0.011700	5.511E-05
	Glaucophane				*Plateau age: n/a*				*Integrated age: 15.2 ± 0.9 Ma (MSWD: 51)*																								
1.0		*Step A*	19.89	2.05	19.438	0.032	2.274	0.013	0.060	0.015	0.043	0.013	0.059	0.001	0.782	0.242	0.027	0.019	10.931	0.934	0.097	0.536	0.023	0.112	0.009	0.040	0.011	0.028	0.010	0.010	0.000	0.011695	5.506E-05
2.0		*Step B*	21.51	0.74	13.412	0.037	4.151	0.013	0.066	0.014	0.092	0.014	0.032	0.000	0.917	0.138	0.007	0.010	31.300	1.011	0.035	0.524	0.022	0.112	0.009	0.038	0.010	0.048	0.010	0.010	0.000	0.011695	5.506E-05
2.5		*Step C*	9.00	1.27	5.363	0.034	2.072	0.014	0.045	0.015	0.182	0.013	0.016	0.000	3.651	0.264	0.025	0.021	16.272	0.421	0.060	0.497	0.023	0.114	0.010	0.046	0.010	0.040	0.010	0.011	0.000	0.011695	5.506E-05
3.0		*Step D*	-1.55	2.11	1.580	0.050	1.652	0.014	0.049	0.015	0.354	0.014	0.008	0.001	8.912	0.369	0.050	0.027	-7.571	-0.073	0.098	3.954	0.021	0.126	0.010	0.038	0.010	0.040	0.010	0.023	0.000	0.011695	5.506E-05
3.1		*Step E*	-0.32	1.59	5.614	0.032	1.827	0.014	0.065	0.015	0.364	0.014	0.021	0.000	8.294	0.322	0.063	0.023	-0.492	-0.015	0.074	0.570	0.021	0.140	0.009	0.036	0.011	0.053	0.010	0.012	0.000	0.011695	5.506E-05
3.3		*Step F*	5.23	1.84	4.819	0.033	1.614	0.014	0.039	0.017	0.328	0.014	0.017	0.000	8.457	0.371	0.030	0.030	8.167	0.244	0.086	0.537	0.023	0.136	0.009	0.042	0.011	0.047	0.010	0.012	0.000	0.011695	5.506E-05
3.5		*Step G*	4.31	2.06	4.614	0.032	1.384	0.014	0.062	0.016	0.321	0.014	0.016	0.000	9.683	0.439	0.089	0.034	6.029	0.201	0.096	0.531	0.023	0.125	0.009	0.027	0.011	0.045	0.009	0.010	0.000	0.011695	5.506E-05
4.0		*Step H*	7.23	1.60	6.714	0.033	1.852	0.015	0.064	0.015	0.451	0.015	0.023	0.000	10.169	0.339	0.060	0.023	9.308	0.338	0.075	0.604	0.022	0.138	0.009	0.041	0.010	0.074	0.009	0.012	0.000	0.011695	5.506E-05
6.2		*Step I*	23.54	0.92	9.410	0.033	3.493	0.015	0.055	0.016	0.644	0.014	0.022	0.000	7.689	0.166	0.008	0.013	41.000